Impedance-Based Analysis of the Cellular Response to Microparticles: Theory, Assay Development and Model Study

DISSERTATION ZUR ERLANGUNG DES DOKTORGRADES DER NATURWISSENSCHAFTEN (DR. RER. NAT.) DER FAKULTÄT CHEMIE UND PHARMAZIE

DER UNIVERSITÄT REGENSBURG

vorgelegt von

Michaela Sperber

aus Regensburg

im Jahr 2015

Die vorliegende Arbeit wurde in der Zeit von Dezember 2010 bis Dezember 2015 unter der Gesamtleitung von Prof. Dr. Joachim Wegener am Lehrstuhl für Analytische Chemie, Chemo- und Biosensorik der Universität Regensburg angefertigt.

Prüfungsgesuch eingereicht am: 22. Dezember 2015

Tag der mündlichen Prüfung: 19. Februar 2016

Prüfungsausschuss:

Vorsitzender: PD Dr. Sabine Amslinger

Prof. Dr. Joachim Wegener

Prof. Dr. Antje J. Bäumner

PD Dr. Miriam Breunig

Für meine Familie und Wolfgang

”Ich habe keine besondere Begabung,

sondern bin nur leidenschaftlich neugierig.“

Albert Einstein

OUTLINE

OUTLINE

1 Label-Free Cell-Based Biosensors

In former times, living animals were used to detect dangerous gases e.g. canaries were taken into coal mines since 1911 to alert the coal miners about an increase in carbon monoxide or methane concentrations. Canaries are able to detect lower concentrations of toxic gases compared to humans. Their signal – termination of their loud chirp and falling down from their perch – clearly indicated the workers a high toxic gas concentration at the ground and initiated the workers to exit quickly the coal mines. Finally, modern portable electronic gas sensors were favored over the canaries and replaced the birds to detect harmful gases in mines [a].

Today, a huge variety of different biosensors are known, which are applied to detect environmental pollutants [1, 2], for agricultural monitoring [3, 4], for medical analysis [5, 6], to control food quality and safety [7, 8] or in drug development [9, 10] (**Fig. 1.1 A**).

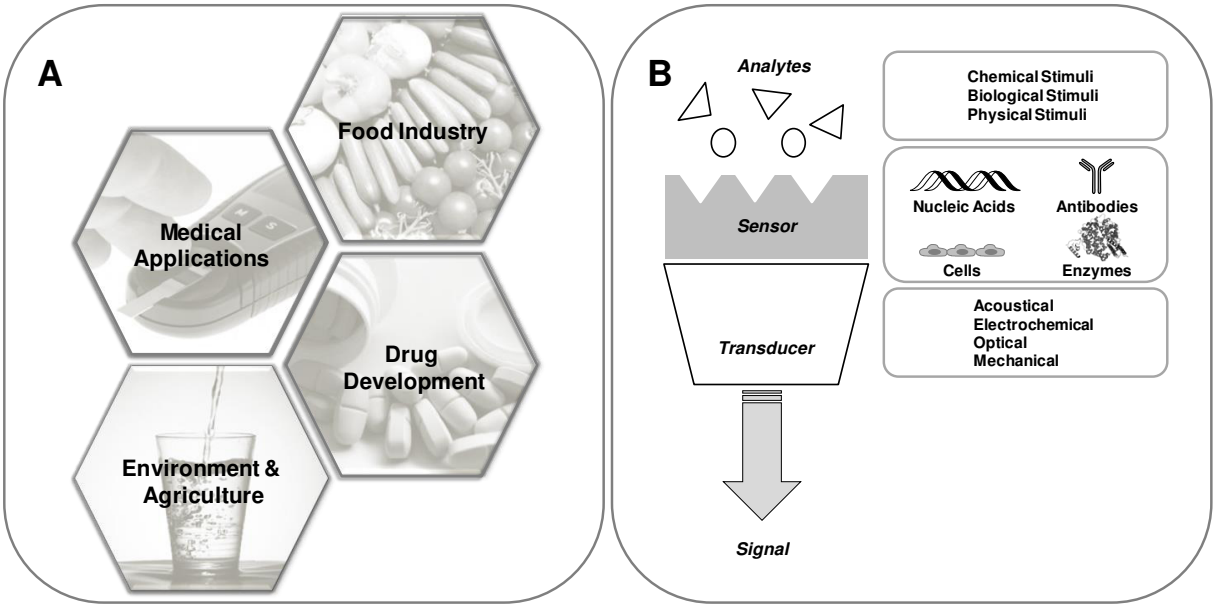

Fig. 1.1: A: Applications of biosensors in daily life. **B:** Schematic principle of a biosensor: A sensoric device is connected to a transducer which converts the response of the biological sensor to a specific analyte into a measureable parameter e.g. voltage or current. In biosensoric applications the sensoric device consists of a biological element like nucleic acids, antibodies, enzymes or even whole cells or tissues.

[a] http://news.bbc.co.uk/onthisday/hi/dates/stories/december/30/newsid_2547000/2547587.stm

Development of biosensors is a promising part of research in the field of analytical biology. Therefore, biosensors were rapidly established and combined with modern principles like nanotechnology [11] or biomimetic approaches [12], especially molecularly imprinted polymers to generate e.g. artificial receptors or antibodies [13]. The term biosensor describes the assembly of a biological sensoric device, like enzymes, antibodies or even whole cells, connected to a transducer, which later provides bioanalytical information after detecting a specific analyte (**Fig. 1.1 B**). If the biological sensing device consists of living cells - accordingly the biosensor belongs to the group of cell-based biosensors - the biological response of cells after exposure to a certain analyte is converted via a transducer into an electrical, acoustical, optical or mechanical signal.

A huge variety of proliferating cell lines originating from different tissues and species are commercially available in cell culture collections, like *American Type Culture Collection* (ATCC) or *Deutsche Sammlung von Mikroorganismen und Zellkulturen GmbH* (DSMZ). Beyond the established cell lines, genetic modifications allow to develop cells which over-express e.g. a specific target receptor, ion channel or reporter gene. Cell-based biosensors are regarded as an intermediate between complex testing in living animals and simple molecular assay system. Using established cell lines or genetically modified cells as recognition elements in the cell-based assays, allows an analysis of enzymes, receptors or ion channels in their natural environment without extracting material from living cells. Therefore, they allow to analyze the response of living cells to the addition of a certain analyte in a physiological environment [14].

Cell-based biosensors provide a high selectivity as well as rapid responses to physical, or chemical stimuli [15, 16]. Advantageously, they offer a cheap sensing device [14] and a longer life time compared to enzymatic sensors however, they are limited to the life time of the cells. An ECIS-based toxicity sensor was developed for the US Army in which rainbow trout gill epithelial (RTgill-W) cells are used to detect chemical contamination of drinking water [17]. The fluidic ECIS sensing chip with an established monolayer of RTgill-W cells could be stored at 6 °C for up to 78 weeks without any impact on cell viability [18].

As living cells are immobilized to the surface of the transducer and serve as sensing element, natural environmental conditions are necessary to perform analysis with whole cell biosensors [19]. Therefore, cells have to grow on the transducer surface [20-22] and require special surface characteristics regarding roughness and hydrophilicity [14].

1.1 Biosensors for Analysis of Cell Metabolism and Cell Morphology

Ion-selective field-effect transistors (ISFET) and *light addressable potentiometric sensors* (LAPS) provide label-free techniques which are suitable to detect and analyze the metabolism of living cells. These promising approaches can analyze changes in pH value or other specific ion concentrations and are both based on the semiconductor technology. Small changes in cell morphology after addition of a certain analyte can be observed either using an optical approach like *surface plasmon resonance* (SPR), a mechanical biosensing technique like *quartz crystal microbalance* (QCM) or an electrochemical biosensor based on impedance spectroscopy like *electric cell-substrate impedance sensing* (ECIS). In the following, these different label-free cell-based biosensor techniques (**Fig. 1.2**) are characterized regarding their ability to detect changes in the metabolism of cells (**A, B**) or to analyze cellular responses after recognition of an analyte resulting in cell morphology alterations (**C** – **E**).

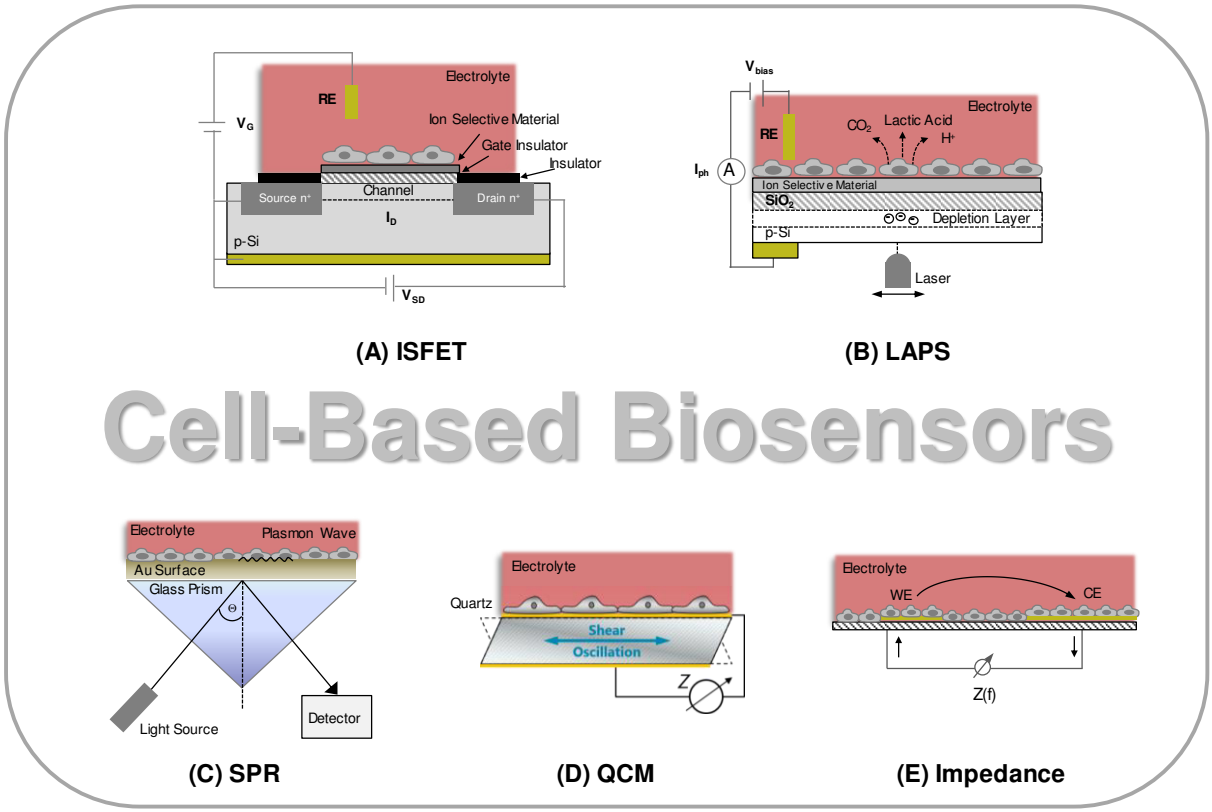

Fig. 1.2: Survey of different whole-cell based biosensors. Schematic illustration of two metabolic cell-based biosensors: ISFET (**A**) and LAPS (**B**) which are both based on the semiconductor technology. **C** – **E** illustrate cell-based biosensors to monitor surface coverage and changes in cell morphology using an optical (**C**), mechanical (**D**) or electrochemical approach (**E**). SPR (**C**) detects changes in refractive index near the gold surface, whereas QCM (**D**) is applicable to monitor changes in mass loading and viscoelastic properties. Electric impedance spectroscopy (**E**) is sensitive for small changes in cell shape due to the fact that the cells behave like insulating particles and force the current to flow around the cell bodies. V_G: gate voltage, V_{DS}: voltage between drain and source, I_D: drain current, V_{bias}: dc bias voltage, I_{ph}: photocurrent, RE: reference electrode, WE: working electrode, CE: counter electrode. Scheme of QCM principle was kindly provided by M. Oberleitner.

(A) Ion-Selective Field-Effect Transistor (ISFET)

Ion-selective field-effect transistor (ISFET) is one of the most popular electrical biosensors. Bergveld (1970) focused on neurophysiological measurements based on FET technology [23] and later in 1991 Fromherz et al. applied cell-based ISEFTs to detect action potentials of neurons [24].

The general setup of a field-effect transistor consists of a metal gate as well as one source and drain region, separated from each other by a short channel which is covered by the gate insulator. The material of the gate insulator in most cases is SiO_2. In ISFET applications the metal gate is replaced by a reference electrode, an ion-selective membrane and an electrolyte. Optionally, a second layer of Si_3N_4, Al_2O_3 or Ta_2O_5 as a pH sensitive layer is added [25]. In **Fig. 1.2 A** a n-channel ISFET is schematically shown where a n-doped source and n-doped drain was introduced into a p-doped Si chip. By applying a positive gate voltage (V_G) with respect to the p-doped Si chip a carrier-depletion region is created under the gate and electrons are detracted from the substrate into the channel region. If sufficient electrons are induced by V_{TH} (threshold voltage) under the gate an electrically conducting channel between source and drain is generated. By applying a voltage between drain and source (V_{DS}) current can ancillary flow via the mobile electrons through this n-channel. The detectable current flow I_D in ISFET biosensors is influenced by the presence of charged biomolecules, pH values or other ions on the sensor surface and is recorded as a function of V_G [26]. During cellular metabolism acidic products are generated like CO_2, H^+ and lactic acid that induce a change in pH value of the cellular environment which can be monitored by ISFET [27]. They change V_G and therefore, increase or decrease the depletion zone, which leads to a change in current flow. Accordingly, ISFETs can be applied to monitor changes in charge densities and a variety of different biological samples including enzymes [28], DNA [29] or cells [30] are successfully applied as bio-recognition element to enhance sensitivity and specificity of the biosensoric device. In the following the introduction will only focus on cell-based ISFETs - living cells are used as recognition element - which seem to be a promising technology for pharmacological and biomedical applications [31]. Applications of cell-based ISFETs mainly focus on measuring extracellular acidification as protons are known to be an important regulator in living cells [21]. Due to the fact that living cells respond with activation or inactivation of several, different pathways after the addition of external stimuli, the development of ISFET based sensors focus on non-invasive detection of multiple parameters [25]. One example of online and non-invasive recording of different parameters was published by Baumann et al. (1999) using a so-called *cell monitoring system* (CMS) [32]. Lehmann et al. (2001) measured the acidification and respiration of adherent cells in real-time using an

ISFET based sensor [33]. Another important application of ISFETs is to detect extracellular and intracellular potentials in electrogenic cells like neurons [24, 34] or cardiac myocytes [35, 36].

(B) Light Addressable Potentiometric Sensor (LAPS)

A second potentiometric semiconductor device, which is commonly used as cell-based biosensor, is the *light addressable potentiometric sensor* (LAPS). It was first described in 1988 by Hafeman et al. [37] and further improved in the following years to achieve better sensitivity, stability as well as biocompatibility. LAPS enables to monitor any event which influences the surface potential, like changes of ion concentrations [38], redox effects [39] and especially in cell-based approaches extracellular acidification and changes in pH value of living cells caused by cellular metabolism [27].

The setup consists of an electrolyte-insulator-semiconductor (EIS) structure e.g. $Si/SiO_2/Si_3N_4$ in contact with an electrolyte containing buffer, an additional reference electrode on the side of the insulator surface and an ohmic contact on the back side. The additional layer of Si_3N_4 is introduced into the LAPS device due to the higher sensitivity towards H^+. In contrast to ISFET, where the entire insulating layer serves as sensing surface, the sensing spots in the LAPS device are defined by illumination with a modulated light source [40]. By applying an external dc bias voltage (V_{bias}) a depletion layer is generated under the gate insulator. When the modulated light source, with appropriate photon energy, illuminates single spots of the LAPS chip from the backside charge carriers in the semiconductor layer are created [21]. In the depletion layer, electrons further move towards the silicon bulk whereas holes accumulate at the silicon insulator interphase [41]. Accordingly, the detectable photocurrent (I_{ph}) is dependent on V_{bias}, on the local surface potential which is dependent on the ion concentration as well as on the illumination [21]. Changes of pH value or of a specific analyte on the sensing surface can be detected either in constant-voltage or constant-current mode. The first detects the ac photocurrent (I_{ph}) as a function of time and position by using a constant V_{bias} and the second records V_{bias} time-dependently while keeping I_{ph} constant [40]. LAPS is not only applicable to the detection of H^+ but also sensitive to a variety of substances including heavy metal ions [42], alkali and alkaline earth metal ions [43] by modifying the sensor surface and implementing an ion selective membrane.

In conclusion, LAPS as biosensor is applied in many studies regarding cell biology or pharmacology to monitor ligand-receptor interactions and signaling mechanism [44-47], to detect excitable cells like neurons [48, 49], or to study the influence of drugs on cardiomyocytes [50, 51]. Further development of LAPS as biosensor evolve into multi LAPS applications, which allow

simultaneous detection of H^+, Na^+, K^+ and Ca^{2+} by using different sensitive membranes which are introduced at separated areas on a single LAPS surface [52-54].

The remaining methods in the survey (**Fig. 1.2**), *surface plasmon resonance* (SPR), *quartz crystal microbalance* (QCM) and impedance based setups like *electric cell-substrate impedance sensing* (ECIS) are applicable to detect cell morphology changes and changes in sensor surface coverage.

(C) Surface Plasmon Resonance (SPR)

SPR is an optical technique which is widely applied to study bimolecular interactions on the sensor surface. SPR uses the establishment of an evanescent field under total internal reflection of an incident light beam. The generation of an evanescent field excites surface plasmons in the adjacent thin gold layer. The conditions of total internal reflection depend on the wavelength of the polarized light, the angle of incidence and the refractive index near the gold surface. The SPR setup consists of a polarized light source, a high refractive index prism covered with a thin metal layer mostly gold and a CCD chip to detect the reflected light. When resonance conditions are fulfilled surface plasmon waves are generated near the gold surface and the evanescent field can subsequently penetrate into adsorbed material for instance adherent cells on the gold surface. The penetration depth of SPR using visible light is below 200 nm [22].

SPR measurements can be performed by measuring changes in reflectivity, which is the intensity of the reflected light, at a constant angle of incidence (kinetic measurement type) or by detecting the angle of minimum reflectivity (angle scan mode). In cell-based biosensor applications mammalian cells are cultured on top of the gold surface and cellular response to external stimuli can be measured by SPR. Accordingly, SPR offers a label-free technique to monitor changes in cell-substrate interactions, however it is not suitable to detect changes, processes or interactions of materials which occur deeper in the cells. SPR technique was successfully applied to detect cell adhesion on the gold surface [55], changes inside cell morphology [56-58] or cellular responses caused by intracellular signaling [59, 60]. In conclusion, SPR provides a label-free and non-invasive method to detect changes which occur near the sensor surface with a high time resolution.

(D) Quartz Crystal Microbalance (QCM)

QCM is an acoustic technique to study cell-surface interaction and cellular response in a label-free and non-invasive manner. The core component is a piezoelectrical quartz resonator which can be excited to perform mechanical shear oscillations parallel to the crystal surface [22]. The piezoelectric effect was first described by J. and P. Curie in 1880 who monitored electrical polarization e.g. in quartz after applying mechanical stress and detected a voltage which is proportional to the applied stress [61]. The linear relation between the resonance frequency shift of a sensor crystal to the change in mass on the quartz surface was established by Sauerbrey, as long as the material on the quartz surface behaves like a rigid material [62]. A further step towards application of QCM as biosensor was done by Nomura and Okuhara who first performed QCM in liquid environment in 1982 [63]. The basic component of a QCM consists of a thin circular piezoelectric AT-cut α-quartz disk sandwiched between two gold electrodes. One electrode is located on each side of the quartz and allows the application of an external alternating electric field. Due to the piezoelectric properties of the α-quartz any mechanical deformation causes an electrical potential difference at the quartz surface and vice versa [64]. After applying an oscillating potential difference the piezoelectric quartz starts to perform mechanical shear oscillations at the resonator's resonance frequency which is influenced by the adsorbed mass on the sensor surface as well as by changes in viscosity of the liquid [65]. For adherent cells on the quartz surface, which behave like viscoelastic bodies, the linear relation between frequency change and adsorbed mass is no longer valid [66]. Nevertheless, QCM offers the advantage of being non-invasive and provides information about surface-near processes of the cell. For a 5 MHz quartz resonator the decay length of the shear-wave in water is ~ 250 nm at RT [67].

In conclusion, the QCM technique is a powerful label-free technique to monitor the response of adherent cells to chemical, physical and biological stimuli in their environment after adhesion on the quartz surface. Therefore, this technique was successfully applied to detect cell adhesion [68-71], cellular response to different drugs [72, 73], changes in their environment like osmolarity [74] or addition of cytotoxic compounds [75, 76].

(E) Impedance Spectroscopy

Impedance spectroscopy as an electrochemical approach in cell-based biosensors can be realized in different setups. Cells can be cultivated on porous filter membranes, whereas one electrode is located above and one below the cell layer or cells are directly grown on top of the electrodes, which serve as culture substrate for anchorage-dependent cells. The latter principle is the basis of *electric cell-substrate impedance sensing* (ECIS) which was introduced by Giaever and Keese in 1984 [77]. This technique provides a promising tool for studying cell surface interactions and changes in cell morphology by measuring the electrical impedance. The measurement principle will be introduced in more detail later (**chapter 3.3**). In this setup, adherent cells are cultured on two co-planar gold-film electrodes. The cells behave like dielectric particles and the current is forced to flow around and through the cells. Therefore, even small changes in cell shape can be recorded and analyzed with high sensitivity in the impedance signal. To summarize all advantages and limitations of ECIS, it provides a label-free and non-invasive method to detect cellular processes like cell migration and cell vitality or even small micromotion of cells with high time-resolution. The experiment can be performed automatically and up to date 96 different wells can be monitored simultaneously. The electrochemical principle is limited to conducting and electrochemically well-behaved electrode materials like gold or indium tin oxide.

1.2 Biological Phenomena Monitored with Cell-Based Biosensors

Label-free biosensors monitor responses of whole cells to a certain stimulus or to changes in their environment with high time resolution and in a non-invasive way [78]. **Fig. 1.3** shows a survey of different cellular events which can be monitored by whole cell biosensors in a label-free manner.

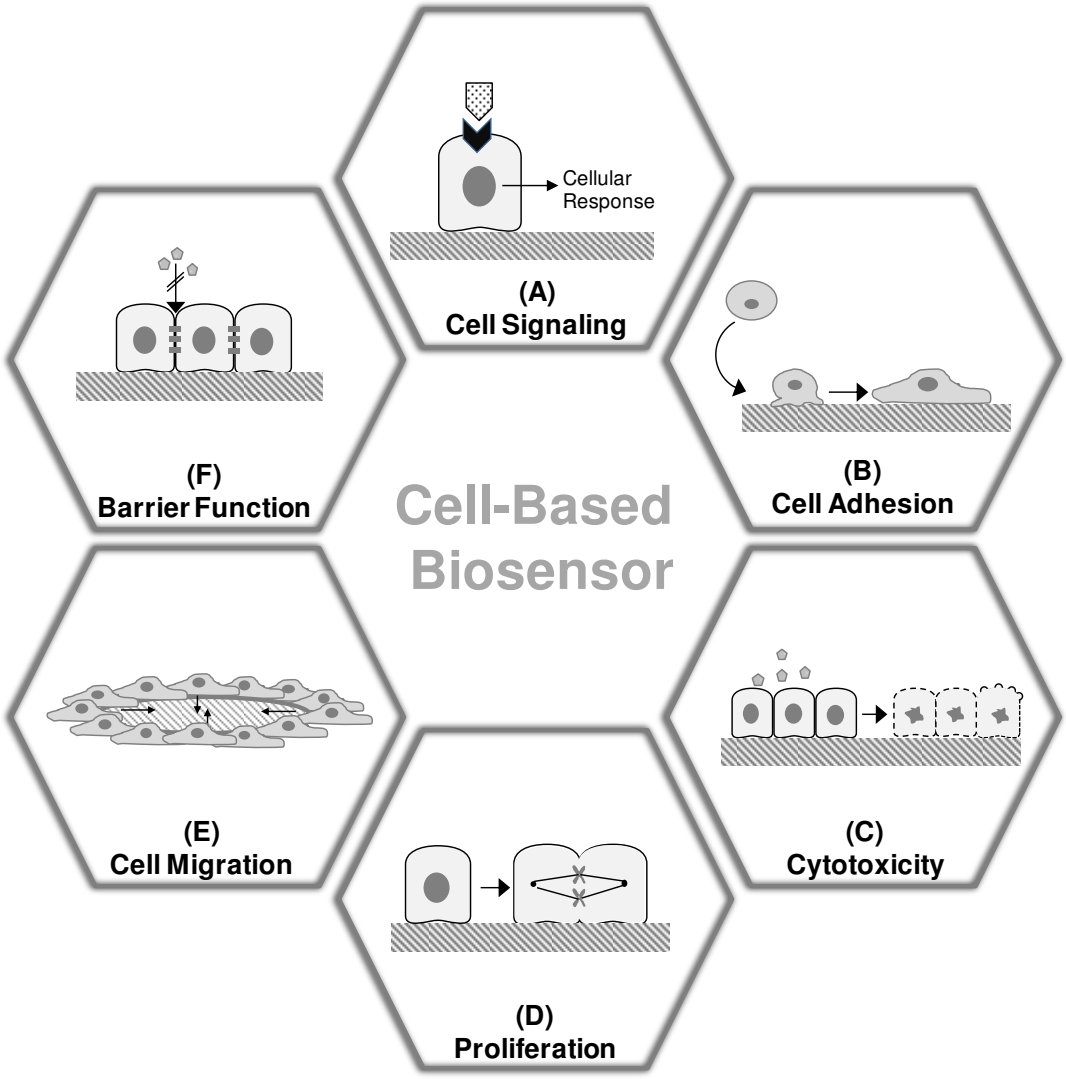

Fig. 1.3: Survey of different biological applications of label-free whole-cell based biosensors: Cell signaling after ligand binding to a membrane-bound receptor which activates cellular cascades subsequently inducing a cellular response (**A**). Monitoring of cell adhesion and cell spreading on the biosensor surface (**B**) or the analysis of cytotoxicity after introducing external stimuli like (nano-) particles or pharmaceutical drugs (**C**). Analysis of cellular proliferation (**D**), collective cell migration (**E**) or the establishment of barrier function between cells hindering substances to diffuse on paracellular pathways (**F**).

Cell-based biosensors can monitor cellular responses after binding of an analyte to a membrane-bound receptor which finally causes a certain cellular response (**A**). Wegener et al. (1999) used a confluent monolayer of *bovine aortic endothelial cells* (BAEC) grown on gold-film electrodes to monitor β-adrenergic stimulation with impedance measurements [79]. Yu

et al. (2006) described a non-invasive and label-free technique based on impedance recordings to study morphological changes due to histamine stimulation of GPCR signaling pathways using H1/CHO cells [80]. Fang et al. (2007) used a *resonant waveguide grating* (RWG) biosensor to record GPCR ligand induced changes in *dynamic mass redistribution* (DMR) of adherent human epidermoid carcinoma cells by ATP or thrombin [81]. Goral et al. (2011) [82] developed a whole-cell based RWG biosensor with microfluidics, which controls the exposure of the agonist, to monitor changes in DMR of A549 cells. Addition of thrombin to A549 cells stimulates protease activated receptor-1 (PAR_1) signaling and subsequent causes pro-inflammatory responses and disruption of endothelial barrier [83].

A second approach of cell-based biosensors is the analysis of cell adhesion and cell spreading on the biosensor surface (**B**) as it is important for cell survival. These studies support our knowledge about the adhesion process which might be necessary for development and optimization of biomaterials e.g. medical applications [22]. Impedimetric biosensors allow to monitor the kinetics of cell attachment in real-time as already demonstrated in 1984 by Giaever and Keese who detected attachment and spreading of fibroblasts on gold-film electrodes by means of the impedance signal [77]. Wegener et al. (2000) demonstrated that impedance recordings are suitable to detect increasing electrode surface coverage with MDCK II cells on different protein coatings in particular by analyzing the capacitance at high frequency [84]. Angstmann et al. (2011) employed a non-invasive impedance-based assay to monitor cell adhesion and cell differentiation of mesenchymal stromal/stem cells which can be a promising tool for therapeutic applications [85]. Holmes et al. (1997) applied SPR technique to study differences in adhesion and binding of *Staphylococcus epidermis* and *Staphylococcus aureus* on fibronectin coated surfaces and found different interactions with fibronectin fragments for both bacteria [86]. Adhesion and spreading of *baby hamster kidney* (*BHK*) cells was monitored using optical waveguide light mode spectroscopy in a study of Hug et al. (2001) [87]. Fang et al. investigated cell attachment and spreading by using a RWG biosensor and analyzed the effect of vincristine - a plant alkaloid which inhibits microtubule assembly and binding to tubulin - on attachment of A431 cells on the sensor surface [88]. QCM is a promising tool to monitor cell attachment on the quartz surface as it is correlated to an decrease in resonance frequency depending on surface coverage [22]. Different groups applied QCM for detecting cell attachment with high time resolution of e.g. MDCK cells and murine 3T3 fibroblasts [69], MKE cells and CHO cells [89] as well as detachment of *African green monkey kidney* cells induced by chemicals or virus infection [90]. Marx et al. utilized QCM to investigate biologically active drugs which alters cellular attachment and spreading by recording the response of adherent cells on the addition of cytoskeleton binding drugs nocodazole and taxol [72].

Further studies address the effect of external stimuli like pharmaceutical drugs, (nano)-particles or cytotoxic agents on anchorage-dependent cells using cell-based biosensors which provide a promising tool in drug development and discovery (**C**). Cell response after the addition of a certain stimulus is characterized by an integrative or holistic signal without any molecular information about the mechanism [78] [91]. Arndt et al. (2004) analyzed the effect of apoptosis induced by cycloheximide on confluent micro-vessel endothelial cells cultured to confluence on gold-film electrodes using impedance analysis [92]. A similar study was performed by Solly et al. (2004), who induced apoptosis in human ovarian cells (A2780) by introducing doxorubicin and detecting cell response by *real-time cell electronic sensing* (RT-CES) technology which is based on impedance recordings [93]. Curtis et al. (2009) used cell-based impedance sensing to detect toxicity of drinking water in a portable automated and long-term stable fluidic device. This setup allows the detection of toxins in drinking water over several months using bovine pulmonary artery endothelial cells or bovine lung microvessel endothelial cells [94]. Liu et al. (2009) used a chip with a micro-electrode array and impedance spectroscopy to detect the chemosensitivity of human oesophageal cancer cell line (KYSE30) after the addition of the anti-cancer drug cisplatin (10 – 50 µM) [95]. The research on nanoparticle synthesis as well as the evaluation of their biological hazards has received considerable attentions over the last years. Therefore, some studies were performed with different nanoscale materials regarding cytotoxicity using cell-based biosensors. Hondroulis et al. (2010) applied the electrical impedance sensing system (EIS) to monitor the cytotoxic time profiles of nanoparticles made of gold and silver as well as single walled carbon nanotubes (SWCNTs) with CCL-153 and RTgill-W1 cells [91]. Tarantola et al. (2011) provided an *in vitro* toxicity study of spherical and rod-like gold nanoparticles using a double biosensor approach of QCM and ECIS which pointed to a higher toxicity of spherical-shaped compared to the rod-shaped nanomaterial [96].

A cell-based biosensor also provides high sensitivity to monitor cell proliferation and thus increasing cell coverage of the sensor surface (**D**). Wodnicka et al. (2000) investigated cell proliferation using a novel fluorescent Oxygen BioSensor technology platform where a continuous real-time detection of dissolved oxygen concentration was realized based on the quenching effect of $Ru(DPP)_3Cl_2$ by oxygen. The oxygen-permeable sensor was placed at the bottom of multi-well plates. A good correlation between cell number and the fluorescence signal was found for prokaryotic and eukaryotic cells [97]. Yun et al. (2010) impedimetrically monitored proliferation of osteoblasts (U2-OS) under different magnesium ion concentrations (0 – 200 mM) using interdigitated electrodes and found a moderate inhibition of cell proliferation in absence of Mg^{2+} and for Mg^{2+}-concentrations above 5 mM [98]. Biosensor applications are not limited to mammalian cells but also applicable for detecting bacterial growth of *Escherichia coli* on the sensing surface by analyzing the shift in resonance

frequency of a micromechanical oscillator [99]. Therefore, it is suitable to perform a rapid antibiotic susceptibility screening [100].

Collective cell migration (**E**) is essential in many biological processes and many assays were developed to further characterize wound healing or cell migration [101]. Beyond many microscopic and optical assays, also some cell-based biosensors are available to monitor migration of adherent cells. The first impedimetric migration study was published in 1997 by Noiri et al. studying the migration of endothelial cells over 20 h after electropermeabilization with direct current (dc) [102]. This was further improved by Keese et al. (2004) who described a highly reproducible approach where a defined wound is created in a confluent cell layer by applying a high voltage pulse to cells on a gold-film electrode followed by real-time monitoring of cellular migration into the wounded area. The authors provided several ECIS recordings to characterize the migratory behavior of different adherent cell lines [103]. Other studies used impedance recording after electrical wounding of adherent cells to investigate the influence of ADAM (*a disintegrin and metalloproteinase*) family enzymes to cellular migration of colonic epithelial cells [104] or to study the impact of EPLIN-α (*epithelial protein lost in neoplasm*) expression on migration of breast cancer cells [105]. Fang et al. (1998) analyzed the migration of human keratinocytes in dc electric fields in terms of the effect of extracellular calcium and growth factors [106] as well as the influence of *epidermal growth factor receptor* (EGFR) kinase activity [107]. Another strategy was used by Wang et al. (2008) who established *self-assembled monolayers* (SAMs) on the electrode surface which inhibit cell adhesion on the surface. After applying a dc pulse to destroy the SAMs, cells start to migrate onto the electrode which is analyzed by impedance recordings and allows a quantitative comparison of migration speed of different cell lines [108].

Label-free biosensors are useful to further study the complexity of cell barrier function (**F**) of e.g. blood-brain barrier or epithelial cell barrier. The most applicable technique to determine and measure the electrical resistance and the permeability of the blood-brain barrier is to impedimetrically monitor the transepithelial electrical resistance (TER) [109]. Hartmann et al. (2007) analyzed the influence of endogenous extracellular matrix (ECM) derived from glia or non-glia cells on cell barrier properties of cerebral endothelial cells which were grown on gold-film electrodes [110]. Seebach et al. (2000) investigated the effect of shear stress on epithelial barrier function upon applying varying laminar fluid shear stresses (0.5 dyn/cm^2 - 50 dyn/cm^2). They used an impedance based setup and found a shear-stress-dependent upregulation of the TER [111]. To further support the understanding of drug development and drug delivery Rempe et al. (2011) used modified nanoparticles which are able to overcome the blood-brain barrier and analyzed their influence on the TER of porcine brain capillary endothelial cells grown on filter inserts [112]. The well-known effect of hydrocortisone on cell

barrier function was analyzed impedimetrically by Weidenfeller et al. (2005) using primary cultured mouse brain endothelial cells adherently grown on gold-film electrodes as well as on permeable filters to determine the TER [113]. A miniaturized impedance biosensor was established by Sun et al. (2010) and measured the disruption of epithelial barrier of a human bronchial epithelial cell line by increasing the concentration of EGTA (*ethylene glycol-bis(2-aminoethyl-ether)-N,N,N',N' tetraacetic acid*) [114]. A dual biosensor surface, consisting of an electrical and an optical biosensor, was described by Michaelis et al. (2013), to achieve multi parametric cell profiling. They combined impedance recordings with SPR and analyzed simultaneously the response of confluent MDCK II cells grown on a sensor chip upon addition of 5 µM cytochalasin D with both techniques [115] showing disruption of actin cytoskeleton and barrier forming cell-cell contacts [116].

2 Objective

In recent years the biological response to nanoscale particles has received considerable attention. This interest was driven by the enormous number of potential applications of nanoparticles on the one hand and their potential health hazards on the other. A lot of studies are published which evaluate the influence and risk to human body caused by nanoparticles or nanomaterials. However, much less is known about the impact of microparticles, i.e. materials with lateral dimensions in the single digit µm range, on human health and environment. Thus, it was the objective of this thesis to study the impact of micrometer-sized silica particles (Ø = 2 µm) on vitality, migration, proliferation and gap junctional intercellular communication of adherent mammalian cells (NRK, *normal rat kidney*) *in vitro* using different label-free, impedance-based assays that are referred as ECIS (*electric cell-substrate impedance sensing*) technique in the literature.

Thus, this thesis is divided into three main chapters focusing on

(i) Theoretical Studies on Data Interpretation
(ii) Assay Development to Study Gap Junctional Intercellular Communication
(iii) Influence of Silica Particles on Mammalian Cells.

This project is intended to serve as a model study on the information content of multimodal impedance-based assays to assess the biological response of mammalian cells to microscale particles. In literature different techniques are used to study one specific cellular response, however, most of them require the use of additional labels that may interfere with the outcome of the assay and do not allow to run several assays sequentially on one cell population. Our aim was to investigate the cellular response upon exposure to silica microparticles as model material using a label-free technique which allows the sequential analysis of particle impact on different levels of cell physiology. To extend this analysis to cell-cell communication a new assay format should be developed which allows the quantification of gap junctional intercellular communication between adjacent cells within a sequence of assays addressing other hallmarks along the interaction of microparticles with mammalian cells. To avoid misinterpretation of impedance data and to facilitate data analysis, the experimental impedance data were supported by theoretical studies. Using a LabVIEW-based software, impedance spectra for different cellular scenarios were simulated and compared to real impedance experiments.

3 Materials and Methods

3.1 Cell Culture Techniques

All cell culture work was performed under sterile conditions under a laminar flow hood (HERAsafe®, Thermo Scientific, München) and by using sterile medium and buffer solutions. All pipette tips (10 µL, 100 µL and 1000 µL) as well as glass pipettes and reaction tubes (500 µL, 1.5 mL and 2.0 mL) were sterilized using an autoclave (DX-45, Systec, Wettenberg). For routine cell culture cells were grown in culture flasks made of polystyrene with a growth area of 25 cm^2 or 75 cm^2 in 4 mL or 10 mL culture medium. Cells were kept in an ordinary cell culture incubator (Thermo Fisher Scientific Inc.) which provides a constant temperature of 37 °C and 5 % CO_2.

3.1.1 Cell Lines

This work includes experiments with the following, adherently growing cell lines: the epithelial-like cell line NRK-52E (*normal rat kidney*, strain 52E), originates from rat kidney and was first described by De Larco and Todaro in 1978 [117]. They show a weak barrier function for ions and small molecules. Adherent NRK cells grow in monolayers and show cobblestone morphology (**Fig. 3.1 A**). MDCK cells (*Madin-Darby Canine Kidney*, Strain I and II) originating from a female cocker spaniel's kidney were first isolated in 1958 by Madin and Darby [118]. Two different cell subtypes are known: MDCK I (**Fig. 3.1 B**) and MDCK II (**C**) which are different in their ability to form a tight barrier for small molecules and ions. For microscopic analysis MDCK II pABCG2 EYFP (enhanced *yellow fluorescent protein*) cells were used which are stably transfected with the plasmid pABCG2-EYFP (**Fig. 3.1 C**). This plasmid carries genes for a fusion protein from the membrane associated ABC-transporter (*ATP-binding cassette*) system G2 and EYFP. These cells were kindly provided by M. Seidl.

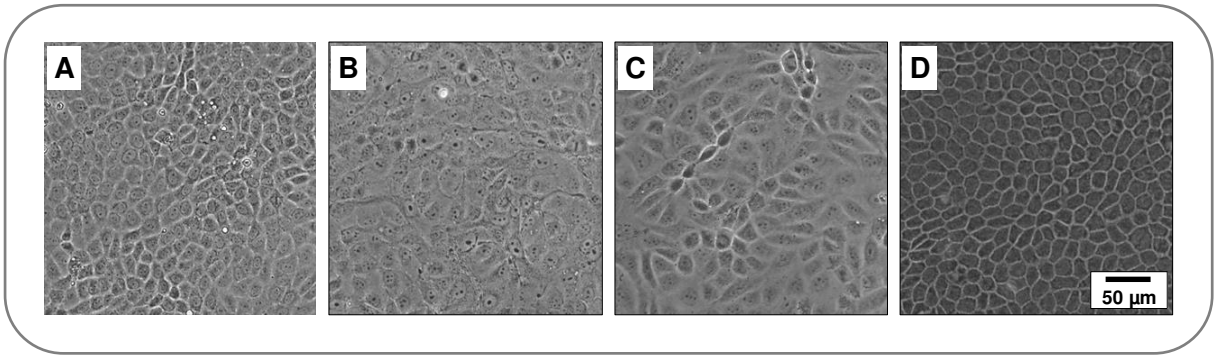

Fig. 3.1: Phase-contrast images of different cell lines used in experiments: NRK (**A**), MDCK I (**B**), MDCK II (**C**), MDCK II pABCG2 EYFP cells (**D**).

3.1.2 Subculturing

Once a week, when cells reached 100 % confluence, cells were trypsinized and transferred in low seeding densities to a new culture flask using the cell type specific subculturing protocol (**Tab. 3.1**). Therefore, all buffer solutions and the cell culture medium were pre-warmed to 37 °C in a water bath (TW12, Julabo, Seelbach). First, medium was removed and cells were washed twice with PBS^{--} to remove medium residues and dead cells. Afterwards, cells were incubated with 1 mM EDTA (*ethylenediaminetetraacetic acid*) solution in PBS^{--} for ~ 10 min to complex bivalent cations, which are necessary for the formation of cell-cell-contacts and cell-extracellular matrix contacts. Cells were finally detached from the culture surface by adding 0.05 % or 0.25 % (w/v) solution of trypsin in PBS^{--}. After 10 min of incubation at 37 °C the culture flask was tapped on a solid surface to facilitate and assist cell detachment. To stop the activity of the enzyme, 10 mL of pre-warmed medium were added, and the cell suspension was centrifuged at room temperature for 10 min at 110 x g. Then, cells were resuspended in culture medium and seeded in culture flasks or other appropriate substrates for different experiments. For routine cell passage a 1:20 dilution referenced to the growth area was used and culture medium was exchanged every other day.

Tab. 3.1: Subculturing protocol for different cell lines.

Cell Type	Incubation with PBS^{--}	Incubation with EDTA/PBS^{--}	Trypsin Concentration (w/v) / Incubation Time
NRK-52E	-	10 min	0.05 % / 10 min
MDCK II pABCG2 EYFP	-	10 min	0.05 % / 10 min
MDCK I	3 x 5 min	2 x 10 min	0.25 % / 10 – 15 min
MDCK II	-	10 min	0.05 % / 10 min

3.1.3 Medium and Buffer Composition

For each cell type different compositions of the culture medium optimized for cell type specific requirements were necessary and are listed in **Tab. 3.2**. Additionally, compositions of different buffers used for cell culture experiments during this work are summarized in **Tab. 3.3**.

Tab. 3.2: Medium composition for different cell lines used in this work.

Cell Line	Cell Culture Medium	FCS	Glutamine	Penicillin and Streptomycin
NRK-52E	DMEM 3.7 g/L $NaHCO_3$ 4.5 g/L D-Glucose	5 % (v/v)	2 mM	100 µg/mL
MDCK II, MDCK I	MEM Eagle 2.2 g/L $NaHCO_3$ 1 g/L D-Glucose	5 % (v/v)	4 mM	100 µg/mL

Tab. 3.3: Composition of different buffers used for cell culture experiments and cell culture work.

Buffer	Composition	Supplier
PBS^{--}	140 mM NaCl 2.7 mM KCl 8.1 mM Na_2HPO_4 1.5 mM KH_2PO_4	Sigma-Aldrich
PBS^{++}	PBS^{--} with 0.9 mM Ca^{2+} 0.5 mM Mg^{2+}	Sigma-Aldrich
EDTA solution	1 mM EDTA in PBS^{--}	Sigma-Aldrich
$Trypsin_{0.25}$/EDTA	0.25 % (w/v) trypsin 1 mM EDTA in PBS^{--}	Sigma-Aldrich
$Trypsin_{0.05}$/EDTA	0.05 % (w/v) trypsin 1 mM EDTA in PBS^{--}	Sigma-Aldrich
$EBSS^{++}$	$EBSS^{--}$ with 1.8 mM $CaCl_2$ 0.8 mM $MgSO_4 \cdot 7\ H_2O$	Sigma-Aldrich
$EBSS^{--}$	5.3 mM KCl 26.2 mM $NaHCO_3$ 117.2 mM NaCl 1.0 mM $NaH_2PO_4 \cdot H_2O$ 5.6 mM D-Glucose	Life Technologies

3.1.4 Cryopreservation and Recultivation

For cryopreservation of adherent cells, cells were cultured in standard culture flasks with a growth area of 75 cm^2 until 80 % confluence was reached. Cells were then trypsinized using the cell type specific protocol as detailed in **chapter 3.1.2**. After centrifugation, the cell pellet was resuspended in a cryoprotective solution of FCS (Biochrom) containing 10 % DMSO (*dimethyl sulfoxide*). DMSO, a cryoprotective substance, can prevent intracellular ice crystal formation and thus cell membrane damages which may otherwise lead to necrosis. The cell suspension was split into 1.5 mL aliquots and was then frozen in cryovials using a two-step process. First, cells were slowly cooled down to - 80 °C, with a constant cooling rate of 1 °C/min using an isopropanol bath. Subsequently, cells were transferred to liquid nitrogen for long term storage.

For recultivation of cells stored in liquid nitrogen, cryovials were removed from the tank and warmed to - 20 °C for ~ 1 – 2 h. Afterwards, cells were quickly thawed in a 37 °C water bath and transferred into a sterile centrifugation tube. Carefully, 10 mL pre-warmed culture medium was added dropwise to the cells and the cell suspension was centrifuged at 110 x g for 10 min at room temperature. Cells were seeded in three culture flasks (25 cm^2) in different densities (1:2, 1:4 and 1:8) with respect to their growth area. After 24 h culture medium was exchanged and cells were subcultivated using the routine protocol described in **chapter 3.1.2** when reaching confluence**.**

3.2 Physical Background of Impedance Spectroscopy

Impedance spectroscopy is a non-invasive method to investigate electrical properties of a huge variety of materials or systems. The basic principle is the analysis of the impedance *Z* of a dielectric system as a function of frequency which describes the ability of the system to resist current flow when using alternating current (ac). The application of low amplitudes of alternating current for excitation allows non-invasive impedance recordings even in sensitive biological or cellular systems. In the following, a brief introduction in this versatile method is given with regard to its physical background.

According to Ohm's law the impedance *Z* is defined in **Eq. 3.1** as the ratio of the applied alternating voltage *U (t)* and the resulting alternating current *I (t)*.

$$Z = \frac{U\,(t)}{I\,(t)} = \frac{U_0 \cdot sin\,(\omega t)}{I_0 \cdot sin\,(\omega t - \varphi\,)} \qquad \textbf{Eq. 3.1}$$

with *U(t)* : voltage at time *t*, U_0 : amplitude of voltage, *I(t)* : current at time *t*, I_0 : amplitude of current, ω : angular frequency, *t* : time; φ : phase shift between voltage *U(t)* and current *I(t)*.

In a perfectly resistive system current and voltage of ac circuits are in phase whereas electric elements with capacitive or inductive properties are characterized by a phase shift between voltage and current (**Fig. 3.2 A**). A more appropriate description of *U(t)* and *I(t)* is therefore given in the complex notation shown in **Eq. 3.2** and **Eq. 3.3**:

$$U\,(t) = U_0 \cdot e^{i\omega t} \qquad \textbf{Eq. 3.2}$$

$$I\,(t) = I_0 \cdot e^{i(\omega t - \varphi)} \qquad \textbf{Eq. 3.3}$$

Consequently, based on **Eq. 3.1** the complex impedance *Z* is defined by the exponential function

$$Z = \frac{U_0 \cdot e^{i\omega t}}{I_0 \cdot e^{i(\omega t - \varphi)}} = \frac{U_0}{I_0} \cdot e^{i\varphi} = |Z| \cdot e^{i\varphi} \qquad \textbf{Eq. 3.4}$$

$$\textit{with } i = \sqrt{-1}$$

A graphical presentation of the complex impedance *Z* is shown in the Gaussian plane in **Fig. 3.2 B** where the length of the vector indicates the magnitude of impedance *|Z|* and the angle between the x-axis and the vector describes the phase shift φ.

In Cartesian coordinates the real and imaginary components of the impedance *Z* can be extracted. The real impedance contributions *Z'* (resistance) arise from current in-phase with the voltage and imaginary contributions *Z''* (reactance) result from 90° out-of-phase currents. The complex impedance *Z* is defined by

$$Z = Z' + i \cdot Z'' \qquad \textbf{Eq. 3.5}$$

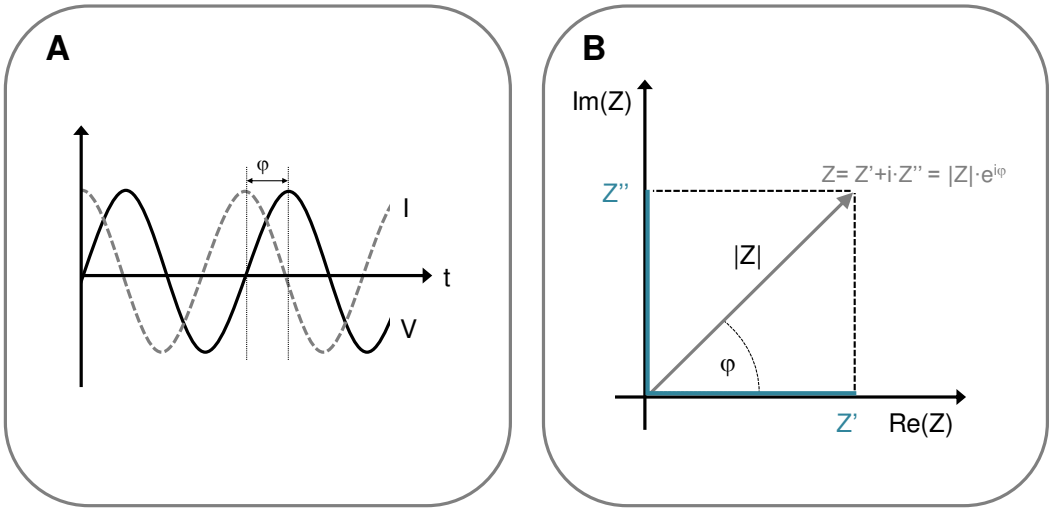

Fig. 3.2: A: Graphical scheme of the phase shift between current-time function (**grey**, dashed) and voltage-time function (**black**, solid). **B:** Graphical representation of impedance *Z* in a Gaussian plane by using a real *Re(Z)* and imaginary *Im(Z)* axis. The length of the vector represents the magnitude of impedance *|Z|*. The angle φ between the real axis and the vector reflects the phase shift between voltage and current. The resistance *Z'* and reactance *Z''* can be extracted from the real and imaginary axis.

The two terms Z' and Z'' can be further characterized using **Eq. 3.6** and **Eq 3.7**.

$$Z' = Re(Z) = |Z| \cdot \cos\varphi \qquad \textbf{Eq. 3.6}$$

$$Z'' = Im(Z) = |Z| \cdot \sin\varphi \qquad \textbf{Eq. 3.7}$$

$$|Z| = \sqrt{(Z')^2 + (Z'')^2} \qquad \textbf{Eq. 3.8}$$

$$\varphi = \arctan\left(\frac{Z''}{Z'}\right) \qquad \textbf{Eq. 3.9}$$

Equivalent Circuit Model

The basic principles to calculate the total impedance *Z* of a given system are described by Ohm's law as well as Kirchhoff's circuit laws (**Fig. 3.3**). To analyze impedance data equivalent circuit models are developed by using common ideal electrical elements, like resistor and capacitor in combination with non-ideal elements (constant phase element; CPE) which should mimic the electric frequency response of the system under study (**Tab. 3.4**).

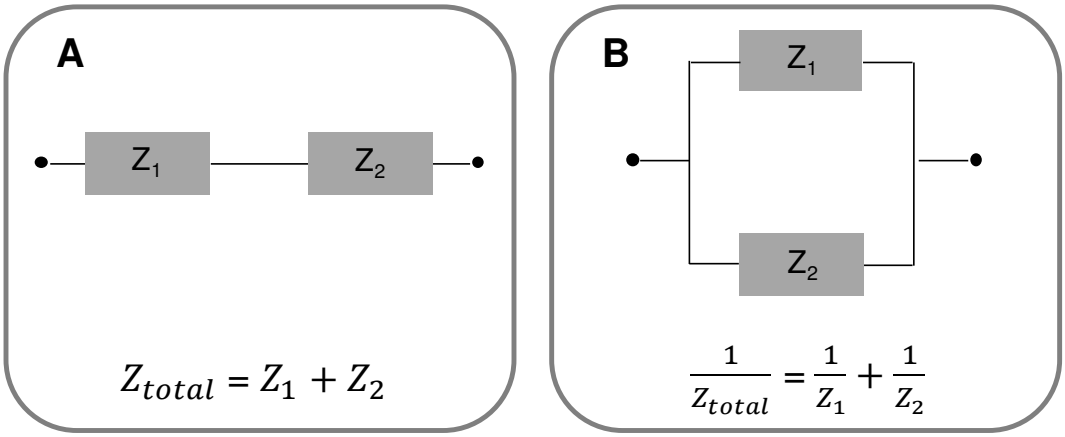

Fig. 3.3: Schematic presentation of the Kirchhoff's law to calculate the total impedance of an equivalent circuit with elements Z_1 and Z_2 in series (**A**) or in parallel (**B**). For impedance elements in series the total impedance is the sum of its individual impedances. When the two impedance elements are in parallel, the total impedance *Z* is defined by the reciprocal of the sum of the reciprocals of the corresponding individual impedances.

By using **Eq. 3.5** and **Eq. 3.8** the real and imaginary impedance contribution can be determined for the different electrical elements and the corresponding phase shift φ can be calculated using **Eq. 3.9**.

Tab. 3.4: Overview of ideal and empirical equivalent circuit elements with their contribution to the impedance as well as phase shift between voltage and current.

Electrical Element	Abbreviation	Parameter	Impedance *Z*	Phase Shift φ
Resistor	*R*	*R*	*R*	0
Capacitor	*C*	*C*	$\frac{1}{(i\omega C)}$	$-\frac{\pi}{2}$
Constant Phase Element	CPE	*A* *n* (0 < *n* < 1)	$(i\omega)^{-n}.\frac{1}{A}$	$-n \cdot \frac{\pi}{2}$

The ideal and frequency independent resistor *R* has an influence on the amplitude of the current but no phase shift between voltage and current is observed. The magnitude of impedance $|Z|$ is defined by $Z' = R$ whereas $Z'' = 0$. However, a frequency-dependent impedance is found by using a capacitor as ideal electrical element. The capacitor *C* provides no contribution to Z' and $|Z|$ is determined by $Z'' = (-\omega C)^{-1}$. The impedance of an ideal capacitor decreases with increasing frequency and a phase shift φ of the current of – 90° is found.

In addition to the ideal elements a constant phase element (CPE) is necessary to describe the interface impedance between a noble metal electrode (e.g. gold electrode) which is covered with an electrolyte containing liquid (e.g. physiological buffer or culture medium). This CPE is defined by the two parameters *A* and *n* and further characterizes the non-ideal capacitive behavior of the electrode. For $n = 0$ the CPE behaves like an ideal resistor and consequently $|Z|_{CPE} = A^{-1}$ resulting in a frequency independent impedance signal without any phase shift φ between current and voltage. If $n = 1$ the CPE is identical with an ideal capacitor with $|Z|_{CPE} = (i\omega A)^{-1}$ and causes a phase shift $\varphi = -\frac{\pi}{2}$. The parameter *n* indicates that the CPE as non-ideal capacitor behaves partly like both elements - capacitor and resistor - and describes best the behavior of a noble metal electrode in combination with conducting supernatants [119].

3.3 Electric Cell-Substrate Impedance Sensing

Electric Cell-Substrate Impedance Sensing (ECIS) is a very versatile technique to monitor adherent cells, which are grown directly on small gold-film electrodes, in a non-invasive manner combined with high time-resolution. This technique was first described in literature in 1984 by Giaever and Keese [77] and offers the possibility to detect the morphological response of adherent cells after the addition of an external stimulus.

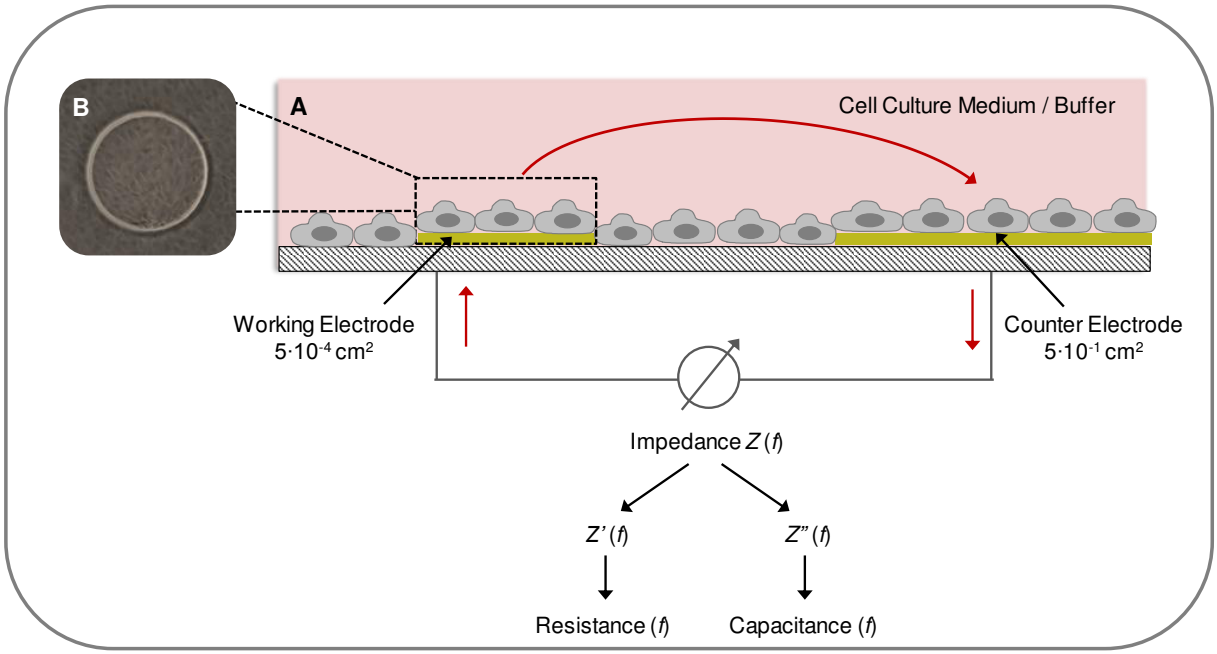

Fig. 3.4: A: Schematic principle of the ECIS technique: Adherent cells are grown on top of gold-film electrodes. After applying alternating current (red arrows; for clarity only drawn unidirectionally) an electric connection between the small working electrode and the significantly larger counter electrode is realized by the supernatant buffer or cell culture medium. The frequency-dependent impedance *Z (f)* of the cellular system can be split into its real component *Z' (f)* representing the resistance of the system and imaginary component *Z'' (f)* from which the capacitance can be calculated. **B:** Phase-contrast image of a working electrode (8W1E) confluently covered with NRK cells. The diameter of the working electrode is 250 µm.

A schematic overview of the ECIS technique is shown in **Fig. 3.4**. The ECIS principle is characterized by a two-electrode setup – a larger counter electrode ($5{\cdot}10^{-1}$ cm^2) and a significantly smaller working electrode ($5{\cdot}10^{-4}$ cm^2) which are electrically connected via an electrolyte containing solution e.g. physiological buffer or cell culture medium. Adherent cells are directly grown on the co-planar gold-film electrodes and the impedance $Z(f)$ is analyzed as a function of frequency by using a weak sinusoidal ac voltage. The measured impedance $Z(f)$ can be converted into $Z'(f)$ and $Z''(f)$ - representing the real and the imaginary components of the system.

Due to the large size difference of the small working electrode compared to the much larger counter electrode the measured total impedance $Z(f)$ is dominated by the cells grown on the small working electrode. This can be explained by the higher voltage drop as well as the

higher measured current density at the working electrode, thus the working electrode serve as a bottleneck for current flow. In contrast, the impedance contribution of the counter electrode to the total impedance $Z(f)$ was found to be below 1 % and can therefore be neglected [120]. The high sensitivity of the ECIS technique that allows monitoring of cell morphology changes without the need for additional labeling originates from the close proximity between cells and gold-film electrode – as the gold-film electrodes serve as growth substrate as well as sensoric device – and the size difference between working and counter electrode. For the ECIS technique the general relation exists: the smaller the electrode size the higher the sensitivity for detecting changes in cellular morphology.

When cells are grown on the electrode surface, the dielectric properties of the plasma membrane causes an increase of impedance Z compared to a cell-free electrode over a wide frequency range (**Fig. 3.5 A)**. The current flow is frequency-dependent and can be explained by two different pathways (**Fig. 3.5 B**). For low frequencies ($f \leq 10$ kHz), the alternating current is forced to flow around the insulating cell bodies, which means it flows through the narrow gap between electrode and cell membrane and subsequently through cell-cell contacts between neighboring cells. Only in the high frequency range ($f > 10$ kHz) the current can couple capacitively through the basal and apical cell membrane. This offers the possibility to monitor and analyze cell-cell contacts in the low frequency range whereas the higher frequency range is more appropriate to analyze electrode coverage.

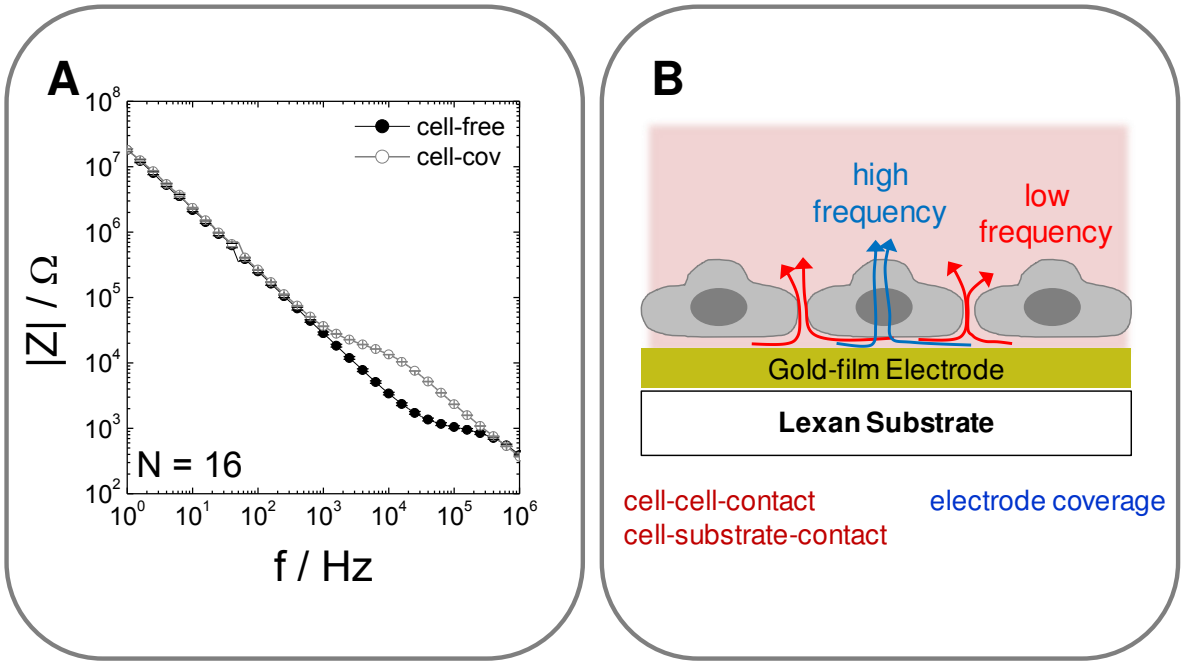

Fig. 3.5: A: Frequency-dependent impedance spectra for a cell-free and NRK cell-covered 8W1E electrode layout (Mean ± SE; N = 16). **B:** Schematic of frequency-dependent current pathways of a cell-covered (cell-cov) electrode. At lower frequencies (**red**) the current flows around the cell bodies through the narrow subcellular gap between cells and electrode and through the intercellular space. At high frequencies current can couple capacitively across the membrane (**blue**). In the intermediate frequency range the current flow can be described by paracellular and transcellular pathways.

The frequency-dependent changes of the impedance signal $Z(f)$ can be used to analyze effects on membrane properties (C_m), intercellular resistance (R_b) or sub-cellular impedance (α) by using the model provided by Giaever and Kesse [121] which will be further described in detail in **chapter 4.1.1**.

3.3.1 Experimental Setup

As described above, ECIS is a versatile tool to monitor changes in cell morphology in a non-invasive manner and with a high time resolution. The non-invasiveness is realized by using a weak sinusoidal ac voltage (10 – 50 mV) at varying frequencies (f = 1 Hz – 10^6 Hz) and the complex impedance Z is monitored as a function of frequency.

For most experiments the commercially available devices ECIS 1600R or ECIS Zθ (Applied BioPhysics, Troy, NY, USA) were used to perform ECIS measurements. Voltages for measurements with the commercial setups are given as *rms*. In this setup the impedance analyzer, frequency generator, microcontroller and the relay are integrated in one component. The array holder, which enables simultaneous data recording of 16 different wells is placed in a humidified incubator (37 °C, 5 % CO_2), whereas all electronic devices are located outside. The ECIS device is connected to an ordinary computer for data storage and recording and is operated by the commercially available ECIS software which also enables data analysis after finishing an experiment.

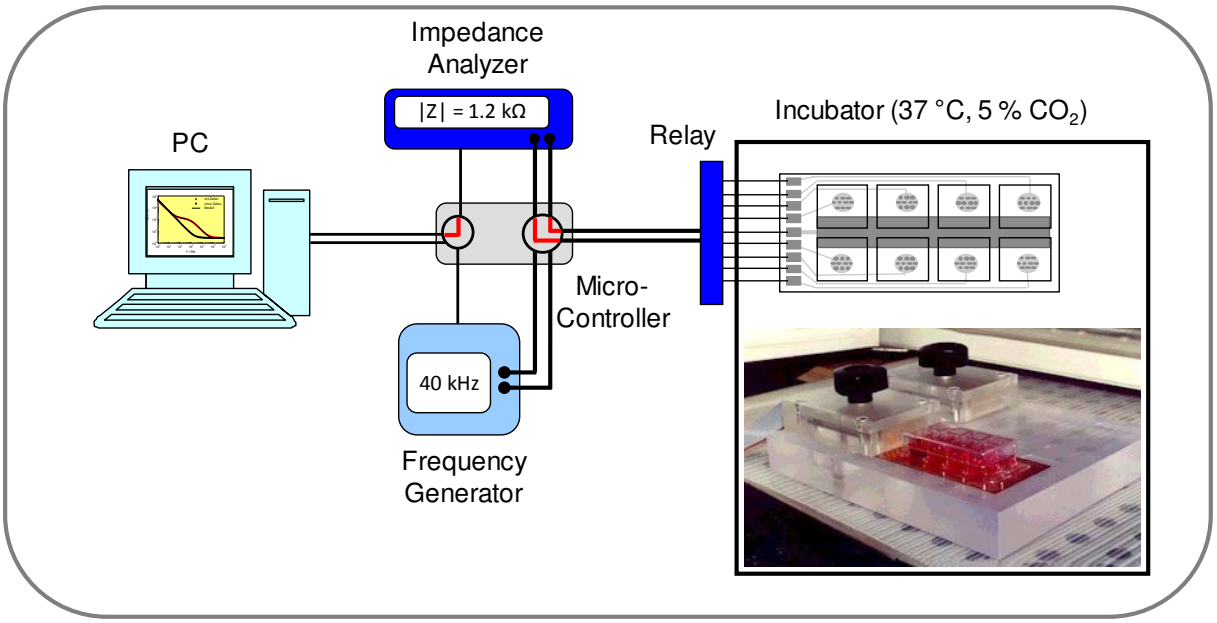

Fig. 3.6: Scheme of the home-made setup for ECIS recordings: the electrode holder is placed in a humidified cell culture incubator which provides constant temperature and CO_2 conditions during the measurement. A microcontroller enables to switch between impedance analyzer and frequency generator for pulse application. The relay offers the possibility to individually address single wells and the whole setup is connected to a computer for data recording.

Alternatively, a home-made setup (**Fig. 3.6**) was used consisting of an impedance analyzer (SI-1260, Solartron Instruments, Farnborough, UK) and a frequency generator (type 33120A, Hewlett Packard; Böblingen) which are connected via a microcontroller to an ordinary computer. A commercially available array holder (Applied BioPhysics, Troy, NY, USA) allows the electrical connection of two 8-well-electrode arrays and a relay enables addressing of individual electrodes. The home-made device is controlled by a LabVIEW-based software written by J. Wegener. A frequency range from 1 Hz to 10^6 Hz was covered depending on the experiment and data was taken at 61 different frequencies in maximum. Frequency-dependent impedance of cell-covered electrodes was recorded with an ac voltage amplitude of 70 mV [b].

3.3.2 Basic Experimental Procedure

ECIS experiments were performed with an established confluent cell layer grown on the appropriate electrode layout (**chapter 3.3.4**). Therefore, NRK cells were seeded at least two days prior to the experiment in defined seeding densities using a volume of 400 µL. Without exception cell culture medium was exchanged one day prior to the experiment. Immediately before starting the experiment culture medium was aspirated and, dependent on the experimental design, buffer or culture medium was added using variable volumes (120 µL - 200 µL). For long-term analysis 100 µL ddH_2O was added into the reservoirs between wells of the LabTek® chamber to minimize solvent evaporation and the wells were always covered with a polystyrene lid to guarantee sterile conditions. The precise experimental instructions are given with the corresponding experiments in the results.

A different experimental procedure was used in ECIS experiments analyzing cellular proliferation as well as establishment of epithelial barrier function. There, experiments were started with a cell-free electrode where cells were seeded in a defined low density and the establishment of a confluent cell layer was monitored in a time-dependent manner.

[b] Voltage is given as *peak to peak* value (pp)

3.3.3 Different Modes of ECIS Recordings within the Commercially Available ECIS Setup

In the commercially available software different measurement modes can be selected depending on the experimental design. It offers the possibility to obtain data of impedance *Z* as a function of frequency over a wide frequency range, at a single frequency or in a high time-resolution mode for detecting micromotion of cells. In the following the three different ways of collecting data are presented in more detail.

Multi-Frequency/Time (MFT) Experiments

In the MFT mode the complex impedance *Z* is measured over a frequency range of 62.5 Hz - 64 kHz at 11 pre-determined frequencies (62.5, 125, 250, 500, 1000, 2000, 4000, 8000, 16000, 32000, 64000 Hz). This measurement mode offers the possibility to analyze the cell response in a frequency-dependent manner and is suitable for e.g. cytotoxicity screening as well as wound healing experiments. Also for proliferation analysis this measurement type is advantageous due to the opportunity to analyze cell coverage at high frequency as well as establishment of barrier function at low frequencies simultaneously during one experiment. When the ECIS model (**chapter 4**) is applied to experimental multi-frequency impedance data of a cell-covered electrode the cell-related parameters R_b, α and C_m can be fitted through a least square optimization algorithm. The time-resolution in a MFT experiment of eight wells was determined to ~ 1.3 min.

Single Frequency/Time (SFT) Experiments

To further enhance time resolution SFT experiments are used to monitor changes in cell morphology at one defined frequency which can be selected and adjusted to the cell type and electrode layout in the beginning of the experiment. For eight wells a time-resolution of ~ 4 s can be realized.

Rapid Time Collect (RTC) Experiments

RTC mode was performed to detect micromotion - small cell morphology fluctuations of a confluent cell layer - which originate from the non-rigid connection between cells and the electrode surface. Micromotion of adherent cells correlates with their metabolic activity and

can be analyzed as impedance fluctuations at 4 kHz. To investigate the influence of silica particles on cell viability and metabolic activity, RTC measurements were performed using one or two points per second and data sets of 15 min for each well. Subsequent to ECIS recordings data were analyzed using increment analysis provided by a LabVIEW-based software written by J. Wegener. During this analysis data was divided into data windows of 64 s and was further analyzed regarding mean value and variance. By analyzing data periods of 15 min a motility index was calculated which represents the metabolic activity. Detailed information about data analysis is given in **chapter 6.3.3.5**.

To study the beating of cardiomyocytes data acquisition was further improved with respect to time resolution. The cardiomyocytes were analyzed with a time resolution of 64 points per second or even 128 points per second over different time periods. Detailed information is given in **chapter 6.3.6.3**.

3.3.4 Electrode Layouts

Different electrode layouts, commercially available from Applied BioPhysics (Troy / NY, USA) were used for ECIS measurements depending on experimental requirements. **Fig. 3.7** shows micrographs of (**A**) 8W1E, (**B**) 8W10E, (**C**) 8W4E-micro and (**D**) 8W10E$^+$ electrode layouts. The base substrate is in most cases *Lexan®,* a 0.51 mm thick polycarbonate substrate, except for 8W1E which was also available with a transparent *polyethylene terephthalate* (PET) substrate (thickness 0.25 mm). The individual electrode layout is generated by sputter deposition of gold followed by a photolithographic step. The 8-well-chamber glued on top of the base substrate is made of polystyrene and creates eight different compartments with a growth area of ~ 0.8 cm^2 and a volume of 150 µL – 400 µL.

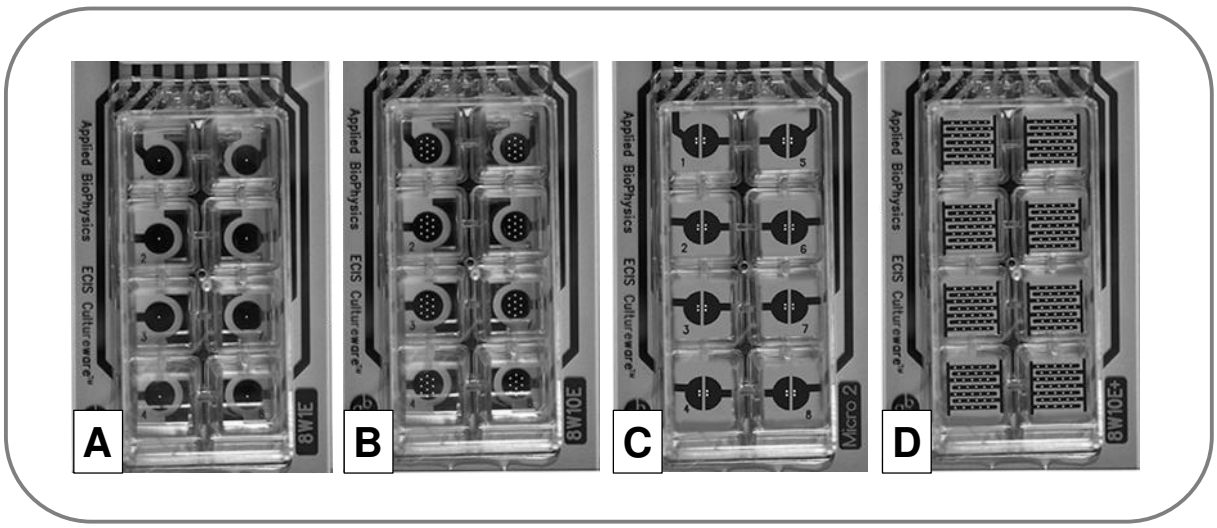

Fig. 3.7: Electrode layouts used for standard ECIS experiments 8W1E (**A**), 8W10E (**B**), 8W4E-micro (**C**), 8W10E$^+$ (**D**). Photographs were taken from http://www.biophysics.com/cultureware.php.

Depending on the application the respective layout was chosen to achieve the best result and highest information content. **Tab. 3.5** shows the different electrode layouts with their major applications during this work. The layouts have different numbers of active electrodes per well, from a single electrode in 8W1E layout to 40 electrodes in a 8W10E$^+$ layout as well as different electrode areas.

Tab. 3.5: Characteristics of different commercially available array types regarding electrode area and number of electrodes in each well. For each array type the major applications are listed in the last column.

Layout	Total Area	Electrodes / Well	Major Application
8W1E	0.05 mm^2	1	Migration, Cytotoxicity, Micromotion, Electroporation
8W10E	0.5 mm^2	10	Co-culture Experiments, Epithelial Barrier Function, Cell attachment/Spreading
8W4E-micro	0.2 mm^2	4	Electroporation
8W10E$^+$	2.0 mm^2	40	Proliferation

The most heavily applied layout type is 8W1E (**A**), which has a single working electrode in each well with a diameter of 250 µm. The counter electrode is approximately 500-fold larger (A ~ 0.25 cm^2) which guarantees that the measured impedance is dominated by cells located on top of the working electrode. During this work 8W1E electrodes were mainly applied to analyze the effect of silica particles regarding cytotoxicity, migration or micromotion.

To increase the maximum number of measured cells 8W10E (**B**) electrodes were used that have a larger electrode area in total. This array type has ten individually working electrodes, each with a diameter of 250 µm. They are arranged in parallel and combined with a counter electrode, which is similar to the 8W1E layout. Their standard applications were to analyze the effect of drugs on epithelial barrier function or to study the inhomogeneity of cells on the electrode in “co-culture” experiments, where different ratios of two cell types were seeded simultaneously.

Some electroporation experiments were done with 8W1E electrodes, but the disadvantage is, that the electroporation efficiency can be analyzed only on a single working electrode. To analyze the dye uptake after *in situ* electroporation at different positions in one well it is more

efficient to use 8W4E-micro (**C**) arrays where one well contains four electrodes with a diameter of 250 µm.

A more specific array type with an interdigitated electrode structure is the 8W10E$^+$ (**D**) array. Each well contains two sets of 20 circular electrodes (d = 250 µm) located on interdigitated fingers. This electrode structure offers the opportunity to analyze impedance integratedover the entire area of 0.8 cm^2 and also to average over a high number of cells. Therefore, it is very useful for impedimetric proliferation studies with only low cell densities present in the well at the beginning of the experiment.

Additional, to these commercially available electrode layouts array modifications as well as some special electrode structures were used during this work. They will be introduced in the context of the respective chapter.

3.3.5 Data Presentation of ECIS Recordings

Normally, impedance is recorded time-dependently at different frequencies in the MFT mode and therefore, a variety of frequencies as well as $|Z|$, R and C values can be used for the analysis of cellular responses.

Often, $|Z|$ was applied to analyze morphological changes at varying frequencies (500 Hz – 32 kHz) depending on the experiment, cell types and electrode structures. In the graphs either the absolute values of $|Z|$ (**Fig. 3.8 A**) or the normalized values of $|Z|$ termed $|Z|_{norm}$ (**B**) are presented as a function of time. Data normalization was performed using the last impedance value before substances were added or electroporation or wounding occurred. Normalized data provides a better comparison between different wells or even between different experiments. Similar procedures of normalization were applied for time-courses of R and C. To further analyze changes in cell coverage of the electrodes the capacitance at 32 kHz was used due to the linear dependency between capacitance and electrode coverage which is given in the high frequency range.

The frequency-dependent spectra of $|Z|$, R and C were plotted (**C**) beside the time-dependent analysis. This graph provides the basis for the normalized presentation where the cell-covered impedance spectrum is divided by the spectrum of the same cell-free electrode (**D**). This data presentation allows the determination of the most sensitive frequency which can be used for further analysis of the data in single frequency recordings.

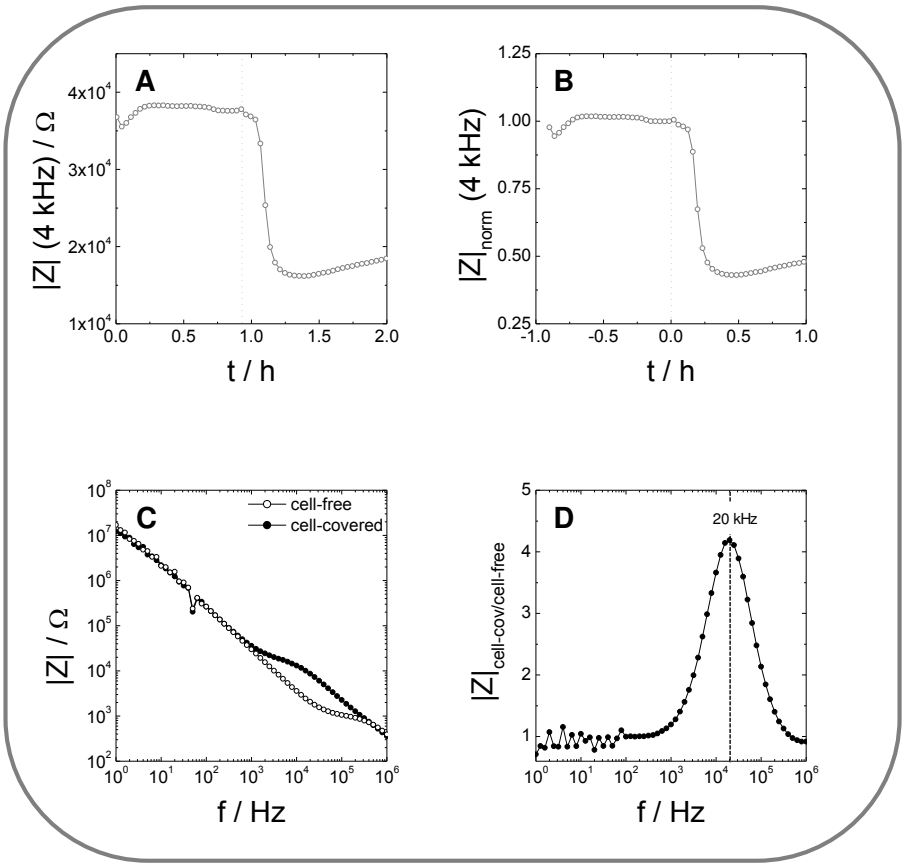

Fig. 3.8: Different types of ECIS data presentation depending on the experiment: **A:** Time-course of the absolute impedance $|Z|$ in Ω at a monitoring frequency of 4 kHz. **B:** Time-course of the normalized impedance ($|Z|_{norm}$) at 4 kHz. $|Z|$ was normalized using the absolute impedance value immediately before the time point of addition (indicated by the dotted line). In some cases normalization was also performed using the value immediately before wounding / electroporation or using the first value which was recorded in the beginning of the experiment. **C:** Frequency-dependent spectrum of $|Z|$ for a cell-free electrode and a cell-covered electrode. **D:** Based on the data presented in (**C)** the cell-covered impedance values were divided by the cell-free values and $|Z|_{cell\text{-}cov./cell\text{-}free}$ was plotted as a function of frequency. This presentation of the impedance data allows evaluation of the most sensitive frequency, here 20 kHz.

3.4 Microscopy Techniques

In this work phase-contrast and fluorescence microscopy were performed. Phase-contrast images served as control for cells in culture flasks or on other culture substrates. Cells on ECIS electrodes were normally analyzed before and after electroporation with a phase contrast microscope. Electroporation or fluorescence labeling by cytochemical stainings were documented using an inverted or upright fluorescence microscope. Mostly, confocal laser scanning microscopy with an upright microscope was used to evaluate uptake efficiency and staining of intracellular cell components.

3.4.1 Confocal Laser Scanning Microscope

Confocal laser scanning microscopy (CLSM) is a microscopic method which only collects fluorescence or reflected light from one specific focal plane whereas out-of-focus fluorescence or scattered light is eliminated by the detector pinhole.

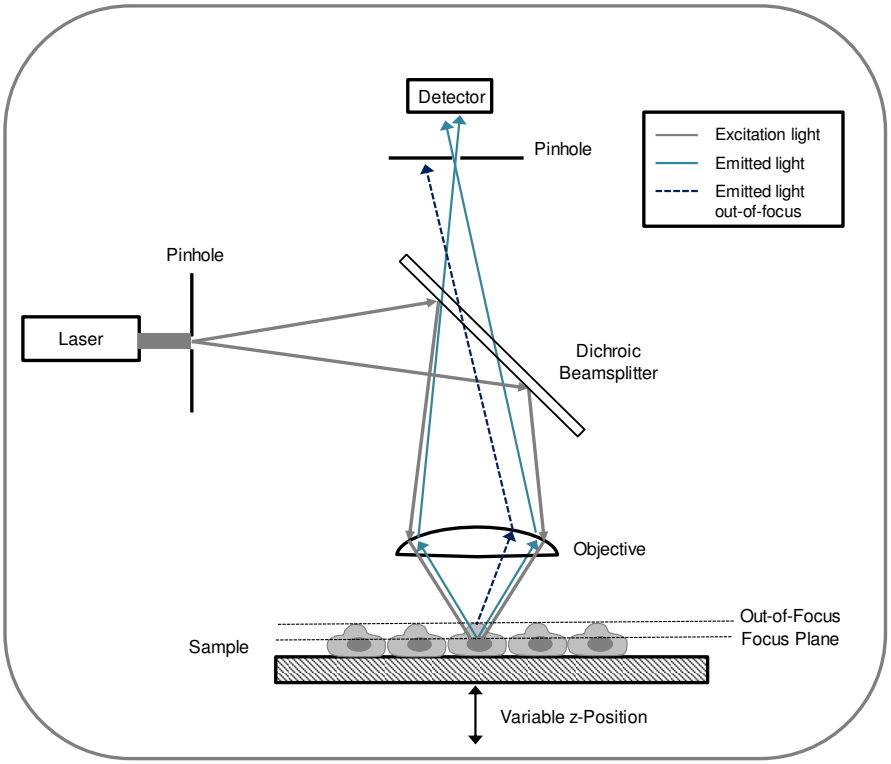

Fig. 3.9: Schematic principle of confocal laser scanning microscopy: Laser excitation light is focused to a thin beam that is used to scan the entire sample point by point. The dichroic mirror exhibits wavelength-dependent characteristics: The excitation wavelength (**grey**) is reflected by the dichroic mirror, whereas fluorescence light (**blue**) passes through it. Only fluorescence light coming from the focal plane is able to pass through the variable pinhole in front of the detector whereas light from out-of-focus planes is selectively blocked.

The principle of confocal laser scanning microscopy (**Fig. 3.9**) was first patented in 1957 by Marvin Minsky and was later applied for three-dimensional as well as time-dependent analysis of cell morphologies and cellular organizations [122]. The principle of this microscopic technique is the combination of a sequential point-by-point illumination with pinhole apertures to eliminate the out-of-focus light. The laser light beam is focused on the cellular sample by an objective and the emitted light from the sample with a characteristic wavelength can pass the dichroic mirror. Only emitted light from the focus plane passes the detection pinhole and is recorded by the detector, whereas reflected or emitted light from other planes is excluded. The variable size of the detection pinhole defines the axial resolution of the obtained images. By scanning the sample in a defined xy-plane and collecting the position-dependent fluorescence information by a photomultiplier tube (PMT) a 2D image is generated. Analysis of different optical sections by varying the z-position of a constant xy-plane - which can be realized and adjusted by a motorized microscope stage - allows a software-based reconstruction and consequently 3D analysis of biological samples. The applied software (Nikon EZ-C1) allows an analysis of the sample from different views (xz, yz and xy) as illustrated in **Fig. 3.10**.

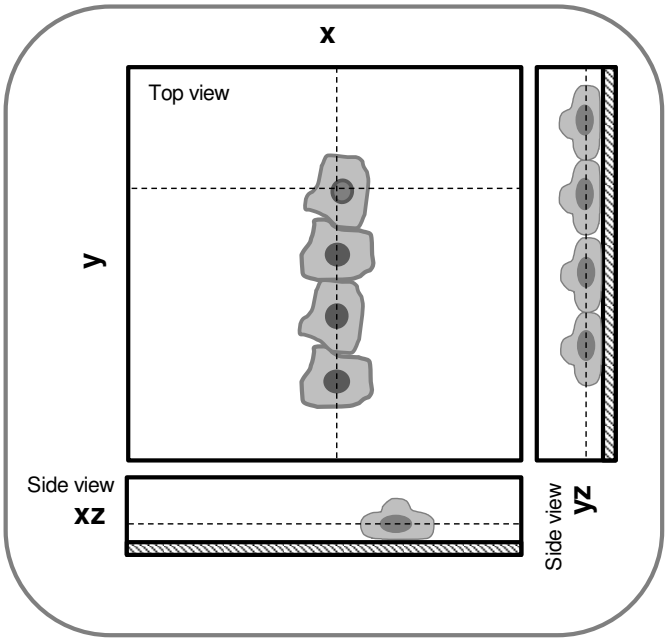

Fig. 3.10: Schematic principle of confocal laser scanning microscopic images. The top view shows an optical confocal xy-section of adherent cells. The corresponding side views (xz, yz) are additionally shown, providing a vertical view of the cell layer. The dashed line indicates the x-position within the yz side view or the y-position within the xz side view, respectively.

Image Recording and Image Presentation

In general, xy-images were recorded using confocal laser scanning microscopy and further analyzed e.g. for dye uptake or to study specific cellular compartments. The images were recorded using 512 x 512 or 1024 x 1024 pixels, often the same field of view was scanned several times (≤ 4) at one defined z-position to get an averaged image. Also z-stacks were recorded for some applications in order to get a side view of cells (xz, yz). Detailed information about array preparation for imaging cells grown on ECIS electrodes e.g. after electroporation is given in **chapter 5.4.1**.

Applied Microscopes

Phase-contrast images were taken with a Nikon Diaphot (Nikon, Tokio, Japan) inverted microscope. Therefore, five different objectives were used: PLAN 4 x / 0.13, E 10 x / 0.25, PLAN 20 x / 0.4, Fluor 40 x / 0.85 and PLAN Apo 60 x / 1.40 Oil.

For *Fluorescence Recovery after Photobleaching* (FRAP) experiments an inverted confocal laser scanning microscope (Zeiss Axiovert 200M) connected to a scanning device (Zeiss, LSM510) in combination with a temperature controlled incubator (XL-3) was used. FRAP experiments were performed using a 40 x objective (Plan-Neofluar 40 x/1.3 oil).

For upright fluorescence or phase-contrast imaging the Nikon Eclipse 90i was used in epi-mode or as a confocal laser scanning microscope. Epi-fluorescence or phase-contrast images were documented by digital cameras, whereas confocal laser scanning microscopic images were digitized by photomultipliers and saved on a computer. The Nikon Eclipse 90i was used in combination with different objectives summarized in **Tab. 3.6**.

Tab. 3.6: Microscopes used in this thesis. The different setups as well as the appropriate objectives are listed.

Microscope	Setup	Objective / Magnification / Numerical Aperture/ Immersion
Nikon Eclipse 90i	**upright**	**PLAN / 10x / 0.25 / -** **NIR Apo / 60x / 1.0 / W**
Nikon Diaphot	**inverted**	**PLAN / 4x / 0.13 / -** **E / 10x / 0.25 / -** **PLAN / 20x / 0.4 / -** **PLAN APO / 60 x / 1.40 / Oil**
Zeiss Axiovert 200M	**inverted**	**PLAN-Neofluar / 40 x / 1.3 / Oil**

3.4.2 Cytochemical Stainings

For further analysis of cellular structures cytochemical stainings together with fluorescence microscopy, mainly confocal laser scanning microscopy, were performed. The corresponding protocols are described below. For detection of the fluorescence signals the appropriate excitation and emission filters were selected. The available combinations for the two different microscopes are listed in **Tab. 3.7**.

Tab. 3.7: Specification of different excitation wavelengths and detectors for confocal laser scanning microscopy as well as filter specifications for epi-fluorescence microscopy. The different filter cubes are characterized regarding their excitation (Ex.) and emission (Em.) wavelengths and the wavelengths of the dichroidic mirror (DM).

Microscope	Mode of Microscopy	Laser Excitation	Detector	Filter Specification for Epi-Fluorescence Exc./DM/Em.
Nikon Eclipse 90i	Confocal Laser Scanning	408 nm 488 nm 543 nm	450/35 515/30 650 LP	---
Nikon Eclipse 90i	Epi-Fluorescence	---	---	340-380 nm/ 400 nm/ 435-485 nm 465-495 nm/ 505 nm/ 515-555 nm 540/25 nm/ 565 nm/ 605/55 nm
Nikon Diaphot	Epi Fluorescence	---	---	BP 420-490 nm/ 510 nm/ LP520 nm BP 510-560 nm/ 580 nm/ LP590 nm 330-380 nm/ 400 nm/ LP420 nm

3.4.2.1 Fixation and Permeabilization

To preserve the cell layer or as pre-treatment to staining of intracellular structures with membrane impermeable dyes or antibodies, cells were fixed with *paraformaldehyde* (PFA). Therefore, cells were washed twice with PBS^{++} to remove medium residues. Afterwards 4 % (w/v) PFA (in PBS^{++}) was added to the cells and incubated for 10 min at RT. After aspirating the fixation reagent, cells were washed twice with PBS^{++}. If necessary, cells were permeabilized by adding 0.5 % (v/v) Triton-X-100 (in PBS^{++}) for 10 min at RT. Finally, cells were washed with PBS^{++} to remove the detergent. These cells were used for subsequent stainings or stored in the fridge under PBS^{++} until use.

3.4.2.2 Live/Dead® Staining with Calcein AM and Ethidium Homodimer

Simultaneous staining of living and dead cells was performed by using a two-color Live/Dead® Cell Viability Assay (Molecular Probes) which includes *calcein acetoxymethylester* (CaAM) and *ethidium homodimer-1* (EthD-1). By combining both dyes, vital cells show a characteristic green fluorescence in the cytoplasm, whereas dead cells show a red fluorescence in the cell nuclei (**Fig. 3.11**).

The principle of this assay is that the non-fluorescent, membrane permeable dye CaAM can diffuse into the cytoplasm of cells, where intracellular esterases of living cells cleave the

ester groups. The product is the membrane impermeable and fluorescent calcein, which remains in the cytoplasm. Therefore, only living cells show a characteristic green fluorescence of calcein (ex./em. 494 nm/517 nm) inside the cytoplasm. On the other hand EthD-1, a DNA-intercalating dye, is excluded by intact plasma membranes of living cells and can only enter cells when membrane integrity is destroyed. If EthD-1 (ex./em. 528/617 nm) enters the cell due to membrane damages, which are characteristic for dead or necrotic cells, and subsequently binds to DNA the fluorescence intensity of the dye is enhanced about 40-fold, shown by the red fluorescence in the nuclei.

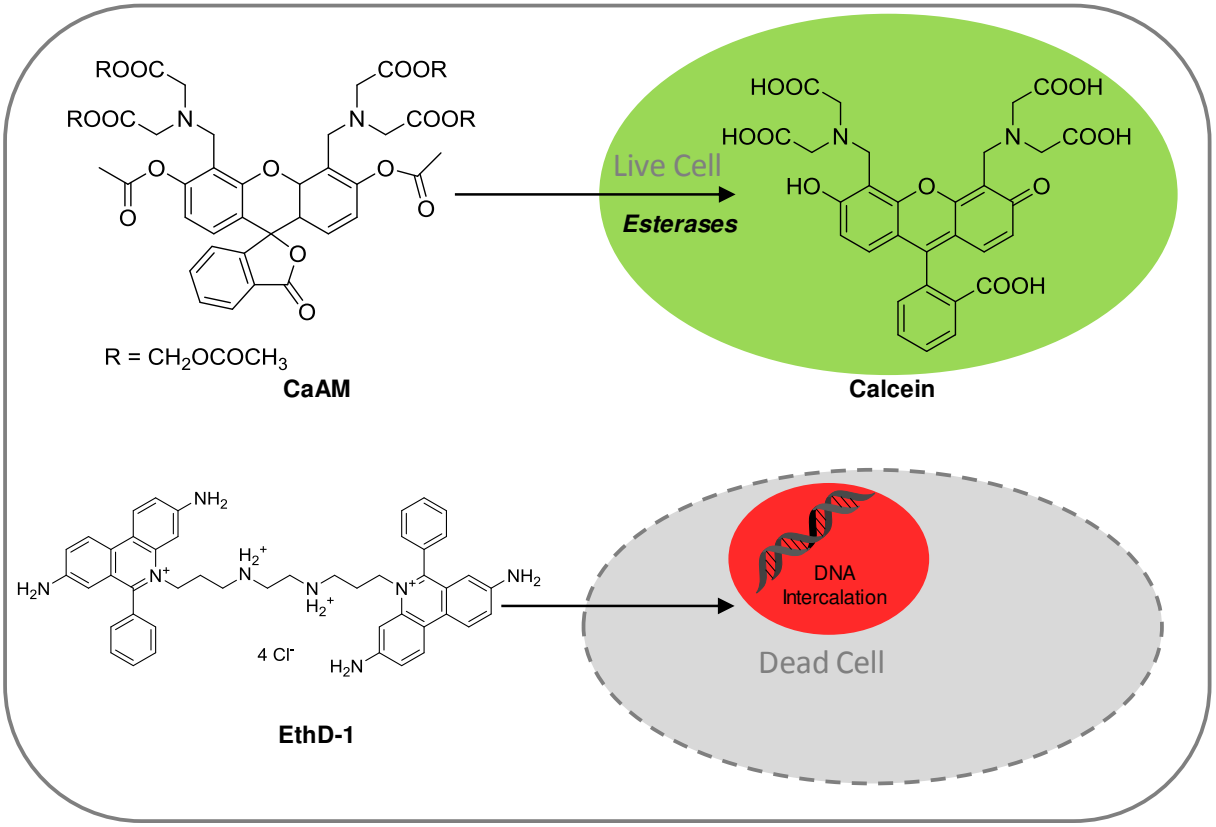

Fig. 3.11: Principle of the Live/Dead® Cell Viability Assay: Living cells show a green cytoplasmic fluorescence, whereas dead cells show a characteristic red fluorescence in the cell nuclei.

For the live/dead stain, these two dyes were applied in combination or individually using the following standard protocol:

A 2 mM stock solution of EthD-1 (in DMSO/H_2O) was diluted in PBS^{++} to a final concentration of 4 µM and the stock solution of CaAM, available in a concentration of 4 mM or 1 mM, was diluted to a working concentration of 1 µM - 3 µM. First, cells were carefully washed once with PBS^{++} and then the freshly prepared staining solution of CaAM and EthD-1 in PBS^{++} was added and incubated for 30 min at 37 °C in the dark. Afterwards, the staining solution was

either removed and cells were washed with PBS^{++} or cells were analyzed microscopically in presence of the staining solution depending on the experiment.

3.4.2.3 Actin Cytoskeleton Staining with TRITC/Alexa Phalloidin

Actin cytoskeleton was stained using a fluorescently labeled phalloidin, a fungal phallotoxin (*Amanita phalloides*) which has a strong affinity to filamentous actin structures. Thereby, phalloidin disturbs the dynamics of filament disassembly.

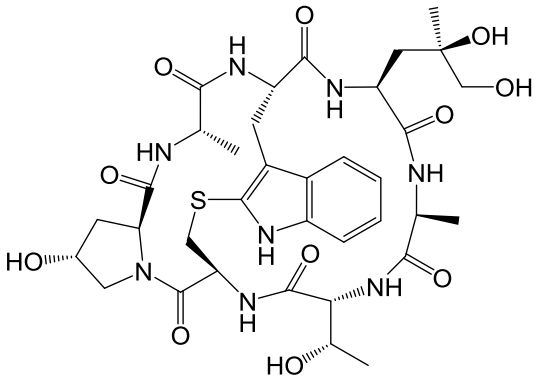

Fig. 3.12: Chemical structure of phalloidin.

In this work, two different fluorescently labeled phalloidins were used: TRITC phalloidin (*tetramethyl rhodamine-isothiocyanate*) with an excitation of the fluorophore at 550 nm and an emission at 570 nm or Alexa Fluor® 488 phalloidin, a green fluorescent dye which is excited at 495 nm and has a characteristic emission at 518 nm.

For visualizing the cytoskeleton, cells were fixed and permeabilized as described above. Afterwards, cells were incubated with a freshly prepared staining solution containing 3 µg/mL TRITC phalloidin or 87 µg/mL Alexa Fluor® 488 phalloidin for 40 min at 37 °C. The corresponding stock solutions containing 0.3 mg/mL TRITC-labeled or 8.7 mg/mL Alexa Fluor® 488-labeled phalloidin in ethanol were stored at - 20 °C. After removing the staining solution, cells were washed three times with PBS^{++} to get rid of unbound dye.

3.4.2.4 Cell Nuclei Staining with DAPI

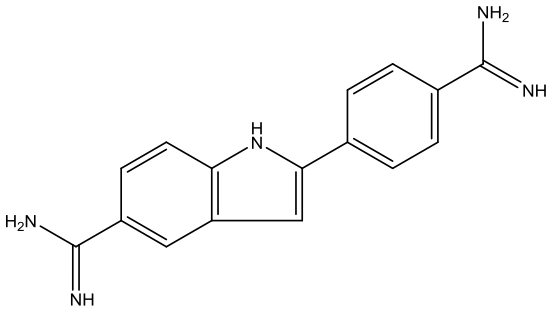

Fig. 3.13: Chemical Structure of DAPI.

For staining the cell nuclei, the blue fluorescent DAPI (*4',6-diamidino-2-phenylindole*) (ex. /em. 358 nm/ 461 nm) was used. DAPI binds strongly to the minor groove of AT-rich parts in the double stranded DNA and by intercalation the fluorescence intensity is enhanced about 20-fold. In order to stain the DNA content of mammalian cells, they were fixed and

permeabilized using the standard protocol. Subsequently, a 100 ng/mL DAPI stock solution was diluted 1:10 in PBS^{++}, and cells were incubated with 10 ng/mL staining solution for ~ 1 min. Afterwards, cells were washed three times with PBS^{++} to remove unbound dye.

3.4.2.5 Membrane Staining with DiI

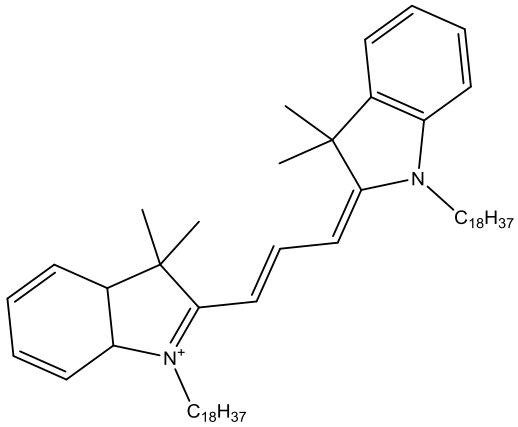

Fig. 3.14: Chemical structure of DiI.

By using the lipid soluble stain DiI (*1,1'–dioctadecyl-3,3,3',3'- tetramethylindocarbocyanine*) the cell membrane of mammalian cells was labeled and visualized for microscopic purposes. This fluorescent dye, with a characteristic excitation at 549 nm and an emission at 565 nm, selectively labels cell membranes by intercalating the two C_{18}-hydrocarbon chains into the lipid bilayer.

The stock solution of DiI (3 mg/mL in DMF) was ultrasonicated for 10 min before preparing a 1:1000 dilution in PBS^{++}. After removal of the culture medium and washing the cells with PBS^{++} the DiI staining solution was added and incubated by slightly shaking the substrate with the cells for 30 min. Cells were washed twice with PBS^{++} and then analyzed microscopically.

3.4.2.6 Immunostaining of Occludin

For visualizing the tight junction protein occludin, a classical indirect immunostaining was performed using a monoclonal, primary antibody against occludin and a polyclonal secondary antibody, which binds to the constant region of the primary antibody and is labeled with a fluorescent dye. The applied antibodies are characterized in **Tab. 3.8**.

Tab. 3.8: Antibodies used for the indirect immunostaining of occludin.

Antibody	Type	Donor Species	Concentration	Supplier
Anti-occludin	Primary, monoclonal, unlabeled	Mouse	2.5 µg/mL	invitrogen
Anti-mouse	Secondary, polyclonal, Alexa Fluor®546	Rabbit	8 µg/mL	invitrogen

Cells were fixed and permeabilized as described in **chapter 3.4.2.1.** Cells were incubated with 3 % (w/v) BSA (*bovine serum albumin*) in PBS^{++} for 20 min at 37 °C to block unspecific binding sites for the antibodies. After removing BSA, cells were incubated with the primary anti-occludin antibody, diluted 1:200 in PBS^{++} supplemented by 0.5 % (w/v) BSA for 60 min at 37 °C. Then, cells were washed twice with PBS^{++} to remove unbound antibody followed by the addition of a 1:250 dilution of the anti-mouse-Alexa Fluor® 546 secondary antibody (dissolved in PBS^{++} supplemented by 0.5 % (w/v) BSA). Cells were incubated for 40 min at 37 °C and finally washed three times with PBS^{++}.

3.4.2.7 PrestoBlue® Assay

The PrestoBlue® cell viability assay (Invitrogen) was applied to identify a potential cytotoxicity of particles or substances. It detects the mitochondrial (metabolic) activity of cells and was performed according to the manufacturer's instructions. NRK cells were seeded in a 96-well plate and grown to confluence. One day before the assay was started the cell culture medium was replaced by fresh medium to ensure a standardized metabolic situation during particle /substance exposure. Cells were usually incubated with different concentrations of particles/substances made up in culture medium or buffer for 24 h. One hour before terminating the incubation 0.5 % (v/v) Triton X-100 was added to those wells used as positive controls to induce cell lysis. The supernatant media was then removed and replaced by 100 µL – 200 µL PrestoBlue® reagent (diluted 1:10 in PBS^{++}). After 1 – 2 h of incubation at 37 °C in the dark, fluorescence was recorded at 590 nm at an excitation wavelength of 544 nm using an Ascent Reader (Labsystems).

4 Systematic Characterization of the Monitoring Parameters Based On the ECIS Model

4.1 Introducing Remarks

Impedance recordings of a system under study are used for an integral description or they are further analyzed in order to determine the individual impedance contributions arising from inherent dielectric features within the sample. Thus, in addition to the experimental analysis of a cell layer on thin-film electrodes, this system can be dissected by theoretical modeling (**Fig. 4.1**). These theoretical models are based on equivalent circuits or differential equations.

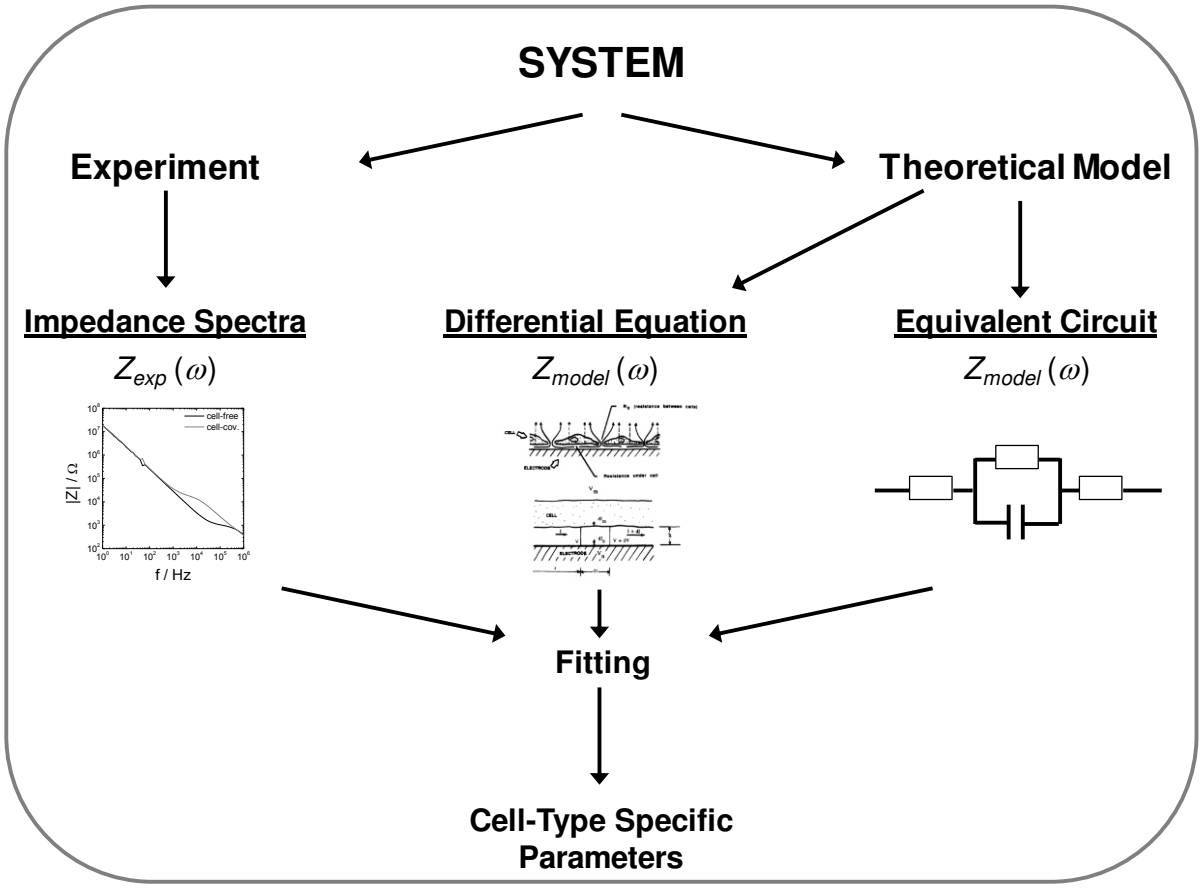

Fig. 4.1: A cellular system can be characterized using impedance measurements or theoretical models. Theoretically, the system can be described using equivalent circuit models or by differential equations. The theoretical models enable a separation of the total signal into individual, specific parameters. Scheme of $Z_{model}(\omega)$ was adapted from Giaever and Keese (1991) [121].

A common technique to analyze impedance data is to create an equivalent circuit using ideal and empirical circuit elements. Ideally, the equivalent circuit represents the same frequency-dependent electric properties as the biological system under study. The corresponding equivalent circuit models for cell-free (**A**) and cell-covered (**B**) gold-film electrodes are provided in **Fig. 4.2**.

A cell-free electrode submersed in medium or buffer can be described by an equivalent circuit consisting of a constant phase element (CPE) connected to an ohmic resistor (R_{bulk}) in series [123]. To describe the impedance contributions of the cell layer an additional frequency-

dependent impedance element (Z_{cl}) is added in series with R_{bulk} and CPE. The total impedance is then calculated in consideration of Ohm's and Kirchhoff's laws (**Fig. 3.3**).

R_{bulk} represents the resistive contribution of the bulk electrolyte. In one ideal element it combines the resistance of the electrolyte itself and the additional constriction resistance due to the electric field compression. The empirical CPE characterizes the impedance contributions at the electrode-electrolyte interface. The CPE considers the non-ideal behavior of the gold-film electrode in contact with the electrolyte.

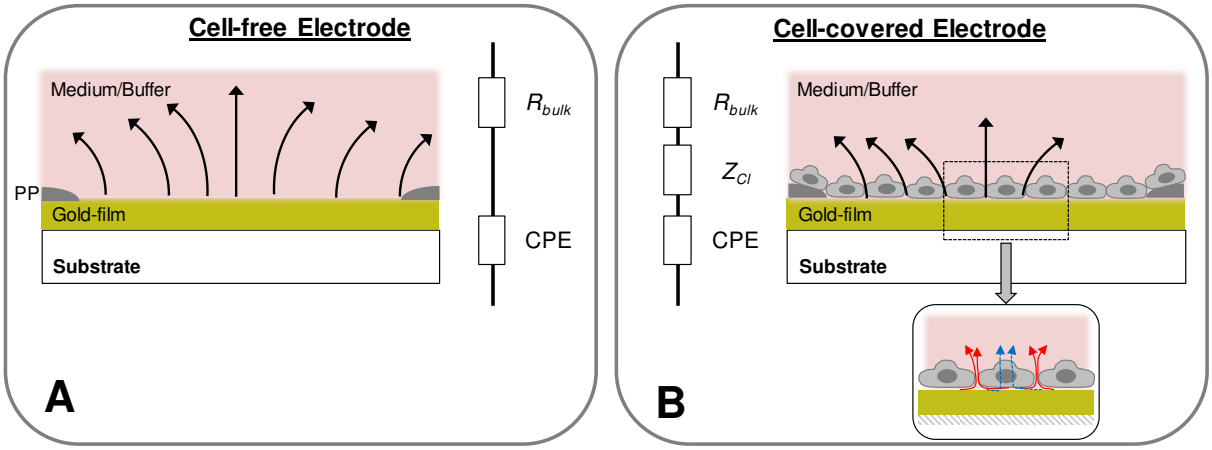

Fig. 4.2: Scheme and corresponding equivalent circuit model for a cell-free (**A**) and cell-covered (**B**) gold-film electrode submersed in medium or buffer. The substrate made of PC or PET is covered with a thin layer of gold. The insulating photopolymer (PP, grey) defines the active area of the gold-film electrodes. **A:** The cell-free electrode can be characterized by a CPE in combination with an ohmic resistor (R_{bulk}) in series. R_{bulk} includes the resistance of the electrolyte and the constriction resistance caused by the electric field compression due to the small working electrode size. **B:** After establishment of a confluent cell layer on the gold-film electrode the equivalent circuit is extended by an additional impedance element (Z_{cl}) in series. Z_{cl} described the frequency-dependent contributions arising from the cell layer as schematically depicted in the insert. For low frequencies (**red**) the current flows through the subcellular gap and through cell-cell-contacts, while for high frequencies (**blue**) the current can couple across the cell membranes.

Current will always take the pathways with the lowest impedance. Therefore, the current flow of a cell-covered electrode can in approximation be separated into two distinct pathways (insert, **Fig. 4.2 B**).

- At low frequencies (≤ 10 kHz) current predominantly passes through the narrow cleft between electrode surface and basal cell membrane before it passes the cell layer into the bulk electrolyte via the paracellular shunt across cell-cell junctions (**red**).
- At high frequencies, current flow is described by the transcellular pathway, where the current couples capacitively through the cell membrane (**blue**).

In between these two extreme situations where the current flow is dominated by one particular pathway, there is a wide frequency range where the current flow is a complex

composition of both ways. In the narrow gap between electrode and cell-membrane the preferred current pathway becomes position-dependent, as current flow across the cell layer faces different impedance contributions arising from the plasma membrane, cell-cell junctions and the subcellular cleft (**Fig. 4.3**). Consequently, in the narrow gap between electrode and cell membrane different position-dependent current pathways exist. However, there is no appropriate equivalent circuit element that can be used to describe the complex situation of frequency- and also position-dependency in the cell-electrode cleft.

The impedance contribution arising from the subcellular cleft can be described by a 2D core-coat conductor, which consists of finite elements of the electrode capacitance (CPE_i) and the membrane capacitance ($C_{basal,\,i}$) as outer dielectric coats and the locally individual finite cleft resistance elements $R_{cleft,i}$ in between [124]. The model based on finite elements of CPE_i, $C_{basal,i}$ and $R_{cleft,i}$ can be applied for the simulation of impedance data.

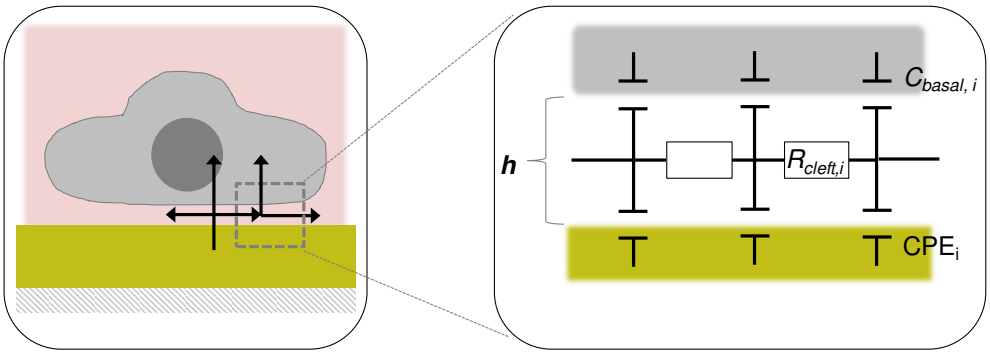

Fig. 4.3: Finite element model of resistance of the aqueous gap between electrode surface and cell membrane. It can be regarded as 2D core-coat conductor with the electrolyte core in the middle, surrounded by electrode surface (CPE_i) and plasma membrane ($C_{basal,i}$). Depending on frequency and position the current flow passes finite elements of R_{cleft} before it flows para- or transcellular into the bulk solution.

4.1.1 The Basic ECIS Model: Core of All Simulation Approaches

In order to achieve a deeper analysis of the frequency-dependent impedance spectra of a cell-covered electrode, Giaever and Kesse (1991) developed a theoretical model, which makes use of a transfer function based on modified Bessel functions [121]. The model, which is based on defined boundary conditions, allows the extraction of three cell-related impedance parameters R_b, α and C_m (**Fig. 4.4**) with,

(i) $\boldsymbol{R_b}$ reflecting the resistance of cell-cell junctions

(ii) $\boldsymbol{\alpha}$ representing the frequency-dependent impedance contributions from cell-matrix adhesion

(iii) $\boldsymbol{C_m}$ quantifying the membrane capacitance

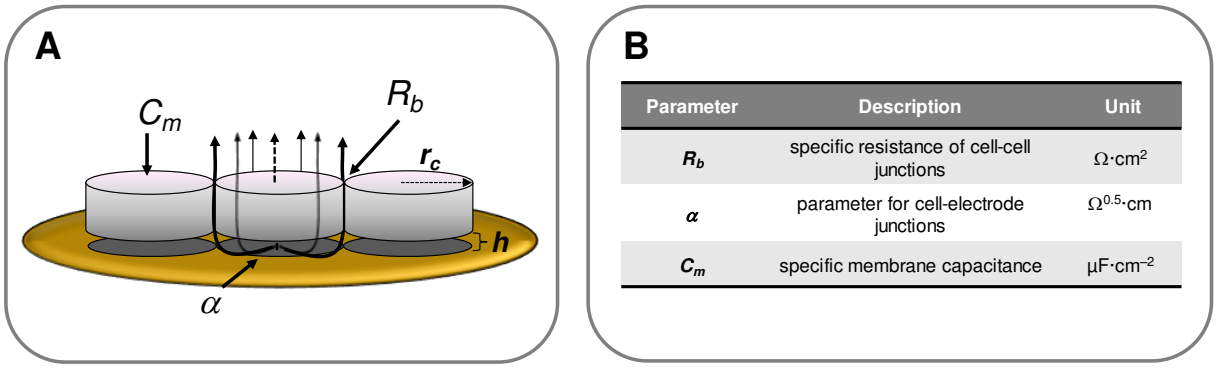

Parameter	Description	Unit
R_b	specific resistance of cell-cell junctions	$\Omega \cdot cm^2$
α	parameter for cell-electrode junctions	$\Omega^{0.5} \cdot cm$
C_m	specific membrane capacitance	$\mu F \cdot cm^{-2}$

Fig. 4.4: Schematic representation of the ECIS model (**A**): Cells are viewed as circular disks, with a radius r_c and located above the electrode surface with a distance *h*. Contributions of the cell layer impedance are quantified by three parameters R_b, α and C_m. R_b describes the resistance of the current pathway, α accounts for the impedance contributions of the cell-electrode junction, and C_m quantifies the capacitive contribution of the plasma membranes. Parameter description and units are provided in (**B**).

In this model cells are regarded as uniform circular disks with a radius r_c, which hover above the electrode surface within a distance *h*. The paracellular and transcellular current flow across the cell layer is indicated by the respective straight and dotted arrow in **Fig. 4.4**. A radial current flow beneath the cell bodies in the cell-electrode space is assumed. Current density across the electrode/electrolyte interface is assumed to be homogeneous.

At low frequencies, the impedance contribution of the cell layer can be described by the parameter α and R_b. R_b represents the impedance contribution due to cell-cell contacts which mirrors the absence or presence of tight junctions and is a measure for the tightness of cell-cell contacts.

The parameter α describes the current flow in the narrow space between electrode and cell membrane and is defined by

$$\alpha = r_c \sqrt{\frac{\rho}{h}} \qquad \textbf{Eq. 4.1}$$

with cell radius r_c, distance between electrode surface and basal membrane h and the specific resistivity of the electrolyte in the gap ρ.

The parameter C_m is dominated by membrane topography and the dielectric properties of the plasma membrane itself. The capacitance C_{cl} of the cell layer is defined by the basal and apical membrane capacitance in series. However, using this model it is only possible to determine the average capacitance of both, apical and basal plasma membranes together and accordingly C_m is defined by the following equation:

$$C_m = 2 \cdot C_{cl} \qquad \textbf{Eq. 4.2}$$

A C_m value significantly different from 1 µF/cm^2 provides an indication for a folded plasma membrane including microvilli or membrane invaginations.

These three cell-related parameters are combined in the following equation to describe the different impedance contributions of a cell layer Z_{total} according to the ECIS model:

$$Z_{total} = \left(\frac{1}{Z_n} \left(\frac{Z_n}{Z_n + Z_m} + \frac{\frac{Z_m}{Z_n + Z_m}}{\frac{\gamma r_c}{2} \cdot \frac{I_0(\gamma r_c)}{I_1(\gamma r_c)} + R_b \left(\frac{1}{Z_n} + \frac{1}{Z_m} \right)} \right) \right)^{-1} \qquad \textbf{Eq. 4.3}$$

with

$$\gamma r_c = r_c \sqrt{\frac{\rho}{h} \left(\frac{1}{Z_n} + \frac{1}{Z_m} \right)} = \alpha \sqrt{\left(\frac{1}{Z_n} + \frac{1}{Z_m} \right)}$$

I_0 and I are modified Bessel functions of the first kind of order 0 and 1, R_b the resistance of cell-cell junctions, ρ the specific electrolyte resistance inside the cell-electrode junction Z_n the impedance of the cell-free electrode and Z_m the total impedance of the apical and basolateral plasma membrane.

The impedance of a cell-free electrode Z_n can be determined in the low frequency range of the spectrum assuming a CPE [123, 124], which indicates a deviation from ideal capacitive behavior of the cell-free electrode determined by the parameter *n*.

$$Z_m = \frac{2}{i\omega\, C_m} \qquad \textbf{Eq. 4.4}$$

$$Z_n = Z_{CPE} = \frac{1}{A(i\omega)^n} \qquad \textbf{Eq. 4.5}$$

with $0 \leq n \leq 1$ and *A* is the boundary resistance

When the transfer function (**Eq. 4.3**) is applied to experimental multi-frequency impedance data of a cell-covered electrode the cell-related parameters can be fitted through a least square optimization algorithm. By applying such analysis on MFT data time-dependent changes in R_b, α and C_m can be extracted.

It should be emphasized once more that the model provided by Giaever and Keese is a non-redundant model to describe the cell-covered gold-film electrode. But the model is only valid when the electrode is completely occupied with uniform and circular-shaped cells. As however different cell types express variable morphologies, cell geometry is a crucial parameter to consider when modeling impedance data. Therefore, Lo and Ferrier (1998) presented an adaption of the basic ECIS model to account for elliptical cells. A remaining drawback of this approach is, however, that the two elliptical axes of the cell type under study have to be determined by microscopic analysis [125]. Lo et al. (1995) considered three different current pathways from the electrode through the cells: In addition to the common paracellular and transcellular current flow the group also included a pathway were current flows in through the lateral membrane and out through the apical membrane [126]. The expansion of the popular ECIS model by additional parameters makes the model redundant and only applicable for simulation.

4.1.2 Simulation Using a LabVIEW-Based Software

As a part of this work, impedance spectra were simulated based on the model of Giaever and Keese using a LabVIEW-based software, written by J. Wegener. The simulation parameters include some experimental determinants, such as electrode size and R_{bulk}. The electrode-type specific area for 8W1E and 8W10E electrodes and the corresponding R_{bulk} values are listed in **Tab. 4.1**. Z_{CPE} is characterized by the parameters A and n. At low frequencies the CPE dominates the impedance spectra whereas R_{bulk} is pronounced in the high frequency range ($> 10^5$ Hz) (**Fig. 4.5**).

Tab. 4.1: Overview of the electrode-type specific parameters used for simulations.

Electrode Type	Area / cm^2	R_{bulk} / Ω	A / $Fs^{n-1} \cdot cm^{-2}$	n
8W1E	$5 \cdot 10^{-4}$	1000	$1.50 \cdot 10^{-5}$	0.95
8W10E	$5 \cdot 10^{-3}$	350	$1.50 \cdot 10^{-5}$	0.95

To simulate the cell-covered impedance spectra, different values for R_b, α and C_m are used and the corresponding Z_{total} is calculated based on the transfer function (**Eq. 4.3**) using the LabVIEW-based software. Establishment of a confluent cell layer on top of the gold-film electrodes causes an increase in impedance in a defined frequency range, creating a shoulder like distortion in the spectrum. The height, width and slope of this shoulder in the impedance spectrum is dependent on the cell-type and therefore on the parameters R_b, α and C_m. As the complex impedance can be split into its real and imaginary part, the simulation software also enables to analyze corresponding changes in the resistance and capacitance spectra.

To illustrate the influence of the cell-related parameters on impedance magnitude $|Z|$ the simulation software was used to generate impedance spectra using defined values for R_b, α and C_m. During the simulation only one parameter was changed, while the other two remained constant. The respective responses of $|Z|$ to changes in R_b, α and C_m are summarized in **Fig. 4.5**.

Changes in R_b ($25 – 200\ \Omega \cdot cm^2$), which mirror alterations in the tightness of cell-cell junctions, are pronounced in the frequency range between 60 – 400 Hz (**A**). An increase in R_b causes a shift of the plateau value to higher impedance values. It simulated the situation that the tightness of cell-barrier function is increasing. The other parts of the spectra are unaffected by changes in R_b. When parameter α is increased stepwise from $5 – 60\ \Omega^{0.5} \cdot cm$

(**B**) changes in the slope of the impedance spectrum are found and the changes are observed in a frequency range between 10 – 4000 Hz. Changes in the parameter C_m (0.5 – 3 µF/cm^2), which defines the membrane capacitance within a cell layer alter the spectrum in the high frequency range between 10^4 – 10^6 Hz (**C**). Here, a shift of the shoulder to lower frequencies is found by increasing C_m.

The physical ECIS model with a minimum of parameters provides a non-redundant model which completely describes the frequency-dependent impedance of a cell-covered electrode. Moreover, the survey of simulated impedance spectra presented in **Fig. 4.5** clearly demonstrates that the ECIS model allows distinguishing between changes in the three parameters R_b, α and C_m such that these can be analyzed separately.

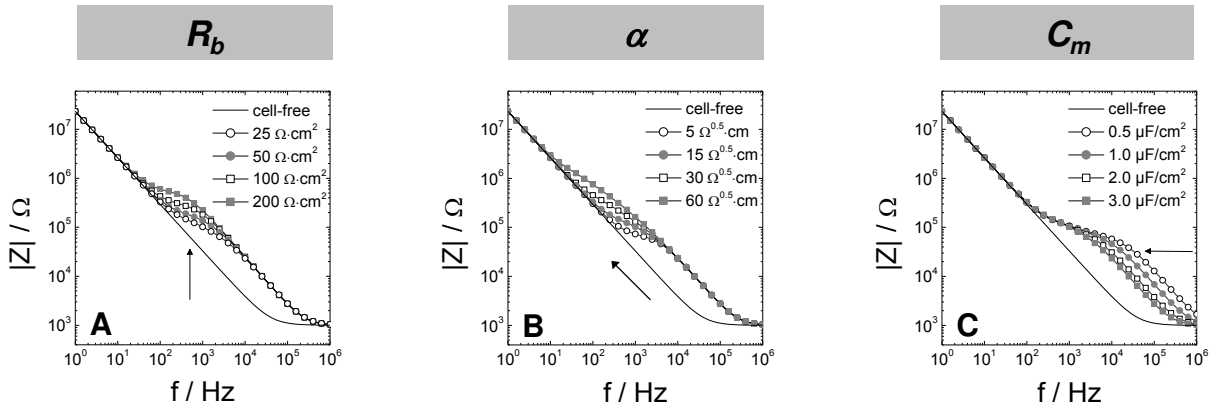

Fig. 4.5: Simulated impedance spectra for cell-free (line) and cell-covered (symbols) 8W1E electrodes using different cell-related parameters R_b, α and C_m. **A:** Variation of R_b (25 – 200 Ω·cm^2), α = 15 Ω$^{0.5}$·cm, C_m = 3 µF/cm^2, **B:** Variation of α (5 – 60 Ω$^{0.5}$·cm), R_b = 25 Ω·cm^2, C_m = 3 µF/cm^2, **C:** Variation of C_m (0.5 – 3 µF/cm^2), R_b = 25 Ω·cm^2, α = 15 Ω$^{0.5}$·cm. Parameters for the 8W1E electrodes were used as specified in **Tab. 4.1**.

4.2 Objective

The aim of this chapter was to attain a better understanding for the frequency-dependent impedance of cell-covered electrodes and to avoid misinterpretation of experimental data. Two aspects should be analyzed in more detail using simulations, which are based on the well-known ECIS model:

(i) the influence of the cell-related parameter R_b, used as indicator for barrier function, on changes in $|Z|$ and R at different frequencies and

(ii) the influence of different sorts of inhomogeneity within the cell layer on measurement outcome, regarding the monitoring parameters $|Z|$, R and C as a function of f

Resistance at a frequency of 4 kHz is frequently used as the preferred parameter to monitor barrier function in epithelial and endothelial cells. This approach, however, bears the risk of data misinterpretation due to the frequency dependent behavior of resistance. This work should provide a systematic guideline for correct data interpretation in the future.

Moreover, inhomogeneity within the cell layers has been suspected to have major influence on overall outcome of data modelling and interpretation, but has not been studied systematically. Here, different scenarios were simulated and supported by experimental data to show their quantitative effects on typical monitoring parameters $|Z|$, R and C.

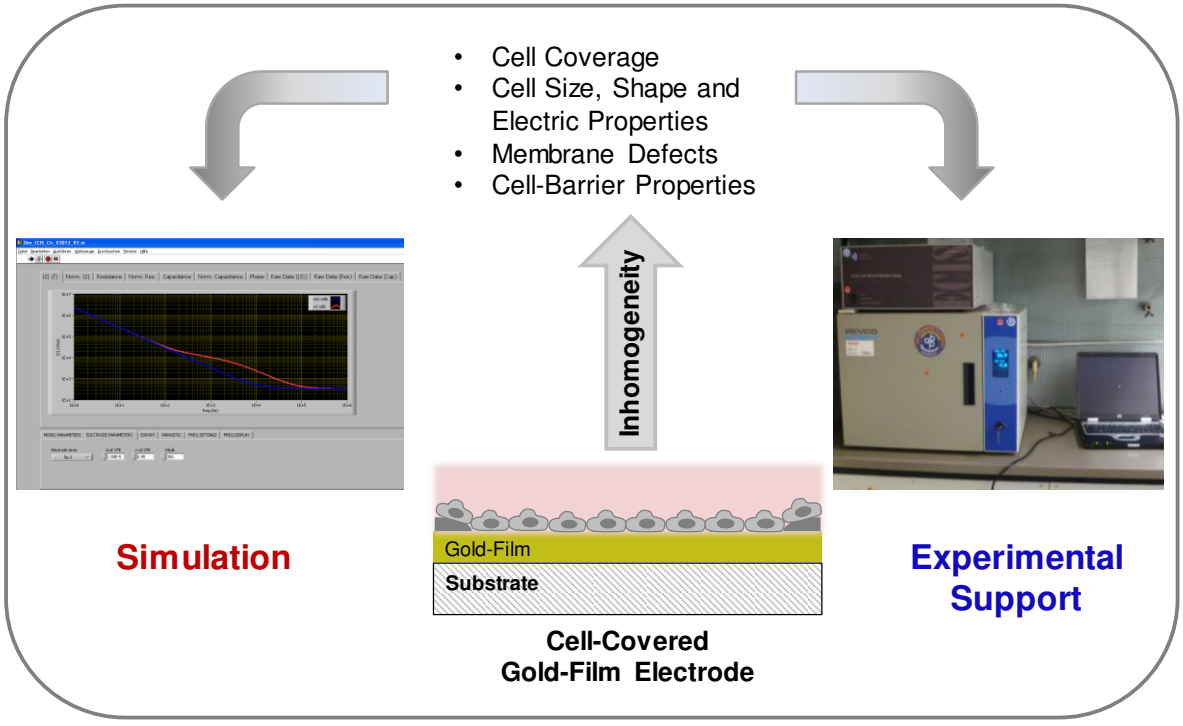

Fig. 4.6: Overview of the simulation project where the results of the computed data were compared and supported by experimental data.

4.3 Materials and Methods

4.3.1 Impedimetric Analysis to Support Simulation Results

4.3.1.1 Treatment with Cytochalasin D

For monitoring the effect of cytochalasin D on the epithelial barrier function of MDCK II cells, cells were grown to confluence on 8W1E or 8W10E electrodes. One day prior to the experiment culture medium was exchanged. To record a baseline in MFT mode, cells were incubated with 200 µL culture medium supplemented with 5 % FCS for ~ 1 h. A 5 mg/mL cytochalasin D stock solution (in DMSO, stored at -20 °C) was diluted in culture medium to a final concentration of 4 µg/mL (8 µM). After recording the baseline, 200 µL of cytochalasin D was added to the cells to yield a final concentration of 4 µM and impedance changes during and after treatment were monitored with non-invasive ECIS recordings. To analyze if impedimetric changes are due to introducing DMSO or only due to the addition itself, DMSO or culture medium was added to individual wells as control. The cellular response was detected over several hours and changes in impedance and resistance signals were extracted at 500 Hz, 4 kHz and 32 kHz.

To analyze reversibility of the effect of cytochalasin D on binding to actin, cells were prepared as described above. After the addition of 4 µM cytochalasin D, the effect of cytochalasin D on epithelial barrier function was monitored for at least 1.5 h. Afterwards, cytochalasin D solution was aspirated, cells were washed once with medium and finally 300 µL medium were added under the laminar flow hood. Immediately after the exchange ECIS recording was resumed and recovery was monitored in a time-resolved manner.

4.3.1.2 Cell Seeding In Absence or Presence of Calcium

Seeding of MDCK II cells in absence or presence of Ca^{2+} was analyzed with non-invasive ECIS recordings using a 8W10E or 8W1E electrode layout. Cells were trypsinized using the MDCK II-specific protocol (**chapter 3.1.2**). After centrifugation, cells were resuspended either in $EBSS^{++}$ containing both, Ca^{2+} and Mg^{2+}, $EBSS^{--}$ supplemented with 0.5 mM Mg^{2+} or $EBSS^{--}$ supplemented with 1 mM Ca^{2+}. Cells were counted using a Bürker hemocytometer and seeded upon fibronectin coated (50 µg/mL, 60 min, RT) electrodes using a density of 495 000 cells/cm^2 in the corresponding buffer. Cell adhesion and spreading was monitored over 20 h following impedance or resistance at 500 Hz, 4 kHz or 32 kHz.

4.3.1.3 Co-Culture of Different Cell Types

Co-cultures were established using NRK cells (designated as cell type A) in combination with MDCK II pABCG2 EYFP cells (cell type B). For this experiment cells were trypsinized using the cell type specific protocol and suspensions were diluted to a density of 500 000 cells/mL. In the following step, cell types were mixed in different ratios (100 % A, 75 % A + 25 % B, 50 % A + 50 % B, 25 % A + 75 % B, 100 % B) and seeded on 8W10E electrode arrays using a final cell number of 250 000 cells/cm^2. Finally, cell adhesion and spreading was monitored over at least 24 h. Data was analyzed using the impedance, resistance and capacitance at 500 Hz, 4 kHz and 32 kHz. Since MDCK II pABCG2 EYFP cells express a yellow fluorescent membrane protein electrode coverage with this cell-type was visualized by confocal laser scanning microscopy.

4.3.1.4 Membrane Opening Due To Saponin Treatment

MDCK II cells were grown to confluence on a 8W10E electrode layout. One day prior to the experiment the culture medium was exchanged. Baseline was recorded in culture medium or EBSS^{++}. Saponin dilutions to final concentrations of 0.02 % or 0.03 % were made from a freshly-prepared saponin stock solution (1 % in EBSS^{++}). After recording a short baseline, saponin was added and changes in $|Z|$, R and C were analyzed at 500 Hz, 4 kHz and 32 kHz.

4.3.1.5 Special Electrode Layouts for Impedance Recordings

To support simulations in which the electrode coverage was modified ranging from cell-free to completely cell-covered with defined degrees of cell coverages it was necessary to create a large cell culturing chamber on top of the array that encompasses all eight working electrodes and the common counter electrode (**Fig. 4.7**). For this purpose, the base of a commercially available 8W1E electrode layout, without the 8-well-chamber (**A**), was equipped with a self-made PDMS chamber. The PDMS chamber was cut from a ~ 0.5 cm thick PDMS layer to a size of ~ 2 cm x 5 cm. The chamber was mounted with silicon glue onto the base with the electrode layout (**B**). To guarantee sterile conditions and prevent fluid evaporation during cell culture and measurements the PDMS chamber was capped with a polystyrene lid (**C**). The modified electrode array was kept in argon plasma for 30 s before cell culture use. For cell seeding as well as for cell cultivation a volume of 2 mL was used.

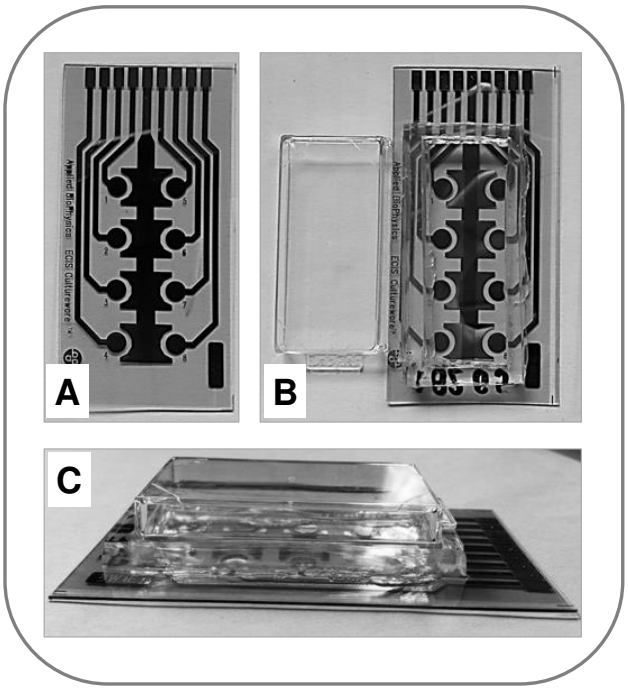

Fig. 4.7: Modified 8W1E gold-film electrode layout for the experimental support of the simulation regarding varying electrode coverage with cells. A plain 8W1E array base, without 8-well-chamber, was used (**A**). A PDMS frame was glued on top of the Lexan® substrate surrounding all eight working electrodes. Top view (**B**) and side view (**C**) of the modified electrode array.

In order to mimic the effect of gradual electrode coverage, MDCK II cells were seeded in a density of 600 000 cells/mL (V = 2 mL) into the PDMS reservoir of the modified 8W1E array. 24 h before the experiment was started culture medium was exchanged. After recording a baseline, the cells on a single electrode (electrode A) were wounded by applying an invasive wounding pulse (40 kHz, 5 V, 1.25 s or 15 s). Afterwards, three spectra of electrode A against the common counter electrode were measured in the normal ECIS mode. Subsequently, the measurement was switched to a second measurement type, in which all eight electrodes were arranged in parallel and measured against the common counter electrode. Three spectra of this “8 against CE” designated measurement mode were recorded, before switching back to normal mode and repeating the cycle initiated by wounding pulse application on electrode B. The purpose of the “8 against CE” mode is that it allows an exact description of the electrode coverage when used in combination with consecutive wounding of individual electrodes. The described cycle was repeated until all eight electrodes were wounded reflecting the situation of 0 % electrode coverage. Changes in $|Z|$, R and C were extracted at 500 Hz, 4 kHz and 32 kHz.

The analysis of electrode coverage in presence of $[Fe(CN)_6]^{3-/4-}$ was performed using the same protocol as described above, except that the measurement was performed in presence of 2 mM $[Fe(CN)_6]^{3-/4-}$ in culture medium.

4.3.2 Microscopic Monitoring of Membrane Disruption after Saponin Treatment

Microscopic analysis was performed with a confocal laser scanning microscope together with a temperature-controlled stage to keep the temperature at 37 °C during the entire experiment. MDCK II cells were grown to confluence in a petridish (9.5 cm^2) and the medium was exchanged one day prior to the experiment. In the beginning of the experiment the medium was removed, 1 mL PBS^{++} was added and cells were equilibrated for 30 min at 37 °C under atmospheric CO_2 environment. Saponin dilutions were made from a freshly-prepared 1 % saponin stock solution (in PBS^{++}) and diluted with FITC dextran solution (1 mg/mL, PBS^{++}) to final concentrations of 0.02 % or 0.03 %. Cells were placed in the 37 °C heating device and PBS^{++} was replaced by the saponin-containing FITC dextran solution. Confocal microscopic analysis was performed using a 60 x objective. To monitor changes in cell layer integrity a defined, optical xy-plane pre-set in z-direction was selected and observed in a time-dependent manner.

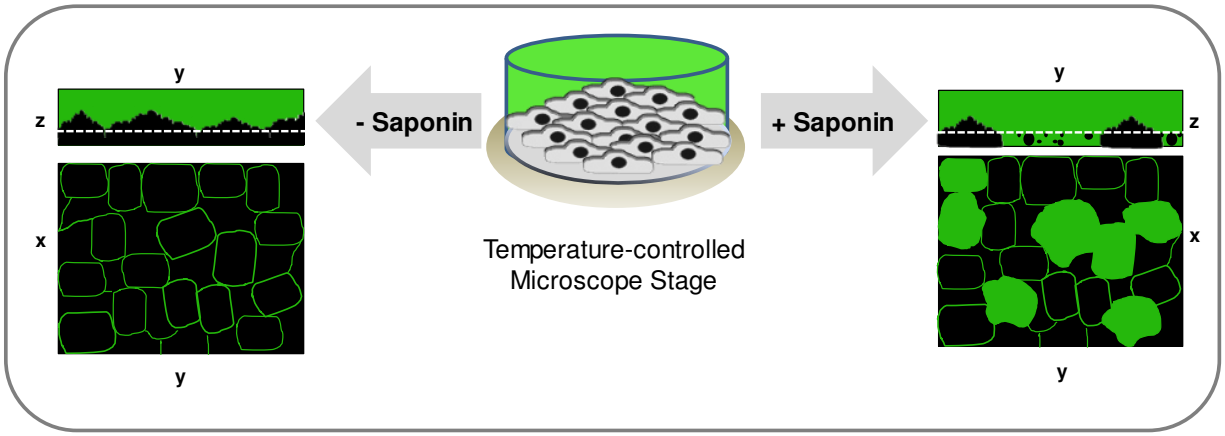

Fig. 4.8: Schematic presentation of the microscopic analysis of membrane opening due to the addition of saponin using an extracellular, green-fluorescent FITC dextran solution for contrast. As long as the plasma membrane stayed intact, FITC dextran solution was excluded from cells' interior and cytoplasm remained dark. After disruption of the membrane integrity by saponin, FITC dextran could diffuse into the cytoplasm leading to a green fluorescence signal.

Image analysis was performed using ImageJ. The contrast was enhanced by about 0.4 % and subsequently the pixels above a brightness threshold of 125 were analyzed for each micrograph.

4.3.3 Dye Diffusion across an Epithelial Cell Monolayer after Cytochalasin D Treatment

Epithelial MDCK II cells were cultured on a porous filter membrane (Corning) until reaching confluence. The polycarbonate membrane has a thickness of 10 µm and a pore density of $1 \cdot 10^8$ pores/cm^2, each pore with a diameter of 0.4 µm. One day prior to the experiment the culture medium was exchanged. For the experiment 500 µL FITC dextran solution (4 kDa, 2 mg/mL in PBS^{++}) was added to the upper compartment and the dye flux into the lower compartment (1.5 mL PBS^{++}) across an untreated MDCK II cell layer was monitored over 60 min. After recording a baseline over 60 min 4 µM cytochalasin D or 0.4 ‰ DMSO as control were added to the lower compartment. Afterwards, the permeation of FITC dextran across the untreated MDCK II layer and after opening epithelial junctions with cytochalasin D was measured over 3 h (**Fig. 4.9**). Cells were kept at 37 °C and cells were removed from the incubator only for the measurement. The fluorescence intensity of the buffer in the lower compartment was measured every 10 min with an Ascent Reader (λ_{exc} = 485 nm / λ_{em} = 538 nm). Therefore, filters were placed in empty wells of a 12-well-plate and immediately after measurement each filter was returned in its respective well. In each well 97 different positions were measured and the mean value as well as standard error was calculated. Afterwards, data were corrected for the fluorescence intensity of PBS^{++} resulting in ΔI_{538nm}.

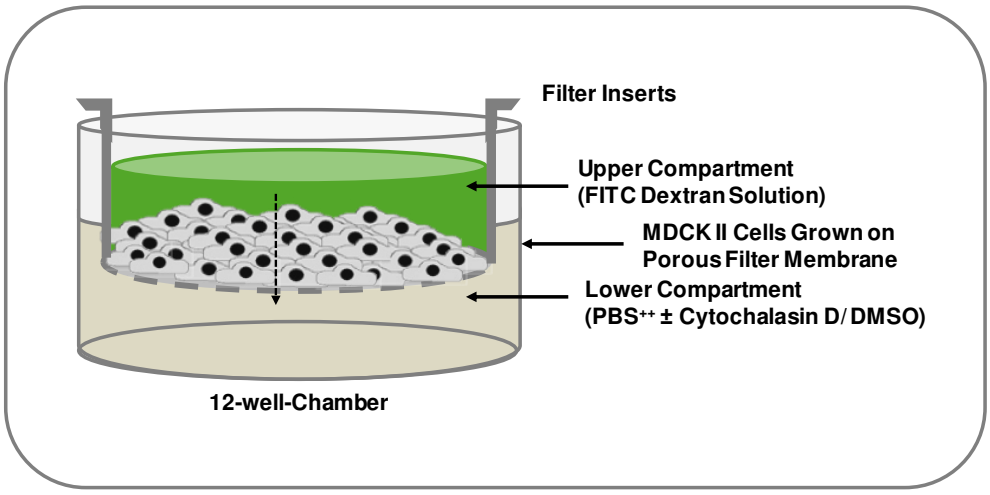

Fig. 4.9: Schematic presentation of the filter experiments: MDCK II cells were grown on porous filter membranes and diffusion of FITC dextran solution from the upper into the lower compartment after cytochalasin D treatment was analyzed in a time-dependent manner.

4.4 Opening and Closing of Intercellular Junctions

Throughout the ECIS literature the resistance is commonly used as a measure for the permeability of endothelial or epithelial cell layers [110, 127]. Historically, 4 kHz is the preferred frequency to monitor barrier function, which simplifies the comparison with other studies in literature. The analysis of endothelial barrier function with non-invasive ECIS recordings was first introduced by Tiruppathi et al. (1992), who exposed bovine pulmonary microvascular endothelial cells, grown on gold-film electrodes, to α-thrombin in varying concentrations. The changes in the endothelial barrier, as a result of thrombin-mediated disruption of cell-cell junctions, were analyzed using the resistance at 4 kHz [128]. Immediately after the addition of thrombin a biphasic decrease in R_{4kHz} was found which was related to an increase in endothelial permeability. In the following, also Ellis et al. (1999) focused on the effect of thrombin and histamine on human pulmonary artery endothelial cells using impedance sensing [129]. Hartmann et al. (2007) further addressed the maturation of endothelial barrier by brain capillary endothelial cells on differently pre-coated ECIS electrodes, but using the resistance at 400 Hz [110]. Additionally, other studies focused on endothelial barrier function under different conditions like disturbed flow fields [130] or cyclic stretch [131] using ECIS.

An increase in resistance is interpreted as a strengthening of endothelial or epithelial barrier function and vice versa. This interpretation is straightforward and intuitive in particular as the *transepithelial electrical resistance* (TER) has been used as a measure for endothelial and epithelial tightness for decades [132-134]. However, this interpretation may fail in certain cases when the native resistance readings recorded by ECIS are used, and especially when cells are characterized by a high R_b value.

In this part of the thesis the ambiguities of resistance readings were investigated using MDCK II cells as model cell line for moderately tight epithelial cells. The effect of an increase or decrease of R_b was analyzed theoretically and supported by experimental data on changes in epithelial barrier properties.

Experimental support for the conclusions was gathered in two ways addressing disruption and formation of cell-cell junctions:

(i) Established epithelial cell layers were treated with cytochalasin D, an actin cytoskeleton disrupting drug, which leads to destabilization and finally opening of intercellular junctions. ECIS data was recorded during exposure and analyzed for the frequency-dependent changes in resistance and impedance.

(ii) Suspended epithelial cells were seeded on ECIS electrode and the *de novo* formation of epithelial junctions was monitored for ~ 20 h by multi-frequency ECIS readings in presence and absence of Ca^{2+}. It is well-known that Ca^{2+} is needed in the medium for cell-cell junctions to form [135-137].

Additionally, the effect of cytochalasin D on MDCK II barrier function was analyzed in a classical permeation assay, where cells were cultured on porous filter substrates and dye diffusion between two compartments across the cell layer is measured. In this study, FITC dextran diffusion from the upper into the lower compartment was monitored in absence or presence of cytochalasin D.

Our LabVIEW-based software allows simulation of opening and closing cell barriers by varying values for R_b. By stepwise reducing R_b, the corresponding increase in intercellular permeability of a cell layer is simulated. The accompanying changes in resistance and impedance at 500 Hz, 4 kHz and 32 kHz were extracted and analyzed in a frequency-dependent manner.

4.4.1 Quantification of Dye Diffusion through Layers of MDCK II Cells after Cytochalasin D Treatment

Dye diffusion through a confluent cell monolayer grown on a porous filter membrane is a common technique to characterize the barrier function of a cell layer [138-140]. In this experiment the flux of a fluorescent dye (FITC dextran, 4 kDa in PBS^{++}) from the top chamber into the bottom chamber across a confluent MDCK II cell layer was measured. Cytochalasin D was chosen as model substance to manipulate the tightness of epithelial cell layers. It is known to open intercellular junctions and is widespread in literature to manipulate the integrity of cell barrier function [132, 141, 142]. Cytochalasin D inhibits the dynamic polymerization of actin monomers at the end of actin filaments [116] and causes a reduction of filamentous actin. In literature a concentration of 4 µM cytochalasin D is described to increase tight junction permeability in MDCK cells which is reflected by a significant decrease in TER by 42 % within 60 min [143].

To quantify the dynamic changes in barrier function upon exposure to cytochalasin D, the time-dependent permeation of FITC dextran across MDCK II cell layers was determined in absence and in presence of 4 µM cytochalasin D.

Fig. 4.10 visualizes the changes in the epithelial barrier function of MDCK II cells after the addition of cytochalasin D (t = 60 min, ↓). Fluorescence intensity of the lower compartment

was monitored over 60 min to establish the basal permeability of an untreated MDCK II cell layer. $\Delta I_{538\,nm}$ only showed a minimal increase to 1.3 ± 0.1 (●) and 1.0 ± 0.1 (□), respectively, indicating nearly no dye flux through the intact cell layer. After 60 min either 0.4 ‰ DMSO (□) as control or 4 µM cytochalasin D (●) were added and a clear difference between control cells and cells treated with the actin-binding drug was found.

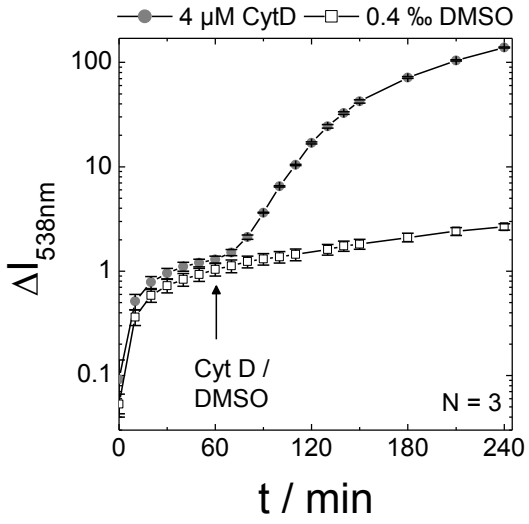

Fig. 4.10: Influence of 4 µM cytochalasin D (Cyt D) on epithelial barrier function: Time-course of fluorescence intensity ($\Delta I_{538\,nm}$) in the lower compartment before and after addition of 4 µM Cyt D (●) or 0.4 ‰ DMSO (□). Time-point of addition (t = 60 min) is indicated by the arrow. After weakening of epithelial barrier function by Cyt D the fluorescence intensity increased, whereas DMSO did not have any significant influence on MDCK II barrier function. Over 4 h there was nearly no dye diffusion of FITC dextran from the upper compartment to the lower under control conditions (Mean ± SE; N = 3).

A constant increase in fluorescence intensity due to increasing permeation of the FITC-labeled tracer from the upper to the lower compartment was monitored whereas the control population in presence of 0.4 ‰ DMSO nearly showed a constant $\Delta I_{538\,nm}$-value over time. Three hours after addition, MDCK II cells in presence of cytochalasin D showed a high fluorescence intensity of 139 ± 1 compared to the control population with 2.7 ± 0.2 indicating the loss of epithelial barrier function in presence of the actin-binding drug. This classical assay clearly demonstrated that 4 µM cytochalasin D significantly reduced the tightness of epithelial barrier function.

4.4.2 Destruction of Epithelial Barrier Function after Treatment with Cytochalasin D Monitored with ECIS

The classic filter experiment to study cell barrier function (**Fig. 4.10**) clearly showed an increasing permeability for FITC dextran over time which is an evidence of the loss of tight junctions after cytochalasin D treatment.

Time-resolved ECIS-measurements enable monitoring of the response of MDCK II cells after the addition of cytochalasin D at different frequencies. The impedance recordings were performed with two different electrode layouts containing ten electrodes (8W10E) or one working electrode (8W1E) per well.

First, the experiment was performed with the cells on the 8W10E electrode layout. After recording a short baseline, Cytochalasin D, DMSO or medium as control were added at $t = 0$ h as indicated by the dashed line (**Fig. 4.11**)**. Fig. 4.11** shows the time-course of $|Z|_{norm}$ (**A1 – C1**) and R_{norm} (**A2 – C2**) of MDCK II cells after the addition of different compounds (medium, DMSO, cytochalasin D) at 500 Hz (■), 4 kHz (●) and 32 kHz (▲). The addition of culture medium (**A**) or 0.4 ‰ DMSO (**B**) only caused a slight dip due to the addition of the different solutions. $|Z|_{norm}$ (**A1; B1**) and R_{norm} (**A2; B2**) remained stable over time under both conditions independent of the frequency, indicating no cellular response of MDCK II cells.

Cytochalasin D caused a decrease in Z_{norm} for all three frequencies, however, with frequency-dependent magnitudes and kinetics. At 500 Hz $|Z|_{norm}$ immediately dropped down and within one hour a stable value of ~ 0.4 was reached. At 4 kHz the decrease of $|Z|_{norm}$ showed a slightly delayed response compared to the signal at 500 Hz and a decrease to ~ 0.4 at $t = 2.5$ h was found. At high frequencies (32 kHz), the presence of cytochalasin D only caused a slight and almost linear decrease to ~ 0.9 within 2.5 h of monitoring.

The time-course of R_{norm} for MDCK II cells in presence of cytochalasin D also revealed frequency-dependent differences in the sign of the signal (**C2**). At 500 Hz (■) the response was very similar compared to $|Z|_{norm}$ at the same frequency. In presence of 4 µM cytochalasin D a steep decrease to ~ 0.2 within one hour was observed. At 4 kHz R_{norm} showed an increase to ~ 1.2 within 20 min after adding the drug followed by a decrease to ~ 0.7 until the end of experiment ($t = 2.5$ h). In contrast, the analysis at 32 kHz disclosed a slight, but persistent increase of R_{norm} to ~ 1.1 after introducing cytochalasin D.

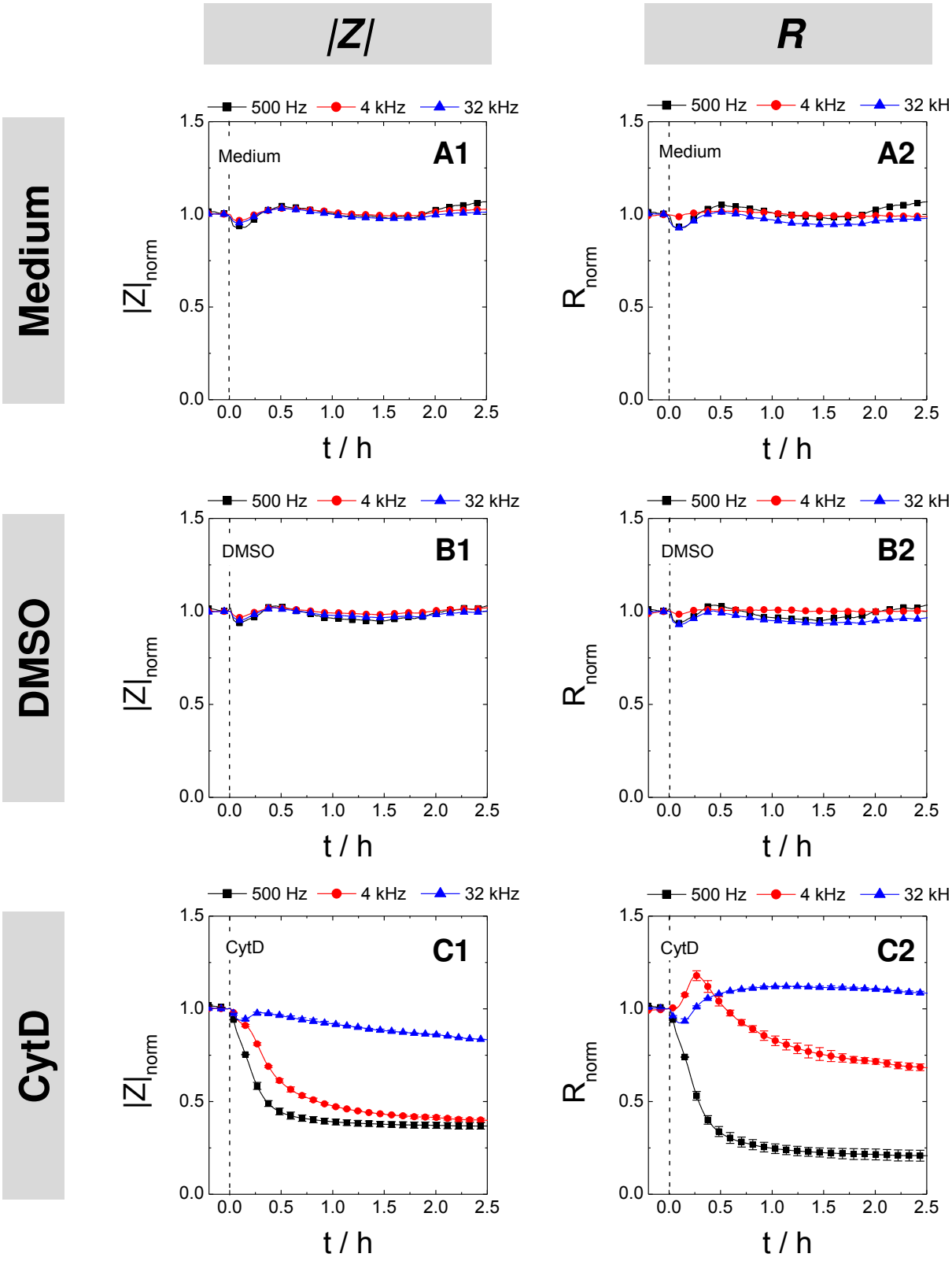

Fig. 4.11: Typical time-course of $|Z|_{norm}$ (**1**) and R_{norm} (**2**) at 500 Hz (■), 4 kHz (●) and 32 kHz (▲) to monitor the response of MDCK II cells grown on a **8W10E** electrode layout upon addition of medium (**A**), 0.4 ‰ DMSO (**B**) or 4 µM cytochalasin D (**C**). For MDCK II cells treated with cytochalasin D Mean values ± SD are shown (N = 2); medium and DMSO controls were run as singles during the experiment. Data were normalized to the time-point immediately before addition.

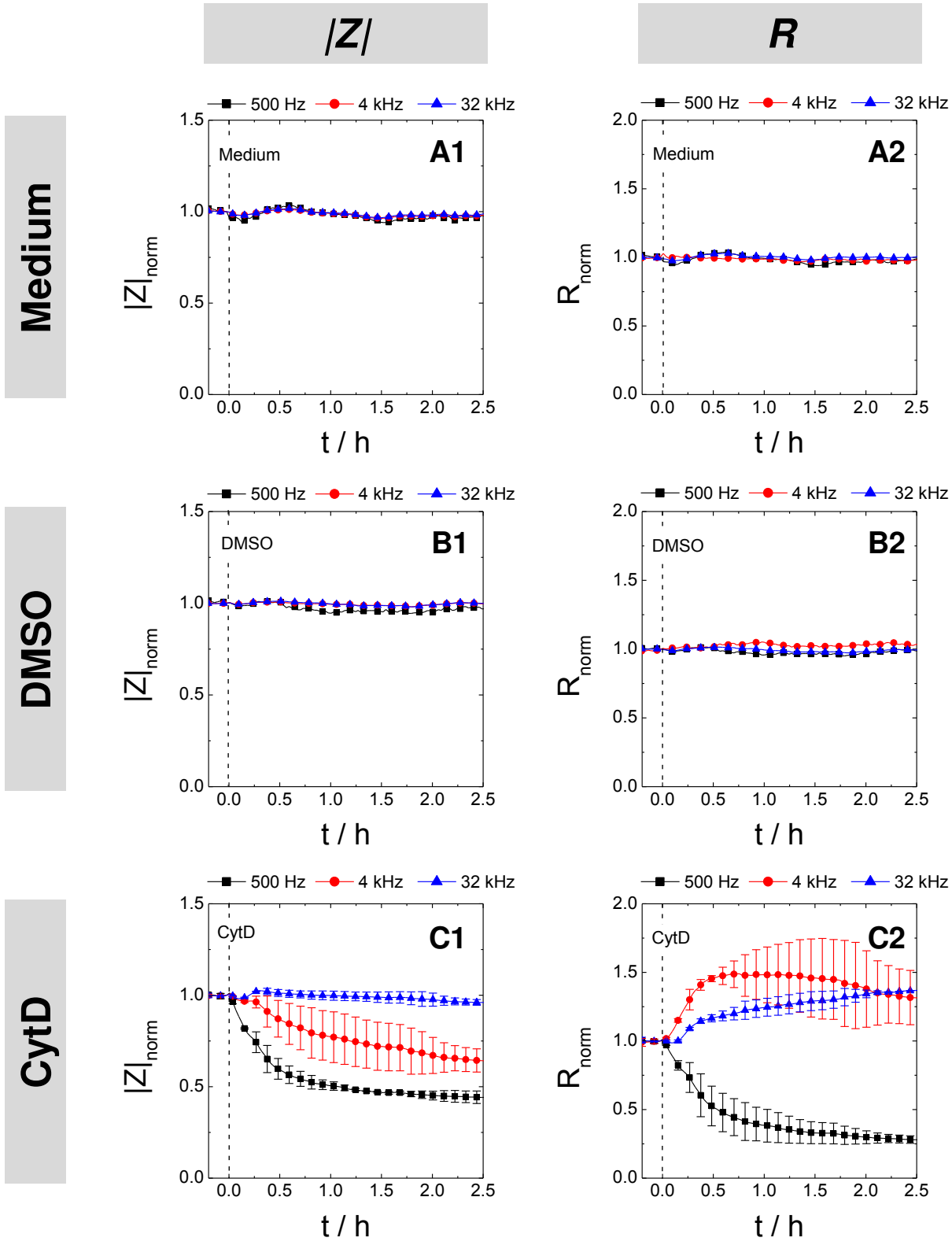

Fig. 4.12: Typical time-course of $|Z|_{norm}$ (**1**) and R_{norm} (**2**) at 500 Hz (■), 4 kHz (●) and 32 kHz (▲) to monitor the response of MDCK II cells grown on a **8W1E** electrode layout upon addition of medium (**A**), 0.4 ‰ DMSO (**B**) or 4 µM cytochalasin D (**C**). For MDCK II cells treated with cytochalasin D Mean values ± SD are shown (N = 2); medium and DMSO controls were run as singles during the experiment. Data were normalized to the time-point immediately before addition.

The same experiment was repeated using a 8W1E electrode layout. Impedance and resistance data after addition of cytochalasin D to MDCK II cells are summarized in **Fig. 4.12**.

Similar to the ECIS data recorded with the 8W10E electrode layout neither the addition of medium nor 0.4 ‰ DMSO had a significant effect on $|Z|_{norm}$ (**A1; B1**) or R_{norm} (**A2; B2**). Independent of the frequency a stable signal was observed over the entire observation time.

However, introducing cytochalasin D resulted in a decrease in $|Z|_{norm}$ to 0.4 (■) and 0.6 (●), respectively, until the end of experiment, when monitored at 500 Hz or 4 kHz (**C1**). At 32 kHz (▲), $|Z|_{norm}$ remained constant over time at ~ 1.0 which clearly indicates the different sensitivities of $|Z|$ depending on the frequency to analyze changes in epithelial barrier function.

The analysis of MDCK II cells in presence of cytochalasin D using R_{norm} provided an even more pronounced frequency-dependent response (**C2**). At 500 Hz (■) the loss of epithelial barrier integrity was indicated by a decrease to ~ 0.3 within 2.5 h. In contrast, at 4 kHz, the addition of cytochalasin D caused an increase to ~ 1.5 during the first 30 min after cytochalasin D addition, followed by a slow decrease to 1.3 until t = 2.5 h (●). Also at 32 kHz (▲) an increase of R_{norm} to ~ 1.4 was detected after the addition of 4 µM cytochalasin D.

Interestingly, in ECIS epithelial barrier disruption by cytochalasin D, which was successfully demonstrated in the dye permeation experiment (**Fig. 4.10**) is shown as decrease or increase in R_{norm}, depending on the frequency selected for monitoring. Obviously, the sensitivity of impedance and resistance for changes in epithelial barrier function is strongly dependent on the frequency. However, the impedance signal was not prone to artifacts, as the loss of epithelial barrier was always correctly reflected by a decrease in $|Z|_{norm}$, most significantly at lower frequencies.

4.4.3 Reversible Effect of Cytochalasin D

Stevenson and Begg (1994) showed that cells are still vital after removing 2.0 µg/mL cytochalasin D from the culture medium and that they are able to re-establish tight epithelial barriers within 1.5 h [135]. With showing this reversible effect in a single ECIS experiment it was possible to demonstrate the frequency-dependent changes in resistance during both, dynamic opening and closing of the epithelial barrier using the same toxin. MDCK II cells were grown on 8W10E or 8W1E electrodes and treated with 4 µM cytochalasin D. After

opening epithelial barriers, cytochalasin D was removed and ECIS recording was continued for additional 90 – 130 min in drug-free culture medium.

Fig. 4.13 summarizes the time-course of normalized impedance (**1**) and normalized resistance (**2**) of MDCK II cells grown on 8W10E electrodes after the addition of 4 µM cytochalasin D or DMSO at $t = 0$ h, as indicated by the dashed line. The cellular response was monitored at the three different frequencies of 500 Hz (**A**), 4 kHz (**B**) and 32 kHz (**C**). In good agreement with the results shown in **Fig. 4.11** $|Z|_{norm}$ decreased after the addition of cytochalasin D (**A1 – C1**). At 500 Hz (**A1**) a decrease of $|Z|_{norm}$ to ~ 0.63 was observed within 30 min. After removing the actin-binding drug from the supernatant, a recovery of $|Z|_{norm}$ was observed indicating closing of epithelial barriers and re-establishment of tight junctions. Within ~ 1 h $|Z|_{norm}$ reached pre-treatment impedance levels and even showed a further increase to ~ 1.1 until the end of experiment ($t = 4$ h). At 4 kHz (**B1**) also an immediate decrease of $|Z|_{norm}$ to ~ 0.52 was found after adding cytochalasin D and the re-establishment of the endothelial barrier function was represented by an increase in $|Z|_{norm}$ back to ~ 1.0. At both frequencies (**A1; B1**) cells did not show any response after the addition of DMSO and only a slow rise in $|Z|_{norm}$ after removing DMSO was found. At 32 kHz (**C1**) the addition of cytochalasin D, and therefore opening of cell-cell junctions, only caused a small decrease in $|Z|_{norm}$ to ~ 0.9. After replacing cytochalasin D by medium a strong increase to higher impedance values (~ 1.1) was found, followed by a decrease to ~1.0 at $t = 4$ h. The time-course of $|Z|_{norm}$ for cells in presence of DMSO showed an unstable signal. However, $|Z|_{norm}$ immediately before changing to culture medium ($t = 1.7$ h) and in the end of the experiment ($t = 4$ h) showed impedance values of ~ 1.0, indicating no influence on MDCK II cells. Analysis of R_{norm} at 500 Hz (**A2**) showed that the resistance dropped down to ~ 0.26 after adding cytochalasin D. After removing cytochalasin D at $t = 1.7$ h recovery in R_{norm} took place within 2 h and R_{norm} showed slightly enhanced values of ~ 1.1 at the end of experiment. At 4 kHz (**B2**) a first transient increase to ~ 1.2 was observed and followed by a decrease to ~ 0.8. After removing cytochalasin D ($t = 1.7$ h) R_{norm} immediately showed a transient increase to ~ 1.3 followed by a decrease to ~ 0.97. Thus, transient maxima in R_{norm} at 4 kHz were found in both steps, the barrier opening and closing process, and seems to be a typical feature in monitoring epithelial barrier kinetics, which should be noted as a potential critical point in data interpretation. At higher frequencies (**C2**), the effect for changes in epithelial barrier on R_{norm} was weak, which clearly indicates that R at 32 kHz is not very sensitive for changes in barrier integrity, as induced by cytochalasin D. After adding cytochalasin D only a slight increase (~ 1.1) was observed. After changing back to culture medium ($t = 1.7$ h) the signal of the control population as well as the signal of cells pre-treated with cytochalasin D showed similar R_{norm} values of ~ 1.0 at the end of the experiment.

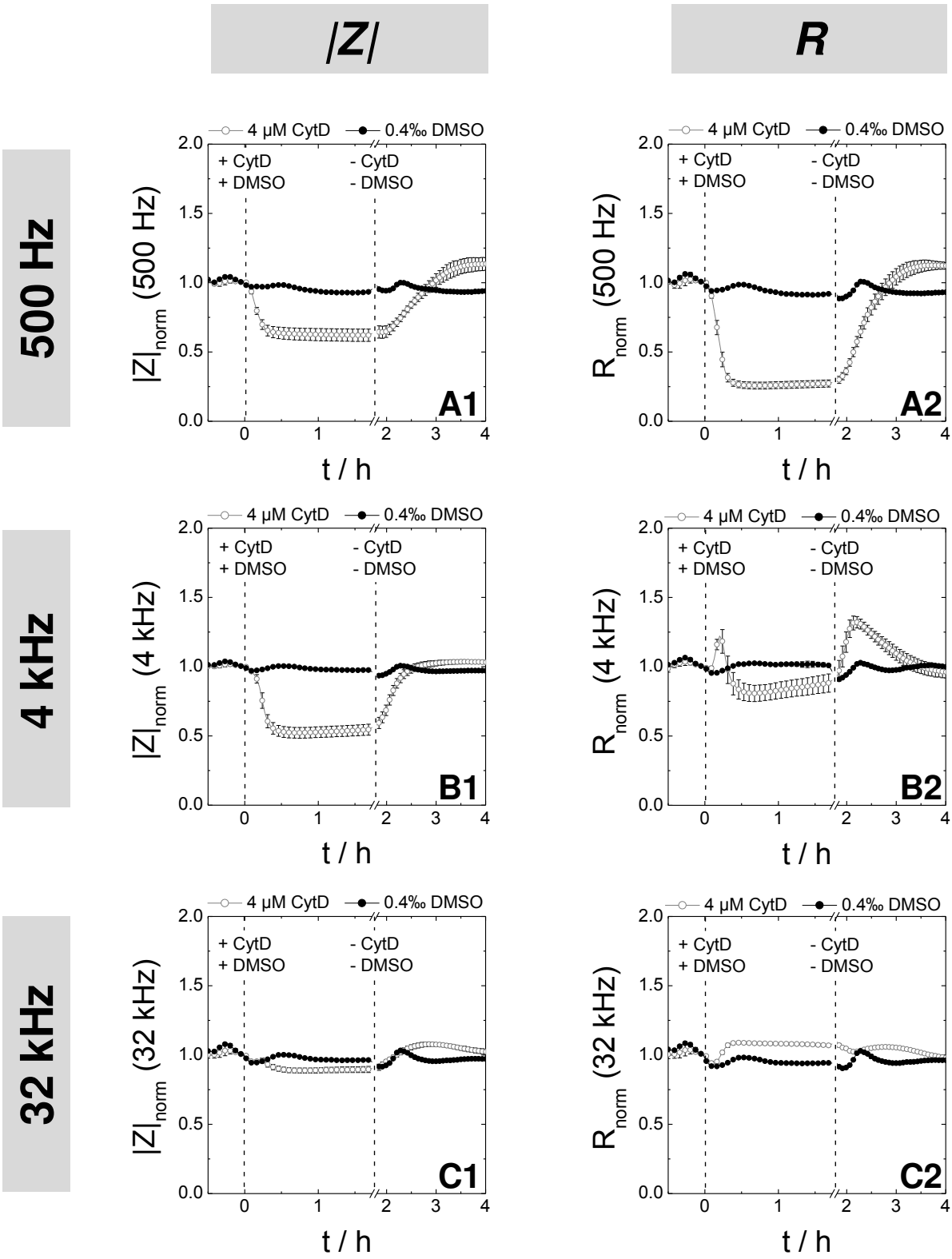

Fig. 4.13: Typical time-course of impedance magnitude |*Z*| (**1**) and resistance *R* (**2**) of MDCK II cells grown on **8W10E** electrodes during cytochalasin D treatment and after exchange to medium at 500 Hz (**A**), 4 kHz (**B**) and 32 kHz (**C**). After recording a baseline, cells were either treated with 4 µM cytochalasin D (○) or 0.4 ‰ DMSO (●) at *t* = 0 h. After 1.8 h the measurement was paused and cytochalasin D or DMSO were removed from the supernatant and replaced by culture medium. In the following, the recovery of epithelial barrier function was monitored with ECIS. Values were normalized to the values before addition of DMSO or cytochalasin D. In the diagram Mean value ± SD for cytochalasin D (N = 6) and DMSO treated cells (N = 2) are shown.

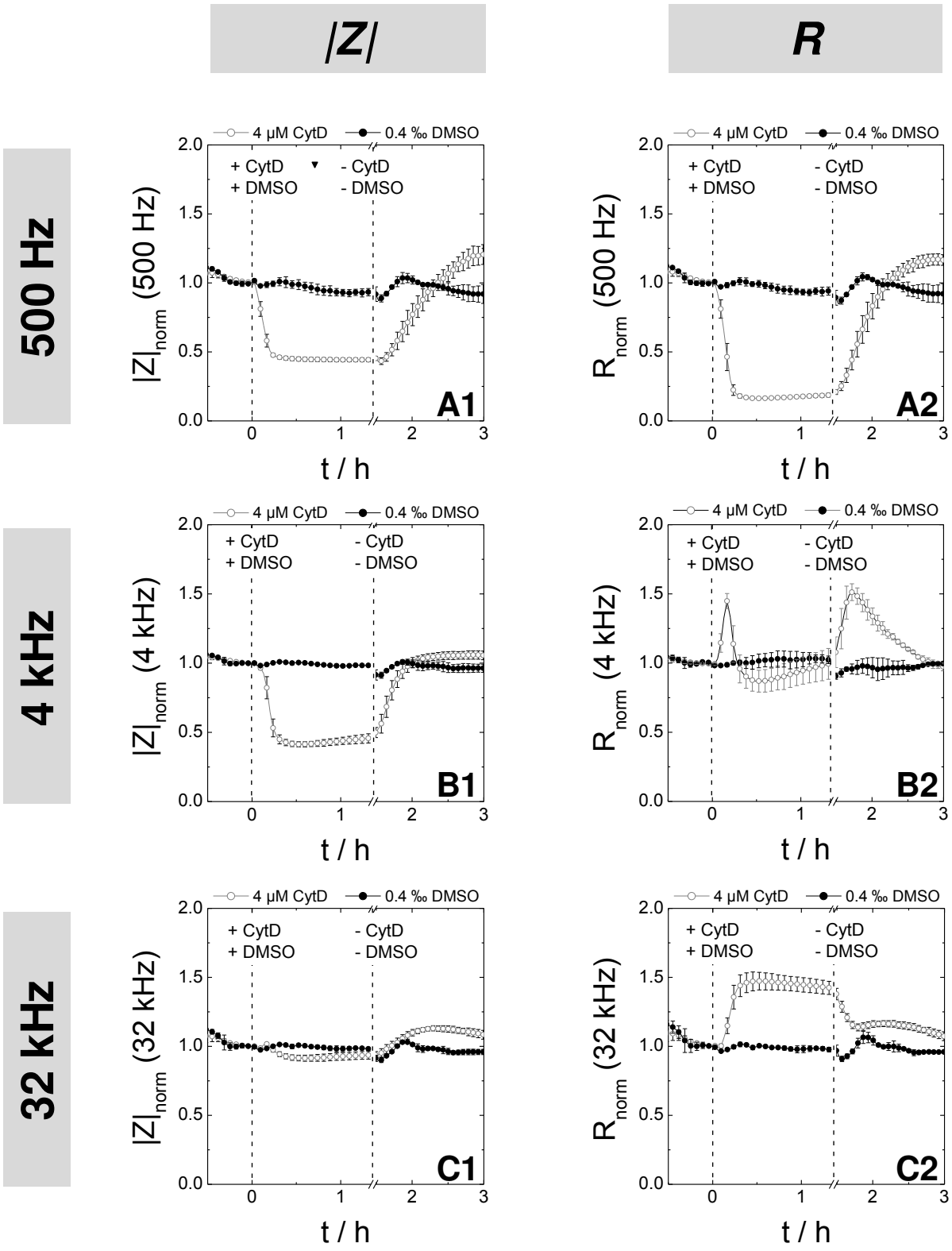

Fig. 4.14: Typical time-course of impedance magnitude |*Z*| (**1**) and resistance *R* (**2**) of MDCK II cells grown on **8W1E** electrodes during cytochalasin D treatment and after exchange to medium at 500 Hz (**A**), 4 kHz (**B**) and 32 kHz (**C**). After recording a baseline, cells were either treated with 4 µM cytochalasin D (○) or 0.4 ‰ DMSO (●) at *t* = 0 h. After 1.3 h the measurement was paused and cytochalasin D or DMSO were removed from the supernatant and replaced by culture medium. In the following, the recovery of epithelial barrier function was monitored with ECIS. Values were normalized to the values before addition of DMSO or cytochalasin D. In the diagram Mean value ± SD for cytochalasin D (N = 6) and DMSO treated cells (N = 2) are shown.

The destruction and re-establishment of epithelial barrier function after cytochalasin D treatment was also analyzed with MDCK II cells grown on 8W1E electrodes (**Fig. 4.14**). In the time-course of $|Z|_{norm}$ (**A1 – C1**) the expected trend was observed: A reduction in R_b caused by the addition of cytochalasin D was reflected by a decrease in $|Z|_{norm}$ to ~ 0.44 at 500 Hz (**A1**) and to ~ 0.41 at 4 kHz (**B1**) immediately after the addition, whereas treatment with DMSO did not affect the impedance signal. Only small changes in $|Z|_{norm}$ were found after the addition of either cytochalasin D or DMSO using a monitoring frequency of 32 kHz (**C1**), indicating that the impedance at this frequency is mostly sensitive for electrode coverage instead of changes in cell-cell contacts.

However, analyzing R_{norm} at 500 Hz (**A2**), 4 kHz (**B2**) and 32 kHz (**C2**) the ambiguities of resistance readings became apparent: At 500 Hz a decrease in barrier integrity was reflected by a decrease in R_{norm} to ~ 0.17. After the addition of medium the recovery of the epithelial barrier caused an increase in R_{norm} to ~ 1.2. In the medium frequency range, at 4 kHz (**B2**), the time-course of R_{norm} revealed a completely different curve profile. After introducing cytochalasin D the signal increased to ~ 1.4, followed by a decrease to the initial value within one hour. After changing back to culture medium (t = 1.3 h) the time-course of R_{norm} again provided a significant peak with ~ 1.5 that was followed by a decrease to ~ 1.0 until the end of resistance recordings at t = 3.0 h. Even though it is well known and undisputed that cytochalasin D increases tight junction permeability R_{norm} at 32 kHz (**C2**) counter-intuitively increased to ~ 1.5 after cytochalasin D addition. After removing the drug R_{norm} decreased to ~ 1.1 until the experiment was stopped.

4.4.4 Cell Seeding in Absence or Presence of Calcium

In a second ECIS assay, suspended epithelial MDCK II cells were seeded on fibronectin pre-coated ECIS gold-film electrodes (8W1E; 8W10E) and the formation of epithelial junctions was monitored over 20 h in absence and presence of Ca^{2+}. For this purpose, one cell population was seeded in $EBSS^{++}$ which contains Mg^{2+} and Ca^{2+}, one population in buffer only containing Ca^{2+} and another population was inoculated as a suspension in buffer supplemented with Mg^{2+} as the only divalent cation. It is known, that Ca^{2+} is necessary to form tight junctions [135-137].

Fig. 4.15 summarizes the frequency dependent changes in the time-course of $|Z|_{norm}$ (**1**) and R_{norm} (**2**) at 500 Hz (**A**), 4 kHz (**B**) and 32 kHz (**C**) for cell seeding and spreading of MDCK II cells on 8W10E.

At 500 Hz a significant increase in $|Z|_{norm}$ (**A1**) to ~ 2.1 and R_{norm} (**A2**) to ~ 20 was found only when Ca^{2+} was present, indicating the formation of cell-cell contacts as well as tight junctions within this cell layer. Cells cultivated in $EBSS^{++}$ showed a maximum in $|Z|_{norm}$ and R_{norm} ~ 8 h after cell seeding. In contrast, when only Ca^{2+} was present but no Mg^{2+} the maximum was reached with a delay of ~ 6 h. In absence of Ca^{2+} no evidence of cell junction formation was found at 500 Hz, as $|Z|_{norm}$ and R_{norm} remained at a low level close to starting values.

At 4 kHz (**B1**) cells seeded in $EBSS^{++}$ showed a constant increase in $|Z|_{norm}$ until a maximum of ~ 3.7 was reached at $t = 6.5$ h. In contrast, cells in presence of Ca^{2+} reached their maximum ($|Z|_{norm} = 4.0$) ~ 12 h after cell seeding. Cells in presence of Mg^{2+} only showed a transient increase immediately after cell seeding, followed by a stable impedance level which was close to the value of the fibronectin coated but cell-free electrode. In the time-course of resistance (**B2**) MDCK II cells in $EBSS^{++}$ showed a continuous increase in R_{norm} to ~ 9.2 ($t = 4$ h), whereas cells only in presence of Ca^{2+} showed a slight retardation with nearly the same maximum of R_{norm} at $t = 8.5$ h. In absence of Ca^{2+} R_{norm} increased during the first two hours to ~ 4.5 but decreased in the following to ~ 2.2. When cell seeding and spreading was analyzed at 32 kHz in absence or presence of Ca^{2+} different responses were found using $|Z|_{norm}$ (**C1**) or R_{norm} (**C2**). MDCK II cells in $EBSS^{++}$ and buffer only containing Mg^{2+} provided similar time-courses in $|Z|_{norm}$ during the first 2 h. Afterwards, cells without Calcium showed a decrease of $|Z|_{norm}$ to ~ 1.9, whereas $|Z|_{norm}$ for cells in $EBSS^{++}$ further increased to ~ 3.4 followed by a slight decrease to ~ 3.0 ($t = 18$ h). The increase in $|Z|_{norm}$ for cells in $EBSS^{--}$ buffer only containing Ca^{2+} showed a less steep slope compared to cells in presence of Mg^{2+}. However, 18 h after cell seeding these cells showed the highest $|Z|_{norm}$ level of ~ 3.0.

When cell seeding and spreading was monitored using R_{norm} at 32 kHz (**C2**) cell seeding in $EBSS^{++}$ and $EBSS^{-+}$ supplemented with 0.5 mM Mg^{2+} showed a similar time course profile with a transient R_{norm}-maximum ~ 2 h after cell seeding. Cells in absence of Ca^{2+} reached their maximum of R_{norm} (~ 2.4) at $t = 5$ h. In the end of experiment, R_{norm} at 32 kHz of cells in absence of Ca^{2+} ($R_{norm} = 2.0$), when no formation of tight junctions was possible, was insignificantly different to those cells where cell-cell contacts were formed.

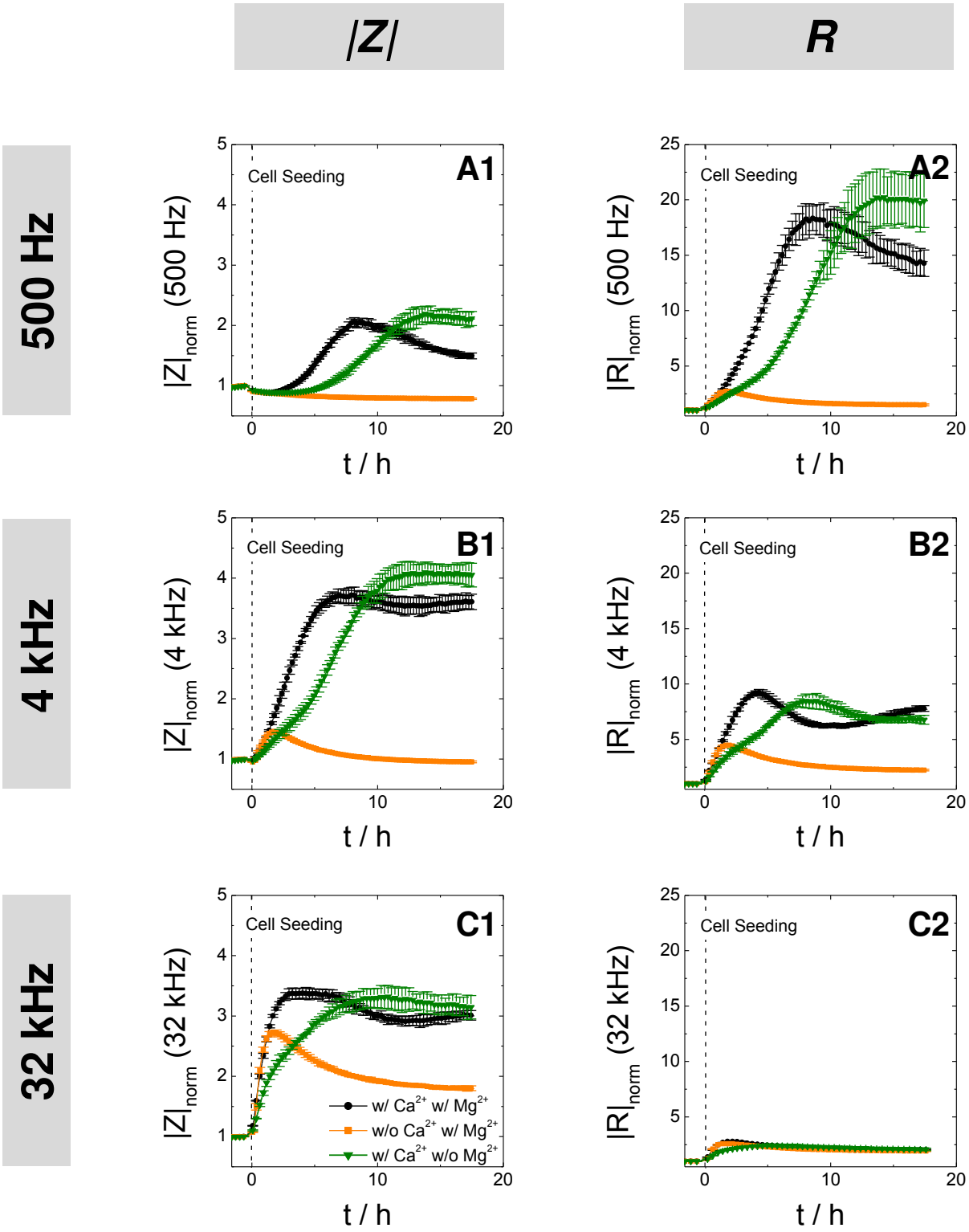

Fig. 4.15: Typical time-courses of normalized impedance magnitude $|Z|_{norm}$ (**1**) and normalized resistance R_{norm} (**2**) for seeding MDCK II cells on a **8W10E** electrode layout monitored at 500 Hz (**A**), 4 kHz (**B**) and 32 kHz (**C**) in absence or presence of Ca^{2+}. The experiment started with a cell-free, fibronectin pre-coated 8W10E electrode layout in the respective buffer. At $t = 0$ h cells were seeded using different conditions: Cell seeding and spreading of MDCK II cells in $EBSS^{++}$ (●), w/o Ca^{2+} ($EBSS^{--}$ + 0.5 mM $MgCl_2$) (■) or w/o Mg^{2+} ($EBSS^{--}$ + 1.0 mM $CaCl_2$) (▼) (Mean ± SD; N = 2). Data were normalized to the respective cell-free values.

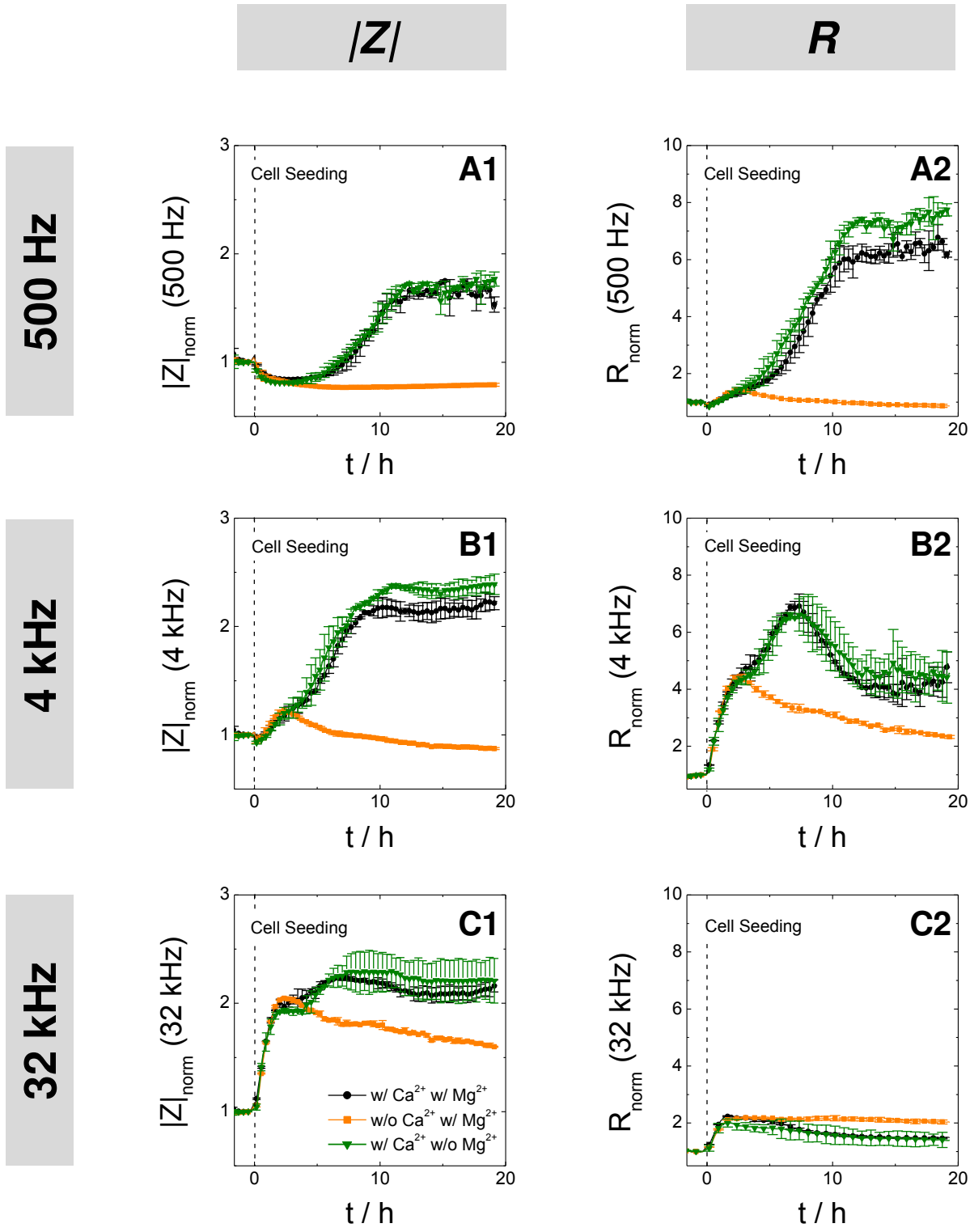

Fig. 4.16: Typical time-courses of normalized impedance magnitude $|Z|_{norm}$ (**1**) and normalized resistance R_{norm} (**2**) for seeding MDCK II cells on a **8W1E** electrode layout monitored at 500 Hz (**A**), 4 kHz (**B**) and 32 kHz (**C**) in absence or presence of Ca^{2+}. The experiment started with a cell-free, fibronectin pre-coated 8W1E electrode layout in the respective buffer. At $t = 0$ h cells were seeded using different conditions: Cell seeding and spreading of MDCK II cells in $EBSS^{++}$ (●), w/o Ca^{2+} ($EBSS^{--}$ + 0.5 mM $MgCl_2$) (■) or w/o Mg^{2+} ($EBSS^{--}$ + 1.0 mM $CaCl_2$) (▼) (Mean ± SD; N = 2). Data were normalized to the respective cell-free values.

Cell seeding of MDCK II cells on fibronectin pre-coated electrodes in absence or presence of Ca^{2+} was also studied using a 8W1E electrode layout (**Fig. 4.16**). In the time-course of $|Z|_{norm}$ at 500 Hz (**A1**) cells in $EBSS^{++}$ or in buffer only containing Ca^{2+} simultaneously reached their maximum of ~ 1.7 at t = 12 h. Cells without Ca^{2+} did not show any changes in $|Z|_{norm}$ at 500 Hz and the impedance 20 h after cell seeding was significantly lower compared to the cells in presence of Ca^{2+}. At 4 kHz (**B1**) the $|Z|_{norm}$ signal clearly revealed that only in presence of Ca^{2+} an increase to ~ 2.2 – 2.4 was observed as a result of cell-junction formation. In contrast, cells in absence of Ca^{2+} provided an impedance value similar to the value of a cell-free electrode (~ 0.9). At higher frequencies, shown at 32 kHz (**C1**), $|Z|_{norm}$ was more sensitive for the analysis of electrode coverage with cells as for the detection of tight junctions formation. Nevertheless, cells without calcium showed the lowest $|Z|_{norm}$ value after 20 h with ~ 1.6 compared to cells in $EBSS^{++}$ or cells in buffer with Ca^{2+} (~ 2.2).

The resistance recording at 500 Hz (**A2**) for MDCK II cells in presence of Ca^{2+} showed significantly higher R_{norm} values (~ 6 – 8) compared to cells cultivated in Ca^{2+}-free environment, which remained stable at ~ 1. In the medium frequency range at 4 kHz (**B2**) the resistance readings showed the characteristic curve shape with a temporary maximum of R_{norm} followed by a decrease. Cells in $EBSS^{++}$ or in buffer only supplemented with Ca^{2+} reached their transient maximum of ~ 6.6 – 6.9 around 7.5 h after cell seeding, followed by a decrease to final R_{norm} values of ~ 4.2 – 4.7 When only Mg^{2+} was present in the buffer cells showed a similar time-course of R_{norm} up to 3 h (~ 4.4). Afterwards, the R_{norm} decreased to ~ 2.3. During the first two hours after cell seeding the different cell populations showed similar time courses of R_{norm} at 32 kHz (**C2**). Afterwards, cells in presence of Ca^{2+} showed a decrease and R_{norm} values of ~ 1.5 were recorded at the end of experiment. In contrast, cells which were cultivated in presence of Mg^{2+} showed the highest R_{norm} of ~ 2.0 at t = 19 h.

Subsequent to the ECIS recordings cytochemical stainings were performed to proof the absence of tight junction formation when Ca^{2+} was not present during cell adhesion and spreading. Therefore, cells were stained with Phalloidin Alexa Fluor 488 (**chapter 3.4.2.3**) and DAPI (**chapter 3.4.2.4**) to visualize the actin cytoskeleton and the cell nuclei. Additionally, the tight junction associated protein Occludin was stained using a monoclonal, primary antibody against Occludin and a polyclonal, fluorescently labeled secondary antibody (**chapter 3.4.2.6**).

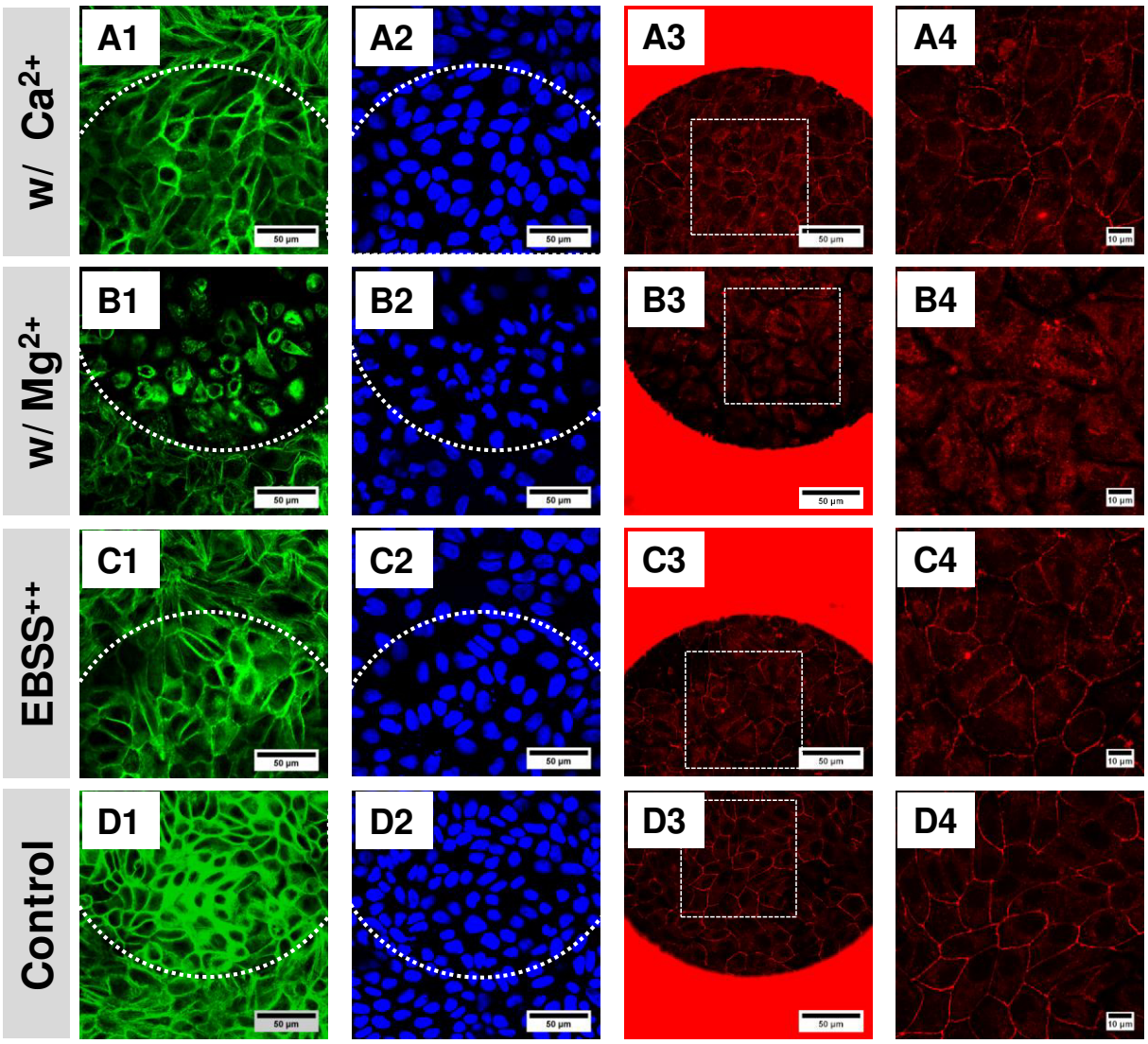

Fig. 4.17: Confocal fluorescence micrographs of MDCK II cells 20 h after cell seeding in absence of Mg^{2+} ($EBSS^{--}$ + 1.0 mM Ca^{2+}) (**A**), in absence of Ca^{2+} ($EBSS^{--}$ + 0.5 mM Mg^{2+}) (**B**), in $EBSS^{++}$ (**C**) or in culture medium (**D**) after actin cytoskeleton stain with phalloidin Alexa Fluor 488 (**1; green**), nuclei stain with DAPI (**2; blue**) and localization of tight junction associated Occludin (**3; red**). The fluorescence micrographs (**1 – 3**) show the distribution of all these cellular components at the same position, for cells directly located on or next to the working electrode. Additionally a higher magnification (**4**) for the Occludin localization presented in **D** is shown, indicated by the dotted rectangle. The scale bar represents 50 µm (**1 – 3**) or 10 µm (**4**).

The fluorescence micrographs shown in **Fig. 4.17** clearly indicate that only when Ca^{2+} was present Occludin was localized at the cell-cell borders (**A4; C4; D4**). In contrast, after cell adhesion and spreading only in presence of Mg^{2+}, a weak and diffuse fluorescence signal was detected inside the cytoplasm caused by unspecific binding. Also differences in the development of the actin cytoskeleton were found (**A1 – D1**). In presence of Ca^{2+} the different structures of the actin cytoskeleton, containing stress fibers, actin belt and microvilli could be visualized. In contrast, phalloidin labeling of cells that were cultured in absence of Ca^{2+} (**B**) did not show a homogeneous staining of the actin structures. The cell nuclei stain with DAPI differed from the control population with respect to number and shape of cell nuclei.

4.4.5 Simulation for Different Types of Barrier-Forming Cell Lines

In the following the above described problem, that the same changes in epithelial barrier function are reflected by significantly different changes in resistance depending on the monitoring frequency, was addressed theoretically on the basis of the ECIS model provided by Giaever and Keese (1991) [144]. Different experimental scenarios were calculated using a LabVIEW-based software written by J. Wegener. The effect of opening and closing of all junctions for different types of barrier-forming cell layers were simulated. The cell layers were described by their characteristic parameters R_b, α and C_m provided in **Tab. 4.2**.

Tab. 4.2: Overview of the different model cell cases used for the simulation of opening and closing epithelial barrier junctions with their characteristic parameters R_b, α and C_m which were provided by J. Wegener.

Cell Type	R_b / Ω·cm^2	α / Ω$^{0.5}$·cm	C_m / µF·cm^{-2}
Small Fibroblast	2	5	1
Big Fibroblast	5	10	1
Moderately Tight Epithelial Cells	25	15	3
Tight Epithelial Cells	500	25	3

After calculating a spectrum for a confluent cell layer with the respective, cell-type specific parameters α, R_b and C_m (**Tab. 4.2**) only R_b was systematically increased or decreased stepwise. The corresponding impedance (**1**) and resistance (**2**) spectra were extracted (**A**) and normalized to the spectra of a cell-free 8W1E or 8W10E gold-film electrode, respectively (**B**). The calculated impedance and resistance spectra ($|Z|_{\text{cell-cov/cell-free}}$, $R_{\text{cell-cov/cell-free}}$) for the different cell types with their individual starting values (**Tab. 4.2**) (●) served as reference for the spectra in which R_b was increased or decreased (**C**) resulting in $\Delta|Z|_{\text{cell-cov/cell-free}}$ and $\Delta R_{\text{cell-cov/cell-free}}$. The entire procedure of data analysis is exemplarily shown for moderately tight epithelial cells (R_b = 25 Ω·cm^2, α = 15 Ω$^{0.5}$·cm, C_m = 3 µF/cm^2) grown on 8W1E electrodes in **Fig. 4.18.**

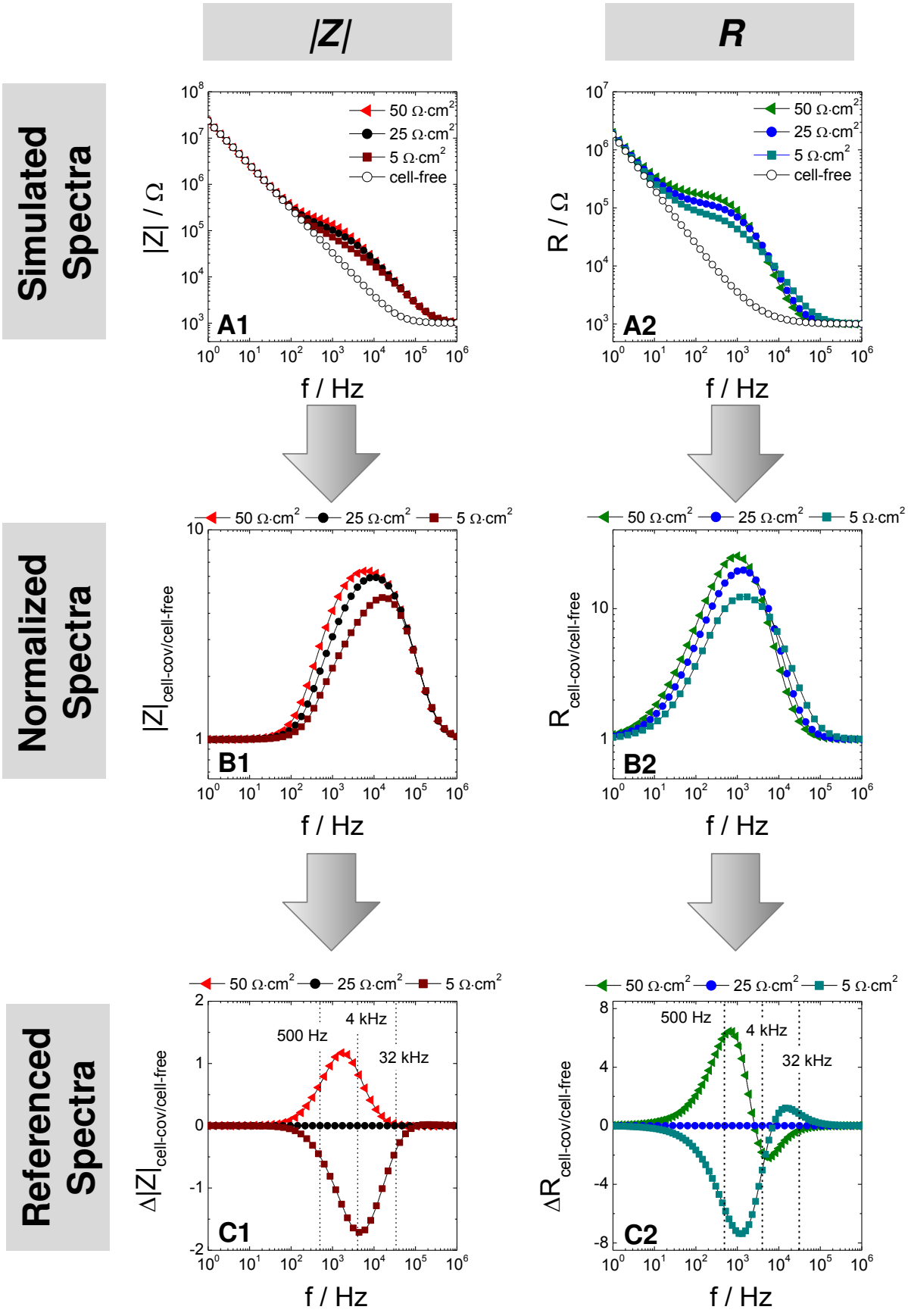

Fig. 4.18: Schematic representation of data conversion: Frequency-dependent $|Z|$ (**1**) or R (**2**) spectra were calculated using the LabVIEW-based software with varying R_b values (**A**). In the following, spectra were divided by the cell-free spectra of an 8W1E electrode layout (○) resulting in a maximum curve of the normalized data (**B**). Curves were referenced to the curve of cell-type specific starting values (●) by subtracting it from the others (■,◀) (**C**).

The changes in impedance and in the resistance signal due to increasing or decreasing R_b values for different model cell types are summarized in **Fig. 4.19** (8W10E) and **Fig. 4.20** (8W1E). **Fig. 4.19** clearly demonstrates that independent of the cell type the changes in normalized Impedance $\Delta|Z|_{\text{cell-cov/cell-free}}$ (**A1 – D1**) give similar curve profiles using the 8W10E electrode layout: By increasing R_b (◄), representing the scenario of strengthening of cellular junctions, the normalized impedance increases compared to the reference signal. By decreasing R_b (■) a decrease in $\Delta|Z|_{\text{cell-cov/cell-free}}$ is found.

The resistance spectra $\Delta R_{\text{cell-cov/cell-free}}$, in contrast, significantly differ between model cell types, which can roughly be grouped into model fibroblasts and model epithelial cells (**A2 – D2**). Resistance curves for model fibroblasts are very similar to the respective ones for impedance from $f = 1 - 10^5$ Hz. Profiles for model epithelial cells, however, cross the baseline and change sign from positive to negative $\Delta R_{\text{cell-cov/cell-free}}$ values or vice versa. The frequency at which the inversion occurred was the lower, the higher R_b of the model cell type (**A2 – D2**). Small model fibroblasts (**A2**) exhibit a cross-over frequency at ~ 90 kHz (◄), whereas this zero-crossing in the $\Delta R_{\text{cell-cov/cell-free}}$ spectra for moderately tight model epithelial cells (**C2**) is found at ~ 2.6 kHz (◄) and 7.2 kHz (■) for R_b increases or decreases, respectively. Simulated spectra for tight model epithelial cells (**D2**) provided the cross-over frequency at ~ 140 Hz (◄) and 280 Hz (■).

The same simulation was repeated for an 8W1E electrode (**Fig. 4.20**) and changes in $\Delta|Z|_{\text{cell-cov/cell-free}}$ (**A1 – D1**) again increase in a model cell type-specific sensitive frequency range by increasing R_b. By decreasing R_b (■), which is similar to the effect of opening cell barriers, the impedance decrease compared to the reference signal (●). The analysis of $\Delta R_{\text{cell-cov/cell-free}}$ (**A2 – D2**) once more shows a cross-over frequency in each diagram, in which the curves change their sign compared to the reference curve and, thus, the relation between resistance and tightness of cell barrier becomes inversed. This effect is more pronounced in the case of model cell types characterized by higher R_b values. (**C; D**). Furthermore, a shift for the cross-over frequency to lower frequencies is observed from **A2 – D2**. Whereas the critical frequency for small model fibroblasts is determined above 75 kHz (**A2**), the frequency of crossover is shifted to ~ 35 kHz for big model fibroblasts (**B2**), 2.5 kHz for moderately tight model epithelial cells (**C2**) and even to 150 Hz for tight model epithelial cells (**D2**). This means, that above a cell-type-specific critical frequency, the resistance increase or decrease inversely correlate to R_b and thus, actual barrier function. In contrast, no cross-over is found in the impedance spectra for all different cell lines (**A1 – D1**).

In summary, the simulation illustrate that impedance provides a robust and sensitive alternative for analysis and quantification of cellular barrier function. In contrast to the response monitored in R, $|Z|$ provides less sensitivity to detect the strength of cell barrier function but $|Z|$ is less prone to artifacts by signal inversion. **Fig. 4.19** and **Fig. 4.20** clearly disclose a strong frequency-dependent sensitivity of resistance and impedance recordings for monitoring changes in barrier function dependent on the cell-type related parameters R_b, α and C_m.

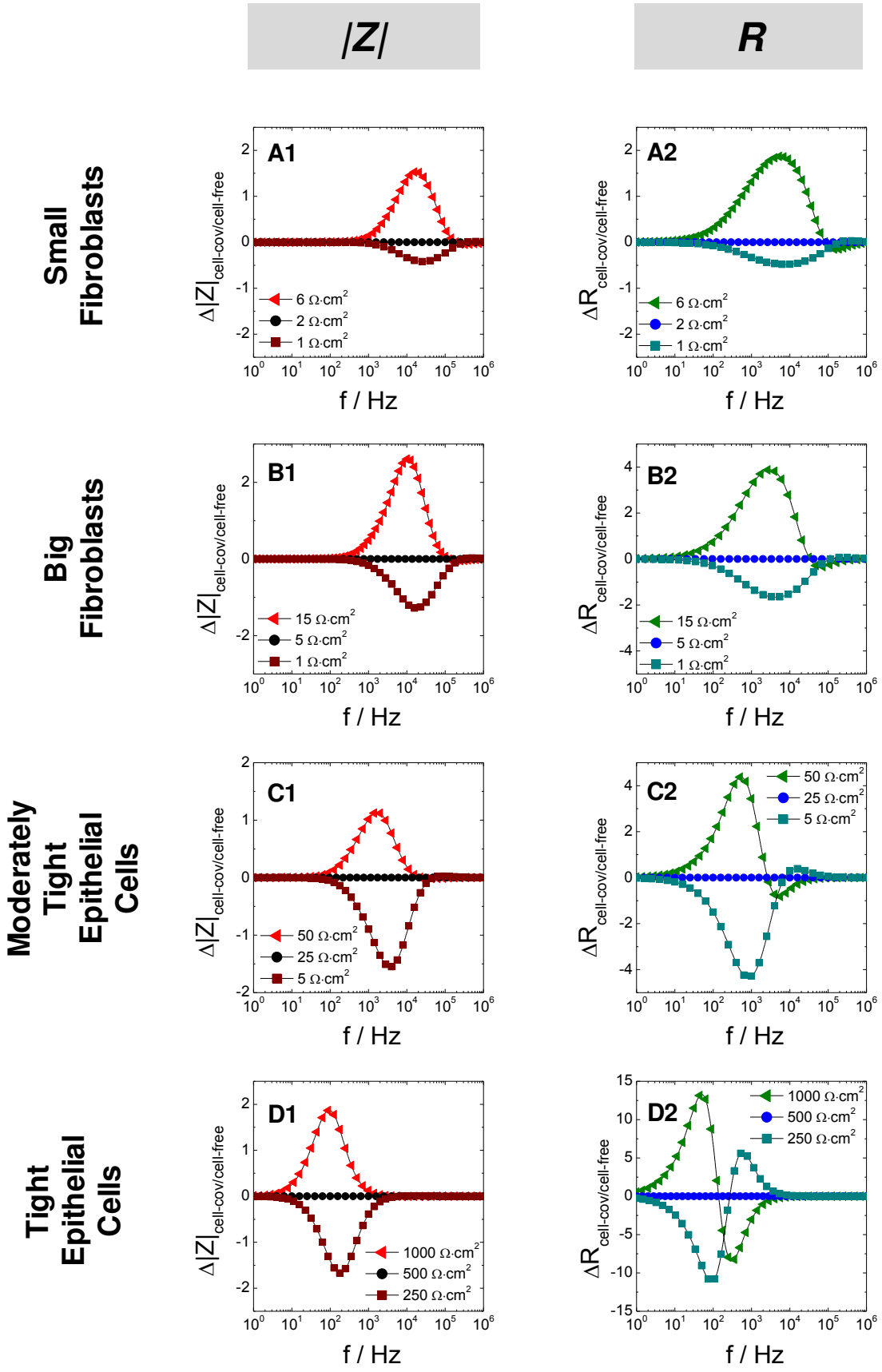

Fig. 4.19: Simulated impedance (**1**) and resistance (**2**) data for **8W10E** electrodes covered with small model fibroblast (**A**), big model fibroblasts (**B**), moderately tight model epithelial cells (**C**) and tight model epithelial cells (**D**) for opening (■) and closing (◄) intercellular junctions. The reference spectrum (●) was subtracted from all normalized spectra. Parameter for the model cell types are summarized in **Tab. 4.2**.

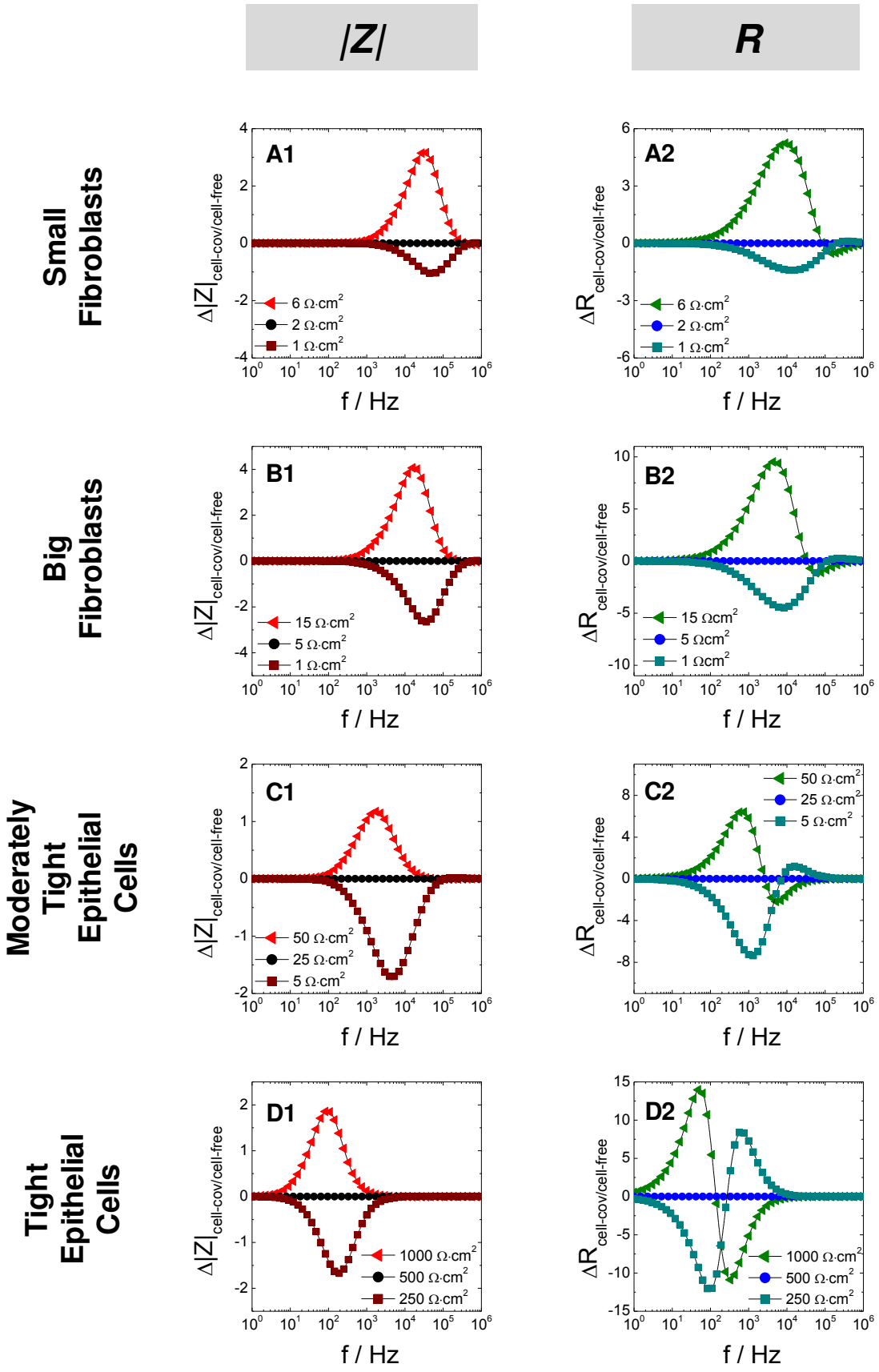

Fig. 4.20: Simulated impedance (**1**) and resistance (**2**) data for **8W1E** electrodes covered with small model fibroblast (**A**), big model fibroblasts (**B**), moderately tight model epithelial cells (**C**) and tight model epithelial cells (**D**) for opening (■) and closing (◄) intercellular junctions. The reference spectrum (●) was subtracted from all normalized spectra. Parameter for the model cell types are summarized in **Tab. 4.2**.

4.4.6 Discussion: Monitoring Changes in Cell-Barrier Properties Using Impedance or Resistance for Analysis

In this work changes in cell-barrier properties were addressed experimentally and theoretically. Different sensitivities were found for impedance magnitude |Z| and resistance R readings when cell-barrier properties are studied. Furthermore, using a monitoring frequency above a cell-type specific critical frequency, a counter-intuitive response of the resistance signal was demonstrated for strengthening or opening of cell junctions.

For the experimental support in this chapter we only focused on MDCK II cells, which are able to form tight junctions [134, 145]. In the first ECIS experiment, the effect of cytochalasin D on the properties of epithelial barrier function of MDCK II cells was analyzed (**Fig. 4.11** and **Fig. 4.12**). It is well known, that cytochalasin D increases the tight junction permeability [146]. Stevenson and Begg (1994) investigated the effect of 2 µg/mL cytochalasin D on the tightness of MDCK II cell-cell junctions. The group reported a significant decrease in TER 60 min after MDCK II cells, grown on permeable filters, were exposed to cytochalasin D [143].

The determination of TER based on a filter experiment, where cells are cultured on permeable membranes, is a classical method for the analysis of the tightness of a cell layer. Therefore, the resistance of the cell-free filter (R_{blank}) is determined and subtracted from the signal of the cell-covered filter (R_{total}) to obtain the cell-specific resistance (R_{tissue}) [147]. TER values are typically determined in the unit of $\Omega \cdot cm^2$ and are obtained by multiplying the calculated R_{tissue} by the effective area of the permeable membrane in units of cm^2. The calculated TER value consequently describes only the resistance arising from the cell layer and is a frequency-independent parameter. High TER-values always characterize tight cell barriers, whereas low TER values indicate leaky cell types. In contrast, during a typical ECIS experiment, the signal of the cell-free electrode is included in the time-course of $|Z|$ and R and a frequency-independent parameter for the tightness of the cell layer is realized by fitting the parameter R_b. In contrast to ECIS, where the application of the ECIS model allows a differentiation between R_b and α, the TER combines the resistance of cell junctions and the resistance of the cell adhesion zone within one value. Using a traditional assay, where the dye diffusion from an upper to the lower compartment across a confluent cell layer grown on a permeable membrane was monitored, the effect of 4 µM cytochalasin D on MDCK II cells was clearly demonstrated (**Fig. 4.10**). A significant increase in dye transfer from the upper to the lower compartment was found after cytochalasin D treatment over 3 h.

Normally, a decrease in the tightness of cell-barrier function should be accompanied with a decrease in impedance or resistance as the current flow via the cell-cell junctions is facilitated. Historically, the resistance is the favored parameter in literature to study changes

in cell-cell contacts. But when the effect of cytochalasin D on MDCK II cell-barrier function was analyzed with ECIS the resistance clearly showed a frequency-dependent response. Only at a monitoring frequency of 500 Hz the strong decrease in resistance immediately after the addition of cytochalasin D correctly indicated the increase in permeability, whereas at 4 kHz and 32 kHz counter-intuitive trends were found, showing a resistance increase for exactly the same process (**Fig. 4.11**; **Fig. 4.12**). At 32 kHz a slight increase in *R* was observed which was more pronounced using the 8W1E layout compared to the 8W10E layout. For a monitoring frequency of 4 kHz a transient increase of *R* for ~ 30 min was found. This characteristic pattern was also found in the reverse process when the dynamics of opening and closing of epithelial barrier function was addressed in a single experiment (**Fig. 4.13** and **Fig. 4.14**). Both processes, opening and strengthening of cell junctions, respectively, provided a characteristic transient maximum of *R* at 4 kHz which recovered back to baseline values. In the end of the experiment, cells were able to re-establish tight epithelial barriers after removing cytochalasin D.

During the experiments to analyze the effect of cytochalasin D changes of the tightness of cell-cell contacts within a confluent cell layer were monitored. Moreover, the *de novo* formation of cell-cell contacts was studied immediately after cell seeding of MDCK II cells and the response of |Z| and R was extracted at 500 Hz, 4 kHz and 32 kHz.

During this second assay cell adhesion and spreading of MDCK II cells on fibronectin pre-coated gold-film electrodes were investigated when either Ca^{2+} or Mg^{2+} was present or under control conditions in presence of both divalent cations (**Fig. 4.15**; **Fig. 4.16**). The important role of the presence of Ca^{2+} for the formation of tight epithelial barriers in MDCK II cells is indisputable and was reported several times [135, 137]. Moreover, integrins which are transmembrane receptors responsible for the attachment and spreading on ECM proteins on the electrode surfaces are dependent on the presence of extracellular divalent cations. Different integrin subtypes have a higher affinity for Ca^{2+} or Mg^{2+} respectively, and are even inhibited by the other cation species [148]. Using the 8W10E electrode layout (**Fig. 4.15**) seeding of MDCK II cells provided a faster increase in $|Z|$ and *R* at 4 kHz and 32 kHz within 2 h in presence of Mg^{2+} compared to cells seeded in Mg^{2+}-free conditions. This led to the conclusion that the integrins of MDCK II cells have a higher sensitivity to Mg^{2+} compared to Ca^{2+} which facilitated the attachment on fibronectin coated gold-film electrodes. The preferred activation of MDCK II integrins via Mg^{2+} cation was also demonstrated by Wegener et al. (2000) [84].

The *de novo* formation of cell-cell contacts, which were confirmed by microscopic images only in presence of Ca^{2+} (**Fig. 4.17**), can be identified by the time-course of *R* and $|Z|$ at 500 Hz. A drastic increase of $|Z|$ and *R* was found in presence of Ca^{2+}, whereas cells in

absence of Ca^{2+} provided a low signal, which was insignificantly different from the cell-free electrode and clearly represented the absence of tight junction formation.

In 1995, Lo et al. analyzed the consequence of the absence and presence of extracellular Ca^{2+} on the junctional resistance of MDCK cells. The group modeled the R_b value of MDCK II cells under standard culture condition to 50 – 60 $\Omega \cdot cm^2$. After removing Ca^{2+} from the supernatant, a quick drop in R_b and α was found [126]. Also other groups found, that the removal or addition of Ca^{2+} in the extracellular buffer, respectively, caused opening or resealing of cell-cell junctions, which is indicated by a decrease or increase of R_b [135, 149].

Using the 8W10E electrode layout (**Fig. 4.15**) similar resistance values at 32 kHz were found for cells in absence of Ca^{2+} and cells cultured in $EBSS^{++}$. The resistance recordings at 32 kHz for cells cultured on 8W1E (**Fig. 4.16**) electrodes even showed the highest resistance level for MDCK II cell seeding in absence of Ca^{2+}. Both results may lead to misinterpretations and may pretend the formation of strong epithelial cell barriers but microscopic images clearly demonstrated the absence of tight junction formation (**Fig. 4.17 B**).

At 4 kHz, a transient maximum in the time-course of R was found. This characteristic pattern can be explained by the cell-type specific critical frequency, where the relation between R and the tightness of cell-barriers change sign.

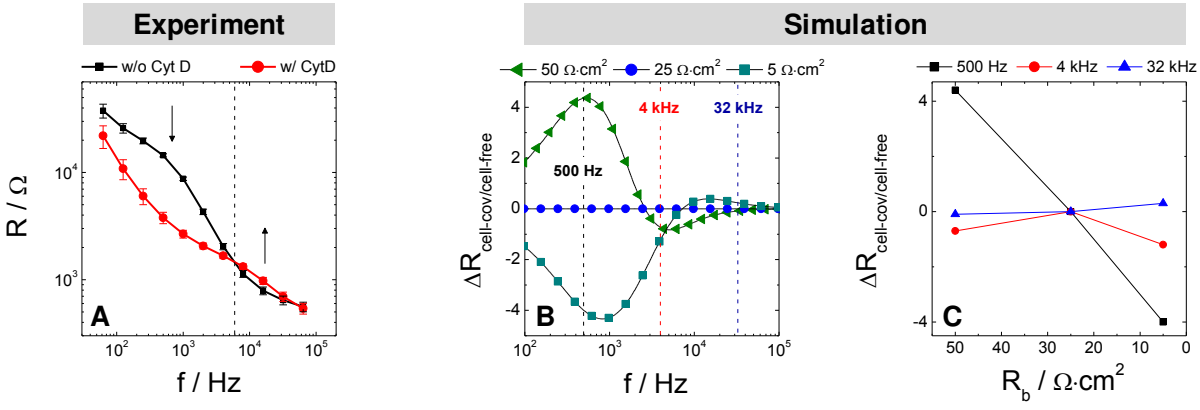

Fig. 4.21: Experimental (**A**) and simulated (**B**) data addressing opening epithelial barrier. **A:** Frequency-dependent spectra of R for MDCK II cells, grown on 8W10E electrodes in absence (**black**) and presence (**red**) of 4 µM cytochalasin D. **B:** Simulated resistance spectra for a model cell type with varying R_b values (5 – 50 $\Omega \cdot cm^2$) whereas the other model parameters were kept constant (α = 15 $\Omega^{0.5} \cdot cm$, C_m = 3 µF/cm^2). **C:** Extracted changes of $\Delta R_{cell\text{-}cov/cell\text{-}free}$ at 500 Hz (■), 4 kHz (●) and 32 kHz (▲).

Fig. 4.21 A clearly shows that the cross-over frequency, which was monitored in the simulated data is not an artifact from the model but was also found in the experimental data. When the frequency-dependent spectra of R was recorded in absence or presence of

cytochalasin D the critical frequency was determined for a confluently MDCK II cell-covered 8W10E layout to ~ 6 kHz. This means, that using a monitoring frequency which is distinctly below 6 kHz the increase in permeability after cytochalasin D treatment is reflected by a decrease in *R* whereas beyond this frequency, *R* increased at the same time.

The simulated data clearly shows the ambiguities of resistance readings due to the cross-over frequency in the resistance spectra (**Fig. 4.19**; **Fig. 4.20**). Impedance readings correctly reflected the direction of signal change, as an opening of the cell-barrier was always reflected by a decrease in $|Z|$. These observations were confirmed for both electrode layouts containing one or ten working electrodes per well Simulated data were performed with different model cell types in order to demonstrate that the critical frequency, where the relation between the measured resistance and the strength of cell-cell-contacts reverses, is cell-type specific. The higher the cell-type specific R_b value of the model cell type, the lower the frequency where the cross-over was found in the spectra.

Fig. 4.21 B represents the simulated data for moderately tight model epithelial cells (R_b = 25 Ω·cm^2, α = 15 Ω$^{0.5}$·cm, C_m = 3 µF/cm^2) when the R_b value for the confluent cell layer was increased (R_b = 50 Ω·cm^2) or decreased (R_b = 5 Ω·cm^2), respectively. When the signal changes in *R* are extracted at 500 Hz, 4 kHz and 32 kHz and plotted as a function of R_b (**C**) the transient increase at 4 kHz becomes apparent. Whereas $\Delta R_{cell\text{-}cov/cell\text{-}free}$ provides a small increase when R_b is changed from 50 Ω·cm^2 to 25 Ω·cm^2 the signal shows a decrease when R_b is reduced to 5 Ω·cm^2. At 32 kHz similar $\Delta R_{cell\text{-}cov/cell\text{-}free}$ are obtained for R_b = 50 Ω·cm^2 and R_b = 25 Ω·cm^2 but even a signal increase is found by further reducing the barrier properties (R_b = 5 Ω·cm^2) of the model cell layer. Only at 500 Hz the expected trend was found, where a decrease in the tightness of cell-barrier is mirrored by a decrease in *R* over the entire R_b range.

Also previous publications showed the frequency-dependent trend of the resistance signal. Ghosh et al. already in 1994 analyzed the effect of an external electric field to adherent cells, grown on gold-film electrodes with ECIS. The group monitored the changes in resistance for MDCK cells after pulsing at 4 kHz and recognized an upward spike in resistance, whereas the same measurement at 700 Hz yielded a resistance decrease. Ghosh et al. explained that the different responses are not caused by the pulse itself, but was influenced by the monitoring frequency. They further simulated different scenarios using varying R_b values between 5 – 80 Ω·cm^2 and plotted the resistance ratio of cell-covered and cell-free spectra [150]. In good agreement to our simulated data shown in (**Fig. 4.19**; **Fig. 4.20**) they found a cross-over frequency which was dependent on the R_b value. Using frequencies below this threshold, a decrease in R_b was reflected by a decrease in resistance, whereas analyzing

frequencies above this cross-over a smaller R_b value caused an increase in resistance [150]. This is also consistent with the computed data of Lo et al. (1995) who reported about an increase in R at low frequencies by increasing R_b, whereas the analysis of high frequencies simultaneously yielded a decrease in R [126]. Recently, Stolwijk et al. (2014) published an overview about impedance analysis of endothelial barrier function. After stimulation of HDMEC cells with histamine, they found a decrease in resistance at a monitoring frequency of 400 Hz – 4 kHz indicating a decrease in barrier integrity whereas, using 40 kHz for analysis an increase in resistance at the same time was found. The response of HDMEC cells within the same experiment was further analyzed using the impedance as second monitoring parameter. The addition of histamine to HDMEC cells always resulted in a decrease in impedance signal independent of the monitoring frequency [151].

In summary, the results of our model calculations as well as the supporting ECIS experiments clearly showed the ambiguities of resistance interpretation as described in the beginning. However, qualitative outcome of impedance magnitude readings were largely unaffected by choice of monitoring frequency. As supported by simulated data and experimental data $|Z|$ provides correct correlation of barrier function and signal sign.

The take-home massages for this study consequently are, that:

- ✓ compared to changes in $R_{500\,Hz}$, $|Z|_{500\,Hz}$ provides less sensitivity to monitor the response MDCK II cells to the addition of cytochalasin D. Using higher monitoring frequencies the signal changes in $|Z|$ becomes less prominent but always shows a correct signal sign instead of R
- ✓ the smaller the size of the electrode the more drastic the effect in R above the cell-type specific cross-over frequency
- ✓ using the resistance R as parameter to characterize changes in cell-barrier function requires a proper selection of the right frequency in advance which should be below the cell-type specific cross-over frequency
- ✓ for unexperienced users it is recommended to use the parameter $|Z|$ instead of R as $|Z|$ provides a correct correlation with barrier function independent of the monitoring frequency

4.5 Inhomogeneity of Electrode Coverage

As described in the introduction of the ECIS model (**chapter 4.1.1**) the model is only valid for a uniformly cell-covered electrode. According to the model, the entire cell population covering the electrode is described by a set of integral values for R_b, α and C_m. Based on the model it is, thus, not appropriate to fit the cell-related model parameters to non-confluent electrodes or to an inhomogeneous cell population. Uniform cell coverage does, however, not reflect the *de facto* situation on the electrode during ECIS experiments. Moreover, individual cells within the cell population will never behave exactly the same or simultaneously to experimental manipulation. This uncertainty about model validity in real cell systems often holds back ECIS users from routine application of the model. However, the influence of gaps in electrode coverage or inhomogeneity within the cell layer has never been studied systematically. With the LabVIEW-based software *Z*, *R* and *C* were calculated after introducing a certain degree of inhomogeneity. For this purpose, four different scenarios were simulated, which were also mimicked experimentally (**Fig. 4.22**):

i. Defined cell-free gaps in the cell layer
ii. Different properties of individual cells within the cell layer
iii. Membrane defects
iv. Inhomogeneous cell-junction formation within the cell layer

Simulations for the described scenarios (**i – iv**) were performed using the parameters, which are summarized in **Tab. 4.3**.

Tab. 4.3: Overview of the parameters of R_b, α and C_m as applied in the simulations regarding the inhomogeneity of electrode coverage. The electrode coverage was varied using different ratios of situation A and B.

Simulation	Situation A	Situation B
Cell-Free Gaps	**Cell-covered** $R_b = 25\ \Omega{\cdot}cm^2$ $\alpha = 15\ \Omega^{0.5}{\cdot}cm$ $C_m = 3.0\ \mu F/cm^2$	**Cell-free**
Different Cellular Properties	**Cell Type A** $R_b = 25\ \Omega{\cdot}cm^2$ $\alpha = 15\ \Omega^{0.5}{\cdot}cm$ $C_m = 3.0\ \mu F/cm^2$	**Cell Type B** $R_b = 5\ \Omega{\cdot}cm^2$ $\alpha = 8\ \Omega^{0.5}{\cdot}cm$ $C_m = 3.0\ \mu F/cm^2$
Membrane Defects	**Intact membrane** $R_b = 25\ \Omega{\cdot}cm^2$ $\alpha = 15\ \Omega^{0.5}{\cdot}cm$ $C_m = 3.0\ \mu F/cm^2$ $R_m = 1{\cdot}10^{12}\ \Omega{\cdot}cm^2$	**Open membrane** $R_b = 25\ \Omega{\cdot}cm^2$ $\alpha = 15\ \Omega^{0.5}{\cdot}cm$ $C_m = 3.0\ \mu F/cm^2$ $R_m = 0.1\ \Omega{\cdot}cm^2$
Inhomogeneous Cell-Junction Formation	**Tight Junction** $R_b = 25\ \Omega{\cdot}cm^2$ $\alpha = 15\ \Omega^{0.5}{\cdot}cm$ $C_m = 3.0\ \mu F/cm^2$	**Open Junction** $R_b = 1\ \Omega{\cdot}cm^2$ $\alpha = 15\ \Omega^{0.5}{\cdot}cm$ $C_m = 3.0\ \mu F/cm^2$

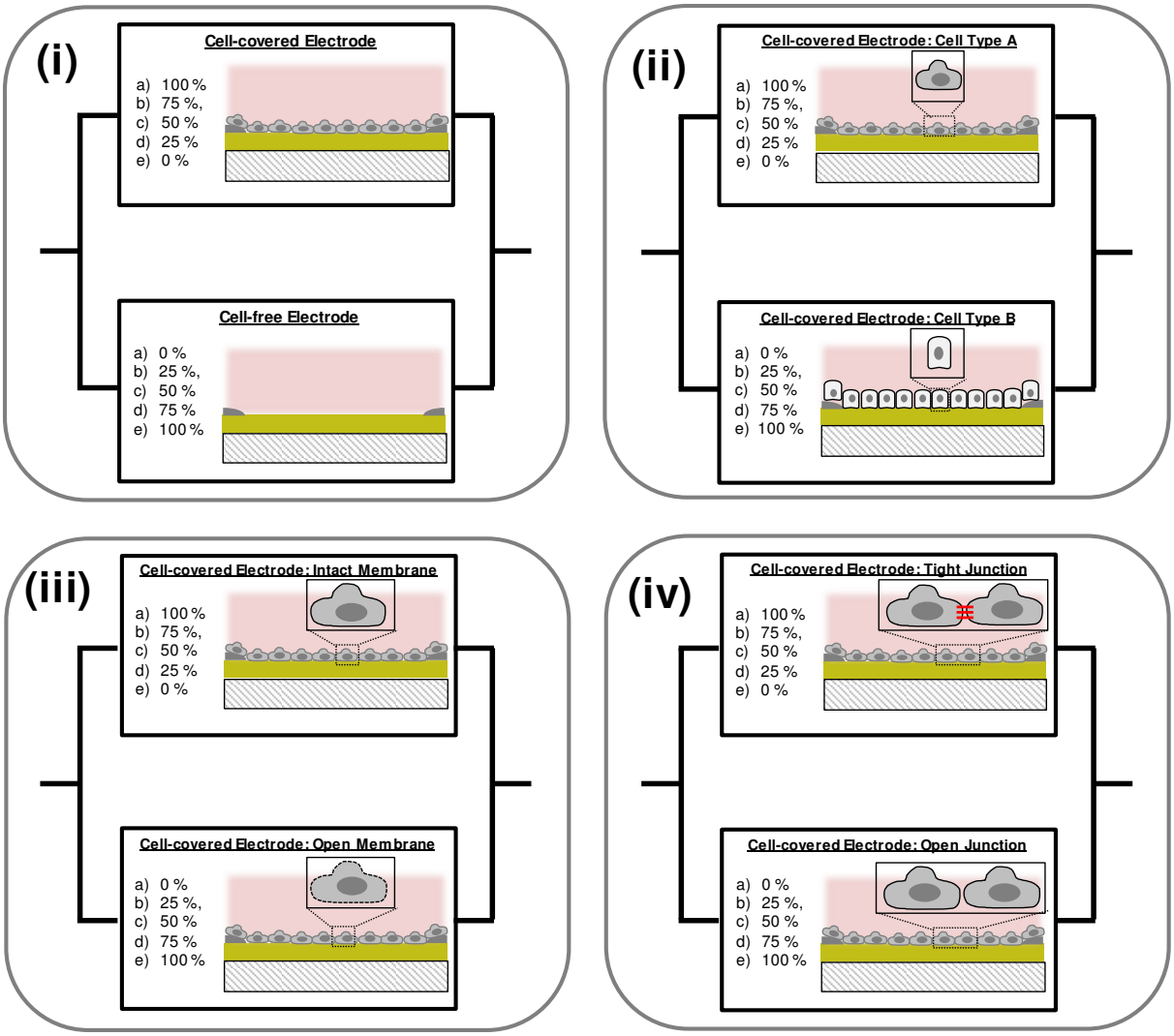

Fig. 4.22: Schematic overview of the different simulation scenarios using: defined, cell-free gaps in the cell layer (**i**), different cellular properties by assuming two different cell types (**ii**), cells with variable membrane properties (**iii**) or cells with tight and open junctions (**iv**). Z_{cl} was calculated using two impedance elements aligned in parallel. Each situation (A; B) is represented by one impedance contribution. **a – e** indicates the respective electrode coverage for situation A + B which was varied between 0 – 100 % during the simulation. In all simulation experiment the sum of the two electrode coverages was kept to 100 %.

4.5.1 Variation of Cell-Free and Cell-Covered Area on the Electrode

To analyze the effect of incomplete electrode coverage with cells on impedance, resistance and capacitance spectra were simulated for a set of pre-defined electrode coverages. In addition, signal changes in $|Z|$, R and C were extracted at three typical monitoring frequencies. To proof our findings experimental support was performed in the following way: A special ECIS setup was used in which two different measurement types allow (i) to individually address a single working electrode for the sequential application of invasive wounding pulses to stepwise reduce the initially confluent cell layer until eight cell-free working electrodes were formed (ii) to measure the combined signal of all eight working electrodes in parallel against the common counter electrode (**chapter 4.3.1.5**).

4.5.1.1 Experimental Background

The initially confluent cell layer grown on all eight electrodes of a 8W1E electrode layout with PDMS chamber (**chapter 4.3.1.5**) was removed stepwise by killing the population of individual working electrode which received an invasive wounding pulse during the normal ECIS mode. The parameters of the wounding pulse were set to 40 kHz, 1.25 s and 5 V. The fluorescence micrographs after live/dead stain clearly indicated, that a pulse duration of 1.25 s was sufficient to kill the cells on top of the working electrode (**Fig. 4.23**). Cells in the periphery of the electrode remained unaffected by the wounding pulse and still showed a green fluorescence in the cytoplasm, which is an indicator for viable cells. These settings did not show any influence on the electrode structure and similar electric properties for the electrodes were found before and after pulsing.

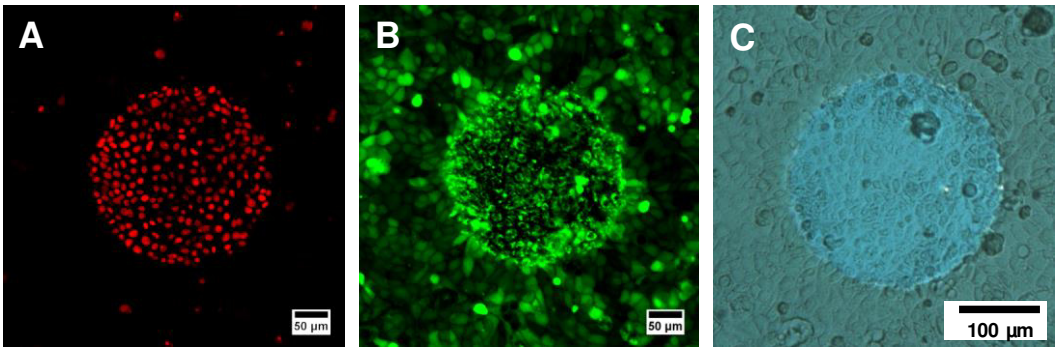

Fig. 4.23: A; B: Typical confocal fluorescence micrographs of MDCKI II cells after live/dead staining using Ethidium Homodimer (**A**) and Calcein AM (**B**). Cells grown on 8W1E electrodes were selectively wounded by an invasive pulse of 40 kHz, 1.25 s and 5 V. Dead cells on the electrode were stained red by Ethidium Homodimer, while vital cells in the periphery exhibited green fluorescence. **C:** Phase-contrast micrograph of the working electrode after applying the wounding pulse. The scale bar represents 50 µm (**A; B**) or 100 µm (**C**).

Consecutively, cells on individual electrodes were wounded by applying an invasive voltage pulse (40 kHz, 5 V, 1.25 s) and the resulting signal “8 against CE” was extracted in the

following. The frequency-dependent changes of $|Z|$, R and C in a frequency range between 1 – 10^6 Hz for the electrode set with cell coverage ranging from 0 – 100 % are summarized in **Fig. 4.24** (**A1 – C1**).

In the spectra of the impedance magnitude $|Z|$ (**A1**) a cell coverage-dependent decrease in $|Z|$ was observed between 10^2 Hz – 10^5 Hz. The low frequency range (f = 1 – 10^2 Hz) as well as the high frequency range (f = 10^5 – 10^6 Hz) remained unaffected by variations in electrode coverage. In the resistance spectra (**B1**) two different trends were observed. Between 10 Hz – 16 kHz a decrease of R was found for the stepwise reduction of cell coverage of the electrode. However, above 20 kHz the cell-layer with maximum coverage of 100 % showed a lower resistance than the completely cell-free electrode set. In the capacitance spectra (**C1**) the signal increased with decreasing electrode coverage for frequencies between 5 kHz – 50 kHz.

For further analysis of the experimental data, the impedance, resistance and capacitance spectra of the (8 against CE) electrode set were normalized by dividing the individual spectra with varying degrees of cell coverage by the corresponding cell-free values. The normalized data presentation is shown in **Fig. 4.24** (**A2 – C2**).

The normalized data presentation of $|Z|_{\text{cell-cov/cell-free}}$ (**A2**) with cell coverages between 100 % – 0 % brings out the sensitive frequency range between 10^2 Hz – 10^5 Hz very clearly. A stepwise decrease of the peak height at the most sensitive frequency of ~ 4 kHz was observed for decreasing electrode coverage with cells, which dropped from 4.5 (100 %) to 2.4 (75 %) and 1.6 (50 %). The shape of $|Z|_{\text{cell-cov/cell-free}}$ significantly changed from spectra with cell coverage of the electrode set of 50 % and below. There, a more flat curve shape without a peak maximum was found. $R_{\text{cell-cov/cell-free}}$ (**B2**) showed two different trends depending on the degree of cell-coverage. First, a decrease of the peak maximum was observed and additionally, a shift of the peak center to lower frequencies was found. For 100 % cell-coverage $R_{\text{cell-cov/cell-free}}$ showed its maximum of ~ 13.5 at ~ 600 Hz. By stepwise reducing the cell-coverage the peak maximum shifted to 300 Hz (75 %), 250 Hz (50 %) and 200 Hz (25 %). A strong dependency on the electrode coverage was found for $C_{\text{cell-cov/cell-free}}$ (**C2**). When the cell-coverage was reduced by 25 % the $C_{\text{cell-cov/cell-free}}$ signal at 4 kHz showed an increase of ~ 0.2. Signal changes in C were found to be directly proportional to the cell-coverage. The changes in $|Z|_{\text{norm}}$, R_{norm} and C_{norm} from the experiment were extracted at three different frequencies (500 Hz, 4 kHz, 32 kHz) and plotted as a function of electrode coverage (**A3 – C3**). $|Z|_{\text{norm}}$ (**A3**) provided a maximum change in impedance magnitude at 4 kHz for the cell-coverage experiment. R_{norm} (**B3**) showed the maximum change using 500 Hz and increased with increasing cell coverage. At 32 kHz even a small decrease in R_{norm} was observed when cell coverage ranged between 63 % – 100 %. The best analysis of electrode

coverage could be realized by using C_{norm} (**C3**) where a linear dependency between the signal and the electrode coverage was found at 32 kHz and 4 kHz.

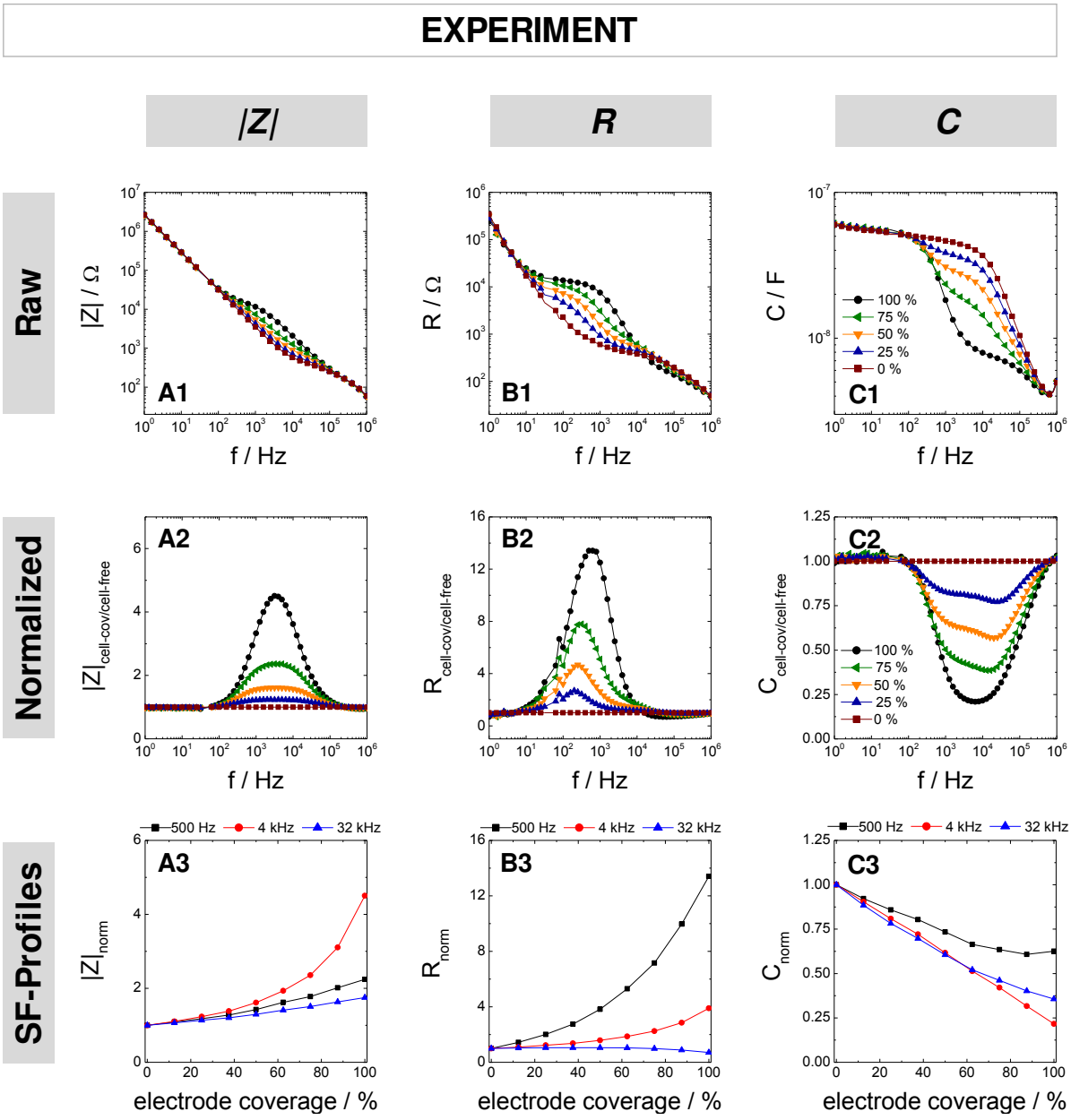

Fig. 4.24: Survey of experimental data addressing the influence of varying electrode coverage with MDCK II cells on $|Z|$ (**A**), R (**B**) and C (**C**) using a 8W1E electrode layout surrounded by a PDMS chamber. Electrode were wounded sequentially by an invasive voltage pulse of 40 kHz, 5 V and 1.25 ms. After each wounding step spectra were recorded in the modified "8 against CE" measurement mode. **1:** Frequency-dependent $|Z|$ (**A1**), R (**B1**) and C (**C1**) spectra (f = 1 Hz – 10^6 Hz) recorded in the "8 against CE" measurement mode [‡c]. **2:** Normalized $|Z|$, R and C spectra: $|Z|_{cell\text{-}cov/cell\text{-}free}$ (**A2**), $R_{cell\text{-}cov/cell\text{-}free}$ (**B2**), $C_{cell\text{-}cov/cell\text{-}free}$ (**C2**) were obtained by dividing values from the respective cell-covered electrodes by the corresponding cell-free values (■) [‡]. **3:** *Single frequency* (SF)-profiles of $|Z|_{norm}$ (**A3**), R_{norm} (**B3**) and C_{norm} (**C3**) at 500 Hz (■), 4 kHz (●) and 32 kHz (▲) depending on the electrode coverage (0 – 100 %). Data were normalized by the respective cell-free values. For clarity, only every other spectrum is shown in **1 + 2**. From the experiment also data with cell coverages of 87.5 %, 62.5 %, 37.5 %, 12.5 % were obtained (**Fig. S 1**).

[c] Data recorded at 40 Hz and 50 Hz are influenced by the powerline interference and were removed from experimentally obtained impedance spectra, which are denoted with [‡].

4.5.1.2 Simulation Using Varying Percentage of Cell-Free and Cell-Covered Area

To investigate the effects of gaps of electrode coverage on $|Z|$, R and C simulations were performed in which the degree of cell coverage of an 8W10E electrode layout was reduced stepwise. Simulations were additionally performed for a 8W1E electrode layout using the same cell-related parameters and the results can be found in **Fig. S 2**.

The resulting changes in $|Z|$, R and C in a frequency range between 1 Hz – 10^6 Hz were extracted. **Fig. 4.25** summarizes the simulated spectra for $|Z|$ (**A1**), R (**B1**) and C (**C1**) for an electrode coverage of 0 – 100 % using a model cell type described by $R_b = 25\ \Omega{\cdot}cm^2$, $\alpha = 15\ \Omega^{0.5}{\cdot}cm$, $C_m = 3.0\ \mu F/cm^2$. The spectra were divided by the respective spectrum of a cell-free 8W10E electrode resulting in $|Z|_{cell\text{-}cov/cell\text{-}free}$ (**A2**), $R_{cell\text{-}cov/cell\text{-}free}$ (**B2**) and $C_{cell\text{-}cov/cell\text{-}free}$ (**C2**). As expected, $|Z|_{cell\text{-}cov/cell\text{-}free}$ (**A2**) decreases by reducing the electrode coverage. When cell coverage is changed from 100 % to 75 % a strong decrease in $|Z|_{cell\text{-}cov/cell\text{-}free}$ at 4 kHz from 5.0 to 2.5 is observed, whereas only small further changes are detected assuming an electrode coverage of 50 % (1.6) or 25 % (1.2). The analysis of $R_{cell\text{-}cov/cell\text{-}free}$ (**B2**) yields a constant decrease in the peak height from 12 (100 %) to 6.6 (75 %), 3.8 (50 %) and 2.2 (25 %). Additionally, the maximum is shifted to lower frequencies. While a confluent cell layer shows a maximum difference between cell-covered and cell-free at ~ 800 Hz, the most sensitive frequency is found at ~ 230 Hz using electrode coverage of 25 %. $C_{cell\text{-}cov/cell\text{-}free}$ (**C2**) provides a linear relation between electrode coverage and normalized capacitance above a frequency of 10^4 Hz. Here, a stepwise decrease of cell-coverage causes an increase in $C_{cell\text{-}cov/cell\text{-}free}$ from 0.2 (100 %) to 0.4 (75 %), 0.6 (50 %) and 0.8 (25 %).

The changes in $|Z|_{norm}$, R_{norm} and C_{norm} were extracted at 500 Hz, 4 kHz and 32 kHz and plotted as a function of electrode coverage (**A3 – C3**). The changes in $|Z|_{norm}$ (**A3**) provide a high sensitivity for changes in electrode coverage using a monitoring frequency of 4 kHz. Here, $|Z|_{norm}$ shows a continuous increase from 1 to 5 by increasing the cell-coverage from 0 – 100 %. At 500 Hz a linear dependency is found, however, the signal changes between cell-free and cell-covered electrode are low. Computed data for $|Z|_{norm}$ at 32 kHz indicate that $|Z|_{norm}$ is not useful to analyze small changes in electrode coverage. A nearly stable signal is monitored for electrode coverages between 0 % and 70 %. Afterwards, an increase of $|Z|_{norm}$ only to ~ 2.3 is found. R_{norm} at 500 Hz (**B2**) shows an increase from 1 to ~ 12 by increasing the percentage of cell coverage until confluence. The analysis of R_{norm} at 4 kHz provides almost no signal change between 0 – 60 % and only shows an increase to ~ 6 by further enhancing the cell coverage to 100 %. At 32 kHz, no changes in R_{norm} are found. The simulated C_{norm} signals provide a good correlation to the respective electrode coverage using

4 kHz and 32 kHz (**C2**). For these frequencies, a linear relationship is found which is advantageous for the detection of even small changes in cells' settlement on the electrode.

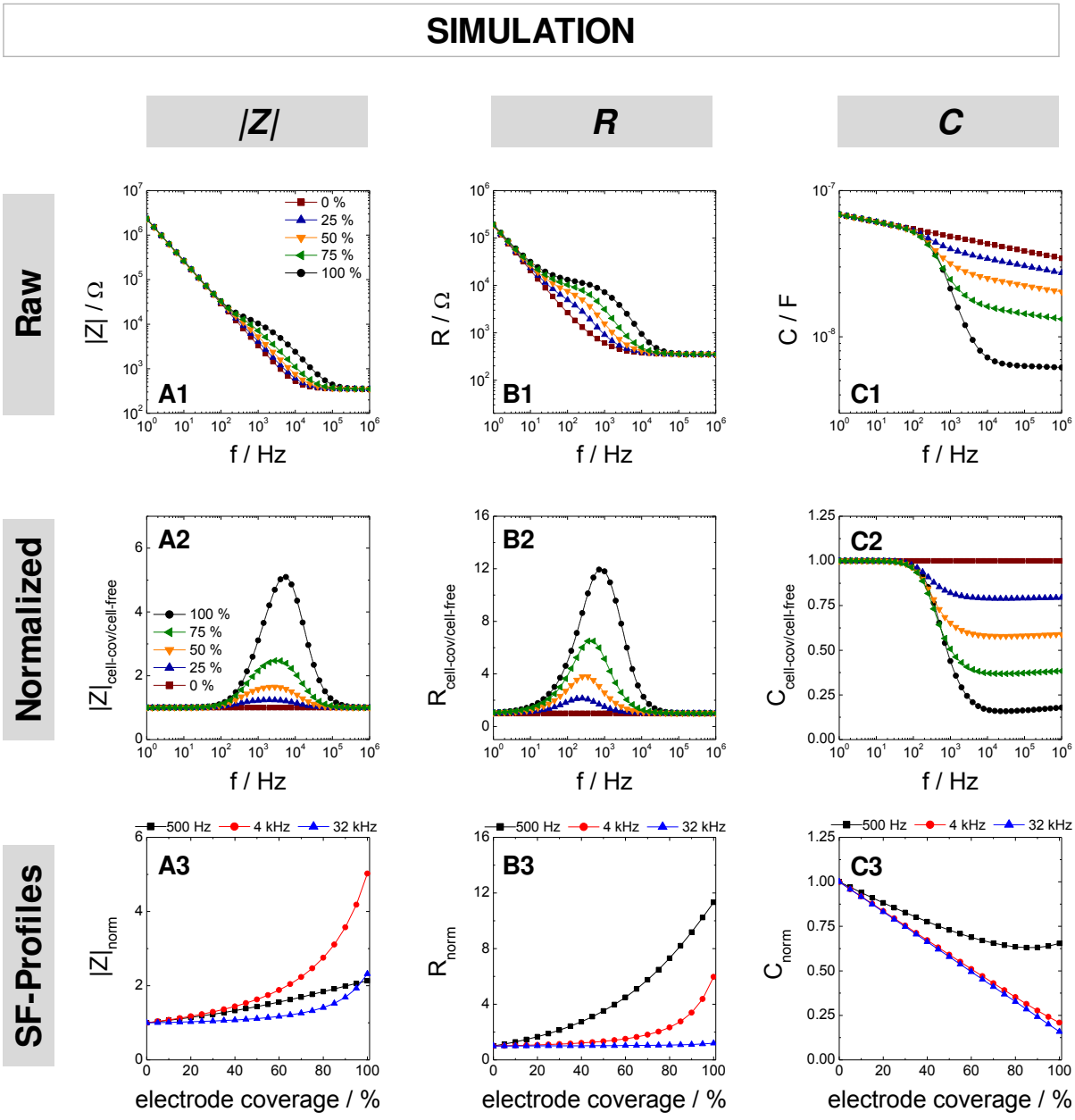

Fig. 4.25: Survey of simulated data focusing on changes in $|Z|$, R and C dependent on the electrode coverage with a model cell layer. The electrode parameters were used as described in **Tab. 4.1** and the model cell layer was characterized by $R_b = 25\ \Omega{\cdot}cm^2$, $\alpha = 15\ \Omega^{0.5}{\cdot}cm$, $C_m = 3.0\ \mu F/cm^2$. **1:** Simulated frequency-dependent $|Z|$ (**A1**), R (**B1**) and C (**C1**) spectra ($f = 1$ Hz – 10^6 Hz) for cell-free (■) and differently cell-covered 8W10E electrode layout. **2:** Normalized $|Z|$, R and C spectra for discretely varied electrode coverage with a model cell layer. The normalized spectra $|Z|_{cell\text{-}cov/cell\text{-}free}$ (**A2**), $R_{cell\text{-}cov/cell\text{-}free}$ (**B2**), $C_{cell\text{-}cov/cell\text{-}free}$ (**C2**) were obtained by dividing values from cell-covered electrodes by the respective cell-free values of a 8W10E layout. **3:** *Single frequency* (SF)-profiles of $|Z|_{norm}$ (**A3**), R_{norm} (**B3**) and C_{norm} (**C3**) at 500 Hz (■), 4 kHz (●) and 32 kHz (▲) depending on the electrode coverage (0 – 100 %). Simulated data were normalized by the respective cell-free values.

4.5.2 Impedance Studies Addressing the Electrode Coverage Using the Redox Mediator $[Fe(CN)_6]^{3-/4-}$

The application of the ECIS model is only valid for confluent electrodes. The basic idea of this project was to characterize the degree of cell coverage by an additional charge-transfer resistance (R_{CT}) during ECIS recordings. If R_{CT} depends on electrode cell coverage, the level of R_{CT} can be used for the investigations of even small gaps within the cell layer in the low frequency range.

4.5.2.1 Principle

The principle of ECIS recordings in presence of the redox mediator $[Fe(CN)_6]^{3-/4-}$ is summarized in **Fig. 4.26** with the respective equivalent circuit for a cell-covered gold-film electrode (**A**).

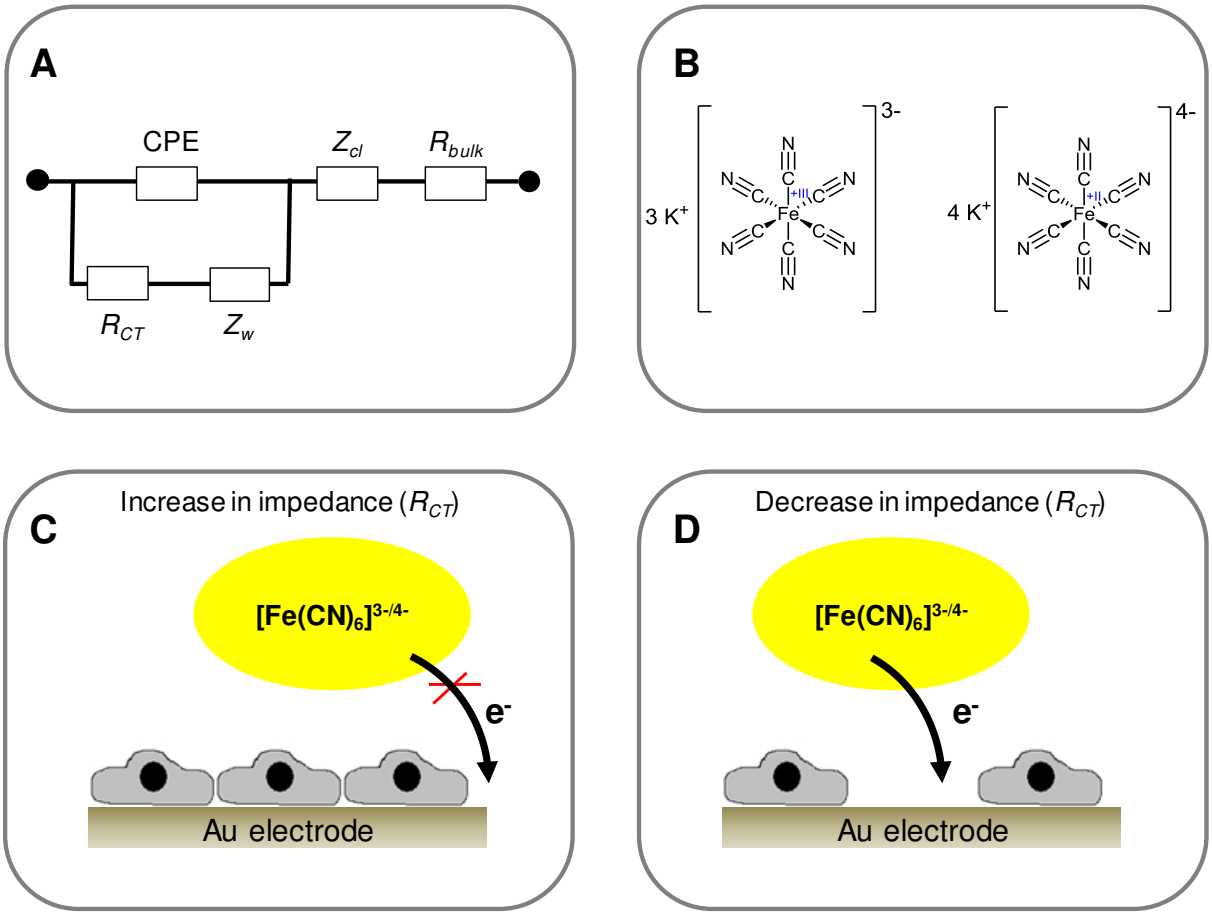

Fig. 4.26: A: Equivalent circuit for a cell-covered electrode in presence of $[Fe(CN)_6]^{3-/4-}$. **B:** Chemical structure of $K_3[Fe(CN)_6]$ and $K_4[Fe(CN)_6]$. **C; D:** Schematic principle of impedance measurements in presence of $K_4[Fe(CN)_6]^{3-/4-}$ shown for a gold-film electrode confluently-covered with cells (**C**) and for an electrode including cell-free areas (**D**).

In contrast to a normal, non-faradaic impedance measurement, in which the corresponding equivalent circuit consists of a CPE connected in series with the impedance contribution arising from the cell layer (Z_{Cl}) and the bulk resistance (R_{bulk}) (**Fig. 4.2 B**), additional circuit elements are necessary to describe the ability for charge-transfer between mediator and electrode. R_{CT} describes the interfacial electron transfer resistance and the Warburg's impedance (Z_w) includes the diffusion of the redox probe in solution, R_{ct} and Z_w are aligned in parallel with the CPE. In faradaic impedance measurements $|Z|$ is usually determined in presence of a redox probe like $[Fe(CN)_6]^{3-/4-}$ (**B**) but also $Co(bpy)_3^{3+}$ or *ferrocenium hexafluorophosphate* are widely used [152].

The principle of impedance analysis in presence of $[Fe(CN)_6]^{3-/4-}$ for a confluently cell-covered gold-film electrode and a gold-film electrodes which includes cell-free regions is illustrated in **Fig. 4.26 C – D**. After establishment of a confluent cell layer and due to the insulating properties of the cell membrane the interfacial electron transfer between redox probe and electrode is hindered, resulting in an increase of R_{CT}. However, when the electrode is only sparsely covered with cells the electron transfer is facilitated, resulting in a lower R_{CT}. In the following study the negatively charged redox mediator $[Fe(CN)_6]^{3-/4-}$ was used in a 1:1 mixture based on molar concentrations to study the effect of varying electrode coverages on $|Z|$, R and C.

4.5.2.2 Concentration-Dependent Impact of $[Fe(CN)_6]^{3-/4-}$ on ECIS Recordings

To analyze the charge-transfer resistance (R_{CT}) in presence of different concentrations of the redox mediator $[Fe(CN)_6]^{3-/4-}$ ECIS measurements were performed with a cell-free 8W10E gold-film electrode layout. After recording a short baseline in culture medium different concentrations (0.5 mM; 2.0 mM; 15 mM) of $[Fe(CN)_6]^{3-/4-}$ were added and the changes in $|Z|$, R and C were analyzed in a frequency-dependent manner (**Fig. 4.27**).

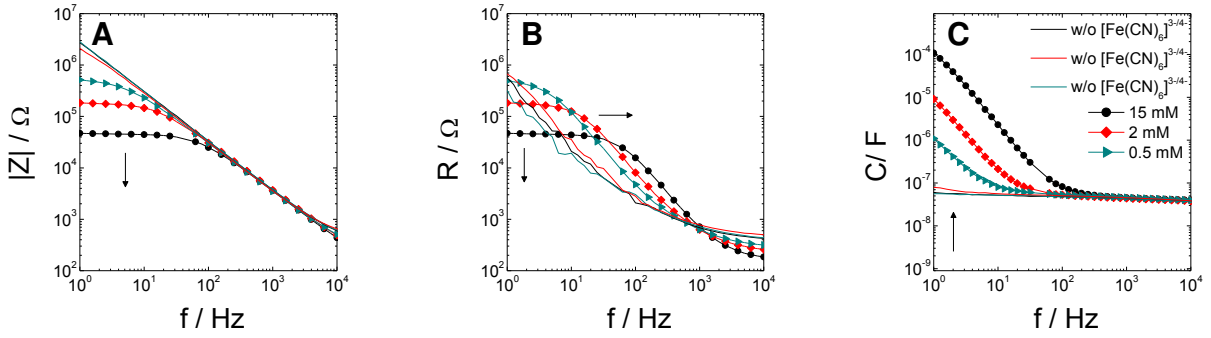

Fig. 4.27: Spectra of impedance magnitude $|Z|$ (**A**), resistance R (**B**) and capacitance C (**C**) as a function of frequency (1 Hz – 10^4 Hz) before (**line**) and after (**line + symbols**) addition of different concentrations (0.5 mM; 2 mM; 15 mM) of $[Fe(CN)_6]^{3-/4-}$ to a cell-free 8W10E electrode layout [‡].

Fig. 4.27 (**A**) clearly demonstrates a decrease of |Z| between 1 - 10^2 Hz dependent on the applied concentration of $[Fe(CN)_6]^{3-/4-}$. For the highest concentration (15 mM) $|Z|$ at 1 Hz decreased from $2.8 \cdot 10^6\,\Omega$ in $[Fe(CN)_6]^{3-/4-}$-free medium to $4.7 \cdot 10^4\,\Omega$. Using 2 mM $[Fe(CN)_6]^{3-/4-}$ a decrease to $1.8 \cdot 10^5\,\Omega$ was observed, whereas the lowest concentration of 0.5 mM resulted in an impedance decrease to $5.1 \cdot 10^5\,\Omega$. The resistance spectra (**B**) showed not only a drop in values at the low frequency regime, but an additional shift of the entire spectrum to higher frequencies. In presence of 15 mM $[Fe(CN)_6]^{3-/4-}$ a decrease to $4.7 \cdot 10^4\,\Omega$ compared to the signal without $[Fe(CN)_6]^{3-/4-}$ ($5.7 \cdot 10^5\,\Omega$) was observed from 1 Hz to 6.3 Hz. The analysis of higher frequencies (above 6.3 Hz) yielded an increase in R in presence of the redox mediator. This effect was also found for 2 mM $[Fe(CN)_6]^{3-/4-}$ with a point of inflection at 3.2 Hz, whereas the lowest concentration provided a higher resistance signal compared to the signal without redox mediator over the entire frequency range. In the frequency-dependent capacitance spectra (C) an increase of C was found in the low frequency range dependent on the applied $[Fe(CN)_6]^{3-/4-}$ concentration. Using 1 Hz for the analysis, C increased compared to the signal in medium to $1.1 \cdot 10^{-6}$ F (0.5 mM), $9.1 \cdot 10^{-6}$ F (2 mM) and $1.1 \cdot 10^{-4}$ F (15 mM).

Changes in the resistance signal were complex as the observed trend strongly depends on the frequency. Using the redox mediator in cell-based experiments the effect of R_{CT} and the position of the point of inflection will strongly depend on a combination of $[Fe(CN)_6]^{3-/4-}$ effect

and the cell-related parameters R_b, α and C_m. Based on these findings the analysis of resistance was excluded for further data analysis, and the focus was only on changes in $|Z|$ and C instead. In the following, a concentration of 2 mM was chosen. This concentration was low enough not to induce any cytotoxicity during cellular studies (**Fig. S 3 A**), and was high enough to be useful for the detection of R_{CT}.

4.5.2.3 Use of $[Fe(CN)_6]^{3-/4-}$ to Study Gradual Electrode Coverages

The additional R_{CT} caused by the presence of 2 mM $[Fe(CN)_6]^{3-/4-}$ in culture medium was analyzed with respect to decreasing cell-coverage with cells. The experiment started with a confluent cell-covered 8W1E gold-film electrode layout housed in a PDMS chamber (**Fig. 4.7**). Eight cell-covered working electrodes in parallel allowed measuring the overall spectra of $|Z|$ and C for 100 % confluence. Afterwards, a single well was selectively wounded by an invasive voltage pulse (40 kHz, 5V, 15 s) and subsequently the overall spectra of $|Z|$ and C for all eight electrodes in parallel (87.5 % cell coverage) was recorded in the "8 against CE" mode. The cell-coverage was reduced stepwise until all eight working electrodes were wounded (0 %). **Fig. 4.28** summarizes the changes in $|Z|$ (**A**) and C (**B**) spectra (1 Hz – 10^6 Hz) for decreasing electrode coverages with MDCK II cells between 100 % – 0 % in presence of 2 mM $[Fe(CN)_6]^{3-/4-}$.

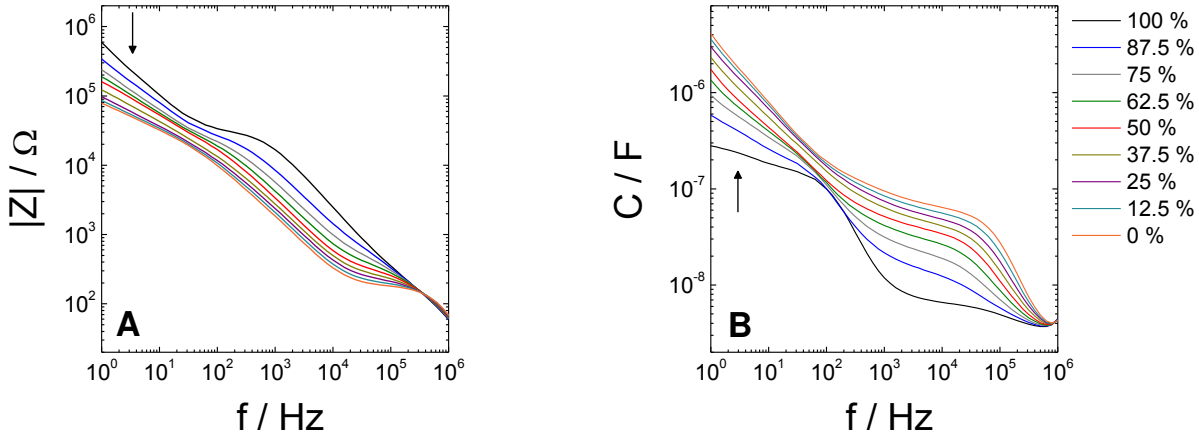

Fig. 4.28: $|Z|$ (**A**) and C (**B**) spectra (1 Hz - 10^6 Hz.) for a differently MDCK II cell-covered and cell-free 8W1E electrode layout when all eight wells are housed in a PDMS chamber in presence of 2 mM $[Fe(CN)_6]^{3-/4-}$. A software modification allowed measuring the overall signal of $|Z|$ and C of all eight WEs in parallel against the common counter electrode ‡.

Changes in electrode coverage were distinct over the whole frequency-range (1 – 10^5 Hz). With decreasing cell coverage the impedance decreased compared to the impedance values for 100 % coverage (**A**). In the low frequency range (1 – 100 Hz) the signal changes in $|Z|$

were caused by the changes in R_{CT}. In the middle frequency range (10^2 – 10^5 Hz) the signal was dominated by the impedance contribution of the cell-layer and therefore, provided information about the degree of cell-coverage. Only in the high frequency-range the impedance values were independent of the electrode coverage and the signal was dominated by parasitic impedance contributions arising from the electronic equipment.

In the capacitance spectra (**B**) a decrease in cell-coverage of the electrodes resulted in an increase of C over the measured frequency-range (1 – 10^6 Hz). Again, changes in C in the low frequency range provided information about changes in R_{CT}, whereas the contribution of the cell layer dominated the position of the plateau in the capacitance spectra (1.5 kHz – 40 kHz).

To emphasize the effect of cell-coverage on R_{CT} the changes of $|Z|$ and C at 1 Hz were extracted and plotted as a function of electrode coverage (**Fig. 4.29**). Data were normalized using the respective value of $|Z|$ and C at 1 Hz for 100 % cell-coverage as reference. Different dependencies were found for $|Z|$ (**A**) and C (**B**) by stepwise reducing the cell-coverage on the electrodes: Whereas $|Z|_{1\ Hz}$ showed an exponential curve progression $C_{1\ Hz}$ provided an almost linear relationship to the electrode coverage.

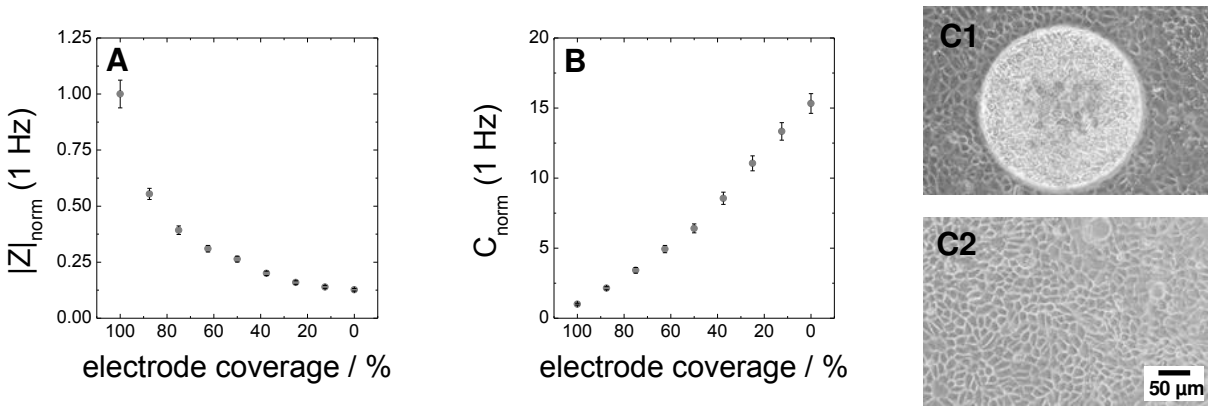

Fig. 4.29: Normalized signal changes of $|Z|$ (**A**) and C (**B**) at 1 Hz to analyze the stepwise reduction in cell-coverage in presence of $[Fe(CN)_6]^{3-/4-}$. Normalized data was obtained by dividing the values by the respective values for 100 % coverage. Phase-contrast micrographs (**C**) of MDCK II cells after wounding (40 kHz, 15 s, 5 V) on the working electrode (**C1**). Cells in the periphery of the electrode show a MDCK II cell-type characteristic cell morphology, indicating healthy cells even in presence of 2 mM $[Fe(CN)_6]^{3-/4-}$ (**C2**). The scale bar represents 50 µm.

At the end of the experiment, cells were documented using phase-contrast microscopy. Cells on the electrode, which were selectively killed by an invasive voltage pulse, showed changes in their morphology (**C1**). In contrast to cells in the periphery no defined cell boundaries were found for cells on top of the electrode. Phase-contrast micrographs additionally revealed no

cell damages in the periphery of the electrode after incubation with 2 mM $[Fe(CN)_6]^{3-/4-}$, indicating no cytotoxicity of the redox mediator itself (**C2**).

The response of each electrode was monitored using the normal ECIS analysis mode in which each working electrode was analyzed individually. The $|Z|$ spectra of two wells before and after pulse application (40 kHz, 5 V, 15 s) are summarized in **Fig. 4.30 A**. After pulse application, a significantly decrease in $|Z|$ between 50 Hz – 20 kHz was found indicating successful wounding of the cell layer. Moreover, in some wells the impedance spectra between 1 Hz – 2 kHz was completely shifted to lower impedance levels (blue line). At these frequencies, the signal is sensitive to changes in the electrode structure. One exemplary phase-contrast image of cells after wounding using 40 kHz, 5 V, 15 s is provided in **Fig. 4.30 B**. The alterations of the electrode structures, which already appeared in the impedance data, were also confirmed in phase-contrast images after pulse application. The white circle along the border of the electrode suggested alterations of the gold-film structure.

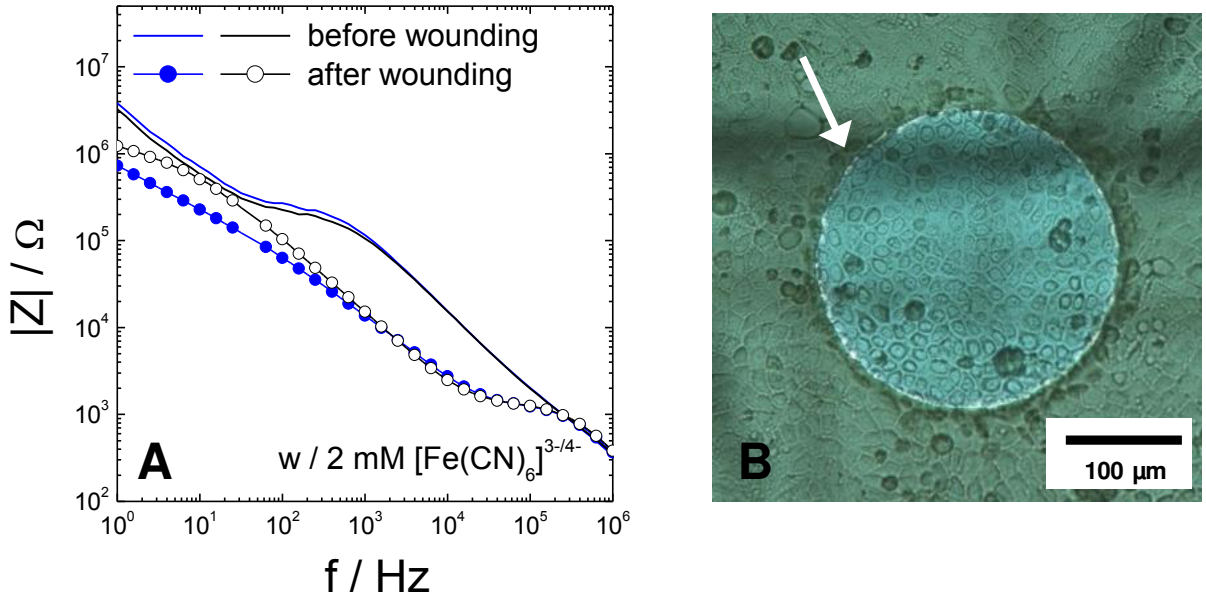

Fig. 4.30: A: Impedance spectra of two MDCK II cell-covered 8W1E electrodes in presence of the redox mediator 2 mM $[Fe(CN)_6]^{3-/4-}$ before (**line**) and after wounding (●; ○) using an invasive wounding pulse (40 kHz, 5 V, 15 s) ‡. **B:** Phase-contrast image of a 8W1E electrode covered with MDCK II cells at the end of experiment. After pulse application electrode damages were found in the phase-contrast image, highlighted by the arrow.

4.5.2.4 Simulations

To support the results yielded from experimental impedance recordings, in which the electrode coverage was reduced stepwise by applying subsequent wounding pulses, a simulation was performed using a modified LabVIEW software. The parameters which were applied during the simulation process are summarized in **Tab. 4.4**. The parameter R_{CT} (cell-free) was taken from a previous cell-free ECIS experiment, in which data were recorded in absence and presence of 2 mM $[Fe(CN)_6]^{3-/4-}$ (**Fig. S 3 B**).

Tab. 4.4: Overview of the different parameters used for the simulation regarding the influence of an additional R_{CT} and varying electrode coverages with cells (100 % – 0 %). As illustrated in **Fig. 4.26** R_{CT} depends on the fraction of cell coverage. In presence of a confluent model cell layer R_{CT} (cell-cov.) was set to 10^6 Ω·cm^2. For a cell-free electrode R_{CT} (cell-free) was determined to 2375 Ω·cm^2.

Parameter	Value /	Unit
R_b	25	Ω·cm^2
α	15	Ω$^{0.5}$·cm
C_m	3	µF·cm^{-2}
R_{CT} (cell-free)	2375	Ω·cm^2
R_{CT} (cell-cov.)	10^6	Ω·cm^2
A	$1.5 \cdot 10^{-5}$	Fs^{n-1}·cm^{-2}
n	0.95	
R_{bulk}	150	Ω
Area	$4 \cdot 10^{-3}$	cm^2

The spectra were calculated using electrode coverages similar to the impedance recordings presented before (100 % – 0 %). **Fig. 4.31** provides a summary of the simulated impedance (**A**) and capacitance (**B**) data. In good agreement with **Fig. 4.28 A** a decrease in $|Z|$ in the low frequency range was found by decreasing the fraction of cell coverage. In contrast to the experimental impedance data the simulated spectra only showed a coverage-dependent decrease from 1 Hz – 7 Hz. Similar impedance values were found in the simulated data from 10 – 120 Hz. The analysis of frequencies between 150 Hz – 400 kHz also yielded a cell-coverage dependent decrease in $|Z|$ values, when the cell coverage was reduced stepwise from 100 % to 0 % electrode coverage. The analysis of the same phenomena in the capacitance signal (**B**) showed an increase in *C* between 1 Hz – 25 Hz by increasing the cell-free area. Additionally, the analysis of C using frequencies above 300 Hz also showed a coverage-dependent increase. To analyze the changes in R_{CT} due to varying electrode

coverages with the model cell type (R_b = 25 Ω·cm^2, α = 15 Ω$^{0.5}$·cm, C_m = 3.0 µF/cm^2) the changes in $|Z|$ (**A2**) and C (**B2**) were extracted at 1 Hz and analyzed as a function of electrode coverage. The diagrams provided a hyperbolic decrease in $|Z|$ as well as an increase in C depending on the coverage.

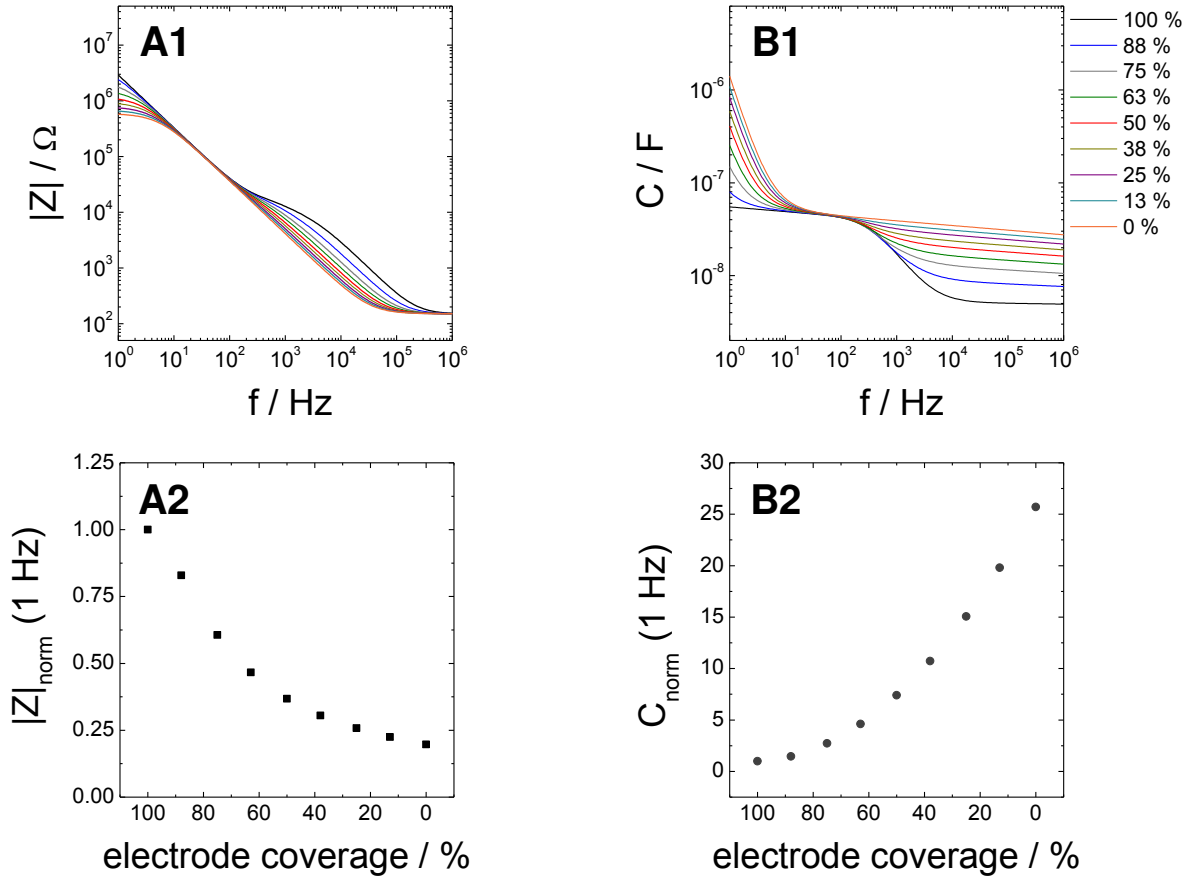

Fig. 4.31: 1: Simulated impedance (**A**) and capacitance (**B**) spectra for decreasing electrode coverages (100 % – 0 %) with cells (R_b = 25 Ω·cm^2, α = 15 Ω$^{0.5}$·cm, C_m = 3.0 µF/cm^2) in presence of charge transfer across the electrode / electrolyte interface. **2:** Normalized extracted changes of $|Z|$ (**A**) and C (**B**) at 1 Hz dependent on the electrode coverage with cells. Data was normalized by the respective value obtained for 100 % coverage.

4.5.3 Inhomogeneity of the Cell Population on the Electrode

The aim of the simulation project was to study the inhomogeneity of a cell population on a confluently cell-covered electrode. In the model of Giaever and Keese the whole cell population located on the electrode is characterized by a uniform parameter of α, R_b and C_m. However, microscopic analysis of the electrode coverage always provides differences in cell size and shape. This clearly shows that the assumption of the ECIS model that cells are regarded as uniform does not reflect the real situation on the electrode. We addressed this topic by calculating impedance data in which the electrode was occupied by two different cell types which are different in their electric properties. For this purpose, in different scenarios the ratio of these two cell types was changed systematically, while keeping an overall 100 % of electrode coverage.

To support the computed data, experimental ECIS recordings were performed to study the effect of inhomogeneity of the cell population on the electrode. For this purpose, co-cultures of two different cell types, NRK and MDCK II pABCG2 EYFP cells, which are genetically modified and carry an EYFP labeling in the plasma membrane, were seeded at defined ratios. Subsequent to the ECIS recordings microscopic analysis of the electrode coverage was performed using DAPI staining. The additional EYFP labeling of the plasma membrane of MDCK II cells allowed a differentiation between NRK and MDCK II cells.

4.5.3.1 Experimental Background

As described in **chapter 4.3.1.3** co-culture experiments were performed by seeding two different cell types simultaneously using defined seeding densities. Prior to the ECIS recordings, microscopic studies have proven that these cell types are viable when cultivated in co-culture. **Fig. 4.32** shows phase-contrast images of NRK cells (**A**), of MDCK II cells (**B**) and of co-cultures of both cell types (**C;D**). Cellular proliferation was unaffected during the co-culture experiment and cell viability was not impaired by the non-ideal growth media (a mixture of both cell-type specific medium compositions). In the co-culture of NRK and MDCK II cells insular structures were found, which can be an indicator for a preferred formation of cell-cell-contacts within one cell type.

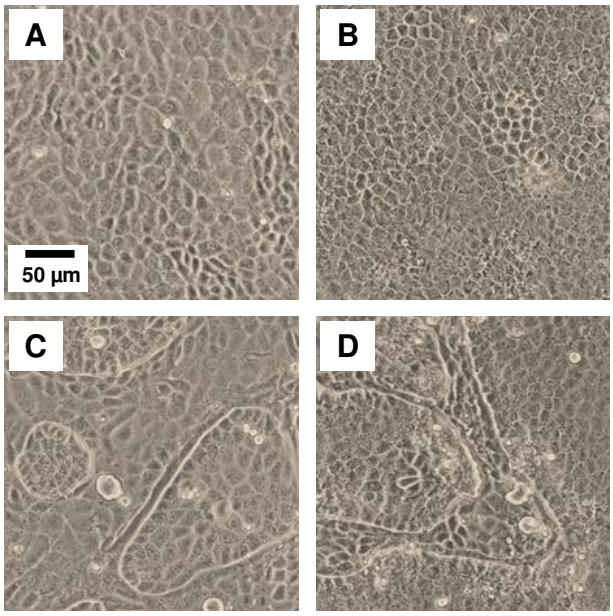

Fig. 4.32: Phase-contrast images of NRK cells (**A**) and MDCK II cells (**B**) after 4 days of cultivation using a seeding density of 45 000 cells/cm^2. Co-cultures of MDCK II cells and NRK cells (**C;D**) were grown in a 1:1 mixture of NRK and MDCK II medium. Cellular proliferation of the co-cultures was analyzed 4 days after cell seeding using initial cell numbers of 5500 cells/cm^2 (**C**) or 22 000 cells/cm^2 (**D**) for each cell type. Images were taken using a 20 x objective.

Since no influences on cell viability were found ECIS experiments were performed (**chapter 4.3.1.3**). Different ratios of MDCK II pABCG2 EYFP cells and NRK cells were seeded simultaneously in defined seeding densities using 8W10E electrode layouts. To support the ECIS recordings and to proof the cell composition on the electrode cells were fixed and cell nuclei were stained with DAPI at the end of the experiment, ~ 20 h after cell-seeding. The additional EYFP-labeling of the plasma membrane of MDCK II pABCG2 EYFP cells facilitated the identification of both cell types. **Fig. 4.33** exemplarily shows one electrode for each condition where the percentages of MDCK II pABCG2 EYFP cells increased from **B1** – **E1** indicated by an increase in green fluorescence intensity within the image section. The DAPI staining in **A2** – **E2** indicated the formation of a confluent cell layer in each well. However, the pure population of MDCK II pABCG2 EYFP cells (**E1)** did not exhibit a homogenous green fluorescence over the entire field of view using one z-position. Nevertheless, a significant difference was found for the different ratios of 3:1 NRK : MDCK II (**B1**), 1:1 (**C1**) and 1:3 NRK : MDCK II (**D1**). Thus, the initially used seeding density of the respective cell types correlates well with the distribution of those two cell types on top of the electrode.

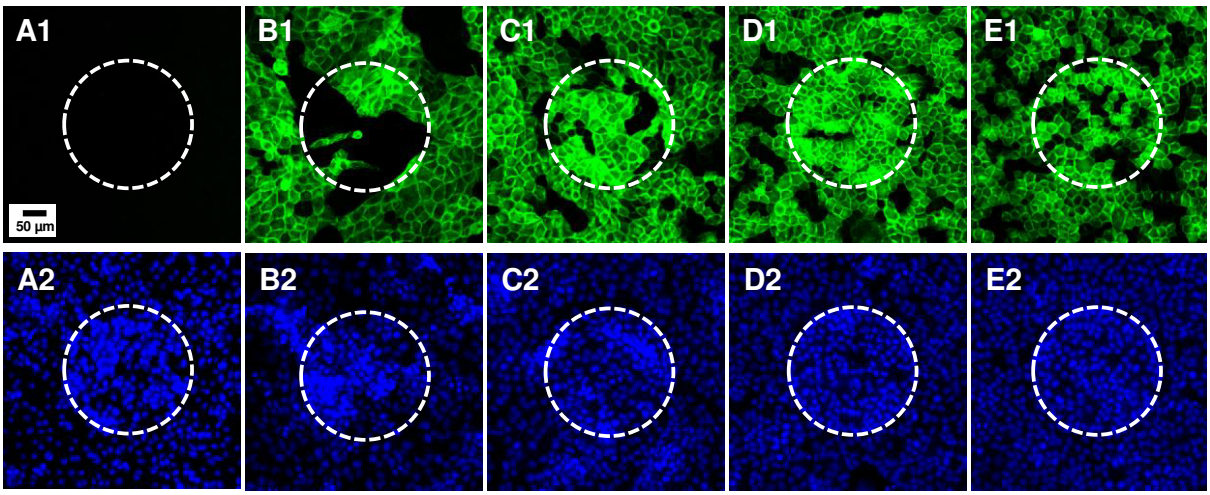

Fig. 4.33: Confocal laser scanning micrographs for NRK cells (**A**), MDCK II pABCG2 EYFP cells (**E**) and different co-cultures with varying ratios (**B – D**) on a 8W10E gold-film electrode layout 20 h after seeding 250 000 cells/cm^2: **B:** 3:1, **C:** 1:1, **D:** 1:3. Images were taken after staining of the cell nuclei with DAPI (**2**). The green fluorescence resulted from the EYFP-labeling of the MDCK II pABCG2 EYFP cells (**1**). For each condition one electrode is shown exemplarily. The position of the electrode is indicated by the white dashed circle. Images were taken using a 10 x objective.

A survey of typical experimental data of a co-culture experiment is provided in **Fig. 4.34**. Here, the raw data of $|Z|$ (**A1**), R (**B1**) and C (**C1**) 20 h after cell seeding on an 8W10E electrode layout in a frequency range between 1 – 10^6 Hz is provided. The impedance magnitude $|Z|$ (**A1**) showed cell-type related changes in the frequency range between 100 Hz – 16 kHz. NRK cells were characterized by a significantly lower plateau level compared to the MDCK II pABCG2 EYFP cells. Co-cultures, when one cell type was present at higher proportion resulted in spectra which were dominated by the predominant cell type and only provided small aberrations compared to the pure population. The 1:1 co-culture of NRK and MDCK II pABCG2 EYFP was characterized by a spectrum which was positioned in between the two pure populations. The analysis of R (**B1**) clearly showed the distinct resistance spectra depending on the cell composition. An increase in the plateau levels was found by increasing MDCK II pABCG2 EYFP content. The composition of the cell population also provided a change in the capacitance spectra. A shift to lower frequencies was found for increasing the content of MDCK II pABCG2 EYFP cells (**C1**). Even when one cell type was added in low proportion to the other cell population, the signal could be discriminated in $|Z|$, R and C from the respective pure population.

To further analyze the effect of different cell coverages the experimental data were normalized to a cell-free 8W10E electrode layout (**A2 – C2**). In the normalized impedance spectra (**A2**) a shift to higher frequencies as well as a decrease in signal height was observed by changing the electrode coverage from MDCK II pABCG2 EYFP to NRK cells. A good separation in $|Z|_{\text{cell-cov/cell-free}}$ was found for the co-cultures depending on the ratios of each cell line. A co-population of 50 % NRK and 50 % MDCK II pABCG2 EYFP was located

between both spectra of the corresponding pure populations. The spectra of co-cultures, when one population was added in excess approached spectra of the respective pure population. The most sensitive frequency was found at ~ 10 kHz for MDCK II pABCG2 EYFP cells and at ~ 25 kHz for NRK cells. The presentation of $R_{\text{cell-cov/cell-free}}$ (**B2**) provided a significant decrease in the maximum from 23.0 for 100 % MDCK II pABCG2 EYFP cells or co-cultured when this cell type was applied in excess to 6.6 for NRK cells. Also in $R_{\text{cell-cov/cell-free}}$ the spectrum with 50 % - 50 % mixture of NRK and MDCK II pABCG2 EYFP cells was located in between the spectra of the pure cultures and showed its maximum at 13.3. The decrease in signal height was also combined with a shift of the maximum to higher frequencies. In $C_{\text{cell-cov/cell-free}}$ (**C2**) a shift to higher frequencies was observed by increasing the content of NRK cells and a clear separation of the different conditions was possible. After establishment of a confluent cell layer (t = 20 h) changes in $|Z|$, R and C at 500 Hz, 4 kHz and 32 kHz were extracted (**A3 – C3**) and normalized to the respective value of a pure MDCK II pABCG2 EYFP cell population.

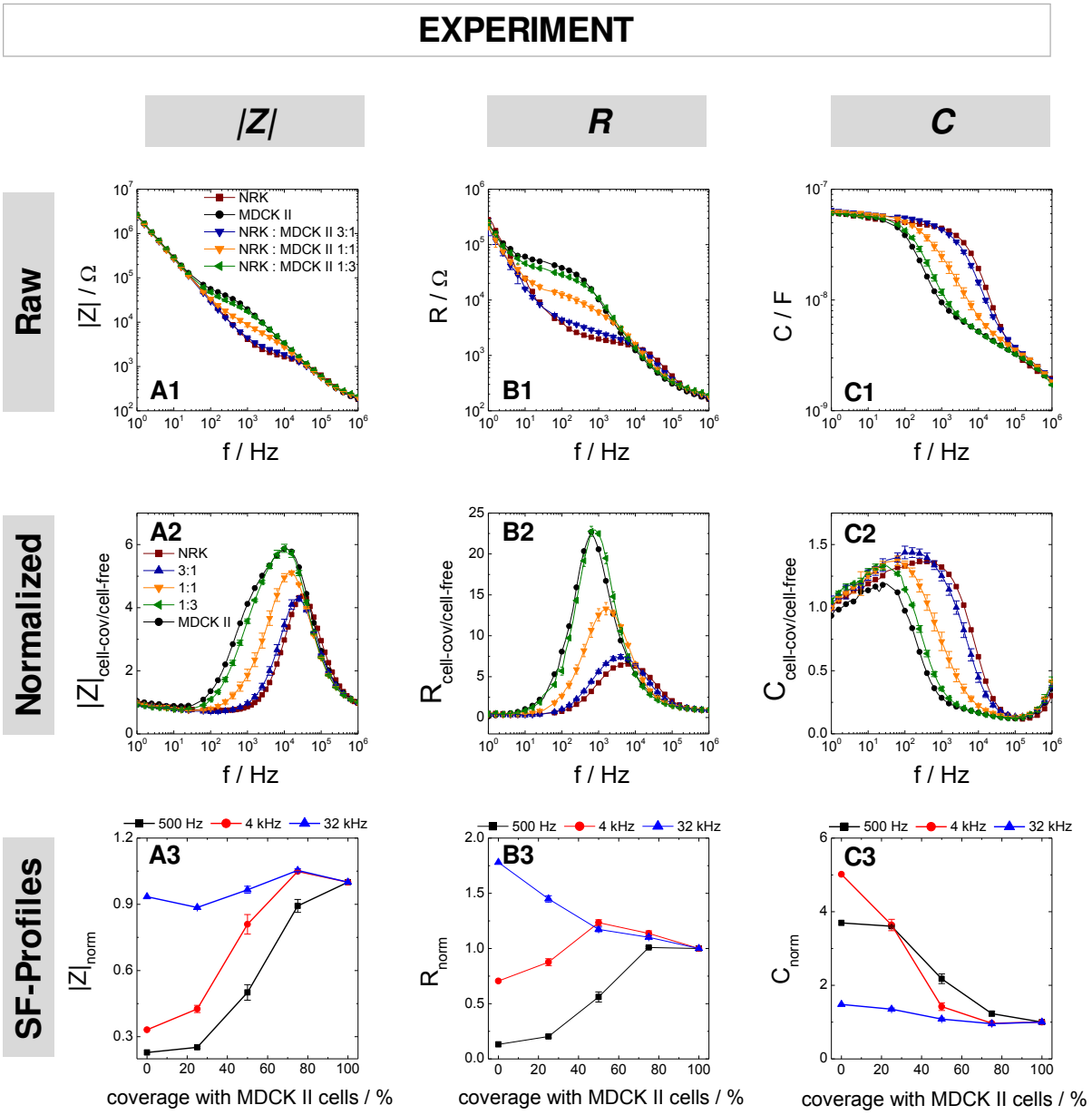

Fig. 4.34: Summary of experimentally obtained $|Z|$ (**A**), R (**B**) and C (**C**) data for discretely varied electrode coverage of MDCK II cells and NRK cells using a 8W10E electrode layout. **1:** Frequency-dependent $|Z|$ (**A1**), R (**B1**) and C (**C1**) raw spectra (f = 1 Hz – 10^6 Hz) ‡. **2:** Normalized $|Z|$, R and C spectra for discretely varied electrode coverage. The normalized spectra $|Z|_{\text{cell-cov/cell-free}}$ (**A2**), $R_{\text{cell-cov/cell-free}}$ (**B2**), $C_{\text{cell-cov/cell-free}}$ (**C2**) were obtained by dividing values from cell-covered electrodes by the respective values of a cell-free 8W10E electrode layout ‡. **3:** *Single frequency* (SF)-profiles of $|Z|_{\text{norm}}$ (**A3**), R_{norm} (**B3**) and C_{norm} (**C3**) at 500 Hz (■), 4 kHz (●) and 40 kHz (▲) dependent on the electrode coverage (0 – 100 %). The data were normalized by the respective values for a 100 % coverage of MDCK II pABCG2 EYFP cells. For co-cultures Mean values ± SD (N = 2) of a typical experiment are shown.

4.5.3.2 Simulation to Study the Inhomogeneity of a Cell Population

To investigate the influence of a cell layer, when cells show a low or high degree of inhomogeneity regarding their electrical properties, a simulation was performed and the content of a cell layer was varied using two model cell types. The simulation starts with a confluent model cell layer of type A, which is described by $R_b = 25\ \Omega{\cdot}cm^2$, $\alpha = 15\ \Omega^{0.5}{\cdot}cm$ and $C_m = 3\ \mu F/cm^2$ on a 8W10E electrode layout. In the following steps the amount of a second model cell type B, characterized by $R_b = 5\ \Omega{\cdot}cm^2$, $\alpha = 8\ \Omega^{0.5}{\cdot}cm$ and $C_m = 3\ \mu F/cm^2$ is increased stepwise, without changing the overall degree of confluence. **Fig. 4.35** summarizes the frequency-dependent changes of $|Z|$ (**A1**), R (**B1**) and C (**C1**) of simulated raw data for different ratios of cell type A and B on the electrode.

In the impedance spectra (**A1**) the increasing amount of cell type B is reflected by a decrease in the plateau value. This effect is even more pronounced in R (**B1**) between 50 Hz – 1000 Hz. However, also here a frequency-dependent trend of R is observed. The analysis of frequencies $> 10^4$ Hz provides an increase in R by reducing the content of cell type B. In the capacitance spectra (**C1**) a shift to higher frequencies is found by varying the population and increasing the content of cell type B.

The corresponding normalized spectra of $|Z|_{\text{cell-cov/cell-free}}$, $R_{\text{cell-cov/cell-free}}$ and $C_{\text{cell-cov/cell-free}}$ are shown in (**A2 – B2**). By modifying the cell layer $|Z|_{\text{cell-cov/cell-free}}$ (**A2**) clearly indicates a shift of the most sensitive frequency to higher frequencies as well as a decrease in the peak height by increasing the content of cell type B. Using a confluent cell layer of type A the maximum of 5.1 is found at ~ 5 kHz, whereas cell layer B is characterized by a maximum signal of 3.3 at ~ 9 kHz. In the normalized data R (**B**) also shifts to lower frequencies as well as a decrease in peak height is found. This diagram also emphasized the cross-over frequency at ~ 6 kHz above which the observed trend of decreasing R values for decreasing coverage of cell type A is inverted. The analysis of higher frequencies show a higher value of $R_{\text{cell-cov/cell-free}}$ for cell layer B compared to the signal of 100 % coverage of type A. The decreasing content of cell type A is indicated by a shift to higher frequencies between 100 Hz – 40 kHz in $C_{\text{cell-cov/cell-free}}$ (**C**).

To summarize the computed data the changes in $|Z|$, R and C were extracted at 500 Hz, 4 kHz and 32 kHz and normalized to the respective signal of a confluent coverage of cell type A. These normalized changes are plotted against the percentage cell coverage of cell type A (**A3** – **C3**).

A steady rise of $|Z|$ at 500 Hz as well as at 4 kHz is observed by increasing the percentage of cell type A (**A3**). As expected, $|Z|$ at 32 kHz almost stays constant for al mixtures as the electrode coverage in all simulation scenarios is assumed to be confluent. R_{norm} (**B3**) showed

different directions of curve development for low and medium frequencies compared to high frequencies. Whereas at 500 Hz and 4 kHz an increase from 0.35 or 0.77 to 1.0 is found, R_{norm} at 32 kHz shows a counter-intuitive decrease from 1.3 to 1.0. C_{norm} at 32 kHz is sensitive to changes in cell coverage and no significant change is detected by varying the content of cell type A (**C3**). Also at 500 Hz, only a weak response in C_{norm} depending on the cell coverage is found, without any significant change between 50 – 100 %. However, a noticeable signal change is observed at 4 kHz where C_{norm} decreased in a linear manner when the amount of model cells described by the parameter $R_b = 25\ \Omega \cdot cm^2$, $\alpha = 15\ \Omega^{0.5} \cdot cm$ and $C_m = 3\ \mu F/cm^2$ increased. Simulation for a 8W1E ECIS electrode layout with identical cell-related parameters for cell type A and B can be found in **Fig. S 4**.

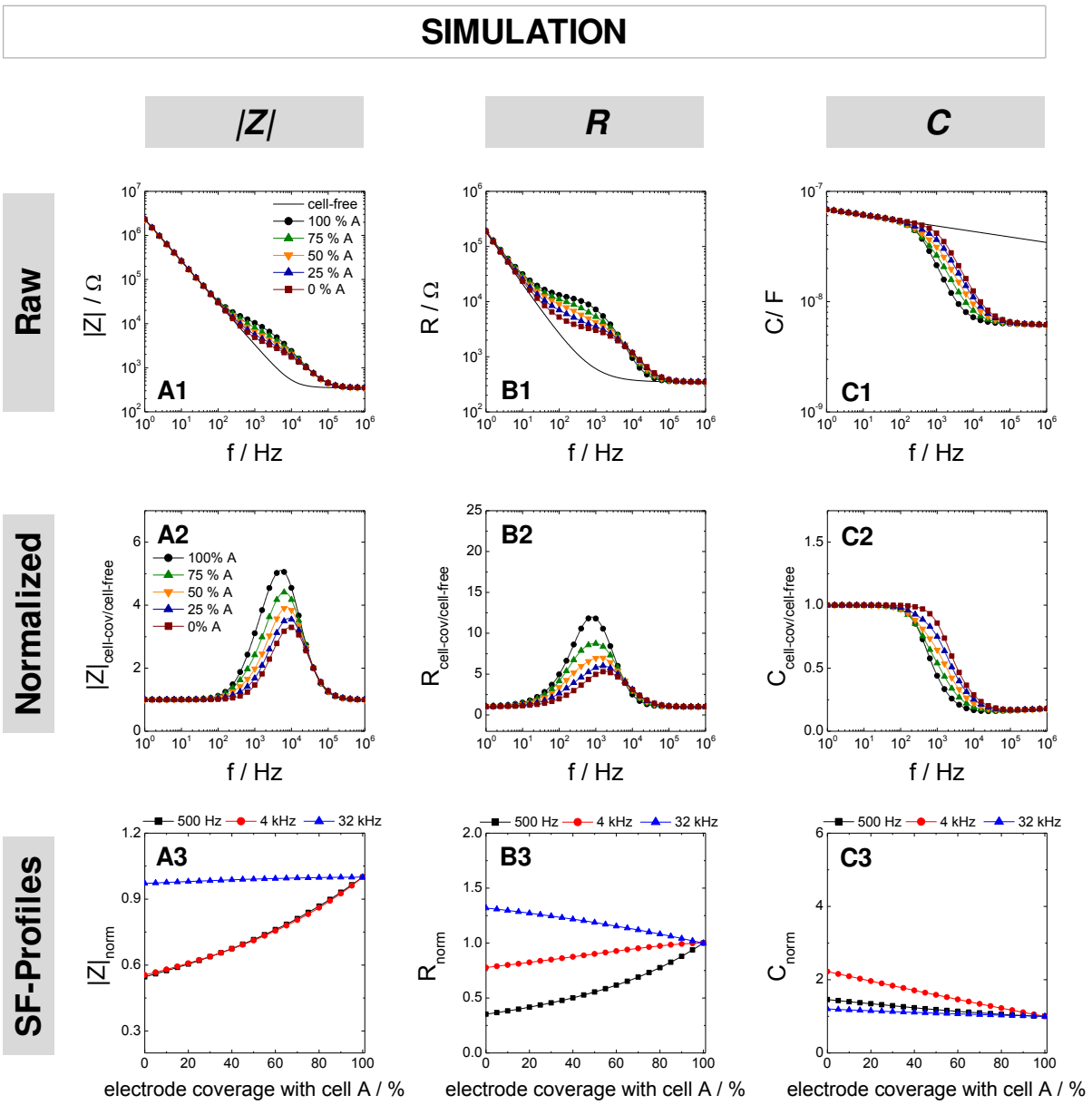

Fig. 4.35: Summary of simulated $|Z|$ (**A**), R (**B**) and C (**C**) data for discretely varied electrode coverage with a model cell type A (R_b = 25 Ω·cm^2, α = 15 Ω$^{0.5}$·cm, C_m = 3.0 µF/cm^2) and B (R_b = 5 Ω·cm^2, α = 8 Ω$^{0.5}$·cm and C_m = 3 µF/cm^2) for a 8W10E electrode layout. **1:** Simulated frequency-dependent $|Z|$ (**A1**), R (**B1**) and C (**C1**) raw spectra (f = 1 Hz – 10^6 Hz) for cell-free (line) and a differently cell-covered (line + symbol) 8W10E electrode layout. **2:** Normalized spectra were obtained by dividing values from cell-covered electrodes by the respective values of a cell-free electrode. **3:** *Single frequency* (SF)-profiles of $|Z|_{norm}$ (**A3**), R_{norm} (**B3**) and C_{norm} (**C3**) at 500 Hz (■), 4 kHz (●) and 32 kHz (▲) depending on the electrode coverage (0 – 100 %). The data were normalized by the values for 100 % coverage with cell type A.

4.5.4 Open Membrane

Another approach to study the inhomogeneity of electrode coverage was performed by increasing the percentage of cells with permeabilized cell membranes. By adding saponin, a mixture of different amphipathic glycosides, the cell membrane loses its barrier properties which under normal conditions prevent free-diffusion of substances (e.g. fluorescent dyes). To address this topic experimentally, the response of MDCK II cells before, during and after saponin exposure was analyzed impedimetrically. The aim of this simulation was to analyze the effect of increasing membrane permeabilization on $|Z|$, R and C signals at different frequencies. Additionally, it should be proven, if it is possible to distinguish between open plasma membrane and open cell-cell-contacts by the evaluation of impedimetric data.

4.5.4.1 Microscopic Analysis

As described in **chapter 4.3.2** cells were treated with saponin in presence of extracellular FITC dextran solution (in PBS^{++}) to monitor microscopically membrane opening in a time-dependent manner. A z-plane was chosen in the middle of the cell bodies where no fluorescence intensity was found at the beginning due to dye exclusion by intact plasma membranes. **Fig. 4.36** summarizes the time-dependent permeabilization process of the plasma membrane after the addition of 0.03 % (**A**) or 0.02 % (**B**) saponin. An increase in green fluorescent MDCK II cells was found after saponin treatment. Images were taken every minute after exposure to saponin and examples are exemplarily shown at t = 4 min, 8 min, 14 min, 18 min and 32 min.

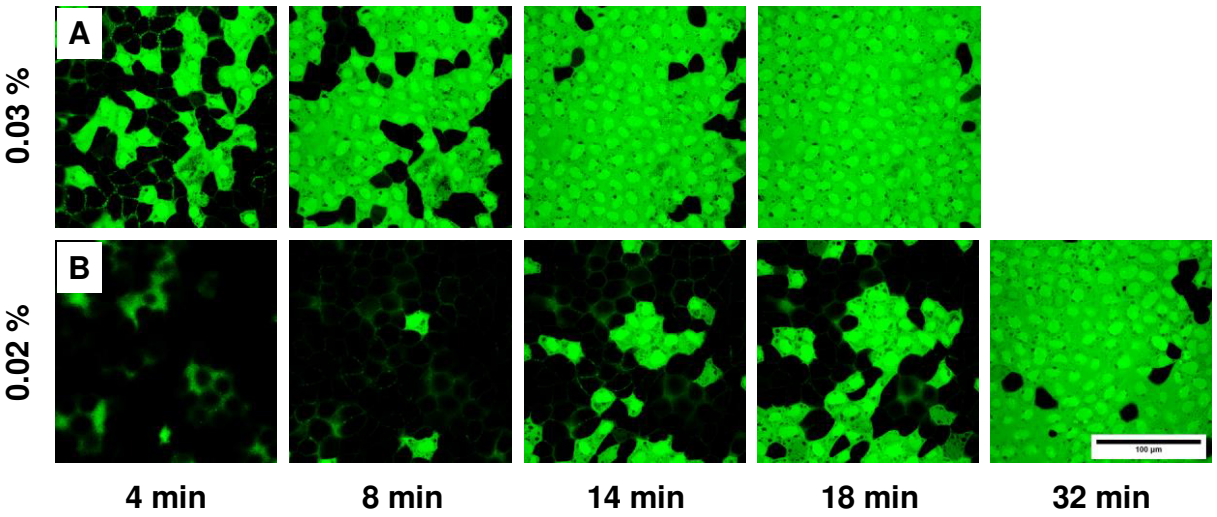

Fig. 4.36: Typical confocal fluorescence micrographs of MDCK II cells after addition of 0.03 % (**A**) or 0.02 % (**B**) saponin in PBS^{++} supplemented with 1 mg/mL FITC dextran at 37 °C. Time-dependent opening of the membrane caused by saponin is indicated by an increase in green fluorescent MDCK II cells. Images were taken every 60 s with 60 x magnification. The scale bar represents 100 µm.

Three different fluorescence micrographs per condition and time-point were analyzed using ImageJ and the amount of fluorescent pixels (with a brightness of 125 and above) were determined for the different conditions (**Fig. 4.37**).

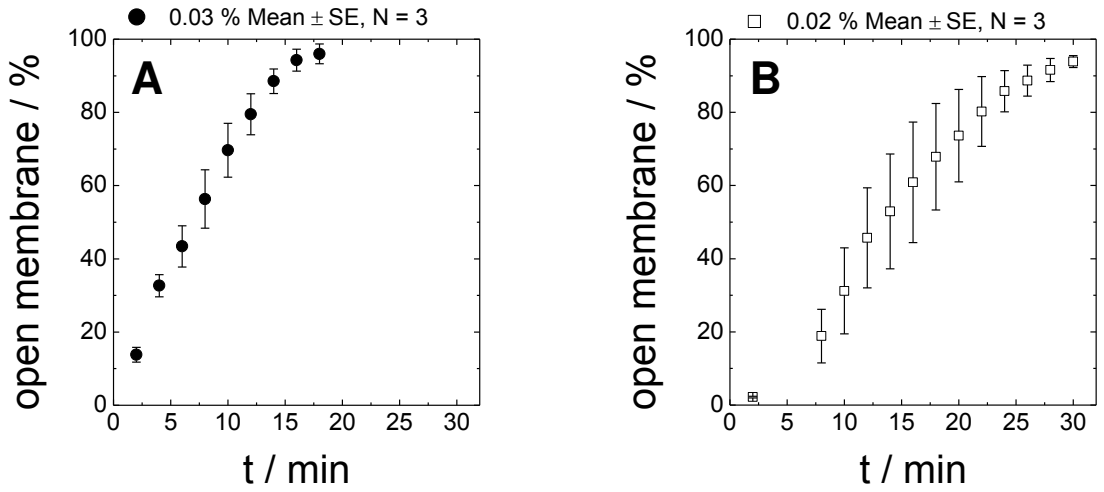

Fig. 4.37: Quantification of time-dependent permeabilization of the plasma membrane of MDCK II cells in presence of 0.03 % (**A**) and 0.02 % (**B**) saponin. The calculated fluorescent pixels were divided by the total number of pixels per image ($1.05 \cdot 10^6$) to obtain the percentage of cells with open membrane. For each time-point three images per condition were analyzed. (Mean value ± SE; N = 3).

After treatment with 0.03 % saponin (**A**), a fast increase in fluorescence intensity was observed indicating a constant reduction of cells with intact plasma membranes. Within 18 min almost all cells in the field of view showed permeable membranes and consequently FITC dextran was able to diffuse into cell bodies. By decreasing the concentration to 0.02 % saponin (**B**) the process of dye-penetration was slower. Membrane opening started around 8 min after saponin addition. The permeabilization of almost the entire cell population took more than 30 min. This microscopic study clearly showed the mode of action of the amphipathic glycosides: Gradual opening of the plasma membrane of adherent cells delayed in time, with the applied saponin concentration determining the speed of the process. For the following ECIS experiment a concentration of 0.02 % was used, which should facilitate an analysis of time-dependent degrees of membrane permeabilization within one cell population during the experiment.

4.5.4.2 Membrane Permeabilization after Saponin Treatment Monitored with ECIS

The cellular response of a confluent MDCK II monolayer was measured during and after treatment with 0.02 % saponin with a high time-resolution using ECIS. Only one well was monitored over 15 min using MFT mode data acquisition to achieve a better time resolution.

The frequency-dependent changes in spectra of $|Z|$ (**A1**), R (**B1**) and C (**C1**) in a frequency range of $10 – 10^5$ Hz after different incubation times in presence of 0.02 % saponin are summarized in **Fig. 4.38**. The time-course of $|Z|_{norm}$, R_{norm} and C_{norm} of MDCK II cell response after the addition of saponin were further extracted at 500 Hz, 4 kHz and 32 kHz (**A2 – C2**). The time point of saponin addition was indicated by the arrow and data were normalized to the respective values immediately before addition. After adding saponin to MDCK II cells $|Z|_{norm}$ showed a significant decrease for all three frequencies (**A2**). Around 2.5 min after the addition the signal became almost constant for the remaining observation time at 0.25 (4 kHz), 0.34 (32 kHz) and 0.48 (500 Hz). Also in R_{norm} (**B2**) a decrease to 0.07 (500 Hz) and 0.18 (4 kHz) was detected. However, the response of MDCK II cells monitored at 32 kHz first provided an increase to 1.1 immediately after the addition, followed by a decrease to 0.57 (32 kHz). C_{norm} at 500 Hz showed a small increase to 1.7 due to the permeabilization of the plasma membrane of MDCK II cells (**C2**). At 4 kHz also a fast increase to 3.6 within 5 min was detected, which further increased to 3.9 until the end of the experiment. The response of MDCK II cells in C_{norm} at 32 kHz showed a bi-phasic process. During the first 5 min an increase to 3.4 was observed, followed by a further increase to 4.5 (t = 13.5 h).

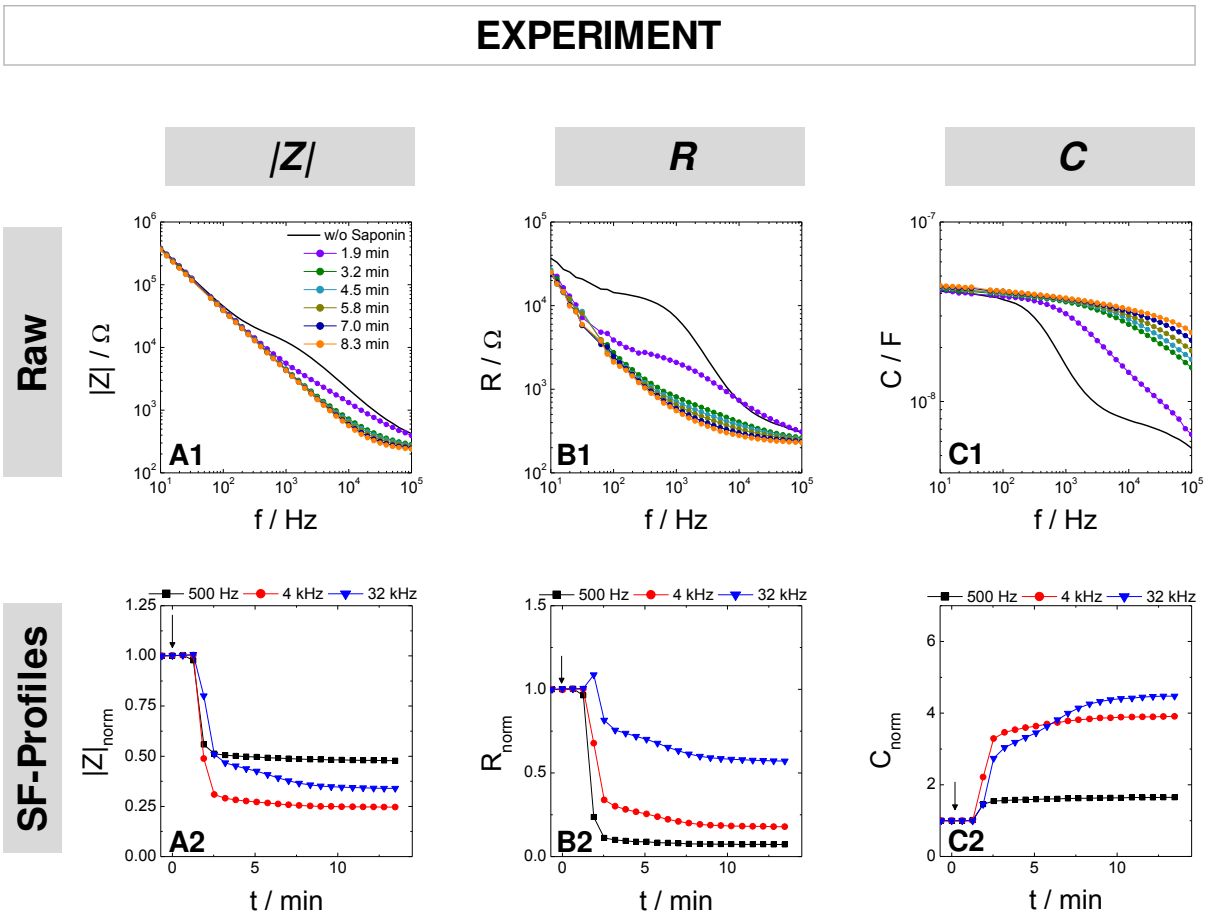

Fig. 4.38: Survey of experimental data to study the response of MDCK II cells confluently grown on 8W10E electrodes before and after the addition of 0.02 % saponin. **1:** $|Z|$ (**A1**), R (**B1**) and C (**C1**) spectra in a frequency range between 10^1 – 10^5 Hz in absence (—) and presence (●) of 0.02 % saponin [‡]. Spectra were recorded at t = 1.9 min – 8.3 min after saponin addition. **2:** Time-course of $|Z|_{norm}$ (**A2**), R_{norm} (**B2**) and C_{norm} (**C2**) of MDCK II cells on 8W10E electrodes before and after the addition of saponin, which were extracted at 500 Hz (■), 4 kHz (●) and 32 kHz (▲). Data were normalized to the time-point immediately before addition, indicated by the arrow.

4.5.4.3 Simulated Data

The simulations were performed with the LabVIEW-based software assuming that in the beginning the electrode of a 8W10E (**Fig. 4.39**) or 8W1E (**Fig. S 5**) layout was confluently covered with a model cell population. The model cell layer is described by the cell-related parameter $R_b = 25\ \Omega{\cdot}cm^2$, $\alpha = 15\ \Omega^{0.5}{\cdot}cm$, $C_m = 3\ \mu F/cm^2$ and $R_m = 1{\cdot}10^{12}\ \Omega{\cdot}cm^2$. A high R_m value is characteristic for an intact plasma membrane. In the following, the electrode coverage was changed stepwise and the fraction of cells exhibiting an open plasma membrane ($R_m = 0.1\ \Omega{\cdot}cm^2$) was successively increased.

The spectra of $|Z|$ (**A1**), R (**B1**) and C (**C1**) with varying percentages of cells with permeabilized plasma membrane were calculated for a 8W10E electrode layout using a frequency range between 1 – 10^6 Hz (**Fig. 4.39**). For the frequency-dependent changes in $|Z|$ (**A1**) an increase in percentage of cells without intact cell membrane causes a decrease in the impedance signal. When the electrode is occupied with 100 % permeabilized cells only a small difference compared to the signal of a cell-free electrode in the high frequency range is found. In the resistance spectra (**B1**) an increase of permeabilized cells is reflected by a shift of the shoulder to the lower frequency range and by a decrease of the plateau value. The most prominent changes are found in the capacitance spectra (**C1**). Here, a stepwise increase, dependent on the percentage of cells with open membrane was recorded between 10^4 – 10^5 Hz.

The $|Z|$, R and C spectra were normalized using the respective cell-free values of a 8W10E electrode (**A2 – C2**). An increase in the percentage of cells with open membrane causes a decrease in the maximum of $|Z|_{cell\text{-}cov/cell\text{-}free}$ (**A2**). While a confluent cell layer with an intact cell membrane provides a maximum of ~ 5.1 at 5 kHz, the peak height for partially or completely permeabilized cell layers decreases to 2.5 (25 %), 1.7 (50 %), 1.3 (75 %) and 1.1 (100 %). This is also accompanied by a shift of the most sensitive frequency. By permeabilization of the plasma membrane the sensitive frequency is changed from 5.2 kHz for a confluent, intact cell layer to 3.5 kHz (25 %), 3.2 kHz (50 %) and 2.6 kHz (75 %), respectively. When the plasma membranes of all electrode-covering cells are permeabilized $|Z|_{cell\text{-}cov/cell\text{-}free}$ only reveals a small difference compared to a cell-free 8W10E electrode between 10^4 – 10^6 Hz. In $R_{cell\text{-}cov/cell\text{-}free}$ (**B2**) two different effects are found by varying the cell membrane properties on the electrode surface. First, the peak height decreases by increasing the ratio of cells with permeabilized cell membranes and second, the width of the signal is getting smaller, which also causes a shift of the most sensitive frequency from 800 Hz (0 %) to 400 Hz (25 %), 300 Hz (50 %) and 200 Hz (75 %). For $C_{cell\text{-}cov/cell\text{-}free}$ (**C2**) a successive increase is observed at 32 kHz upon increasing the number of permeabilized cells from 0.16 (0 %) to 0.35 (25 %),

0.56 (50 %) and 0.77 (75 %). When 100 % of the cells provide open membranes the signal at this frequency did not show any difference to a cell-free electrode.

The survey of changes in $|Z|_{norm}$, R_{norm} and C_{norm} which were extracted at 500 Hz, 4 kHz and 32 kHz are shown in (**A3 – C3**). Data were normalized to the signal when the entire electrode was covered with cells having an intact plasma membrane. By analyzing subsequent opening of the plasma membrane in $|Z|$ a continuous decrease independent of the frequency is found (**A3**). At 500 Hz and 32 kHz the signal decreases to a minimum of ~ 0.47 for 100 % open membranes. However, a major difference is found in the signal profiles. At 500 Hz $|Z|_{norm}$ shows a decrease by increasing the fraction of open membrane. At 32 kHz $|Z|_{norm}$ provides an asymptotic response profile. When the 8W10E electrode was confluently covered with cells with open membrane $|Z|_{norm}$ at 4 kHz provides a decrease to ~ 0.20. In R_{norm} (**B3**) at 500 Hz and 4 kHz the signal decreases to ~ 0.10 or ~ 0.18, respectively, when all cells exhibit an open membrane. However, at 4 kHz no significant changes are found between 50 % – 100 % cells with permeabilized plasma membranes. At 32 kHz the signal first shows a slightly increase to ~ 1.1 and a marginal decrease to ~ 0.92 is recorded after that. Also the signal change in C_{norm} (**C3**) shows a strong frequency-dependent sensitivity. At 4 kHz and 32 kHz a linear dependency of signal increase to the ratio of cells with open membrane is found. At 32 kHz the signal shows an increase to maximal 6.2, whereas at 4 kHz the maximum increase of C_{norm} is 4.8. C_{norm} at 500 Hz is not suitable for analyzing the increasing portion of cells with open membrane, since C_{norm} only provides a weak increase to 1.5.

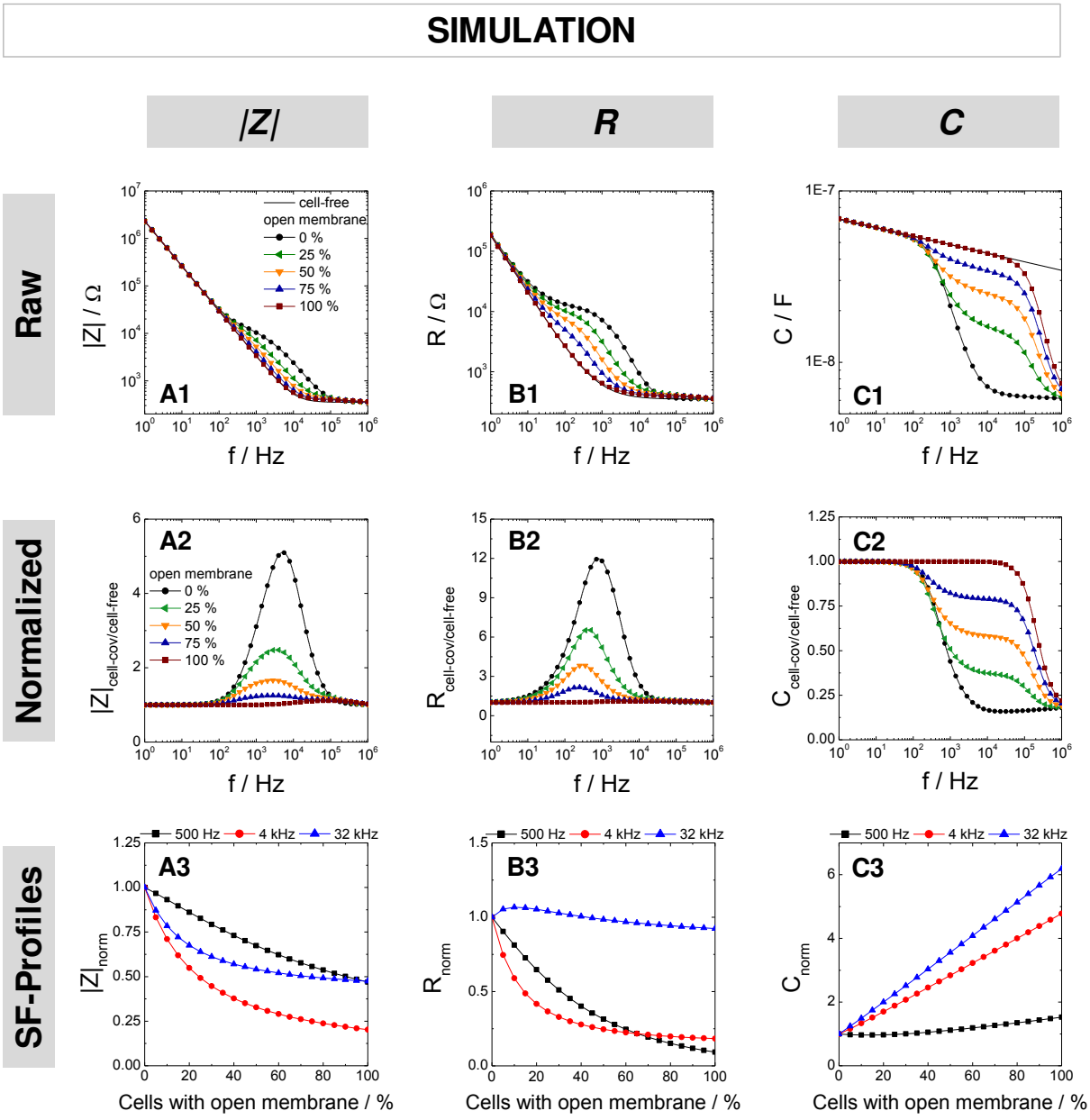

Fig. 4.39: Survey of simulated data addressing the changes of $|Z|$ (**A**), R (**B**) and C (**C**) by stepwise increasing the portion of cells with open membrane. **1:** Simulated frequency-dependent spectra of $|Z|$ (**A1**), R (**B1**) and C (**C1**) for model cells mixed with a with varying portion of cells with "open membrane". Opening of cell membrane was simulated by reducing the R_m value to 0.1 $\Omega \cdot cm^2$·. The untreated model cell layer is described by $R_b = 25\ \Omega \cdot cm^2$, $\alpha = 15\ \Omega^{0.5} \cdot cm$, $C_m = 3\ \mu F/cm^2$ and $R_m = 1 \cdot 10^{12}\ \Omega \cdot cm^2$. **2:** Normalized $|Z|_{cell\text{-}cov/cell\text{-}free}$ (**A2**), $R_{cell\text{-}cov/cell\text{-}free}$ (**B2**) and $C_{cell\text{-}cov/cell\text{-}free}$ (**C2**) spectra. Spectra were obtained by dividing the simulated spectra (0 %– 100 %) by the values of a cell-free 8W10E layout. **3:** *Single frequency* (SF)-profiles of $|Z|_{norm}$ (**A3**), R_{norm} (**B3**) and C_{norm} (**C3**) at 500 Hz (■), 4 kHz (●) and 32 kHz (▲). Data were normalized to the respective values of a non-treated model population with an intact plasma membrane.

4.5.5 Open Junctions

In **chapter 4.4** it was pointed out that using the resistance as monitoring parameter for epithelial barrier function might lead to misinterpretation when choosing an improper frequency. In this former study, the R_b value of the entire cell population on top of the gold-film electrode was varied stepwise and the corresponding spectra were calculated. This chapter focuses instead on the relative increase of cells with open junctions embedded in a layer of cells with regular junctions and the resulting changes in $|Z|$, R and C. For this purpose, a confluent electrode coverage with cells characterized by intact cell-cell-contacts or with open junctions was assumed and the ratio of these two populations was varied stepwise.

4.5.5.1 Experimental Support

The impedimetric measurements in (**Fig. 4.40**) summarize the response of MDCK II cells on a 8W10E (**A1 – C1**) or 8W1E (**A2 – C2**) electrode layout after the addition of 4 µM cytochalasin D, which leads to opening of epithelial barrier functions [d].

As already discussed in **chapter 4.4** $|Z|_{norm}$ (**A**) provided a frequency-dependent sensitivity for the analysis of epithelial barrier tightness for both layouts. At 500 Hz and 4 kHz a significant decrease of $|Z|$ was observed, whereas $|Z|_{norm}$ at 32 kHz only provided a slight decrease during the whole experiment. Only at a monitoring frequency of 500 Hz R_{norm} (**B**) showed a strong decrease in resistance immediately after the addition, indicating the increase in permeability. In contrast, at 4 kHz a characteristic transient resistance increase was recorded for both electrode layouts. At 32 kHz only a slight increase was detected using 8W10E electrodes (**B1**) and a significant increase to ~ 1.5 was found for 8W1E (**B2**). The time-dependent analysis of C_{norm} on a 8W10E electrode layout (**C1**) only provided an increase to ~ 2.1 at 4 kHz, whereas at 500 Hz and 32 kHz only small increases to 1.3 – 1.4 were observed. Using a 8W1E electrode layout (**C2**) opening of epithelial barrier function was indicated by an increase to ~ 2.9 (4 kHz), ~ 1.8 (500 Hz) or ~ 1.2 (32 kHz).

[d] Time-courses of $|Z|$ and R presented in **Fig. 4.34** were extracted from **Fig. 4.13** and **Fig 4.14** within one hour after cytochalasin D treatment.

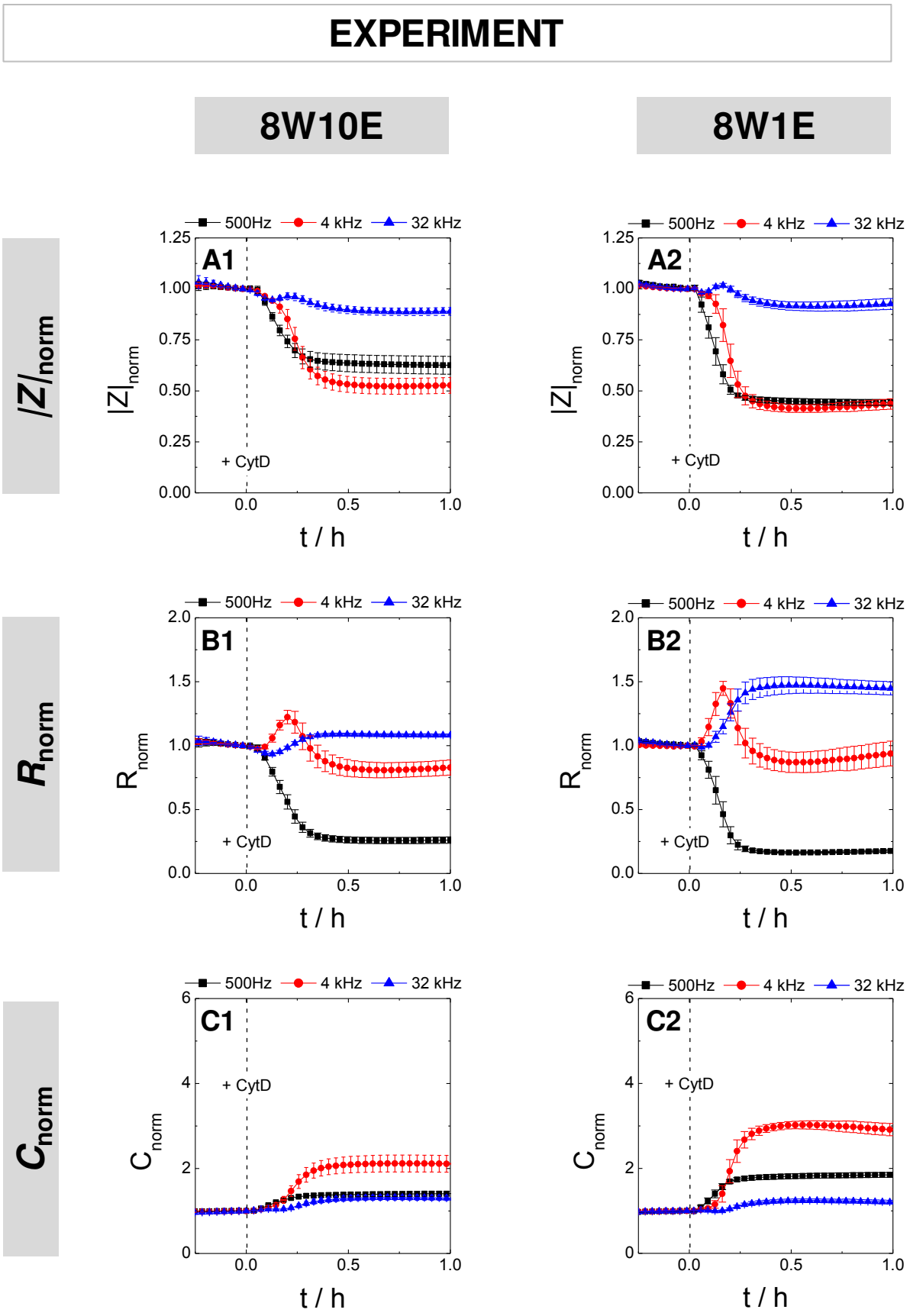

Fig. 4.40: Typical time-courses of $|Z|_{norm}$ (**A**), R_{norm} (**B**) and C_{norm} (**C**) for MDCK II cells before and after the addition of 4 µM cytochalasin D ($t = 0$ h) using a 8W10E (**1**) or 8W1E (**2**) electrode layout. The cellular response was monitored at 500 Hz (■), 4 kHz (●) and 32 kHz (▲). Data were normalized to the respective values immediately before the actin-binding drug was added. (Mean ± SD; N ≥ 5).

4.5.5.2 Computed Data for Successive Opening of Epithelial Barrier Function

To analyze the effect of an increasing fraction of cells without tight epithelial barriers different scenarios were simulated for both electrode layouts. Simulation started with a confluently cell-covered electrode with an intact cell-barrier using a model cell population characterized by $R_b = 25\ \Omega{\cdot}cm^2$, $\alpha = 15\ \Omega^{0.5}{\cdot}cm$ and $C_m = 3\ \mu F/cm^2$. Subsequently, the electrode coverage with cells which are not able to form tight junctions was increased stepwise. Thus, only R_b was reduced, while the other parameters were kept constant. The model cell layer with open junctions is characterized by $R_b = 1\ \Omega{\cdot}cm^2$, $\alpha = 15\ \Omega^{0.5}{\cdot}cm$ and $C_m = 3\ \mu F/cm^2$. The relative coverage with cells described by $R_b = 1\ \Omega{\cdot}cm^2$ was increased from 0 % – 100 %. The simulated data for 8W10E and 8W1E electrodes are summarized in **Fig. 4.41** and **Fig. 4.42**, respectively.

By increasing the percentage of cells with open junctions a decrease in $|Z|$ between $f = 10^2 – 10^5$ Hz is found (**A1**). In the frequency-dependent spectra of R (**B1**) an increase of cells characterized by $R_b = 1\ \Omega{\cdot}cm^2$ causes frequency-dependent changes and for both layouts a cross-over frequency is present. Using a 8W10E electrode layout (**Fig. 4.41 B1**) R decreases with increasing ratio of cells characterized by open junctions using frequencies between $1 – 10^4$ Hz. In contrast, the analysis of frequencies above 10^4 Hz provides an increase in R by increasing the ratio of open junctions. For the 8W1E layout (**Fig. 4.42 B1**) also a cross-over at 10^4 Hz is found beyond which the relation between resistance signal and strength of cell-cell contacts is inversed. In the frequency-dependent changes in C only small changes are observed for the different expression of epithelial barrier function on the electrode. Increasing the amount of cells with low R_b causes a shift of the C_{norm} minimum to higher frequencies (**C1**).

In the following step the data were normalized (**A2 – C2**) to values of a cell-free 8W10E (**Fig. 4.41**) or 8W1E (**Fig. 4.42**) electrode layout. The most sensitive frequencies of $|Z|_{cell\text{-}cov/cell\text{-}free}$ are determined for a 8W10E layout between 5 – 7 kHz (**A1**), with no significant changes in curve shape upon changing the fraction of the low R_b cell population. For a 8W1E electrode layout the peak center of $|Z|_{cell\text{-}cov/cell\text{-}free}$ is located between 10 – 20 kHz (**A2**). The changes in $R_{cell\text{-}cov/cell\text{-}free}$ (**B2**) emphasize the point of inflection for both layouts at ~ 10 kHz. The most sensitive frequency was found at 800 Hz (8W10E) and 1300 Hz (8W1E), respectively, without showing significant changes in curve shape. However, a decrease of the peak maximum occurs. For the 8W10E layout (**Fig. 4.41 B2**) the maximum decreases from 12.0 (0 %) to 10.1 (25 %), 8.7 (50 %), 7.6 (75 %) and 6.7 (100 %). The 8W1E layout (**Fig. 4.42 B2**) exhibits a decrease from 19.7 (100 %) – 10.5 (0 %). In $C_{cell\text{-}cov/cell\text{-}free}$ a shift of the spectrum's minimum to higher frequencies by increasing the fraction of cells without tight junctions is observed which comes along with a change in the curve slope (**C2**).

To highlight the changes due to increasing the percentage of cells with open junctions, the changes in $|Z|_{norm}$, R_{norm} and C_{norm} were extracted at 500 Hz, 4 kHz and 32 kHz (**A3 – C3**). Values were normalized to the respective values of a confluent cell layer with tight cell-barriers.

At 500 Hz the increasing ratio of cells characterized by $R_b = 1\ \Omega cm^2$ causes a decrease of $|Z|_{norm}$ to 0.73 for both layouts. Under the assumption of having a 100 % coverage of cells with open junctions $|Z|_{norm}$ at 4 kHz shows a decrease to 0.61 (**8W10E**) or 0.60 (**8W1E**). In contrast, at 32 kHz only small signal changes are found indicated by a slight decrease to 0.90 (**8W10E**) and 0.80 (**8W1E**). The analysis of R_{norm} provides a frequency-dependent trend: Simulation for increasing percentage of low R_b cells on the 8W10E electrode type results in an increase to 1.2 (32 kHz), whereas values decrease to 0.67 and 0.60 for 4 kHz and 500 Hz, respectively. Using a 8W1E electrode layout an increase in R_{norm} to 1.5 is found for 32 kHz whereas at 500 Hz and 4 kHz a decrease to 0.56 and 0.64 is observed. In C_{norm} (**C3**) the signal at 500 Hz and 32 kHz is not influenced by varying the electrode coverage using different ratios of cell-barrier forming cells. Only at 4 kHz a small increase to ~ 1.7 is detected.

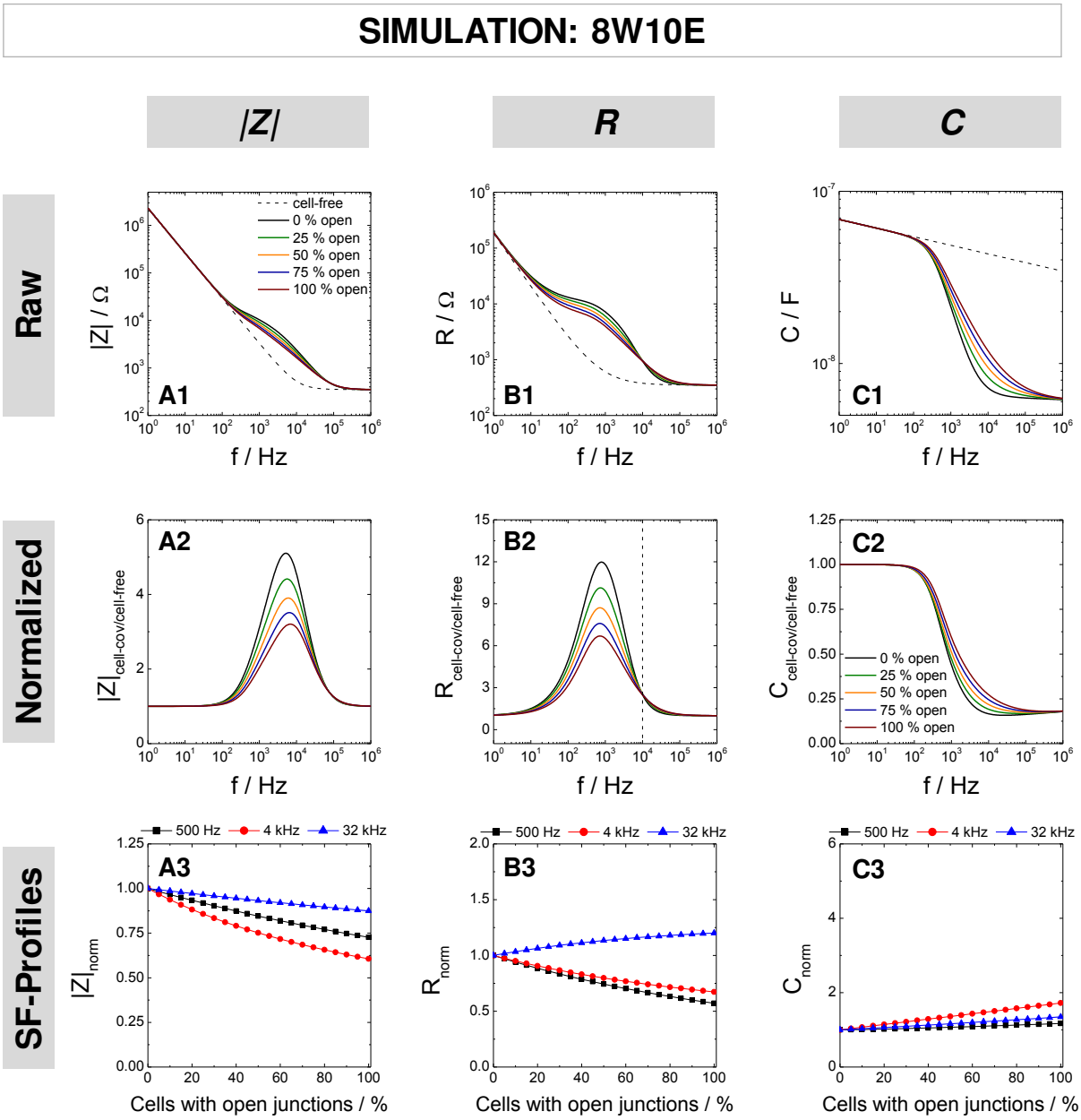

Fig. 4.41: Summary of the simulated data for increasing fraction of cells with open junctions. Data were calculated using the parameter for a 8W10E electrode layout (**Tab. 4.1**) and assuming a model cell layer with intact (R_b = 25 Ω·cm^2, α = 15 Ω$^{0.5}$·cm and C_m = 3 µF/cm^2) or open (R_b = 1 Ω·cm^2, α = 15 Ω$^{0.5}$·cm, C_m = 3 µF/cm^2) cell junction. The fraction of cells without tight junctions (R_b = 1 Ω·cm^2) was increased stepwise 0 – 100 %. **1:** Simulated frequency-dependent spectra of $|Z|$ (**A1**), R (**B1**) and C (**C1**) for different fractions of model cells with open junctions located on a 8W10E electrode layout. **2:** Normalized spectra of $|Z|_{cell\text{-}cov/cell\text{-}free}$ (**A2**), $R_{cell\text{-}cov/cell\text{-}free}$ (**B2**) and $C_{cell\text{-}cov/cell\text{-}free}$ (**C2**) were obtained by dividing the simulated spectra (0 % – 100 %) by the values of a cell-free 8W10E layout. **3:** *Single frequency* (SF)-profiles of $|Z|_{norm}$ (**A3**), R_{norm} (**B3**) and C_{norm} (**C3**) at 500 Hz (■), 4 kHz (●) and 32 kHz (▲). Data were normalized to the respective values of a model population with tight cell-barrier properties (R_b = 25 Ω·cm^2, α = 15 Ω$^{0.5}$·cm and C_m = 3 µF/cm^2).

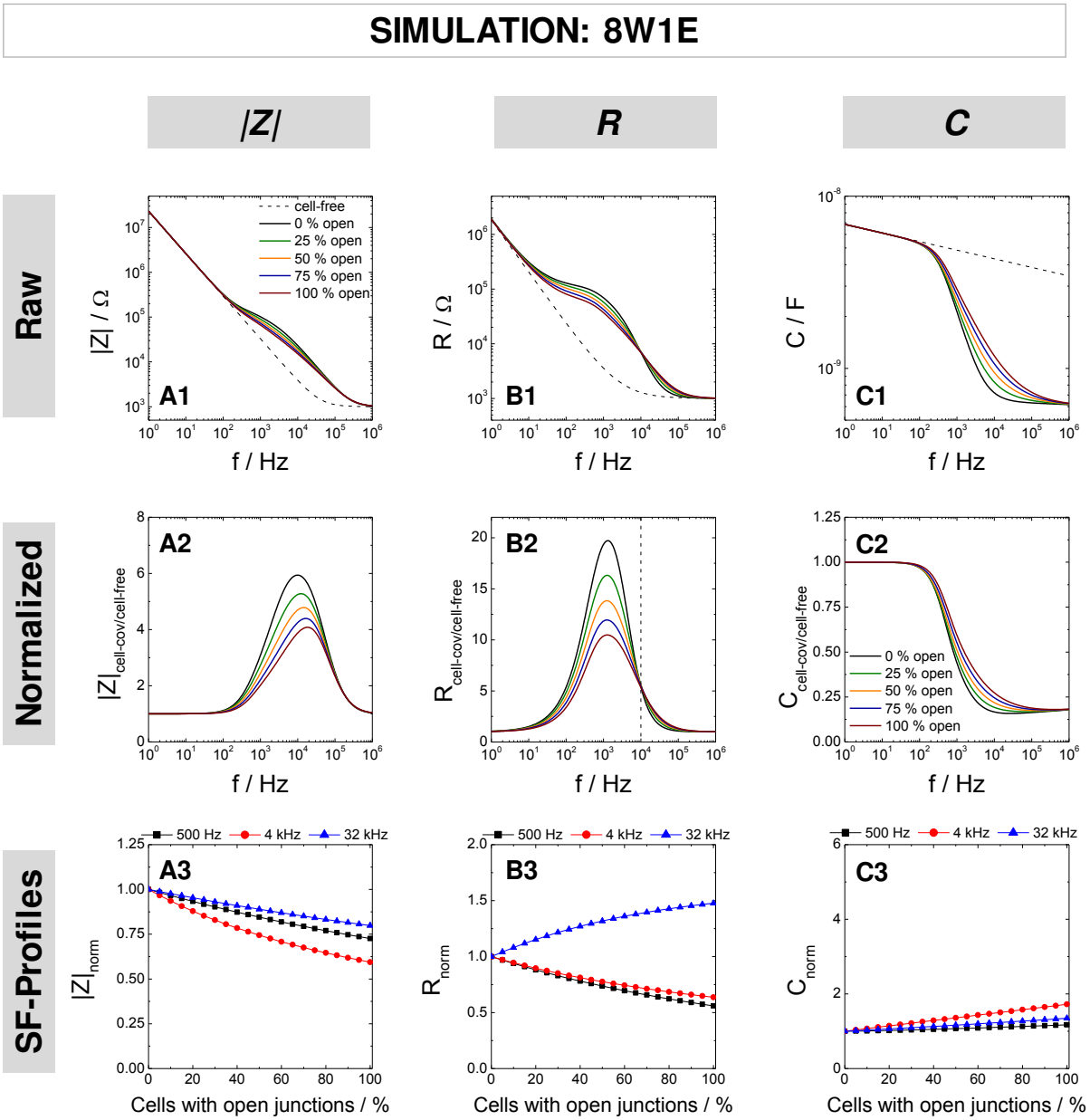

Fig. 4.42: Summary of the simulated data for increasing fraction of cells with open junctions. Data were simulated using the parameter for a 8W1E electrode layout (**Tab. 4.1**) and assuming a model cell layer with intact (R_b = 25 Ω·cm^2, α = 15 Ω$^{0.5}$·cm and C_m = 3 µF/cm^2) or open (R_b = 1 Ω·cm^2, α = 15 Ω$^{0.5}$·cm, C_m = 3 µF/cm^2) cell junction. The fraction of cells without tight junctions (R_b = 1 Ω·cm^2) was increased stepwise 0 – 100 %. **1:** Simulated frequency-dependent spectra of $|Z|$ (**A1**), R (**B1**) and C (**C1**) for different fractions of model cells with open junctions located on a 8W1E electrode layout. **2:** Normalized spectra of $|Z|_{cell\text{-}cov/cell\text{-}free}$ (**A2**), $R_{cell\text{-}cov/cell\text{-}free}$ (**B2**) and $C_{cell\text{-}cov/cell\text{-}free}$ (**C2**) were obtained by dividing the simulated spectra (0 %– 100 %) by the values of a cell-free 8W1E layout. **3:** *Single frequency* (SF)-profiles of $|Z|_{norm}$ (**A3**), R_{norm} (**B3**) and C_{norm} (**C3**) at 500 Hz (■), 4 kHz (●) and 32 kHz (▲). Data were normalized to the respective values of a model population with tight cell-barrier properties (R_b = 25 Ω·cm^2, α = 15 Ω$^{0.5}$·cm and C_m = 3 µF/cm^2).

4.5.6 Discussion: Influences of an Inhomogeneous Electrode Coverage

A deeper analysis of multi-frequency impedance data based on the ECIS model developed by Giaever and Keese only allows the determination of R_b, α and C_m under defined boundary conditions. Then, the cell-related parameters can be fitted for every impedance spectrum and the time-dependent analysis of these parameters can provide further insight into the cellular process at work, and which part of the cell responded to the addition of a certain stimulus. However, it is always only an approximation to the real situation during the experiment. In this study we addressed the different assumptions of the ECIS model by simulating impedance spectra in which the electrode coverage with different cell populations was changed systematically to model an inhomogeneous electrode coverage.

4.5.6.1 Variation of Cell Coverage

If the requirement of a confluent cell layer is not complied, the quantification of the cell-related parameters is not meaningful using the ECIS model. In a first project the effect of cell-free gaps on |Z|, R and C were analyzed theoretically and experimentally. Therefore, the cell-free parts within a cell layer were increased systematically and the resulting spectra were calculated using a LabVIEW-based software.

One important requirement to apply the ECIS model to experimentally obtained data is the assumption that the cell layer on the electrode is confluent. This excludes the existence of cell-free parts on the electrode, even to a very low extent. However, the consequences of inhomogeneity within the cell layer covering the electrode have never been investigated systematically. In this project the influence of changes in the electrode coverage on $|Z|$, R and C of ECIS readings was studied by systematic simulations and experiments. In different experimental approaches the cell-coverage at the working electrode was changed stepwise.

$|Z|_{norm}$ as monitoring parameter turned out not to be applicable for the analysis of cell coverage between 0 – 50 % (**Fig. 4.24** and **Fig. 4.25**) independent of the frequency. Between 50 – 100 % cell coverage $|Z|_{norm}$ at 4 kHz provided a strong increase and showed a high sensitivity to identify small cell-free gaps within the cell layer. $|Z|_{norm}$ at 32 kHz only changed marginally for low cell coverages but then provided an almost linear signal increase.

The analysis of C is recommended instead of $|Z|$ to investigate the cell coverage of gold-film electrodes as the experimental approach (**Fig. 4.24**) provided a linear dependency of C at 4 kHz and 32 kHz to the degree of cell-coverage. In the simulated data (**Fig. 4.25**) cell-free portions between 5 – 95 % were included to simulations and the corresponding $|Z|$, R and C profiles were calculated. In good agreement to the experimental data, C_{norm} at 4 kHz and

32 kHz provided a linear response to different degrees of electrode coverage. Even low fractions of cell-free electrode area caused a decrease in C_{norm}. Therefore, C turned out to be the best parameter for the analysis of the electrode coverage with similar sensitivities at 4 kHz and 32 kHz. Further simulations (**Fig. 4.43**) showed that the trend of C_{norm} for increasing coverage at 4 kHz is dependent on the tightness of cell-cell contacts and only showed a linear response for high R_b values. In contrast, changes in C_{norm} at 32 kHz were independent of the R_b value and therefore a monitoring frequency of 32 kHz is recommended for the analysis of the degree of cell coverage. Also Wegener et al. (2000) suggested an analysis of C at 40 kHz to monitor cell attachment and spreading on gold-film electrodes and pointed to a linear dependency of the signal on cell coverage [84].

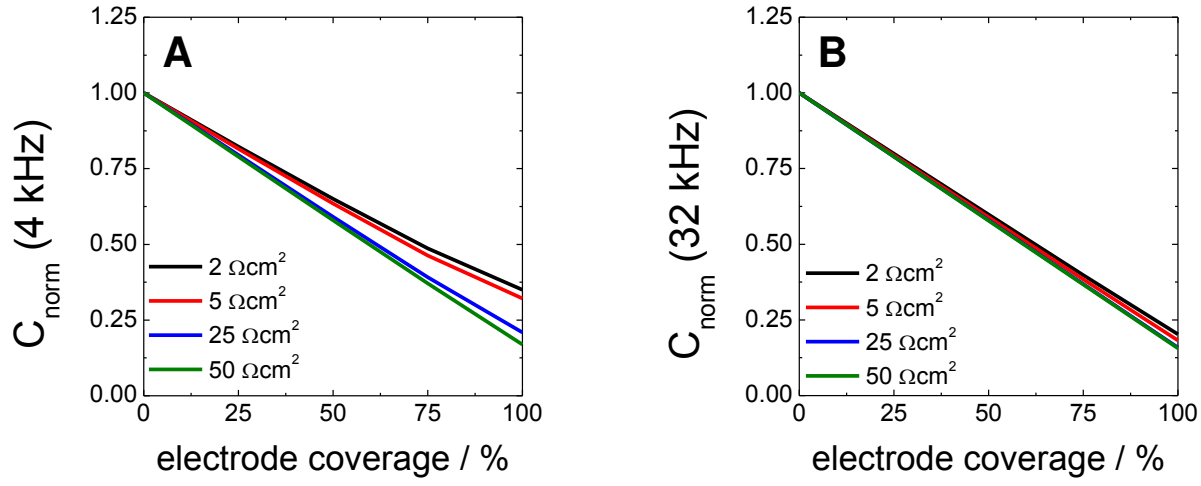

Fig. 4.43: Simulated data addressing the decrease in C_{norm} at 4 kHz (**A**) and 32 kHz (**B**) depending on the electrode coverage of a 8W10E layout with a model cell layer (α = 15 $\Omega^{0.5}$·cm, C_m = 3.0 µF/cm^2) and assuming different R_b values (2 – 50 Ω·cm^2). Data were normalized to the respective values of a cell-free 8W10E electrode.

It should be mentioned, that the electrode area was different in the experimental and theoretical approach. In the experiment the total electrode area of the "8 against CE" mode was $4 \cdot 10^{-3}$ cm^2 whereas the electrode area of the simulation was set to $5 \cdot 10^{-3}$ cm^2 (which corresponds to the area of a 8W10E electrode layout)[e]. Moreover, the normalizations $|Z|_{cell\text{-}cov/cell\text{-}free}$, $R_{cell\text{-}cov/cell\text{-}free}$ and $C_{cell\text{-}cov/cell\text{-}free}$ in the experimental study were calculated based on the signal, after all eight electrodes were wounded. In this situation the electrodes are still covered by cell debris and, thus, cannot be regarded as 100 % clean and cell-free electrode, as assumed for simulations. In contrast, during the simulation the cell-free spectrum for a 8W10E layout was calculated. This can explain the different shapes of the capacitance signals **C2** in the experimental (**Fig. 4.24**) and theoretical (**Fig. 4.25**) approach.

[e] The LabVIEW-based software (Version 5) only allowed the simulation of typical electrode areas of commercially available electrode layouts. Therefore, the area for an 8W10E layout was chosen for the simulation.

One prominent deviation between experimental data and calculated data is pronounced in the high frequency range ($10^5 – 10^6$ Hz). In the simulated spectra **Fig. 4.25** (**A1; B1**) the signal in $|Z|$ and R is characterized by a horizontal, stable value, which is dominated by the value of R_{bulk}. In contrast, the spectra obtained during the ECIS experiment (**Fig. 4.24**) provided a further decrease in $|Z|$ and R between $10^5 – 10^6$ Hz below the level of R_{bulk}. This can be explained by parasitic impedance contributions arising from the electronic equipment.

4.5.6.2 Analysis of Electrode Coverage Based on R_{CT}

ECIS experiments were performed in presence of 2 mM $[Fe(CN)_6]^{3-/4-}$ *to obtain information about the degree of cell coverage of the electrode based on changes in* R_{CT}.

In literature, the concept of faradaic impedance spectroscopy is used to investigate several cellular processes. Zhao et al. (2012) analyzed changes in membrane permeability of MDCK II cells after initiating cell anoxia by adding FCCP (*carbonycyanide-p-(trifluoromethoxy)phenyl-hydrazone*). For this study, the group used gelatin-modified glassy carbon electrodes in presence of 5 mM $[Fe(CN)_6]^{3-/4-}$ and detected a steady decrease in charge-transfer resistance with increasing incubation times [153]. Primiceri et al. (2011) suggested an assay to study cell migration based on electrochemical impedance spectroscopy in presence of 10 mM $[Fe(CN)_6]^{3-/4-}$ .In this study hepatocellular carcinoma (HCC) cells were cultivated on a porous membrane located between an upper and a lower compartment. After migration of HCC cells through the membrane, cells reached the interdigitated gold electrodes deposited at the bottom of the lower compartment, indicated by a significant increase in R_{CT} [154]. Other groups monitored the cell attachment, spreading or proliferation using electrochemical impedance spectroscopy. Guo et al. (2006) analyzed attachment and proliferation of cancer cells on ITO slides in presence of 1 mM $[Fe(CN)_6]^{3-/4-}$. They found an increase in electron-transfer resistance with increasing incubation time when cell proliferation led to an increase in cell-coverage [155]. Feng et al. (2011) used redox-mediated impedance spectroscopy to investigate the immobilization of cancer cells on the electrode surface. The group first immobilized aptamers on graphene-modified electrodes which selectively allowed binding of cancer cells to the electrode surface. A semi logarithmic dependency of R_{CT} on HeLa cell concentration was found [156]. This technique also enables to quantify electrode coverages with microorganisms. The *E. coli* cell concentration was quantified based on changes in R_{CT} after immobilization of anti- *E. coli* antibodies using gold [157] or ITO [158] as electrode material. In these studies, a linear dependency of the increase in R_{CT} on the logarithmic *E. coli* concentration was found. Heiskanen et al. (2008) further

investigated adhesion of *Saccharomyces cerevisiae* on cysteine-modified gold electrodes using impedance spectroscopy in presence of 10 mM $[Fe(CN)_6]^{3-/4-}$ [159].

In this work, the influence of decreasing electrode coverages on R_{CT} were investigated experimentally (**Fig. 4.29**) and theoretically (**Fig. 4.31)**. It was found that R_{CT} is dependent on electrode coverage. At 1 Hz a decrease in cell-coverage is characterized by a decrease in $|Z|$ and an increase in C, respectively. The analysis is independent of the cell type and the cell-related parameters R_b, α and C_m as the impedance at this frequency is dominated by the CPE.

Often, a linear dependency of changes in R_{CT} to the cell number was found using a semi logarithmic scale [156, 157, 160]. According to these reports a quantification of the electrode coverage based on R_{CT} is possible. Thus, the aim of this part was to calculate the electrode coverage in presence of the redox mediator by the additional charge transfer resistance at 1 Hz.

The analysis of the extracted changes in $|Z|_{norm}$ at 1 Hz, 500 Hz, 4 kHz and 32 kHz (**Fig. 4.44**) offered significant differences between the experimental data and the simulation (**A1; A2**). During the ECIS experiment $|Z|_{norm}$ at 1 Hz – 4 kHz provided similar trends upon decreasing the cell-coverage. In contrast, in the simulated data a significant difference was found for $|Z|_{norm}$ at 500 Hz and the other frequencies. At 500 Hz only a signal change from 1.0 (cell-covered) to 0.47 (cell-free) was observed. That means that the $|Z|_{norm}$ at 500 Hz was unaffected by the presence of $[Fe(CN)_6]^{3-/4-}$ as it showed similar trends as in **Fig. 4.25** when the simulation was performed in absence of the redox mediator. The analysis of 1 Hz, 4 kHz and 32 kHz provided an exponential decrease with a signal of 0.19 – 0.22 for a cell-free electrode. Consequently, $|Z|_{norm}$ at 1 Hz showed the same sensitivity as $|Z|$ at 32 kHz.

The sequential wounding pulse application during the “8 against CE” measurement allowed a precise determination of the overall electrode coverage of all eight working electrodes with a total electrode area of $4 \cdot 10^{-3}$ cm^2. After wounding one electrode to reduce the overall cell-coverage to 87.5 %, $|Z|_{norm}$ at 1 Hz significantly decreased to ~ 0.55. During the simulation also a decrease of electrode coverages to 88 % and 75 % resulted in the most intense decreases of $|Z|_{norm}$ at 1 Hz to 0.82 and 0.60, respectively, indicating that only a 100 % cell-covered electrode with epithelial cells was able to form a diffusion barrier, to completely prevent charge-transfer to the gold electrode. During the experiment $|Z|_{norm}$ at 1 Hz only changed marginal by decreasing the electrode coverage from 25 % to 0 % (**Fig. 4.29 A**). A correlation of experimentally obtained $|Z|_{norm}$ changes to the computed data (**Fig. 4.31 A2)** clearly supported these findings. Changes of the electrode coverage between 0.25 % – 0 %

were not indicated by a significant difference in $|Z|_{norm}$ also in the simulated data and $|Z|_{norm}$ remained almost unaffected.

For further analysis also changes in C at 1 Hz were quantified during the experiment (**Fig. 4.29 B**) and the simulation (**Fig. 4.31 B2**). Simulated data and the experiment are in good agreement and both studies provided an increase in C_{norm} by decreasing the electrode coverage. The increase in the simulated data was significantly higher compared to the experiment. This can be a consequence of the different meaning of the term “cell-free” during the experiment and the simulation. Whereas “cell-free” in the simulated data corresponds to a clean electrode surface without any cellular material “cell-free” in the experimental approach corresponds to permeabilized cells, which were killed by an invasive wounding pulse. After pulse application cell debris remained on the electrode, which can be the reason for the lower signal increase of C_{norm} compared to the simulation.

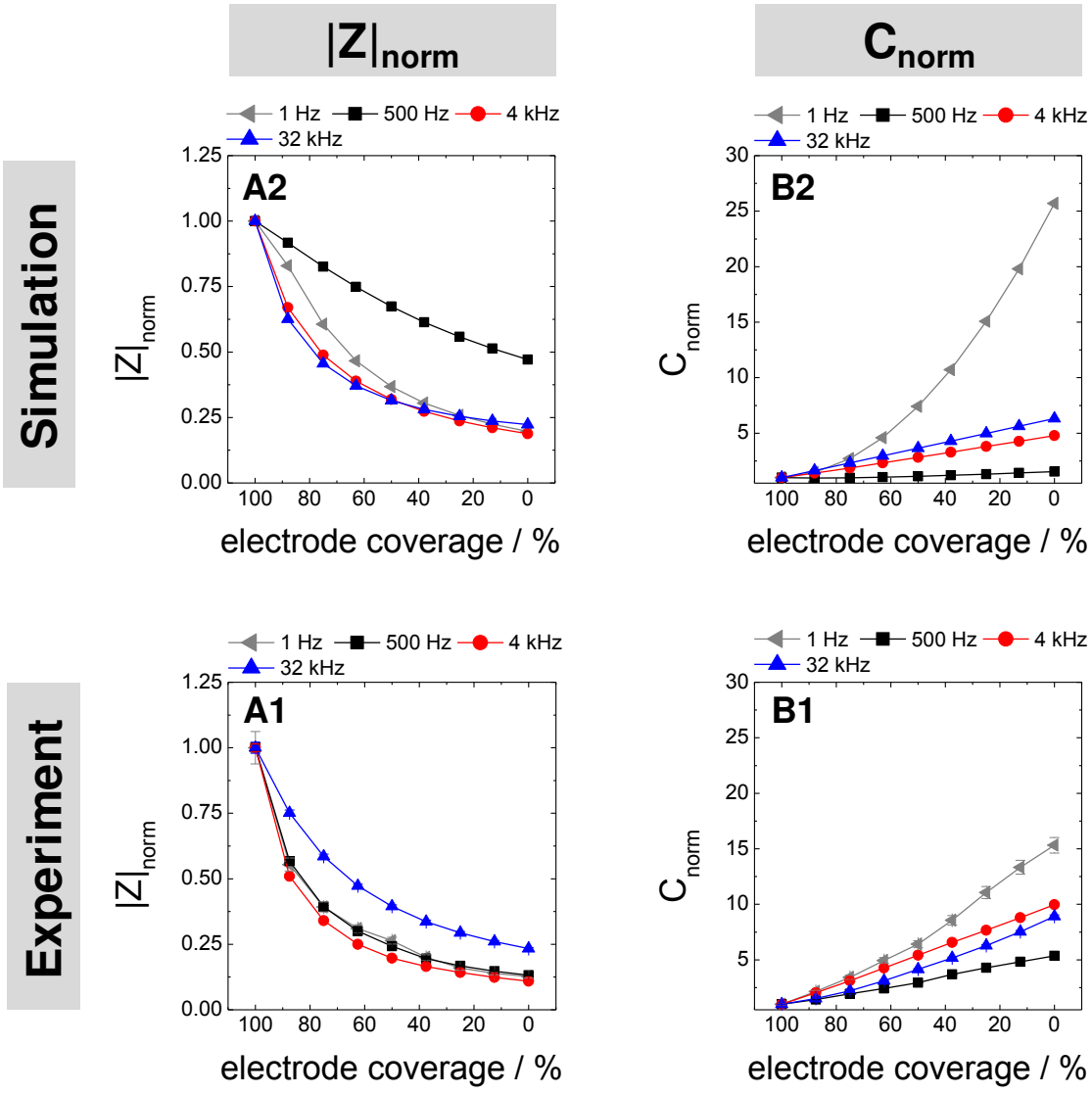

Fig. 4.44: Experimental (**1**) and computed (**2**) data addressing the effect of decreasing electrode coverage with cells in presence of a redox mediator. Changes of $|Z|_{norm}$ (**A**) and C_{norm} (**B**) were extracted at 1 Hz (◀), 500 Hz (■), 4 kHz (●) and 32 kHz (▲) and normalized to the value for 100 % cell coverage.

One problem, which strongly influenced the analysis of the experimentally obtained data, was that in some wells electrode damages were observed after pulse application. These changes in the electrode properties were documented in phase-contrast images and in the frequency-dependent impedance spectra (**Fig. 4.30**). These frequency-dependent differences in $|Z|$ and C spectra of simulated and experimental data were also demonstrated in **Fig. 4.28** and **Fig. 4.31**. During modification of the electrode coverage by invasive wounding pulse application a coverage-dependent response was found over the whole frequency range between 1 – 10^5 Hz. This finding can explain the similar $|Z|_{norm}$ trends at 1 Hz and 500 Hz in the experimental data. Moreover, these observed shifts in the spectra to lower impedance levels also impaired the analysis of data at 500 Hz and 4 kHz. In contrast, $|Z|_{norm}$ values between 10 – 100 Hz in the computed data remained unaffected by the variation of the electrode coverage.

In summary, $|Z|_{norm}$ and C_{norm} at 1 Hz were significantly different for cell-free and cell-covered electrodes but further improvements are necessary to define the degree of electrode coverage based on R_{CT} in ECIS experiments when cells are analyzed in presence of the redox mediator.

4.5.6.3 Effect of a Inhomogeneous Cell Population

In the next scenario, the electrode was assumed to be covered by different fractions of two different cell types and each of the two cell types was defined by a specific set of parameters R_b, α and C_m. Experimentally, the inhomogeneity was generated by seeding a co-culture of two cell-types, NRK and MDCK II at different ratios.

A second assumption of the ECIS model is that a homogenous cell population with similar electrical and morphological characteristics is required for meaningful outcome of the analysis. For this purpose simulations based on the ECIS model included varying ratios of two model cell types, each defined by a set of characteristic parameters R_b, α and C_m.

In the experimental approach the composition of the cell layer was varied by simultaneously seeding defined densities of both cell types. A co-culture of two different cell-types was performed using NRK and MDCK II cells. However, the exact composition of the cell layer, which after cell adhesion and spreading populates the electrode surface *de facto*, occurred by chance. This was also confirmed by the microscopic images at the end of experiment, which showed that the cell distribution on top of the electrode does not correspond entirely to the initially seeded ratio of NRK and MDCK II cells (**Fig. 4.33**). The naturally occurring diversity within one cell population, however, is difficult to characterize and to manipulate.

The spectra of $|Z|$, R and C ~ 20 h after cell seeding provided different signals dependent on the cell layer composition (**Fig. 4.34**). Using 50 % of each cell type and a final seeding density of 250 000 cells/cm^2 resulted in $|Z|$, R and C spectra which were found in between the responses of MDCK II cells or NRK cells, when seeded separately. When one cell population dominated the population, which corresponds to 75 % of the total cell density, the signal resembled the one of the respective pure population but, however, did not provide a complete conformity. These results clearly indicate, that even a diversity within a cell population of a moderate extent has an influence on the impedance recordings and is visible in $|Z|$, R and C. Using the normalized data presentation, in which the spectra were divided by the corresponding cell-free values of an 8W10E electrode layout (**Fig. 4.34 A2 – C2**) showed, that a cell population consisting of one cell type or one dominating cell type will show similar electric properties with respect to the most sensitive frequency or peak height and shape. However, no complete congruence was obtained for these populations, which indicates that even small variations within a cell layer can be detected impedimetrically. A co-cultivation of both cell types when applied in equal ratios provided an intermediate electrical response.

Using the LabVIEW-based software different scenarios were calculated, in which the cell layer consists of two cell types in varying ratios (**Fig. 4.35**). The frequency-dependent $|Z|$, R

and *C* spectra provided composition-dependent signals (**A1 – C1**). A decrease of the plateau level in |Z| between $f = 500$ Hz – 5 kHz was found which was dependent on the cell layer composition. This should not be disregarded by ECIS users when the R_b value is determined by fitting based on experimentally obtained MFT data. The simulation clearly showed that it strongly depends on the homogeneity within the cell layer.

In contrast to the ECIS experiment, in which only the cellular content in each well could be controlled by the initially used seeding densities, the population on top of the gold-film electrodes was selectively changed during the simulation. This might also be the explanation why the different curves, especially in $C_{\text{cell-cov/cell-free}}$ (**Fig. 4.35 C2**) provided an equally-spaced shift of the shoulder to higher frequencies by increasing the content of cell type B in contrast to the experimentally obtained data (**Fig. 4.34 C2**). But the experimental and simulated data of |Z|, R and C both provided the same trends, showing a dependency on the cell layer composition. Both studies emphasized that even a low degree of inhomogeneity within one cell population was sufficient to influence |*Z*|, *R* and *C* over a broad frequency range.

The ECIS model provides an excellent source to achieve a better understanding about individual components (R_b, α and C_m) during an experiment. But the natural variance within a cell population should not be disregarded, when the cell-related parameters for the whole population are fitted based on ECIS experiments.

4.5.6.4 Differentiating Different Routes across the Cell Layer: "Open Membrane" vs. "Open Junction"

The ratio between untreated cells and manipulated cells, either modifying membrane properties or cell junctions, was varied to mimic different sorts of defects in a cell layer. Differences in the response profiles were found which allowed a differentiation between "open membrane" and "open junctions" based on the extracted profiles of $|Z|_{norm}$, R_{norm} and C_{norm}.

Normally, during impedance recordings, the integrative response of one cell population is recorded without any additional information about an exact mechanism of where current passes the cell layer. Based on the ECIS model the quantification of the cell-related parameters allows to distinguish what caused impedance change. This can be a useful tool to discriminate the mode of action of different experimental stimulants, to distinguish effects on membrane properties or cell-cell contacts.

In this work, simulations were performed in which either membrane properties (R_m) or cell-junction (R_b) were changed discretely. The effect of increasing the fraction of permeabilized cell membranes for cells adhered on top of the electrode was studied in more detail (**chapter 4.5.4**). The experimental approach included experiments with MDCK II cells and impedance recordings were performed before, during and after the addition of 0.02 % saponin (**Fig. 4.38**). Saponin is known to induce pore formation in cells [161, 162] and artificial membranes [163]. The mechanism of membrane permeabilization could be due to formation of complexes with cholesterol [163].

The analysis of $|Z|$ and R at three different frequencies (**A2 – C2**) yielded a decrease of $|Z|$ and R immediately after the addition of saponin. A stable signal was observed after 10 min of incubation independent of the frequency. Wassler et al. (1987) investigated the degree of permeabilization of the plasma membranes of rat hepatocytes after saponin treatment using LDH (lactate dehydrogenase) assay. The group found a complete release of the enzyme within 20 min after incubation with 0.1 mg/mL (0.01 %) saponin [164]. The most prominent changes were observed in the capacitance signal. Whereas at 500 Hz and 4 kHz the permeabilization of the plasma membrane was indicated by an increase in C_{norm} the signal at 32 kHz provided a bi-phasic response: A first increase of C_{norm} to ~ 3.3 within 5 min followed by a second step where the C_{norm} increased to ~ 4.5 until the end of experiment. In the experimental part, only the representative time-course of one well after the addition of 0.02 % saponin was exemplarily shown. However, the analysis of four different wells (**Fig. S 6**) always provided a first increase of C_{norm} to 3.1 ± 0.2 and a second step to 4.6 ± 0.2 (Mean $\pm$ SD). A hypothesis to explain this phenomenon was that this two-step process

shows the sequential permeabilization of the apical and basal membrane, however, requires further investigations.

In our study we analyzed the effect of saponin on MDCK II cells using microscopic and impedimetric analysis. In the microscopic approach, the permeability of FITC dextran into the cytoplasm of 0.02 % saponin-treated MDCK II cells was analyzed over 30 min. A time-dependent increase in fluorescence signal within the cell layer was found. Using a higher concentration provided a faster permeabilization process and the whole cell layer within one image section was completely permeabilized within 18 min (**Fig. 4.36**). In order to analyze the stepwise increase in membrane permeability 0.02 % saponin was used for the ECIS experiment which provided the slower kinetic in the dye penetration study. The impedimetric analysis of MDCK II cells before and after treatment with 0.02 % saponin provided a faster time-course compared to the microscopic study. Here, immediately after the addition a decrease in $|Z|$ and R was found, while C started to increase. Independent of the parameter used for analysis no time-lag was found between addition and cellular response. One possible reason could be that this lag period describes the formation of increasing pore sizes so that the FITC dextran can diffuse in the cytoplasm, whereas impedimetric recordings do not require an exact defect size and even small changes in membrane properties significantly change current flow.

In the second experimental approach an inhomogeneity on the electrode surface was generated by varying the degree of cells with tight cell-junctions and cells with open cell junctions. The model substance cytochalasin D was applied to generate opening of cell-cell contacts within a confluent cell layer of MDCK II cells (**Fig. 4.40**), as already discussed in **chapter 4.4**. Additionally, simulations were performed in which the variance in the cell layer regarding their ability to form tight junctions was addressed theoretically (**Fig. 4.41** and **Fig. 4.42**).

Using the simulated data, in which selectively one parameter was changed and the others remained unaltered, the effect of opening of cell membranes or decreasing junctional tightness was analyzed in $|Z|$, R and C. Significant differences were found in the changes in C_{norm} at three different frequencies between changes in cell membrane properties and changes in cell junctions (**Fig. 4.45**). Alterations in membrane properties are indicated by a steep increase in C_{norm} to 6.2 (32 kHz) and 4.7 (4 kHz) according to the computed data. At 500 Hz only small changes were found. In contrast, variations addressing the tightness of cell-junctions within one cell population only showed small changes in C_{norm} for all three tested frequencies.

These findings were compared to the signal changes in C_{norm} from the experimentally obtained data (**Fig. 4.45**) by either varying the membrane properties by the addition of saponin (**A2**) or by changing junctional tightness by cytochalasin D (**B2**). Also the experimental data disclosed a significant difference between both cellular alterations. In good agreement to the simulated data, also C_{norm} of MDCK II cells after the addition of Saponin provided an increase to 4.5 (32 kHz) and 3.9 (4 kHz) whereas C_{norm} at 500 Hz remained unaffected. The signal increase of C at 4 kHz and 32 kHz were significantly lower in the experimental approach compared to the simulated data. This can be due to cell debris which remained on the electrode. When the same cell type was treated with cytochalasin D instead, C_{norm} at 500 Hz and 32 kHz did not provide any significant response. Only at 4 kHz a small increase to ~ 2.1 within 1 h was found.

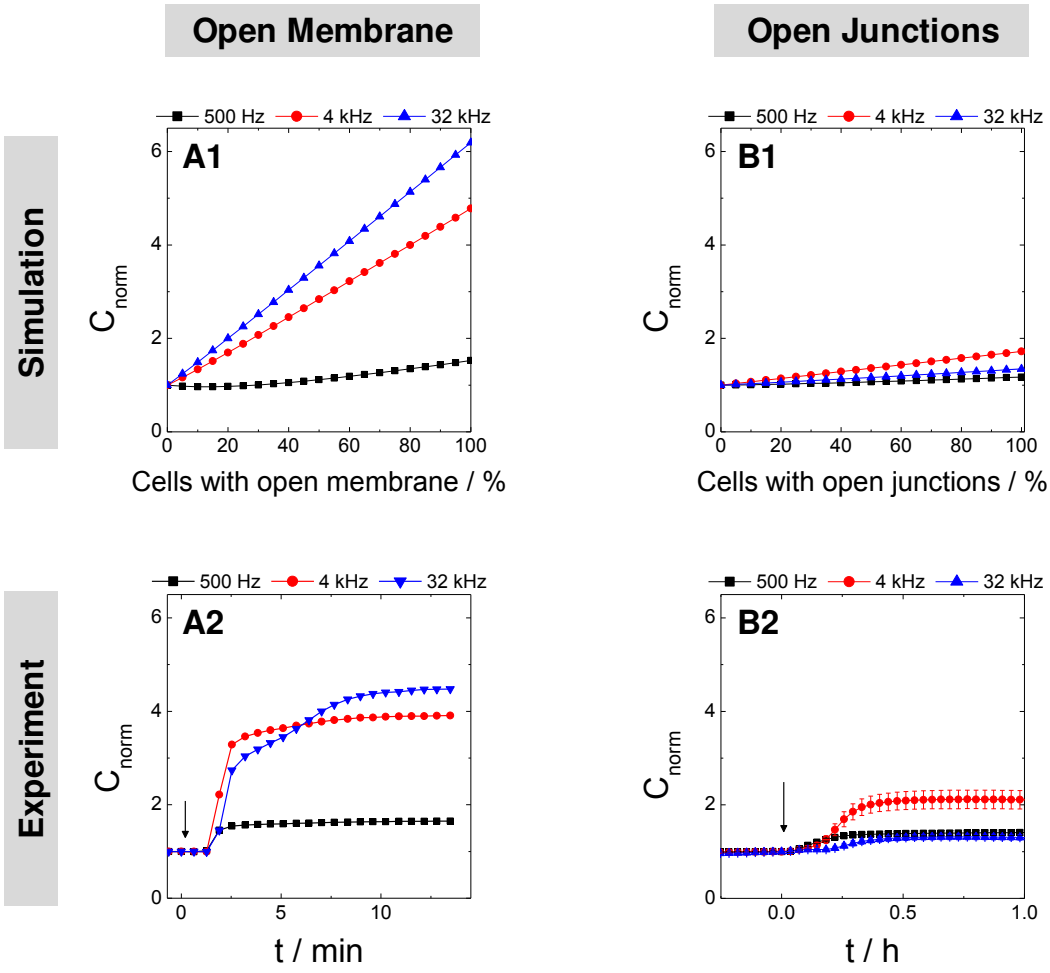

Fig. 4.45: Data comparison between simulated (**1**) and experimental (**2**) data for open membrane (**A**) and open junctions (**B**) based on the capacitance signal.

The calculated and experimental data clearly showed that a differentiation of both processes is possible by the analysis of C_{norm}. Using the MDCK II cell type for the experimental support and moderately tight epithelial model cells (R_b = 25 $\Omega \cdot cm^2$, α = 15 $\Omega^{0.5} \cdot cm$, C_m = 3.0 µF/cm^2) showed the most prominent changes in C in a frequency range between 4 kHz and 32 kHz using the 8W10E electrode layout. Therefore, the simulation project provided a further insight into cell-related processes based on impedance recording and assisted the data interpretation with respect to different current routes across the cell layer without modeling experimental data.

The take-home massages for **chapter 4.5** are, that:

- ✓ the degree of cell-coverage can be determined by the signal change in C with the highest sensitivity at high frequencies (32 kHz)
- ✓ when the cell layer is characterized by high R_b values also the analysis of C at 4 kHz showed a linear response to the degree of cell coverage
- ✓ small changes in the electrode coverage also provided strong signal changes in R at 500 Hz or $|Z|$ at 4 kHz, which are the most sensitive parameter combinations to study cell-cell contacts. To selectively extract changes in cell-barrier function a multi-parametric readout is advantageous to ensure that no changes in the degree of cell coverage exist
- ✓ permeabilization of the plasma membrane by saponin led to a significant increase in C using a monitoring frequency of 4 kHz and 32 kHz
- ✓ in contrast, C remained almost stable at 32 kHz after decreasing the tightness of epithelial barrier function in presence of cytochalasin D
- ✓ inhomogeneity within the cell population with respect to size and their electric properties provided a strong influence on the impedimetric readout. A homogenous and intact cell layer is required, especially when R_b, α and C_m are calculated

4.6 Summary and Outlook

Cell-free gaps in electrode coverage or inhomogeneity within the cell layer are considered as limiting parameter of ECIS model validity. Here, a systematic analysis of these individual factors was performed to proof this and to deduce suitable monitoring parameters for different cellular scenarios. Therefore, simulations based on the well-known ECIS model were performed and additionally supported by experimental data.

The first topic focused on changes in barrier-forming cell junctions, characterized by the cell-related parameter R_b. The tightness of epithelial barrier function between neighboring MDCK II cells was modulated using the substance cytochalasin D. Experimental and simulated data provided a frequency-dependent sensitivity of resistance and impedance magnitude to detect changes in barrier function. Simulated data using different model cell types provided a cell type-specific cross-over frequency in the resistance spectra, beyond which the relation between the tightness of cell-barrier functions and the resistance signal is inverted. In contrast, weakening of barrier function is indicated by a decrease in $|Z|$ independent of the frequency using the impedance magnitude as monitoring parameter.

Moreover, the key requirement of the ECIS model to have uniform electrode coverage, without any cell-free gaps was studied systematically in order to extract general guidelines for determining optimal monitoring parameter-frequency combinations. The simulations and the experimental approach revealed a high sensitivity of C_{norm} at high frequency to selectively identify even low portions of cell-free areas on the electrode. Furthermore, experiments for cell-free and gradually cell-covered gold-film electrodes were performed in presence of $[Fe(CN)_6]^{3-/4-}$. The R_{CT} was analyzed at 1 Hz by a decrease in $|Z|$ or an increase in C, respectively.

Also, the assumption of having a uniform cell layer was analyzed, by generating experimentally or via simulation an electrode coverage which consisted of two different cell types. It was found, that even small deviations from uniform electrode coverage have an influence on $|Z|$, R and C. Simulated and experimental data clearly showed that, the mechanism of inducing “open membranes” can be distinguished from open barriers, by analyzing the changes in C_{norm}. Only when cell membranes do not longer form an intact barrier, a strong increase in C_{norm} was found. Additionally, a multi-parametric readout is favored as an influence on barrier properties also involves a significant decrease in $|Z|$ or R at 500 Hz.

In summary, a good agreement was achieved between simulated data and the experimental support. A possible limitation of our approach might be that only model parameters were used instead of fitting the parameters from the experiment. Of course, the simulated can

come to better agreement with the experimental data when the parameters R_b, α and C_m were calculated from the experimental data using the ECIS model. These fitted parameters can then be used in the following for the simulation of a certain cellular scenario. However, fitting the cell-related parameters requires flawless frequency-dependent spectra which could be addressed by further projects.

The natural variance within one cell population prevents that one specific set of cell-related parameters R_b, α and C_m correctly characterizes the entire population. A Gaussian distribution will reflect more precisely the cell population adhered to the electrode. In this study only two different values for R_b, α and C_m were assumed during a simulation. In the future, a simulation in which the cell-related parameters are varied within a Gaussian distribution could provide a more sophisticated approach to investigate the influence of inhomogeneous cell layers. A future application for the faradaic ECIS experiments in presence of $[Fe(CN)_6]^{3-/4-}$ could be the analysis of increasing permeabilization of the plasma membrane after the addition of saponin. A change in R_{CT} requires the permeabilization of both, apical and basal plasma membrane. We established a hypothesis that the bi-phasic time-course of capacitance at high frequencies represents the stepwise permeabilization of the membranes. First the apical membrane is affected by saponin before the basal membrane is permeabilized. To proof the hypothesis, the analysis of the time-courses of $|Z|$ at 1 Hz and C at high frequencies (32 kHz) could be helpful, as a decrease in R_{CT} should then appear simultaneously with the second increase in C_{norm} at 32 kHz.

5 Assay to Study Gap Junctional Intercellular Communication

5.1 Introduction to Gap Junctional Intercellular Communication

The scientist Theodor Wilhelm Engelmann recognized already in 1877, long before gap junctional intercellular communication was discovered, that the "death of a cardiac cell does not result in death of the neighboring cells" [165]. In 1875 he dissected frogs and found that heart contraction is caused by the heart itself and is not neurogenic in origin as believed before at this time. He supported the hypothesis that an "excitation wave was conducted directly from one muscle cell to another" [166]. This happened ~ 80 years before electric coupling in myocardium (1952) and neurons (1957) via gap junctions was discovered [167, 168].

The name "gap junction" is based on the narrow, extracellular gap of ~ 2 nm between the plasma membranes of two adjacent cells [169, 170]. Gap junctions represent a unique type of intercellular junctions, which allows the direct connection between the cytoplasm of adjacent cells (**Fig. 5.1**). Each channel consists of two hemichannels called **connexons** which are formed from six polypeptides (**connexins**). If two hemichannels, each located in the plasma membrane of neighboring cells, dock together a functional pore is created. Depending on the connexin distribution the pore diameter can vary between 8 – 16 Å [171-176]. Through this intercellular connection between the cytoplasm of two cells, the diffusion and exchange of molecules smaller than 1 kDa e.g. amino acids, small peptides, water, cations, anions, second messengers (cAMP, IP_3) and electric signals is possible. A brief introduction is provided below to give an overview on structure and organization as well as regulation and analysis of gap junctional intercellular communication.

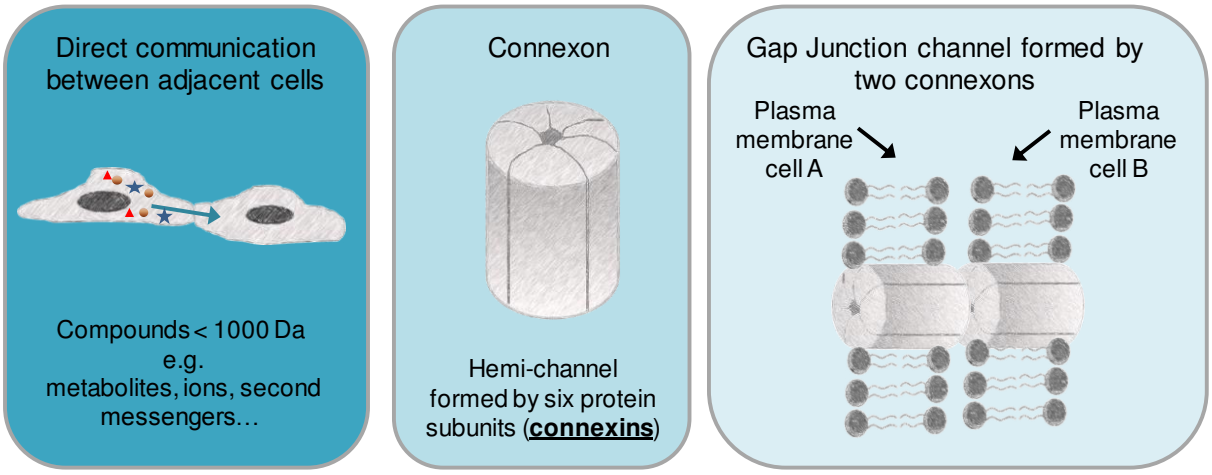

Fig. 5.1: Overview of gap junctional intercellular communication: Gap junctional intercellular communication allows the exchange of small compounds (< 1 kDa). A connexon is formed from six protein subunits and a functional channel is made of two connexons, located in two adjacent cell membranes.

5.1.1 Structural Characteristic and Organization

Gap Junctions are formed by clustering two connexons of two neighboring cells, resulting in bridging of the extracellular gap and directly connecting the adjacent cytoplasms (**Fig. 5.2 A**). Up to now, 20 connexins are known in mouse and 21 in human genome [177] which differ in their molecular size between 23 – 62 kDa [178]. Connexins are labeled according to their molecular weights, e.g. connexin with a molecular weight of 26 kDa is named as Cx26. Gap junctions possess a high diversity due to the plurality of different connexins that can form a connexon. The connexon can be homomeric (made of one single type of connexin) or heteomeric (assembly of different connexins). Consequently, also the assembly of two connexons can create a homotypic or a heterotypic junction (**Fig. 5.2 B**). Due to the high diversity of connexins the number of different channels is immense. However, some assembly combinations seems to be prohibited [179]. Gap junctions appear as *plaques* [180] with varying sizes from less than 100 nm up to several micrometers [181, 182]. *Plaques* are formed in the cell membrane by a few or up to thousands of channels, as confirmed by atomic force microscopy [183], freeze fracture analysis [184] or fluorescence microscopy [185-187]. Gap junction plaques were found to be dynamic structures proven by time-lapse imaging and fluorescence microscopy [188-190].

The structural and microscopic observation of gap junctions already started several years before the connexins were identified and cloned for the first time in 1986 [191, 192]. Electron microscopic studies of intercalated discs from frog, mouse and guinea pig cardiac muscles in 1958 pointed to characteristic regions between adjacent cells [193]. Already in 1963 hexagonal subunits were identified in electrical synapses of goldfish brains [194] and later also in liver plasma membranes [195]. Further research on this topic verified the presence of these hexagonally packed structures in mouse heart and liver in 1967 [196]. In 1970, Uehara and Burnstoc confirmed by electron microscopy the presence of gap junctions between smooth muscle cells [197].

First evidence and low resolution topological information about the organization of gap junctions was provided by Zimmer et al. in 1987, which is still valid up to now [198]. Each connexin independent of their molecular weight shows a characteristic tetraspan transmembrane protein structure (**Fig. 5.2 C**) resulting in two extracellular loops and one intracellular loop with the N- and C-termini located intracellularly [199]. In 1999, Unger et al. proved by electron crystallography that the hexameric structure of connexons is formed by six individual proteins each with four transmembrane structures folded in α-helices [200]. Ten years later, Maeda et al. further investigated this structural characteristic using x-ray crystallography and offered a high resolution structure of Cx26 gap junction channel (**D**) [201].

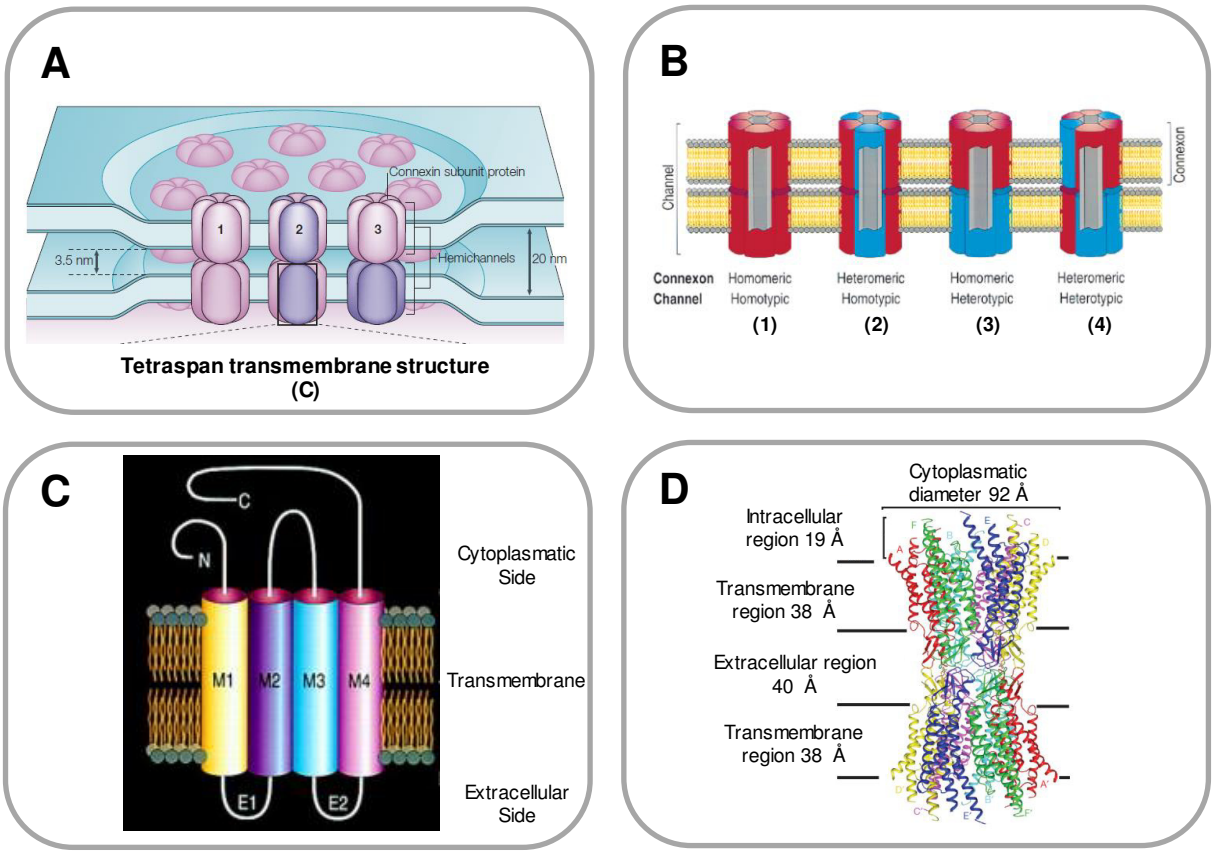

Fig. 5.2: A: Schematic structure of gap junctions formed by docking of two hemi-channels which are located in the plasma membranes of adjacent cells. **B:** Different types of gap junction channels: Hemichannels can be formed by six identical connexins resulting in a homomeric connexon (**1+3**). Heteromeric (**2+4**) are assembled from different connexin. The resulting channel, consisting of two connexons can be homotypic or heterotypic if it consists either of two identical (**1+2**) or different connexons (**3+4**). **C:** Connexins show a characteristic tetraspan transmembrane structure resulting in two extracellular loops and one loop at the cytoplasmatic side. Additionally, the C- and N-terminus are located on the cytoplasmatic side. **D:** X-ray structure of a Cx26 gap junction channel in side view discovered by Maeda et al. (2009). The extracellular region results in an "intercellular" gap of 40 Å. Images were taken with permission from Sohl et al. (2005) [202] (**A**), Kumar and Gilula (1996) [199] (**B+C**) and Maeda et al. (2009) [201] (**D**).

The connexin composition has a strong influence on pore size, passage of dyes, ions and endogenous metabolites through the channel as well as on regulation modes [172, 203]. Different studies focused on the permeability properties of different connexin isoforms and channels using fluorescent tracers of different sizes and charges [204] or by measuring the flux of cytoplasmatic molecules [205, 206]. Significant differences were found in the intercellular transfer e.g. for ATP and adenosine for different connexins (Cx32, Cx43) [207].

5.1.2 Regulation of Gap Junctions

The permeability of gap junction channels is regulated by different parameters and gap junction closure leads to metabolical and electrical uncoupling of adjacent cells. This seems to have a protective background as healthy cells can be separated from damaged cells to maintain normal cellular functions [208]. Switching between open and closed gap junctions is often described as "gating". The progress in research focusing on gating of gap junctions are relatively slow compared to studies on other channels in the plasma membrane due to the high diversity of connexin assemblies [209]. Many studies are focusing on the regulation of gap junctions, however the molecular mechanism of chemical gating is not completely decoded.

Several working hypotheses for the mechanism of channel closure can be found in literature like rotation of connexins [210, 211] or "ball and chain model" [212-214] which is also known as "particle-receptor model" [213, 215]. In this model, an interaction of a so-called CT domain with the receptor domain is considered. Other mechanisms suggest a "cork-type model" also known as "plug gating mechanism" [216] where a physical obstruction by Calmodulin (CaM; ***ca****lcium-****modul****ated prote****in***) [217] or another plug is assumed.

The unique structure of gap junctions is regulated in multiple ways differing in the timescale of regulation from slower to faster processes. Slower regulation is obtained by altering the number of channels on the cell surface by modifying the connexin biosynthesis, plaque assembly as well as the lifetime of a gap junction. Among others, a fast regulation of gap junctional intercellular communication is achieved by:

(i) Chemical Gating Including pH And Calcium-Dependency

Acidification of the cytoplasm leads to channel closure with varying sensitivities dependent on the connexin isoform [218]. The uncoupling effect of pH changes was found and confirmed in different cell types like insect gland cells [219], cardiac cells [220] and crayfish axons [221] among others. Depending on the connexins different sensitivities to changes in intracellular pH are reported. By decreasing the pH from 7.6 to 6.5 a decrease in the junctional conductance in Cx32 to ~ 80 % compared to the control values was found [222] and for Cx38 even a decrease to 0 % was observed [223]. Further studies by Stergiopoulos et al. regarding the $[pH]_i$ sensitivity of eight different connexin channels proved that Cx50 as well as Cx46 are strongly pH sensitive connexins whereas Cx32 was the least sensitive one [224].

The effect of calcium on gap junctional intercellular communication was an early topic of research and has long been postulated to have a crucial role in the regulation of gap junctions. Already in 1967, a decrease of gap junctional intercellular communication caused

by intracellular Ca^{2+} ions was published by Loewenstein et al. [225]. Oliveira-Castro and Loewenstein (1971) showed that the dye transfer of fluorescein between salivary gland cells was blocked when there is an excess of calcium in the cytoplasm [226]. Furthermore, De Mello (1975) confirmed that intracellular injection of Ca^{2+} in heart cells caused electrically uncoupling of the cells [227]. The first microscopic evidence was given by Unwin and Zampighi (1980) and Unwin and Ennis (1984) as they analyzed gap junction structures by electron microscopy in absence and presence of Ca^{2+} [210, 211] They suggested a model that the transition from the open to the closed configuration may occur by rotation of the subunits. Müller et al. (2002) detected a reduction of the extracellular channel diameter of Cx26 after injection of Ca^{2+} by atomic force microscopy [228]. The channel closing effect of calcium was further characterized by Ishihara et al. who performed *Fluorescence Recovery after Photobleaching* (FRAP) experiments under different extracellular calcium concentrations [229]. The group found a dose-dependent decrease in gap junctional intercellular communication between osteocytes by increasing the Ca^{2+} concentration. Using microinjection Jongen et al. found that the number of dye-coupled cells in mouse epidermis was increasing with increasing the calcium concentration from 0.05 mM to 1.2 mM. The group reported that the calcium-dependency of Cx43 mediated gap junctional intercellular communication is directly controlled by the calcium-dependent adhesion molecule E-cadherin [230]. Calcium significantly stops gap junctional intercellular communication between damaged cells, however, the role of Ca^{2+} as a physiological modulator is still under discussion [165].

(ii) Inhibitors

Many different inhibitors are available which have an influence on gap junctional intercellular communication [231]. Unfortunately, most inhibitors are not selective and can also bind to other cellular structures [231]. Two different types of inhibitors, the long chain alcohols 1-octanol or 1-heptanol and *2-Amino-ethoxydiphenyl borate* (2-APB), are presented in more detail.

- **Long Chain Alcohols**

Classic inhibitors of gap junctional intercellular communication are long chain alcohols, especially octanol and heptanol, which are described in literature to reversibly reduce gap junctional intercellular communication [232]. A proposed mechanism of action assumes that these alcohols cause changes in the membrane fluidity and lead to contraction ("squeezing") of intercellular channels [233]. However, no evidence was found for a Cx-dependent selectivity of these inhibitors [234]. Using both alcohols, a concentration-dependent reduction in dye diffusion were found in intact retina [235] and were reported to block gap junctional intercellular communication in insect cells [236], rat glial cells [237] as well as in mammalian cells [238]. The working concentrations for 1-heptanol varied between 1 - 3 mM and for octanol lower concentrations, between 0.5 - 1.0 mM, were published [231]. Furthermore, change in $[pH]_i$ was reported after inhibition of gap junctional intercellular communication with 1-octanol and 1-heptanol [239]. Pappas et al. (1996) found an intracellular acidification after applying 1 mM 1-octanol to astrocytes. In a further study the effect of 1-heptanol on cardiac gap junctions was analyzed. Takens-Kwak et al. (1992) hypothesized a non-specific action of 1-heptanol. They claimed that 1-heptanol induces changes in the lipid membrane which alters gap junctional intercellular communication [240].

- ***2-Aminoethoxydiphenyl borate*** **(2-APB)**

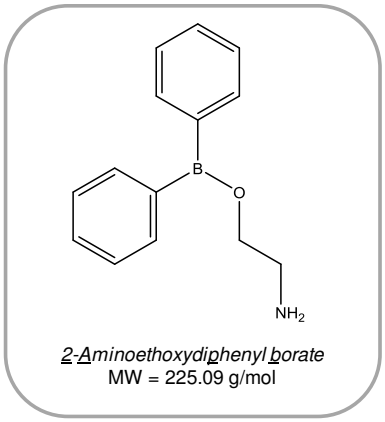

Fig. 5.3: Molecular structure of 2-Amino-ethoxydiphenyl borate used as reversible inhibitor for gap junctional intercellular communication.

2-APB is a commonly used inhibitor of IP3 (inositol triphosphate) receptor [241] and TRP (transient receptor potential) channels [242]. However, 2-APB is also known as inhibitor for gap junctional intercellular communication and it reversibly blocks electric coupling through Cx50 in N2A cells [243]. Yang et al. (2003) found a reversible inhibitory effect of 2-APB in TM4 Sertoli cells. Additionally, a reduced expression of Cx43 protein was confirmed by western blotting assay after treatment with 50 µM 2-APB [244]. The mechanism is hypothesized to occur at the extracellular junction site, as the inhibition was reversible when 2-APB was removed from the extracellular solution even in presence of intracellular 2-APB [245]. In a study from Ye et al. (2011) 100 µM 2-APB were found to completely inhibit Cx43-mediated dye transfer in NRK cells using a microfluidic device. They confirmed the reversible effect of 2-APB after washing out from the extracellular environment. They concluded that 2-APB may either interact directly with the connexin proteins or have an influence on the conformation of the proteins by interacting with the lipid

membrane [246]. Further investigations regarding the effect of 2-APB on homomeric Cx32 and heteromeric Cx26/32 channels yielded a reversible inhibition of both types in HeLa cells, whereas homomeric Cx26 channels were not blocked by 2-APB [247].

Connexin Biosynthesis and Turn-Over

Slower regulation of gap junctional intercellular communication is achieved by modifying the connexin biosynthesis. Connexins have a high turn-over rate compared to other membrane proteins and their life cycle (**Fig. 5.4**) can be divided into three main steps [248]:

- **(A)** **Gap junction formation**: Protein assembly into connexons, translocation of the hemichannels to the cell surface, channel formation by docking of two connexons of adjacent cells and subsequent clustering into plaques.
- **(B)** **Internalization**: Removing of gap junctions from the cell surface
- **(C)** **Degradation**: Lysosomal and proteasomal degradation [249]

The short half-life of different connexins originating from different cell types were summarized by Berthoud et al. [250]. The half-life of Cx32 was determined to ~ 2.5 – 3 h [251-253] and even faster for Cx43 (1 – 3 h) [254, 255]. Thus, it is a dynamic process of gap junction formation and degradation of gap junctions. The degree of gap junction efficiency is directly controlled by channel formation, association to plaques and channel degradation [256]. Consequently, cells can up- or down regulate the degree of gap junctional coupling as a response to the physiological requirements.

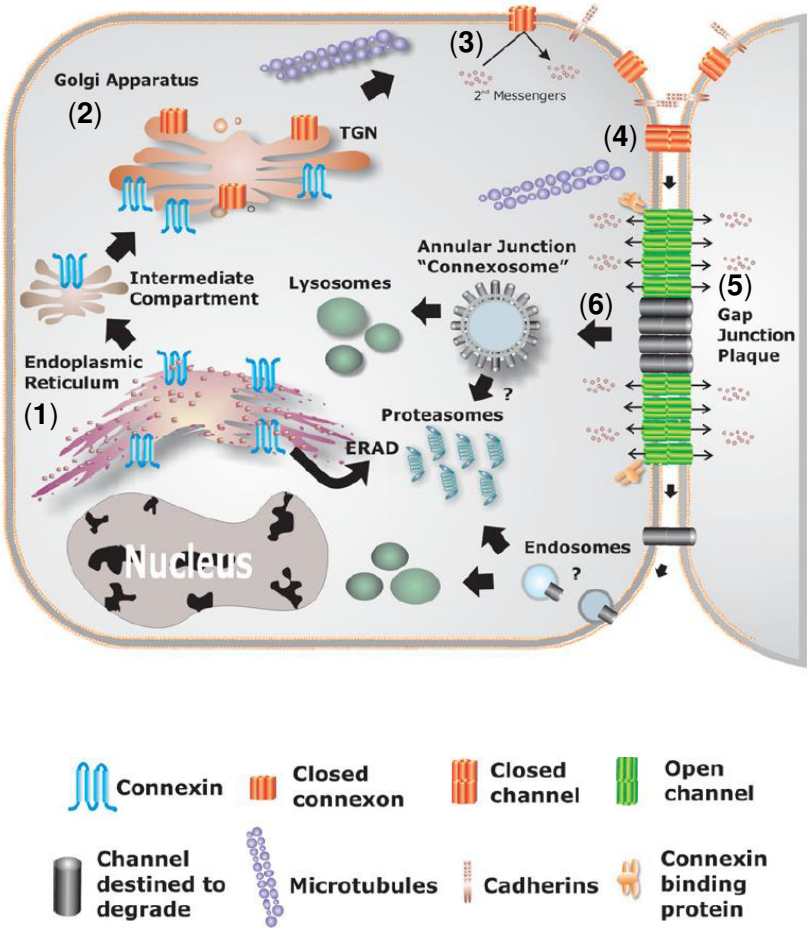

Fig. 5.4: Overview of connexin life cycle: **1:** Synthesis on ER-bound ribosomes, **2:** Oligomerization in the TGN, **3:** Transport to the plasma membrane, **4:** Gap junction channel formation, **5:** Assembly in plaques, **6:** Gap junction degradation. Image was reproduced with permission, from Laird (2006), Biochemical Journal, **394**, 527 – 543. [256] © the Biochemical Society. (Numbers were inserted for clarity).

Connexin polypeptides are synthesized by ribosomes in the endoplasmic reticulum and subsequently oligomerized into connexons in the trans-golgi-network (TGN). Connexins are transported from Golgi to the plasma membrane and after incorporation in the plasma membrane, the hemichannels can freely diffuse within the lipid bilayer [257]. Two connexons from neighboring cells can dock together to form a functional gap junction channel. Thereby, regenerated channels are always added at the edges of the plaques whereas older channels, which will be removed soon from the cell membrane, are located in the center [186, 258]. Internalization of gap junctions was previously described to occur by formation of annular junctions [259, 260] which are also called connexosomes [256]. In this process one cell internalizes the entire gap junction or fragments of it. The degradation of gap junctions was investigated by microinjection studies using antibodies [189] or by microscopic analysis of labeled connexins [258, 261]. Other studies pointed to an internalization of gap junctions by endosomal pathways like clathrin-mediated [262] and clathrin-independent mechanism [263].

5.1.3 Role of Gap Junctional Intercellular Communication for Cell and Tissue Physiology

Most cells in normal tissues are communicating via gap junctions except skeletal muscle, erythrocytes and lymphocytes [199]. The great importance of gap junctions for different cell functions is reflected in several gating mechanism (**chapter 5.1.2**) as well as in diversity of different connexins. Gap junctional intercellular communication is regarded as a key mechanism in homeostatic control [264, 265]. It is essential for various cellular functions like growth control, cellular differentiation or regulation of apoptosis [265-267].

Early studies focused on the negative correlation between cell growth and the capability to communicate with each other via gap junctions [268, 269]. The high importance of gap junctional intercellular communication can also be affirmed by the presence of gap junctions in most developmental systems already starting from early stages of embryogenesis [270, 271]. A general task of gap junctional intercellular communication is to provide a rapid way of communication within a tissue. This plays an important role in spreading electric waves in cardiac tissues which coordinate repeated cycles of synchronized contraction and relaxation, resulting in rhythmic and synchronized contraction of many individual cardiac myocytes [272, 273]. The transfer and exchange of signals via gap junctions was also found between astrocytes [274] as well as in coordination of hormonal action and secretion [275] like triggering the insulin release [276].

Connexin gene mutations as well as changes in localization or expression of the proteins are the reason for different connexin-linked or connexin-dysregulated diseases [277]. Already in 1966, first evidence for a connection between gap junctional intercellular communication and carcinogenesis was found. Human cancer cells showed a reduction of gap junctional intercellular communication [278]. More than 40 years later it is still questionable, if deficient gap junction communication is a requirement or a consequence of tumor formation [279]. Aberrations in the connexin expression are also involved in cardiac ischemia and cardiac hypertrophy [199]. Mutations in the connexins are responsible for different diseases. The first one, which is reported in context with a mutation in the gene for Cx32 is x-linked Charcot-Marie-Tooth disease [280]. Additionally, mutations in Cx26 and Cx31 are known to lead to deafness [281]. Different diseases are caused by mutations in Cx31. Missense or nonsense mutations in the second extracellular loop were also identified to induce deafness, whereas other mutations in the second membrane domain have been associated with skin disorder erythrokeratoderma variabilis (EKV) [282]. Other mutations of connexins e.g. Cx37, Cx46, C40, Cx43 and Cx50 are associated with cataract [283] or heart abnormality [284].

5.1.4 Common Techniques to Analyze Gap Junctional Intercellular Communication *in vitro*

Due to the importance of gap junctions in many biological processes as well as in regulation of cell growth and cell death, many techniques are known to study gap junctional intercellular communication *in vitro*. Techniques based on conductance measurements via dual patch clamp [285] or based on endogenous compound transfer e.g. by using radiolabeled nucleotides [286] have been developed. But by far, most techniques use dye transfer analysis. The most popular assays based on dye transfer are schematically depicted in **Fig. 5.5 (A-G)** and briefly explained below including a discussion about their individual advantages and disadvantages [287].

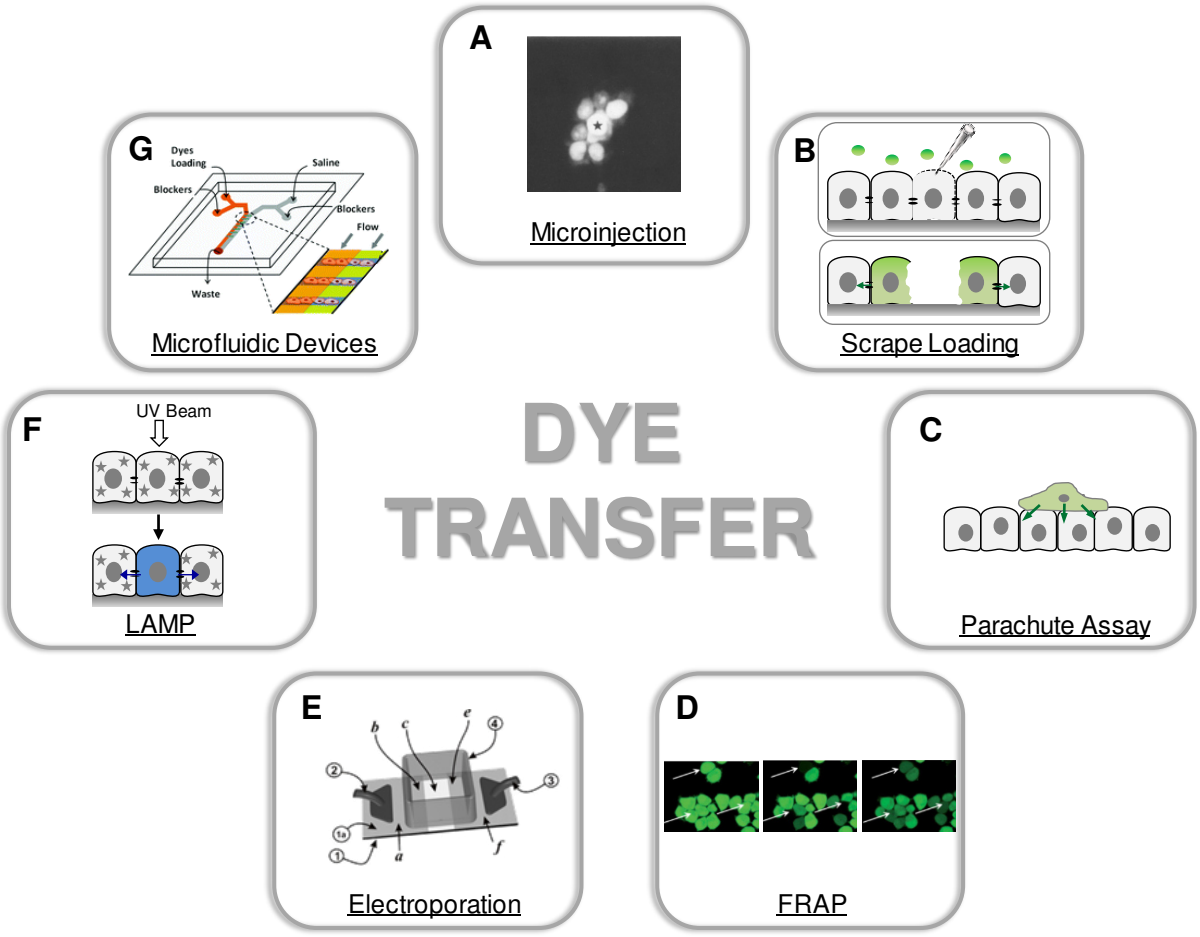

Fig. 5.5: Overview of most popular dye transfer techniques to analyze gap junctional intercellular communication: Microinjection [204] (**A**), scrape loading (**B**), parachute assay (**C**), *Fluorescence Recovery After Photobleaching* (FRAP) [288] (**D**), electroporation [289] (**E**), *Local Activation of a Molecular fluorescent Probe* (LAMP) (**F**) or microfluidic devices [246] (**G**). The techniques differ in the method used for loading the cells with a small, fluorescent gap junction-permeable dye and initiation of the gap junctional transport process. Images in **A** ; **D; E** and **G** were taken with permission from the declared references.

(A) Microinjection

Microinjection was first described by Loewenstein and Kanno in 1964. They successfully loaded salivary gland cells from *Drosophila flavorepleta* larvae with fluorescein by using intracellular micropipettes. They discovered that the dye diffused from one cell to the next via gap junctions [290]. Microinjection assays for the detection of gap junctional activity utilize direct injection of a membrane-impermeable but gap junction-permeable dye to one target cell. Injection of the fluorescent dye from the micropipette lumen into a single cell is realized using a pressure or electrical pulse. Different dyes are used as fluorescent tracers such as Lucifer Yellow, Calcein, Propidium Iodide, Alexa Fluor 488, Cascade Blue and others. The microinjection-based technique benefits from the selectivity of loading a single and defined cell with the fluorescent tracer. The injection procedure is well-defined which also enables studies on dye transfer kinetics. Typically, only the intercellular communication of the microinjected cell is analyzed. However, this invasive technique requires specialized equipment and technical skills to prevent cell death during the experiment. Normally, microinjection is a low throughput technique and is not practical for parallel analysis of many cells. The results are limited to microscopic observations where the number of dye-coupled cells is counted and sometimes variations in the initial concentration of the dye are observed.

(B) Scrape Loading

Scrape Loading is a simple and fast method to evaluate the presence or absence of gap junctional intercellular communication. It was first described in 1987 by El-Fouly et al. [291] as a direct and rapid technique to monitor dye transfer of Lucifer Yellow with a molecular weight of 457.2 Da into adjacent cells. For this purpose, cell monolayers were scraped or scratched with a scalpel, needle or pipette tip in presence of a gap junction-permeable, but membrane-impermeable dye. Due to local disruption of the membrane the dye is incorporated by cells along the lesion. The fluorescent dye subsequently diffuses from the primary loaded cells into the neighboring ones if they are connected via gap junctions. The distance of dye diffusion is used as a measure for the degree of gap junctional intercellular communication. By combining Lucifer Yellow with another fluorescent dye beyond the size limit for gap junctional transfer like Rhodamine Dextran the initially stained cells can be clearly defined. The big advantage of this traditional method is that no special equipment or special technical skills are necessary to perform a successful experiment. As the size of the lesion defines the amount of initially stained cells, a large number of cells can be analyzed simultaneously. However, this method has the disadvantage that neither low density cultures nor 3D models can be used. McKarns and Doolittle showed that dye loading of the scraped cells is not uniform and that it has an influence on dye transfer into recipients. Therefore, they argue that this method is not suited for a quantitative analysis of concentration-dependent effects of

substances. Additionally, they raise concern that cell damages can cause changes in pH, Ca^{2+} concentration or generate free radicals which are described to regulate gap junctional intercellular communication [292]. Nevertheless, this method is applied in many studies to investigate gap junctional intercellular communication of different cell types as well as in whole tissue sections like skin [293], primary tissue [294] or central nervous system [295].

(C) Parachute Assay

Another dye transfer-based assay is the so-called parachute assay, first described by Goldberg et al. in 1995 [296]. While the presence of gap junctions can be confirmed and analyzed by the scratch assay and microinjection technique, the parachute assay is suitable to investigate gap junction de novo formation. This assay requires pre-staining of a single cell suspension with a small gap junction-permeable dye. These single, pre-stained cells are then added to a confluent, unstained acceptor cell population. If gap junctions are consecutively formed between donor and acceptor cells the dye can diffuse into the monolayer. Dye spreading can finally be analyzed by using fluorescence microscopy. In more refined approaches a second dye is used - either staining the donor or acceptor cells - which has a high molecular weight to prevent dye transfer through gap junctions. In some approaches the dye transfer is detected via flow cytometry which also offers the possibility to yield quantitative and precise data for a huge cell population. Tomasetto et al. (1993) presented a two-dye method in which the recipient cells were pre-stained with an irreversibly membrane binding dye and the donor population was stained with Calcein. After gap junction formation, cells were analyzed by flow cytometry regarding double positive cells containing both dyes [297]. However, this assay is time-consuming and cannot be used to analyze gap junction formation within tissues. Additionally, local differences of dye transfer within the cell layer are found. The big advantage of the method is that the membrane remains intact during the whole assay by using the membrane-permeable tracer dye Calcein AM.

(D) Fluorescence Recovery After Photobleaching (FRAP)

The advantage of loading cells with initially membrane-permeable dyes is also applied in the so called FRAP assay. The gap-FRAP method was first described by Wade et al. in 1986 who monitored the redistribution of the dye as a function of time in human teratocarcinoma cells [298]. In contrast to the previously described techniques where only a small population is loaded, the entire cell layer is stained for the FRAP assay. Typically, 5(6)-carboxy-fluorescein diacetate (CFDA) or Calcein AM which remains in the cytoplasm after hydrolysis by intracellular esterases are used, which both have a low molecular weight of 376 Da or 622 Da. Subsequently, a single cell is photobleached by using a high power laser beam. If cells are connected via gap junctions, dye movement from the adjacent cells into the

photobleached cell is monitored by time-resolved fluorescence microscopy using low laser power. As the recovery process is monitored over several minutes, kinetic curves can be analyzed to quantify and compare gap junctional intercellular communication between different cell types or after adding gap junction-modulating substances. Benefits of the FRAP assay compared to other techniques are its non-invasiveness and its fast and easily quantifiable detection approach. Gap junction intercellular communication can be monitored in real-time without any cell injuries due to injection or other mechanical manipulation during the dye-loading process. However, potential phototoxicity due to the intense laser illumination as well as photobleaching of the surrounding non-targeted cells may cause problems.

(E) Electroporation

As described in more detail in **chapter 5.2** electroporation can be used to introduce membrane impermeable fluorescent dyes into the cytoplasm of adherent cells by creating transient pores via brief electric pulses. This method is also used to selectively load a defined cell population with e.g. Lucifer Yellow, followed by the analysis of dye transfer into adjacent non-electroporated cells via gap junctions. Raptis et al. developed and published a setup in 1994 which consists of a half ITO-coated glass substrate [299] to study gap junctional intercellular communication. The layout was further improved in the following years [289]. After applying an electric pulse in presence of Lucifer Yellow the cells grown on the conductive ITO substrate are loaded with the tracer dye. The subsequent migration of Lucifer Yellow into the non-electroporated cells grown on the non-conductive part of the slide was analyzed to investigate gap junctional intercellular communication. The dye transfer was analyzed using fluorescence microscopy in combination with digital image analysis [300]. This technique can be used for all adherent cell lines and represents a rapid, precise and highly reproducible assay with a minimum of interference with cellular physiology compared to other techniques [301]. With this approach successful studies e.g. regarding regulation of gap junctional intercellular communication [302, 303] or changes in gap junctional intercellular communication during tumor development [304] were performed. De Vuyst et al. (2008) presented another dye transfer assay to investigate gap junctional intercellular communication based on electroporation called ELDT – *Electroporation Loading and Dye Transfer*. In their study they compared ELDT results directly with results obtained by scrape loading assay and found a higher degree of gap junctional intercellular communication in their electroporation based assay. They explained the decrease in dye transfer analyzed in the scratch assay with the interference due to cell death and membrane disruption which leads to the release of intracellular content and intracellular signals [305].

Disadvantageously, electroporation parameters must be adjusted for each cell line prior to the gap junctional intercellular communication assay. However, this method enables the analysis of the dye transfer over a large population in a fast and precise assay.

(F) Local Activation Of Molecular Fluorescent Probe (LAMP)

LAMP as a new imaging assay to analyze gap junctional intercellular communication was described in 2005 by Dakin et al. [306]. In this assay cells are loaded with a membrane permeable, caged coumarin fluorophore (NPE-HCCC2/AM) which is hydrolyzed by intracellular esterases to generate the membrane impermeable non-fluorescent dye NPE-HCCC2. In the next step local uncaging of the dye is performed using a small and defined UV beam that is focused on a single cell to produce the blue fluorescent and gap junction-permeable compound HCCC2. Afterwards, the dye transfer of HCCC2 from the donor cells to the adjacent receptor cells is detected using continuous fluorescence microscopic analysis. In further studies differently caged tracers were developed [307, 308]. This method was further improved as infrared-LAMP [309] using two-photon uncaging and imaging, which offers the possibility to analyze gap junctional intercellular communication in 3-D. Summarizing the advantages of this technique, LAMP offers the possibility to analyze cell-cell communication non-invasively, conserving the membrane integrity throughout the experiment and to obtain quantitative as well as dynamic information. The assay is applicable for cell monolayers and tissues.

***(G)* Microfluidic Devices**

Microfluidic devices to investigate numerous biological processes and phenomena are widely used in technologies such as immunoassays [310], cell counting [311] and sorting [312, 313], cell culture studies [314], cell manipulation [315] including electroporation [316], and drug screening [313, 317]. This miniaturized method has the big advantage that only small volumes are needed allowing for low reagent consumption, which can be of great interest when working with expensive substances or dyes. Microfluidic devices are a scalable technology which offers the possibility for high throughput screening. By using microfluidic setups for the analysis of gap junctional intercellular communication membrane permeable dyes or molecules can be selectively introduced into cells at a defined area. The dye transfer into the periphery can be analyzed quantitatively. However, this method is limited to the use of membrane permeable molecules and is up to now only suitable for monolayer forming cells [318]. Analysis of 3D models for gap junctional intercellular communication remains a technical challenge [319].

Chen and Lee (2010) demonstrated a non-invasive microfluidic gap junction assay where adherent cells were selectively loaded with Calcein AM by hydrodynamic focusing [318]. By

applying high pressure in the outer inlets and low pressure into the middle one, dye loading selectively occurred in the center of the channel without any cell damages or membrane disruption. They analyzed the subsequent dye transfer of Calcein into the adjacent, unperturbed cells by time-lapse fluorescence microscopy. Ye et al. (2011) also presented a microfluidic method to analyze gap junctions mediated dye transfer between single cells in one dimension, by arranging them in single cell arrays [246]. This technique offers the possibility to follow the time-course of dye uptake and diffusion kinetics as the microfluidic device is rapid and precise. The Y-shaped device requires two parallel streams. One stream contains the membrane and gap junction permeable dye and the second stream is used with a dye-free solution for later analysis of the dye transfer due to gap junction communication. The authors showed successfully the analysis of inhibitory effects and kinetics of dye transfer. To further improve the microfluidic devices a high-throughput assay was developed by Bathany et al. (2011) using a multi-laminar flow to simultaneously analyze dye transfer in different environments, e.g. for drug screening or inhibitor studies [320].

5.2 Theoretical Background of Electroporation

Cell membranes are phospholipid bilayers, which contain a hydrophobic core and hydrophilic surfaces. Their main function is to form a barrier between two fluid compartments [321] and thereby preventing free diffusion of ions and hydrophilic molecules.

Selective and reversible permeabilization of the plasma membrane as a tool to inject extracellular compounds into the cytoplasm is necessary for many biotechnical applications and can be realized also with other strategies including:

(i) **Chemical** permeabilization
(ii) Ultrasound-mediated permeabilization (**sonopration**)
(iii) High intensity laser pulses (**optoinjection, optoporation**):
(iv) Exposure to strong electric fields for a limited period of time (**electroporation**).

First publication regarding electroporation of mammalian cells was published in 1982 by Neumann et al. who analyzed gene transfer in mouse lyoma cells by electroporation [322]. Electroporation describes a well-known phenomenon of reversible perturbation of the plasma membrane by exposing cells to an external electric field, which causes a transient membrane destabilization. Presumably, pore formation enables a temporary free diffusion of membrane-impermeable compounds across the plasma membrane. After a limited period of time membrane resealing occurs, while the substances remain entrapped in the cytoplasm. With this method a variety of different molecules have been introduced into cells such as dyes [323-325], drugs [326-328], radiotracers [329, 330], oligonucleotides [331], antibodies [332], DNA [322, 333] and RNA [334, 335].

Over the last years, the combination of electroporation and chemotherapy called *electrochemotherapy* (ECT) using plate or needle electrodes [336] has received considerable attention as a method for cancer treatment. The first application of bioactive substances in ECT was reported in a first clinical trial in 1991 by Mir et al., who introduced bleomycin into head and neck squamous carcinomas [337]. In good agreement, also other clinical studies with individually-sized tumors from different tissues or organs, pointed to an enhanced effect of bleomycin by ECT. Bleomycin was either applied intravenously [338] or intratumorally [339] before electroporation. More recent studies showed that *irreversible electroporation* (IRE), without using a cytotoxic drugs, may serve as a new technique for cancer cell ablation [340]. To ablate

tumors *in vivo*, the cell membrane is permanently permeabilized by applying short duration electric fields without inducing thermal damages in the tissue [341-343].

In summary, electroporation can be considered as a promising tool to improve cancer therapy, as it was already successfully applied *in vitro*, *in vivo* [344] and in clinical approaches [345] and may be a potential technique for future applications. However, ECT and IRE both require the localization of the electrodes directly into the injured tissue which limits their application [346].

5.2.1 Biophysical Background of Electroporation

Normally, the cell membrane creates a barrier, which prevents molecules from free diffusion across it. However, it is selectively permeable to certain ions, including Na^+, K^+ and Cl^-, which causes a natural potential difference ($\Delta\Psi_0$) of around - 40 mV to - 70 mV between the cells' interior ($\Delta\Psi_{in}$) and the surrounding medium ($\Delta\Psi_{out}$). The natural potential difference, arising from the electrochemical ion gradients as well as the asymmetric distribution of charged lipids and glycoproteins in the plasma membrane is defined by **Eq. 5.1**.

$$\Delta\Psi_0 = \Delta\Psi_{in} - \Delta\Psi_{out} \qquad \textbf{Eq. 5.1}$$

Cells in a Direct Current (DC) Electric Field

By applying an external electric field, the permeability of a membrane can be temporarily increased [347, 348]. The application of an external electric field E_i during an electroporation experiment induces a position-dependent change in $\Delta\Psi_0$ [349]. The resulting $\Delta\Psi_{total}$ is defined (**Eq. 5.2**) as the sum of the natural potential difference ($\Delta\Psi_0$) and the electro-induced transmembrane potential difference ($\Delta\Psi_E$).

$$\Delta\Psi_{total} = \Delta\Psi_0 + \Delta\Psi_E \qquad \textbf{Eq. 5.2}$$

Studies with a voltage sensitive fluorescent dye showed that membrane permeabilization is position-dependent [350]. This was also confirmed by theoretical studies that showed a hyperpolarization of the cell membrane facing the anode whereas the opposite cell side is depolarized [351]. Additionally, membrane permeabilization is dependent on cell size and shape, the electric field intensity, and the orientation of the cell in the electric field [352]. The electric field induced membrane potential can be described by **Eq. 5.3** [347, 353].

$$\Psi_E = f \cdot g(\lambda) \cdot r \cdot E \cdot \cos\theta(M) \qquad \textbf{Eq. 5.3}$$

The formula includes the cell radius *r* and the shape factor *f*, which was determined to 1.5 for a spherical cell shape [354]. To consider the different conductivities λ of the cell membrane (λ_m), the cytoplasm (λ_c) and the extracellular medium (λ_i) the factor $g(\lambda)$ is introduced into **Eq. 5.3** [347]. The parameter *E* describes the field strength and $\theta(M)$ defines the angle between the normal to the membrane at a position *M* and the electric field direction.

Permeabilization of the plasma membrane only occurs if the potential difference $\Delta\Psi_{total}$ after applying an electric field has achieved a critical value $\Delta\Psi_{perm}$, which was found to be between 200 mV – 1 V [355] depending on cell type and cell size [356, 357].

$$\Psi_{perm} = f \cdot g(\lambda) \cdot r \cdot E_{perm} \qquad \textbf{Eq. 5.4}$$

Therefore, the external electric field strength must be higher than a cell-type specific threshold (E_{perm}). $E > E_{perm}$ leads to an increase in permeabilized membrane area [349], whereas the area of membrane permeabilization and pore diameter is determined by pulse number and duration, respectively [358]. The maximum value of the electro-induced transmembrane potential difference ($\Delta\Psi_E$) is already achieved after a short charging time τ of around 1 µs [353, 354]. The parameter τ depends on the membrane properties and the conductivity of the cytoplasm and the extracellular medium [359].

Electropermeabilization Using AC Current

In contrast of dc current pulses for electropermeabilization the transmembrane potential difference induced by an ac pulse is described by the frequency-dependent Schwan Equation (**Eq. 5.4**). Compared to the dc pulse, where pulse duration and amplitude are clearly defined, using ac pulses it is the frequency that influences the degree of permeabilization. Marszalek et al. (1990) found that compared to the asymmetric polarization of the membrane using dc, a symmetric polarization and simultaneous dye diffusion from both sides into the whole cell was found for electroporation with ac [360]. Further research dealing with the differences of ac compared to dc current revealed, that for frequencies smaller than 100 kHz, $\Delta\Psi_E$ was similar using ac or dc pulses with similar field strength [347, 361].

$$\Delta\Psi_E = \frac{1.5 \cdot g(\lambda) \cdot r \cdot E \cos\theta(M)}{\sqrt{1+(\omega\tau)^2}} \qquad \textbf{Eq. 5.4}$$

$$E = E_0 \cdot \sin(\omega\tau) \qquad \textbf{Eq. 5.5}$$

5.2.2 Electroporation and Transient Permeabilization of the Cell Membrane

The introduction of membrane impermeable compounds into the cells by electroporation is mediated by a transient dielectric breakdown of the membrane due to an overcritical potential difference. This is realized by the application of an electric pulse with a defined pulse duration between micro- to milliseconds and a well-defined amplitude [362].

Different Steps during Electroporation

According to Teissie et al. (2005) the whole electroporation process can be divided into the following five different steps [363] (**Fig. 5.6 C**):

(i) Initiation or Induction

As explained in **chapter 5.2.1** a change in the membrane structure can be triggered by an electric field E_{perm} when $\Delta\Psi_{total}$ reaches a critical value. The critical field strength E_{perm} is influenced by the cell radius. Therefore, small compartments like intracellular cell organelle membranes and bacteria need a higher E_{perm} than larger mammalian cells [346].

(ii) Expansion

The membrane permeability expansion process was studied by a fluorescence assay by Prausnitz et al. (1995) [364]. They determined the time-scale of this process to be in the order of ms. Weaver and Powell discovered that as long as $\Delta\Psi_{total} \geq \Delta\Psi_{perm}$ pore formation and expansion is favored [365]. The influence of field strength on the geometry of the permeabilized area and the pulse duration on the density of defects were reported using video imaging [358]. They observed that increasing electric field strengths caused a larger area of membrane permeabilization, whereas greater perturbation of the permeabilized area was found using longer pulse durations.

(iii) Stabilization

As soon as $\Delta\Psi_{total} < \Delta\Psi_{perm}$ the membrane still remains leaky for polar compounds [363] however, a strong decrease of cell membrane perforation was reported [358].

(iv) Membrane Resealing

When pulse parameters were properly selected, the membrane integrity completely recovers after electroporation. It was found that membrane permeabilization remains for up to 4 h at 4 °C, whereas at 37 °C, membrane resealing completes in less than 5 min [366]. Normally, the time-scale for membrane resealing under standard culture conditions is often described to

take place within several seconds [363, 367, 368]. Aside from the temperature dependency, the resealing process is influenced by the lipid composition [369, 370] and most likely by protein reorganization [366]. One factor which should not be neglected for the resealing step is the nutritional state of the cells as reported by Rols et al. (1998) [371].

(v) Memory

After membrane resealing the cell membrane reconstructs a barrier towards hydrophilic molecules back to the state before electroporation under common conditions. This prevents the cell from lysis [353]. However, it can take several hours until the original asymmetric lipid distribution is re-established [372, 373].

Pore Models to Explain the Effect of Electric Field on Cell Membranes

Several studies focused on the mechanism of electroporation and how the barrier, formed naturally by a lipid bilayer, can be overcome by membrane impermeable compounds. One model, which is without significant experimental evidence but widely accepted, is the formation of transient hydrophilic pores [355, 374] (**Fig. 5.6 A**). In this model, the applied external electric field is expected to induce lipid fluctuations and subsequent water entrance, which enables the formation of hydrophobic pores in the membrane. Thermal fluctuations of lipids in combination with pore formation were first described by Litster [375] and Taupin et al. [376] in 1975. These hydrophobic pores are subsequently transformed into hydrophilic ones. It is assumed that, this may happen by molecular rearrangement of the lipids in the pore edges where the head groups are expected to turn away from the original membrane-water interface into the core of the bilayer [377].

The Lewis model (2003) explains the formation of pores differently and proposes an interaction between the electric field and the molecules. According to the Lewis model, the transmembrane voltage causes a decrease in the interaction between phospholipid molecules at the membrane-water interface [378]. Pore formation is explained as a result of adjusting the hydrophilic to the hydrophobic forces at the membrane-water interface [355]. This model describes a connection between the electric field and molecular dynamics in the membrane structures. On the basis of this model several molecular simulations dealing with pore formation in membranes were published. In *molecular dynamics* (MD) simulations the motion of individual molecules in defined electric fields is simulated and can be used to explain and monitor pore formation (**Fig. 5.6 B**). They found that “fingers” of water

molecules initiate the entry in the hydrophobic part of the membrane. Later, water channels are formed which can bridge the cell membrane. Subsequently, motion of polar lipid head groups into the interior of the bilayer create hydrophilic pores [379]. Disadvantageously, this computer-based simulation did not include any ions or cellular organelles which may have an influence on the mechanism during electroporation [355].

The current opinion is that small molecules and drugs enter the cells through pores via diffusion while macromolecules and DNA enter the cytoplasm through an electrophoretically driven mechanism after interacting with the destabilized membrane [380].

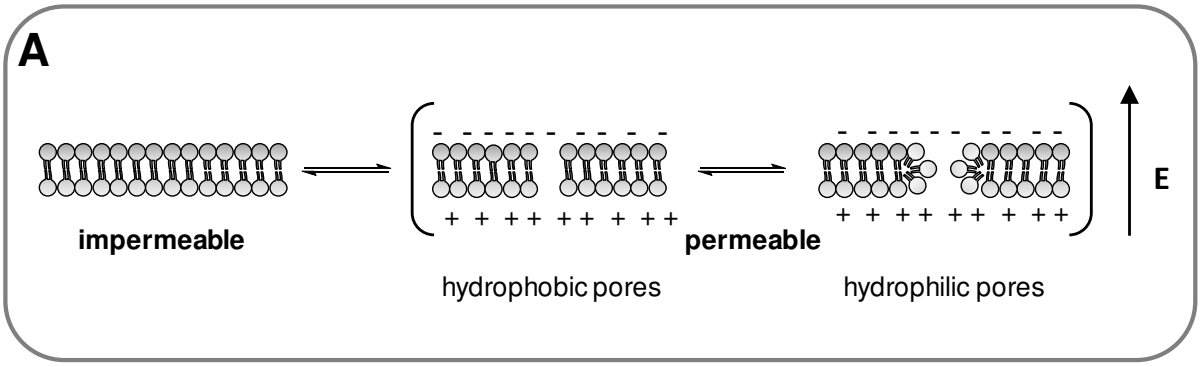

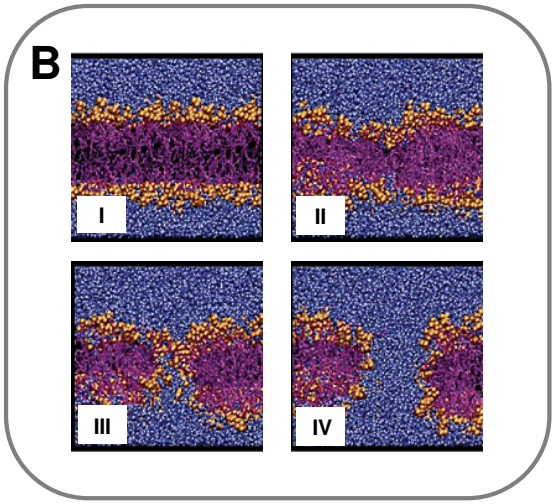

C

Step	Description	Time Scale
Initiation	By applying an external electric field, the transmembrane potential is increased up to a threshold value	µs
Expansion	As long as the supercritical field is present the defects expand	ms
Stabilization	As soon as the field is subcritical membrane recovery and reorganization takes place Cell membrane remain leaky for molecules	ms
Resealing	Reclosure of transient permeable structures	s
Memory	Complete recovery of membrane structures and physiological properties	h

Fig. 5.6: A: Hydrophilic pore model for membrane permeabilization after electroporation according to Neumann et al. (1999) [377]. Upon application of an electric field E interfacial polarization of the membrane (+ ; -) is induced leading to water entrance and pore formation. First hydrophobic defects are produced which are transformed into hydrophilic pores after lipid structure rearrangement. **B:** Simulation of pore formation during application of an electric field of 0.5 V/nm in a *dioleoylphosphatidylcholine* (DOPC) bilayer. Images show simulation snapshots of the pore formation process at 2.4 ns (**I**), 3.04 ns (**II**), 3.35 ns (**III**) and 3.55 ns (**IV**) after starting the application of the electric field: Intact membrane (**I**), water penetration and membrane deformation (**II**), phospholipid rearrangement (**III**), pore has reached its final size (**IV**). Water molecules are shown in blue, lipid chains in purple and their head groups in orange [381]. **C:** Five steps of electroporation according to Teissie et al. (2005) [363]. Images in **B** were taken with permission from Tieleman et al. (2003) [381].

5.2.3 *In Situ* Electroporation of Adherent Cells

Traditionally, electroporation is performed with suspended cells placed in a cuvette between two parallel plate electrodes. For this purpose, cells must first be removed from their growth substrate and the organization as well as the structure of the cell layer is destroyed. One disadvantage of electroporation in suspension is that the voltage drops to some degree across the bulk fluid, which increases the temperature in the electroporation buffer. Because of the energy loss across the bulk rather high voltages are necessary for a successful delivery of membrane impermeable compounds with suspension electroporation. In this context a strong influence on cells' viability is reported. Additionally, cells must be re-plated and adhesion as well as spreading of the cells must be completed before the electroporated cells can be analyzed microscopically. These disadvantages can be overcome by *in situ* electroporation of adherent cells which remain anchored to their growth substrate during the entire experiment.

Different Setups for *In Situ* Electroporation

Different setups are available to perform electroporation with adherent cells and a survey of some available electroporation strategies is given in **Fig. 5.7**.

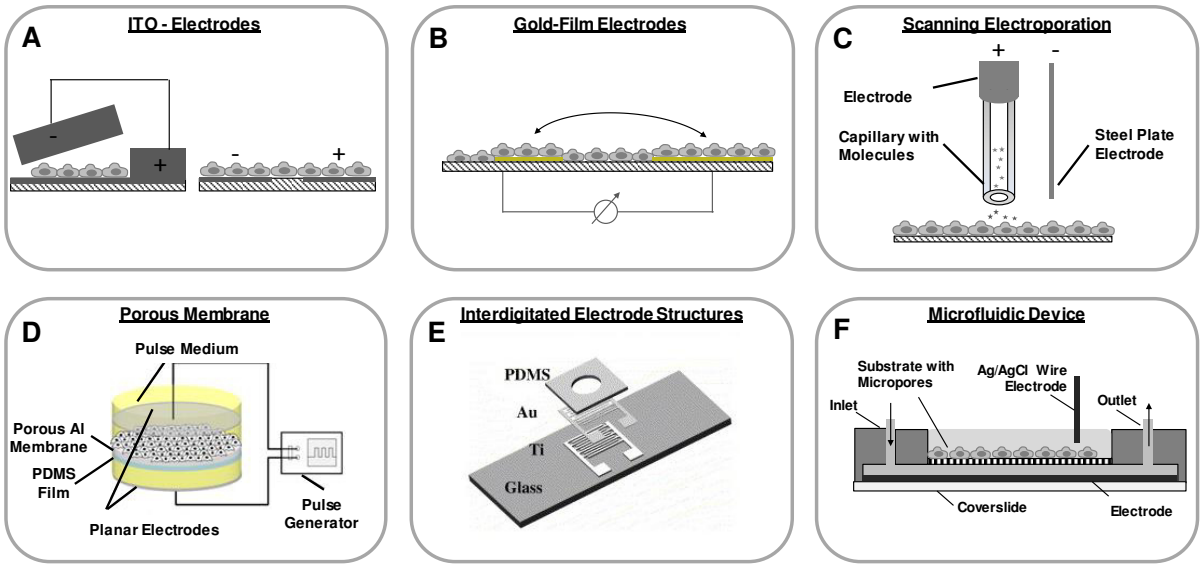

Fig. 5.7: Survey of different setups used for *in situ* electroporation of adherent cells: Electroporation of adherent cells on ITO electrodes using a dipping counter electrode [382] (**left**) or two co-planar ITO electrodes [289] (**right**) and dc pulses (**A**). Another strategy is based on using gold as electrode and growth substrate and by applying ac voltages for cell permeabilization [150, 323, 383] (**B**). Scanning electroporation is performed by using a capillary which can deliver the molecules as well as the electric field for membrane permeabilization. Additionally to the Al electrode in close contact with the capillary a dipping steel plate electrode is used for electroporation of adherent cells grown in a petri dish with dc pulses [384] (**C**). Cells can also be cultivated on porous membranes. Ishibashi et al. optionally inserted a PDMS film underneath to perform localized electroporation in pre-defined regions. Two planar Pt electrodes are used to perform electroporation by applying a dc electric field [385] (**D**). Another electrode structure contains thin-film interdigitated electrodes made of Ti and Au deposited on glass slides [386] and electroporation was performed using ac pulses (**E**). Microfluidic *Localize Electroporation Device* (LEPD) containing one electrode integrated into the solid glass substrate and a dipping Ag/AgCl electrode for dc electroporation. Cells are grown on top of porous membranes containing nano- or microchannels. The microfluidic channel underneath provides the cells continuously fresh medium [387] (**F**). Images in **D-E** were taken with permission from the declared references.

Some groups investigated electrode layouts made of ITO (*indium tin oxide*) or gold for *in situ* electroporation. Raptis and Firth described a simple and rapid procedure for the delivery of antibodies and DNA into adherent F111 cells by *in situ* electroporation using electrically conductive indium-tin oxide as substrate electrode material and a dipping aluminum counter electrode (**A, left**) [299, 382]. Their setup was further improved and adjusted using two coplanar ITO electrodes (**A, right**) [289]. Already in 1993 Ghosh et al. monitored the phenomena of pore formation and resealing in adherent fibroblastic cells grown on small gold-film electrodes (**B**) with impedance measurement in real-time [388]. Later, Wegener et al. (2002) published the combination of electroporation with non-invasive and time-resolved impedance monitoring along the introduction of extracellular and membrane impermeable Lucifer Yellow into the cytoplasm of different adherent cell lines grown on gold-film electrodes [383].

Olofsson et al. (2007) reported about a scanning electroporation setup. Adherent cells are electroporated using an electrolyte-filled capillary. This capillary is surrounded by a cylindrical Al counter electrode and the measurement setup is completed by a dipping steel plate electrode (**C**). The differently sized capillary has several tasks:

(i) Delivery of an electric field, whereas the field of membrane permeabilization can be controlled and selected by a micromanipulator. The electric field is created between the Al electrode and the steel plate electrode.
(ii) Delivery of the non-membrane permeable substances which were introduced into the electroporation buffer-filled capillary.

With this setup either stationary electroporation or scanning electroporation can be performed and the group successfully transfected cells with a nine base pair randomized oligonucleotide and a plasmid [384].

Another setup published in 1995, used transparent microporous filter membranes, made of polyester or polyethylene terephthalate, as solid growth substrate for adherent cells which were positioned between the two electrodes in a common electroporation cuvette. However, a precise positioning of the membrane in the cuvette, which determines the distance to the electrodes, could not be achieved [389]. After electroporation of adherent HUVEC cells on porous filter inserts the alterations in cytoskeletal structures dependent on the applied voltages were investigated by Kanthou et al. (2006) using immunofluorescence staining or western blot analysis [390]. Ishibashi et al. (2007) used porous alumina membrane inserts with a thin PDMS film attached underneath, which includes one or more holes to define the regions of electroporation (**D**). As electrode material they used two planar Pt electrodes - one above and one underneath the cell layer. They showed that electroporation and uptake of

Lucifer Yellow only occurred in those HeLa cells, which were located directly above the holes in the PDMS layer [385].

Microfluidic devices and microchips enjoy an increase in popularity. Some devices have been developed where cells are anchored to the surface during electroporation. Electroporation microchip layouts with interdigitated electrodes (**E**) were used to successfully transfect adherent cells using gold [391] or gold with titanium [386] electrodes. In 2014 a device was presented by Kang et al. which combined the advantages of a microfluidic setup with those of *in situ* electroporation (**F**). In this setup, they used a polycarbonate (PC) membrane with varying pore diameters as growth substrate for HeLa, HT1080 cells and primary neurons. The membrane also separates the cell culture compartment from the microchannel underneath. By using the PC membrane the group could define the positions where electroporation occurred and termed it “localized electroporation”. In this device the medium as well as membrane impermeable compounds were delivered from underneath by using ten microchannels. They successfully introduced propidium iodide as well as a plasmid DNA with a size of 2 MDa [387].

So far, only incorporation of membrane impermeable compounds into multiple cells was presented here. However, there are some new and versatile methods reported, which address the selective loading of single cells with the compounds of interest. Vassanelli (2008) developed a silicon BioChip format with 60 microelectrodes made of gold, where the electrode sizes were adjusted to those of cells (15 µm – 50 µm) [392]. The design allows one single cell to adhere upon one microelectrode. The cell-sized electrodes are addressed individually and single-cell electroporation of CHO-K1 cells in presence of siRNA, DNA plasmid vectors, dyes or antisense-like oligodeoxyribonucleotides (ODNs) was performed.

All these devices presented in this chapter differ with respect to the material and layout of the growth substrate, but they all have in common the big advantage that cells can be manipulated in their natural environment without damaging the surface proteins or cytoskeleton by detaching them from their surface. Of course, only a selection of published and available methods of *in situ* electroporation were presented here and the development of new devices is still a current topic of research [393, 394].

Applications of *In Situ* Electroporation

The method of introducing compounds into cells by electroporation is utilized in some therapeutic or genetic approaches, where active substances are released into the cytoplasm of adherent cells. Aside from the uptake of fluorescent molecules *in situ* electroporation is performed with a medical or biological interest to load cells with peptides [395], enzymes [388], antibodies [382, 396], DNA [389, 397], mRNA [398], siRNA [399, 400] or anti-cancer drugs [327].

Electroporation can be used to study the biological function of a target protein inside living cells and allows selective blocking of single cellular functions. Rui et al. (2002) applied electroporation to introduce anti-TFAR19 antibodies, which are targeted on *TF-1 apoptosis-related gene 19* (TFAR19), into HeLa cells to inhibit apoptosis [396]. Another approach study the interaction and signal transduction in vitro requires non permeable inhibitors disturbing the signal cascade to be introduced by *in situ* electroporation into living cells. Brownell et al. incorporated inhibitors for the epidermal growth factor (EGF) receptor signaling cascade in NiH3T3 cells which were grown on partly conductive ITO slides [401]. The two inhibitors inhibited the EGF-mediated activation of Erk1/2 signaling pathways after delivery into the cytoplasm and were proposed to be a promising tool in cancer therapy.

In situ electroporation can also be used to transfect adherent cells with nucleic acids and therefore provides a good alternative to common transfection methods based on lipofection, virus-mediated transfection or physical methods like sonoporation or microinjection [402]. Zheng and Chang used a pulsed radio-frequency electric field to successfully transfect adherent cells. They introduced plasmid DNA containing the reporter gene β-gal by *in situ* electroporation into COS-M6 and CV-1 cells with high efficiency [397]. In 1999, Teruel et al. applied *in situ* electroporation for the transfection of cultured neurons in a micro volume set up with DNA and RNA [398].

A further approach of *in situ* electroporation was also demonstrated in **chapter 5.1.4** where small membrane non-permeable dyes are introduced into adherent cells and subsequent dye transfer into neighboring cells is monitored [289]. The distance of dye transfer correlates with the degree of gap junction communication and this method offers the possibility to study e.g. the effect of Proto-oncogene tyrosine-protein kinase Src and its effector Stat3 (*Signal transducer and activator of transcription-3*) on gap junctional intercellular communication in adherent cells [302].

Combination of *In Situ* Electroporation with Non-Invasive Impedance Monitoring

In situ electroporation offers a possibility to selectively introduce substances into target cells yielding high efficiencies and high survival rates by using appropriate pulse parameters. Often, electroporation efficiency and successful delivery of the target molecule into the cytoplasm is controlled by optical methods using light or fluorescence microscopy or flow cytometry. Also other bioanalytical methods are used to evaluate the uptake efficiency like western blot [396, 403], immunostaining [401] or special kits to analyze cell viability or apoptosis [404].

Electroporation performed with cells in suspension are sometimes combined with electrical methods to analyze the impact of electric pulses on cell membranes. Kinosita and Tsong used conductance measurements to study the electroporation process in suspensions of erythrocytes [405]. Also Pavlin et al. studied the effect of electroporation of a mouse melanoma cell suspension by using conductivity measurements. They found that the extent of permeabilized tissue can be calculated by detecting the conductivity during the whole process, as an decrease in membrane integrity is reflected by an increase in conductivity [406]. Huang and Rubnisky (1999) developed a microchip used for electroporation and combined it with current measurements to control the process [407] A combination of a 3-D microelectrode layout with impedance sensing was developed by He et al. (2008) who analyzed the response of HeLa cell suspension during electroporation and measured the dynamics in the cell membrane dependent on pulse duration and applied voltage [408].

A more efficient and less time-consuming analysis without using expensive technical devices is the combination of *in situ* electroporation with impedance recordings. Here, all advantages of *in situ* electroporation and those of an electrical readout to monitor the electroporation process and the cellular response in real-time are combined. Adherent cells are grown on small gold-film electrodes which provide a sensor surface to detect small changes in cells' morphology with high sensitivity and in real-time. The gold-film electrode serves as

(i) culture substrate for adherent cells
(ii) electrode to measure and monitor non-invasively cells before and after electroporation (analysis)
(iii) electrode to apply the electroporation voltage for a limited period of time (manipulation).

This combination of these two techniques were successfully applied by Ghosh et al. (1993) to analyze the recovery and regeneration of the cells after applying different electroporation pulses with high time-resolution [388]. Wegener et al. (2002) used this set up for the evaluation of the non-invasive manner of the electroporation process during incorporation of fluorescent dyes [383]. Stolwijk et al. (2011) analyzed the uptake mechanism of differently sized FITC dextrans into adherent cells and further investigated the membrane resealing impedimetrically. Additionally, the response of bioactive compounds like sodium azide and bleomycin after electroporation into NRK cells was monitored in real-time [323].

5.3 Objective and Motivation

Gap junctional intercellular communication plays an important role in many biological processes. Therefore, many methods are known to monitor and analyze this way of communication whereby most methods are based on dye transfer. Each method has its own advantages and limitations (**chapter 5.1.4**) but the basic idea is always similar: A non-toxic and membrane impermeable dye, which is small enough to diffuse through gap junction, is introduced into a single cell or a selected cell population and subsequently the dye transfer to adjacent cells is investigated and quantified.

Our goal was to investigate a new opto-electrical assay, which is based on non-invasive ECIS recordings and electroporation, to facilitate a sequentially analysis of different cell physiological parameters, like cell viability or motility in combination with gap junctional intercellular communication within one cell population (**Fig. 5.8**). For this purpose NRK cells were loaded with the gap junction permeable dye Lucifer Yellow by *in situ* electroporation on the electrode surface. Dye transfer into NRK cells in the periphery of the electrode is then analyzed microscopically. This method offers the advantage of a possible parallelization because commercial ECIS arrays contain eight different compartments which can be pre-treated differently prior to the gap junctional intercellular communication assay. This enables a comparison of the dye transfer within control cells and experimentally manipulated cells, which were exposed to a test substance in advance, during a single experiment with similar cell culture conditions. In the future even high-throughput approaches using 96-well or higher formats may be possible. Pre-loading with Lucifer Yellow by electroporation can be optimized with respect to cell-type and electroporation parameters. The good controllability of the electroporation parameters enables high reproducibility. This and the benefit of automation create big advantage compared to common dye transfer-based techniques.

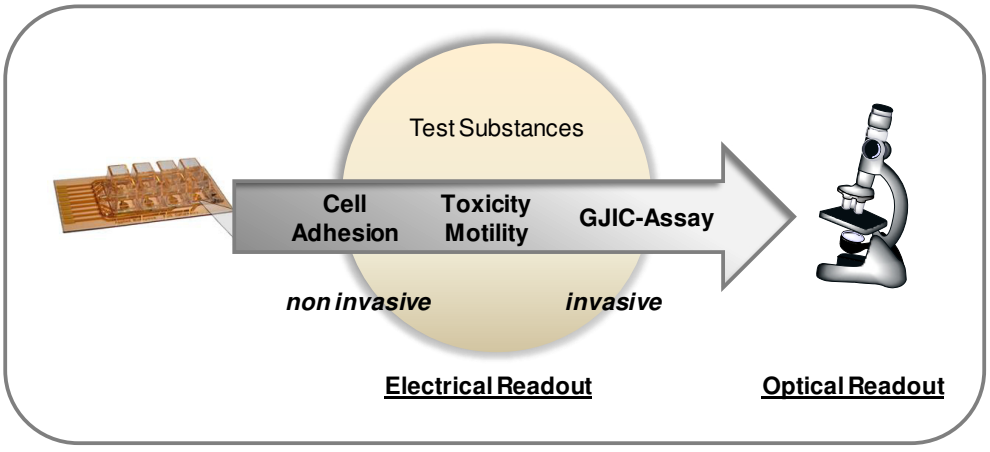

Fig. 5.8: Schematic overview of the gap junctional intercellular communication assay (GJIC) based on electroporation: The opto-electrical assay allows a sequentially analysis of cellular response to the addition of a certain test substance, like inhibitors or nanoparticles. In a sequence of non-invasive impedance recordings the impact of a test substance on cell adhesion, cell viability or motility can be investigated. Finally, the electroporation-based analysis of dye transfer is performed using an optical readout to evaluate the impact of the test substance on gap junctional intercellular communication.

5.4 Material and Methods for Analysis of Gap Junctional Intercellular Communication Based on *In Situ* Electroporation

5.4.1 Experimental Setup and General Procedure for *In Situ* Electroporation

In this approach non-invasive impedance recording is combined with a short, invasive electroporation pulse to introduce membrane-impermeable compounds into the cytoplasm of adherent NRK cells. The general experimental procedure is divided into three steps (**Fig. 5.9**):

(A) Array preparation: Cell seeding and culturing on the appropriate electrode layout

(B) Electroporation experiment: Impedance recordings of baseline, electroporation pulse and cells' recovery (optional)

(C) Microscopic analysis of electroporation efficiency

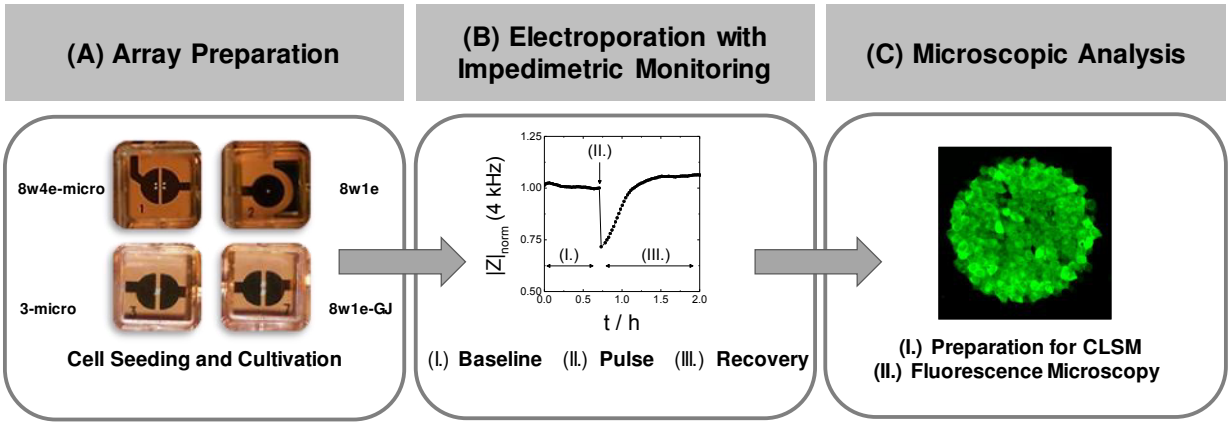

Fig. 5.9: Overview over the three experimental steps for *in situ* electroporation. **A:** Array preparation including cell seeding of NRK cells on the appropriate electrode layout. **B:** Impedimetric analysis starting with a baseline in buffer ($EBSS^{++}$; $EBSS^{-+}$) and followed by the addition of the membrane-impermeable substance to be introduced into the cells. After pulsing cell recovery was monitored for a defined period of time or until fully completed as indicated by re-attaining pre-pulse impedance levels. **C:** Documentation of the cells by confocal laser scanning microscopy.

All electroporation experiments were performed with NRK cells, which were always inoculated onto the appropriate electrode layout in a seeding density of 500 000 cells/mL or 600 000 cells/mL two days prior to the experiment. One day before electroporation, culture medium was exchanged. Impedimetric monitoring was started with recording a baseline in 150 µL – 200 µL $EBSS^{++}$ or $EBSS^{-+}$ (w/ Mg^{2+}, w/o Ca^{2+}) to monitor the equilibration of the cells to the conditions of the measurement setup with non-invasive ECIS recordings. Then, the membrane impermeable substance or dye of interest was added, using a volume of

50 µL - 200 µL depending on the respective compound. After a short equilibration, an invasive electroporation pulse, commonly 40 kHz, 4 V and 200 ms, was applied. Afterwards, the impedance recovery and cellular response after electroporation in presence of substances was monitored by analyzing the time-course of impedance at 4 kHz or 32 kHz. This post-pulse monitoring was only done for 5 min in case of microscopic analysis of gap junctional intercellular communication, or until the impedance reached values similar to those before pulsing. Variations of this protocol for special applications are described in more detail below (**chapter 5.4.2**).

To visualize adherent cells on the gold-film electrodes after electroporation an upright microscope was used. For this purpose, a special preparation of the sample was necessary after ECIS recordings (**Fig. 5.10**). First, cells were washed with PBS^{++} to remove extracellular dye and then covered with 100 µL PBS^{++}. Subsequently, the 8-well-chamber was removed carefully and the remaining *Lexan*® substrate was fixed with Teflon weights in a standard petri dish. For visualizing fluorescence intensities with a 10 x magnification, cells were covered with 100 µL PBS^{++} per well for microscopic analysis. When additional images were taken with a 60 x water immersion objective, the *Lexan*® substrates were carefully flooded with pre-warmed PBS^{++} and a water immersion objective was dipped into the PBS^{++} buffer.

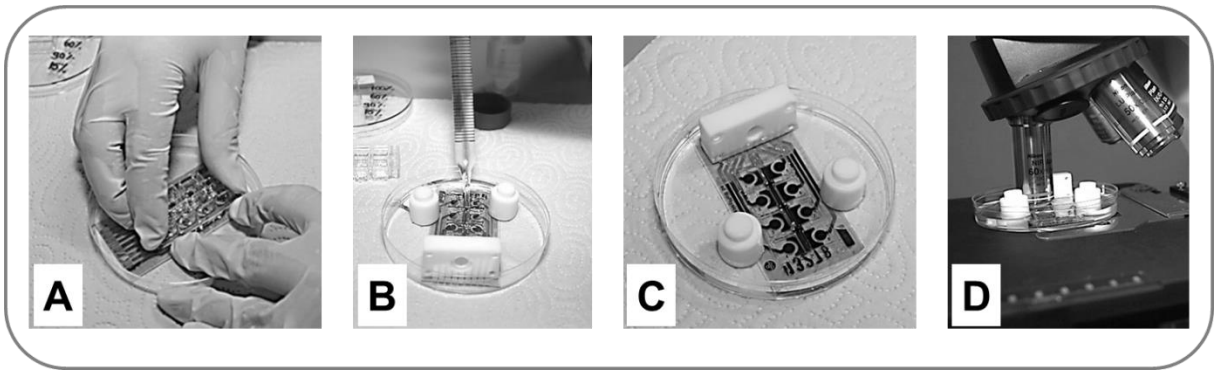

Fig. 5.10: Array preparation for upright microscopy: 8-well-chamber was carefully removed (**A**) and *Lexan*® substrate was fixed with weights (**B;C**). If cells were analyzed with the 60 x water objective, cells were completely covered with ~ 20 mL PBS^{++} and the objective was dipped into the buffer to visualize cells located on the electrodes (**D**).

5.4.2 Protocol Modifications for *In Situ* Electroporation Experiments

Loading of NRK Cells with FITC Dextran

The size-dependent uptake into the cytoplasm of NRK cells was investigated using FITC dextrans as fluorescent probes. Additionally, FITC dextran was also applied to proof the enhanced uptake of membrane impermeable compounds into the cytoplasm by applying more than a single electroporation pulse. Also experiments to optimize the appropriate electroporation parameters for different electrode layouts were carried out in presence of FITC dextran as fluorescent probe.

Therefore, differently-sized FITC dextrans (4 kDa – 2 MDa, Sigma-Aldrich) were prepared in a final concentration of 1 mg/mL in $EBSS^{-+}$ or $EBSS^{++}$. Baseline was recorded in 150 µL buffer and monitored impedimetrically in MFT mode. Subsequently, 50 µL FITC dextran solution (4 mg/mL) were added carefully during recording. NRK cells were electroporated once, twice or three times with constant pulse parameter of 40 kHz, 200 ms and 4 V. Afterwards, impedance recovery was monitored until a stable signal was reached. Then cells were gently washed twice with PBS^{++} to remove extracellular dye and dye uptake was documented using confocal laser scanning microscopy.

Loading of NRK Cells with Sodium Azide

For the electroporation experiments of NRK cells in presence of sodium azide (Merck KGaA) different concentrations (5 mM – 10 mM) were used. Dilutions were made from a 1 M stock solution in $EBSS^{++}$ stored at - 20 °C. In the beginning of an ECIS experiment culture medium was removed and 200 µL $EBSS^{++}$ was added. After an equilibration time of 3 h, 200 µL sodium azide was added and the 1st electroporation pulse (40 kHz, 200 ms, 4 V) was applied 30 min after treatment. In some cases a 2nd pulse was used 30 min later to enhance uptake efficiency. Afterwards the response of NRK cells to the addition of sodium azide was monitored with non-invasive ECIS recordings over several hours.

Loading of NRK Cells with Bleomycin

To load NRK cells with the bioactive compound bleomycin (Sigma-Aldrich), dilutions to a final working concentration 100 µM were made from a 4 mM stock solution in $EBSS^{++}$ stored at - 20 °C. In the beginning of an ECIS experiment culture medium was removed and cells were equilibrated for 2 h in 150 µL $EBSS^{++}$. Afterwards, cells were treated with 100 µL of bleomycin solution and incubated for 30 min before the 1st electroporation pulse (40 kHz,

200 ms, 4 V) was applied. A 2nd pulse was applied 30 min later and cellular response was monitored with non-invasive ECIS recordings over several hours.

To inhibit cell motility 50 µL cytochalasin D (final concentration 1.0 µM) or 50 µL $EBSS^{++}$ as control were added and incubated for 1 h prior to the addition of bleomycin.

Gap Junctional Intercellular Communication Study Based on Electroporation

To study dye transfer between adjacent NRK cells, cells were prepared using a seeding density of 600 000 cells/mL. One day before electroporation culture medium was exchanged. On the day of the gap junctional intercellular communication experiment, medium was completely replaced by 150 µL $EBSS^{-+}$ (w/ 0.5 mM $MgCl_2$) and a baseline was recorded using MFT-mode. After equilibration, a mixture of gap junction permeable Lucifer Yellow (final concentration 2.0 mg/mL, Sigma-Aldrich) and gap junction impermeable TRITC dextran (final concentration 3.0 mg/mL, Sigma-Aldrich) was added. Cells were electroporated by applying a voltage pulse of 40 kHz, 4 V with a pulse duration of 200 ms. In some wells a 2nd electroporation pulse was applied 15 min later to enhance uptake efficiency. ECIS recordings were stopped 5 min after the 2nd electroporation. Subsequently, cells were washed once with 200 µL of washing buffer ($EBSS^{-+}$ supplemented with 10 % FCS). Afterwards, cells were washed twice with 200 µL PBS^{++} and finally 100 µL PBS^{++} were added. The dye transfer due to gap junctional intercellular communication was analyzed by using a confocal laser scanning microscope.

To selectively inhibit gap junctional intercellular communication, 50 µM 2-APB was present during the whole assay. Therefore, cells were pre-incubated with $EBSS^{-+}$ supplemented with 50 µM 2-APB freshly prepared from a 0.4 M stock solution in DMSO or a 5 mM stock solution in $EBSS^{-+}$, both stored at -20 °C. Afterwards a mixture of Lucifer Yellow and TRITC dextran in 50 µM 2-APB in $EBSS^{-+}$ was added to the cells. Cells were electroporated, washed and analyzed as described above except using washing buffer and PBS^{++} containing 50 µM 2-APB.

5.4.3 Gap Junctional Intercellular Communication Study Based on Scrape Loading Assay

The principle of this assay is to scratch a cell monolayer in presence of a membrane impermeable, but gap junction permeable dye, like Lucifer Yellow (**Fig. 5.11**).

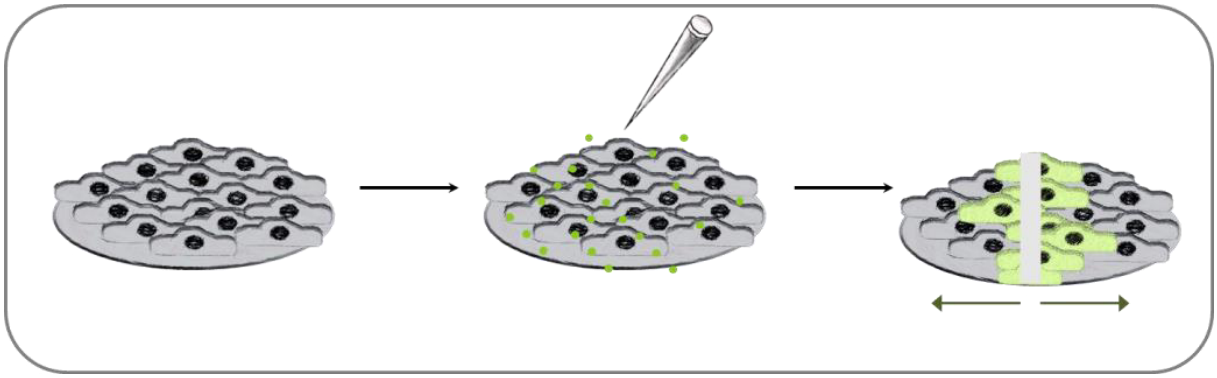

Fig. 5.11: Principle of introducing a membrane impermeable, but gap junction permeable tracer (Lucifer Yellow) into NRK cells by scrape loading assay.

To analyze dye transfer between neighboring cells using the scrape loading technique, cells were grown to confluence in a petridish (9.5 cm^2) or 6-*well*-plate. One day prior to the experiment cell culture medium was exchanged. Immediately before the experiment, the confluent cell layer was washed twice with PBS^{-+} containing $MgCl_2$ but without Ca^{2+}, to remove cell culture medium. Afterwards, Lucifer Yellow in PBS^{-+} (1.5 mg/mL – 2.0 mg/mL) was added to the confluent monolayer of adherent cells. By scraping the cells with a small pipette tip, Lucifer Yellow can enter the cytoplasm of cells, which are located along the path of the tip. Due to gap junctions, Lucifer Yellow can then diffuse into adjacent cells, resulting in a decrease of fluorescence intensity with increasing number of connected cells. The assay was performed with confluent cell layers of adherent MDCK II and NRK cells.

5.4.4 ITO Electrode Fabrication Using Photolithography

For the generation of electrode arrays made from *indium tin oxide* coated (ITO)-PET substrates (Sigma-Aldrich) the following protocol summarized in **Fig. 5.12** was applied. After spin-coating the substrate with photopolymer (AZECI3027, MicroChemicals GmbH) at 2000 rpm for 1 min the substrate was baked for 30 min at 100 °C. Afterwards, the substrate with the photoresist was directly positioned on top of a mask (**Fig. 5.34 A1**), delineating the electrode layout (black) and exposed to UV light for 2 min. In the following step, the photoresist in the area, which was not protected by the first mask, was removed by incubating the foil in a freshly prepared NaOH solution (7 g/L) for 20 s. The substrates were rinsed with dest. water and finally gently moved in $H_2O/HCl/HNO_3$ (47:47:6) for 30 s to etch

the exposed ITO areas. The substrate was washed again with dest. water and dried with N_2. To remove the photoresist completely, the ITO-PET foil was temporary shaken in acetone, washed with water and dried. For the final structure, the substrate was again spin coated with photopolymer (2000 rpm, 1 min) and baked for 30 min at 100 °C. The substrate was then exposed with UV light for 2 min, using a second mask (**Fig. 5.34 A2**) containing the electrode structures (WE,CE and conducting paths). The UV-exposed areas were then developed using again NaOH (7 g/L; 20 s). The electrode layout was rinsed with dest water, dried and finally hard baked for 2 h at 118 °C.

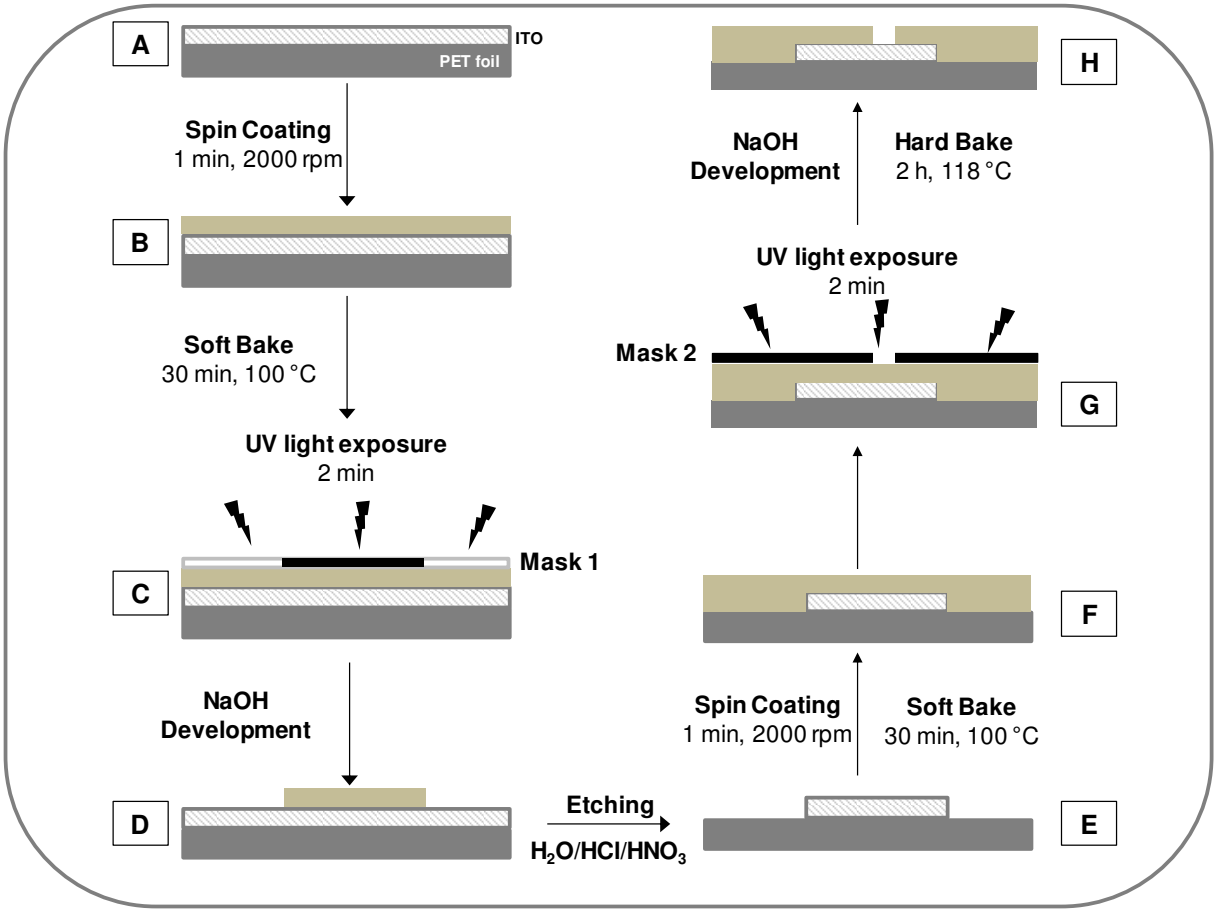

Fig. 5.12: Schematic presentation of ITO electrode fabrication using standard photolithography and lift off technique: Spin coating of the photoresist (**A**) followed by a soft baking step (**B**). UV light exposure with the appropriate mask 1 to protect the photoresist (**C**). The exposed photoresist was removed using NaOH (**D**) and ITO was removed using etching in $H_2O/HCl/HNO_3$ (47:47:6) (**E**). 2nd spin coating process followed by a soft baking step (**F**) and 2 min UV light exposure with mask 2 containing the electrode structures (**G**). NaOH development of the exposed photoresist and hard bake to yield the final ITO electrode structures (**H**).

5.5 *In Situ* Electroporation of Adherent NRK Cells

5.5.1 NRK Cells as Model System for Studying GJIC

At the beginning of the study a suitable cell model for gap junctional intercellular communication assay development was selected. Therefore, the simple and rapid scrape loading assay (**5.1.4 B**) was used to identify gap junctional intercellular communication in two different cell lines MDCK II and NRK, both cell lines originating from renal epithelium (**Fig. 5.13 A;B)**.

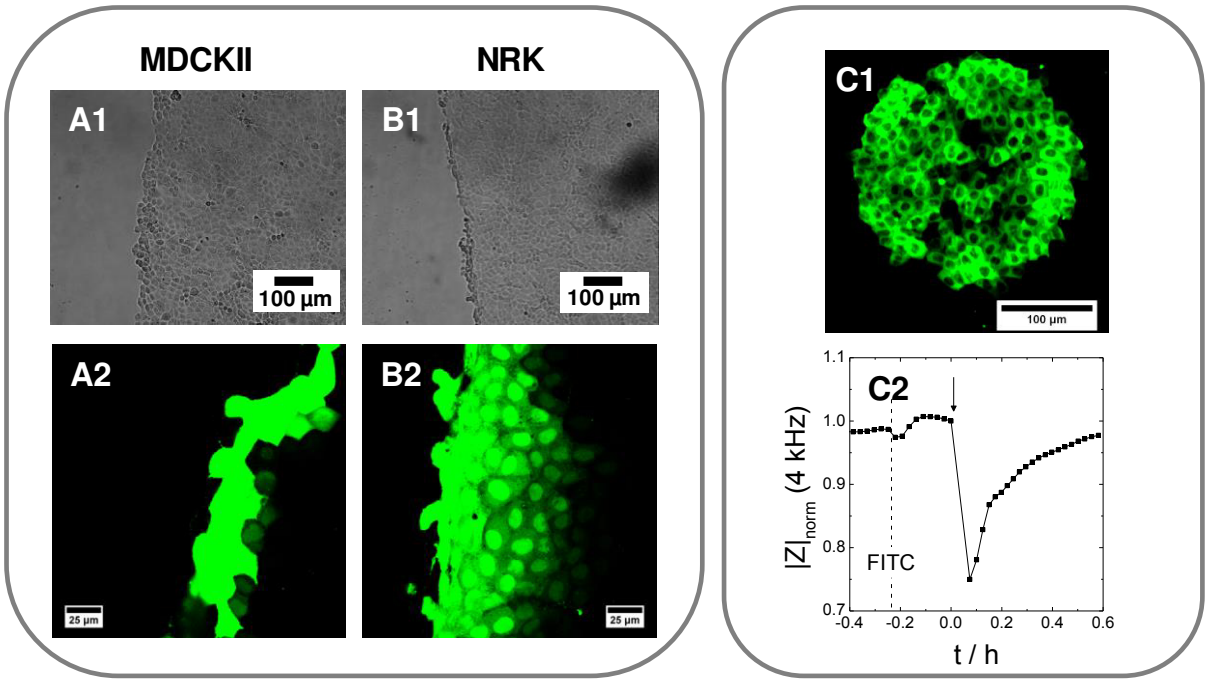

Fig. 5.13: Phase-contrast images (**1**) and confocal fluorescence micrographs (**2**) of MDCK II (**A**) and NRK cells (**B**) after performing the scrape loading assay. After scraping the cell layer in presence of Lucifer Yellow with a small pipet tip dye can diffuse into the wounded cells. Only in case of gap junction-connected cells (**B**) the fluorescent dye can diffuse into the cell monolayer. The distance of dye transfer mirrors the level of gap junction coupling. Fluorescence images were taken using a 60 x W objective at the confocal laser scanning microscope. **C:** Confocal fluorescence micrograph of NRK cells grown on gold-film electrodes after electroporation in presence of 2 MDa FITC dextran (**C1**). Typical time-course of normalized impedance at 4 kHz before and after electroporation (↓, 40 kHz, 4 V and 200 ms) (**C2**). The scale bars correspond to 100 µm (**1**) or 25 µm (**2**).

The fluorescence micrograph in **Fig. 5.13 A2** clearly showed that dye transfer in MDCK II cells was limited to only a small number of neighboring cells indicating a low degree of gap junctional intercellular communication. Therefore, MDCK II cells did not fulfill our requirements to serve as a suitable model for gap junctional intercellular communication. In contrast, NRK cells (**B**) showed a gradual distribution of Lucifer Yellow from the scrape edges into the cell layer, indicating a high gap junction communication efficiency.

A second requirement for the establishment of the new assay format was that model cells have to grow in monolayers on the electrode substrate to allow for incorporation of membrane-impermeable tracer molecules into cells' cytoplasm by *in situ* electroporation. Both conditions were fulfilled for NRK cells and the results of an electroporation experiment regarding the uptake of a fluorescent dye as well as the corresponding impedance recordings are shown in **C**. NRK cells turned out to be an appropriate cell line for the development of a new assay format and were used in this thesis for all electroporation experiments and for studies addressing gap junctional intercellular communication.

5.5.2 Size-Dependent Dye Uptake via Electroporation

The delivery of macromolecules into adherent NRK cells was investigated with differently-sized FITC dextran (4 kDa – 2 MDa) and Lucifer Yellow.

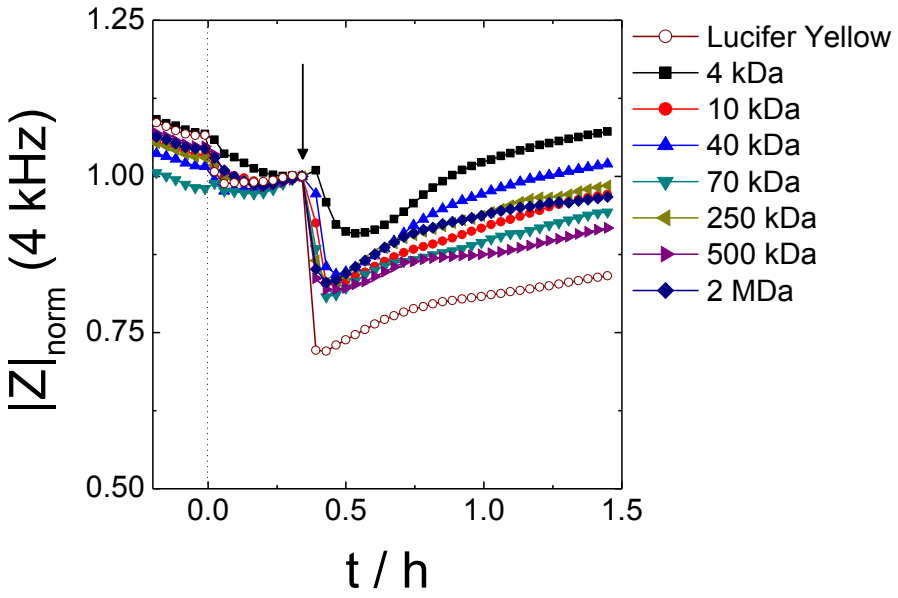

Fig. 5.14: Typical time-course of normalized impedance |*Z*| at 4 kHz before and after electroporation of NRK cells grown on 8W4E-micro array in presence of 4 kDa (■), 10 kDa (●), 40 kDa (▲), 70 kDa (▼), 250 kDa (◀), 500 kDa (▶), 2 MDa (♦) FITC dextran or Lucifer yellow (○) (2 mg/mL in $EBSS^{++}$). Time-point for the addition of the corresponding fluorescent dyes (t = 0 h) is indicated by the dotted line, while the time-point of electroporation (40 kHz, 4 V, 200 ms) is shown by the arrow (↓). The temperature during the whole experiment was set to 24 °C. Impedance values were normalized to the respective impedance values at the time-point of electroporation (t = 0.34 h). ***T*** = 24 °C

The impedance recordings presented in **Fig. 5.14** shows the expected response of NRK cells after applying an electroporation pulse. After pulse application (40 kHz, 200 ms, 4 V) $|Z|_{norm}$ immediately decreased to ~ 0.8. Only cells in presence of Lucifer Yellow showed a lower $|Z|_{norm}$ value of ~ 0.7 immediately after electroporation, whereas cells in presence of 4 kDa FITC dextran only decreased to ~ 0.9. In the following, the impedance signal, independent of the fluorescent tracer, started to increase indicating the recovery process. A small retardation was found for cells electroporated in presence of Lucifer Yellow. Around 1.0 h after pulse

application the experiment was stopped when $|Z|_{norm}$ was almost similar to the value before electroporation. Afterwards, cells were prepared for microscopic analysis and dye uptake was subsequently analyzed using confocal laser scanning microscopy.

Fig. 5.15 clearly showed the uptake of the fluorescent dyes, independent of their size due to transient permeabilization of the plasma membrane after applying the short, invasive voltage pulse. Obviously, the uptake was restricted to the cells that were directly located on top of the electrode whereas unspecific binding of extracellular dye to the cell surface as well as vesicle-mediated uptake was negligible.

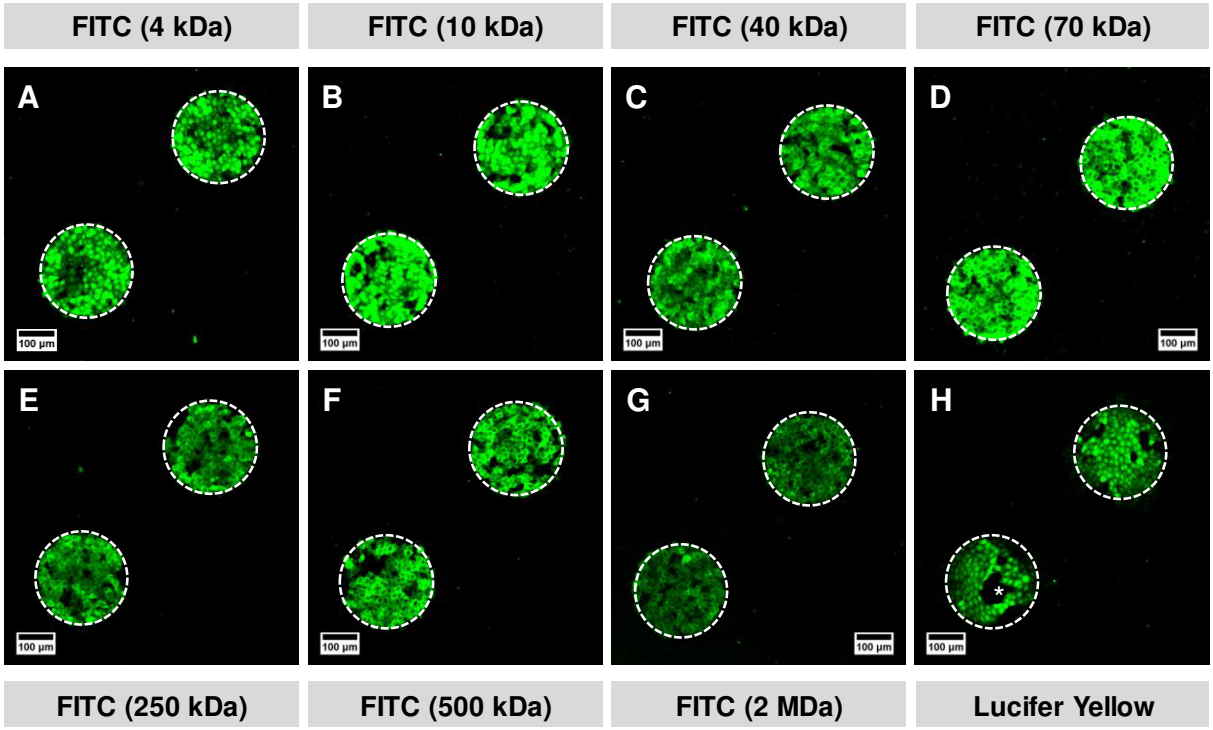

Fig. 5.15: Confocal laser scanning micrographs of NRK cells after electroporation in presence of FITC dextran of 4 kDa (**A**), 10 kDa (**B**), 40 kDa (**C**), 70 kDa (**D**), 250 kDa (**E**), 500 kDa (**F**), 2 MDa (**G**) molecular mass or Lucifer Yellow (**H**) (T = 24 °C). Positions of the electrodes are indicated by white, dashed circles. Images were taken with the 10 x objective using an excitation wavelength of 488 nm and detecting the emission at 515/30 nm. In **H** the star (*) indicates a cell-free area on the electrode, which was confirmed by analyzing the phase-contrast image (**Fig. S 7**). The scale bar corresponds to 100 µm.

To further investigate the uptake in a size-dependent manner, higher magnified images were taken using a 60 x objective. **Fig. 5.16** summarizes fluorescence micrographs of cells grown on the gold-film electrode after loading them with different FITC labeled dextrans (**A-G**) as well as with Lucifer Yellow (**H**) in high magnification. After *in situ* electroporation the fluorescence micrographs shown in **A**, **B** and **H** clearly showed the fluorescence intensity inside the whole cytoplasm even in the nuclei. This effect can be explained by the small size of the fluorophore with 4 kDa (**A**), 40 kDa (**B**) and 457 Da (**H**) as well as with the determined nuclear pore complex exclusion size of 20 - 40 kDa [409]. By increasing the fluorophore sizes

(70 kDa – 2 MDa) the dye uptake was limited to the cytoplasm and the cell nuclei appeared black in the fluorescence images (**C-G**).

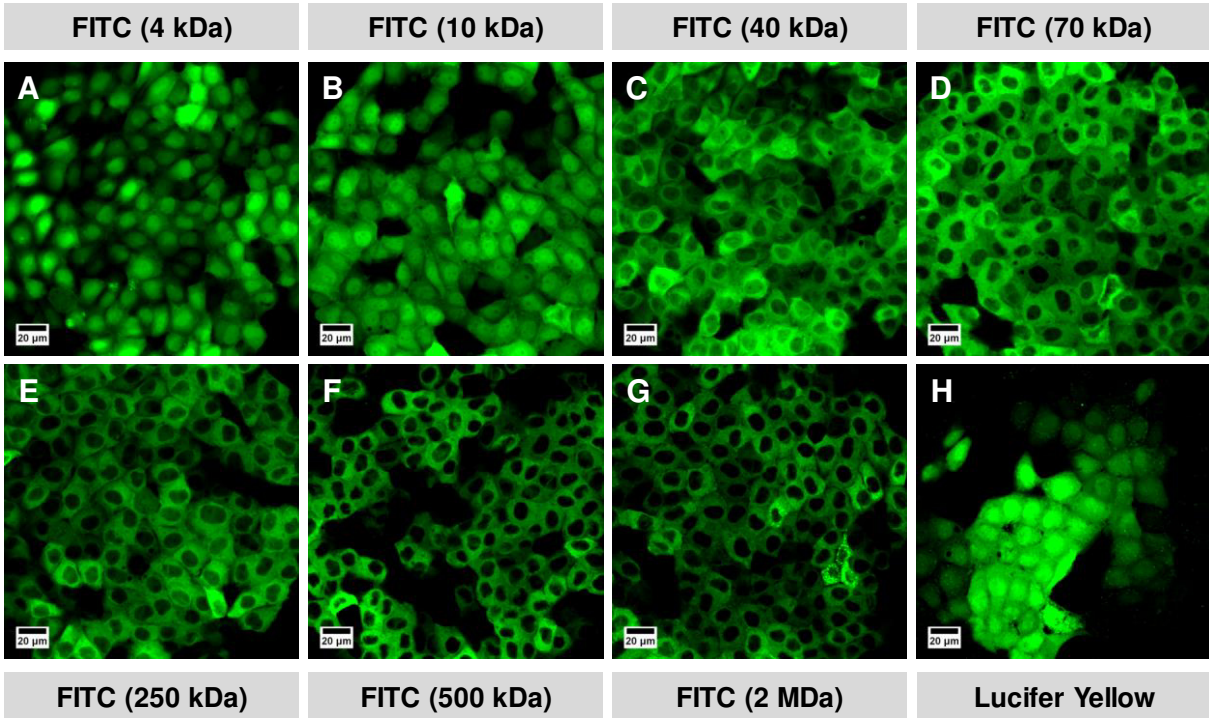

Fig. 5.16: Confocal laser scanning micrographs of NRK cells after electroporation in presence of FITC dextran of 4 kDa (**A**), 10 kDa (**B**), 40 kDa (**C**), 70 kDa (**D**), 250 kDa (**E**), 500 kDa (**F**), 2 MDa (**G**) molecular mass or Lucifer Yellow (**H**) at $T = 24$ °C. Images were taken with the 60 x W objective using an excitation wavelength of 488 nm and detecting the emission at 515/30 nm. The scale bar represents 20 µm.

5.5.3 Improvement of Uptake Efficiency by Applying Sequential Pulses

During a standard electroporation experiment cells were pulsed once with optimized electroporation parameters to guarantee high uptake efficiency as well as high cell viability. In many applications, e.g. expensive dyes or molecules like DNA, it is desirable to reduce the concentrations of the molecule in the extracellular buffer which should be internalized via electroporation. Therefore, the influence of sequential pulses on the electroporation efficiency was analyzed using fluorescent dyes or bioactive molecules.

5.5.3.1 Dye Uptake Study with FITC-Labeled Dextrans

In a proof of concept experiment it was investigated if the uptake of a fluorescent dye (FITC dextran) can be enhanced by applying more than one pulse. For that purpose an electroporation experiment was designed where NRK cells grown on 8W4E-micro electrodes were electroporated once, twice or three times. Additionally, the time between two sequential pulses was varied to analyze the effect on cell loading or viability.

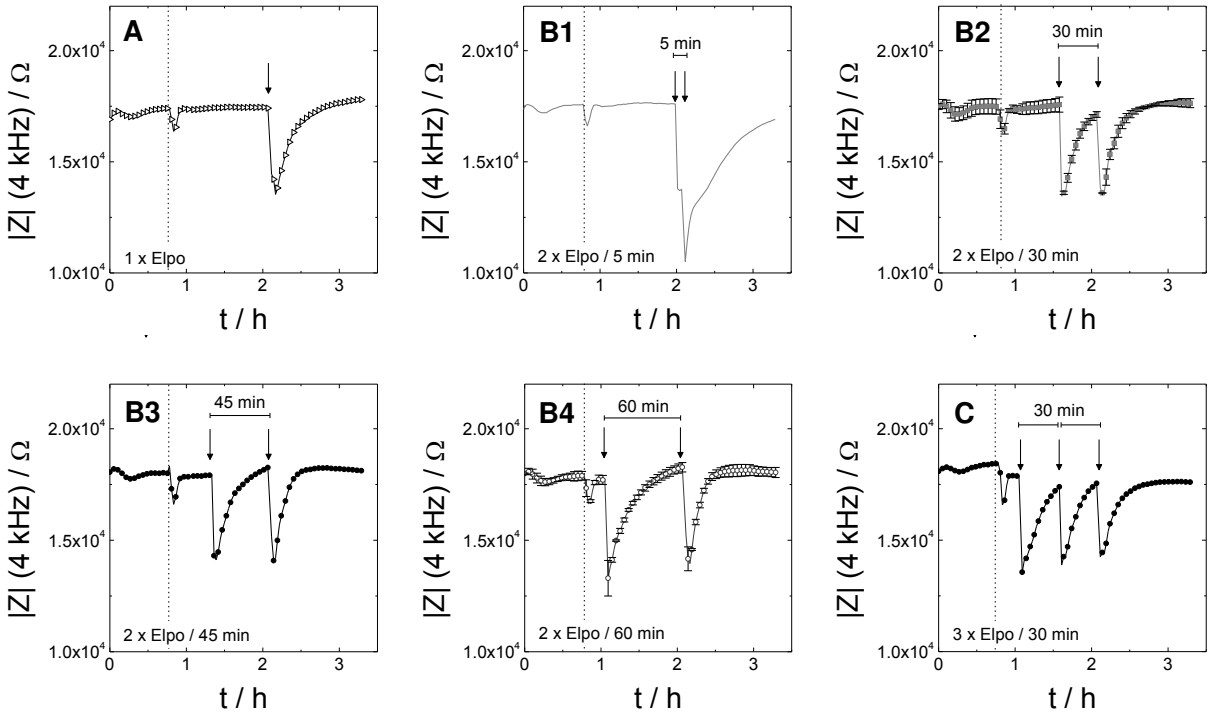

Fig. 5.17: Typical time-course of |*Z*| at 4 kHz before and after electroporation of NRK cells grown on 8W4E-micro electrodes. Cells were electroporated once (**A**), twice (**B**) or three times (**C**) using standard electroporation conditions of 40 kHz, 200 ms and 4 V. The time between two pulses was varied between 5 min (**1**), 30 min (**2**), 45 min (**3**) and 60 min (**4**). For **B2** and **B4** two individual wells are averaged and Mean ± SD are shown in the respective graph. The time between pulses in the three-pulse experiment was 30 min (**C**).

Fig. 5.17 shows the time-course of impedance at 4 kHz for NRK cells before and after electroporation. After recording a baseline in EBSS^{++} FITC dextran (250 kDa) was added and incubated for at least 15 min. The electroporation pulses were applied at individual time-points to guarantee (i) a defined time between the pulses and (ii) the last simultaneous

electroporation event at t = 2.1 h to allow for the same recovery time for all wells until the end of the experiment. For all cell layers the recovery of $|Z|$ after electroporation was similar and recovered to $|Z|$ values between 17.6 kΩ and 18.3 kΩ. The only exception was found for an inter-pulse time of 5 min, which did not show a complete recovery and the recorded $|Z|$ at 4 kHz was finally determined to 16.4 kΩ.

Afterwards, the uptake of the green fluorescent FITC dextran was studied by confocal laser scanning microscopy. The survey of fluorescence micrographs is shown in **Fig. 5.18** where two characteristic electrodes for each condition are shown. All images were taken using a 10 x objective and same gain settings to facilitate the comparison between the different conditions.

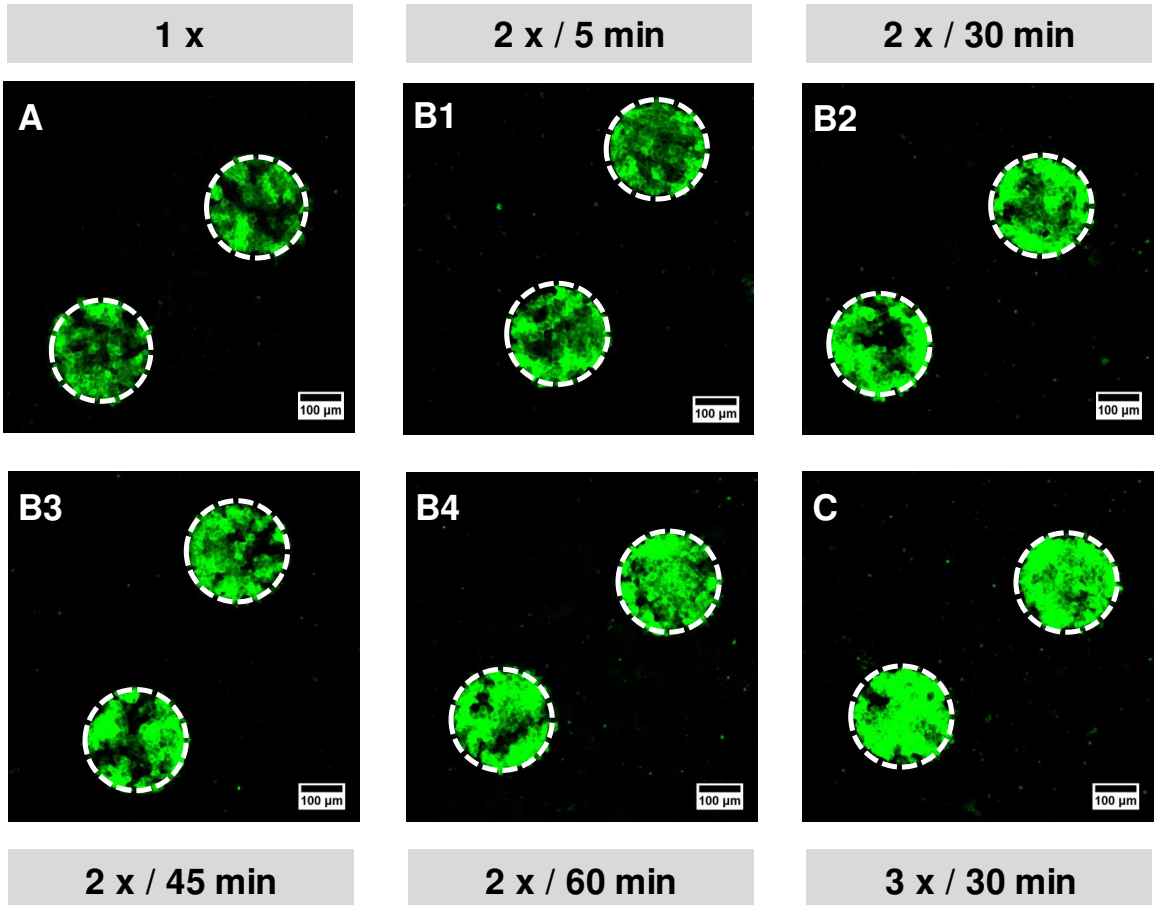

Fig. 5.18: Confocal fluorescence micrographs of NRK cells after applying one (**A**), two (**B**) or three (**C**) sequential electroporation pulses using standard conditions in presence of FITC dextran (250 kDa, 1.0 mg/mL in $EBSS^{++}$). All pictures were taken with 10 x magnification using the same gain settings. The time interval between two pulses was varied between 5 min (**1**), 30 min (**2**), 45 min (**3**) and 60 min (**4**) and for three pulses a gap of 30 min (**C**) was chosen. White circles indicate the positions of the two working electrodes. The scale bar corresponds to 100 µm.

Obviously, the fluorescence intensity of FITC dextran inside the electroporated cells was enhanced by increasing the number of pulses. Similar results were obtained for the different time intervals between the two pulses, which were varied between 5 min and 60 min (**B1 - B4**).

5.5.3.2 Enhanced Uptake of Bioactive Molecules

Further research on the enhanced uptake efficiency by applying multi-pulses was performed using bioactive substances, which exhibit a low extracellular cytotoxicity but a high intracellular cytotoxic activity. After loading the cells with the membrane-impermeable substances by electroporation the combination with non-invasive ECIS recordings allowed impedimetric monitoring of morphological changes within the cell layer as a response to these substances over several hours.

Sodium Azide

Sodium azide is described in the literature to induce apoptotic [410] as well as necrotic [411, 412] processes. Furthermore, sodium azide is well-known for its inhibitory effects on mitochondrial electron transport [413, 414] and it is well-established as a reversible inhibitor of the respiratory chain complex IV [415-417]. It has been proven that the toxicity of the compound is much higher when administered inside the cytoplasm compared to the exposure of sodium azide in solution. For the delivery of NaN_3 into the cytoplasm different strategies like encapsulation in liposomes [418] or electroporation are used.

Sodium azide was used to further characterize the effect of applying sequential multi-pulses to adherently grown NRK cells and subsequent monitoring of the cellular response with ECIS. The concentration of sodium azide was selected such that no cytotoxicity was observed without electroporation [419]. **Fig. 5.19** (**A**) exemplarily shows the result for the electroporation of NRK cells in presence of sodium azide with varying extracellular concentrations and different numbers of pulses.

Immediately after the first electroporation (↓; $t = 0$ h) $|Z|_{norm}$ at 32 kHz steeply dropped down in a concentration-dependent manner. The control population electroporated in presence of $EBSS^{++}$ only decreased to ~ 0.75, whereas $|Z|_{norm}$ of cells in presence of 5.0 mM NaN_3 exhibited a value of 0.64 and 10 mM NaN_3 caused a further decrease to 0.45. This concentration-dependent effect was in conformity with the results of the 2nd pulse which was applied at $t = 0.5$ h. Afterwards, recovery of the cell layer is indicated by an increase in $|Z|_{norm}$. Independent from the applied sodium azide concentration cells which were electroporated twice showed a slower recovery compared to the cells which were only electroporated once using the same concentration. Higher concentrations of sodium azide caused a slower recovery reflected by a delayed recovery of $|Z|_{norm}$. Only for the control population the recovery after the electroporation showed no significant dependency on the number of pulses and recovery under both conditions was completed within ~ 1.3 h after the last pulse. In presence of 5.0 mM NaN_3 a complete impedance recovery to a stable signal took 2.2 h for single electroporation and 5.4 h when including a second pulse. By increasing

the concentration to 10 mM the recovery time increased to 3.3 h for one pulse or 7.2 h by using two pulses until |*Z*| came back to stable values.

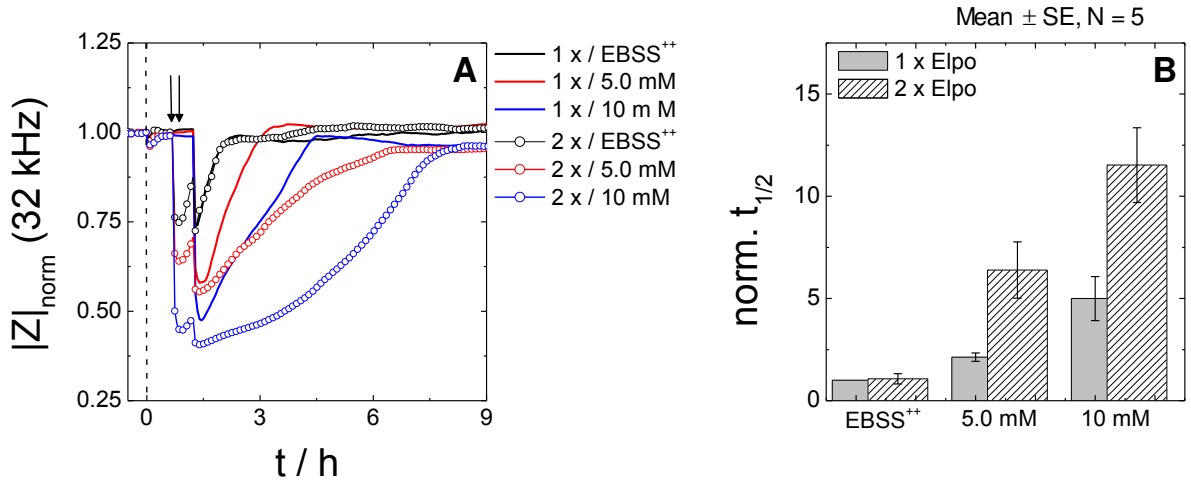

Fig. 5.19: A: Typical time course of $|Z|_{norm}$ at 32 kHz to analyze cellular response of NRK cells grown on 8W1E electrodes after electroporation in presence of EBSS^{++} (**black**) or sodium azide in EBSS^{++} (**red**, **blue**). Concentration of NaN_3 was 5.0 mM (**red**) or 10 mM (**blue**). Cells were either electroporated once (—) or twice (○) with an electroporation pulse of 40 kHz, 4 V and a pulse duration of 200 ms. Impedance values were normalized to the respective impedance values at the time-point of buffer or sodium azide addition (t = - 0.7 h). **B:** Normalized $t_{1/2}$ values of five independent experiments. The $t_{1/2}$ values of the different concentrations and electroporation conditions were normalized to the $t_{1/2}$ values of the control (EBSS^{++}, 1 x) in each experiment (Mean ± SE).

To summarize five independent experiments the $t_{1/2}$ values were extracted and normalized using the following procedure. The impedance value immediately before electroporation was used as the maximum impedance value ($|Z|_{max}$), and the minimum ($|Z|_{min}$) was defined after pulsing. Then, the individual time-points were selected, when the curves were recovered to 50 % of the difference between $|Z|_{max}$ and $|Z|_{min}$. For better comparison, even for different passage numbers, the $t_{1/2}$ values were normalized to the $t_{1/2}$ value of the control cells, which were electroporated once in EBSS^{++}. For data analysis the time-point of the 2nd electroporation event was set to t = 0 h. The column bars clearly show, that in EBSS^{++} the 2nd electroporation event only had a weak influence on the recovery time. The normalized $t_{1/2}$ was determined to 1.1 ± 0.3. After electroporation in presence of 5 mM and 10 mM NaN_3 the recovery of the impedance signal was delayed and reflected in normalized $t_{1/2}$ values of 2.1 ± 0.2 and 5 ± 1. This effect was even more pronounced in cases where a 2nd pulse was applied. In presence of 5 mM NaN_3 the normalized $t_{1/2}$ value was 6 ± 1 and increased to 12 ± 2 for 10 mM NaN_3.

Bleomycin

The anticancer drug bleomycin [420] was used as a second model molecule for bioactive substances. Bleomycin is a complex glycopeptide antibiotic isolated from *Streptomyces verticillus* which is characterized by a low transmembrane permeability and an about 100 – 5000 fold increased cytotoxicity once it is present inside the cell [327, 421]. Bleomycin is known to induce DNA single and double strand breaks and to initiate an apoptotic cascade which finally causes cell death [422-425].

The cell membrane of NRK cells, grown on 8W1E electrodes, was permeabilized by applying a single pulse or multiple pulses, which allows free diffusion of bleomycin into the cytoplasm. After electroporation the response of bleomycin-loaded NRK cells was monitored with ECIS over several hours. The time-course of normalized impedance $|Z|_{norm}$ at 32 kHz was analyzed before and after applying the electroporation pulse to monitor the response of NRK cells after bleomycin addition as well as after cytoplasm delivery via electroporation. The responses of NRK cells after electroporation in presence of $EBSS^{++}$ only (**A**) or 100 µM bleomycin (**B**) are summarized in **Fig. 5.20**. To further emphasize the apoptotic effect of bleomycin cells were co-incubated with cytochalasin D (final concentration 1.0 µM) to inhibit repopulation of the electrode surface with untreated cells from the periphery of the electrode.

As control, NRK cells were electroporated in presence of $EBSS^{++}$ or buffer containing 1.0 µM cytochalasin D using a single or two pulse electroporation with a delay of 30 min (**Fig. 5.20 A)**. When NRK cells were electroporated once either in absence or presence of cytochalasin D no significant difference in the recovery of $|Z|_{norm}$ was found and pre-pulsed $|Z|_{norm}$ values were reached at $t = 3.3$ h. NRK cells, which were electroporated twice in $EBSS^{++}$ showed a complete recovery of $|Z|_{norm}$ at $t = 3.7$ h. Two-pulse electroporation in presence of cytochalasin D resulted in a steeper decrease of $|Z|_{norm}$ immediately after pulsing to 0.57 (1^{st} pulse) or 0.53 (2^{nd} pulse). Impedance recovery for NRK cells in presence of cytochalasin D was delayed compared to the electroporation only in $EBSS^{++}$ buffer. A complete recovery of $|Z|_{norm}$ for NRK cells was recorded at t = 7.9 h.

The response of bleomycin-loaded NRK cells after single (—) or two-pulse (○) electroporation is provided in **Fig. 5.20 B.** NRK cells which were only exposed to a single pulse showed a decrease of $|Z|_{norm}$ to 0.70 immediately after pulse application. Afterwards, $|Z|_{norm}$ recovered to a transient maximum of 0.97 ($t = 6.9$ h) followed by fluctuations in $|Z|_{norm}$ and a final decrease to 0.55 within 16 h. When cells were electroporated twice, the application of the electroporation pulses resulted in a decrease of $|Z|_{norm}$ to 0.87 (1^{st}) and 0.76 (2^{nd}). Afterwards, the transient maximum of $|Z|_{norm}$ was reached at $t = 4.2$ h followed by a decrease to 0.53 ($t = 12.3$ h) which indicates the cell death of NRK cells on the electrode.

To further emphasize the apoptotic effect of bleomycin, NRK cells were additionally electroporated in presence of bleomycin and cytochalasin D using a single (—) or two-pulse (○) protocol (**Fig. 5.20 B**). After one hour of pre-incubation with cytochalasin D, bleomycin was added, indicated by the dashed line. NRK cells which were only exposed to a single pulse provided a decrease of $|Z|_{norm}$ to 0.70 followed by a further decrease to 0.61. A transient maximum of $|Z|_{norm}$ of 0.78 was reached at $t = 5.2$ h followed by a decrease to 0.37 at $t = 10.7$ h. Using the two-pulse protocol a sharp decrease of $|Z|_{norm}$ was detected immediately after pulse application which further decreased to 0.50. The application of the 2nd pulse caused a decrease of $|Z|_{norm}$ to 0.46. The onset of NRK cell death, induced by bleomycin, already started at $t = 4.2$ h and caused a decrease of $|Z|_{norm}$ to 0.37 until $t = 8.5$ h.

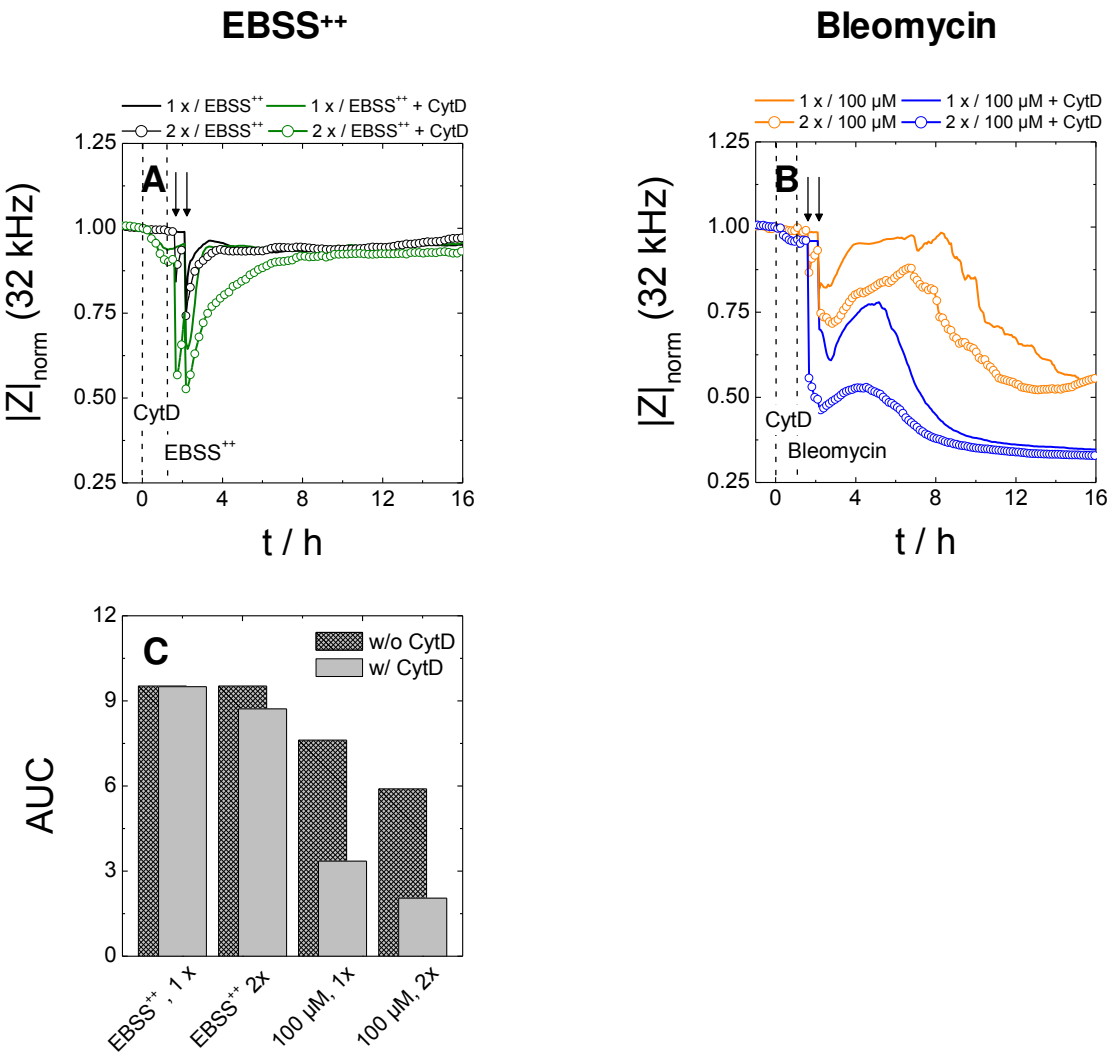

Fig. 5.20: Typical time-courses of normalized impedance $|Z|_{norm}$ at 32 kHz to analyze the response of NRK cells after electroporation in presence of EBSS^{++} (**A**) or 100 µM bleomycin in EBSS^{++} (**B**) using a single (—) or two-pulse protocol (○). Additionally 1 µM cytochalasin D was added to some wells to inhibit cell migration. Impedance values were normalized to the respective impedance values at the time-point of buffer or cytochalasin D addition ($t = 0$ h). **C:** Calculated area under the curve (AUC) of $|Z|_{norm}$ between the time point of the second pulse ($t = 2.2$ h) and the end of experiment ($t = 16$ h) based on a single experiment.

In summary, bleomycin-loaded NRK cells in presence of cytochalasin D provided a minimum in $|Z|_{norm}$ at $t = 8.5$ h (○) and 10.7 h (—) indicating the cell death of NRK cells on the electrode. In absence of cytochalasin D the $|Z|_{norm}$ minimum of 0.55 – 0.56 was found at $t = 12.3$ h (○) and $t = 16$ h (—) showing a slightly higher $|Z|_{norm}$ value than in presence of cytochalasin D ($|Z|_{norm} = 0.37$). Under both conditions, the two pulse experiment resulted in an earlier onset of cell death induced by bleomycin compared to the single pulse experiment indicating a higher uptake efficiency. In absence of cytochalasin D the apoptotic effect of bleomycin was masked by cell migration from the periphery, which resulted in a delay until the apoptotic effect was completely displayed in the time-course of $|Z|_{norm}$.

Additionally, the time-courses of impedance (**A;B**) were analyzed regarding their *area under the curve* (AUC). For this purpose, a constant y-value of 0.25 was chosen as a baseline value for interpretation. The AUC was calculated for the different conditions in the time period after applying the 2nd pulse ($t = 2.17$ h) until the end of experiment ($t = 16.01$ h). The column bars (**Fig. 5.20 C**) represent the AUC in absence (dense pattern) and presence (light grey) of 1.0 µM cytochalasin D. This data presentation also confirms the increase in uptake efficiency for two pulses indicated by a decrease in AUC. Under control conditions cells in presence of one or two electroporation pulses both showed similar AUCs, which reflect a minor impairment of the cells by electroporation itself. Even the addition of cytochalasin D to inhibit cell migration only generated a weak decrease in AUC. NRK cells electroporated twice in EBSS^{++} provided an AUC of 9.5 which insignificantly decreased to 8.7 after two-pulse electroporation in presence of cytochalasin D in EBSS^{++}. Electroporation in presence of bleomycin but in absence of cytochalasin D resulted in AUCs of 7.6 (1 x) and 5.9 (2 x). The effect of bleomycin was even more pronounced in presence of cytochalasin D. After a single pulse electroporation the AUC was reduced to 3.4 and further decreased to 2.1 by applying two pulses. To summarize the results presented in **Fig. 5.20** the bleomycin experiment confirms the finding that a second electroporation pulse enhances compound uptake efficiency, without additional impairment by electrical manipulation.

After performing the impedimetric analysis, cells were further analyzed microscopically using the cell nuclei stain DAPI (**chapter 3.4.2.4**). A survey of the phase-contrast images of the NRK cells on the working electrodes as well as blue fluorescence images of the stained cell nuclei are shown in **Fig. 5.21**. In good agreement with the impedance recordings of NRK cells shown in **Fig. 5.20,** cells which were electroporated in presence of EBSS^{++} (**A**) or 1.0 µM cytochalasin D in EBSS^{++} (**C**) still formed a confluent cell layer in phase-contrast images and fluorescence micrographs after single and two-pulse electroporation. In contrast, cells ~ 15 h after electroporation in presence of 100 µM bleomycin (**B**) independent of the electroporation protocol provided defects in the cell layer. The phase-contrast images (**B1**;

B3) clearly showed dead, round cells directly located on the electrode and cell-free areas. Additionally, some healthy NRK cells, originating from the boarder of the electrode already migrated into the cell-free area on the electrode. The migration of NRK cells, which were not originally loaded with bleomycin during electroporation, was inhibited by adding cytochalasin D in low concentration. In presence of both, bleomycin and cytochalasin D (**D**) the toxic effect of the bioactive compound bleomycin was pronounced. There, the electrode was only occupied by round-shaped, dead cells and no repopulation of the electrode with vital NRK cells, due to migration into the cell-free area could be observed. The survey of images clearly indicates that the cytotoxic effect of bleomycin was limited to the position of the electrodes, where the cell membrane was transiently permeabilized by electroporation. The cells around the electrode showed a vital morphology without any characteristics of cytotoxic effects. In presence of bleomycin and cytochalasin D only cells located at the border of the electrode showed abnormalities in cell morphology caused by the toxicity of bleomycin.

Unfortunately, cellular response after electroporation in presence of bleomycin using variable cell passages was significantly different. This variance of cellular response after single pulse electroporation of NRK cells in presence of bleomycin was also reported before by J. Stolwijk (2012) [419]. Nevertheless, bleomycin served as a second model substance for a bioactive drug where a cytotoxic effect could be enhanced by a second pulse. In contrast to the sodium azide results shown before, cell migration can interfere with the cytotoxic effect several hours after incorporation of the compound into the cytoplasm.

In summary, the aim of the multi-pulse electroporation was to show via dye uptake and in presence of bioactive compounds that the uptake efficiency can be enhanced by a second pulse. This was successfully demonstrated by fluorescence micrographs using FITC dextran as fluorescent probe as well as by analyzing impedance recordings in presence of sodium azide and bleomycin.

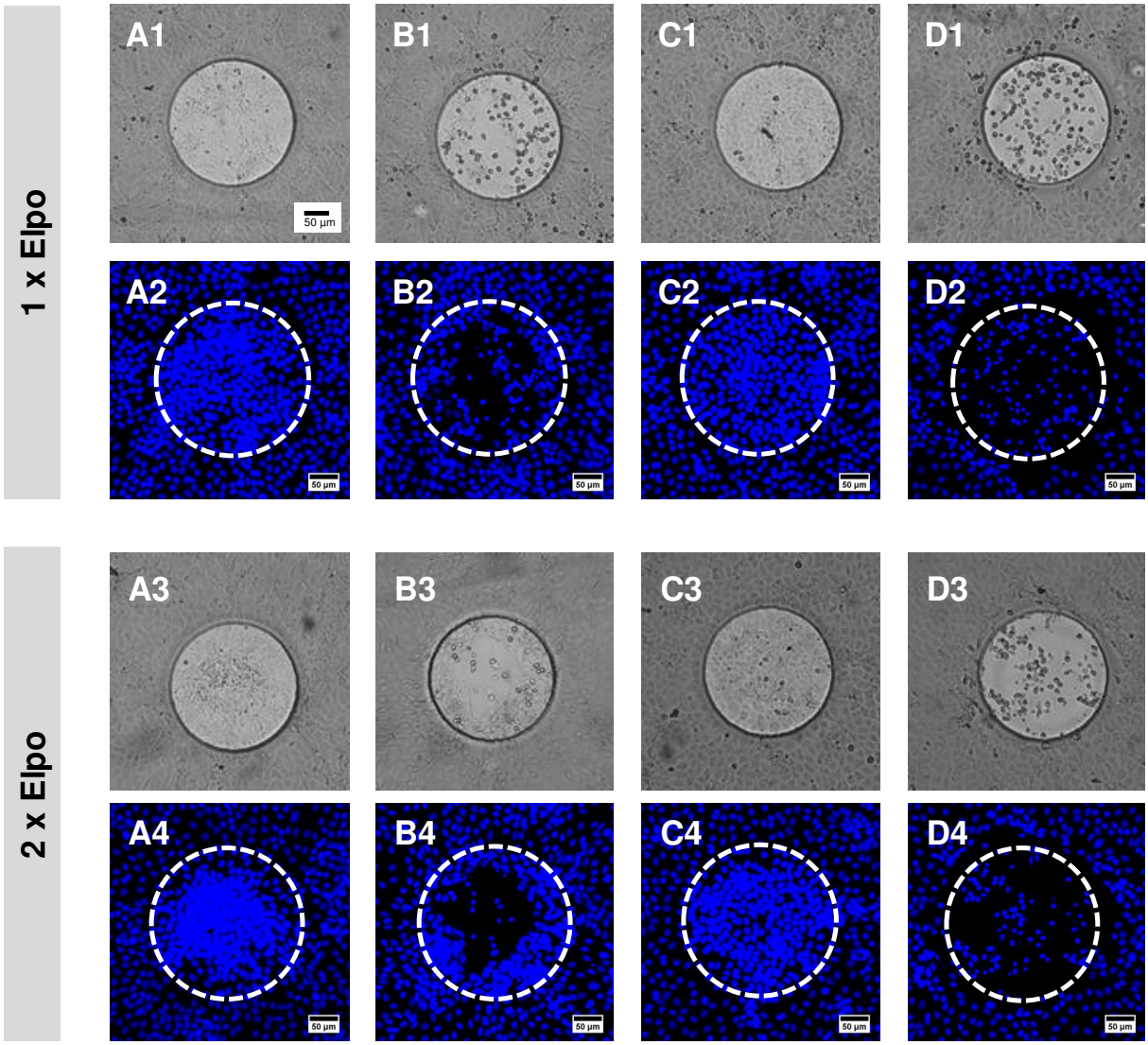

Fig. 5.21: Phase-contrast images (**1;3**) and fluorescence micrographs (**2;4**) of NRK cells, grown on a 8W1E electrode layout, after electroporation in presence of $EBSS^{++}$ (**A**), 100 µM bleomycin (**B**), 1.0 µM cytochalasin D in $EBSS^{++}$ (**C**) or 100 µM bleomycin in $EBSS^{++}$ containing 1.0 µM cytochalasin D (**D**). Cells were pre-incubated with cytochalasin D for 1 h before bleomycin was added. NRK cells were transiently permeabilized by applying a single (**1;2**) or two (**3;4**) electroporation pulses (40 kHz, 200 ms, 4V) with a time delay of 30 min between the pulses. The position of the working electrodes in the fluorescence micrographs are indicated by the dashed, white circles (**2+4**). The image sections of phase-contrast and fluorescence images are different. The scale bar represents 50 µm.

5.5.4 Gap Junctional Intercellular Communication Studies Based on Electroporation

The principle of pre-loading the cells with a gap junction-permeable but membrane-impermeable dye is shown in **Fig. 5.22 A.** A short electric pulse, which is applied to the cell layer in presence of the tracer, causes pore formation and enables the penetration of the dye into the cytoplasm of a large number of cells. To investigate cell to cell communication the tracer dye must be small enough to pass the gap junctions. If cells are connected via gap junctions a dye transfer from cells located on the electrodes into the periphery is possible and can subsequently be analyzed via fluorescence microscopy (**C**).

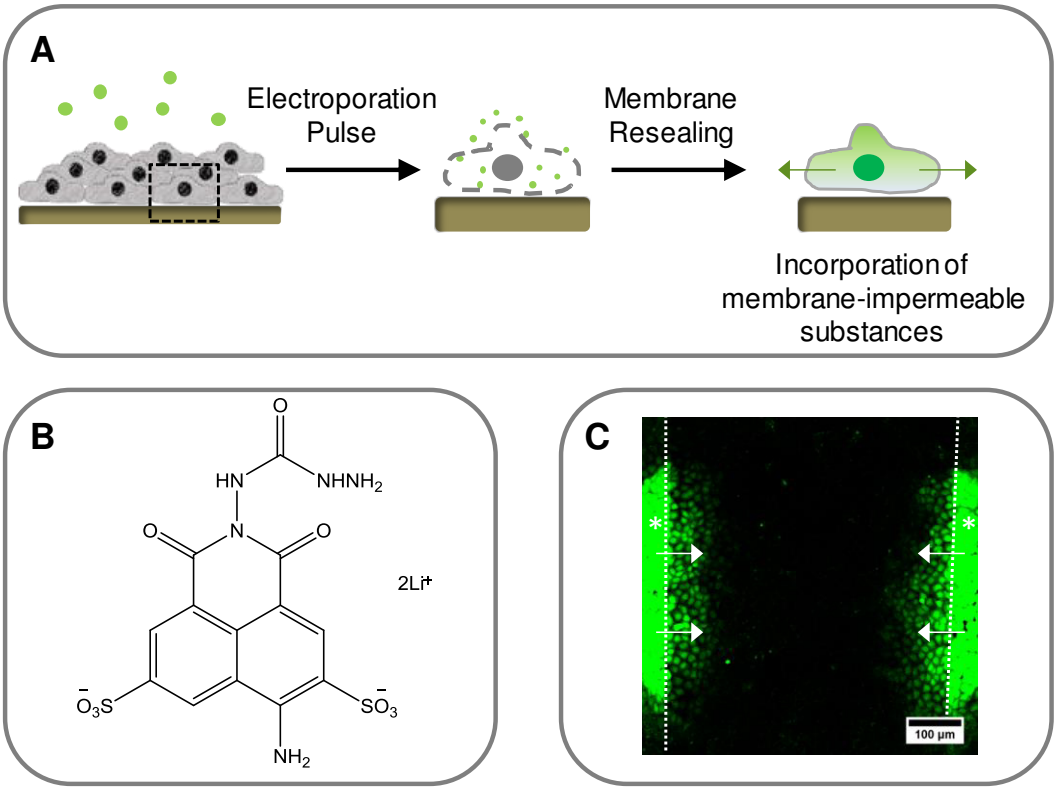

Fig. 5.22: A: Principle of dye uptake via electroporation. **B:** Molecular structure of Lucifer yellow CH dilithium salt (6-amino-2-((hydrazinocarbonyl)amino)-2,3-dihydro-1,3-dioxo- dipotassium salt). The fluorescent dye was used for studying gap junctional intercellular communication. With a molecular weight of 457.3 Da it is small enough to pass through gap junctions which have a size limit of ~1 kDa. **C:** Confocal fluorescence micrograph of a confluent NRK cell layer grown on thin-film electrodes after electroporation. Lucifer yellow can diffuse from electroporated cells on the electrode (indicated by the *) into adjacent NRK cells grown in the photopolymer-free gap through gap junctions. The scale bar represents 100 µm.

For this purpose, Lucifer Yellow CH dilithium salt (in the following only denoted as Lucifer Yellow), which is the most prominent dye used in literature to analyze gap junctional intercellular communication, was used in a final concentration of 2 mg/mL. The dye was first introduced by Stewart in 1978 [426] and is still applied in many methods as tracer compound. Due to its small molecular size of 457.3 Da it can easily pass through gap junctions. A second dye TRITC dextran (155 kDa) was used in the experiment which is excluded from transfer via gap junctions due to its high molecular weight and successfully showed that electroporation is limited to the position of the electrodes.

5.5.4.1 Electroporation in Absence of Calcium

It was further investigated if electroporation is possible in absence of calcium as Ca^{2+} is described to inhibit gap junctional intercellular communication. Therefore, the electroporation buffer was modified to EBSS supplemented with 0.5 mM $MgCl_2$ ($EBSS^{-+}$) as the only divalent cation and dye uptake was compared to the results of experiments performed under standard conditions using $EBSS^{++}$.

Dye Uptake Study in Absence or Presence of Ca^{2+} as Divalent Cation

Fig. 5.23 summarizes the impedance recordings at 4 kHz for NRK cells electroporated in presence of Lucifer Yellow or FITC dextran in $EBSS^{-+}$ or $EBSS^{++}$ buffer. At $t = 0$ h FITC dextran or Lucifer Yellow were added to the cells, which were pre-incubated with $EBSS^{-+}$ or $EBSS^{++}$ buffer before. After 20 min cells were electroporated with 40 kHz, 200 ms and 4 V. The time-course of impedance depends on the buffer composition (**Fig. 5.23 A**). In $EBSS^{++}$ the normalized impedance immediately decreased after electroporation to its minimum, whereas in $EBSS^{-+}$ the cellular response seems to follow a different kinetic.

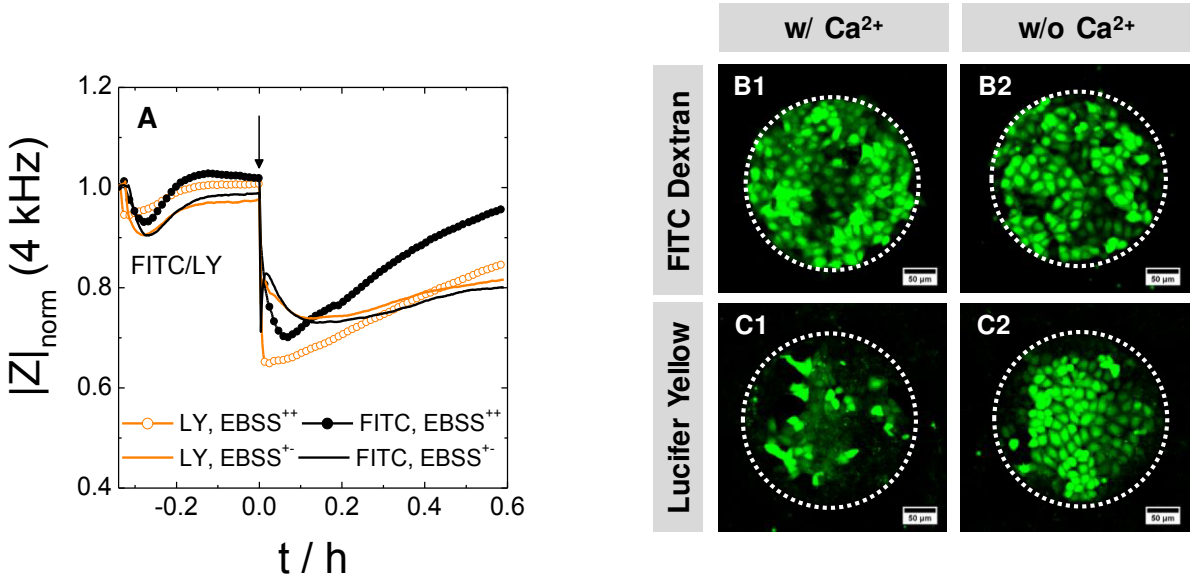

Fig. 5.23: A: Time course of normalized impedance at 4 kHz monitoring NRK cells grown on 8W1E electrodes before and after electroporation in presence of Lucifer Yellow (**orange**) or FITC dextran (**black**) using EBSS buffer with (○) or without Ca^{2+} (—). **B; C:** Confocal fluorescence micrographs of NRK cells after electroporation in presence of FITC dextran (**B**) or Lucifer Yellow (**C**) using buffer with (**1**) or without (**2**) Ca^{2+}. The scale bar represents 50 µm.

Recovery was monitored for ~ 36 min and subsequent dye uptake was analyzed via confocal laser scanning microscopy. **Fig. 5.23** summarizes the uptake of the fluorescent dyes into the cells grown on the small working electrode. Obviously, FITC dextran 4 kDa (**B**) was successfully incorporated homogenously into NRK cells showing a bright green fluorescence inside the cytoplasm and the cell nucleus independent of extracellular Ca^{2+}. In contrast, the

uptake of Lucifer Yellow (**C**), independent of the electroporation conditions, did not show a homogenous dye distribution and uptake was strongly reduced compared to FITC dextran.

Why the uptake and consequently the fluorescence intensity was low in the case of Lucifer Yellow monitored ~ 40 min after electroporation remained unclear. However, as dye uptake in **B1** and **B2** were similar the buffer composition seems to have no influence on the dye uptake and the electroporation process.

Differences in the Time-Course of Electroporation in Absence or Presence of Ca^{2+}

Because impedance recovery showed slight differences between Ca^{2+}-free and Ca^{2+}-containing buffer electroporation kinetics were investigated in more detail. In the following, differences in impedance curve progressions at 4 kHz upon electroporation of NRK cells in $EBSS^{-+}$ (w/o Ca^{2+}) and $EBSS^{++}$ were studied. A survey of impedance recordings in SFT mode for the different buffer compositions of EBSS buffer (with or without Ca^{2+}) is shown in **Fig. 5.24**, with each curve representing the mean value of four independent measurements.

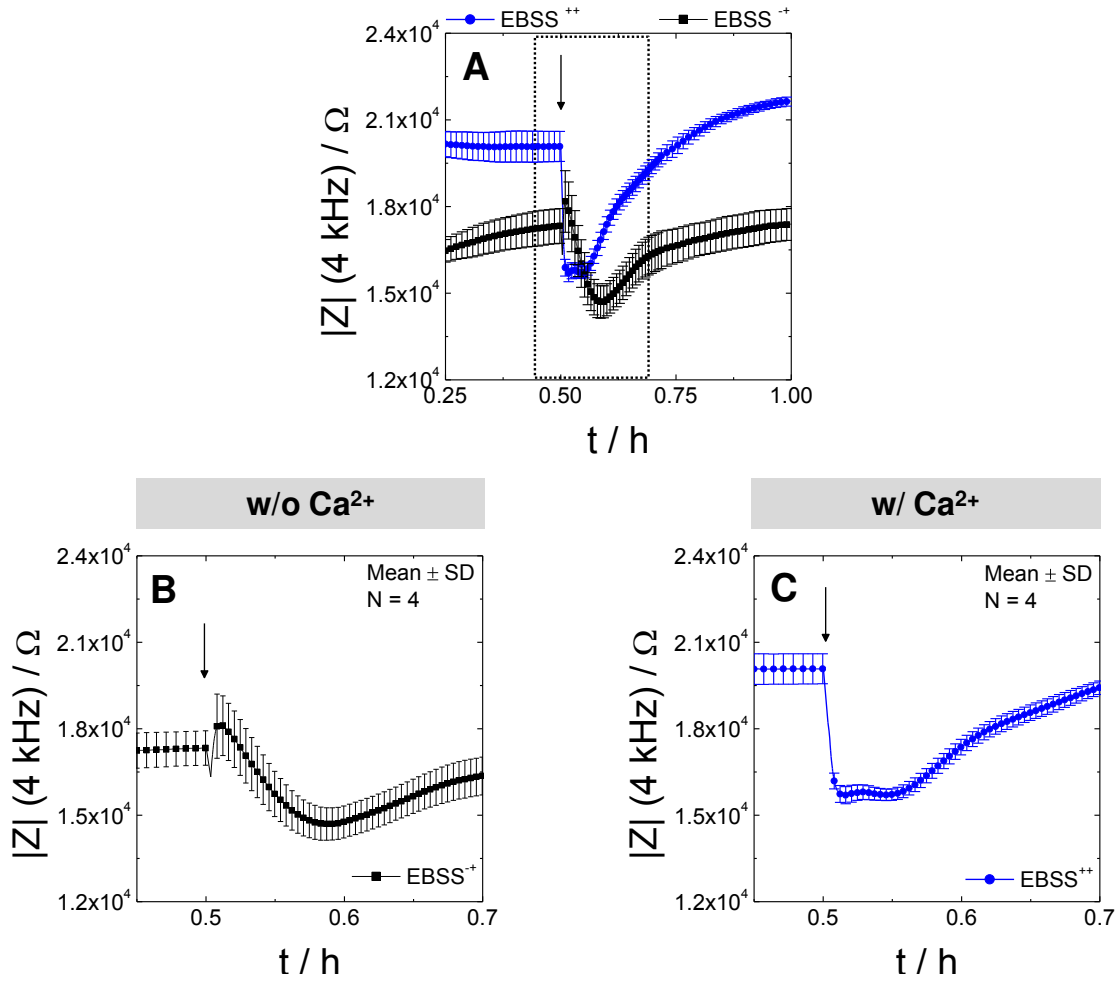

Fig. 5.24: Time-course of |*Z*| at 4 kHz 30 min before, during and 30 min after electroporation of NRK cells grown on a 8W4E-GJ array in $EBSS^{-+}$ and $EBSS^{++}$ monitored in SFT mode (**A**). Zoom-in to the time frame between $t = 0.45$ h and 0.7 h to further emphasize the different time-courses in absence or presence of calcium (**B;C**). Curves represent Mean ± SD of four different wells measured separately to enhance the time-resolution.

Time-course of $|Z|_{4\,kHz}$ for NRK cells incubated with two different buffer compositions are shown in **Fig. 5.24 A**. Baseline was recorded for 30 min in the respective buffer. Immediately before pulsing, the signal for cells in Ca^{2+}-containing buffer showed higher impedance values with $(20 \pm 0.5)\cdot 10^3\ \Omega$ compared to those in buffer without Ca^{2+} which were determined to $(17 \pm 0.6)\cdot 10^3\ \Omega$. After pulsing at $t = 0.5$ h the response to the electroporation pulse with identical parameters (40 kHz, 200 ms, 4 V) caused different impedance recovery profiles. In absence of Ca^{2+} (**B**) the impedance first increased to ~ $18.2\cdot 10^3\ \Omega$ at $t = 0.51$ h, followed by a slow decrease to a transient minimum of $14.7\cdot 10^3\ \Omega$ ($t = 0.59$ h). Afterwards, $|Z|$ increased again and completely recovered within 30 min. A different impedance process was monitored when Ca^{2+} was present (**C**). Here, $|Z|$ immediately showed a sharp decrease to the minimum of ~$15.6\cdot 10^3\ \Omega$, followed by an increase until the initial $|Z|$ value was exceeded ~ 20 min later and settled to $(21.7 \pm 0.2)\cdot 10^3\ \Omega$ at the end of the recording ($t = 1.0$ h).

In summary, electroporation can be performed in absence of Ca^{2+} without any significant difference on the uptake efficiency of FITC dextran. However, the impedimetric profiles recorded at 4 kHz immediately after pulse application followed a different kinetic compared to electroporation in $EBSS^{++}$. Consequently, a Ca^{2+}-free environment was chosen as standard condition for the analysis of gap junctional intercellular communication in the following.

5.5.4.2 Inhibition of GJIC between NRK Cells Using 2-APB

2-APB is a literature-known inhibitor for gap junctional intercellular communication [231] and it was used in several studies to selectively block the dye transfer into adjacent cells without affecting the primary loading with the tracer dye [246, 247, 320].

Microscopic Characterization

Following literature recommendations 100 µM 2-APB was applied in a scratch assay to proof the inhibitory effect on gap junctional intercellular communication between NRK cells. After scratching the dye transfer into neighboring NRK cells with or without inhibitor was monitored using confocal laser scanning microscopy. **Fig. 5.25** shows typical micrographs in absence (**A**) and presence of 2-APB (**B**). Obviously, the dye transfer was inhibited by 2-APB and only cells at the wound border were loaded with Lucifer Yellow.

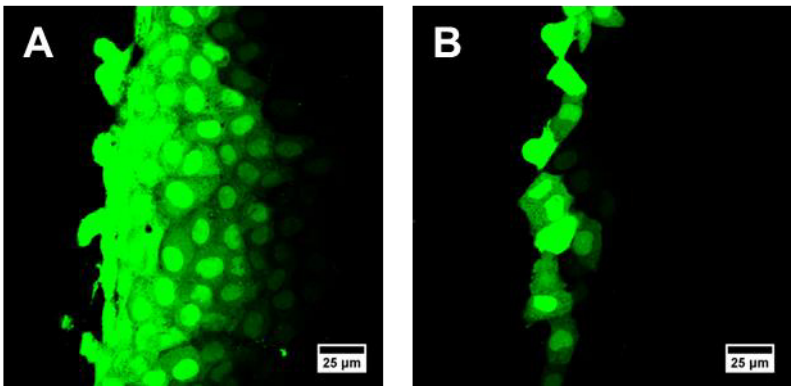

Fig. 5.25: Confocal fluorescence micrographs of NRK cells after scrape loading assay in absence (**A**) or presence of 100 µM 2-APB (**B**). Dye transfer based on gap junctional intercellular communication was strongly inhibited in presence of 2-APB and fluorescence was limited to the cells that were primary loaded with Lucifer Yellow at the scratch edge. The scale bar represents 25 µm.

Impedimetric Analysis of Cellular Response after 2-APB Addition

Before using 2-APB in gap junctional intercellular communication experiments the effect of the drug on NRK cells with and without electroporation was studied by impedance monitoring in order to exclude significant cytotoxicity.

Confluent NRK cells, grown on 8W1E electrodes were either incubated in $EBSS^{++}$ or $EBSS^{-+}$ (w/o Ca^{2+}) and treated with increasing concentrations of 2-APB (50 µM – 100 µM). Cells were subsequently electroporated twice (delay 15 min) in presence of 2-APB or buffer only and cellular response was monitored over 30 h. To extract the toxicity of 2-APB remaining in the extracellular fluid for the entire experiment, cells were additionally monitored at least 24 h in presence of the inhibitor without electroporation.

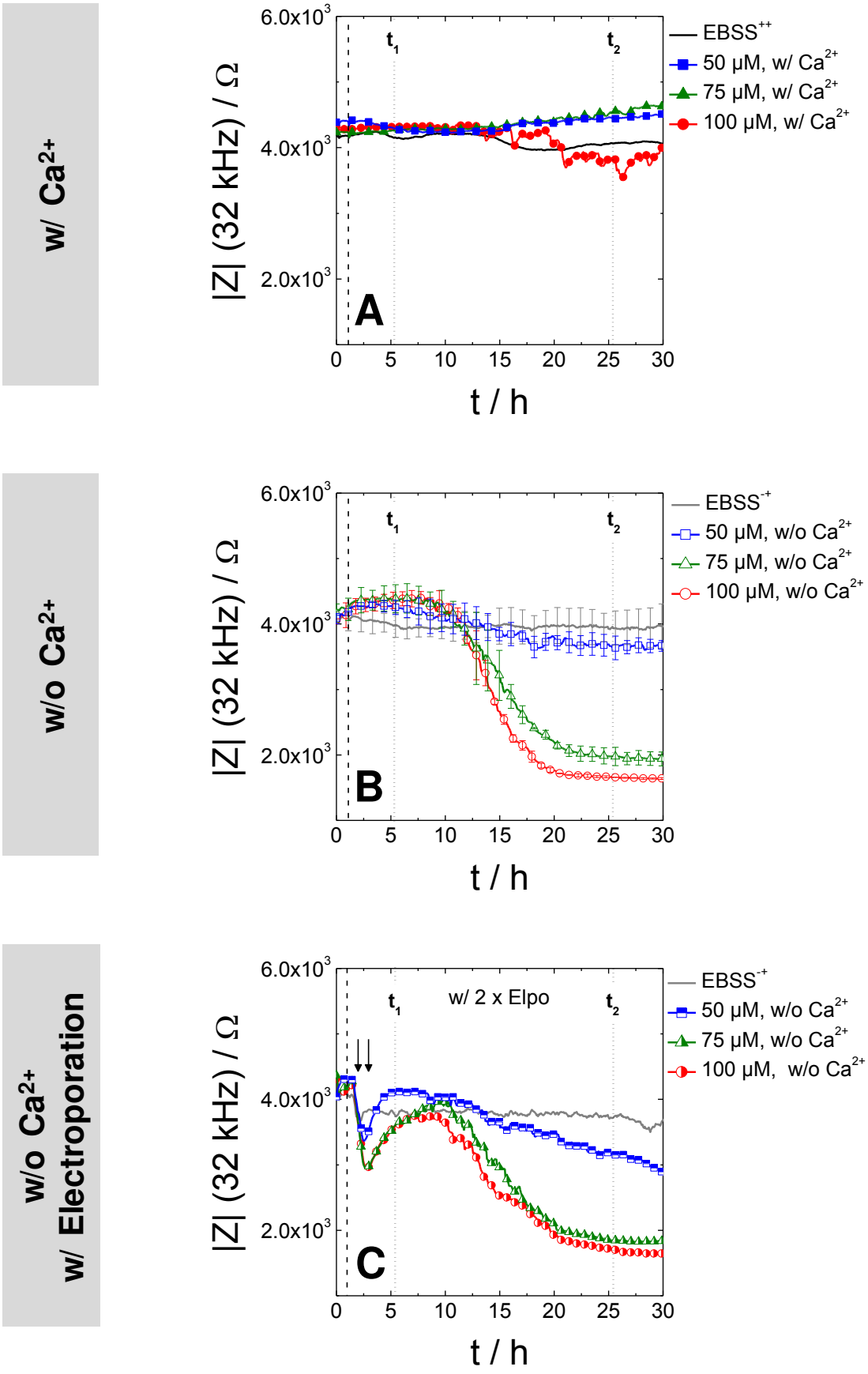

Fig. 5.26: Time-course of the impedance magnitude *|Z|* at 32 kHz to monitor the response of NRK cells to the addition of 2-APB with varying concentrations (50 µM, 75 µM, 100 µM) using $EBSS^{++}$ (w/ Ca^{2+}) (**A**), $EBSS^{-+}$ (w/o Ca^{2+}) (**B**) or $EBSS^{-+}$ and cytoplasm delivery of the compound by *in situ* electroporation (2 x, 40 kHz, 200 ms, 4 V) (**C**). (N = 1 or Mean ± SD for N = 2). The time-point of addition is indicated by the dashed line and the two electroporation pulses are shown by the arrow. The incubation times of 4 h (t_1) and 24 h (t_2) with 2-APB are indicated by the dotted lines.

Fig. 5.26 exemplarily shows typical time-courses after adding 2-APB to the buffer (w/ or w/o Ca^{2+}) (**A;B**) and after electroporation in presence of 2-APB (**C**). Obviously, the response of NRK cells to the addition of 2-APB was dependent on the presence of Ca^{2+} in the buffer. In $EBSS^{++}$ (**A**; **black** symbols) no toxic effects were found within 30 h independent of the 2-APB concentration. The magnitude of impedance $|Z|$ for cells in presence of $EBSS^{++}$ remained constant over the entire experiment at ~ $4.1 \cdot 10^3\,\Omega$ and even in presence of 100 µM 2-APB an impedance magnitude $|Z|$ of $3.7 \cdot 10^3\,\Omega$ was found after 30 h. For lower concentrations of 2-APB slightly increased impedance values of $4.6 \cdot 10^3\,\Omega$ (75 µM) and $4.5 \cdot 10^3\,\Omega$ (50 µM) compared to the control were found.

By removing Ca^{2+} from the extracellular environment (**B**), a concentration-dependent trend was monitored for 2-APB. Only the lowest concentration of 2-APB (50 µM) showed similar impedance values ($3.7 \cdot 10^3\,\Omega$) compared to the controls in $EBSS^{-+}$ and the controls in $EBSS^{++}$. However, in presence of higher concentrations a cytotoxic effect, indicated by a decrease in $|Z|$ to $1.7 \cdot 10^3\,\Omega$ was found 20.5 h after adding 100 µM 2-APB to NRK cells. A slow delay of the cytotoxic effect was monitored using 75 µM 2-APB and impedance dropped down to $2.0 \cdot 10^3\,\Omega$ after 22.7 hours of incubation. In contrast, no cytotoxic effects were detected for the same concentrations in Ca^{2+}-containing buffer for the same time frame of 30 h (**A**).

In the next step, the effect of 2-APB after transient permeabilization of the plasma membrane for access to the cytoplasm in Ca^{2+}-free buffer was studied (**C**). Therefore, cells were incubated in presence of 2-APB and electroporated twice and the response of NRK cells was monitored over time. For higher concentrations, 100 µM and 75 µM, similar time-courses were found for cells, with or without electroporation. Similar to the results shown in (**B**) $|Z|_{32\,kHz}$ dropped down to $1.7 \cdot 10^3\,\Omega$ in presence of 100 µM and to $1.9 \cdot 10^3\,\Omega$ in presence of 75 µM 2-APB. The only difference was found for 50 µM 2-APB, which only caused cytotoxic effects after applying two electroporation pulses resulting in a slight decrease in impedance ~ 10 h after electroporation. In contrast, the same extracellular concentration of 2-APB (**B**) in absence of calcium did not show any effects, as already discussed before.

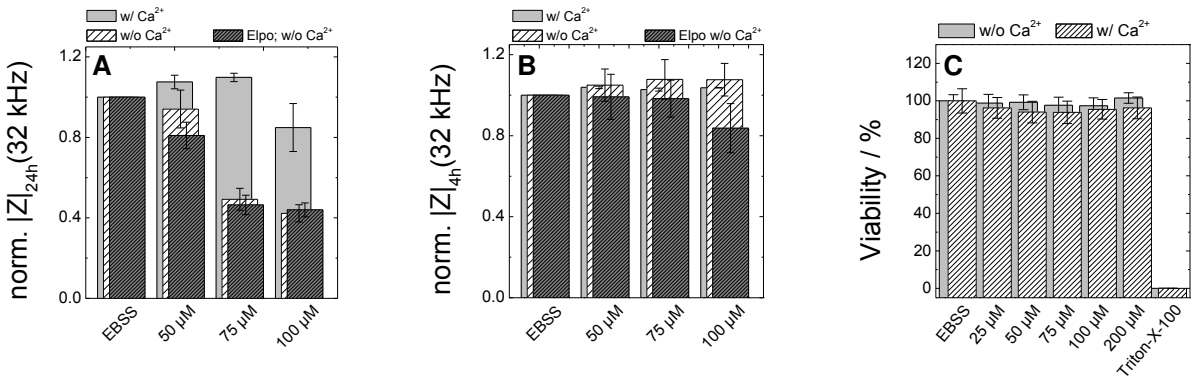

Fig. 5.27: A; B: Response of NRK cells 24 h (**A**) and 4 h (**B**) after the addition of 2-APB (50µM, 75 µM, 100 µM). Impedance magnitude $|Z|$ was normalized to the values of the respective control ($EBSS^{++}$, $EBSS^{-+}$ and $EBSS^{-+}$ with electroporation). The column bars represent two independent measurements (Mean ± SD, N = 2 – 4). **C:** PrestoBlue® assay to analyze cell viability for different concentrations of 2-APB after an incubation time of 4 h. The PrestoBlue® assay was performed as single experiment (N = 8; Mean ± SD).

An overview of two independent experiments is provided in the column bars in **Fig. 5.27** (**A; B**) representing the mean value of impedance and the corresponding standard deviation. For this purpose, impedance values ($|Z|_{32\,kHz}$) were taken 24 h (**A**) or 4 h (**B**) after adding 2-APB in different concentration and normalized to the corresponding control values of $EBSS^{++}$, $EBSS^{-+}$ or $EBSS^{-+}$ with electroporation respectively.

In conclusion, the results obtained with NRK cells in absence of Ca^{2+} after 24 h (t_2) of incubation showed similar results with or without electroporation. In presence of 100 µM 2-APB the normalized impedance at 32 kHz dropped down to 0.42 ± 0.04 ($EBSS^{-+}$) or 0.44 ± 0.03 after electroporation. By using 75 µM 2-APB nearly the same cytotoxic effects were monitored with impedance values of 0.49 ± 0.05 and 0.47 ± 0.05. With a concentration of 50 µM the effect of 2-APB on NRK cells was weak and $|Z|_{norm}$ values of 0.94 ± 0.09 and 0.81 ± 0.07 were recorded. In presence of Ca^{2+} the calculated mean values of $|Z|_{norm}$ after 24 h were similar to those of the control with 0.8 ± 0.1 (100 µM), 1.10 ± 0.02 (75 µM) and 1.08 ± 0.03 (50 µM).

For the later application in the gap junctional intercellular communication assay the total time of the assay starting with the ECIS recordings until the final documentation with confocal laser scanning microscopy was set to be maximum 4 h. Therefore, the signals after 4 h (t_1) of incubation were extracted (**B**) and additionally analyzed by a PrestoBlue® assay in absence or presence of Ca^{2+} (**C**). After 4 h of incubation no indications for a cytotoxic effect of 2-APB in $EBSS^{-+}$ and $EBSS^{++}$ were found independent of the applied concentration. Only after applying invasive electroporation pulses, the normalized $|Z|_{32\,kHz}$ signal for NRK cells in presence of 100 µM 2-APB showed a small deviation from the respective control value with

0.8 ± 0.1. For lower concentrations (75 µM, 50 µM), even with electroporation, similar values as for the control were achieved, indicating no cellular response. The metabolic activities of NRK cells in $EBSS^{-+}$ and $EBSS^{++}$ were further investigated using PrestoBlue® assay. In this assay the blue and non-fluorescent dye is converted into a pink, fluorescent dye only by healthy and metabolically active cells. NRK cells were incubated with 2-APB (25 µM – 200 µM) in absence or presence of Ca^{2+} for 4 h before the PrestoBlue® reagent was added. The calculated viabilities (**C**) show that cells were viable over the whole concentration range and that no cytotoxic effects were found.

The ECIS data as well as the results of the colorimetric assay assure that a concentration of 50 µM can be used for selectively blocking gap junctional intercellular communication without affecting cells' viability for the intended time frame of the here developed gap junctional intercellular communication assay.

5.5.4.3 Dye Uptake Study to Analyze the Effect of Recovery Time on Uptake Efficiency

In the following the dye uptake was analyzed dependent on the post-pulse period without monitoring the complete recovery process with non-invasive ECIS technique. For that purpose, an electroporation experiment was designed where the pulses were applied to confluently grown NRK cells varying the time frame between electroporation and termination of impedance monitoring.

Fig. 5.28 shows the impedance recordings at 4 kHz (**A**) and 32 kHz (**B**) for NRK cells confluently grown on 8W1E electrodes. A baseline in $EBSS^{-+}$ was recorded for ~ 0.6 h before FITC dextran (4 kDa, 2 mg/mL) was added. Afterwards, cells were pulsed (↓) with constant pulse parameters of 40 kHz, 4 V and a pulse duration of 200 ms with different time frames between electroporation and the endpoint of the experiment. At 4 kHz (**A**) |*Z*| first increased and then decreased due to the electroporation pulse, whereas at 32 kHz (**B**) an immediate decrease was observed. Afterwards, |*Z*| increased indicating the process of membrane resealing and cell recovery. The measurement was stopped 20 min (■), 15 min (●), 10 min (▼) or 5 min (♦) after pulsing.

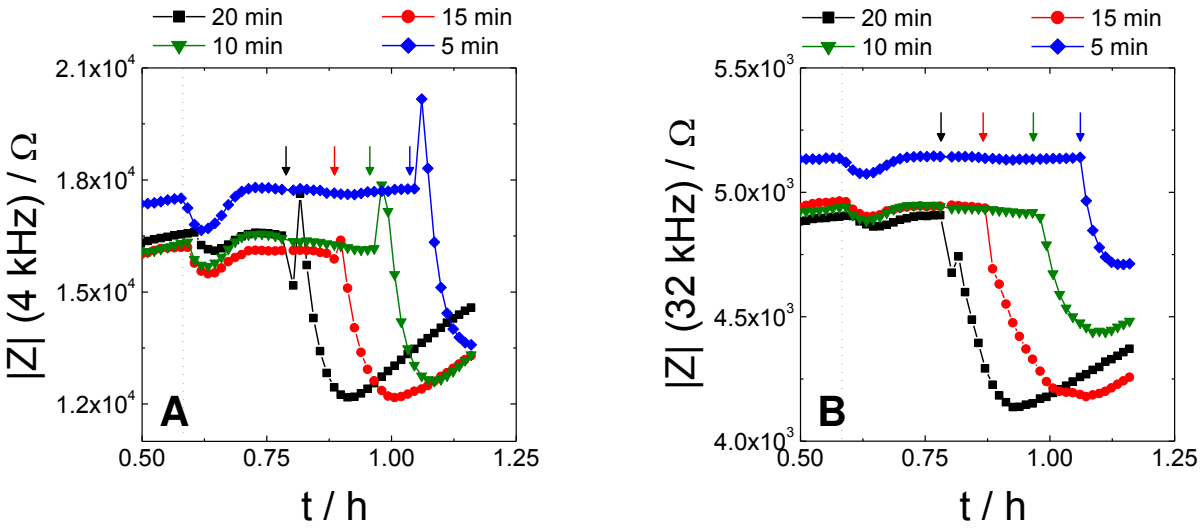

Fig. 5.28: Time-courses of impedance magnitude |Z| at 4 kHz (**A**) and 32 kHz (**B**) before and after electroporation of NRK cells grown on 8W1E electrodes in presence of FITC dextran (4 kDa) in $EBSS^{-+}$ (containing 0.5 mM $MgCl_2$). Electroporation (40 kHz, 200 ms, 4 V) occurred 20 min (■), 15 min (●), 10 min (▼) or 5 min (♦) before the experiment was stopped and the dye uptake was analyzed microscopically. The time point of FITC dextran addition is marked with the dotted line, whereas the respective electroporation events are labeled with the arrows.

Afterwards, the dye solution was aspirated and the cells were washed once with a buffer containing 10 % FCS, which was also applied in other gap junctional intercellular communication assays [304] to facilitate resealing of the membrane [427]. With additional two washing steps using PBS^{++} the unincorporated dye was removed. Then, the dye uptake was

immediately analyzed using confocal laser scanning microscopy. The different cell layers exposed to decreasing recovery times are shown in **Fig. 5.29** (**A-D**) in fluorescence (**1**) as well as in phase-contrast (**2**) micrographs to evaluate the dye uptake and cell layer integrity. Loading efficiency of NRK cells on the electrodes (indicated by the white, dashed circle) was similar for all conditions and did not depend on the recovery time. In the phase-contrast images confluent cell layers were found, indicating no cell damage due to the electroporation pulse or the fast washing procedure and the subsequent microscopic analysis.

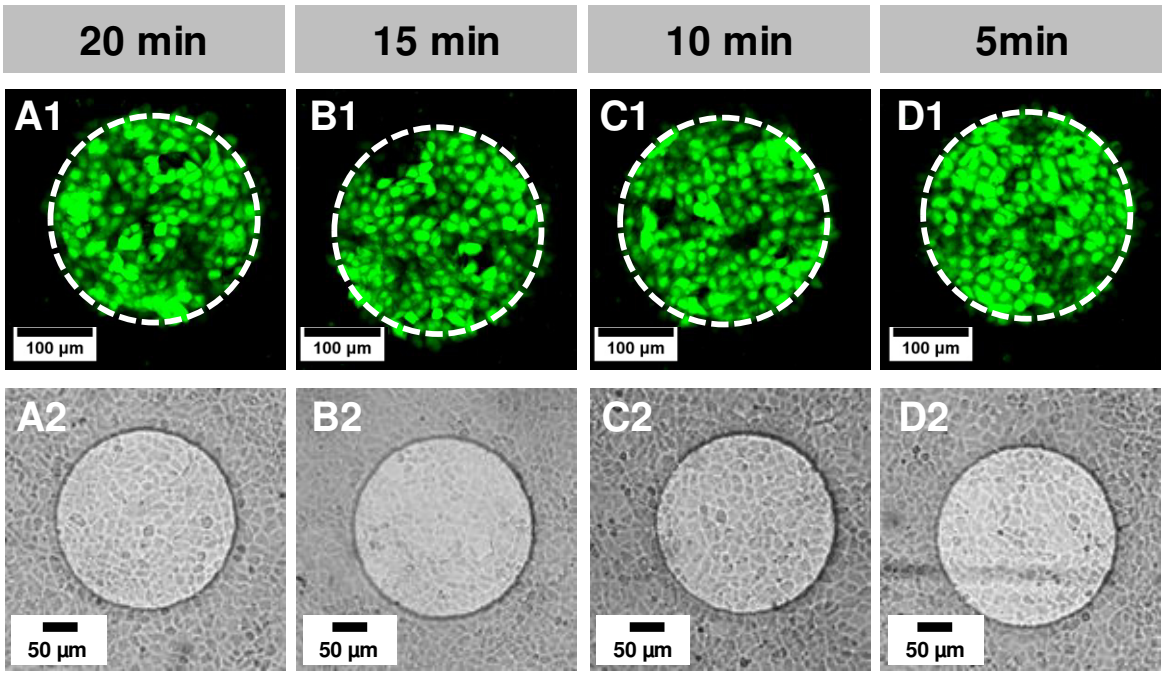

Fig. 5.29: Fluorescence micrographs (**1**) and phase-contrast images (**2**) after electroporation in presence of FITC dextran (4 kDa, 2 mg/mL in $EBSS^{-+}$). Cells were pulsed 20 min (**A**), 15 min (**B**), 10 min (**C**) or 5 min (**D**) before the experiment was stopped. The scale bars represent 100 µm (**1**) or 50 µm (**2**).

These results emphasized, that for the future use in the gap junctional intercellular communication assay a microscopic detection of dye transfer into the adjacent cells will be possible already after 5 min.

In the following the dye uptake of Lucifer Yellow was analyzed with respect to recovery time. Therefore, NRK cells were grown to confluence on 1st generation gold-film electrodes (**chapter 5.5.4.4.3**) and a baseline was recorded in $EBSS^{-+}$. After 30 min a mixture of Lucifer Yellow (2 mg/mL) and TRITC dextran (3 mg/mL) was added and cells were either pulsed 60 min or 5 min before the experiment was stopped. **Fig. 5.30** shows the time course of

normalized impedance at 16 kHz [f] (**A**) and a survey of fluorescence micrographs (**B;C**) of green-fluorescent Lucifer Yellow and red fluorescent TRITC dextran of the same position taken 60 min (**B**) or 5 min (**C**) after pulsing.

The uptake efficiency was significantly different for the green fluorescent Lucifer Yellow (**B1;C1**) using a recovery time of 60 min and 5 min. Analysis 5 min after electroporation provided a successful uptake of Lucifer Yellow into the cytoplasm indicated by a homogeneous and bright fluorescence intensity. For longer incubation times, with same microscopic settings only a weak green fluorescence intensity was found inside the cytoplasm of cells located on the electrode. However, TRITC dextran was in both cases successfully incorporated into NRK cells by electroporation indicated by a bright red fluorescence intensity shown in **B2** and **C2**. In the red channel no significant difference was found for an incubation time of 60 min and 5 min.

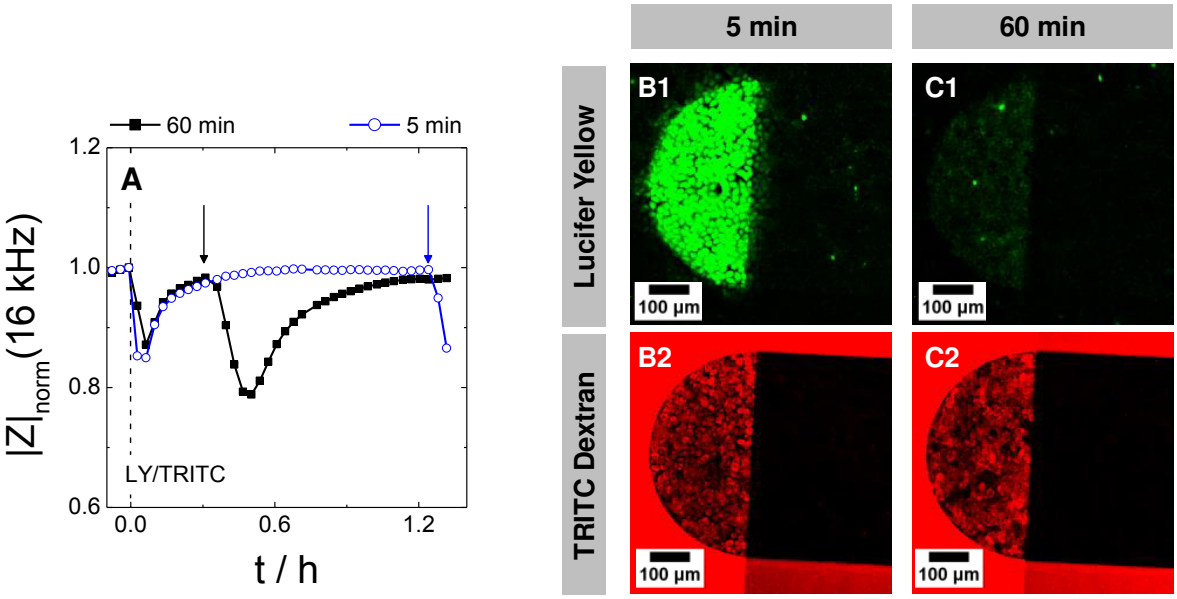

Fig. 5.30: A: Time course of normalized impedance at 16 kHz for NRK cells confluently grown on 1st generation gold-film electrodes before and after electroporation in presence of Lucifer Yellow and TRITC dextran. Experiment was stopped 60 min (**black**) or 5 min (**blue**) after the electroporation pulse. **B; C:** Confocal fluorescence micrographs of NRK cells after electroporation in presence of Lucifer Yellow (**1**) and TRITC dextran (**2**) 5 min (**B**) and 60 min (**C**) after pulse application. One characteristic semi-circular electrode for each condition is presented. The scale bar represents 100 µm.

[f] In contrast to the experiments before, the 1st and 2nd generation gold-film electrode layout was used which will be introduced in **chapter 5.5.4.4.3**. |*Z*| at 16 kHz was selected as monitoring parameter during the experiment as the most sensitive frequency was determined to ~ 25 kHz.

To further analyze the disappearance of Lucifer Yellow after 60 min the experiment was repeated using different inhibitors:

(i) **2-APB** - a literature-known inhibitor for gap junctional intercellular communication

(ii) **Sulfinpyrazone** - an inhibitor for *organic anion transporters* (OAT)

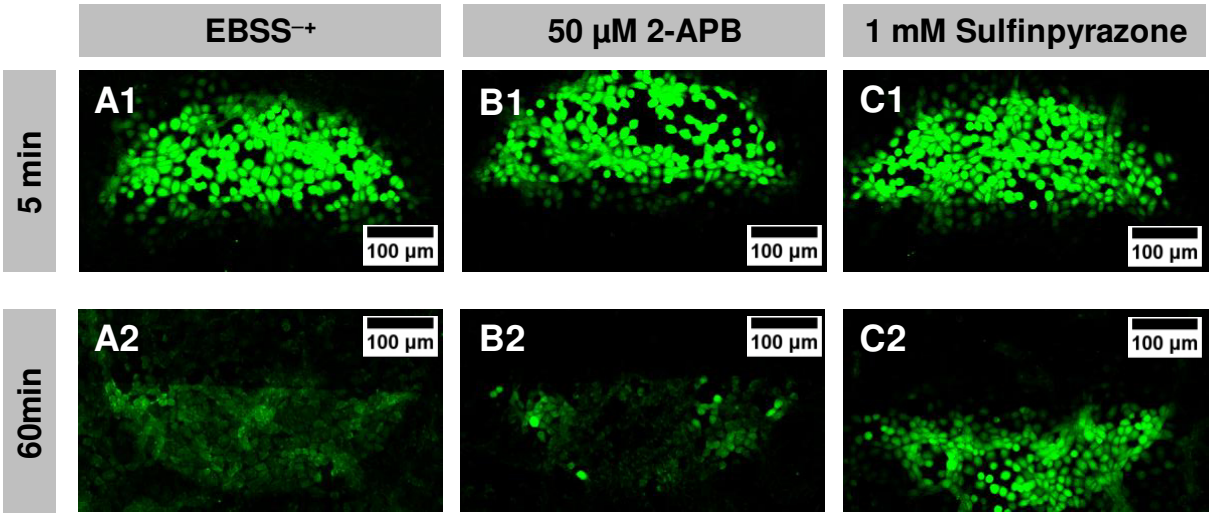

Fig. 5.31: Confocal fluorescence micrographs of NRK cells after electroporation in presence of Lucifer Yellow using the 8W4E-GJ gold-film electrode layout. Cells were electroporated in EBSS^{-+} (**A**), in presence of the inhibitor 50 µM 2-APB (**B**) or 1 mM Sulfinpyrazone (**C**). Incorporation of Lucifer Yellow was analyzed 5 min (**1**) or 60 min (**2**) after electroporation. For each condition one characteristic "semi-elliptical" electrode is shown. The scale bar represents 100 µm.

Fig. 5.31 shows a survey of fluorescence micrographs of NRK cells after electroporation in presence of Lucifer Yellow. The dye uptake was documented 5 min (**1**) or 60 min (**2**) after electroporation. Under control conditions, electroporation in presence of Lucifer Yellow in EBSS^{-+} buffer, the dye was incorporated into the cytoplasm of NRK cells after 5 min (**A1**). Again a significant decrease in fluorescence intensity was found when cells were imaged 60 min after pulsing (**A2**). When the same experiment was performed in presence of 50 µM 2-APB, an inhibitor for gap junctional intercellular communication, similar results were found. After 5 min cells on the electrode showed a bright green fluorescence intensity (**B2**), whereas after 60 min only a weak fluorescence signal was detected (**B2**). Therefore, a reduction of Lucifer Yellow intensity on the electrode was not caused by a dilution of the dye via dye transfer based on cell-cell communication. Additionally, NRK cells were electroporated in presence of 1 mM Sulfinpyrazone, which is known to inhibit OAT. When 1 mM Sulfinpyrazone was present during the electroporation process the dye loading inside the cytoplasm of NRK cells was similar and independent of the recovery time (**C1;C2**) and the dye efflux of Lucifer Yellow was completely inhibited by the addition of the inhibitor for OAT [428].

Furthermore, the ECIS recording of NRK cells in presence of Lucifer Yellow was stopped 5 min after electroporation. Before cells were analyzed by confocal laser scanning microscopy cells were stored at 4 °C for an additional hour to study the temperature-dependency of the dye efflux. The fluorescence micrographs in **Fig. 5.32** revealed the presence of Lucifer Yellow-stained NRK cytoplasm on top of the electrode when NRK cells were incubated at 4 °C (**C**). The dye efflux was clearly inhibited by decreasing the temperature indicating an energy-dependent process.

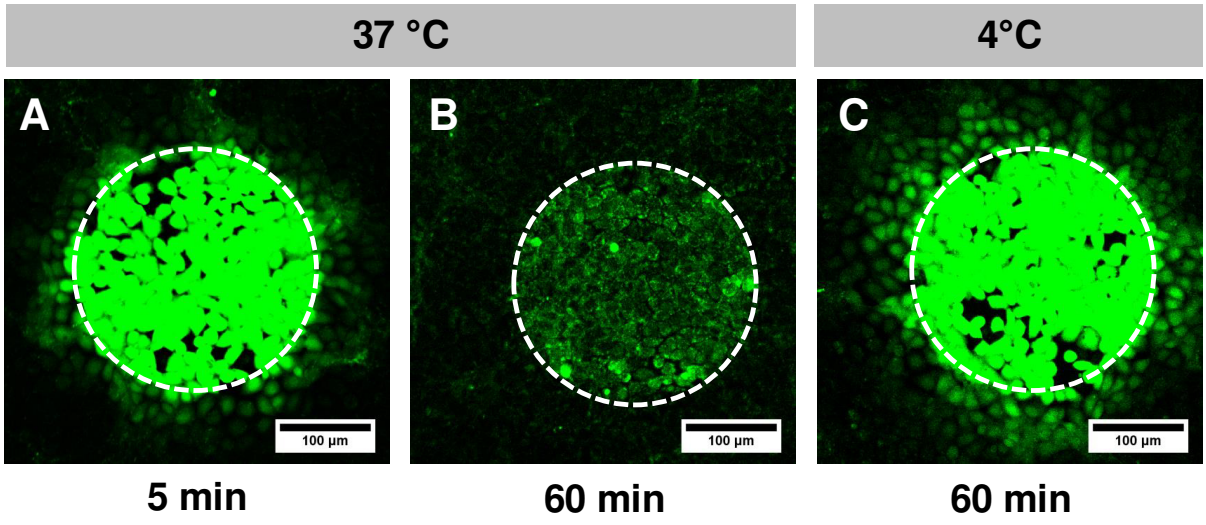

Fig. 5.32: Confocal fluorescence micrographs of NRK cells after electroporation in presence of Lucifer Yellow using the 8W1E gold-film electrode layout. Incorporation of Lucifer Yellow was analyzed 5 min (**A**) or 60 min (**B**) after electroporation at 37 °C. Confocal fluorescence micrograph of NRK cells electroporated at 37 °C then stored at 4 °C for 60 min before the dye uptake was analyzed using confocal laser scanning microscopy (**C**). The scale bar corresponds to 100 µm.

In summary, the time-dependent uptake efficiency of fluorescent dyes after electroporation showed that the analysis of dye uptake can be performed within 5 min after pulsing. When using FITC dextran no significant differences in dye loading efficiency was found dependent on the delay between pulse application and termination of impedance monitoring. When Lucifer Yellow was used as fluorescent tracer instead, the analysis after 5 min was even favored, due to the higher fluorescence intensity on the electrode compared to 60 min recovery.

5.5.4.4 Modification of the Electrode Layout

5.5.4.4.1 Circular Gold-Film Electrode Layout (8W4E-micro)

First experiments to study gap junctional intercellular communication were performed using a 8W4E-micro electrode layout, containing four circular gold-film electrodes with a diameter of 250 µm per well. Cells were either pulsed once (40 kHz, 200 ms and 4 V) or twice to investigate if a 2nd pulse influences gap junctional intercellular communication. In a previous study the delay between two pulses was varied between 10 min – 30 min (**Fig. S 9**). It was found that a delay of 15 min between the two pulses was best and used in the following studies.

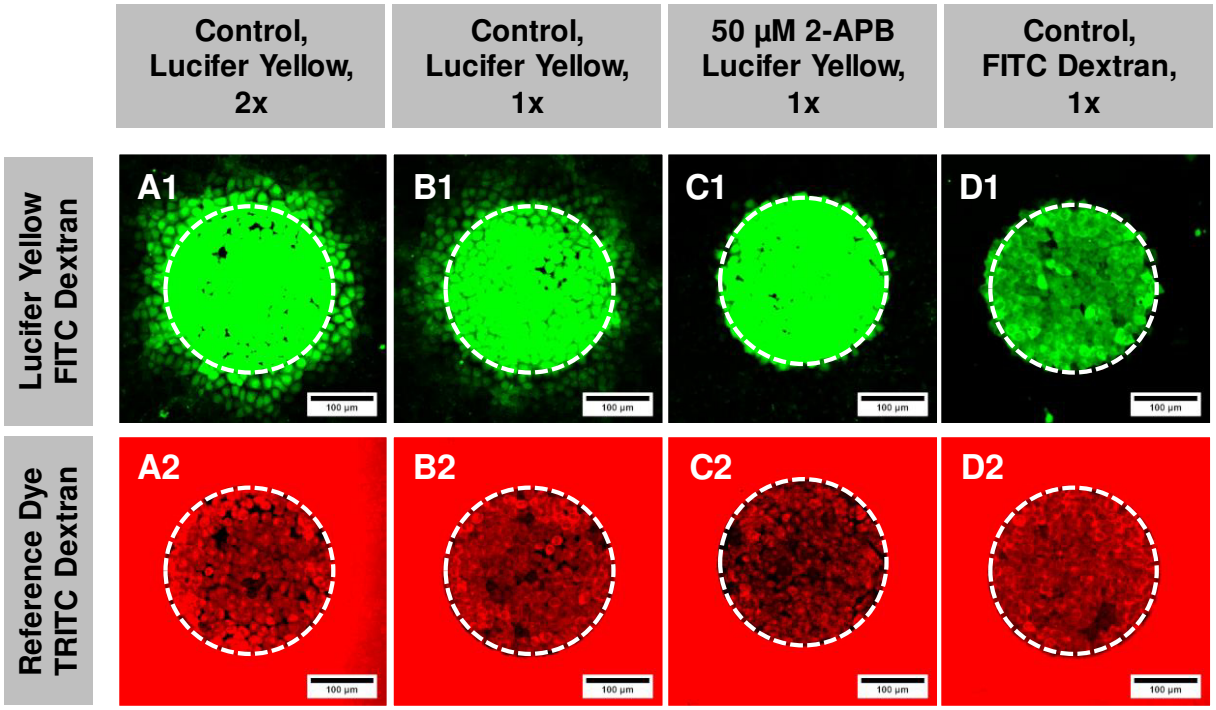

Fig. 5.33: Confocal fluorescence micrographs of NRK cells grown on 8W4E-micro electrodes after applying two pulses (**A**) or after single pulse electroporation (40 kHz, 200 ms, 4 V) (**B-D**) in presence of Lucifer Yellow (**A1-C1**) and TRITC dextran (**A2-D2**) in $EBSS^{-+}$ (**A;B;D**) or in $EBSS^{-+}$ containing 50 µM 2-APB (**C**). FITC dextran (250 kDa) (**D1**) and TRITC dextran (155 kDa) (**A2-D2**) was used as fluorescent compound to investigate the size limit for gap junction-mediated transport. White circles indicate the position of the small working electrode. Images were taken using 10 x objective. The scale bar corresponds to 100 µm.

Fig. 5.33 exemplarily shows NRK cells on one electrode in a 8W4E-micro electrode layout after electroporation in presence of differently-sized fluorescent dyes. The dye transfer into the adjacent cells only occurred for Lucifer Yellow with a molecular weight of 457 Da (**A1; B1**) but not if the inhibitor 2-APB was present (**C1**). If the molecular weight exceeds a limit for the permeability of the connexons of ~ 1 kDa, the fluorescence intensity was limited to the cells adhered to the working electrode. This was successfully demonstrated in **D1**, where

electroporation was conducted in presence of FITC dextran (MW 250 kDa). After selectively loading NRK cells on the electrode surface with Lucifer Yellow, the dye diffused into neighboring cells and green fluorescence was also detected in the periphery of the actual electrode area. Enhanced fluorescence intensity was found within the cell population on and surrounding the electrode after applying two pulses (**B1**) compared to the single-pulse experiment (**A1**). The incorporation of the red fluorescence TRITC dextran (MW 155 kDa) could only be visualized at the position of the gold-film electrode (**A2 – D2**). In the surrounding periphery the red auto fluorescence of the insulating polymer prohibited the analysis of the surrounding NRK cells. However, the red fluorescent dye was applied as reference dye which should distinguish between primary loading due to electroporation and fluorescence signals due to dye diffusion based on gap junctional intercellular communication.

In this experiment the dye transfer due to gap junctional intercellular communication between NRK cells was successfully detected after electroporation. Nevertheless, the 8W4E-micro electrode type with four circular gold-film electrodes in each well was not optimal, as a proper detection of the reference dye TRITC dextran was impeded by auto fluorescence of the insulating polymer.

5.5.4.4.2 ITO Electrode Layout

For the investigation of dye transfer after *in situ* electroporation the electrode layout was further improved. ITO was chosen as electrode material which provides good electrical conductivity and optical transparency. This enables a microscopic analysis from the bottom using an inverted fluorescence microscope without any special array preparation prior to the experiment. A new electrode layout was designed using semi-elliptical ITO electrodes instead of circular electrodes. Additionally, the photopolymer in the bordering ITO-free area was removed to eliminate the red auto fluorescence signal next to the electrode. This provides the opportunity to distinguish between pre-loaded cells and cells which were loaded by dye transfer through gap junctions using the red fluorescence TRITC dextran as reference dye. The dye transfer can then be analyzed along a straight line which facilitates the quantification of gap junctional intercellular communication.

The layout of the ITO electrode array is shown in **Fig. 5.34**. The ITO 8-well array was fabricated using standard photolithography processes and lift of techniques with an ITO-PET foil (Sigma-Aldrich, USA) as substrate **(Fig. 5.12**).

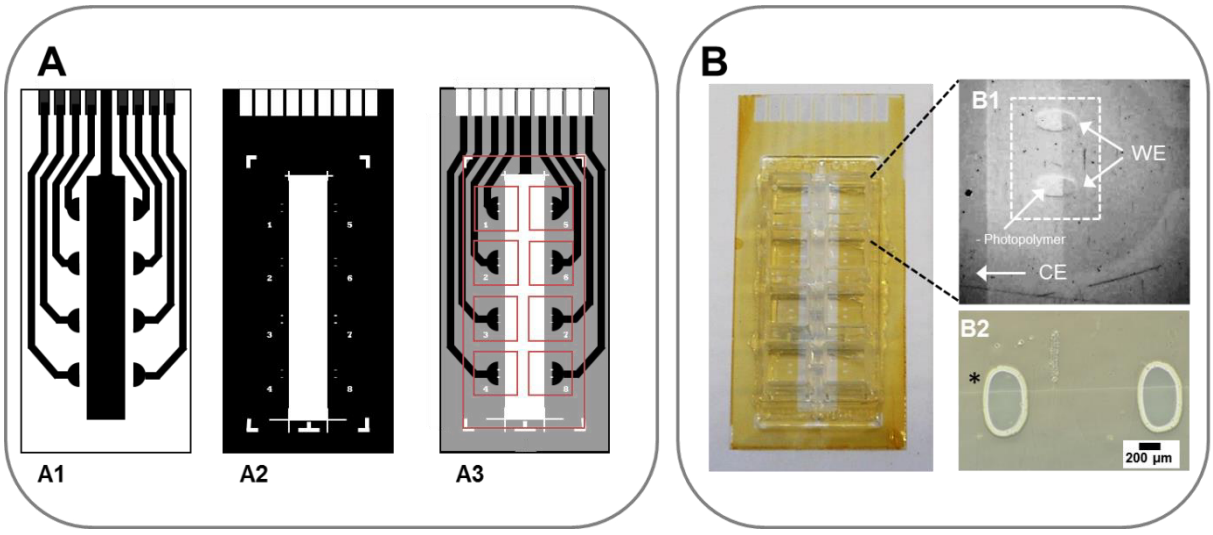

Fig. 5.34: A: Different masks for the fabrication of the ITO layout by standard photolithography (**1; 2**). After a first spin coating step with the photopolymer **A1** represents the mask for the first UV illumination step. After NaOH treatment ITO in the surrounding area, which was not protected by **A1** is removed by etching in $H_2O/HCl/HNO_3$. After a second spin-coating process the UV irradiation was done using mask **A2** to expose the working electrodes (WE), the large counter electrode (CE) and the contact areas. An overlay of both masks and the position of the LabTek 8-well-chamber mounting position is shown in **A3.** In the final product each well contains two semi-elliptical electrodes. **B:** Photographical image of the final ITO-PET electrode array. **B1** provides a photograph of one well, where the position of the CE as well as the two WE are shown. Additionally, the photopolymer was removed in the ITO-free periphery of the WE to facilitate data analysis of dye transfer. **B2** shows microscopic images of the two WE, taken with a 10 x objective. The ITO WEs are indicated with the *.

The size of the ITO-PET foil was adjusted to the standard size of the commercially available 8-well electrode arrays with a width of 3.5 cm and a length of 7.5 cm. The characteristics of this ITO coated PET foil substrate are shown in **Tab. 5.1**.

Tab. 5.1: Characteristics of the ITO-PET foils used for the preparation of the electrode layout.

ITO PET Foil	
Foil thickness	**0.127 mm**
Surface resistivity	**60 Ω /sq**
Thickness ITO coating	**100 nm**

Impedimetric Measurements and Electrode Characterization of the ITO-PET Electrodes

To further characterize the self-fabricated electrodes, frequency-dependent spectra of $|Z|$, R and C were measured in a frequency range between 1 Hz and 10^6 Hz. Data were recorded before and ~ 24 h after cell seeding of NRK cells with a seeding density of 500 000 cells/mL. **Fig. 5.35** presents a survey of the frequency-dependent data as well as the calculation of the sensitive frequencies for each quantity. **A – C** clearly show that the ITO electrode layout allows detecting cells grown upon the electrodes, as the $|Z|$, R and C spectra for cell-free and cell-covered electrodes differed in a cell-type specific frequency range. Depending on the parameter analyzed the sensitive frequency range varied between $10^3 – 10^5$ Hz for $|Z|$ (**D**), $10^2 – 10^5$ Hz for R (**E**) as well as $2.5 \cdot 10^3 – 5 \cdot 10^5$ Hz for C (**F**).

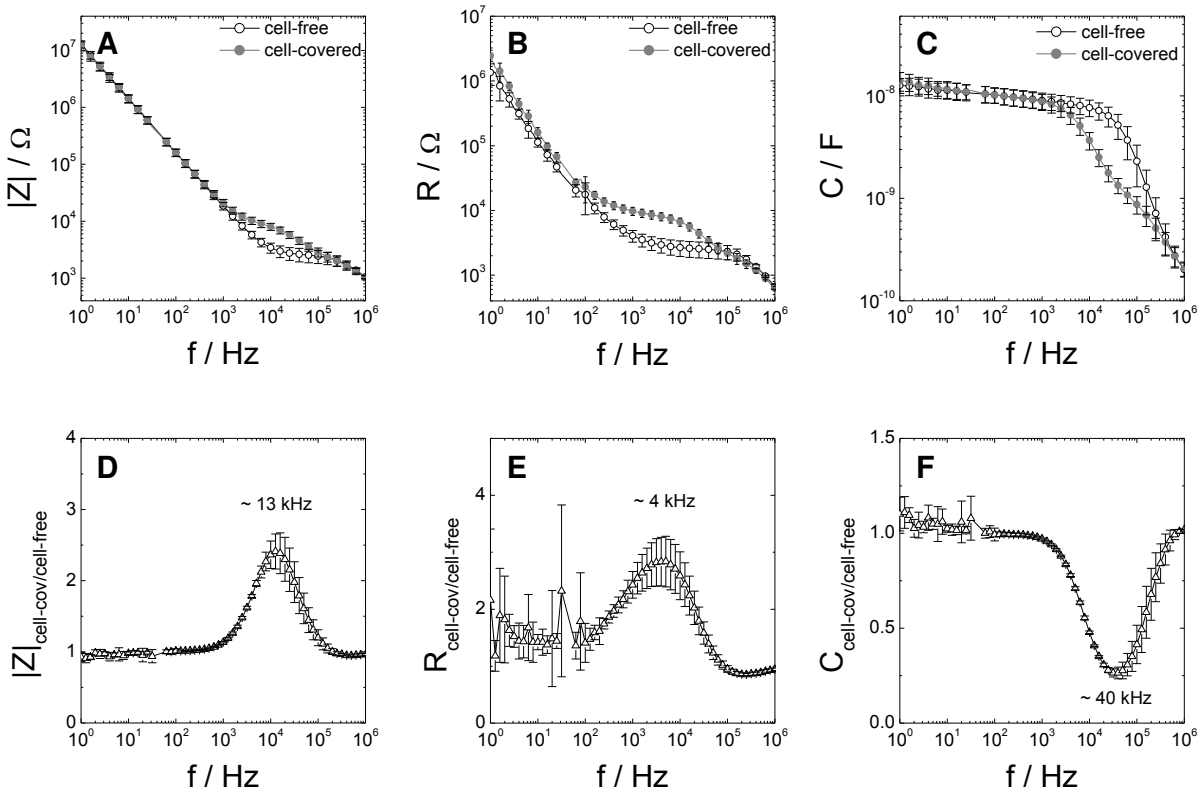

Fig. 5.35: Frequency-dependent impedance (**A**) resistance (**B**) and capacitance (**C**) spectra for cell-free (○) and NRK cell-covered (●) electrode using the self-fabricated ITO foil electrode layout (Mean ± SD, N = 8) [‡g]. The sensitive frequencies were determined by calculating $Z_{\text{cell-cov/cell-free}}$ (**D**), $R_{\text{cell-cov/cell-free}}$ (**E**) and $C_{\text{cell-cov/cell-free}}$ (**F**) which were obtained by dividing values from cell-covered electrodes by the corresponding cell-free values. This way, the sensitive frequencies for $|Z|$, R and C were determined to 13 kHz (**D**), 4 kHz (**E**) and 40 kHz (**F**).

[g] The high standard deviations in **E** are a consequence of the high standard deviations of the cell-covered and cell-free resistance spectra in the low frequency range between $1 – 10^2$ Hz (**B**) and the calculation of $R_{\text{cell-cov/cell-free}}$ by dividing values from cell-covered electrodes by the corresponding cell-free values. As already explained in **chapter 4,** data recorded at 40 Hz and 50 Hz are influenced by the powerline interference and were removed from experimentally obtained impedance spectra, which are denoted with [‡].

As the electrode structures were fabricated by standard photolithography process (**chapter 5.4.4**) the positioning of the second UV irradiation mask (**Fig. 5.34 A2**) was crucial for the electrode positioning and therefore for the size of the active ITO working electrodes. Moreover, the electrode size is essential for an efficient electroporation experiment. For the later application similar dye loading of cells on the electrodes in all eight wells and therefore similar electrode sizes are required to evaluate differences in gap junctional intercellular communication. The produced electrode arrays were controlled with respect to uniform electrode areas.

The 16 different ITO working electrodes were documented in phase-contrast and the active electrode areas were quantified using ImageJ. The electrode area significantly differed from well to well and was calculated to $(5.6 \pm 0.3) \cdot 10^{-2}$ mm^2 (Mean ± SE; N = 16). The reason for this variation might be that the second irradiation mask defines both, the active electrode area as well as the photopolymer-free gap for dye transfer analysis. The idea was that one half of the elliptical structure with a size of 300 µm x 600 µm and a theoretical area of 0.14 mm^2 should define the electrode whereas the second half should provide the polymer-free area. The theoretical area of the elliptical structure in the mask fits quite well with the calculated area based on microscopic images (0.15 ± 0.01 mm^2, Mean ± SD, N = 8). However, the exact positioning of the mask for the second irradiation step turned out to be difficult to control and generates inhomogeneous electrode areas.

Electroporation of NRK Cells Grown on ITO-PET Electrode Layouts

Even if the electrode size differed from well to well a proof of principle experiment was performed to analyze dye uptake after applying an invasive electroporation pulse in presence of FITC dextran. Therefore, FITC dextran (10 kDa, 2 mg/mL in EBSS^{++}) was added to a confluent cell layer of NRK cells and different electroporation pulses with varying voltages and pulse durations were applied to investigate the optimal conditions with high uptake efficiency and without cell damages. Cells were monitored non-invasively before and after applying the pulses with a monitoring frequency of 10 kHz, which was determined as sensitive frequency for $|Z|$ in **Fig. 5.35**.

After electroporation of NRK cells on ITO electrodes $|Z|$ recovered to pre-pulse values for all pulse settings (**Fig. 5.36 A**). After finishing the experiment, cells were washed twice and dye uptake was controlled via inverted epi-fluorescence microscopy. **B1** and **B2** show an exemplary phase-contrast and fluorescence micrograph of one electrode after electroporation in presence of FITC dextran and an electroporation pulse of 4 V, 500 ms and

40 kHz. Unfortunately, relatively high fluorescence background was detected which may interfere with the analysis of dye transfer in the later application to study gap junctional intercellular communication.

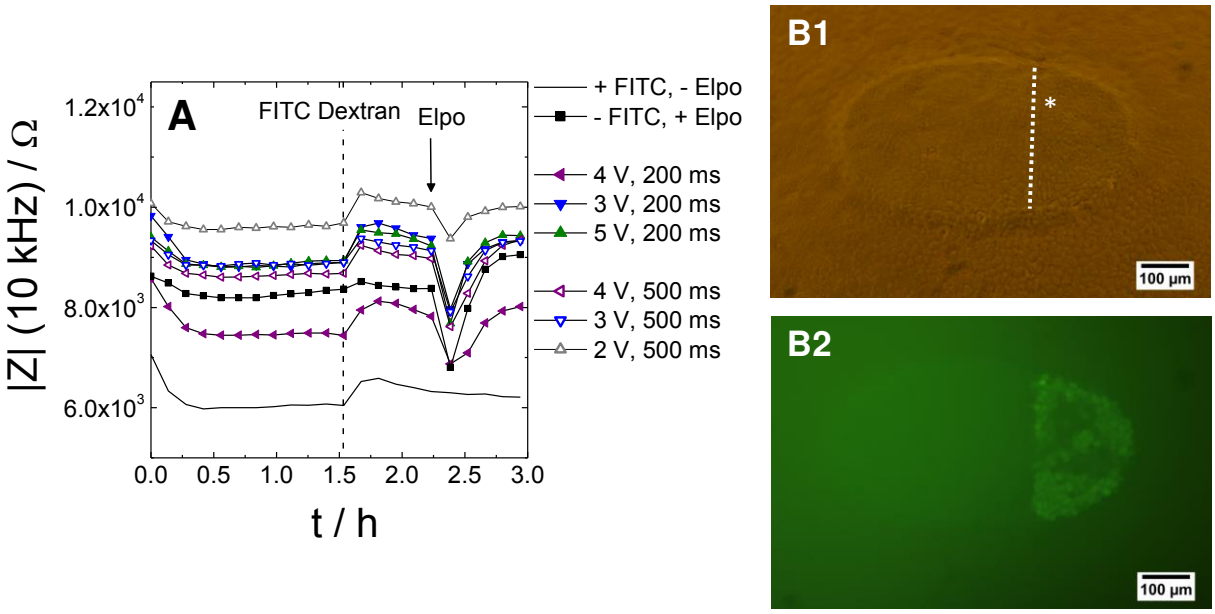

Fig. 5.36: A: Time-course of |*Z*| at 10 kHz to monitor the cellular response before and after electroporation. Confluent NRK cell layers were incubated with FITC dextran for ~30 min before different electroporation pulses were applied. The pulse duration was varied between 200 ms (filled symbols) and 500 ms (open symbols) whereas voltages were varied between 2 V – 5 V. After pulsing, recovery of |*Z*| was monitored for around 30 min before dye uptake was analyzed microscopically. **B:** Phase-contrast (**1**) and fluorescence micrograph (**2**) of NRK cells after applying an electroporation pulse of 4 V and 500 ms. Position of the small semi-circular electrode in **B1** is labeled with * and the borderline to the photopolymer-free gap is symbolized by the dotted line.

In this first electroporation experiment a successful application of the designed layout for impedimetric analysis of adherent cells could be shown. However, (i) problems to fabricate uniform electrode structures and (ii) difficulties with the microscopic detection of the dye uptake became apparent.

5.5.4.4.3 1st and 2nd Generation Gold-Film Electrode Layout

Further research on the assay development was based on gold-film electrodes which seemed to be a better candidate because

(i) commercial fabrication of the gold-film electrodes should provide uniform electrode areas and

(ii) high fluorescence background detected with the ITO array prohibited the analysis of dye transfer.

Therefore, the ITO electrode layout was further improved and a new design was developed (**Fig. S 8**) which was fabricated by Applied BioPhysics as gold-film electrode layout.

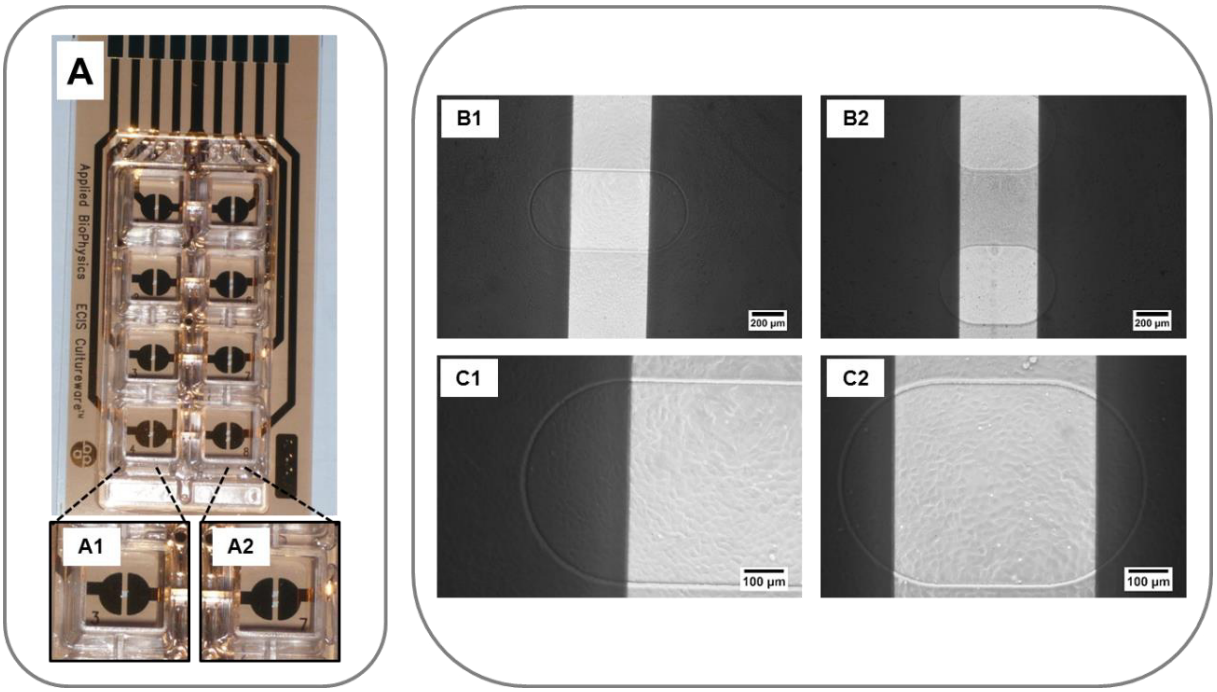

Fig. 5.37: A: Photograph of the 1st generation gold electrode layout which was fabricated by Applied BioPhysics using *Lexan*® or PET substrate and standard photolithography processes. The eight well chambers contain two different electrode layouts each present in four wells. Well 1 – 4 contains two semi-circled electrodes (2E) with a diameter of 500 µm (**A1**) and well 5 – 8 (4E) consists of four approximately semi-elliptical electrodes (~ 420 µm x ~ 120 µm) (**A2**). To facilitate the microscopic analysis the photopolymer was removed in the gap. **B; C:** Phase-contrast images of the two electrode layouts after establishment of a confluent NRK cell layer taken with a 4 x objective (**B**) or 10 x objective (**C**) shown for the 2E (**1**) and 4E (**2**) layout.

As shown in **Fig. 5.37 A** the 1st generation ECIS gold-film array contains two different electrode layouts four wells of each type. **A1** shows an enlarged photograph of the 2E electrode layout which is present in well 1 – 4. This layout contains two semi-circular electrode structures, each with a diameter of 500 µm which are separated by a photopolymer-free gap of ~ 500 µm. The active electrode area of one semi-circled electrode was determined to approximately 0.098 mm^2. In the remaining four wells four “semi-elliptical” working electrodes (4E) are present (**A2**) each with an area of around 0.040 mm^2 and also containing a photopolymer-free area for microscopic analysis of the dye transfer. In the 4E

electrode layout the active electrode is characterized by two “semi-elliptical” electrodes and consequently the total surface area is ~ 0.08 mm^2.

Impedimetric Characterization

To further characterize the two different electrode structures, impedance analysis was performed under cell-free and cell-covered conditions. **Fig. 5.38** summarizes spectra for $|Z|$ (**A**), R (**B**) and C (**C**) in a frequency range between 1 Hz – 10^6 Hz for the 2E (○; ●) and 4E (□; ■) electrode layout. For both layouts the mean values with the corresponding standard deviations are shown (N = 4). After formation of a confluent NRK cell layer clear differences due to the insulating properties of the cells were found in the cell-covered spectra compared to the cell-free data. For both electrode layouts, 2E and 4E, the respective $|Z|$, R and C spectra (**A-C**) showed similar behavior. NRK cells are dominating the impedimetric signal over a broad frequency range. For $|Z|_{\text{cell-cov./cell-free}}$ changes were found between 10^3 Hz – 10^6 Hz and the most sensitive frequency for $|Z|$ was ~ 25 kHz for both layouts (**D**). By analyzing $R_{\text{cell-cov/cell-free}}$ (**E**) the sensitive frequency was found to be at ~ 6 kHz and the contribution of the cell layer was visible between 10^2 Hz – 10^5 Hz. However changes in $C_{\text{cell-cov./cell-free}}$ were demonstrated in the higher frequency range, with a maximum change at ~ 63 kHz (**F**).

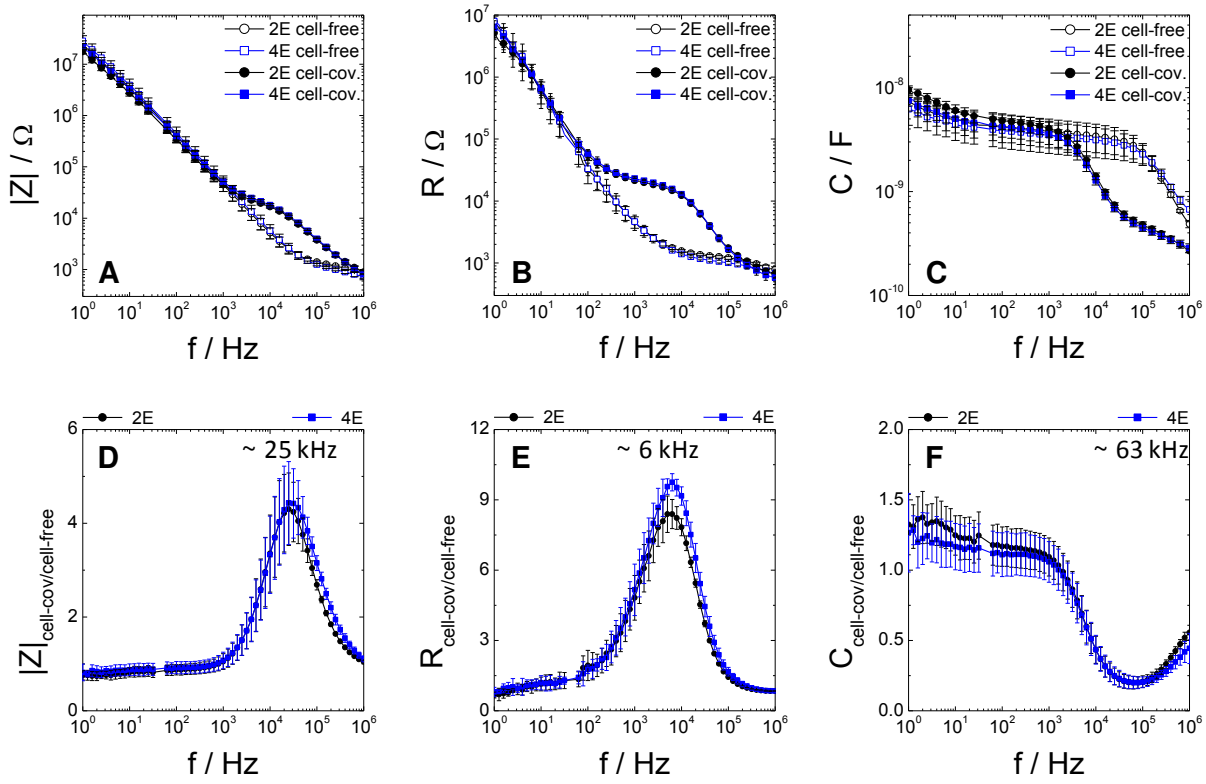

Fig. 5.38: $|Z|$ (**A**), R (**B**) and C (**C**) spectra for cell-free (○; □) and cell-covered (●; ■) 2E (**black**) and 4E (**blue**) electrode layout shown in a frequency range between 1 Hz - 10^6 Hz ‡. For extraction of the most sensitive frequency the normalized spectra are shown in (**D** – **F**) which were obtained by dividing values from cell-covered electrodes by the corresponding cell-free values. This way, the sensitive frequencies for $|Z|$, R and C were determined to 25 kHz (**D**), 6 kHz (**E**) and 63 kHz (**F**). (Mean ± SD, N = 4).

Investigation of the Electroporation Parameters

To evaluate the optimal electroporation parameters for the subsequent application in the gap junctions analysis assay cells grown on the 1st generation ECIS array were electroporated in presence of FITC dextran (250 kDa, 1 mg/mL in EBSS^{-+}) choosing different electroporation parameters. The voltage was varied between 3 V – 5 V and the frequency as well as the pulse duration were kept constant (40 kHz, 200 ms).

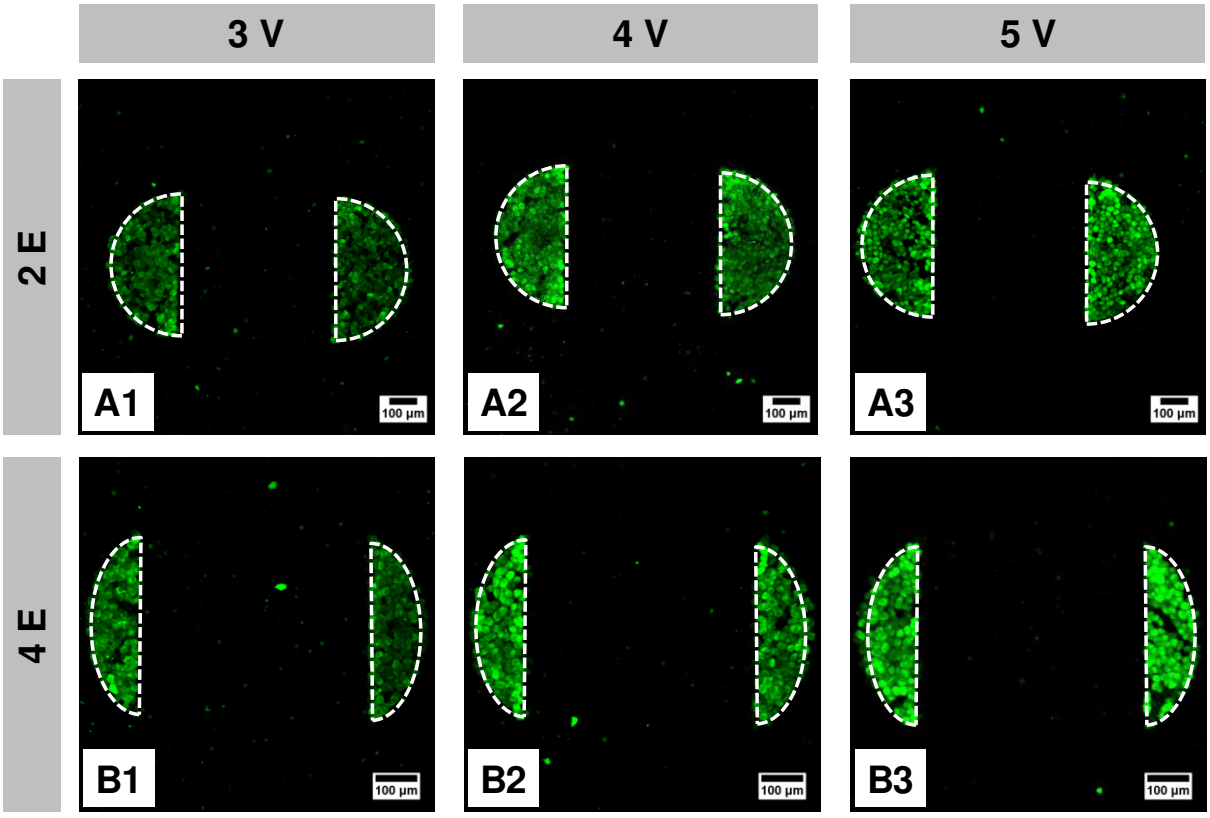

Fig. 5.39: Confocal fluorescence micrographs after electroporation of NRK cells grown on the 2E (**A**) or 4E (**B**) electrode layout in presence of FITC dextran (250 kDa, 1 mg/mL in EBSS^{-+}) using voltages of 3 V (**1**), 4 V (**2**) or 5 V (**3**). The positions of the semi-circled (**A**) or the "semi-elliptical" (**B**) electrodes are defined by the dashed, white lines. Images were taken using the 10 x objective and field zooms of 1.0 (**A**) or 1.5 (**B**). The scale bar corresponds to 100 µm.

The survey of fluorescence micrographs in **Fig. 5.39** clearly shows that cells with green fluorescent FITC dextran inside the cytoplasm are located directly on top of the semi-circular or "semi-elliptical" electrodes. In addition, for both electrode layouts an increase in fluorescence intensity was found by increasing the voltage from 3.0 V to 4.0 V. A further increase to 5.0 V also showed bright fluorescence, although the fluorescence signal was not as homogenous as in the case of 4.0 V. **Fig. 5.40** exemplarily shows fluorescence micrographs of one electrode after electroporation under each condition using a higher magnification. In good agreement with the images taken with the 10 x objective, the best and most homogenous result was found after applying the pulse with 4.0 V. Regardless of

electrode type 2E or 4E, pulse parameters of 40 kHz, 200 ms and 4 V were found to yield the best results.

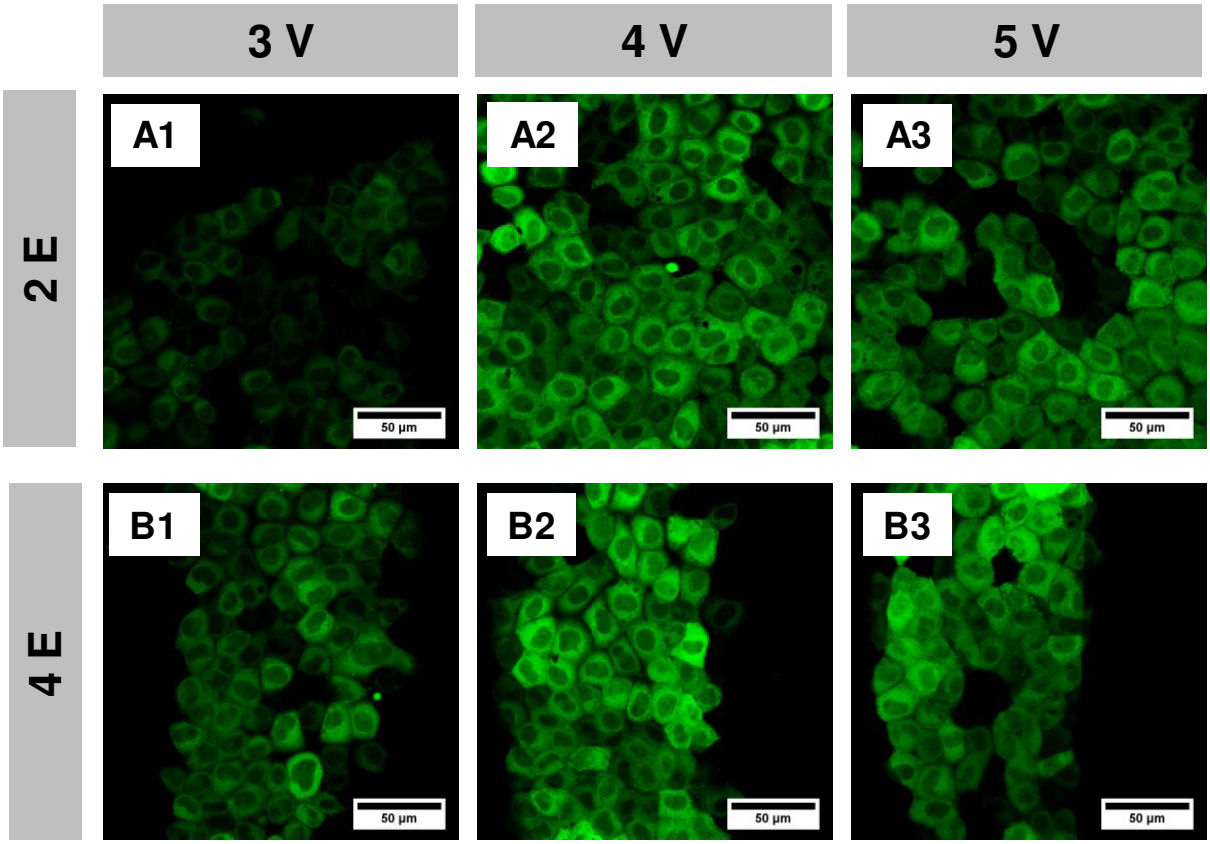

Fig. 5.40: Confocal fluorescence micrographs after electroporation of NRK cells grown on the 2E (**A**) or 4E (**B**) electrode layout in presence of FITC dextran (250 kDa, 1 mg/mL in $EBSS^{-+}$) using varying voltages of 3 V (**1**), 4 V (**2**) and 5 V (**3**). Images were taken using the 60 x W objective. The uptake efficiency clearly depended on the applied voltage. The scale bar corresponds to 50 µm.

To further improve the statistic evaluation of electroporation studies investigating gap junctional intercellular communication the electrode layout was modified. In this 2nd generation layout, only the electrode layout containing four electrodes per well (4E), was implemented in all eight wells. In this new array, called **8W4E-GJ**, four different positions can be analyzed in each well with respect to dye transfer through gap junctions.

5.5.4.5 Quantification and Dye Transfer Analysis Using 8W4E-GJ Electrode Layout

For the investigation of gap junctional intercellular communication with the new impedance based opto-electrical assay the electroporation of NRK cells was performed in presence of two differently-sized fluorescent dyes: TRITC dextran (155 kDa) and Lucifer Yellow (457.3 Da). The 8W4E-GJ gold-film electrode layout allows for quantification of dye transfer at four different positions in one well. Therefore, a strategy was developed to analyze the confocal laser scanning micrographs.

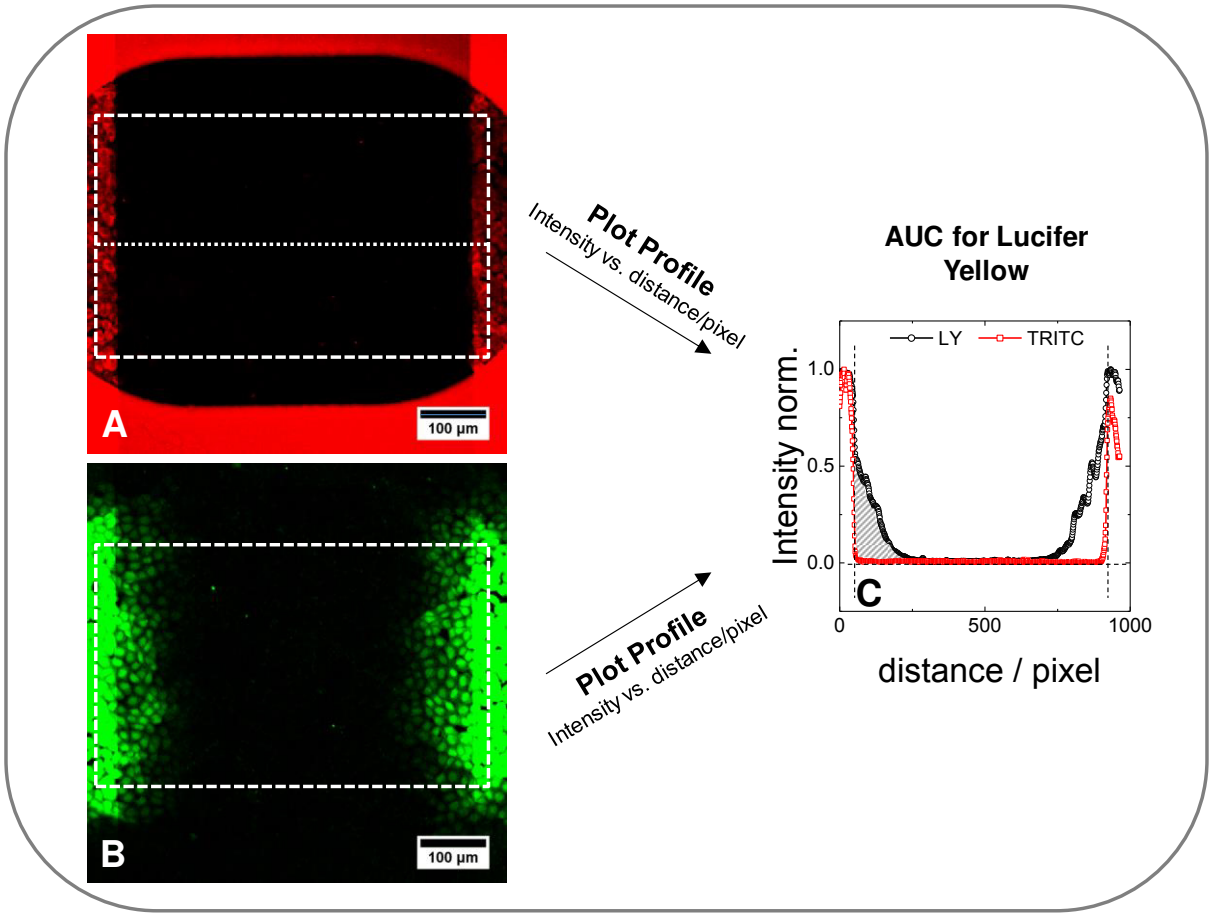

Fig. 5.41: Dye transfer analysis based on calculation of the *area under the curve* (AUC) of the intensity profile of Lucifer Yellow: The fluorescence micrographs recorded from Lucifer Yellow and TRITC-loaded cells on 8W4E-GJ electrodes were analyzed separately (**A;B**). A similar region of interest (white, dashed square) with a defined size was analyzed in the green and red channel regarding their pixel intensity as a function of distance. The plot profiles were normalized to their maximum value and the AUC of Lucifer Yellow was analyzed using the normalized intensity of TRITC dextran as integration limits on the x-axis whereas the y-value was set to zero.

Lucifer Yellow and TRITC dextran fluorescence micrographs from the same position within the sample were recorded separately and image analysis was performed using ImageJ. A constant region of interest (ROI) with dimensions of 370 µm x 600 µm was chosen for further analysis. This ROI was positioned with the left and right frame directly over the “semi-elliptical” electrodes, whereas the main focus of this ROI was located in the photopolymer-

free gap between the two electrodes. In the following the same ROI was individually analyzed for the green and the red channel. For each channel the intensity profile within the ROI was calculated where the x-axis represents the horizontal distance through the ROI and the y-axis displays the vertically averaged pixel intensity within the red and green channel, respectively. The images of the red channel (**A**) were suitable for detecting the incorporation of TRITC dextran into NRK cells on the gold-film electrodes as a result of electroporation, whereas the green channel (**B**) allowed the analysis of primary loading and dye transfer of Lucifer Yellow via gap junctional intercellular communication. In the following the plot profiles of Lucifer Yellow and TRITC dextran were normalized with respect to their maximum values (Intensity norm.) and plotted as a function of pixel distance (**C**). Based on this diagram the area under the curve (AUC) of Lucifer Yellow was calculated. For this purpose, the y-threshold was set to zero and the limits of integration on the x axis were adapted to the respective normalized intensity profile of TRITC dextran. Consequently, only the dye transfer into the photopolymer-free gap was analyzed, whereas the intensities directly on the electrode as a consequence of primary loading were excluded from the AUC calculation. For better comparison of different experiments the calculated AUC were normalized to the respective AUC in presence of the inhibitor 2-APB. For the analysis of dye transfer after single and two pulse electroporation the AUC data were normalized to the value after single electroporation. For the final presentation of different diffusion properties the distance in pixel was transferred to a µm-scale.

5.5.4.5.1 Dye Transfer after Single and Two-Pulse Electroporation

In the following the optimized 8W4E-GJ electrode layout was used to analyze the effect of pulse number, one or two pulses, on dye transfer via gap junctional intercellular communication.

Fig. 5.42 exemplarily shows fluorescence micrographs of NRK cells after single electroporation (**1**) and two-pulse electroporation (**2**) and the normalized intensity plot for the different examples (**C**). The green channels (**A1 – A2**) showed a bright intensity of Lucifer Yellow on the gold-film electrode as well as green fluorescence intensity in the gap. The fluorescence intensity decreased with increasing distance from the electrode. Obviously, in **B1 – B2** the red fluorescence of TRITC dextran (155 kDa) was strictly limited to cells directly on the gold-film electrodes. Due to the size limit of gap junctions of 1 kDa no dye transfer of the reference dye TRITC dextran was found in the adjacent cells located in the gap between the electrodes. As described before, the rectangular ROI was chosen for the red and green channel and analyzed separately with respect to the intensity of each channel.

The two diagrams **C1** and **C2** clearly demonstrated a sharp decline of the normalized intensity of TRITC dextran, whereas the decrease in the green channel was smoother and clearly exceeded the border of the electrode. Additionally, a significant effect of the second pulse was found in the fluorescence micrographs as well as in the intensity plot. The dye transfer into the gap was enhanced for two electroporation events resulting in a higher fluorescence intensity.

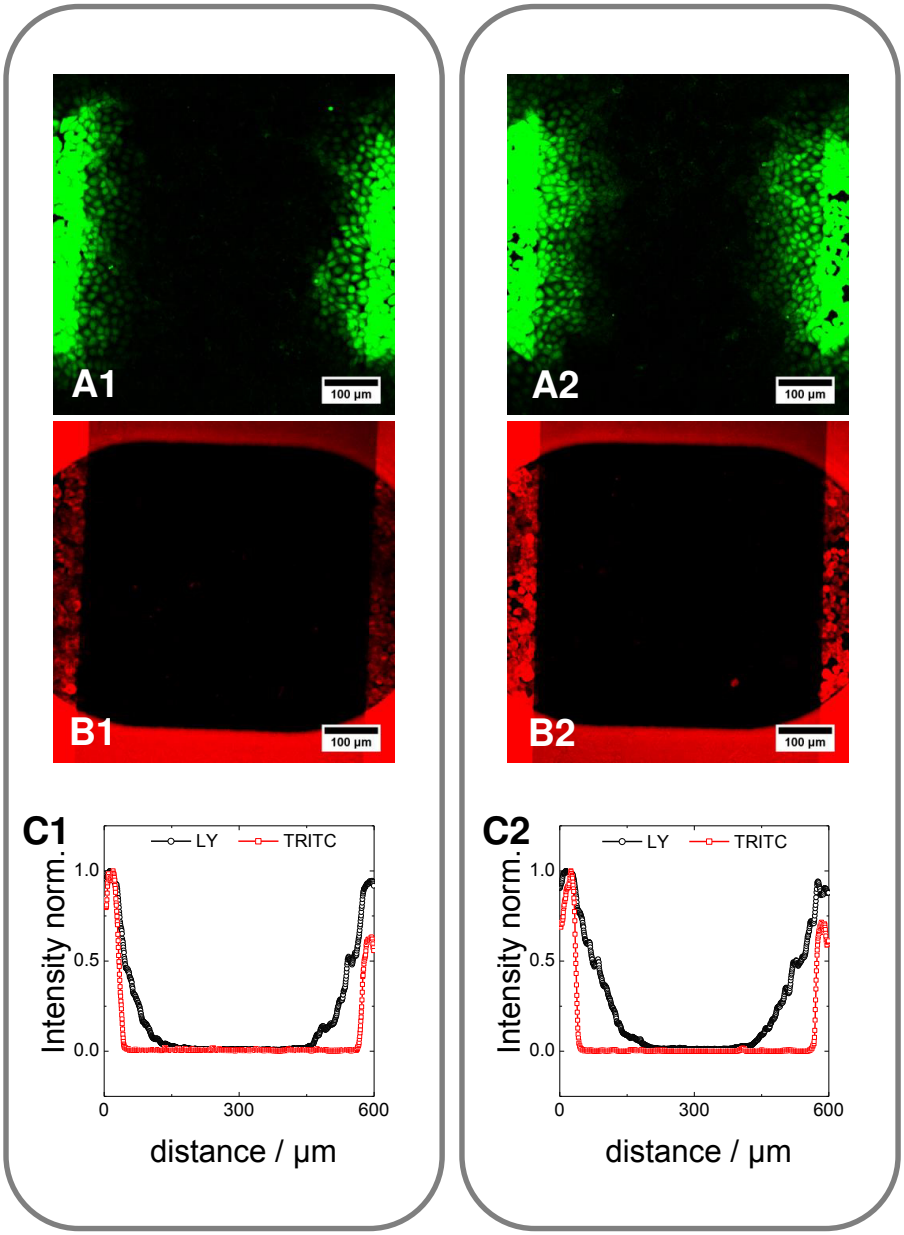

Fig. 5.42: Confocal fluorescence micrographs of NRK cells after electroporation in presence of Lucifer Yellow (**green**, **A**) and TRITC dextran (**red**, **B**) using a single electroporation pulse (**1**) or two pulses (**2**) that were 15 min apart. Obviously, Lucifer Yellow was transported via gap junctions into the neighboring cells (**A**). Cells located directly on the gold-film electrode showed a bright green fluorescence, whereas the intensity of Lucifer Yellow in the gap was decreasing with increasing distance from the electrode. Due to size exclusion of gap junctions for substances above 1 kDa TRITC dextran was only detected inside the cytoplasm of cells grown directly on the electrode (**B**). Normalized intensity was plotted as a function of distance (**C**) for TRITC dextran (□) and Lucifer Yellow (○).The scale bar corresponds to 100 µm.

In good agreement with the results obtained in the experiment with circular gold-film electrodes (**chapter 5.5.4.1**) also for the new electrode layout the intensity of the dye transfer via gap junctional intercellular communication was enhanced by a second electroporation pulse. **Fig. 5.43 C** shows the results from three independent experiments where seven images are summarized**.** The calculated AUC for the two pulse experiments were normalized to the AUC of the single pulse experiment. However, different cell passages clearly showed deviations regarding their degree of gap junctions-mediated dye transfer even though experimental conditions like seeding density, days on the electrode and medium exchange prior to the experiment were strictly controlled. In some cases dye transfer into a high number of adjacent cells was found (**A**) and in other experiments, NRK cells only showed a weak ability to conduct transport of Lucifer Yellow into neighboring cells (**B**). In summary, a higher AUC and thus an increase in dye transfer was achieved by applying two electroporation pulses compared to single electroporation only.

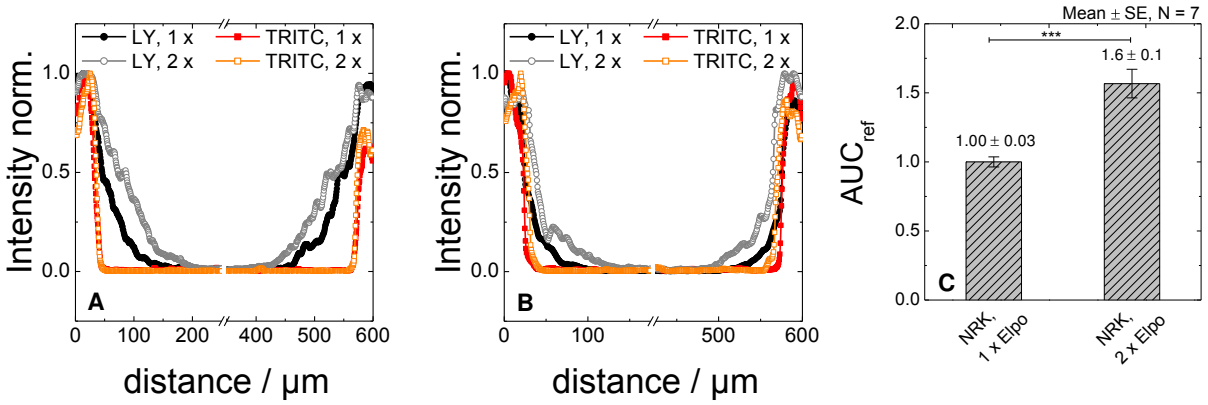

Fig. 5.43: A;B: Normalized intensity as a function of distance for examples of high (**A**) and medium (**B**) gap junctional intercellular communication between different passages of NRK cells after single (filled symbols) and two-pulse electroporation (open symbols) in presence of Lucifer Yellow (○; ●) and TRITC dextran (□; ■). **C:** Column diagram of AUC_{ref} for NRK cells after single and two-pulse electroporation. Values were normalized to the AUC obtained with NRK cells after single electroporation (Mean ± SE; N = 7). Significance was determined by a two-sample t-test using a significance level of 0.01 (***).

5.5.4.5.2 Studying the Influence of 2-APB and Calcium

The electroporation-mediated gap junctional intercellular communication (GJIC) assay in presence of Lucifer Yellow and TRITC dextran was conducted for control cells in buffer w/o Ca^{2+} (**1**), in presence of the literature-known GJIC inhibitor 50 µM 2-APB (**2**), and in presence of Ca^{2+} which is a natural regulator (**chapter 5.1.2**) of GJIC (**3**). **Fig. 5.44** exemplarily shows a survey of fluorescence micrographs after electroporation in presence of Lucifer Yellow and TRITC dextran (**A; B**) and the normalized intensity diagram for the red and the green channel in a defined ROI (**C**). As different cell passages clearly showed deviations regarding their degree of gap junctional intercellular communication only one typical image per condition is shown in the following.

TRITC dextran (155 KDa) was exclusively detected inside the cytoplasm of cells which were attached on top of the "semi-elliptical" gold-film electrodes and served as reference dye to identify cells which were loaded by electroporation (**B**). Consequently, the photopolymer-free gap of ~ 500 µm, where no electroporation occurred completely appeared black in the red channel (**B1 – B3**) indicating no dye transfer.

However, in the green images the fluorescence signal was not limited to the cells on the electrode, but dye diffusion into neighboring cells was observed (**A1**). In presence of 2-APB the most intense fluorescence was co-localized with the TRITC staining, indicating a successful inhibition of gap junctions communication by the presence of 50 µm 2-APB (**A2**). Additionally, the effect of Ca^{2+} was studied using the electroporation-loading method. Here, also a dye transfer into the periphery of the electrode was observed (**A3**). The different effects of probe size, inhibitor and calcium on dye transfer through gap junctions are again summarized in the normalized intensity diagram (**C1 – C3**).

Obviously a strong difference was found for the profiles of Lucifer Yellow under control conditions in Ca^{2+}-free buffer (**1**) and in presence of 50 µM 2-APB (**2**): In presence of extracellular inhibitor 2-APB no significant differences in the intensity profiles between the red fluorescent TRITC dextran and the green fluorescent Lucifer Yellow were found. The corresponding AUC (as explained in **chapter 5.5.4.5**) for Lucifer Yellow was calculated to 105 for NRK control cells compared to 28 for cells in presence of the inhibitor.

By performing the electroporation in presence of calcium a clear difference regarding the fluorescence intensity of adjacent cells in the photopolymer-free area was found compared to the control cells. Even in presence of Ca^{2+}, Lucifer Yellow was transported via gap junctions from the primary loaded cells, into the neighboring cells in the periphery of the electrode, however with lower efficiency. In presence of Ca^{2+} dye transfer was more inhomogeneous along the straight edge of the electrode compared to the control population. Thus, the

intensity profile of Lucifer Yellow in presence of Ca^{2+} (**3**) was decreasing much steeper compared to the control cells in **1** resulting in an AUC of 49.

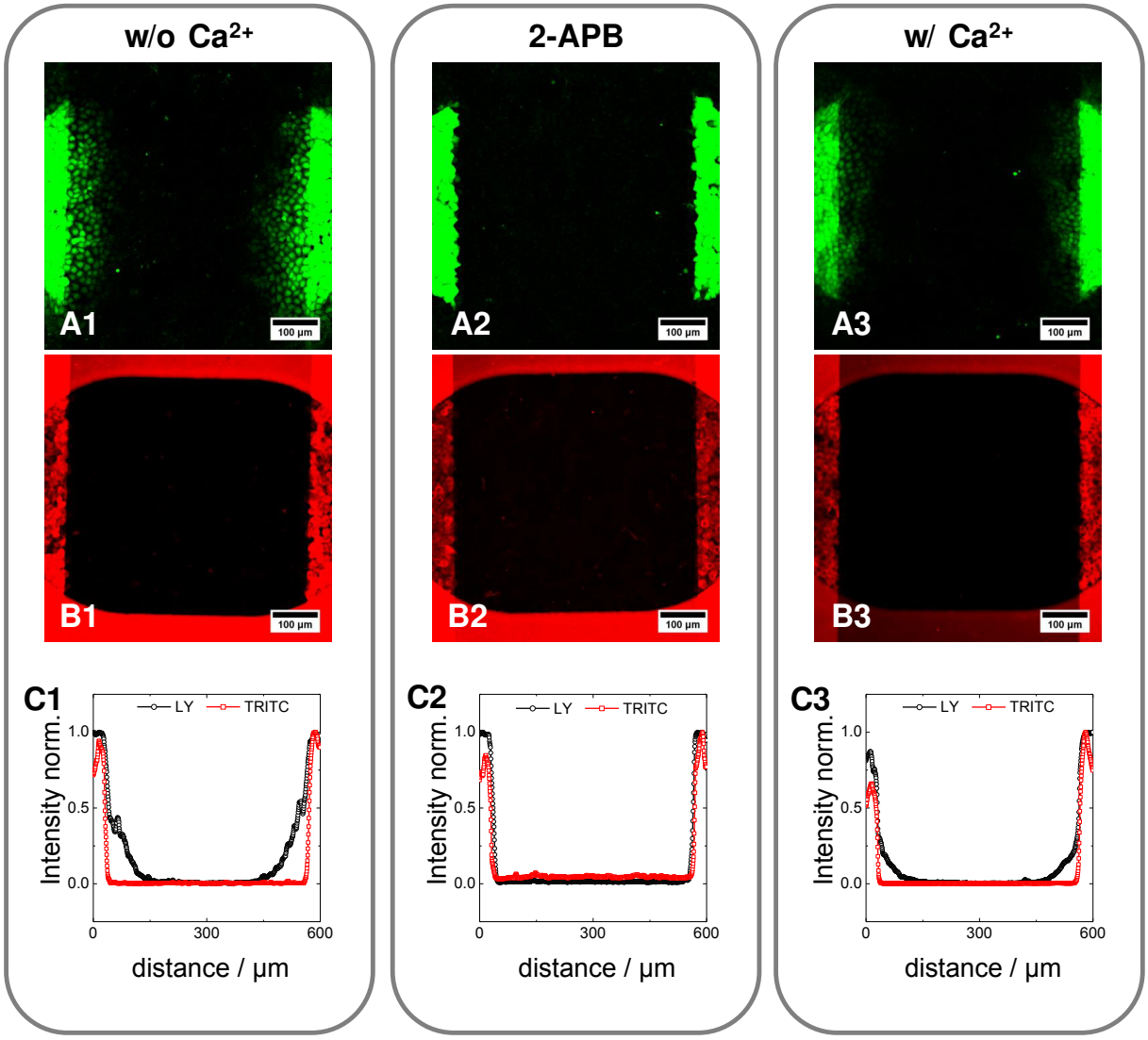

Fig. 5.44: A; B: Confocal fluorescence micrographs of NRK cells after two-pulse electroporation in presence of Lucifer Yellow (**A**) and TRITC dextran (155 kDa) (**B**). Cells were either electroporated in $EBSS^{-+}$ (w/o Ca^{2+}) (**1**), in $EBSS^{-+}$ supplemented with 50 µM 2-APB (**2**) or $EBSS^{++}$ (w/ Ca^{2+}) (**3**). **C:** Normalized intensities of the red and green channel as a function of distance in a defined ROI. The scale bar corresponds to 100 µm.

As emphasized before, the ability of cells to communicate with each other seems to be influenced by many parameters including the cell passage. Therefore, the different experiments can differ in their individual results for dye transfer efficiency. For statistic reasons, data of AUCs under different conditions were normalized using the AUC of cells in presence of the extremely efficient gap junction uncoupler 2-APB in each experiment as reference (AUC_{ref}).

The diagram **Fig. 5.45** summarizes the results of at least three independent experiments where 13 – 16 different sets of images were analyzed regarding their intensity profiles and AUCs.

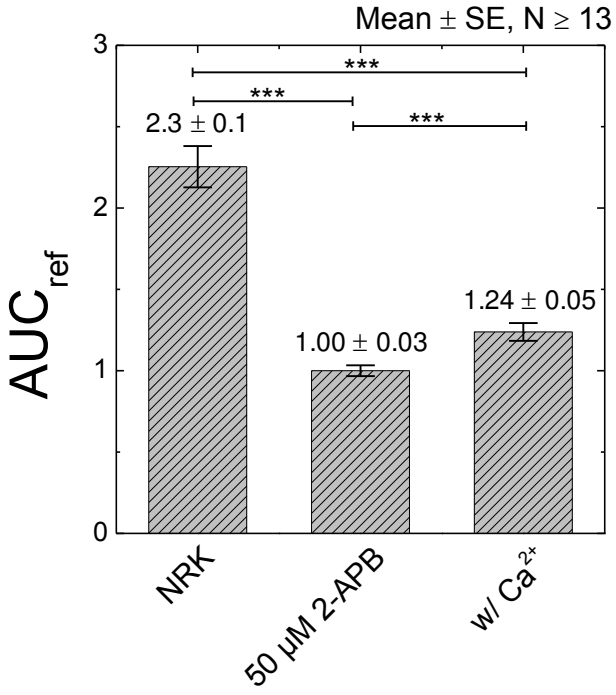

Fig. 5.45: Summary of normalized AUC values of NRK cells, cells in presence of inhibitor and cells electroporated in Ca^{2+}-containing buffer from at least three independent experiments (Mean ± SE; N ≥ 13). Individual AUC values were referenced to the AUC of cells in presence of 2-APB. Significance was determined by a two-sample t-test using a significance level of 0.01 (***).

For NRK cells under control conditions the mean AUC_{ref} was 2.3 ± 0.1 and could be clearly distinguished from the populations with inhibited gap junctional intercellular communication in presence of 50 µM 2-APB (1.00 ± 0.03). Even when the inhibitor did not completely inhibit the dye transfer in some images, Lucifer Yellow propagation was restricted to one or two adjacent cells at the border of the electrode. The dye transfer in presence of Ca^{2+} revealed a clear difference compared to the control cells electroporated in a Ca^{2+}-free environment, which was reflected by an averaged AUC_{ref} of 1.24 ± 0.05.

5.6 Discussion

5.6.1 Improved Electroporation Efficiency by Two-Pulse Electroporation

In this work a dependency of the number of electric pulses on uptake efficiency was confirmed for in situ electroporation of NRK cells grown on ECIS electrodes. A significant increase in fluorescence intensity of cells after electroporation in presence of FITC dextran was achieved with two or three pulses as compared to using only one electroporation pulse. This improvement of electroporation efficiency was also demonstrated using the bioactive compounds sodium azide and bleomycin.

Electroporation describes a technique where the permeability of the cell membrane is increased by pore formation while an electric field is applied [361, 429]. The idea of this thesis' study was, to enhance the uptake efficiency by applying more than just a single *in situ* electroporation pulse, but using two or three sequential pulses.

Ghartey-Tagoe et al. (2004) reported that the total time span of the electroporation pulses defines the uptake efficiency, as they achieved equal results with a single long pulse or multiple shorter pulses [430]. However, Canatella et al. (2009) reported a decrease in cell viability when using a single long pulse compared to multiple short pulses for electroporation of suspended prostate cancer cells [431]. In good agreement, also Kim et al. (2007) found a better transfection and survival rate for the multi-pulse application compared to a single long pulse electroporation when suspended mammalian cells were addressed[432]. The enhanced activity of bioactive compounds after electroporation-mediated uptake into acceptor cells was further described for the delivery of the peptide drug Cyclosporin A into skin [433]. Moreover, the principle of applying more pulses for efficient DNA transfection was performed with *in vivo* tumor models [434], liver cells [435] and muscle cells [344, 436]. Additionally, the multi-pulse protocol was used for the transfection of mammalian cells, like HEK-293 and CHO cells [432] or Caco-2 and T84 cell monolayers [430]. The principle of improving the uptake efficiency by using multiple-pulse electroporation was also successfully demonstrated for transfection of diatom *Phaeodactylum tricornutum* [437] and the uptake of FITC dextran into *Saccharomyces cerevisiae* [438].

For *in situ* electroporation of adherently grown NRK cells, an increase in fluorescence intensity was found after two and three-pulse electroporation in presence of FITC dextran as compared to the single-pulse electroporation (**Fig. 5.18**). Independent of the delay time (5 – 60 min) between individual pulses, the impedance recovered to the pre-pulse level within less than one hour (**Fig. 5.17**) and microscopic analysis revealed that cell layers remained intact. The influence of electroporation pulse number was further investigated

regarding its impact on increasing the cytotoxicity of the bioactive substances sodium azide and bleomycin.

Sodium azide is well-known for its inhibitory effects on mitochondrial electron transport [413, 414] and the respiratory chain complex IV [415-417]. Additionally, it leads to apoptotic [410] and necrotic [411, 412] processes inside the cell. Sato et al. (2008) analyzed the response of rat SCC131 cells to the exposure of NaN_3 with concentrations between 1 mM – 100 mM over 72 h using an XTT assay. In presence of 5 mM NaN_3 the fraction of dead cells increased from 34 % (48 h) to 66 % after 72 h of incubation. Additionally, the group found a significantly decreased content of cellular ATP after 48 h of incubation with 5 mM NaN_3 [439]. Selvatici et al. (2009) analyzed cell viability of rat cortical neuronal cells 24 h after a 10 – 30 min exposure to NaN_3 (1 – 10 mM) using an MTT assay. They found a concentration and incubation time-dependent decrease in cell viability [440]. However, it is reported, that the effect of sodium azide is enhanced when the substance has free access to the cytoplasm of the cells. To overcome the natural diffusion barrier of the cell membrane, Raicu and Mixich encapsulated sodium azide into liposomes and delivered the substance into HEp-2 cells. They found an aberration of the chromatid and chromosome structure in human HEp-2 cells and the effect of encapsulated NaN_3 was significantly higher compared to the addition of free NaN_3 in medium [418]. Stolwijk et al. (2011) introduced 1.5 mM – 15 mM NaN_3 into NRK cells by *in situ* electroporation and monitored the cells over 4 h. Within this period of time the normalized impedance at 4 kHz recovered completely for a concentration of 5 mM, whereas the impedance recovery after electroporation was slightly delayed for 10 mM NaN_3 [323].

These results are in good agreement with the impedance recordings presented in **Fig. 5.19** where the normalized impedance at 32 kHz recovers within ~ 2.5 h for NRK cells electroporated once in presence of 5 mM NaN_3. In presence of 10 mM, however, the pre-pulse values were only reached with a significant delay ~ 3.5 h after electroporation. Applying a second pulse was associated with a longer time period (~ 5.2 h or ~ 7.1 h) until the impedance recovered to its pre-pulse level in a concentration-dependent manner. Further analysis of different experiments regarding the time point until the impedance recovered to 50 % of the pre-pulse value also yielded an increase in norm. $t_{1/2}$ for the two-pulse protocol as compared to the single electroporation experiment in presence of the same NaN_3 concentration (**Fig. 5.19 B**).

The second bioactive compound used for multi-pulse *in situ* electroporation studies was bleomycin. Bleomycin is characterized by a low transmembrane permeability and a high intracellular toxicity [441]. Different groups investigated the effect of bleomycin after electroporation and found an increase in cytotoxicity by 300 – 5000 -fold [327, 442]. During electroporation, bleomycin gains free access to the cytoplasm and subsequently causes

single and double strand breaks to the genetic material inside the cell [443]. Bleomycin is used as anti-tumor drug in electrochemotherapy [336, 444, 445] and has been successful applied during *in vivo* mouse studies [446] and in clinical trials [447]. For this purpose, bleomycin was applied in increasing concentrations from ~ 7 – 350 µM [448, 449]. A combination of *in situ* electroporation and time-resolved impedance recordings after introducing different concentrations of bleomycin was provided by Stolwijk et al. (2011). Here, extracellular bleomycin (100 µM) did not cause any cellular response, whereas for the same concentration being delivered into NRK cells by electroporation a drastic decrease in normalized impedance was found, indicating the cytotoxic effect of bleomycin [323].

In this study the effect of single and two-pulse electroporation of NRK cells in presence of 100 µM bleomycin was monitored finding an enhanced cytotoxicity after applying two pulses (**Fig. 5.20**). Also confocal laser scanning microscopy images after staining the nuclei with DAPI confirmed the cytotoxic effects of bleomycin after delivery into the cytoplasm as round, dead cells were found on top of the electrode (**Fig. 5.21**). The effect of bleomycin was emphasized by inhibiting the migration of unaffected cells from the electrode periphery into the center using cytochalasin D.

In summary, two-pulse *in situ* electroporation significantly enhances loading efficiency for anchorage-dependent cells. This is a crucial advantage especially when extracellular concentrations of the compound are limited due to costs or physico-chemical properties. For the assay development to investigate the gap junctional intercellular communication only two pulses were used with a constant time delay of 15 min in between the pulses.

5.6.2 Assay Development for Gap Junctional Intercellular Communication Screening

5.6.2.1 Requirements for the Model Cell System

For the development of a new gap junctional intercellular communication assay NRK cells were chosen as a model system. Active gap junctional intercellular communication between neighboring NRK cells was proven by dye transfer after scrape loading (**Fig. 5.13**). *A second requirement for the establishment of a new assay format was that NRK cells can be efficiently loaded with tracer dyes by in situ electroporation. Using FITC dextran homogenous dye loading after electroporation was demonstrated (***Fig. 5.29***). In addition, the combination of in situ electroporation with non-invasive ECIS measurements allowed for monitoring of cell layer integrity.*

In literature NRK cells are described to communicate via gap junctions (**Tab. 5.2**). Yao et al. (2010) found that NRK cells are expressing abundant Cx43 as analyzed by Western blot analysis. The authors found a dye transfer into surrounding cells after injection of Lucifer Yellow into single cells via microinjection experiments [450]. Further research addressing gap junctional intercellular communication between NRK cells was provided by Shao et al. (2005). After transiently transfecting NRK cells with Cx43-targeted siRNAs they monitored a reduction of Cx43 expression by Western blot analysis and also a decrease of Cx43 plaques at cell-cell interphases revealed by immunofluorescence microscopy [451]. Jordan et al. (2001) used double-immunolabeling of ZO-1 and Cx43 in NRK-52E cells and reported on a co-localization of both patterns which were predominantly found at the cell boundaries [189].

Tab. 5.2: Survey of structural and functional studies on gap junctions using NRK-52E cells.

Method	Reference
Microinjection	Yao et al. (2010) [450] Feldman et al. (1997) [452]
Western Blot	Shin et al. (2001) [453] Yao et al. (2010) [450]
Immunofluorescence	Savarin et al. (2010) [454] Berthoud et al. (2001) [455]

NRK cells are known as a reliable system for electroporation. Electroporation-mediated transfection of suspended NRK cells with plasmids of interest has been performed with high efficiency [456-458]. However, *in situ* electroporation, with adherent cells being electroporated, holds some advantages compared to the electroporation procedure in suspension: Using anchorage-dependent cells, membrane proteins and the cytoskeleton remain intact and functional during the entire process which also facilitates membrane resealing and recovery. In cell suspensions typically high voltage amplitudes are applied, since a high fraction of the applied voltage drops across the bulk, leading to an unwanted increase in buffer temperature. This disadvantage can be completely avoided by *in situ* electroporation. Wegener et al. (2002) performed *in situ* electroporation of NRK cells on thin-film electrodes and studied the impact of frequency, voltage amplitude and pulse duration on electroporation efficiency quantified by the dye uptake Lucifer Yellow [383]. Further research was published by Stolwijk et al. (2011) who studied the time-course of dye uptake and membrane resealing of NRK cells after electroporation using sinusoidal voltage pulses of 40 kHz, 200 ms and 4 V [323].

In this thesis NRK cells on top of the working electrode were loaded via electroporation with fluorescent dyes. The effect of temperature on pore formation, recovery and uptake during *in situ* electroporation of NRK cells was investigated using differently sized fluorescent probes (460 Da – 2 MDa) at a temperature of ~ 24 °C (**Fig. 5.15**). The results were compared with electroporation-mediated dye uptakes presented by Stolwijk et al. (2011) [323]. Adherent NRK cells can be successfully loaded with fluorescent probes with a molecular weight up to 2 MDa, which corresponds to a hydrodynamic radius of about 15 – 20 nm [459, 460], at 37 °C [323] and 24 °C (**Fig. 5.15**). After electroporation of NRK cells in presence of Lucifer Yellow or FITC dextran (4 – 10 kDa) dye uptake was detected in the entire cytoplasm (**Fig. 5.16**). Using fluorescent dyes with a molecular size of 40 kDa and above resulted in fluorescence signals of FITC-labeled dextrans (40 kDa – 2 MDa) which were excluded from the cell nucleus which can be explained due to the nuclear pore complex exclusion size of 20 – 40 kDa [409]. Fluorescence micrographs with homogeneous fluorescence intensities across the entire electrode area were found for all FITC dextrans (4 kDa – 2 MDa) whereas electroporation of NRK cells in presence of Lucifer Yellow resulted in a more inhomogeneous dye distribution on top of the working electrode.

5.6.2.2 Protocol Optimization for the Opto-Electrical Assay

Gap junctional intercellular communication between NRK cells was investigated using a new opto-electrical assay, when Lucifer Yellow and TRITC dextran were introduced by in situ electroporation into cells directly grown on ECIS gold-film electrodes. To establish a standardized assay the optimization of experimental conditions like buffer composition and time-point of microscopic analysis was necessary.

Gap junctional intercellular communication can be analyzed using different methods. The most sensitive approach to analyze the functionality and the electrical properties of gap junctions is dual whole-cell patch clamp [287]. Moreover, dye transfer-based assays like scrape loading [291], FRAP analysis [288] or microinjection [461] are popular methods. Another principle to selectively load a small cell population with a gap junction-permeable dye is realized by electroporation. One protocol to study gap junctional intercellular communication based on electroporation was published by Raptis et al. in 1994. In their setup, cells were grown on a glass slide that was partly coated with a thin film of electrically conductive ITO. Cells on the ITO side were loaded with Lucifer Yellow by electroporation. Afterwards, cells along the border between ITO and glass were analyzed with respect to dye transfer of Lucifer Yellow into the non-electroporated cells [299]. Moreover, this setup was used by Brownell et al. (1996) to study the effect of cellular c-Ras proteins on gap junctional intercellular communication between mouse mesenchymal cell line (10T1/2 fibroblasts) [462] and by Vultur et al. (2003) to investigate cell-cell communication in cells derived from differently-aged urethane-induced tumors [304]. The layout was further improved and adjusted using two coplanar ITO electrodes to analyze the dye transfer via gap junctions [289, 302]. Geletu et al. (2012) found that high cell density upregulates gap junctional intercellular communication in mouse lung epithelial type II cell line (E10) by analyzing transfer of Lucifer Yellow after electroporation on two co-planar ITO electrodes. The level of Cx43 protein was also determined as a function of cell density by Western blotting. They found a significant increase in both, dye transfer and Cx43 protein level, for E10 cells that were three days post-confluent compared to the same cell line with 90 % confluence [302]. This indicates that gap junction functionality depends on cell-cell contacts and adherens junction formation [463]. Using *in situ* bipolar electroporation De Vuyst et al. (2008) developed an assay to selectively load a small strip-like area of adherent, gap junction competent cells with the fluorescent tracer 6-carboxyfluorescein and monitored the dye transfer at room temperature into connected cells [305].

The effect of calcium on dye transfer was investigated by performing an electroporation experiment in absence and in presence of Ca^{2+}. A decrease in dye transfer ability for NRK cells was found in buffer supplemented with Ca^{2+}.

Calcium is known to have a regulatory effect on gap junctional intercellular communication. By closing gap junctions adjacent cells are electrically and metabolically uncoupled from their neighbors. This has a protective reason, as healthy cells can be separated from damaged or dying neighboring ones [217]. It is assumed that compared to rapid but incomplete channel closure mediated by transjunctional voltages (V_j), changes in Ca^{2+} and H^+ result in a slower but complete gap junctions uncoupling [464]. The role of Ca^{2+} as regulator of gap junctional intercellular communication was addressed by different studies in which dye transfer [306] or junctional conductance [465] were reduced by an increase in intracellular Ca^{2+} concentration. Gap junctional intercellular communication is not gated by other divalent cations and even Mg^{2+} ions with concentrations in the millimolar range did not show any effect on cell-cell communication [218]. The gating mechanism of Ca^{2+} is proposed to be mediated via calmodulin (CaM) as intermediate [208, 466]. This hypothesis was supported by immunofluorescence microscopy when a co-localization of CaM and Cx32 was found in HeLa cells expressing Cx32 [467]. The precise mechanism by which CaM regulates cell-cell communication is still unknown, however it is assumed that CaM interacts directly with some connexins [468, 469]. Lurtz and Louis (2007) analyzed the regulation of Cx43 by Ca^{2+} and proposed two different ways of action [470]. One possible mechanism includes binding of Calcium to cytosolic CaM followed by the association of the Ca^{2+}/CaM complex to the cytoplasmatic part of Cx43 which subsequently induces a conformational change. Alternatively, a calcium-independent association of CaM to Cx43 is proposed where Ca^{2+} induces a conformational change in Cx43 and thus inhibits cell-cell communication. Conformational changes in the extracellular entrance of Cx26 hemichannels were found by Müller et al. (2002). In this study, a decrease in channel diameter from ~ 15 Å to ~ 6 Å was found after the injection of 0.5 mM Ca^{2+} [228]. However, it is not verified if channel closure occurs directly due to increasing Ca^{2+} concentration or if pH changes in combination with calcium ions are responsible for the gating mechanism [471]. Dakin et al. (2005) used three different methods to increase the intracellular Ca^{2+} concentration in intact human fibroblasts: Neither the application of bradykinin, an agonist for the cell surface receptor which finally induces Ca^{2+} release from internal stores, nor the addition of a Ca^{2+} ionophore could inhibit the dye transfer between intact human fibroblasts. However, Thapsigargin (Tg)-induced capacitive Ca^{2+} influx through the plasma membrane store-operated Ca^{2+}-channels significantly inhibided the dye transfer in their study [306]. However, the exact mechanism of Ca^{2+} action is still under investigation and the regulatory role of Ca^{2+} as a physiological modulator is still in dispute [165].

In this work, the effect of calcium after electroporation in presence of $EBSS^{++}$ resulted in a decrease of dye transfer into neighboring cells indicated by a decrease of the corresponding AUC for Lucifer Yellow compared to the experiment in Ca^{2+}-free environment (**Fig. 5.45**). However, the dye transfer was not completely inhibited when 1.0 mM Ca^{2+} was present.

The protocol was further adjusted by determining the best time-point for microscopic analysis. The time-dependent uptake of the fluorescent dyes Lucifer Yellow, TRITC dextran and FITC dextran was investigated. Lucifer Yellow showed a time-dependent behavior whereas similar dye uptakes into the cytoplasm of NRK cells were found using FITC dextran and TRITC dextran.

FITC dextran (4 kDa) did not show any significant difference in dye loading when the dye uptake was analyzed microscopically 5 min or 20 min after electroporation (**Fig. 5.29**). When the fluorescent probe was Lucifer Yellow instead the microscopic images showed a clear time-dependency. The microscopic analysis of NRK cells around 60 min after pulsing in presence of TRITC dextran (155 kDa) and Lucifer Yellow only provided weak and inhomogeneous green fluorescence intensity on top of the electrode, which was almost similar to the background signal but the red-fluorescent TRITC dextran was regularly incorporated into the NRK cells indicating a successful pulse application. In contrast, the fluorescence micrographs of NRK cells 5 min after pulsing were characterized by a high green and red fluorescence intensity at the position of the electrode (**Fig. 5.30**).

Trying to find an explanation for this time-dependent phenomenon two different aspects were taken into account:

(i) One possible explanation could be, that due to gap junctional intercellular communication Lucifer Yellow is transported via these channels into neighboring cells resulting in a significant decrease in intensity on the electrode when delay times between pulsing and microscopic inspection became too long. The dye-dependency can be explained as only Lucifer Yellow can be transported via connexons into adjacent cells whereas FITC dextran is excluded due to the size above 1 kDa from gap junctions-mediated dye transfer.

(ii) The second hypothesis was that the Lucifer Yellow is transported from the cytoplasm of NRK cells back into the extracellular compartment via organic

anion transporters (OATs). Lucifer Yellow is described in literature as a substrate of OATs .

The potential efflux of Lucifer Yellow was further investigated using two different inhibitors. The presence of 50 µM 2-APB during the in situ electroporation did not show any differences compared to the inhibitor-free control and only showed a weak fluorescence signal for cells on the electrode after 60 min (**Fig. 5.31**) indicating that gap junctional intercellular communication is not the reason for the observed decrease in fluorescence intensity. The addition of 1 mM sulfinpyrazone, a literature-known inhibitor for organic anion transporters (OAT), provided similar fluorescence intensities under both conditions. Independent of the post-pulse incubation time of 5 min or 60 min, high fluorescence intensities were detected inside the cells on top of the working electrode which showed that Lucifer Yellow remained inside the cytoplasm over the entire experiment.

When cells after electroporation were additionally stored at 4 °C for 60 min before analyzing dye-uptake into adherent NRK cells via confocal laser scanning microscopy resulted in a homogenous dye loading on top of the electrode. The temperature-dependent dye efflux indicated an energy-dependent efflux mechanism of Lucifer Yellow. Consequently, a dye efflux of Lucifer Yellow via OATs was considered. OATs are present in different epithelial cells and were also identified in rat kidney and liver [472]. NRK-52E cells were described by Sauvant et al. (2006) to be suitable for organic anion transporter studies. They found, that NRK-52E cells express two types of organic anion transporters, rOAT1 and rOAT3 using reverse transcription-PCR [473]. Different fluorescent organic dyes are used to study the energy-dependent transport via OATs like Fura-2 [428], Carboxyfluorescein derivates [474] or Lucifer Yellow [475]. Dinchuk et al. (1992) analyzed dye efflux of Lucifer Yellow in lymphocytes. In this study dye loading was performed using electroporation of suspended Jurkat cells in presence of Lucifer Yellow. They monitored a rapid dye efflux and the fluorescent dye was completely eliminated from the cytoplasm within 2 h. In good agreement to our results, dye efflux was completely inhibited by the presence of 1 mM Sulfinpyrazone. Additionally, the efflux of Lucifer Yellow via organic anion transporter was found to be an energy-dependent process which was completely inhibited by incubation at 4 °C [325].

In summary, our experimental setup can be used as a new assay format to study OATs in adherent cells based on *in situ* electroporation. It allows introducing membrane-impermeable OAT substrates into a selected cell population by *in situ* electroporation and subsequently dye efflux mediated by OATs can be analyzed.

The gap junctional intercellular communication assay was finally performed using a two-pulse protocol where cells were electroporated in buffer without Ca^{2+}. Impedance analysis was stopped 5 min after the second pulse without recording the complete recovery process with ECIS. After several washing steps cells were analyzed immediately using confocal laser scanning microscopy regarding the transfer of Lucifer Yellow into adjacent cells.

As the dye transfer between gap junctions-connected cells is known to be a fast process the analysis of Lucifer Yellow transfer into adjacent NRK cells was analyzed already 5 min after pulsing. Raptis et al. (1994) performed a kinetic study of the dye transfer investigating a time frame between 30 s and 10 min after electroporation and found that dye transfer was completed within 3 min [299]. In good agreement, Lucifer Yellow movement from electroporated cells into neighboring ones was also analyzed by other groups 2 min [300] or 5 min [304] after electroporation. After performing bipolar *in situ* electroporation of C6 glioma cells in presence of 6-carboxyfluorescein, dye uptake and transfer was even analyzed 30 min after electroporation [305].

In this work, an enhanced uptake of Lucifer Yellow into the cytoplasm of NRK cells grown on the electrode was established using the two pulse protocol. Additionally, the quantification of dye diffusion into adjacent cells was simplified by the increase of Lucifer Yellow uptake on the electrode (**Fig. 5.43**). Impedance recordings were stopped 5 min after applying the 2nd electroporation pulse. The confocal laser scanning micrographs successfully revealed transfer of Lucifer Yellow from the primary loaded cells on the electrode into the photopolymer-free gap via gap junctions (**Fig. 5.42**). As already discussed above, a shorter post-pulse period was preferred, as longer incubation times led to Lucifer Yellow efflux from the cytoplasm and did not allow an analysis of dye transfer via gap junctions. The experimental setup finally allowed a quantification of Lucifer Yellow transfer from pre-loaded cells into neighboring NRK cells. 2-APB was found to inhibit gap junctional intercellular communication between NRK cells as a significant decrease in dye transfer was found compared to the control cells.

2-APB is described in literature as a blocker of intracellular Ca^{2+}-signaling by inhibition of IP_3-induced Ca^{2+}-release and TRP channels including store-operated Ca^{2+} channels [476]. Additionally, Harks et al. (2003) showed that 2-APB completely and reversibly blocks gap junctional intercellular communication between NRK-49F fibroblasts due to electrical and chemical uncoupling of the cells. They found that within 0.5 min after adding 50 µM 2-APB the steady state current was partially reduced. After washing out, the current returned to its initial level. The group suggested an extracellular mode of action since applying a higher concentration within the patch pipette did not affect electrical coupling between NRK-49F cells [245]. A dose-dependent and reversible inhibition of Cx50 gap junction channels was

found by Bai et al. (2006) using dual-patch clamp analysis of neuroblastoma cells (N2A) [243]. The group pointed to a connexin-dependent inhibition efficiency for 2-APB which can be useful for selectively blocking certain channel types. This characteristic set 2-APB apart from other uncoupling substances which exhibit poor selectivity for different channel types. Using low concentrations of 2-APB (20 µM) gap junctional intercellular communication between channels composed of Cx36, Cx40 and Cx50 were selectively blocked with IC_{50}-values between 3 µM and 4 µM. On the other hand an IC_{50}-value of 51.6 µM was found for Cx43 channels [243]. Bathany et al. (2010) also analyzed the inhibitory effect 100 µM of 2-APB on dye transfer between NRK-49F cells using a microfluidics-based assay. An inhibition of 89 ± 7 % was found for the relative fluorescence intensity of 5-(6)-carboxyfluorescein diacetate (CFDA) in a defined region. Additionally, they observed similar inhibitions using three different fluorescent dyes, Calcein, Oregon Green 488 and CFDA in presence of 100 µM 2-APB [320]. The sensitivity of Cx43 channels towards the literature-known inhibitors, 100 µM 2-APB and 0.8 mM 1-heptanol were analyzed by Ye et al. (2011) in multiple 1-D cell arrays in real-time. In NRK-49F cells a complete and reversible inhibition of CFDA transfer was found after 2-APB was applied to the system. In presence of heptanol dye transfer was reduced to the first acceptor cell [246] by non-selective modulation of the lipid structure around the connexins [240]. Another mechanism for the action of 2-APB was hypothesized by Ye et al. (2011). The authors suggested that 2-APB may interact directly with the connexins or change the conformation of connexins by interaction with the local lipid membrane [246]. Another strategy to inhibit gap junctional intercellular communication was pursued by Raptis et al. (1994) who blocked dye transfer between F111 cells by acetate treatment [299]. De Vuyst et al. (2008) incubated Cx32 or Cx43 stably transfected C6 cells with 25 µM carbenoxolone to decrease gap junctional intercellular communication [305].

In this study, the fluorescence micrographs and the corresponding position-dependent intensity profiles clearly showed a strong influence on gap junctional intercellular communication between NRK cells to the presence of 2-APB (**Fig. 5.44**). Quantification of intercellular communication between NRK cells was performed by analysis of fluorescent dye transfer of Lucifer Yellow and TRITC dextran using a plot profile and subsequent calculation of the AUC of Lucifer Yellow in a defined region of interest (ROI). A constant ROI with a size of 370 µm x 600 µm was chosen to analyze the dye transfer into adjacent cell. Image analysis was performed with ImageJ, where this ROI was analyzed in a separated plot profile for the red and green channel and subsequently normalized to the maximum intensity value. As the electroporation was performed in presence of gap junction-permeable Lucifer Yellow and TRITC dextran as reference dye the intensity plot of the red channel served as control for primary loading. The dye transfer was than quantified using the AUC which under these conditions only considers the dye transfer into the photopolymer-free gap whereas the

position of the electrode is excluded (**Fig. 5.41**). This way of data analysis provided good information about the degree of gap junctional intercellular communication and showed significant differences between cells in presence of the inhibitor and for control cells. Dye transfer between control cells was 2.3 times higher compared to gap junctional intercellular communication in presence of 2-APB (**Fig. 5.45**). Image analysis of gap junctional intercellular communication is achieved in an acceptable expenditure of time and the mean values of at least two different images per well and condition can be used for quantification.

5.6.2.3 Electrode Layout Development for the Study of Gap Junctional Intercellular Communication

During assay development for the study of gap junctional intercellular communication different gold-film electrode layouts were applied and evaluated regarding their applicability to analyze dye transfer via gap junctions.

In the beginning circular gold-film electrodes were used. **Fig. 5.33** clearly showed differences in dye transfer using the small Lucifer Yellow and the bigger-sized FITC dextran. While the fluorescence intensity of FITC dextran was exactly determined by the electrode area, the small green fluorescent Lucifer Yellow was also detected in cells near the periphery of the electrode. This observation is consistent with the size-exclusion of gap junction channels which was determined to be 1 kDa [477]. The diffusion of Lucifer Yellow through gap junctions was even more pronounced after applying two pulses with an inter-pulse delay of 15 min. Naturally, the fluorescence intensity in the cytoplasm of cells located in the periphery of the electrode border decreased with increasing distance to the electrode. Unfortunately, the red auto fluorescence of the insulating photopolymer prevented the use of TRITC dextran as reference dye to differentiate between dye transfer via gap junctions and dye loading via electroporation. Therefore, a new electrode layout was designed where the photopolymer was removed to facilitate image analysis and to quantify the dye transfer based on gap junctional intercellular communication. The designed layout (8W4E-GJ) was finally produced as gold-film electrodes by Applied BioPhysics. In this layout, each well contains four “semi-elliptical” electrodes and a straight border separates the active gold-film electrodes from a photopolymer-free gap which is used for microscopic dye transfer analysis. The electroporation parameters for NRK cells on gold-film electrodes have been optimized for different layouts and cell types with respect to pulse duration, voltage amplitude and frequency. Evaluation of the loading efficiency and screening for the best pulse parameters are often performed using fluorescent dyes [385, 429, 431], like Lucifer Yellow [383], Propidium Iodide [478] or differently-sized FITC dextrans [323]. The loading efficiency of adherent cells with

membrane-impermeable molecules during electroporation requires sufficient permeabilization of the plasma membrane which can be affected by the pulse parameters. Therefore, it is necessary that the major part of the voltage drops across the cells in order to realize a high degree of membrane permeabilization. Simulations performed by C. Hartmann et al. (2003) showed that using a frequency between 5 – 100 kHz guarantees that a high fraction of the applied voltage pulse drops across the cell layer [479]. Above this frequency the major part is applied to the electrolyte which causes a temperature increase due to joule heating. Wegener et al. (2002) pointed to electrode damages by using ac pulses with frequencies smaller than 10 kHz, which can be explained by a major voltage drop across the electrode-electrolyte interface and induction of electrochemical reactions which may lead to electrode rupture [383]. The cell-type specific optimal electroporation parameters depend on the electrical properties of the cells which are described according to Giaever and Keese by α, R_b and C_m. Using frequency-dependent spectra of $|Z|_{\text{cell-covered/cell-free}}$ an estimation of the relevant frequency range for a successful delivery of membrane-impermeable substances into the cytoplasm of adherent cells by electroporation is possible.

Using the 8W4E-GJ electrode structure, which was designed for the requirements to study gap junctional intercellular communication, the uptake of fluorescent FITC dextran was proven successfully using different voltages (3 – 5 V) but a constant frequency and pulse duration of 40 kHz and 200 ms. Maximum fluorescence intensity as well as the best homogeneity of dye uptake was achieved for 4 V (**Fig. 5.40**) which was further used for the analysis of gap junctional intercellular communication.

5.6.2.4 Comparison with Common Techniques

After optimization of the experimental protocol, a quantification of dye transfer between adherent cells under different conditions was performed. The new opto-electrical assay to study gap junctional intercellular communication provides some advantages compared to established techniques based on dye transfer.

After adjusting the electroporation parameters for the respective cell type and electrode layout, the experiment is simple and easy and requires no special technical skills. The dye loading with optimized electroporation parameters should result in a homogeneous and efficient loading of cells on the electrode with tracer dye. This was reported as a limitation of the commonly used scrape loading assay where no uniform primary loading was achieved along the scrape which later caused inhomogeneous dye transfer through cell-cell junctions [292]. The opto-electrical assay has one big advantage compared to single cell analysis after microinjection or analysis of a limited cell population in a FRAP assay [287] which is that the efficiency of dye transfer can be analyzed as an average over a larger cell population. Using the 8W4E-GJ electrode layout four electrodes can be used for pre-loading the cells with gap junction-permeable Lucifer Yellow and subsequent for the analysis of dye transfer into adjacent cells. Using the developed setup, eight different conditions can be analyzed simultaneously. This allows the analysis of dye transfer between control cells and differently manipulated cells within one experiment using one cell passage with similar experimental conditions. Doing so, the effect of biological variability especially the degree of gap junctional intercellular communication depending on passage number can be eliminated and differences in dye transfer can be more precisely ascribed to their pre-treatments with compounds. In the current state of research the assay is limited to investigate eight different conditions simultaneously during one assay. However, the commercial ECIS device is also available in 96-well-format and by adjusting the electrode layout, the gap junctional intercellular communication analysis can be a reliable tool for screening applications in 96-well-format in the future. When using optimized parameters for electroporation the membrane is not disrupted permanently but ensures a reversible, transient permeabilization without causing cell death. In the scrape-loading assay however, broken membrane integrity and cell death cannot be disregarded. De Vuyst et al. (2008) monitored a lower coupling efficiency by directly correlating the results of classical scratch assay to those of electroporation-based analysis [305].

However, up to now, the elpo-loading assay is limited to a confluent cell layer and no analysis of low density cultures or small cell populations has been realized. One limitation of the assay is it only allows the quantification of dye transfer at a defined endpoint after electroporation and does not provide any information about the kinetic.

The basic principle of the opto-electrical assay is the combination of non-invasive ECIS recordings with *in situ* electroporation of adherent cells on gold-film electrodes. This enables performing a sequence of impedimetric assay with one cell population including cell adhesion and spreading studies, micromotion analysis or toxicity studies prior to electroporation and microscopic analysis of cell-cell communication. This way, the integrity and full functionality of a cell layer can be well controlled before performing the gap junctional intercellular communication assay. When irregularities within the cell layer become apparent from the initial ECIS assays these can be considered for analysis and discussion of gap junctional intercellular communication data.

5.7 Summary

The goal of this work was to develop a new assay format to study gap junctional intercellular communication within adherent cells. For this purpose, an impedance-based opto-electrical assay was developed: NRK cells were loaded with the gap junction permeable dye Lucifer Yellow by *in situ* electroporation using two electroporation pulses. The dye transfer into NRK cells in the periphery of the electrode was afterwards monitored using confocal laser scanning microscopy. The combination of *in situ* electroporation with non-invasive ECIS measurements allowed recording of cellular properties before and after applying the electroporation pulse of 40 kHz, 200 ms and 4 V.

A Ca^{2+}-free environment was chosen as standard condition for the analysis of gap junctional intercellular communication. A second electroporation pulse was found to enhance dye loading efficiency into NRK cells. This was successfully demonstrated using fluorescent dyes and bioactive compounds like bleomycin or sodium azide. During optimization of the electroporation procedure it was discovered that dye loading efficiency as well as the cells' vitality is not dependent on the recovery time after applying the electroporation pulse. Similar uptake behaviors were found for cells in presence of FITC dextran when microscopic analysis was performed 5 min or 60 min after membrane permeabilization. However, when the fluorescent probe was changed to Lucifer Yellow instead, the microscopic images showed a time-dependency which was interpreted as dye efflux via OATs.

Different electrode layouts and materials were used and assessed regarding their applicability for the analysis of gap junctional intercellular communication. Circular electrodes were not an eligible candidate as the surrounding red fluorescent photopolymer and the circular shape hindered a quantitative analysis of the corresponding micrographs. An electrode layout with "semi-elliptical" electrodes was designed and fabricated using ITO-PET foil as substrate and standard photolithography processes. Based on this design, two follow-up layouts with gold-film electrodes were fabricated by Applied BioPhysics that finally consists of eight wells, each containing four "semi-elliptical" electrodes separated by a 500 µm-sized photo-polymer-free gap (8W4E-GJ).

Finally, a protocol for an electroporation-based opto-electrical assay was developed using the two fluorescent dyes Lucifer Yellow and TRITC dextran. Image analysis was performed by ImageJ examining the plot profile in a defined ROI. Subsequently, the AUC between the gap junction permeable Lucifer Yellow and the gap junctions-impermeable TRITC dextran as integration limit was calculated. An inhibitory effect of 2-APB and Ca^{2+} on gap junctional intercellular communication between NRK cells was successfully demonstrated.

5.8 Outlook

Further research on gap junctional intercellular communication based on the assay that was developed in the scope of this work could address the effect of cell-density and time of cultivation of the NRK cells. Goldenberg at al. (2003) found a higher gap junction coupling ability in low density cell cultures compared to confluent cell layers [480] whereas Geletu et al. (2012) reported about an increase in dye transfer with increasing cell density [302]. Therefore, studying the impact of post-confluence time-period and seeding density on the ability to transfer Lucifer Yellow into neighboring NRK cells can be an interesting topic. The study can be supported by Western Blot analysis to identify the present connexin type in NRK cells and also to quantify the respective connexin content under different conditions. Furthermore, the selectivity of NRK cells to transfer different membrane impermeable dyes regarding different charges and sizes can be investigated. In combination with different gap junction competent cell lines a comparison between charge and size selectivity might help to unravel gap junction mechanism. As electroporation is not limited to 37° C but was also successfully performed at room temperature a temperature-dependent study of dye transfer through the cell-cell junctions can provide a better insight into the complex way of communication.

The time-dependent loss of fluorescence intensity after incorporation of Lucifer Yellow into NRK cells, which was assumed to be a consequence of dye efflux via OATs, can be studied in more detail. This can include experiments with different anionic and cationic dyes which are described as substrates of OATs or OCTs. Additionally, a time-dependent analysis of the efflux of Lucifer Yellow can be an interesting topic. These experiments can provide a further insight into this mechanism and can help to confirm our hypothesis.

6 Studying the Impact of Silica Particles on Cell Physiology Using Multimodal, Label-Free Biosensors

6.1 Introduction

The term “nano”, has become popular in scientific literature during the last decades, is derived from the Greek word “nanos”, which means “dwarf”. “Nano” is today associated with the current state of research not only including nanoparticles or nanomaterial but also keywords like “nanofibers”, “nanocavities”, “nanoelectronics” or “nanocrystals” are some examples of topics which gained an increase in popularity over the last years [481]. The statistic in **Fig. 6.1 A** provides an overview about number of publications connected with the keyword “nanoparticles” since the year 2000 and clearly shows the high interest in modern science to develop new materials based on nanotechnology or to analyze the interactions of these particles with the environment to evaluate their risk.

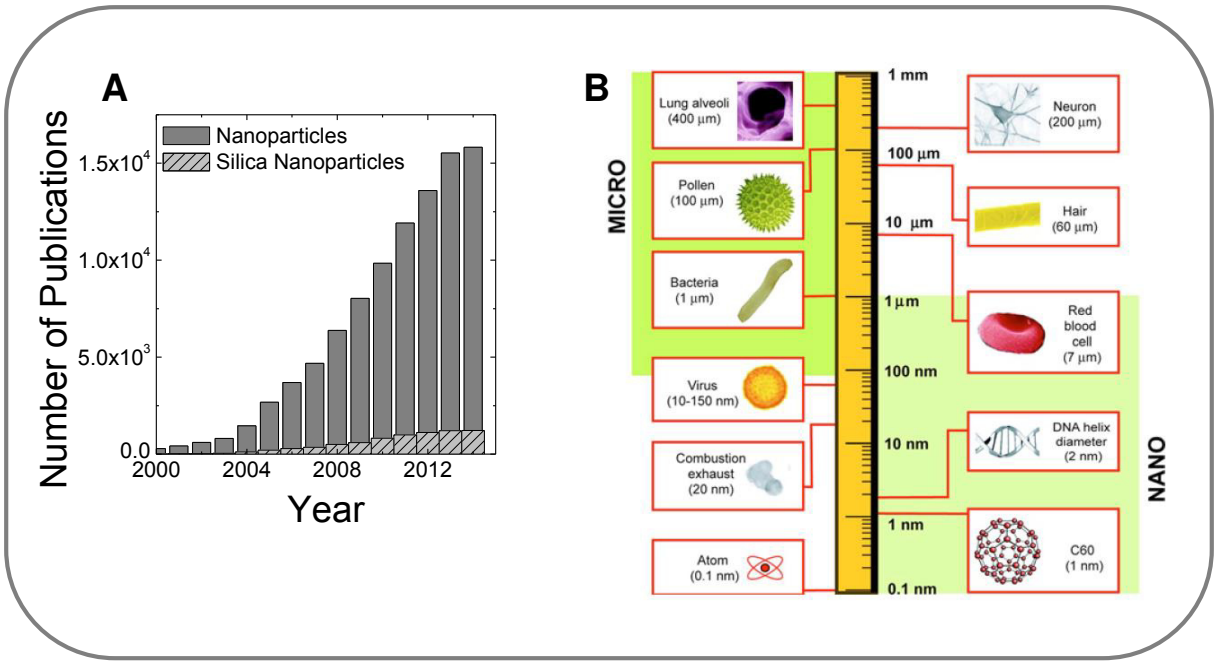

Fig. 6.1: A: Progress in research concerning publications dealing with nanoparticles. The number of publications with the keyword “nanoparticles” or “silica nanoparticles” was taken from Medline[h] over the last 15 years. **B:** Logarithmic length scale to visualize the size of nano- and micro materials compared to biological components adapted with permission from Buzea et al. (2007) [481].

“Nanomaterial” according to the European Commission is defined as “*a natural, incidental or manufactured material containing particles, in an unbound state or as an aggregate or as an agglomerate and where, for 50 % or more of the particles in the number size distribution, one or more external dimensions is in the size range 1 nm - 100 nm*” [i]. However, the definition is not strictly applied and sometimes the term nanoparticle is also applied for sizes up to 1 µm whereas particles with a diameter above 1 µm are categorized as microparticles [481].

[h] www.ncbi.nlm.nih.gov/pubmed

[i] http://ec.europa.eu/environment/chemicals/nanotech/faq/definition_en.htm

In recent years nanoscale particles have received considerable attention due to their unique properties and their application in different areas of life (**Fig. 6.2**): They are applied in cosmetics and health products, in textiles, in paintings and coatings, in energy technologies or in the sector of food and agriculture. Moreover, these particles provide an enormous number of potential applications in biomedical diagnostics and in biosensoric and bioanalytical approaches like the local detection of a specific analyte concentration [482-484].

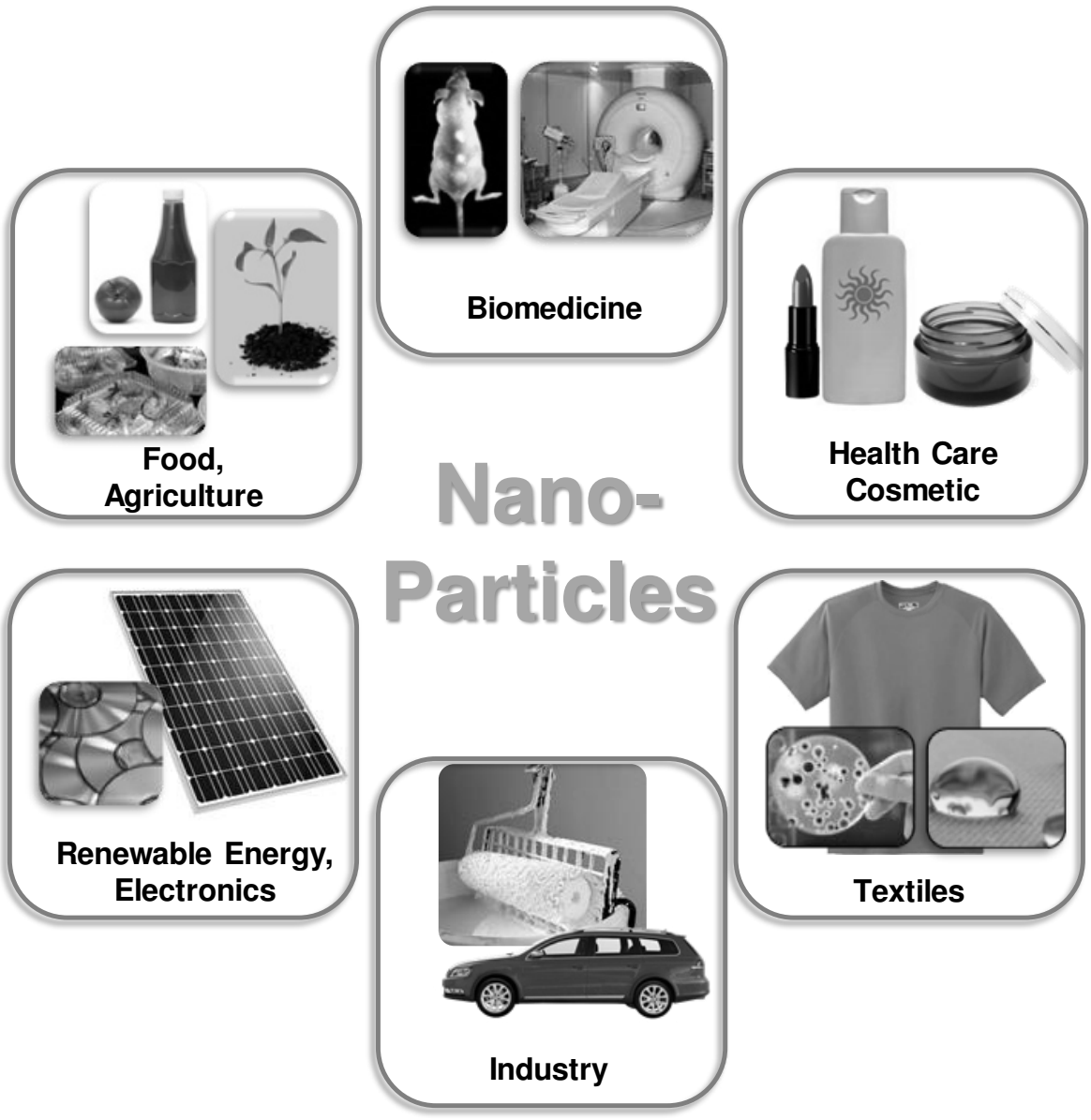

Fig. 6.2: Applications of nanoparticles: In consumer products including cosmetics and textiles, material sciences and electronic engineering, agriculture and food industry and biomedicine.

The properties of nanoparticles depend on the chemical composition, the size and the shape of the particles. Prominent examples of nanoparticles include nanoparticles made of gold or silver, quantum dots (QD), single-wall carbon nanotubes (SWCNT), carbon dots (CD) and titanium dioxide or silica particles. Nanoparticles provide an enormous number of potential applications on the one hand, but on the other, their potential health hazards cannot be

disregarded. Therefore, nanotechnology requires a carefully characterization of the impact and the biological response to nanoparticles to evaluate the risks and opportunities of nanotechnology in combination with biological material.

The impact of (nano-) particles on cell physiology can be analyzed using cell-based assays with an appropriate cell culture model. The cell response is quantified by a label-based or label-free readout.

Many different label-based assays are available to investigate cell-related parameters like cell viability, proliferation or metabolic activity (**Tab. 6.1**). These assays are based on the application of chromophores or fluorescent probes which often react with a certain molecular marker. Subsequently, these labels change their optical properties which allow quantitative description of a certain process. These end-point assays, which only provide information about cellular conditions at one specific time-point, cannot provide any information about the kinetics of cell response. To obtain time-dependent information about cell responses after the addition of a certain stimulus requires replicates which are often limited for reasons of economy. Moreover, these assays only report on a specific pre-defined cell-related parameter and are blind for unexpected cellular responses.

Different strategies are applied in common label-based techniques to investigate cell viability. One principle relies on alterations in membrane integrity and either detects the uptake of a membrane-impermeable dye like Propidium Iodide or Ethidium Homodimer into the cell interior or the efflux of an intracellular molecule, like the enzyme lactate dehydrogenase (LDH) into the supernatant. The readout can be performed by detecting the fluorescence signal where dead cells can be identified by a cell nuclei stain with Ethidium Homodimer or Propidium Iodide. Using the LDH assay red-colored Formazan is produced which can be analyzed by absorbance measurements. When the readout of cell viability relies on metabolic activities MTT, XTT, AlamarBlue® and PrestoBlue® are common assays. The colorless or non-fluorescent precursors are reduced by NADH or $FADH_2$ into a colored or fluorescent derivate and can be quantified by absorbance or fluorescence measurements. Another cell viability assay is based on the hydrolysis of a non-fluorescent dye by intracellular enzymes into a fluorescent tracer. One prominent example is labeling of metabolically active cells by Calcein AM which is converted into the green-fluorescent Calcein by intracellular, active esterases (**Fig. 3.11**).

The analysis of cell proliferation using label-based methods are based on the metabolic activity (as already presented before), on the increase in biomass or on the analysis of DNA/protein synthesis. The increase in biomass detects the total amount of DNA and protein within a sample. Therefore, crystal violet and DAPI are prominent dyes which allow

quantification via absorbance or fluorescence measurements. To evaluate the synthesis of DNA or protein within a sample, differently labeled nucleotides or amino acids are temporary offered in the supernatant and the integration of these components can be used for the analysis of cell proliferation. Labels are available for fluorescence readout which can be performed by fluorescence microscopy and flow cytometry or by the detection of radioactivity when radio-labeled components are used.

Tab. 6.1: Overview of some prominent label-based assays to quantify cell viability or cell proliferation.

Parameter	Indicator	Reagent	Mechanism	Detection
Viability	Dye Exclusion	Ethidium Homodimer, Propidium Iodide	Staining of dead cells (nuclei) with the membrane impermeable dyes	Fluorescence
	Membrane Integrity (LDH Leakage)	Lactate, NAD^+, Diaphorase, Resazurin	Release of intracellular LDH catalyzes the oxidation of Lactate to Pyruvate under NADH production. Reaction cascade leads to the formation of Formazan	Absorbance Fluorescence
	Metabolic Activity (Reducing Coenzymes)	Tetrazolium salts (e.g. MTT, XTT) Resazurin (e.g. PrestoBlue®, AlamarBlue®)	Reduction in presence of coenzymes by living cells	Absorbance Fluorescence
	Enzyme Activity	Calcein AM	Intracellular hydrolysis of the non-fluorescent dye by cellular enzymes leads to staining of the cytoplasm	Fluorescence
Proliferation	Increase in Biomass (Protein)	Crystal Violet	Binding to proteins	Absorbance
	Increase in Biomass (DNA)	DAPI	Binding to DNA	Fluorescence
	Metabolic Activity (Reducing Coenzymes)	Tetrazolium salts (e.g. MTT, XTT) Resazurin (e.g. PrestoBlue®, AlamarBlue®)	Reduction in presence of coenzymes by living cells	Absorbance Fluorescence
	Protein Synthesis	^{3}H-Leu, ^{35}S-Met	Incorporation of radio-labeled amino acids	Scintillation
	DNA Synthesis	^{3}H-Thymidine BrdU EdU	Incorporation of labeled nucleotides	Scintillation Antibodies Click reaction

More convenient is the analysis of the impact of nanoparticles using label-free methods. Here, the cell response is monitored without any additional label using cell-based biosensors where transducers based on acoustical, optical, mechanical or electrochemical methods convert cell responses into a detectable signal. The different label-free methods were already presented in the introduction in **chapter 1**. Using label-free techniques, the cell response is detected as a holistic, integrative signal which does not provide any molecular information about the mechanism behind it. The most prominent principles were shown in **Fig. 1.2** and they all have the common advantage, that these label-free assays are superior to optical assays as (nano-) particles do not interfere with their readout.

6.2 Objective

It was the aim of this chapter was to provide a model study about the information content of multimodal impedance-based assays to assess the cellular response to the addition of (micro)-particles in a label-free manner.

The *in vitro* research about the impact of micrometer-sized silica particles (Ø = 2 µm) on mammalian cell physiology is based on the ECIS-technique (*electric cell-substrate impedance sensing*). Here, the response of mammalian cells can be monitored online with a high time-resolution, instead of analyzing cellular response at one specific end-point. Furthermore, it allows the analysis of multiple cell parameters using one cell population without any additional labeling. The label-free analysis based on impedance measurements is superior to optical assays as the particles do not interfere with the readout. In this chapter a sequential analysis of the cell-related parameters vitality, motility and migration in absence and presence of particles is described. In addition an analysis of the impact of these particles on cell proliferation and gap junctional intercellular communication has been analyzed. Moreover, the analysis of cell-cell communication (presented in **chapter 5**) has been combined with impedimetric measurements and allows an in-depth evaluation of the impact of silica particles on NRK cell physiology within one population.

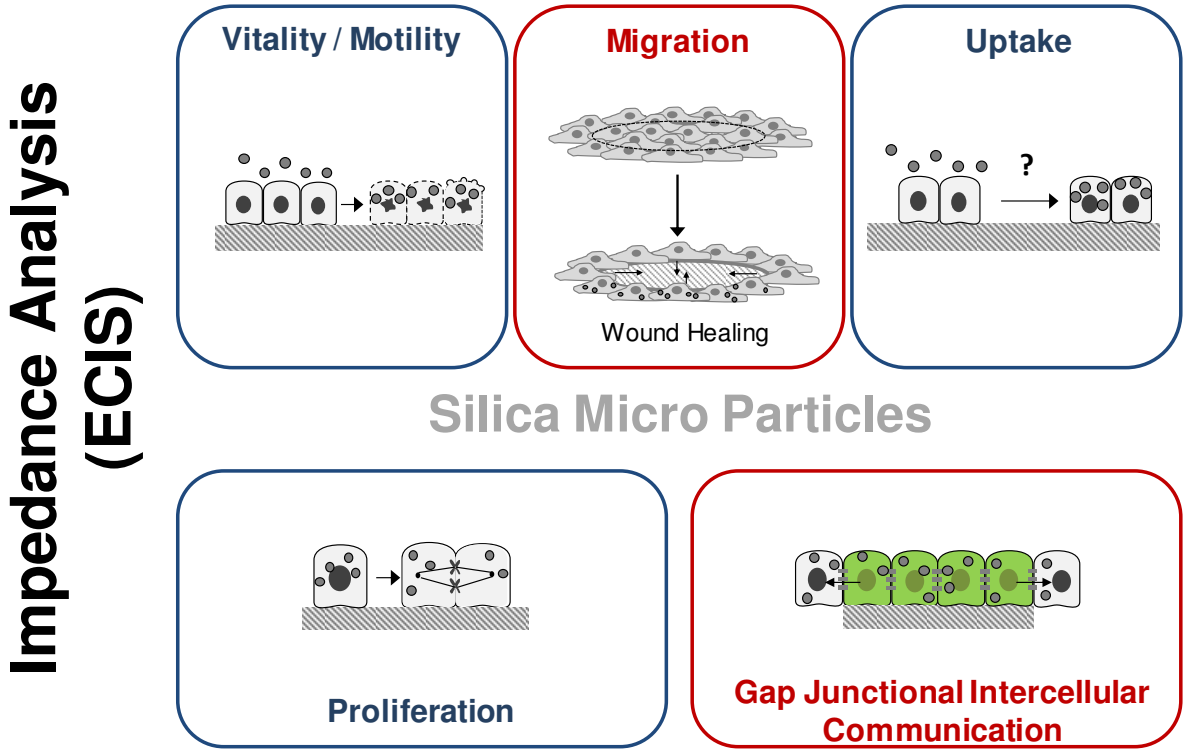

Fig. 6.3: Overview of assays adressubf the impact of silica particles on NRK cell physiology using the ECIS technique. It allows the sequential analysis of different cell-related parameters using non-invasive measurements (**blue**). Additionally, non-invasive recordings after the application of an invasive wounding or electroporation pulse (**red**) can be performed to study cell migration and gap junctional intercellular communication in presence of silica microparticles.

6.3 Materials and Methods

Normally all experiments were performed in serum containing medium. Variations of this standard experimental condition are mentioned in the respective experiments.

6.3.1 Determination of the Zeta Potential

The zeta potential of different particle solutions was measured with a ZetasizerNano ZEN3600 (Malvern Instruments). Therefore, particle stock solutions (**Tab. 6.2**; **Tab. 6.3**) were diluted 1:80 in culture medium supplemented with 10 % FCS (SCM), without FCS (SFM) or in PBS^{++}. One hour after preparation, the stock solutions were diluted 1:5 with dest. water and the zeta potential was measured using three independent measurements.

6.3.2 Microscopic Analysis

6.3.2.1 Time-of-Flight Secondary Ion Mass Spectrometry (ToF-SIMS) Analysis

The principle of SIMS analysis (**Fig. 6.4 A**) includes the bombardment of the cell sample surface with a primary ion beam with high energy (Cs^+ or O_2^+). SIMS imaging was performed using Bi^{3+}-ions after every round of ablation. It leads to the emission of secondary ions originating from the sample surface, which are in the following analyzed in a time-of-flight analyzer with respect to their mass to charge ratio. The sample is investigated layer by layer and the molecular information is registered as a function of depth because of the alternating sputter cycle and analyzing steps. Afterwards, the chemical composition of the cell layer is reconstructed in three dimensions as every spectrum can be assigned to a volume pixel (voxel).

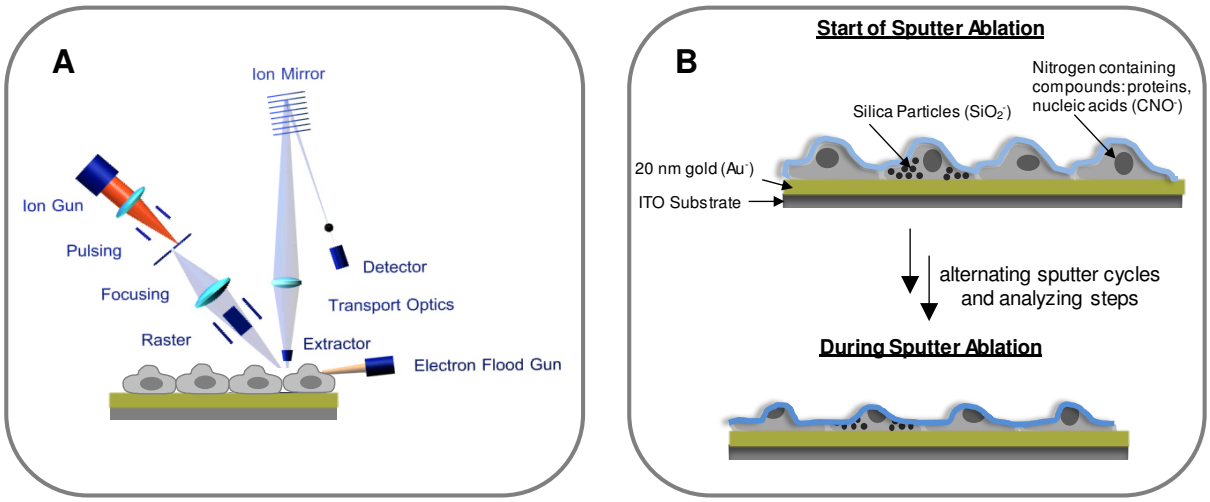

Fig. 6.4: A: Principle of ToF-SIMS analysis, which enables the chemical characterization of a cell sample: The surface is bombarded by ions and resulting secondary ions from the upper surface layer are analyzed with respect of their mass to charge ratio using a time-of-flight analyzer. **B:** Schematic principle of ToF-SIMS analysis to detect and localize silica particles within the cytoplasm of mammalian cells. By using alternating sputter cycles and analyzing steps the cell sample composition can be detected layer by layer and a 3D image of the chemical composition can be created.

For the analysis of particle uptake into NRK cells, cells were grown to confluence on microscopy slides which were sputter-coated with 20 nm ITO and 20 nm Au. When the cell layer was fully established, cells were incubated with silica particles with varying diameters and concentrations for 24 h. Afterwards, culture medium was aspirated and the cell layer was washed twice with PBS^{++} to remove extracellular particles. Cells were fixed with 2.5 % (v/v) GDA in PBS^{++} for 20 min at RT and subsequently washed eight times with water. In the end, water was completely aspirated and sample was dried over night at 37 °C. 3D imaging was performed using a ToF-SIMS.5 instrument and data were recorded in the non-interlaced mode. ToF-SIMS analysis was performed by Tascon GmbH in Münster and more details about image acquisition and experimental procedure can be found in the reference [485].

6.3.2.2 Scanning Electron Microscopy (SEM)

Cells were seeded to confluence on gelatin-coated glass slides (∅ 12 mm) and incubated with silica particles ($4.7 \cdot 10^7$ P/cm^2) for 42 h. For microscopic analysis cells were either washed with PBS^{++} to remove extracellular particles and fixed afterwards or fixed immediately after the end of particle exposure. SEM analysis was performed in the faculty for biology and preclinical medicine by the working group of Prof. Witzgall.

6.3.2.3 Transmission Electron Microscopy (TEM)

Cells were grown to confluence in T25 cell culture flasks and incubated with $3.7 \cdot 10^7$ P/cm^2 for 24 h or 90 h. At the end of particle incubation cells were trypsinized using the cell-type specific protocol. The cell pellet was covered with 1 mL Karnovsky's fixative. Further preparation steps and the image acquisition by TEM microscopy was performed in the University Hospital Regensburg.

6.3.3 Protocols for Impedimetric Measurements

6.3.3.1 Sequence of Impedimetric Assays to Analyze Acute Toxicity, Motility and Cell Migration

ECIS experiments were performed with a confluent NRK cell layer established on 8W1E electrode array. After recording a baseline in culture medium 200 µL of silica particles with increasing concentrations ($7.5 \cdot 10^6$ P/cm^2 – $7.5 \cdot 10^7$ P/cm^2) diluted in culture medium, or culture medium only as control, were added. Impedance was monitored over at least 24 h. Afterwards, RTC measurements were performed (**chapter 6.3.3.5**). Subsequent to the micromotion analysis a MFT experiment was started to analyze cell migration in absence or presence of silica particles. After recording a baseline an invasive voltage pulse (40 kHz,

30 s and 5 V) was applied and all eight wells were wounded simultaneously. Migration of NRK cells in absence or presence of silica particles was analyzed with non-invasive ECIS recordings using |Z| at 32 kHz until a confluent cell layer was re-established.

6.3.3.2 Impedimetric Sequence to Analyze Acute Toxicity in Serum-Free and Serum Containing Medium

ECIS experiments were performed with confluent NRK cell layer established on 8W1E electrode arrays. One day prior the experiment was started 400 µL of serum-free (SFM) or serum containing (SCM) medium was added to NRK cells, respectively. After recording a baseline in 200 µL serum-free or serum containing medium 200 µL of the microparticle solution with a concentration of $3.7 \cdot 10^7$ P/cm^2 were added. Impedance was monitored over at least 72 h after microparticle exposure.

6.3.3.3 Silica Particle Uptake in Absence or Presence of DMA

1 mM DMA (*Dimethyl amiloride*) stock solution was prepared in EBSS^{++} and diluted with culture medium to a final concentration of 100 µM. NRK cells were seeded on 8W1E electrode arrays with a seeding density of 500 000 cells/mL and grown to confluence. One day prior to the experiment medium was renewed. Baseline was recorded in 200 µL culture medium and subsequently DMA was added using a final concentration of 100 µM. After 1 h of pre-incubation in absence or presence of DMA particles in varying concentrations ($1.9 \cdot 10^7$ P/cm^2 – $7.5 \cdot 10^7$ P/cm^2) were added and cellular response was monitored over at least 24 h.

6.3.3.4 ECIS Monitoring of Particle Uptake Dependent on Surface Charge

To analyze the effect of different surface modifications on particle uptake 2 µm silica particles and carboxy or amino modified polystyrene beads were used. ECIS experiments were performed with confluent NRK cell layer established on 8W1E electrode arrays. After recording a baseline in culture medium 200 µL particle solutions ($3.7 \cdot 10^7$ P/cm^2) in culture medium were added. Impedance was monitored over at least 24 h. For the polystyrene beads a pre-treatment was necessary to prevent cytotoxic effects. Therefore, particles were washed four times with medium followed by centrifugation (20 min, 13 000 rpm) before the dilutions in cell culture medium to final concentrations were prepared.

6.3.3.5 RTC Measurements to Analyze Cell Motility

ECIS enables the analysis of cell motion and cell dynamics within a confluent cell layer by detecting the fluctuation in the resistance of a cell-covered electrode using a high time-resolution. This allows analysis of cell motion in the nanometer-scale and correlation with the metabolic activity of the cells. These small changes in cell morphology are often called micromotion. Micromotion or fluctuations of cell shape are metabolically and thermally driven and they change the extracellular current pathways. In this study, micromotion was investigated using the RTC (rapid time collect) mode, where the measurement was performed at one specific frequency (normally 4 kHz) with a time-resolution of 1 point per s over 15 min. The fluctuation in the resistance signal then indicates the dynamics of cells and their metabolic activity.

Analysis and quantification of RTC measurements was performed using a LabVIEW-based software, developed by J. Wegener. With this software the time-course of resistance was analyzed using increment analysis. A data frame of 64 was chosen, which indicates that for further analysis every 64^{th} data point was used. The calculation of the motility index based on every 64^{th} point provided the best sensitivity to detect micromotion with this experimental setup. Therefore, the increments between two subsequent data points i and (i+63) are calculated for the entire experiment. All increments were averaged and the standard deviation to the average was calculated. The standard deviation of the increments (SDI) is a quantitative parameter for the resistance fluctuation in the experiment. A high SDI, also called motility index, indicates a high degree of fluctuation in the recorded time-course due to a metabolically active cell layer.

6.3.3.6 Microscopic and Impedimetric Wound Healing Study in Absence or Presence of Silica Particles

Cells were grown to confluence on 8W1E arrays and culture medium was exchanged one day before starting the experiment. Baseline was recorded in 200 µL culture medium supplemented with FCS. Addition of silica particles (2 µm; $3.7 \cdot 10^7$ P/cm^2) or culture medium as control, occurred during ECIS recordings and the particle uptake was monitored over 24 h. Measurement was temporary paused to remove extracellular particles which were not taken up by the cells, using three washing steps with culture medium. Afterwards, ECIS measurement was restarted and the application of an invasive voltage pulse of 40 kHz, 30 s and 5 V for wounding was performed simultaneously in two wells, one control population and one silica pre-loaded NRK population at a given time. Finally, the ECIS recording was stopped and cells were stained with live/dead stain Calcein AM and Ethidium Homodimer as described in **chapter 3.4.2.2.** The different stages of wound healing were analyzed with confocal laser scanning microscopy.

6.3.3.7 ECIS-Based Analysis of Cell Proliferation

The proliferation experiments started with a cell-free measurement of a 8W10E$^+$ electrode layout which was incubated with culture medium at least for 24 h. For this type of assay cells were grown to confluence in the culture flask for 7 days and a single cell suspension was made following the cell type specific routine for passaging. After centrifugation, cells were counted using a Bürker hemocytometer and the cell suspension was adjusted to 20 000 cells/mL. Then, 400 µL of the cell suspension was seeded into each well and the array was kept in the laminar flow hood for additional 10 min allow for initial cell adhesion. In the following, the electrode array was connected to the ECIS instrument to analyze cell attachment, spreading and cell proliferation. After ~ 20 h medium was exchanged or silica microparticles (2 µm; $3.7 \cdot 10^7$ P/cm^2) were added. The capacitance or the impedance magnitude at 32 kHz was followed with non-invasive ECIS recordings until a confluent cell layer was established.

6.3.4 Label-Based Assays

6.3.4.1 DAPI Staining to Analyze Cell Proliferation

Proliferation analysis of adherent cells is based on the analysis of fluorescence micrographs after cell nuclei staining with blue fluorescent DAPI. Therefore, cells were seeded in a defined, low density of 3400 cells/well in 96-well-plates. At the end of defined incubation times cells were fixed with PFA for 20 min at RT, permeabilized with Triton-X-100 and stained with DAPI (1:10 in PBS^{++}). Cells were washed three times with PBS^{++} and cell proliferation in each well was documented with the inverted microscope (Nikon Diaphot) using a mercury lamp and 10 x magnification objective. Images were analyzed using ImageJ software and the area of fluorescent pixels with a brightness of 255 or the number of nuclei was counted.

6.3.4.2 PrestoBlue® Assay to Analyze Cellular Proliferation

Another optical approach to measure cellular proliferation is performed using the commercially available PrestoBlue® reagent (Invitrogen). Therefore, cells with defined seeding densities were seeded in 37 °C pre-warmed 96-well-plates. After defined incubation times, medium was removed and 200 µL PrestoBlue® (1:10 in PBS^{++}) was added to each well and incubated at 37 °C for 1 h protected from light. As control, 200 µL PrestoBlue® was also added to some cell-free wells. Subsequently, fluorescence intensity of the supernatant was measured (exc. 544 nm, em. 590 nm) using an Ascent Fluoroscan. In order to investigate the influence of silica particles on cell proliferation, a second measurement was

performed after pipetting 100 µL of the supernatant into a cell-free 96-well-plate to exclude an influence of 2 µm silica particles on the readout.

6.3.4.3 PrestoBlue® Assay to Analyze Cytotoxicity

The PrestoBlue® cell viability assay (Invitrogen) was also applied to identify cytotoxicity and was performed according to the manufacturer's instructions. In brief, NRK cells were seeded in a 96-well-plate and grown to confluence. One day before starting the experiment, the cell culture medium was replaced by fresh medium to ensure a standardized metabolic situation during exposure. Particles were diluted in cell culture medium or EBSS buffer. Normally, cells were incubated with the particles for 24 h. One hour before the end of the incubation period 0.5% (v/v) Triton X-100 was added to those wells used as positive controls to induce cell lysis. The supernatant media were then removed and replaced by 200 µL PrestoBlue® reagent (diluted 1:10 in PBS^{++}). After 1 – 2 h of incubation at 37 °C in the dark, 100 µL of the supernatant was transferred into a cell-free 96-well-plate and fluorescence was recorded at 590 nm. For data analysis the detected fluorescence signals were first corrected by the value of the positive control (0.5 % (v/v) Triton-X-100) and the Cytotox-value was calculated using the following equation:

$$\text{Cytotox}\,[\%] = \left(1 - \frac{I_{590\,nm}}{I_{590\,nm}\,(control\ cells)}\right) \cdot\ 100 \qquad \textbf{Eq. 6.1}$$

6.3.5 Analysis of Gap Junctional Intercellular Communication

6.3.5.1 Scrape Loading Assay

The principle and exact protocol of this assay was already presented in **chapter 5.4.3**. To study the influence of silica particles on gap junctional intercellular communication the known protocol was modified. One day prior to the experiment cell culture medium was exchanged or medium was replaced by a silica microparticle solution for the following 24 h. As a negative control, this assay was also performed in presence of 100 µM 2-APB. Therefore, 2-APB was present in every step and also in the PBS^{++} buffer during microscopic analysis.

6.3.5.2 Parachute Assay

The parachute assay allows the analysis of *de novo* gap junction formation. In comparison to the scrape loading assay, the membrane remains intact during the whole process. The principle is based on pre-stained donor cells, which are allowed to adhere on a confluent unstained acceptor cell layer. Depending on the cell specific potential to form gap junctions, dye diffusion into the monolayer can occur and be analyzed microscopically (**Fig. 6.5**).

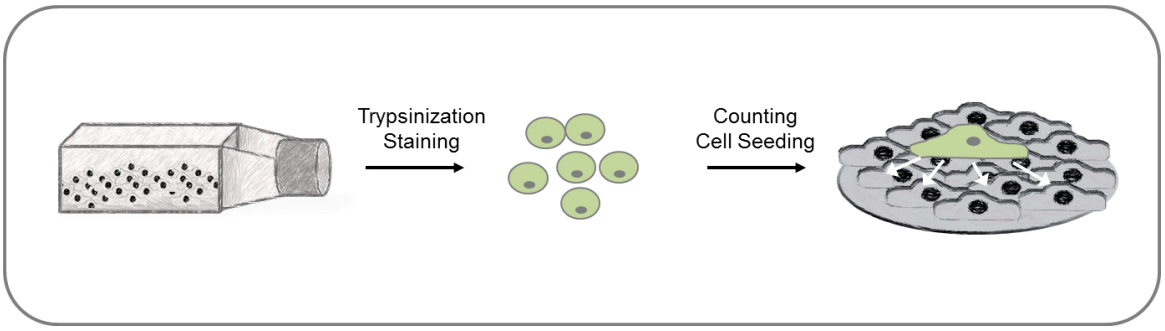

Fig. 6.5: Principle of a parachute assay to study *de novo* formation and functionality of gap junctions: Adhesion of suspended, Calcein AM-stained cells on a monolayer and microscopic analysis of dye diffusion into the acceptor population.

NRK cells of a confluent culture flask were trypsinized following the cell type specific routine for passaging. After centrifugation (RT, 10 min, 110 x g) a single cell suspension was made in PBS^{++} supplemented with 1 mg/L Glucose and containing 3 µM Calcein AM. Cells were incubated with this staining solution for 30 min at 37 °C and 300 rpm. Afterwards, 10 mL medium was added and the cell suspension was centrifuged (RT, 10 min, 110 x g). This washing step was repeated twice to remove the extracellular staining solution. Subsequently, Calcein AM-stained cells were counted and 20 000 to 50 000 cells per well were added to a confluent NRK cell layer established in a 6-well-plate. Stained cells were allowed to adhere and spread for ~ 3 h on top of the confluent cell layer before non-adhered cells were removed by aspirating the supernatant. Cells were incubated for further 30 min before dye

transfer and the formation of gap junctions were analyzed by confocal laser scanning microscopy. When the influence of silica particles on the formation of gap junctions was analyzed the acceptor population was pre-incubated with 2 µm silica particles ($7.5 \cdot 10^6$ P/cm^2; $1.9 \cdot 10^7$ P/cm^2) for 24 h. Pre-loaded NRK cells were washed twice with PBS^{++} before pre-stained cells were added.

6.3.5.3 Fluorescence Recovery after Photobleaching (FRAP) Assay

Another dye transfer-based method to study gap junctional intercellular communication is to monitor dye diffusion microscopically via FRAP assay (**Fig. 6.6**). In this approach the whole cell population was loaded with a small, gap junction permeable tracer molecule (Calcein AM) and subsequently the fluorescence intensity was photo-bleached in a selected area. Afterwards, fluorescence recovery into the cytoplasm of the target cell was monitored microscopically as a function of time.

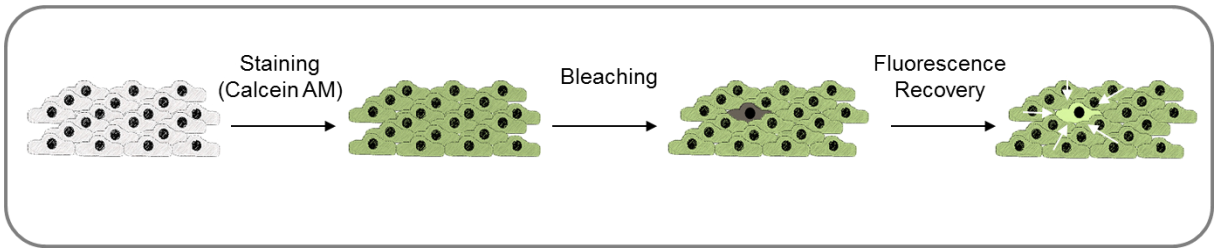

Fig. 6.6: Principle of a FRAP assay: After pre-staining the confluent cell layer with Calcein AM a selected, single cell was bleached by a strong laser pulse and fluorescence recovery was monitored over time.

Therefore, cells were seeded with a density of 250 000 cells/cm^2 in 8-well-chambers glued on top of a cover slip, which later allowed the analysis with an inverted confocal laser scanning microscope. Cells were grown to confluence and stained with Calcein AM (3 µM in PBS^{++}) for 30 min at 37 °C prior to analysis. Afterwards, the staining solution was removed and cells were washed twice with 200 µL PBS^{++}. When gap junction analysis was performed to study the influence of silica particles, cells were pre-incubated with 2 µm silica particles ($3.7 \cdot 10^7$ P/cm^2) for 24 h prior to Calcein AM staining. FRAP assays were performed at a Zeiss inverted microscope (Zeiss Axiovert 200M) connected to a Zeiss LSM 510 scanning device using a 40x/1.3 oil objective. A 488 nm argon laser was used to perform a time-series of 80 – 100 images (512 x 256 pixels) for each cell sample. Single cells were irreversibly photo-bleached by applying a strong laser beam [j] to defined cells. Fluorescence recovery was monitored over time and micrographs were taken every 5 s. FRAP analysis was performed at 37 °C.

[j] An iteration of 125 was used for laser pulse application during the FRAP experiments

As control, gap junctional intercellular communication was inhibited by the addition of 50 µM 2-APB. Therefore, selected cell populations were incubated for at least 15 min with 50 µM 2-APB before the experiment was started. The inhibitor was also present in the buffer during the FRAP experiment.

Data were corrected (**Eq. 6.3**) using a time-dependent correction value (CV) based on **Eq. 6.2** which considered fading of Calcein within an untreated cell. The recovery of the target, photo-bleached cell under different conditions was quantified based on **Eq. 6.4**.

$$\mathrm{CV_{t=x}} = \frac{\mathrm{I_{control,t=0}}}{\mathrm{I_{control,t=x}}} \qquad \textbf{Eq. 6.2}$$

$$\mathrm{I_{bleach,\ t=x}(corr.)} = \mathrm{CV_{t=x}} \cdot \mathrm{I_{bleach,\ t=x}} \qquad \textbf{Eq. 6.3}$$

$$\mathrm{Recovery\ [\%]} = \frac{\mathrm{I_{bleach,\ t=x}(corr.)}}{\mathrm{I_{bleach,\ t=0}(corr.)}} \qquad \textbf{Eq. 6.4}$$

6.3.5.4 Study of Gap Junctional Intercellular Communication in Presence of Silica Particles Based on Electroporation

The underlying protocol to study gap junctional intercellular communication using the opto-electrical assay was described in more detail in **chapter 5.4.3**. Modifications of the basic protocol to investigate the effect of silica particles are described in the following: 24 h after cell seeding NRK cells were pre-incubated with 2 µm silica particles ($3.7 \cdot 10^7$ P/cm^2) for additional 24 h except for the control populations, where only fresh medium was added. Afterwards, non-invasive ECIS recordings were optionally performed to monitor cytotoxicity of the particles during exposure time (MFT experiment) or to analyze the motility of the cells after particle treatment (RTC experiment). Prior to the electroporation experiment, cells were washed twice to remove extracellular particles and the assay was performed according to the basic protocol as described before.

6.3.6 Studies with Cardiomyocytes to Analyze the Influence of Silica Particles

Experiments were performed with Cor.At® mouse embryonic stem cell-derived cardiomyocytes, which were obtained from Axiogenesis. Cells were purchased as frozen cryovials and thawed using the recommended protocol described in **chapter 6.3.6.2**. The cultivation of Cor.At® cells and the experiments were performed at 34 °C and 5 % CO_2. Cor.At® cells were available with or without expressing the green fluorescent protein (GFP) reporter gene. It is known that these cells provide a high ability to perform gap junctional intercellular communication, since they express the cardiac specific Cx43.

6.3.6.1 Materials Used for the Cardiomyocyte Project

Material	Supplier
Cor.At® Cells (w/ or w/o GFP) ($1 \cdot 10^6$ viable cells per cryovials)	Axiogenesis
Cor.At® Culture Medium	Axiogenesis
Fibronectin derived from bovine plasma	Sigma-Aldrich
Puromycin stock solution (10 mg/mL)	Axiogenesis
Isoproterenol hydrochloride	Sigma-Aldrich
2 M stock solution 1-heptanol in DMSO	Sigma-Aldrich

6.3.6.2 Thawing and Seeding Protocol for Cor.At® Cells

Cor.At® culture medium and the puromycin stock solution were thawed over night at 4 °C protected from light. For the selection of cardiomyocytes 50 mL medium was supplemented with 50 µL puromycin stock solution (10 µg/mL). Next day, the cryovial with Cor.At® cells was removed from the gas phase of the nitrogen tank and immediately thawed for 2.75 min at 37 °C in the water bath. Cell suspension was then carefully transferred dropwise to 7 mL culture medium and the cryovial was additionally rinsed once with 1 mL culture medium. Cells were centrifuged at 200 x g for 5 min at RT. The cell pellet was resuspended in 4 mL culture medium supplemented with puromycin resulting in a cell suspension with 250 000 cells/mL.

Prior to cell seeding the appropriate ECIS gold-film electrode arrays (8W4E-micro or 8W4E-GJ) were incubated for at least 24 h with DMEM medium without any supplements. Afterwards, the substrates were coated with fibronectin from bovine plasma (10 µg/mL in PBS^{--}) for 3 h at 34 °C prior to cell seeding. After thawing the cells and preparation of the

cell suspension with 250 000 cells/mL fibronectin solution was removed and immediately replaced by the cell suspension with a final seeding density of 100 000 cells/cm^2. After cell seeding, the ECIS array was kept under the laminar flow hood for 30 min and subsequently transferred into the cell culture incubator (34 °C, 5 % CO_2). Cell attachment and formation of a confluent cell layer was monitored with impedance recordings (MFT). 24 h after cell seeding the medium was exchanged using Cor.At® culture medium supplemented with puromycin. After 48 h the medium was replaced by Cor.At® culture medium without puromycin.

6.3.6.3 Highly Time-Resolved Impedimetric Measurements to Detect Synchronous Beating of Cardiomyocytes

The analysis of synchronous beating of Cor.At® cardiomyocytes cultured on ECIS gold-film electrodes was performed using the RTC measurement mode. Therefore, the software was adjusted by Applied BioPhysics to obtain a resolution of 64 points/s or 128 points/s. The beating efficiency with or without different drugs was recorded over at least 1.8 min per measurement. Data analysis with respect to *beats per minutes* (BPM) was performed by a LabVIEW-based software developed by J. Wegener (2014).

6.4 Influence of Silica Microparticles on Mammalian Cells

6.4.1 Physicochemical Characterization of Silica Microparticles

The main focus of this work was to analyze cellular response upon exposure to silica particles. The analysis of the biocompatibility of a (nano-) material requires a complete physicochemical characterization of the particles in advance.

For this thesis commercially available microparticles made of silicon dioxide (Fluka) with a mean diameter of (2.02 ± 0.04) µm were used. The key parameters of the silica particles are summarized in **Tab. 6.2**.

Tab. 6.2: Physicochemical data of silica particles (∅ 2 µm) as provided from the supplier (Fluka).

Parameter	Silica Particles
Particle Composition	**Silicon Dioxide**
Particle Diameter (Diameter ± SD)	**(2.02 ± 0.04) µm**
Density	**1.8 – 2.0 g/cm^3**
Solid Content	**5 % wt**
Calculated Particle Concentration	**5.99 · 10^9 P/mL**

The uptake of particles by mammalian cells was analyzed with respect to surface charge. Therefore, a second particle type, particles made of polystyrene (Sigma-Aldrich), were applied. Polystyrene beads are available with amine- or carboxylate-modified surfaces and with different fluorescent labels. Their physicochemical characteristics are summarized in **Tab. 6.3**.

Tab. 6.3: Physicochemical data of amine- and carboxylate-modified Polystyrene beads (∅ 2 µm) as provided from the supplier (Sigma-Aldrich).

Parameter	Polystyrene Beads amine-modified	Polystyrene Beads carboxylate-modified
Particle Composition	**Polystyrene**	**Polystyrene**
Dye Characteristics	**Fluorescent blue (λ_{ex} ~ 360 nm; λ_{em} ~ 420 nm)**	**Fluorescent yellow-green (λ_{ex} ~ 470 nm; λ_{em} ~ 505 nm)**
Mean Particle Diameter	**1.90 – 2.20 µm**	**1.80 – 2.20 µm**
Density	**1.04 – 1.06 g/cm³**	**1.04 – 1.05 g/cm³**
Solid Content	**2.5 % wt**	**2.5 % wt**
Calculated Particle Concentration	**5.71 · 10⁹ P/mL**	**5.71 · 10⁹ P/mL**

The zeta potential provides a characteristic parameter to determine the stability of particles in solution and allows characterization of the particle surface charge. The measurements of the zeta potential in different buffer or medium compositions for commercially available silica particles and polystyrene beads with a diameter of 2 µm are summarized in **Fig. 6.7** and **Tab. 6.4**.

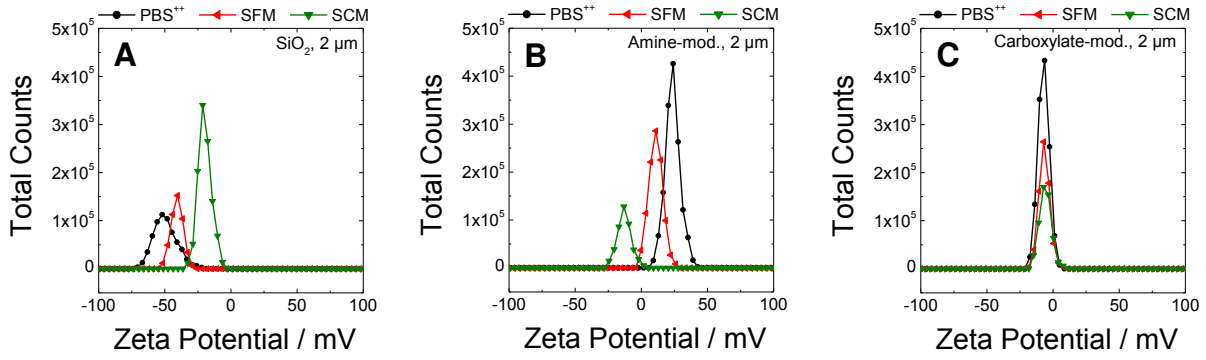

Fig. 6.7: Zeta potential of silica particles (**A**), amine-modified polystyrene beads (**B**), carboxylate-modified polystyrene beads (**C**) measured in PBS^{++} (●), serum-free medium (SFM; ◀) and medium containing FCS (SCM; ▼).

The zeta potential of silica particles exhibited a negative value independent of the buffer or medium composition. In PBS^{++} the corresponding zeta potential was determined to (- 52 ± 1) mV whereas a slight shift to a more positive zeta potential was observed in culture

medium without (- 43 ± 2) mV and with FCS (- 21.1 ± 0.8) mV. As expected, the zeta potential of amine-modified polystyrene beads was positive in PBS^{++} (21 ± 1) mV and serum-free medium (8 ± 1) mV but became negative in presence of FCS (- 14.4 ± 0.7) mV. The zeta potential of carboxylate-modified polystyrene beads was determined at ~ - 7 mV independent of the respective buffer or medium composition.

Tab. 6.4: Zeta potential of silica particles, amine- and carboxylate-modified polystyrene beads. Zeta potentials were determined using three different measurements (Mean ± SE; N = 3).

	Silica Particles	Polystyrene Beads amine-modified	Polystyrene Beads carboxylate-modified
PBS^{++}	(- 52 ± 1) mV	(21 ± 1) mV	(- 7.3 ± 0.8) mV
Serum-free medium (SFM)	(- 43 ± 2) mV	(8 ± 1) mV	(- 6.5 ± 0.3) mV
Serum-containing medium (SCM)	(- 21.1 ± 0.8) mV	(- 14.4 ± 0.7) mV	(- 7.0 ± 0.6) mV

6.4.2 Analysis of Particle Uptake into NRK cells

It is well-known that the number of particles inside the cell normally determines the cytotoxic effect [486] rather than the extracellular concentration. In the beginning of this study it was very important to characterize the uptake of 2 µm silica microparticles into NRK cells in detail. This included studies on temperature-dependency, the mechanism of particle uptake as well as their intracellular localization. The research comprised different methods, like fluorescence microscopy after application of classical staining methods, REM and TEM imaging and ToF-SIMS analysis.

6.4.2.1 Staining Methods

To investigate the uptake mechanism of silica particles into the cytoplasm of NRK cells, confluent cell layers were incubated in presence of particles for 24 h at 4 °C and 37 °C. The incorporation of silica particles into NRK cells was identified as a temperature-dependent process. **Fig. 6.8** summarizes the results after incubation of cells with a suspension of silica particles at 4 °C (**A**) or 37 °C (**B**) in phase-contrast (**1**) and fluorescence micrographs after cell nuclei stain with DAPI (**2**). A significant difference was found in phase-contrast micrographs showing only at 37 °C a densely-packed particle distribution around the nucleus. In contrast at 4 °C particles remained in the supernatant and were not taken up by the cells. These results indicated an membrane-dependent internalization mechanism of silica particles and excluded an uptake via diffusion.

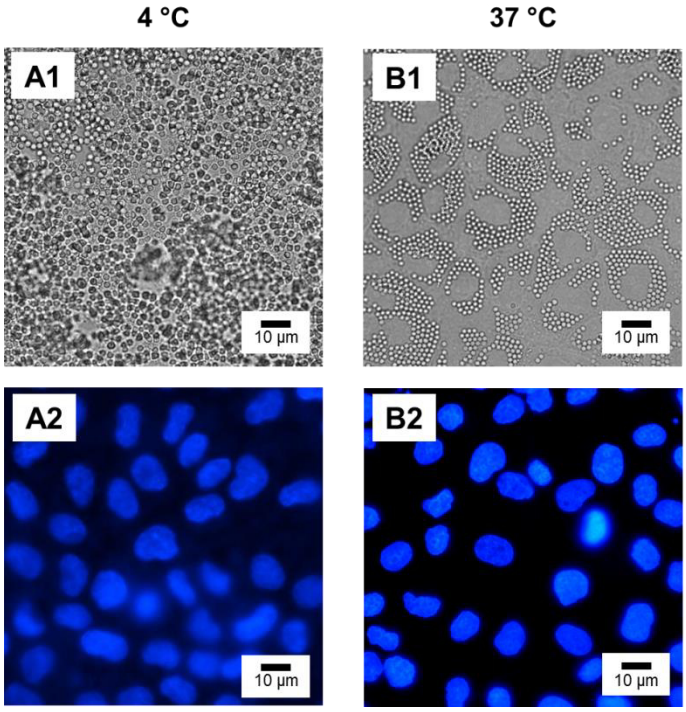

Fig. 6.8: Temperature-dependent uptake of silica particles after incubation at 4 °C (**A**) and 37 °C (**B**) in phase-contrast (**1**) and fluorescence micrograph after cell nuclei stain with DAPI (**2**). The experiment was performed in serum containing medium.

To further characterize the localization within the cytoplasm and to exclude attachment of particles on the cell surface, classical staining methods were applied which allows characterization of the particle interaction in more detail. The combination of phase-contrast images with fluorescent micrographs after cell nuclei stain with DAPI clearly revealed an arrangement of the particles around the cell nucleus (**Fig. 6.9 A+B**). Moreover, an intact cytoskeleton was found after visualization with Phalloidin Alexa Fluor 488 (**C**).

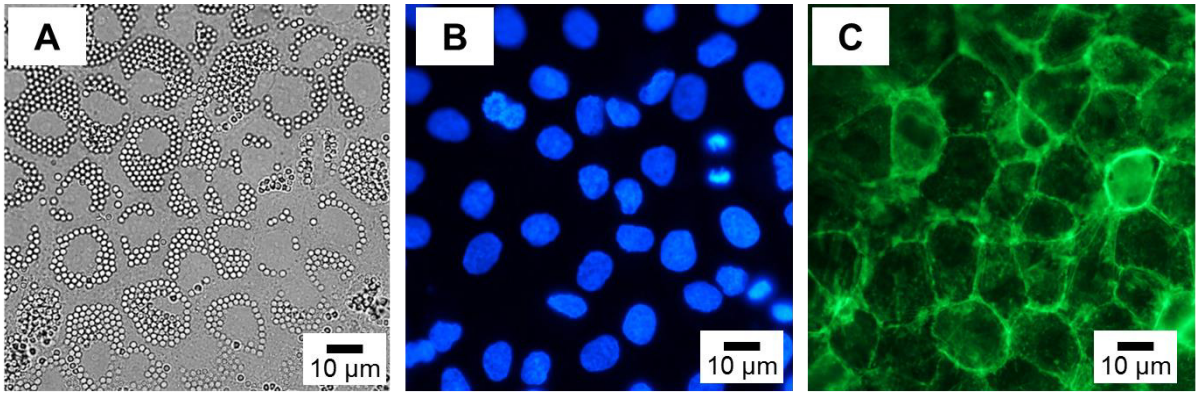

Fig. 6.9: Phase-contrast (**A**) and fluorescence micrographs (**B; C**) of NRK cells after 24 h of incubation in presence of silica particles in serum containing medium. At the end of the experiment cell nuclei were stained with DAPI (**B**; **blue**) and actin cytoskeleton was visualized using Phalloidin Alexa Fluor 488 (**C**; **green**).

The research was further extended by confocal laser scanning microscopic analysis of NRK cells with or without pre-incubation with silica particles (2 µm) after live/dead stain using Calcein AM and Ethidium Homodimer (**Fig. 6.10**). NRK cells without particle incubation (**A**) and cells pre-loaded with silica particles for 24 h (**B**) provided a high cell viability characterized by the green fluorescent cytoplasm. Only some red-stained cell nuclei were detected in both cases, which can be neglected as it corresponds to the normal dynamics of cell growth and cell death within a cell population. A higher magnification of cells in presence of silica particles (**C**) clearly emphasized the uptake into the cytoplasm as the non-fluorescent particles could be visualized within one z-section as black dots inside the green fluorescent cytoplasm located around the green-fluorescent nucleus.

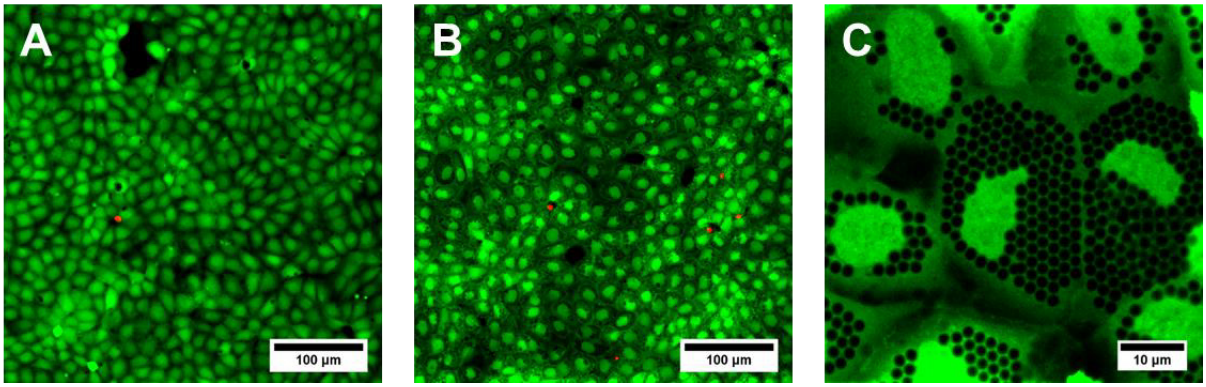

Fig. 6.10: Confocal fluorescence micrographs of NRK cells without particle incubation (**A**) and after 24 h of incubation in presence of silica particles (**B**) in serum containing medium and after live/dead stain with Calcein AM (**green**) and Ethidium Homodimer (**red**). Even in presence of silica particles cells showed high cell viability similar to cells under control conditions. Higher magnification of cells incubated with silica particles (**C**) revealed a densely-packed particle distribution around the cell nucleus inside the Calcein-stained cytoplasm.

Additionally, confocal laser scanning microscopy allowed the re-construction of a 3D image of the cell sample. Therefore, xy images were recorded as a function of variable z-positions which enables the analysis of the sample in side views (xz; yz). After staining the cytoplasm with Calcein AM the supernatant was replaced by TRITC dextran solution to differentiate between particle adhesion on the cell surface and uptake into the cytoplasm. Almost all cells in the field of view provided a high degree of silica particle uptake (**Fig. 6.11**) which was further revealed by the respective side views xz and yz where the black particles were found in the focus plane of the green fluorescent cytoplasm (**B**).

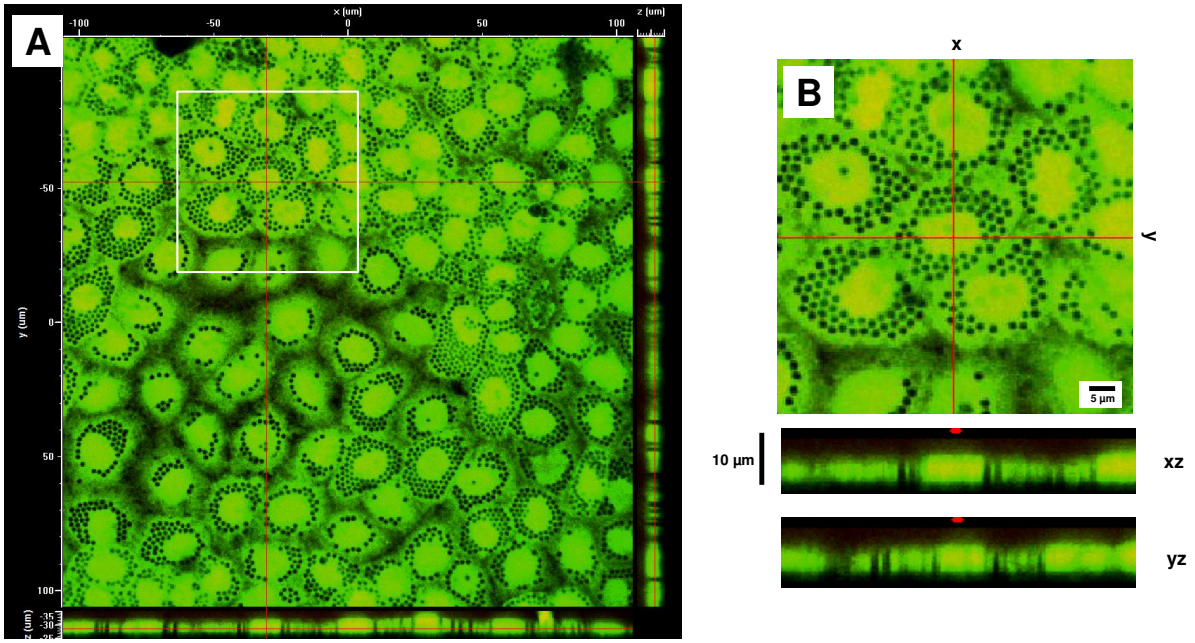

Fig. 6.11: Confocal laser scanning micrographs of NRK cells pre-loaded with silica particles (2 µm; $3.7 \cdot 10^7$ P/cm^2) for 24 h in serum containing medium after Calcein AM stain (**green**) and addition of extracellular TRITC dextran solution (**red**).

The microscopic study of the uptake of silica particles into the cytoplasm of NRK cells was completed performing a membrane stain with DiI which revealed the presence of membrane-coated particles inside the cytoplasm of NRK cells (**Fig. 6.12**).

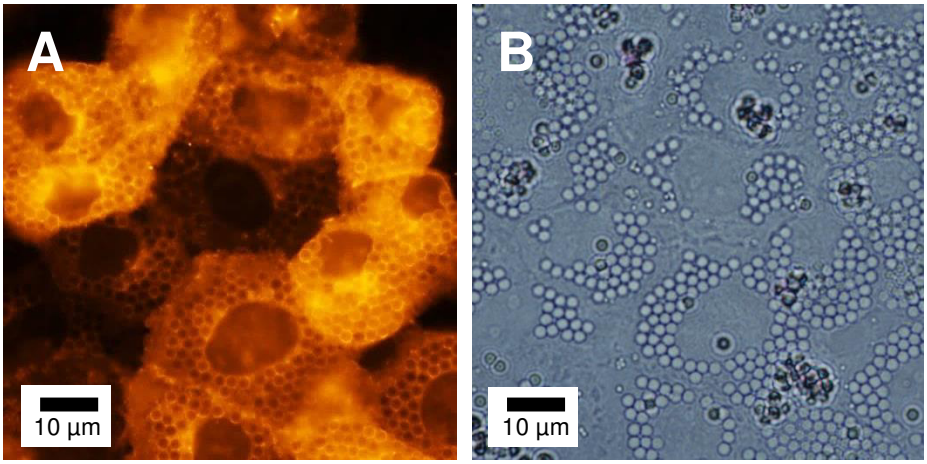

Fig. 6.12: Fluorescence micrograph (**A**) and phase-contrast image (**B**) of NRK cells pre-loaded with silica particles ($3.7 \cdot 10^7$ P/cm^2) for 24 h in serum-containing medium after membrane stain with DiI. The staining revealed membrane-coated particles inside the cytoplasm.

6.4.2.2 Uptake Studies Using Scanning Electron Microscopy (SEM)

Furthermore, silica particle loaded NRK cells and control NRK populations were investigated by SEM. Therefore, cells were either washed after ~ 42 h of incubation with silica particles (2 µm; $4.7 \cdot 10^7$ P/cm^2) to remove particles which were not taken up by NRK cells or were immediately prepared for microscopic analysis. Additionally, control cells were analyzed after incubation with culture medium. **Fig. 6.13** shows a survey of SEM images, which were kindly provided by the working group of Prof. Witzgall (faculty for biology and preclinical medicine; University of Regensburg). When NRK cells were washed with PBS^{++} after particle incubation and before preparation for microscopic analysis (**A**) almost all particles were localized intracellularly and covered with plasma membrane. The filopodia on the cell surface after uptake of silica particles are shown in a higher magnification in **A3**. When the washing steps were skipped some particles in the extracellular space were found, which provided a smooth particle surface (**B**) in contrast to the incorporated microparticles. Control cells showed the cell-type specific morphology and clearly allowed identification of the position of the cell nucleus (**C**).

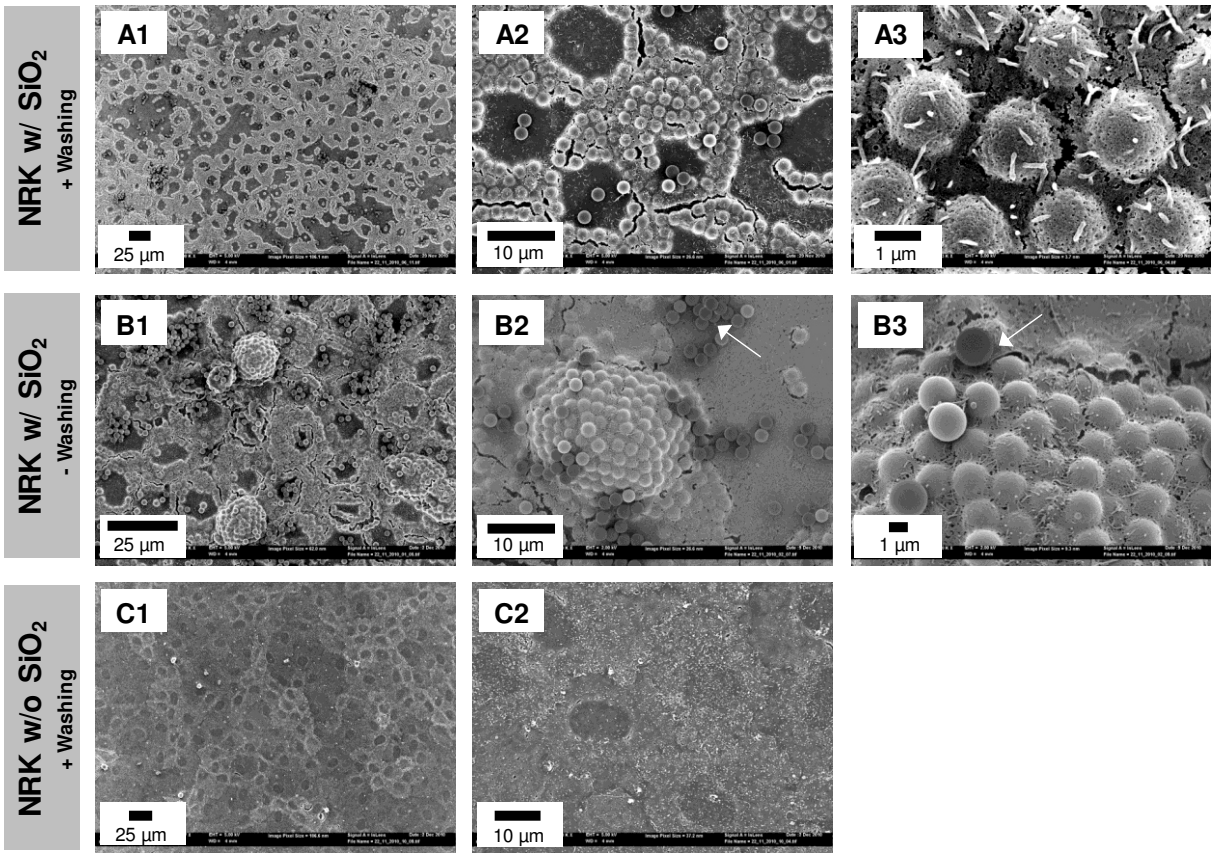

Fig. 6.13: SEM images of NRK cells pre-loaded with silica particles (**A;B**) and control NRK cells (**C**) in different magnifications. After 42 h of incubation cells were fixed with (**A**) or without (**B**) washings steps in advance to remove extracellular particles. Some extracellular particles are highlighted by the white arrow in **B2** and **B3**. The experiment was performed in serum containing medium. SEM images were taken by the working group of Prof. Dr. R. Witzgall in the faculty for biology and preclinical medicine (University of Regensburg).

6.4.2.3 Uptake Studies Using Transmission Electron Microscopy (TEM)

The uptake of silica particles by NRK cells was further investigated by TEM microscopy which provides a higher resolution than normal light microcopy. **Fig. 6.14** shows TEM images of NRK control cells (**A; B**), pure silica particles (**C**) and NRK cells after pre-loading with microparticles (**D; E**). The aim of this study was to obtain a label-free evidence for the membrane-coating around each particle which was found after membrane stain with DiI. Unfortunately, during the preparation for TEM imaging, silica particles cracked when the cell sample was sliced into different sections. The signal could be clearly identified as SiO_2 signal, however, this effect hindered a good analysis of the sample (**C**). When cells were analyzed after pre-incubation with silica particles, particles were found within the cell section (**D**) but the analysis of the particle surface with respect to membrane coating was difficult. Only one image, where particles were located around the nucleus allowed identification of a membrane-coating including two particles (**E1; E2**). The TEM analysis again showed an uptake into the cytoplasm of NRK cells but did not provide new findings about the particle coating inside the cytoplasm.

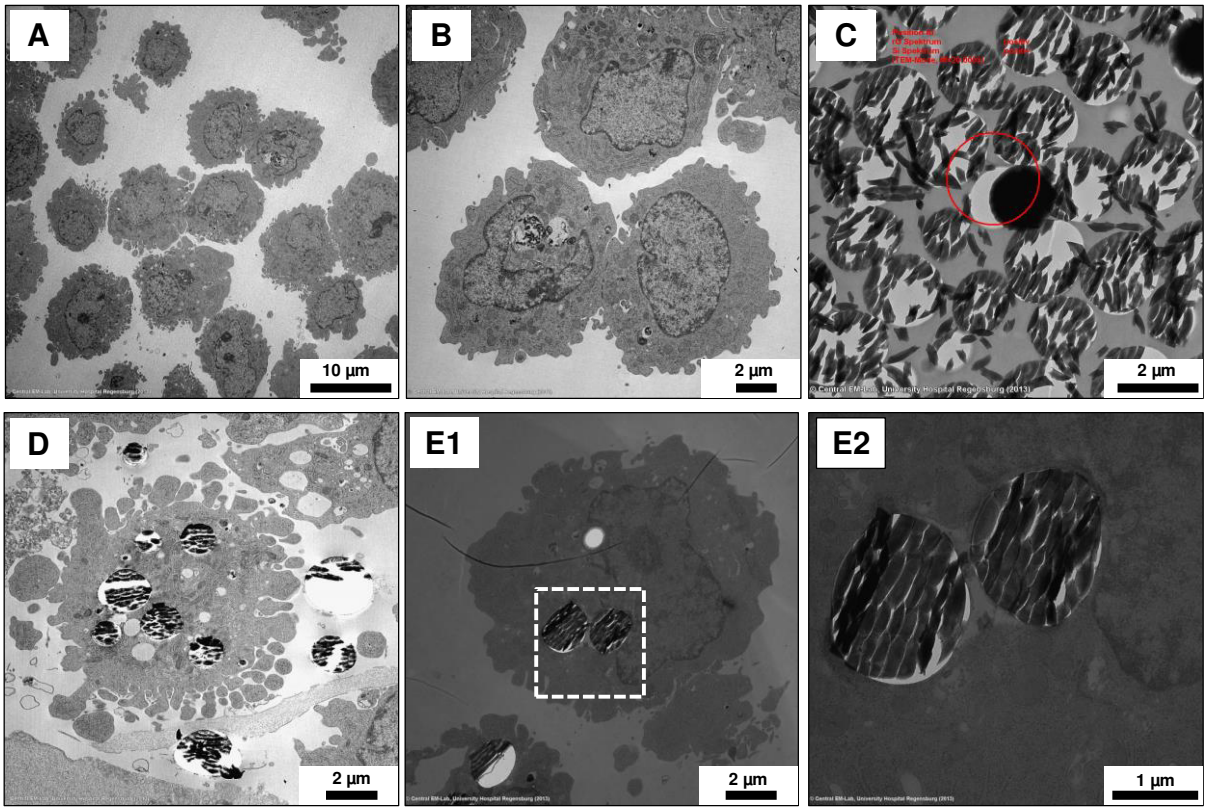

Fig. 6.14: TEM images of NRK cells (**A; B**), silica particles (**C**) and NRK cells pre-incubated with silica particles in different magnifications (**D-E**). The experiment was performed in serum containing medium and images were taken at the university hospital (Regensburg).

6.4.2.4 ToF-SIMS Analysis

3D ToF-SIMS analysis (*time-of-flight secondary ion mass spectrometry*) was performed in cooperation with Tascon GmbH and ION-TOF GmbH in Münster to study the localization of silica particles inside NRK cells. This technique, which is characterized by a subcellular resolution, allows detection of particles even without any additional labeling down to a particle diameter of 150 nm. The localization of nano- and microparticles inside NRK cells was successfully realized by alternating SIMS imaging (Bi_3^+) and sputter erosion (O_2^+ or Cs^+). Only the uptake of 2 µm particles will be presented in more detail and results for the other particle diameters (∅ 150 nm, 500 nm) can be found in the publication Hagenhoff et al. (2013) [485].

NRK cells, grown to confluence on glass slides which were sputter coated with 20 nm Au on top of 20 nm ITO, were loaded with silica particles for 24 h. Prior to ToF-SIMS analysis, cell samples were washed and fixed with 2.5 % (v/v) glutaraldehyde and finally dried overnight. **Fig. 6.15** summarizes the mass resolved (x, y) images for

(A) **SiO_2^-** which characterizes the localization of the silica particles

(B) **CNO^-** originating from nitrogen containing compounds such as proteins and nucleic acids

(C) **Au^-** resulting from the 20 nm Au coating of the growth substrate

before (**1**) and after (**2**) opening the plasma membrane by sputter ablation using Cs^+-ions.

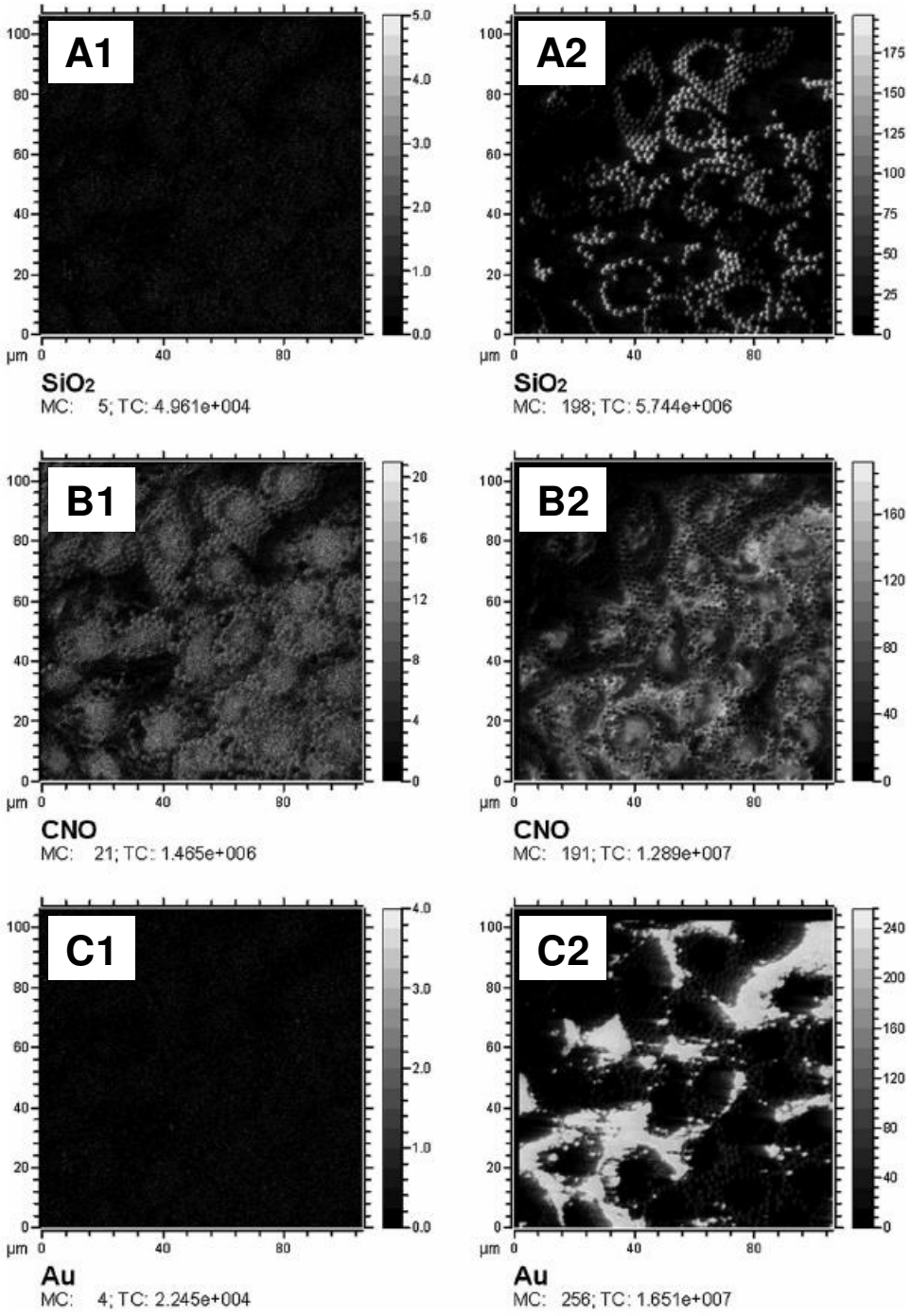

Fig. 6.15: Mass resolved-images attributed to SiO_2^- (**A**), CNO^- (**B**) and Au^- (**C**) for a confluent cell layer of NRK cells after 24 h of pre-incubation with silica particles (2 µm) in serum containing medium before (**1**) and after (**2**) opening the cytoplasm by sputter ablation of the plasma membrane. The individual caption indicates the number of ions found in the entire image (TC; *total counts*) and the most intense pixel (MC; *maximum counts*). Images were performed by Tascon GmbH Münster.

Before opening of the plasma membrane neither a silicon signal (**A1**) nor gold (**C1**) was detected indicating that the sample consisted of a confluent cell layer and that the microparticles (2 µm) were not adhered extracellularly to the apical membrane. When the apical membrane was removed by sputter erosion a high SiO_2^- signal intensity was detected (**A2**) and provided a densely-packed particle distribution around the nucleus which remained dark due to the size limit of the nuclear pore complex. The mass-resolved images of CNO^- ions before opening of the plasma membrane provided a high intensity of CNO^- fragments originating from components of the plasma membrane. Additionally, the presence of particles inside the cells caused topographic undulation of the membrane (**B1**). After sputter ablation also a bright intensity of CNO^- fragments was detected due to the abundance of nitrogen-containing molecules inside the cell. The position of cell nuclei was identified by a homogeneous round appearance of the CNO^- signal which could be clearly distinguished from the more differentiated CNO^- distribution caused by the membrane (**B2**). This label-free method provided a substantial contribution to the study about the uptake of silica particles into NRK cells and their localization in the cytoplasm. After this analysis a sole attachment of silica microparticles on the apical membrane was definitely excluded and a clear evidence of the uptake was realized without any additional labeling.

6.4.3 Impedimetric Monitoring of the Uptake of Silica Particles

The internalization of silica microparticles was further analyzed using the label-free ECIS technique. NRK cells confluently grown on 8W1E electrodes were monitored 40 h in absence or presence of silica particles ($3.7 \cdot 10^7$ P/cm^2). Additionally, the uptake of silica particles was monitored in presence of 100 µM *Dimethylamiloride* (DMA). DMA is an inhibitor of Na^+/H^+-exchange [487] and well-known for its inhibitory effect on micropinocytosis [488]. The uptake of silica particles into the cytoplasm of NRK cells was successfully proven and already demonstrated in **chapter 6.4.2**. Due to the size of the particles an uptake via micropinocytosis was considered. **Fig. 6.16** summarizes the time-course of $|Z|_{norm}$ at 16 kHz over 40 h in absence or presence of silica particles with (**A**) or without (**B**) DMA.

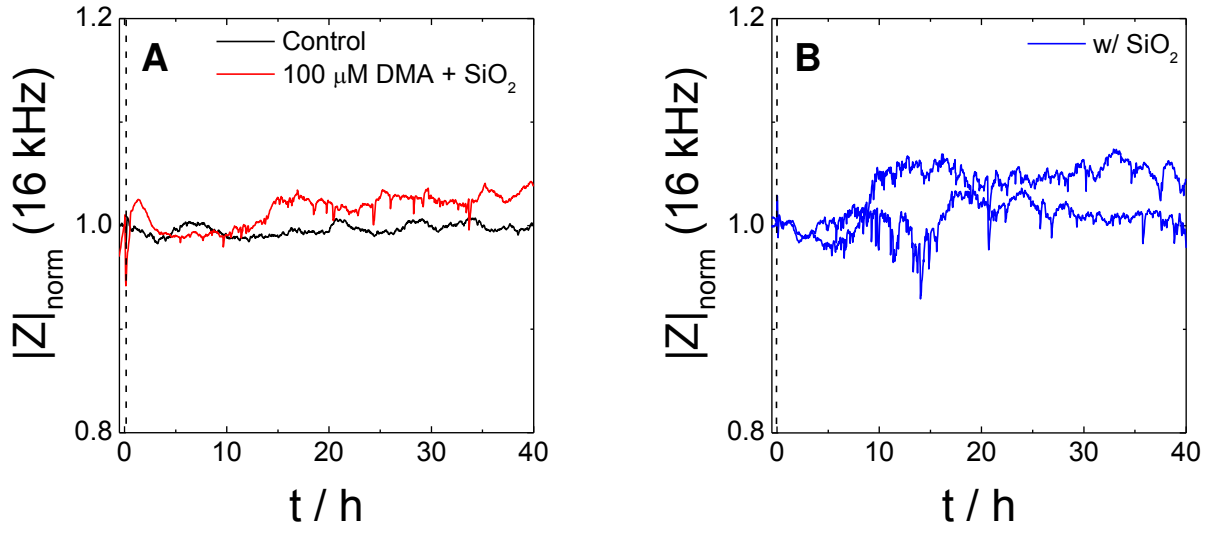

Fig. 6.16: Typical time-course of normalized impedance $|Z|$ at 16 kHz to detect cellular response after the addition of serum containing medium (**A**; **black**) or silica particles (∅ 2 µm; $3.7 \cdot 10^7$ P/cm^2) in presence of 100 µM DMA (**A**; **red**). Furthermore, the response of two different NRK cell populations during 40 h of incubation in presence of silica particles (∅ 2 µm; $3.7 \cdot 10^7$ P/cm^2) in culture medium was observed (**B**; **blue**). Data were normalized to the value immediately before addition of particles or medium. The experiment was performed in serum containing medium.

NRK cells in medium (**black**; **A**) showed a stable $|Z|_{norm}$ signal over time. When NRK cells were incubated with silica particles in presence of DMA (**red**; **A**) $|Z|_{norm}$ showed a slight increase immediately after particle addition. In the following only small fluctuations of the impedance signal were found. After 40 h control cells showed a $|Z|_{norm}$ signal of 1.00 whereas cells incubated with DMA and silica particles were characterized by a slightly higher $|Z|_{norm}$ value of 1.03. In contrast, two different cell populations incubated in culture medium with silica particles (**B**) clearly showed strong fluctuations in the time-course of impedance. The first spikes were found around 5.5 h after particle addition and remained visible over the whole observation time. In the end of the experiment $|Z|_{norm}$ was found at ~ 1.04 and ~ 0.98, respectively.

Additionally, confocal laser scanning micrographs of NRK cells after incubation with silica particles in absence or presence of DMA were recorded after staining the cytoplasm with Calcein AM (**Fig. 6.17**). The uptake of the non-fluorescent silica particles into the cytoplasm was analyzed after 24 h of incubation.

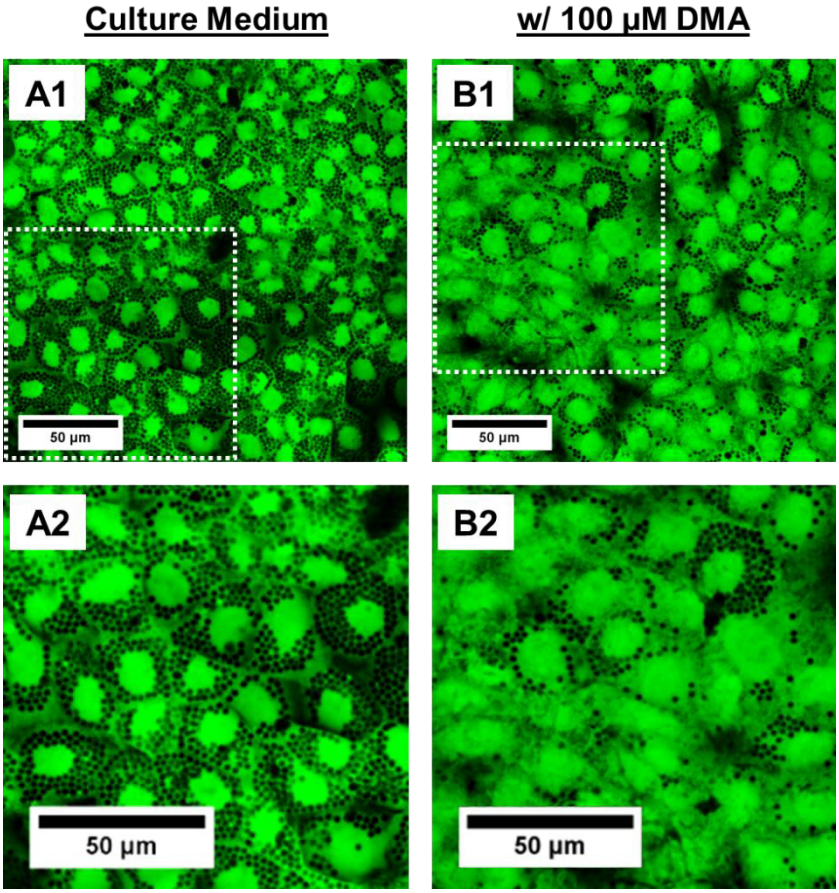

Fig. 6.17: NRK cells after 24 h of incubation with silica particles (∅ 2 µm) in serum containing medium and in absence (**A**) or presence of 100 µM DMA (**B**). To visualize the non-fluorescent silica particles inside the cell the cytoplasm was stained with Calcein AM. The image section indicated by the white, dotted square in **A1** and **B1** is provided in a higher magnification in (**2**).

The fluorescence micrographs showed that the presence of DMA clearly affected the uptake behavior. Whereas under control conditions many particles were taken up by the cells, only some microparticles appeared as black dots inside the cytoplasm in presence of the inhibitor. This provided an optical proof that the uptake of silica particles was significantly inhibited by the presence of DMA.

6.4.3.1 Concentration-Dependency of the Spikes in the Impedance Signal

The origin of the spikes in the impedance signals (**Fig. 6.16 B**) was further addressed using different particle concentrations. The hypothesis was that these spikes can be related to the uptake of particles and their appearance should be promoted by higher concentrations of silica particles in the medium. The same experiment was repeated with increasing concentrations of silica particles of $1.9 \cdot 10^7$ P/cm^2 – $7.5 \cdot 10^7$ P/cm^2. The time-courses of $|Z|_{norm}$ at 16 kHz in absence (**A**) and presence (**B – D**) of silica particles are summarized in **Fig. 6.18**.

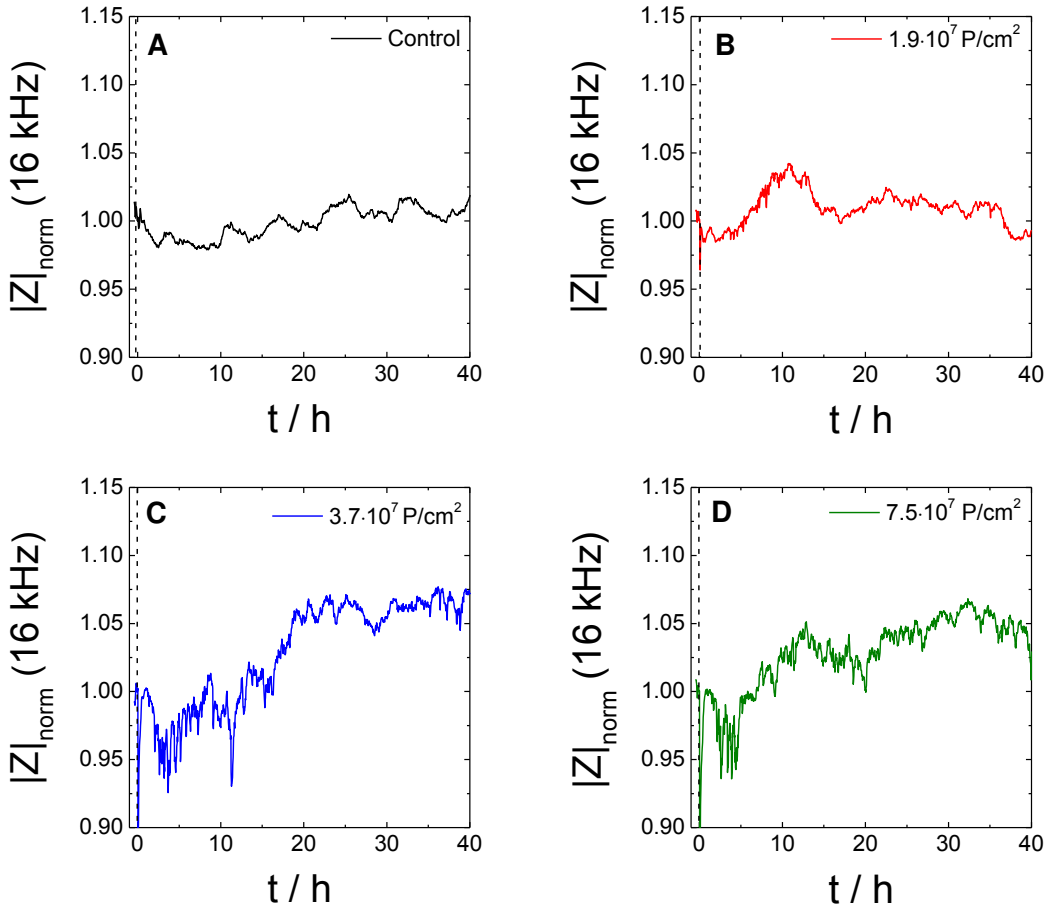

Fig. 6.18: Typical time-courses of the normalized impedance $|Z|$ at 16 kHz for NRK cells in serum containing medium (**A**) and in presence of varying concentrations of silica particles (**B – D**). Data were normalized to the respective impedance value immediately before addition.

The control cells showed an almost stable signal over the observation time of ~ 40 h (**A**). After the addition of silica particles with a concentration of $1.9 \cdot 10^7$ P/cm^2 (**B**) the signal did not provide any significant differences compared to the response of NRK cells after the addition of medium except for small fluctuations in the time-course of impedance. By further increasing the particle concentration to $3.7 \cdot 10^7$ P/cm^2 (**C**) again the sharp spikes in $|Z|_{norm}$ were detected. The first impedance peak already appeared ~ 2 h after addition. When the same concentration of silica particles was added to a cell-free well, no changes in $|Z|_{norm}$ were observed (**Fig. S 10**). The time-course of $|Z|_{norm}$ after addition of the highest

concentration ($7.5 \cdot 10^7$ P/cm^2; **D**) also provided a significantly different impedance signal compared to those for control cells. $|Z|_{norm}$ started to fluctuate ~ 2 h after addition. After 40 h $|Z|_{norm}$ of NRK cells in presence of $3.7 \cdot 10^7$ P/cm^2 and $7.5 \cdot 10^7$ P/cm^2 showed a slightly enhanced normalized impedance signal (1.04 – 1.07) compared to the control cells (1.02).

The time-course of normalized impedance for NRK cells in presence of $1.9 \cdot 10^7$ P/cm^2 (**B**) and the remaining higher concentrations (**C; D**) were different: Whereas for the lowest concentration of silica microparticles no spikes were found in the time-course of impedance, sharp changes in the impedance signals were seen for cells in presence of higher concentrations. However, no significant dependency of the spiking effect on the applied concentrations was found using $3.7 \cdot 10^7$ P/cm^2 and $7.5 \cdot 10^7$ P/cm^2.

6.4.3.2 Particle Uptake Dependent on Surface Charge

For a deeper analysis of these spiking effects, which were thought to be related to the uptake of the microparticles, the phenomena was additionally analyzed using differently charged particles. It is known that the surface charge has a strong influence on cellular uptake of the particles [489-491]. Positively-charged particles show a stronger affinity for the negatively-charged cell membrane [492] and consequently a higher uptake efficiency. Therefore, polystyrene beads with a particle diameter of 2 µm were used, which had either a carboxylate-modified or amine-modified particle surface.

In the following experiment a similar concentration ($3.7 \cdot 10^7$ P/cm^2) of polystyrene beads and silica particles was applied to a confluent NRK cell layer grown on 8W1E electrodes and the time-course of impedance $|Z|_{norm}$ at 16 kHz was analyzed over 40 h (**Fig. 6.19**). Incubation of NRK cells in presence of silica particles again yielded sharp peaks in the impedance signal and after 10 – 30 h the impedance signal increased continuously. At the end of the experiment $|Z|_{norm}$ for NRK cells incubated with silica particles was determined to ~ 1.10. In contrast, NRK control cells, which were incubated in presence of culture medium remained stable over time with $|Z|_{norm}$ of 0.98 after 40 h. Time-course of normalized impedance was insignificantly different for amine- and carboxylate-modified polystyrene beads. Under both conditions, $|Z|_{norm}$ did not show any spikes comparable to the signal fluctuations in presence of silica particles. At the end of experiment $|Z|_{norm}$ was ~ 1.00 independent of surface charge.

Additionally, the uptake of differently-modified polystyrene beads was analyzed in phase-contrast after 24 h of incubations (**B1; B2**). NRK cells showed nearly no uptake of the particles into the cytoplasm in presence of negatively-charged polystyrene beads (**1**). In contrast, a positive charge on the surface of the polystyrene beads resulted in a high cellular

uptake and amine-modified particles were found located around the nucleus inside the cell (**2**).

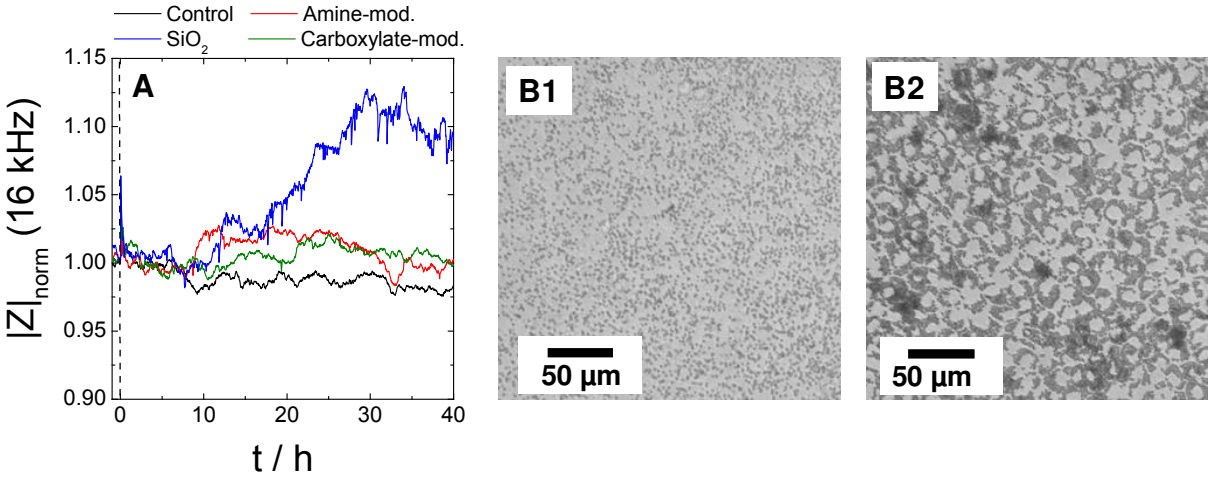

Fig. 6.19: A: Typical time-course of normalized impedance $|Z|$ at 16 kHz to monitor cellular response after addition of serum containing medium (**black**), silica particles (**blue**), amine-modified polystyrene beads (**red**) or carboxylate-modified polystyrene beads (**green**) to a confluent layer of NRK cells using 8W1E electrode layout. Data were normalized to the respective values immediately before addition. **B:** Phase-contrast micrographs of NRK cells after 24 h of incubation in presence of carboxylate-modified (**1**) or amine-modified (**2**) polystyrene beads. Experiments were performed in serum containing medium.

In summary, the experiment showed an uptake of silica particles and amine-modified polystyrene beads into the cells. However, the time-course of impedance $|Z|_{norm}$ was significantly different for both particle types. Moreover, amine-modified particles showed a similar time-course of impedance compared to the carboxylate-modified particles which were not taken up into the cell. This leads to the conclusion that the uptake of microparticles is not necessarily associated with the phenomenon of “spikes” in the time-course of $|Z|_{norm}$. No final judgment was delivered from this experiment which process or cellular phenomenon is related to the sharp spikes in impedance and still requires further investigations.

6.4.4 Sequence of Impedimetric Assays to Analyze the Biocompatibility of Silica Particles

It was one of the objectives of this thesis to study the impact of micrometer-sized silica particles on the vitality of adherent NRK cells, their motility and their ability to migrate. A sequence of three different impedimetric assays – all based on the well-established ECIS-technique – was applied to investigate

(i) acute toxicity
(ii) impact on the metabolically driven micromotion
(iii) impact on cell migration

Using a label-free sequence of different impedimetric assays based on ECIS allowed to assess the biological response of one population of NRK cells to the exposure of silica particles from different perspectives. An overview of the stepwise analysis of particles' impact on NRK cell physiology is provided in **Fig. 6.20**.

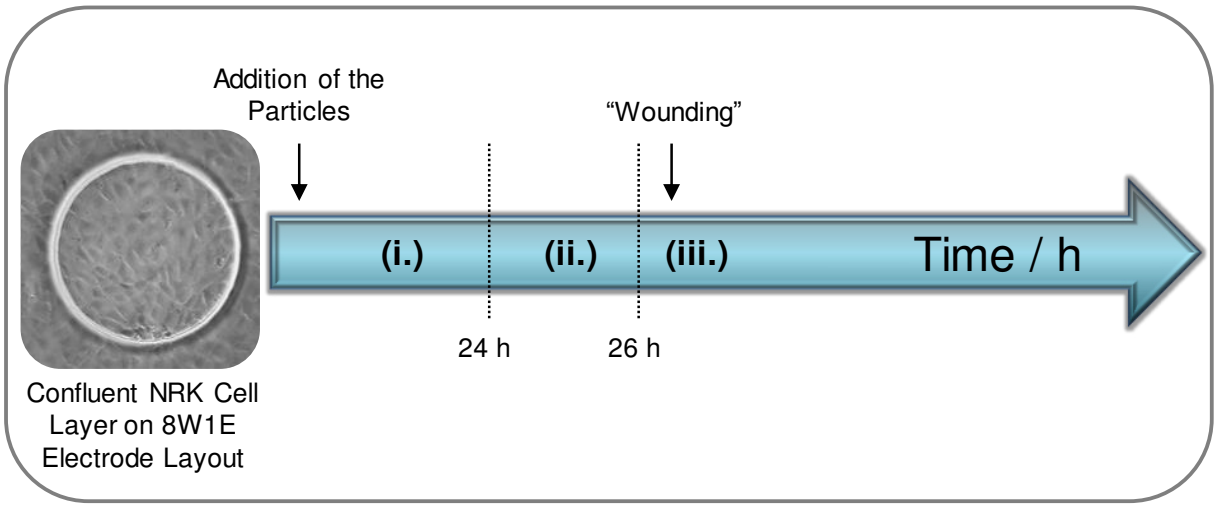

Fig. 6.20: Overview of the sequential analysis of the impact of silica particles on NRK cell physiology: Confluent layers of NRK cells, grown on 8W1E electrodes were analyzed with respect to cytotoxicity after the addition of silica particles in different concentrations for 24 h (**i**). In the following, cell motility in absence or presence of silica particles was analyzed using RTC measurements (**ii**). Finally, cells on top of the electrode were wounded by applying an invasive voltage pulse and cell migration in absence or presence of silica particles was analyzed time-dependently (**iii**).

6.4.4.1 Acute Toxicity

In a first assay the impact of micrometer-sized silica particles (∅ = 2 µm) on vitality of adherent NRK cells was investigated. Time-resolved ECIS recordings can monitor the response of NRK cells, grown to confluence on 8W1E electrodes, to the exposure of silica particles in increasing concentrations ($7.5 \cdot 10^6$ P/cm^2 – $7.5 \cdot 10^7$ P/cm^2) under serum containing conditions. **Fig. 6.21 A** summarizes the cellular response of control cells (■) and cells in

presence of silica particles (●) over a time-period of 24 h. At $t = 0$ h, indicated by the dashed line, particles were added to the confluent NRK cell layer. Afterwards, time-course of normalized impedance $|Z|$ at 4 kHz was recorded over 24 h. Independent of the applied concentration no toxic effects, which would be indicated by a decrease in $|Z|_{norm}$, were found. Using the lowest particle concentration ($7.5 \cdot 10^6$ P/cm^2, ●) the time-course of impedance was similar to that for cells without particles (■) and normalized impedance values of 0.94 – 0.98 were found after 24 h. By increasing the particle concentration even a slight increase in impedance was observed and after 24 h of incubation $|Z|_{norm}$ was determined to ~ 1.05. In summary, during the observation period of 24 h impedance recordings revealed no sign of cytotoxicity.

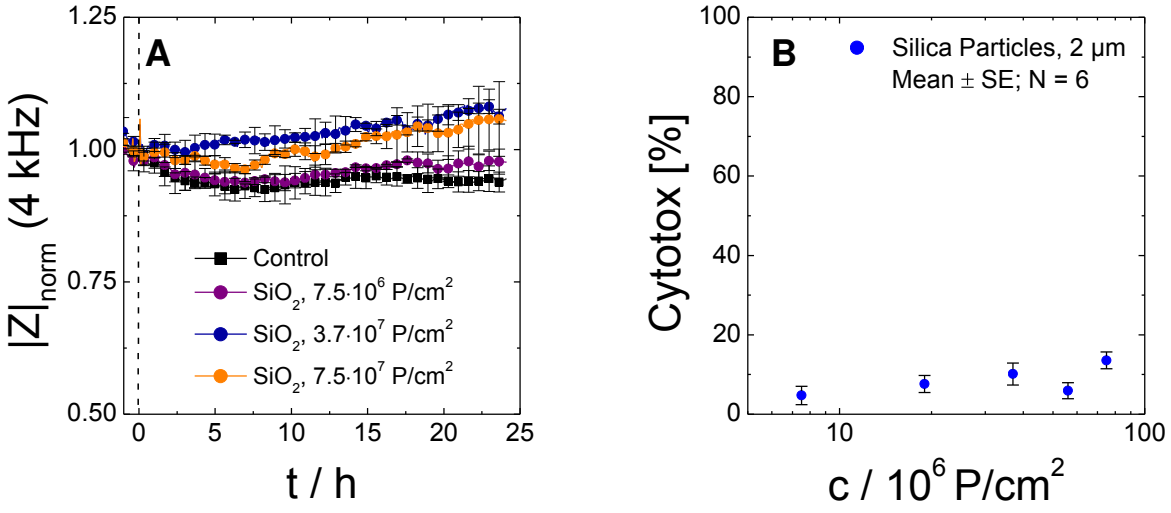

Fig. 6.21: A: Typical time-courses of normalized impedance at 4 kHz to investigate the acute toxicity of silica particles (∅ 2 µm) on NRK cells using increasing concentrations ($7.5 \cdot 10^6$ P/cm^2 – $7.5 \cdot 10^7$ P/cm^2). NRK cells, seeded to confluence on 8W1E, were monitored over 24 h. (Mean ± SD; N = 2). **B:** PrestoBlue® assay to analyze cell viability after 24 h of incubation with silica particles (c = $7.5 \cdot 10^6$ P/cm^2 – $7.5 \cdot 10^7$ P/cm^2). Cell viability was quantified by the ability to convert the blue, non-fluorescent Resazurin into the red, highly-fluorescent Resorufin. The mitochondrial metabolic activity of the cells was quantified by measuring the fluorescence intensity (exc. 544 nm, em. 590 nm) after 2 h of incubation in the dark (Mean ± SE; N = 6). Experiments were performed in serum containing medium.

Additionally, a PrestoBlue® assay, an optical and commonly-used cytotoxicity assay, was performed to analyze cytotoxic effects of silica particles after 24 h of incubation. This assay is based on the conversion of the blue, non-fluorescent Resazurin into the highly-fluorescent Resorufin by healthy and metabolically active cells. PrestoBlue® solution was added to the cell layer after 24 h of incubation with silica particles in presence of serum using a concentration range between $7.5 \cdot 10^6$ P/cm^2 – $7.5 \cdot 10^7$ P/cm^2. The fluorescence intensity was recorded at 590 nm at an excitation wavelength of 544 nm after 2 h of incubation at 37 °C in the dark. Independent of the applied concentration and in good correlation with the impedance data shown in **Fig. 6.21 A** no indications for a cytotoxic effect were found (**B**). Even for the highest particle concentration of $7.5 \cdot 10^7$ P/cm^2 the cytotox value was calculated to (13 ± 1) % indicating no acute cytotoxicity of silica microparticles.

6.4.4.2 Silica Particle Impact on Cell Motility

The micromotion of adherent cells, which is an undisputed indicator for metabolically active cells, can be detected as fluctuations of the resistance by means of RTC (Rapid Time Collect) measurements. The analysis of cellular micromotion was used to further characterize the impact of silica particles on cell physiology since it can detect the onset of cytotoxicity more sensitively compared to normal ECIS experiments [493, 494].

First the micromotion for vital NRK cells and cells after permeabilization with Triton-X-100 was recorded at 4 kHz. A significant difference was found between metabolically active NRK cells and cells which were pre-treated with Triton-X-100 prior to the RTC measurements (**Fig. 6.22**). Vital NRK cells showed a characteristic pattern where fluctuations in R/R_{mean} were found. In contrast, the measurement for NRK cells after Triton-X-100 treatment only provided a drift in R/R_{mean} but no evidence for micromotion of cells due to dynamic changes in cell shape. The data were further quantified as already presented in **chapter 6.3.3.5** by increment analysis in which the standard deviation with a time-frame of 64 s was used. The motility index (**B**) also provided a significant decrease after permeabilization with Triton-X-100. Whereas vital cells showed a motility index of $(10 \pm 2) \cdot 10^{-4}$ the value was significantly lower for cells after permeabilization with $(2.9 \pm 0.9) \cdot 10^{-4}$.

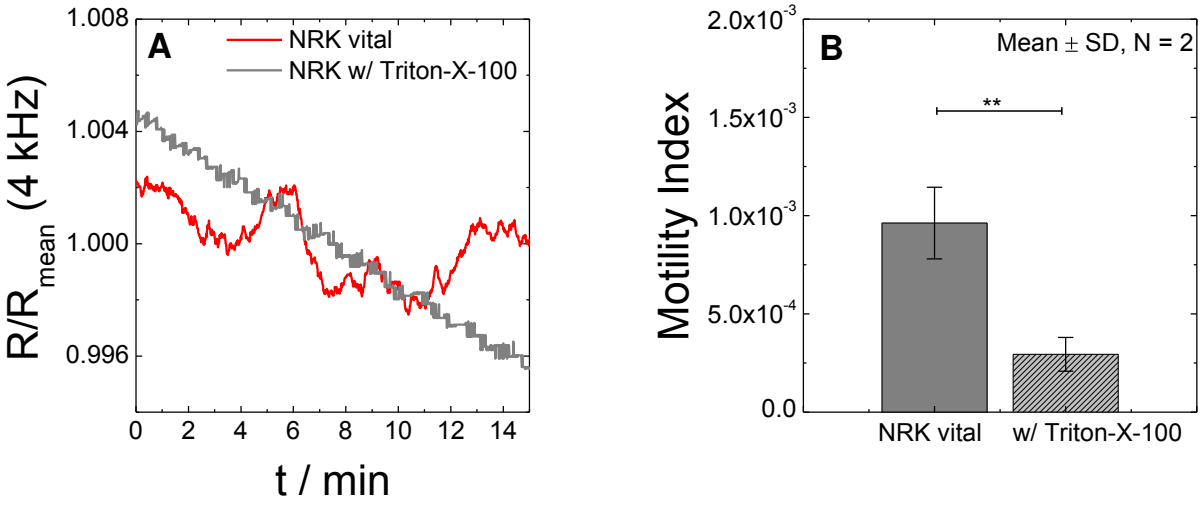

Fig. 6.22: A: Typical time-course of resistance at 4 kHz detected in RTC mode to analyze motility of vital NRK cells and cells after permeabilization with Triton-X-100. Data were recorded for each well over 15 min with a resolution of 1 point per second. For the final presentation data were normalized to the respective mean value. The experiment was performed in serum containing medium. **B:** Quantification of cell motility using a LabVIEW-based software. A high motility index indicates high cell viability (Mean ± SD; N = 2). Significance between the two populations was determined by a two-sample t-test using a significance level of 0.05 (**).

Cell motilities were in the following analyzed in absence or presence of silica particles in different concentrations. The micromotion assay was performed subsequent to the cytotoxicity assay when no indication for cytotoxicity was observed. Therefore, cells were

already pre-loaded with silica particles for 24 h before the high time resolution analysis was performed. **Fig. 6.23** summarizes the results for micromotion studies of NRK cells after pre-incubation with different concentrations of silica particles with a diameter of 2 µm. In the time-course of normalized resistance, no significant changes were found for the different conditions. Cells showed fluctuations in R/R_{mean} independent of the applied particle concentration. The data sets of four different wells per condition were further analyzed by the calculation of the motility index. Control NRK cells in presence of culture medium were characterized by a motility index of $(8 \pm 4) \cdot 10^{-4}$. When cells were pre-incubated with silica particles no significant influence on the motility index was found. With increasing particle concentrations the motility index was determined to $(10 \pm 2) \cdot 10^{-4}$ ($7.5 \cdot 10^{6}$ P/cm^2), $(9 \pm 1) \cdot 10^{-4}$ ($3.7 \cdot 10^{7}$ P/cm^2) or $(12 \pm 5) \cdot 10^{-4}$ ($7.5 \cdot 10^{7}$ P/cm^2). Cellular motility and, thus, metabolic activity was found to remain unaffected by the presence of 2 µm silica particles independent of particle concentration.

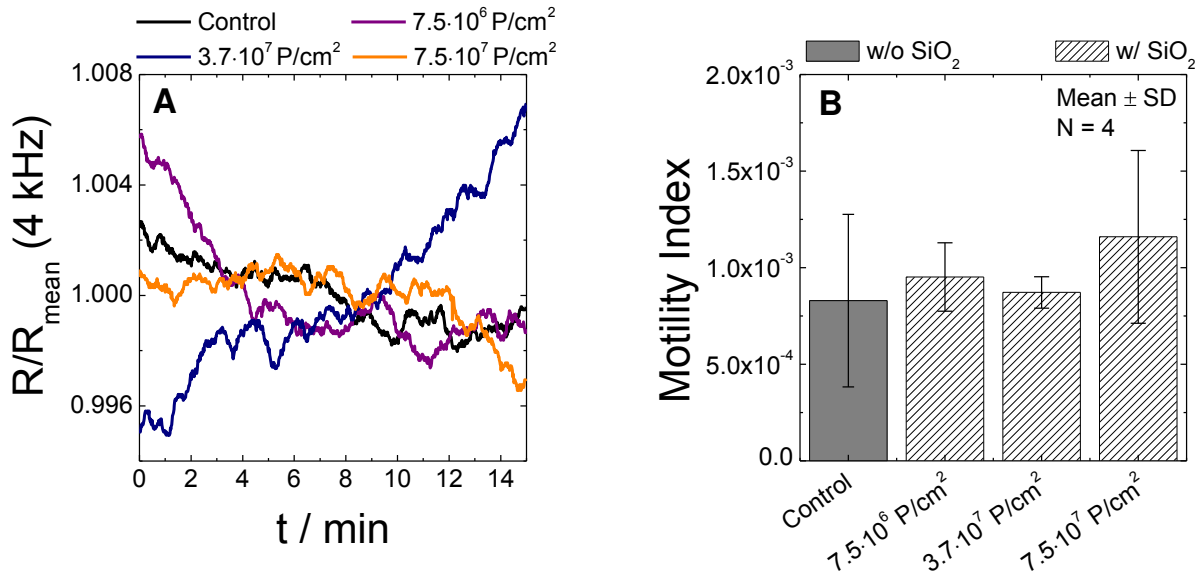

Fig. 6.23: A: Typical RTC measurements at 4 kHz to analyze motility of NRK cells in absence or presence of silica particles of increasing concentrations. For each well a time-record over 15 min at 4 kHz was performed using a time resolution of 1 point/s. Data were normalized to the mean value of each well. Experiments were performed in serum containing medium. **B:** Analysis of RTC data using a LabVIEW-based software. The motility index was calculated for cells in absence or presence of silica particles (Mean ± SD; N = 4). Differences were determined to be not significant by a two-sample t-test using a significance level of 0.05.

6.4.4.3 Impedimetric Wound Healing Assay to Analyze the Impact of Silica Particles on Cell Migration

Cell migration is very important in many different biological processes such as tissue regeneration, embryogenesis, cancer metastasis and wound healing [495, 496]. Collective cell migration describes the phenomenon of concerted migration of a cell monolayer in which single cells are connected mechanically and biochemically through cell-cell adhesion [101]. ECIS provides an electrical method to create a defined wound in a cell monolayer, which is determined by the size of the working electrode. Afterwards cell migration from the electrode periphery into the cell-free area on top of the electrode is monitored electrically with high time-resolution. After analysis of cell viability and cell motility, which did not provide any impact of silica particles on NRK cell physiology, an impedance-based wound healing assay was performed to monitor cell migration in absence or presence of silica particles. It should be emphasized that different microscopy studies clearly revealed the presence of silica particles inside the cells, densely-packed around the nucleus and in some cases even stacked in more layers. In the following, the impact of these incorporated 2 µm particles on wound healing efficiency was investigated.

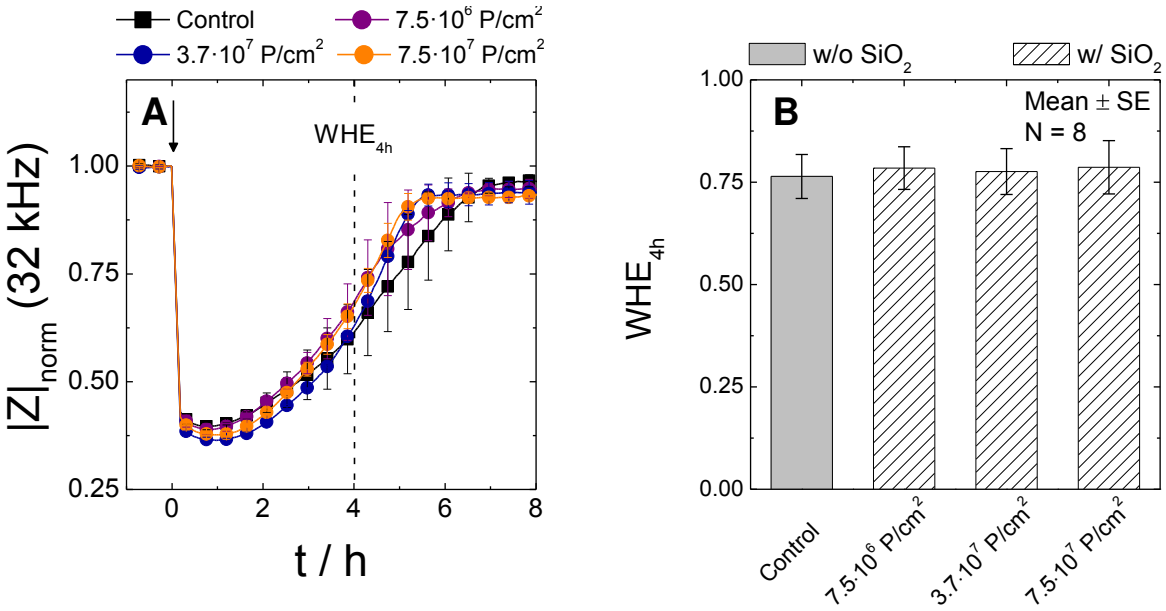

Fig. 6.24: A: Typical time-courses of normalized impedance |*Z*| at 32 kHz to monitor the wound healing efficiency of NRK cells in absence (■) or presence of silica particles (●). After applying an invasive wounding pulse (40 kHz, 30 s, 5 V) a circular wound was created and in the following the migration from cells in the electrode periphery into the cell-free area was monitored time-dependently (Mean ± SD; N = 2). The experiment was performed in serum containing medium. **B:** Wound healing efficiency (WHE) of cells in absence or presence of particles 4 h after wounding. (Mean ± SE, N = 8) of four independent experiments. The WHE_{4h} of control cells and cells pre-loaded with different concentrations of silica particles (∅ 2 µm) were found to be not significantly different, determined by a two sample t-test using a significance level of 0.05.

Fig. 6.24 A exemplarily shows the time-course of normalized impedance at 32 kHz before and after wounding of control cells (■) and NRK cells pre-loaded with 2 µm silica particles (●) in increasing concentrations. Immediately after applying the wounding pulse (40 kHz, 30 s, 5V) $|Z|_{norm}$ at 32 kHz decreased to ~ 0.4 which represents the impedance value of a cell-free electrode, indicating the formation of a circular cell-free wound with a diameter of 250 µm. After a short lag phase $|Z|_{norm}$ started to increase, indicating the migration of NRK cells into the cell-free area to re-establish a confluent cell layer independent of the presence of silica particles. After ~ 5.7 h cells in presence of $3.7 \cdot 10^7$ P/cm^2 and $7.5 \cdot 10^7$ P/cm^2 silica particles reached impedance values similar to those before pulse application (~ 0.93). The control population as well as cells in presence of $7.5 \cdot 10^6$ P/cm^2 showed an insignificantly small delay and re-population of the electrode was completed within 6.5 h.

In order to evaluate different experiments the *wound healing efficiency* (WHE_{4h}) after 4 h (dotted line in **Fig. 6.24 A**) was chosen as parameter and the results of four different experiments (N = 8) are summarized in **Fig. 6.24 B**. The column bars clearly show that wound healing and cell migration were found to remain unaffected by the presence of silica particles – independent of particle concentration. The time-resolved wound healing assays revealed impedance recoveries within four hours (WHE_{4h}) of (0.76 ± 0.05) for control cells. In presence of different concentrations of silica particles WHE_{4h} were found to be (0.78 ± 0.05) ($7.5 \cdot 10^6$ P/cm^2), (0.78 ± 0.06) ($3.7 \cdot 10^7$ P/cm^2) and (0.79 ± 0.07) ($7.5 \cdot 10^7$ P/cm^2).

The migration of NRK cells with or without silica particles ($3.7 \cdot 10^7$ P/cm^2) into the wounded area was additionally monitored microscopically using the live/dead stain with Calcein AM and Ethidium Homodimer (**chapter 3.4.2.2**).

Therefore, NRK cells were wounded electrically (40 kHz, 5 V, 30 s) and cells were allowed to migrate into the cell-free area for defined periods of time. A survey of fluorescence micrographs is shown in **Fig. 6.25** for unloaded NRK cells (**A**) and cells pre-loaded with silica particles for 24 h and stained (**B**) 2.0 h (**1**), 3.0 h (**2**), 4.5 h (**3**) and 6.0 h (**4**) after wounding. The size of the circular wound, created by the invasive voltage pulse is decreasing with increasing wound healing period (**1 – 4**). Cell migration was not inhibited by incorporated 2 µm particles in the cytoplasm of NRK cells. Even a slightly enhanced migration speed was found in presence of particles and complete wound closure was detected 6.0 h after pulsing (**B4**). In the fluorescence micrograph of control cells a small cell-free area was found where only red fluorescence of dead cell nuclei was detected (**A4**).

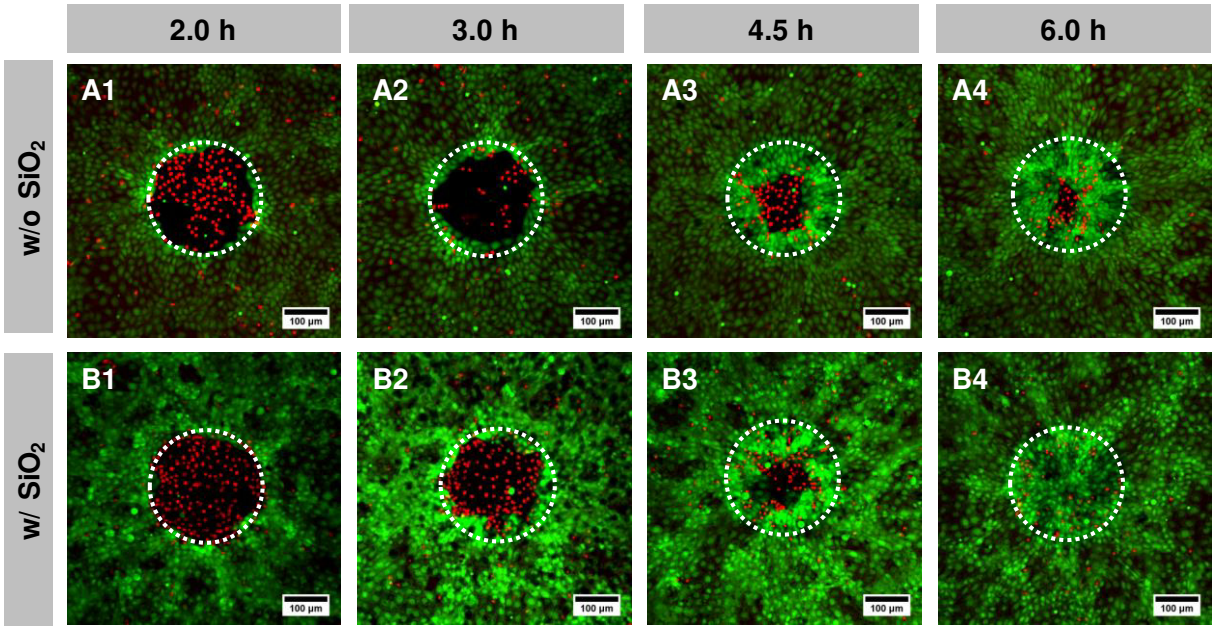

Fig. 6.25: Confocal fluorescence micrographs of NRK cells (**A**) and cells pre-loaded with silica particles (**B**; ∅ 2 µm; $3.7 \cdot 10^7$ P/cm^2) after live/dead stain with Calcein AM (**green**) and Ethidium Homodimer (**red**). Images were taken 2 h (**1**), 3 h (**2**), 4.5 h (**3**) and 6.5 h (**4**) after applying the wounding pulse (40 kHz, 30 s, 5 V). Position of the small working electrode is indicated by the dotted circle. Experiment was performed in serum containing medium. The scale bar represents 100 µm.

In summary, a complete wound closure was monitored in absence or presence of silica particles during the impedimetric wound healing assay. Moreover, similar WHE_{4h}-values were extracted from the time-course of impedance for control populations and NRK cells pre-loaded with silica particles. This indicates that silica particles have no influence on NRK cell migration independent of the applied concentration for a pre-loading period of ~ 24 h.

6.4.5 Long-Term Analysis of Silica Particles' Cytotoxicity in Serum-Free and Serum-Containing Medium

Additionally, the cytotoxic effect of silica particles in serum-free and serum-containing medium was analyzed using an observation time of 72 h. In these experiments only one concentration of silica particles ($3.7 \cdot 10^7$ P/cm^2) was applied to a confluent layer of NRK cells, cultured on 8W1E electrodes. **Fig. 6.26** summarizes the time-course of normalized impedance at 4 kHz (**A**) and 32 kHz (**B**) over 72 h.

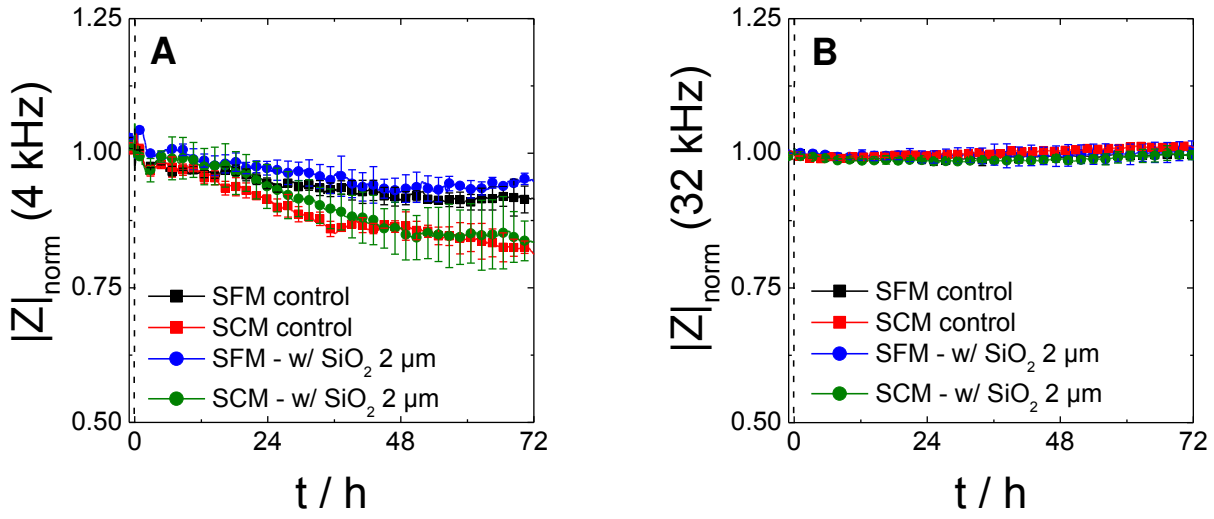

Fig. 6.26: Long-term analysis of cellular response after the addition of silica particles (∅ 2 µm; $3.7 \cdot 10^7$ P/cm^2) in serum-free (SFM) or serum-containing (SCM) medium: Typical time-course of $|Z|_{norm}$ at 4 kHz (**A**) and 32 kHz (**B**). Data were normalized to the start of microparticle exposure, represented by the dashed line (Mean ± SD; N = 2).

Independent of the presence of serum in the culture medium ECIS experiments over an observation time of 72 h revealed no indication of a cytotoxic effect caused by silica particles. At 4 kHz (**A**) cells in presence of particles behaved like the particle-free control in the respective medium in absence or presence of serum. A slight decrease in presence of serum was found in the time-course of $|Z|_{norm}$ at 4 kHz. After 72 h cells in medium supplemented with FCS (●;■) showed lower $|Z|_{norm}$ values (~ 0.83) compared to cells in serum-free medium (●;■) with $|Z|_{norm}$ values between 0.92 and 0.95. However, $|Z|_{norm}$ at 32 kHz, which is a sensitive frequency to analyze changes in cell coverage of the electrode, did not provide any significant differences in the time-course of impedance independent of the presence of silica particles or the medium composition (**B**).

In summary, cell vitality remained unaffected and ECIS experiments revealed no indications of cytotoxicity of silica particles up to an observation period of 72 h.

6.4.6 Analysis of Cell Proliferation

The influence of silica particles on NRK cell physiology was analyzed with respect to its influence on cell proliferation. Therefore, NRK cell division was monitored in absence or presence of silica particles with ECIS. Furthermore, label-based strategies were applied to support the ECIS results with optical methods.

6.4.6.1 Studying the Impact of Silica Particles on Cell Proliferation Using ECIS

To study the influence of silica particles (Ø = 2 µm) on cell proliferation, NRK cells were seeded on the gold electrodes (8W10E$^+$, Applied BioPhysics Inc., USA) in low density (20 000 cells/mL) and cell proliferation in absence or presence of silica particles ($3.7 \cdot 10^7$ P/cm^2) was monitored in a time-resolved manner (**Fig. 6.27**).

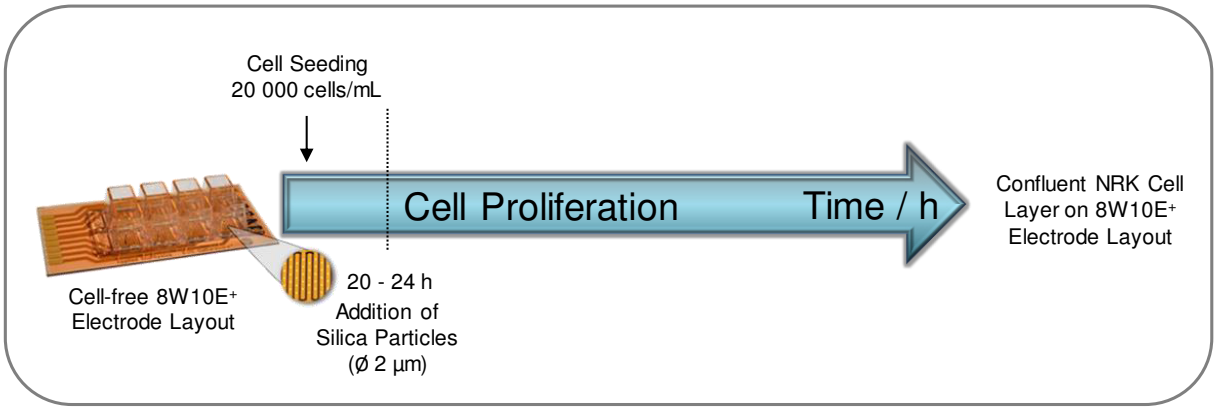

Fig. 6.27: Experimental design to investigate cell proliferation in absence or presence of silica particles using ECIS experiments.

The increasing coverage of 8W10E$^+$ electrodes with NRK cells was analyzed using the time-course of the capacitance and impedance at 32 kHz. Data were normalized to the value of a cell-free electrode. **Fig. 6.28** exemplarily shows the time-courses of capacitance (**A**) and impedance (**B**) for cell proliferation with or without silica particles over 120 h.

Only a small change in C_{norm} to 0.91 was found during the first 22 h after seeding. At that time-point fresh medium was added to control cells (■) and other NRK populations were exposed to silica particles in serum containing medium (○). Afterwards, C_{norm} continuously decreased independent of the experimental condition. After 48 h the C_{norm} value for control cells was (0.67 ± 0.06) whereas cells in presence of silica particles showed an insignificantly higher normalized capacitance signal of (0.70 ± 0.05). A further increase in electrode coverage was observed until $t = 72$ h with C_{norm} mean values of (0.36 ± 0.06) for untreated NRK cells and (0.40 ± 0.10) when silica microparticles were present. A confluent cell layer,

indicated by a constant C_{norm} value of 0.17 ± 0.01 was reached after 104.6 h for control cells and 113.7 h for cells in presence of silica particles.

The analysis of the normalized impedance $|Z|$ at 32 kHz for the same experiment (**B**) did not show any significant change until 48 h after cell seeding. Cells in absence or presence of silica particles only provided a slight increase to ~ 1.2. In contrast, C_{norm} at 48 h already showed a decrease to ~ 0.7 indicating a higher sensitivity of C even to small changes in cell coverage. Afterwards, a strong increase in $|Z|_{norm}$ was observed to ~ 2.2 (t = 72 h) and 3.8 (t = 96 h). The time-course of $|Z|_{norm}$ did not show any significant influence of silica particles on NRK cell proliferation. Control cells showed a stable $|Z|_{norm}$ value of ~ 4.3 after 110 h, whereas $|Z|_{norm}$ for cells in presence of silica particles were characterized by a further increase to ~ 4.6 until the end of experiment.

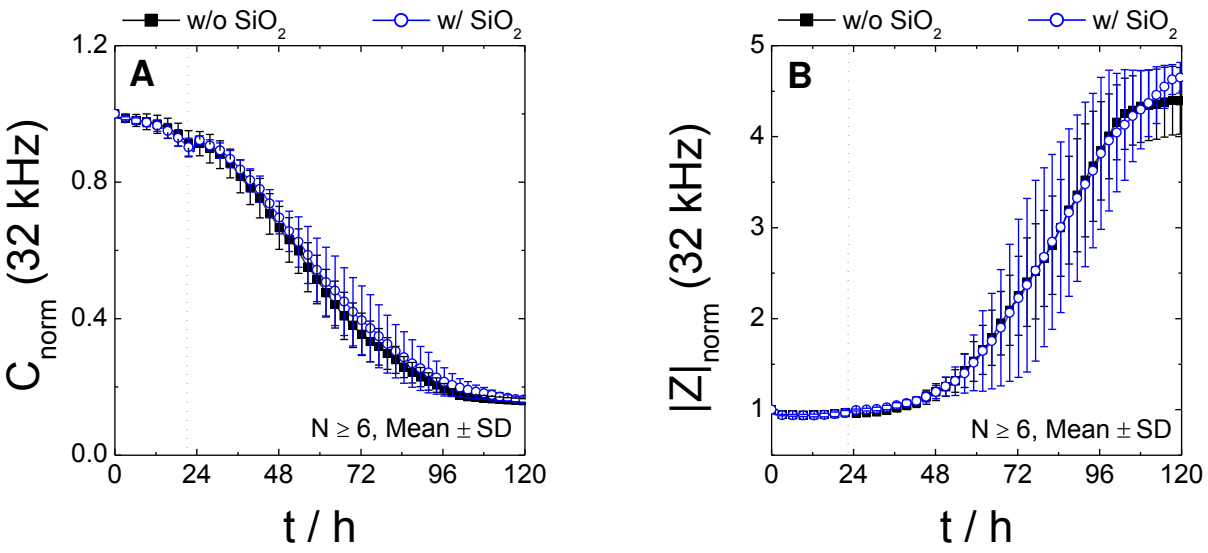

Fig. 6.28: Typical time-courses of normalized capacitance (**A**) and impedance (**B**) at 32 kHz for cell proliferation of NRK cells in absence (■) or presence (○) of silica particles ($3.7 \cdot 10^7$ P/cm^2). The time-point for the addition of particles or fresh medium is indicated by the dotted line. Time-course represents the mean value of at least six different wells within one experiment (Mean ± SD; N ≥ 6). Data were normalized to the respective cell-free value. Experiments were performed in serum containing medium.

At the end of the ECIS recordings the cell coverage was also analyzed microscopically after staining the cell nuclei with DAPI (blue) and the actin cytoskeleton with Alexa Fluor 488 Phalloidin (green). Confocal fluorescence micrographs for one field of view of each condition are exemplarily shown in **Fig. 6.29**. The overview (**1**) of DAPI-stained cell nuclei demonstrated the formation of a confluent cell layer under both conditions. The higher magnification of one field of view on the electrode showed that in presence of silica particles

(**B2**) the amount of cell nuclei was lower compared to the control condition (**A2**). Nevertheless, under both conditions an intact actin cytoskeleton, present in cells on the entire electrode surface, was found.

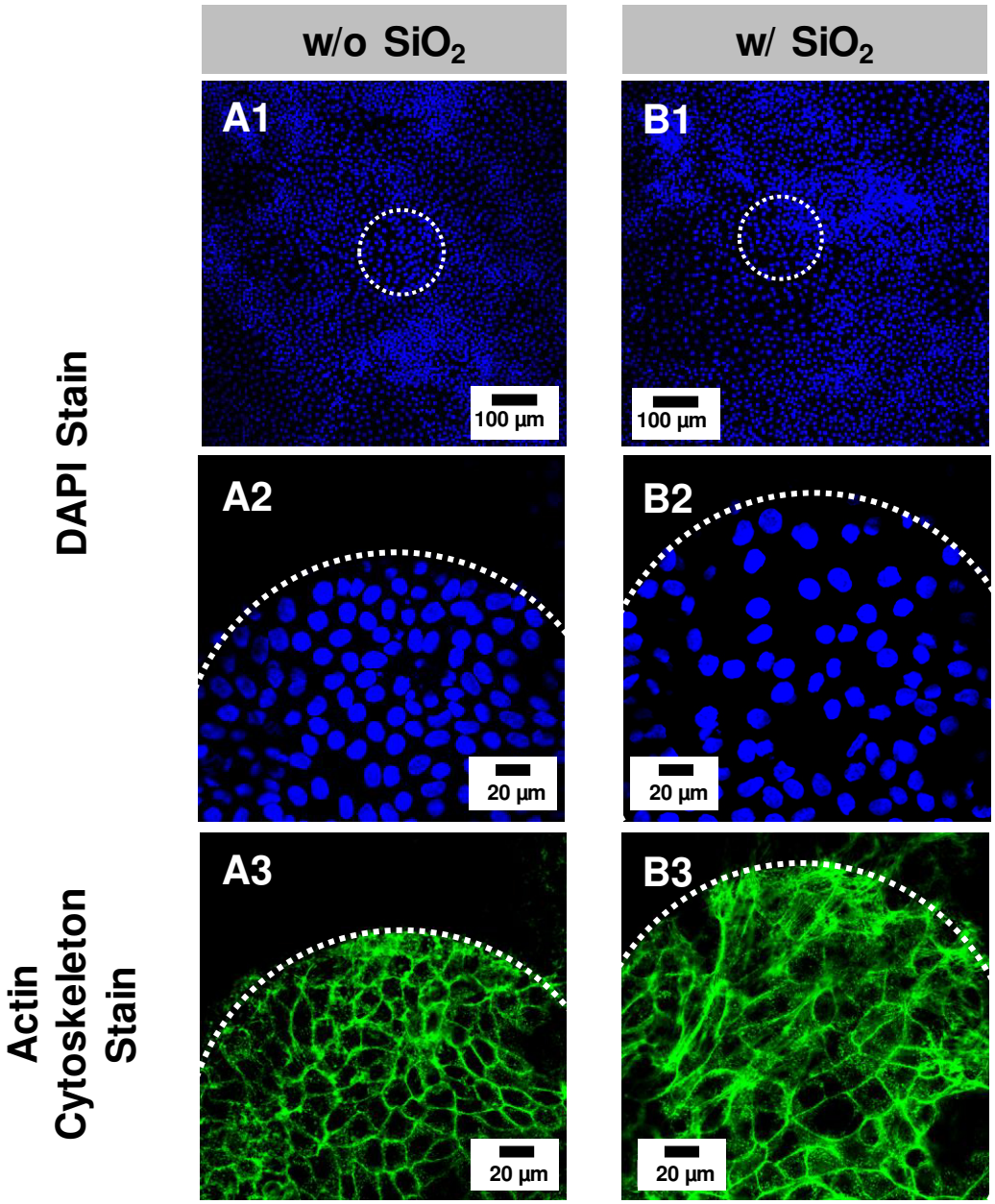

Fig. 6.29: Confocal fluorescence micrographs after cell nuclei stain with DAPI (**1;2**) and actin cytoskeleton stain (**3**) to visualize cell proliferation in absence (**A**) or presence (**B**) of silica particles at the end of impedance recordings. White circle represents the position of one electrode of the interdigitated 8W10E$^+$ electrode layout.

To further characterize cell proliferation, impedance data were analyzed with respect to the time-point of half maximum capacitance decrease ($t_{1/2}$) which corresponds to 50 % cell coverage according to the simulation results (**Fig. 4.25**). Additionally, the slope *s* of capacitance decrease was calculated between C_{norm} values of 0.7 – 0.5 to further quantify

the rate of proliferation. The results of two independent experiments are summarized in **Tab. 6.5**. No significant difference was found for both parameters. In the first experiment the maximum electrode coverage with cells was found after (46 ± 4) h for control cells and after (46 ± 3) h for cells in presence of silica particles.

The slope *s* of C_{norm} between 0.7 – 0.5 was determined to (- 0.016 ± 0.003) 1/h for NRK cells and to (- 0.019 ± 0.003) 1/h in presence of microparticles. Using another passage number the cell proliferation showed a slower proliferation rate compared to the first experiment. However, the $t_{1/2}$-value of (54 ± 4) h for control cells was similar and insignificantly different to the value for cells in presence of silica particles with (57 ± 5) h with similar slopes *s*.

Tab. 6.5: Overview of two independent proliferation experiments for NRK cells in absence or presence of silica particles in serum containing medium. C_{norm} data were analyzed at the time-point where the electrode was covered to 50 % with cells ($t_{1/2}$) and additionally the slopes *s* of the curves were calculated using a linear fit (Mean ± SD).

	$t_{1/2}$ / h	*s* / (1/h)
w/o silica particles (N = 7)	46 ± 4	- 0.016 ± 0.003
w/ silica particles (N = 7)	46 ± 3	- 0.019 ± 0.003
w/o silica particles (N = 6)	54 ± 4	- 0.014 ± 0.002
w/ silica particles (N = 7)	57 ± 5	- 0.014 ± 0.004

In summary, the time-course of cell proliferation was not significantly different in absence or presence of silica particles.

6.4.6.2 Studying the Impact of Silica Particles on Cell Proliferation Using an Optical Assay

Cell proliferation in absence or presence of silica particles (2 µm; $3.7 \cdot 10^7$ P/cm^2) was analyzed microscopically using nuclei stain with DAPI (**chapter 3.4.2.4**). Preliminary experiments showed a good correlation between defined seeding densities and the ImageJ analysis of fluorescence micrographs (**Fig. S 11**). Two different strategies for analysis of fluorescence micrographs were applied using ImageJ software:

(i) Identification of fluorescence area with a brightness of 255
(ii) Analysis of the number of cell nuclei

Cells were seeded in a low seeding density (10 000 cells/cm^2) in 96-well-plates. Similar to the ECIS experiment, cells were allowed to adhere for ~ 20 – 24 h before silica particles were added to the cells. NRK cells were fixed and stained with DAPI after defined periods of incubation (24 h, 48 h, 72 h, 96 h) and quantified by ImageJ.

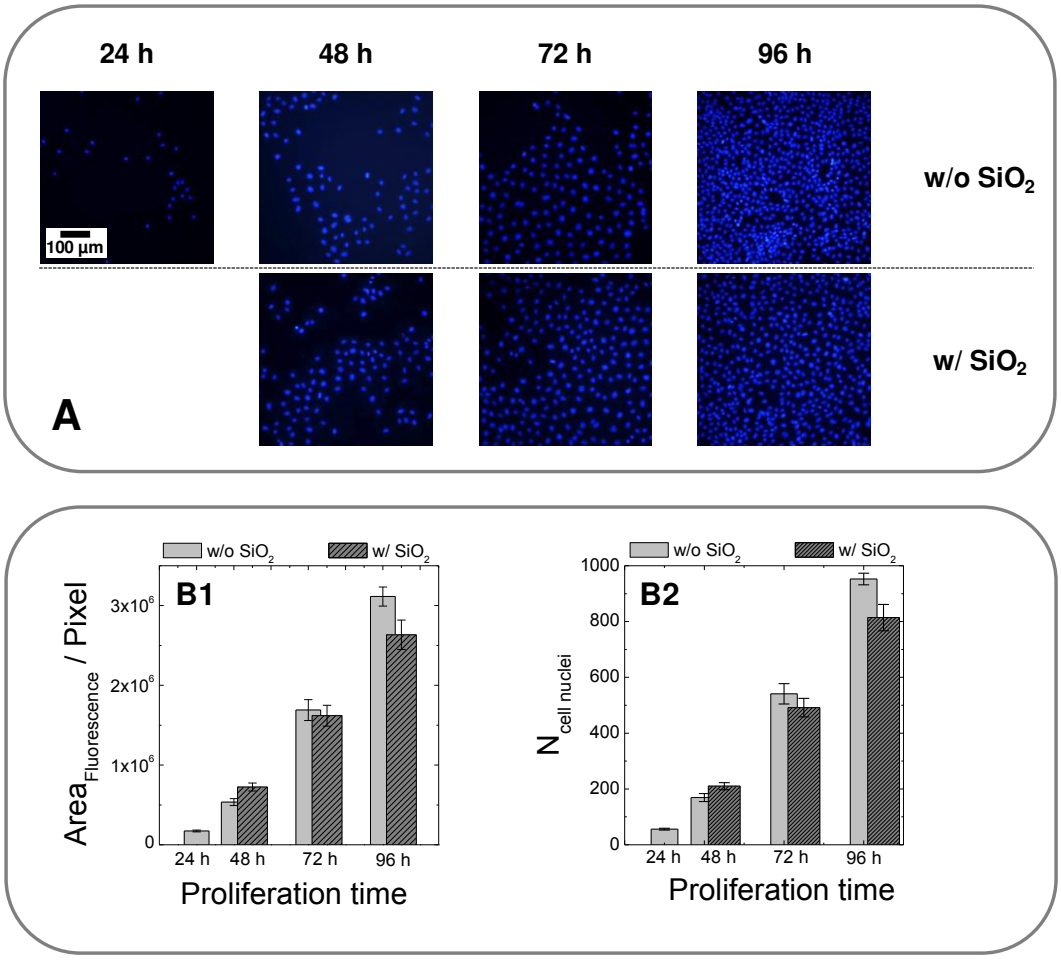

Fig. 6.30: A: Exemplary fluorescence micrographs after cell nuclei stain with DAPI for control NRK cells and cells in presence of silica particles 24 h, 48 h, 72 h and 96 h after cell seeding in serum containing medium. **B:** Analysis of typical fluorescence micrographs (N = 16; Mean ± SE) using ImageJ software to calculate the area of DAPI fluorescence (**B1**) or the number of cell nuclei (**B2**). Experiments were performed in serum containing medium.

The fluorescence micrographs (**Fig. 6.30 A**) clearly showed that independent of the presence of silica particles an increase in the number of DAPI-stained cell nuclei was detected with increasing proliferation time. After 96 h confluent cell layers were found for both conditions. The different fluorescence micrographs for each condition were analyzed with regard to the area of blue fluorescence (**B1**) or the number of cell nuclei (**B2**).

After 48 h the area of fluorescence increased from $(1.7 \pm 0.1)\cdot10^5$ to $(5.4 \pm 0.4)\cdot10^5$ (control) or $(7.3 \pm 0.5)\cdot10^5$ (w/ SiO_2). A further increase was found under both conditions in the following 24 h to $(17 \pm 1)\cdot10^5$ (control) and $(16 \pm 2)\cdot10^5$ (w/ SiO_2). In the end of the proliferation experiment an enhanced area of fluorescence was found for control cells ($(31 \pm 1)\cdot10^5$) compared to cells, incubated in presence of silica particles ($(26 \pm 2)\cdot10^5$).

The second method of analyzing fluorescence micrographs also indicated a similar proliferation behavior in absence and presence of silica particles up to 72 h resulting in (541 ± 37) cell nuclei for control cells and (492 ± 33) for NRK cells in presence of microparticles. In good correlation with the first analysis method also this evaluation yielded higher cell counts for untreated NRK cells (953 ± 21) compared to those with silica particles (814 ± 47) at the end of experiment.

6.4.6.3 Studying the Impact of Silica Particles on Cell Proliferation Using the PrestoBlue® Assay

A second analysis of cell proliferation to support the ECIS data was performed using the PrestoBlue® assay. In a proof of principle experiment it was found that the fluorescence intensity at 590 nm depends on the number of cells per well (**Fig. 6.31 A**). The summary of three independent experiments in which cell proliferation was monitored over 94 h in absence or presence of silica microparticles in serum containing medium indicated an increase in the fluorescence intensity at 590 nm with increasing proliferation time (**Fig. 6.31 B**). No differences for NRK proliferation under both conditions were observed. At $t = 70$ h NRK control cells and cells with silica particles showed similar results (18.0 ± 2.0). The final analysis after 94 h showed a slightly higher intensity for control cells (27 ± 3) compared to cells in presence of microparticles (25 ± 2). The cell-free control (*) independent of the proliferation time always showed a weak signal of ~ 1.6 – 1.7.

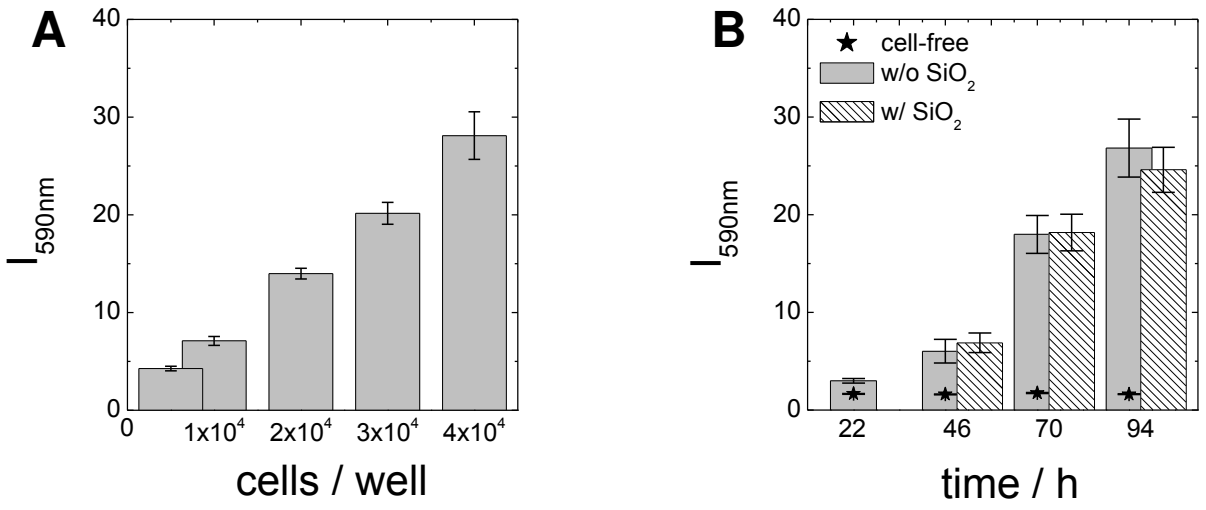

Fig. 6.31: A: Proof of principle experiment to show the validity of the PrestoBlue® assay to monitor cell proliferation. Defined cell densities between 5000 cells/well – 40 000 cells/well were seeded in serum containing medium. Fluorescence intensity was measured at 590 nm (Mean ± SD; N = 8). **B**: Analysis of cell proliferation in absence or presence of silica particles using the PrestoBlue® assay. Summary of three independent experiments in serum containing medium (Mean ± SD; N = 48).

6.4.7 Influence of Silica Particles on Gap Junctional Intercellular Communication

In the following the in-depth analysis of silica particle impact on NRK cell physiology was further extended using dye transfer based assays to analyze cell-cell communication via gap junctions. An introduction to cell-cell communication which mediates the exchange of small molecules via gap junctions was already given in **chapter 5**.

6.4.7.1 Classical Assays to Study Gap Junctional Intercellular Communication

First, the analysis of gap junctional intercellular communication was investigated with common techniques, like scrape loading assay, parachute assay or FRAP analysis. These assaya were performed with NRK cells as model cell line as these cells were found to be connected with its neighbors via gap junctions (**Fig. 5.13**).

First a scrape-loading assay (**chapter 6.3.5.1**) was performed with NRK cells and cells which were pre-loaded with silica particles (∅ 2 µm) 24 h in advance. This assay provides a simple and fast method to show the presence of gap junctions within a cell layer. **Fig. 6.32** summarizes fluorescence (**1**) and phase-contrast (**2**) micrographs of NRK cells in absence (**A**) or presence of silica particles (**B**). Additionally, the assay was performed in presence of the inhibitor 2-APB, which blocked the dye transfer via gap junctions into neighboring cells and only showed a fluorescence signal at the scratch border (**C**).

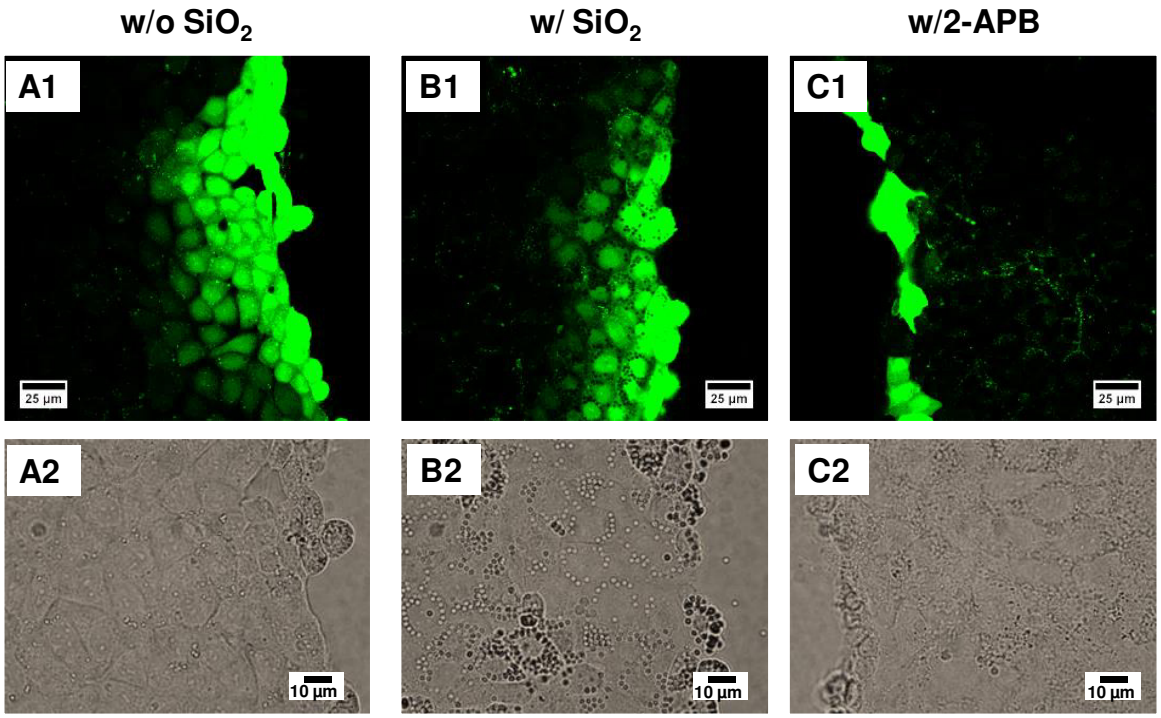

Fig. 6.32: Confocal fluorescence micrographs (**1**) and phase-contrast images (**2**) of NRK cells (**A**), cells pre-loaded with silica particles ($7.5 \cdot 10^6$ P/cm^2; **B**) and cells in presence of the 100 µM 2-APB (**C**). NRK cells were scraped in presence of Lucifer Yellow with a small pipette tip. Lucifer Yellow can then enter the cytoplasm of cells, which are located along the path of the tip. Due to gap junctions, Lucifer Yellow can diffuse into adjacent cells, resulting in a decrease of fluorescence intensity perpendicular to wound line.

After scraping the cells in presence of Lucifer Yellow, the dye could diffuse into the adjacent cells and dye transfer to some neighboring cells was found under control conditions (**A1**). When cells were pre-loaded with silica particles for 24 h the dye transfer was not significantly inhibited by the presence of microparticles (**B1**). Obviously, dye transfer was strictly limited to the cells at the scrape border when 2-APB was present (**C1**).

In the following the *de novo* formation of gap junctions in an NRK cell layer was monitored in absence or presence of silica particles using a parachute assay (**chapter 6.3.5.2**).

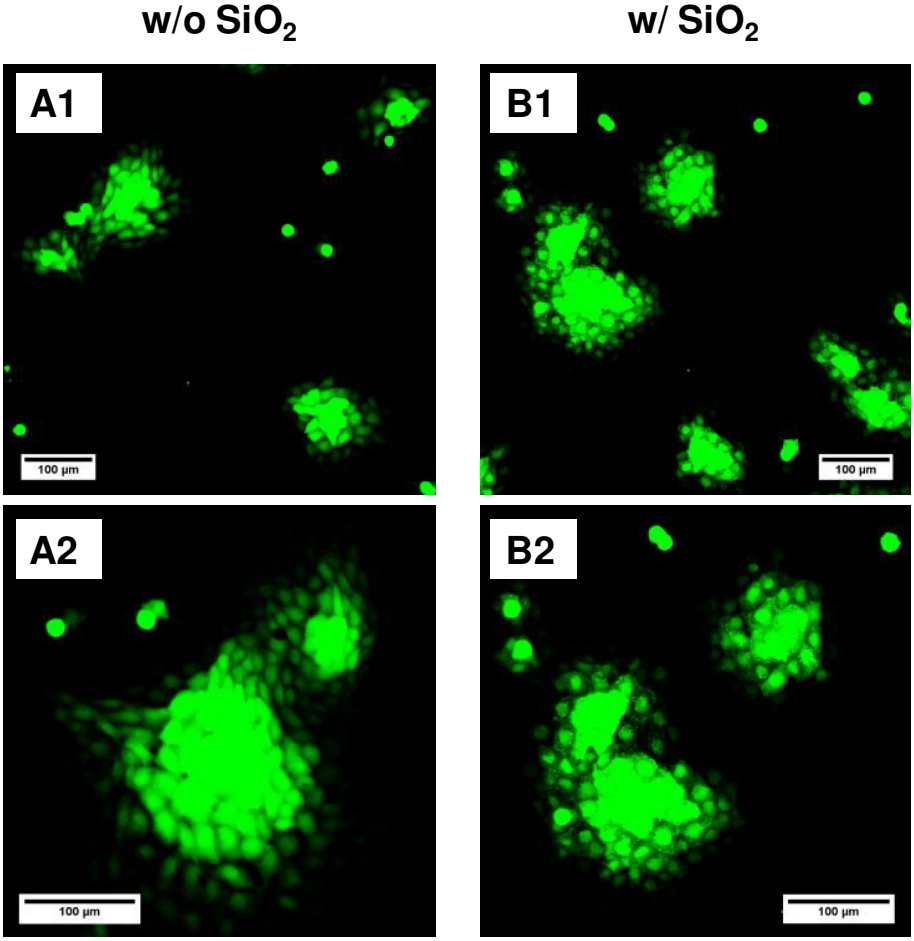

Fig. 6.33: Confocal fluorescence micrographs for NRK cells (**A**) and cells pre-loaded with silica particles (**B**) after formation of gap junctions analyzed via parachute assay. For this assay a particle concentration of $3.7 \cdot 10^7$ P/cm^2 of the 2 µm-sized silica particles was applied to the acceptor cells.

After the formation of gap junctions between the pre-stained donor cells and the unstained acceptor population independent of the absence (**A**) or presence of silica particles (**B**) in the acceptor cells dye diffusion into the monolayer was detected via confocal laser scanning microscopy. In all images pre-stained donor cells were found, which did not form gap junctions with the neighboring unstained cells and no dye transfer into the monolayer was

found. The parachute assay provided similar gap junction coupling of NRK cells without finding any impact of silica particles on the channel formation and function.

A different approach where the gap junctional intercellular communication can be analyzed with a high time-resolution is the FRAP assay (**chapter 6.3.5.3**). Selected cells of a pre-stained cell population were bleached by a highly intense laser pulse and the fluorescence recovery in the cytoplasm of the photo-bleached cell, indicated by an increase in the fluorescence signal to approximately pre-pulse values, was monitored with time.

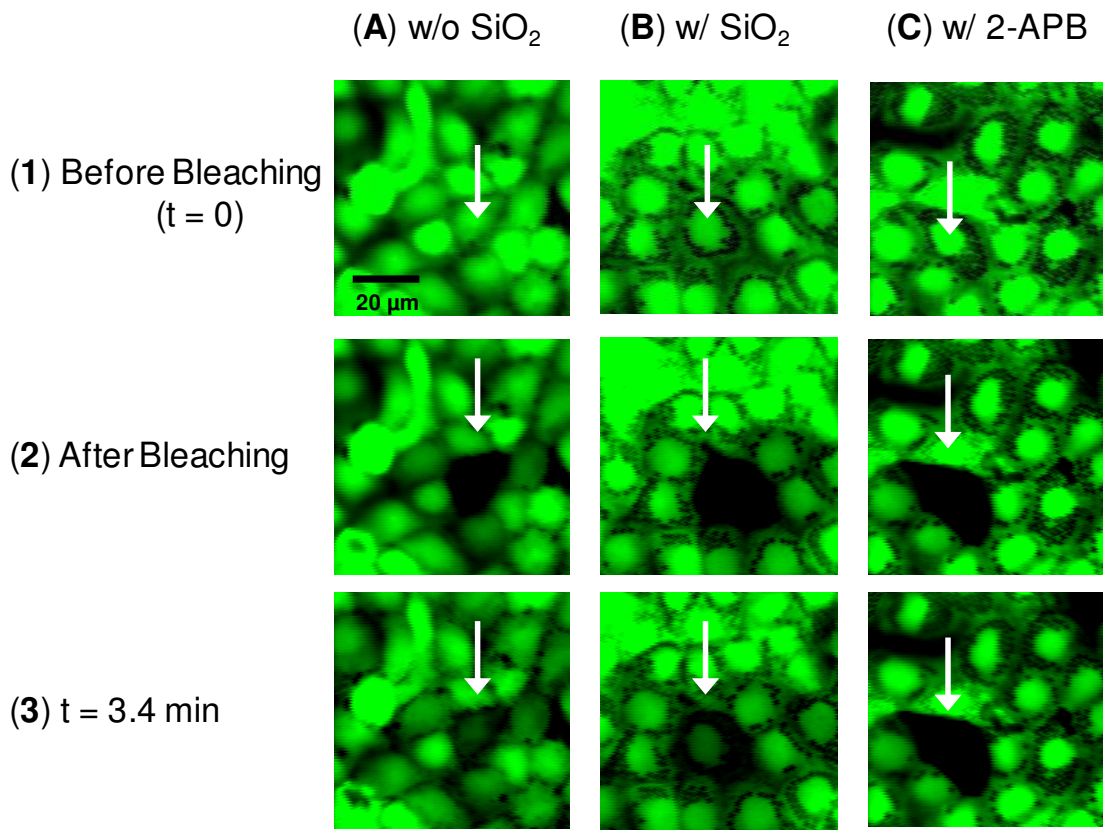

Fig. 6.34: Typical confocal fluorescence micrographs of NRK cells (**A**), cells in presence of silica particles (**B**) or in presence of the gap junction inhibitor 2-APB (**C**) during the FRAP assay. Cells are shown before bleaching (**1**), immediately after bleaching a selected cell (arrow) (**2**) and 3.4 min after bleaching (**3**). Fluorescence recovered in absence and presence of silica particles (**A3; B3**) whereas the target cell remained dark in presence of the inhibitor 2-APB (**C3**). For this assay a particle concentration of $3.7 \cdot 10^7$ P/cm^2 of the 2 µm-sized silica particles in presence of serum was applied to the confluent cell layer 24 h prior to the FRAP experiment.

Fig. 6.34 summarizes fluorescence micrographs of different stages (**1 – 3**) for one target cell, highlighted by the white arrow, during FRAP analysis under different conditions (**A – C**). Significant differences were found in the time-dependent recovery of NRK cells in absence (**A; B**) or presence of the inhibitor 2-APB (**C**). Whereas NRK control cells and cells pre-loaded with silica particles at the end of analysis again provided a green fluorescence inside the cytoplasm, which was most prominent at the position of the cell nuclei, the cytoplasm of the photo-bleached cell remained completely dark when 50 µM 2-APB was present. Further

characterization of the recovery of fluorescence dye inside the cytoplasm of NRK cells was performed using ImageJ. In this analysis the fluorescence intensity of the selected cell was quantified over time. Additionally, one control cell per image was selected, which did not receive a high intensity pulse, and the fluorescence intensity over time was detected to correct for dye fading.

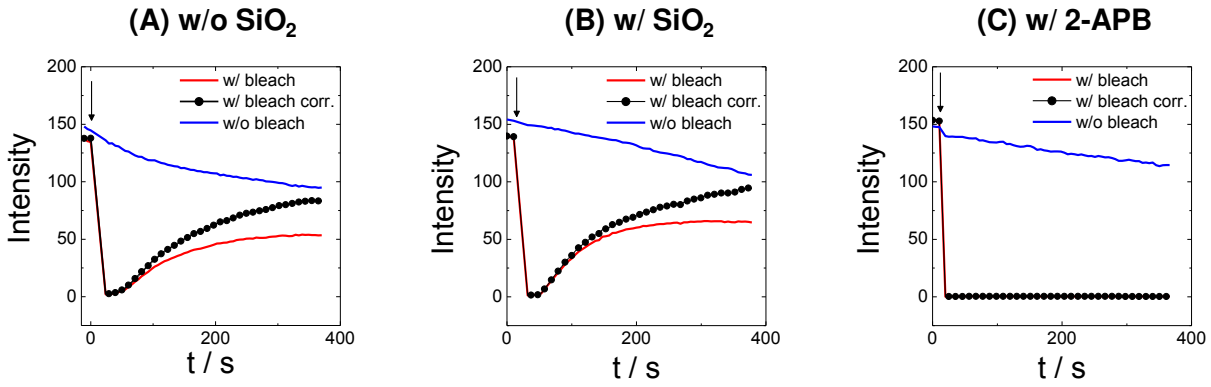

Fig. 6.35: Typical time-courses of fluorescence intensities (**red**) before and after bleaching NRK control cells (**A**), cells which were pre-loaded with silica particles (**B**) and cells in presence of the inhibitor 50 µM 2-APB (**C**). Additionally, the changes in fluorescence intensity of a non-treated cell (**blue**) was monitored over time and used for the correction of fading due to recording the microscopic images every 5 s. A correction value for each image was calculated and used for data correction for the time-course of the bleached target cell (**line with symbol**). Time-point $t = 0$ indicates the last image immediately before bleaching which served as reference for the calculation of the recovery. Curves represent the response of a single cell.

The time-courses of intensities were further processed to eliminate fading of Calcein only due to the microscopic performance. Therefore, a correction value was calculated using the equation **Eq. 6.2**. After initiating the FRAP assay by photo-bleaching (↓) the intensity significantly decreased to 0 followed by a time-dependent increase in fluorescence intensity for NRK control cells (**A**) and cells pre-loaded with silica particles (**B**). In contrast, no change in fluorescence intensity within the cytoplasm of NRK cells was found when the gap junction inhibitor 2-APB (50 µM) was present (**C**). The cytoplasm of the treated cells remained dark over the entire measurement. Obviously, the auto-bleaching effect should not be neglected as even untreated cells provided a decrease in fluorescence intensity over time (**blue**). Using the correction value, this effect can be eliminated and corrected curves (line with symbols) provided a higher recovery compared to the raw data (**red**) and facilitated the comparison of different experiments.

Recovery of the fluorescence signal after photo-bleaching under different conditions was quantified by **Eq. 6.4** and recovery of seven different images for control cells and cells after pre-loading with silica particles are summarized in **Fig. 6.36**. Additionally, four different images in presence of the gap junction inhibitor 2-APB are included in the analysis. Using

NRK cells, the intensity of the calcein fluorescence signal under control conditions recovered to (54 ± 6) % and cells after pre-loading with silica particles recovered to (45 ± 16) %. A significant difference was found for cells in presence of 50 µM 2-APB which showed almost no recovery (0.4 ± 0.6) % during the observation time.

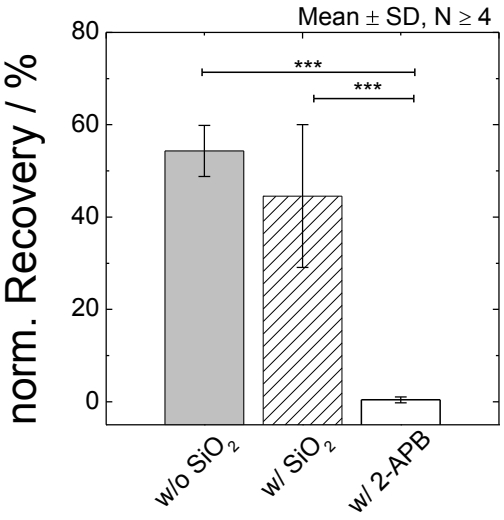

Fig. 6.36: Quantification of fluorescence recovery 6.2 min after photo-bleaching a single NRK cell of a control population, cells pre-loaded with silica particles and cells in presence of 50 µM 2-APB. When cells expressed intact gap junctions Calcein could diffuse from neighboring cells into the targeted cell causing an increase in fluorescence intensity over time. (Mean ± SD; N ≥ 4). Significance between the two populations was determined by a two-sample t-test using a significance level of 0.01 (***).

In this study three different dye transfer based techniques, which are commonly used to study gap junctional intercellular communication, clearly demonstrated the ability of NRK cells to communicate via gap junctional intercellular communication. The presence of silica particles with a diameter of 2 µm did not inhibit or influence the ability to transport Lucifer Yellow via gap junctions. A clear inhibition was obtained when the inhibitor 2-APB was present.

6.4.7.2 Analysis of the Impact of Silica Particles on Gap Junctional Intercellular Communication Using the Developed Opto-Electrical Assay

The common techniques to investigate gap junctional intercellular communication only provide microscopic information about dye transfer via gap junction. However, no further information about the impact on cell physiology and metabolic activity or about cell responses after the addition of silica particles for the same cell population can be obtained from these label-based assays. The opto-electrical assay, which was presented in **chapter 5** was used and applied to investigate the effect of silica particles on NRK gap junctional intercellular communication microscopically. In this assays cells are grown on gold-film electrodes which allows the combination with non-invasive ECIS recordings prior to the microscopic dye-transfer analysis. Doing so, the effect of silica particles on cell vitality, motility and on gap junctional intercellular communication can be studied during one experiment using one NRK cell population.

6.4.7.2.1 Electroporation of NRK Cells Pre-Loaded With Silica Particles

In preliminary experiments it was analyzed if a membrane-impermeable dye can be incorporated into silica pre-loaded NRK cells by *in situ* electroporation in high efficiency and without a negative effect on cell viability. To analyze, if electroporation is possible without any cell damages in presence of microparticles, control and particle-loaded NRK cells were electroporated in presence of FITC dextran (4 kDa, 1 mg/mL) using different voltages (2.5 – 4.0 V) whereas pulse duration and frequency were kept constant (200 ms, 40 kHz). NRK cells were pre-loaded with silica particles (∅ 2 µm; $3.7 \cdot 10^7$ P/cm^2) 24 h prior to the electroporation experiment.

Fig. 6.37 summarizes the time-courses of $|Z|_{norm}$ at 4 kHz before and after electroporation for NRK cells (■) and cells pre-loaded with silica particles (○) using different parameters. Independent of the applied voltage cells recovered within ~ 30 min. Furthermore, the presence of silica particles did not provide any influence on cell recovery since this occurred within the same time-scale. Only after application of two pulses (**D**) cells pre-loaded with silica particles showed a slightly retarded recovery time-course compared to the control population. These results were obtained by a single experiment. It requires further investigations to characterize if these differences in impedance recovery which were observed during the two-pulse experiment are significant.

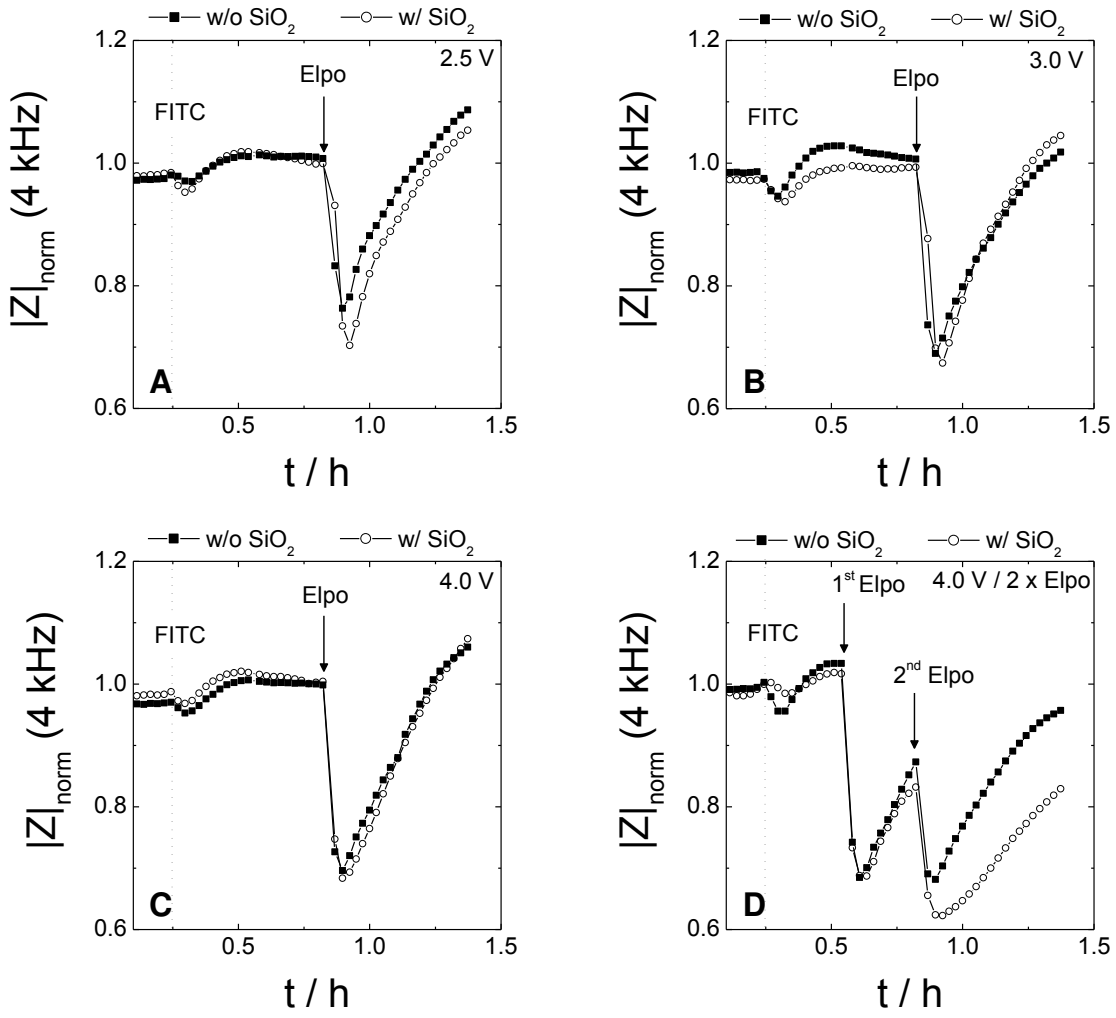

Fig. 6.37: Time-course of normalized impedance at 4 kHz for the electroporation of NRK cells (■) and cells pre-loaded with silica particles (∅ 2 µm; $3.7 \cdot 10^7$ P/cm^2 ;24 h; ○) in presence of FITC dextran (4 kDa, 1 mg/mL in EBSS^{++}) using a 8W1E electrode layout. The applied electroporation pulse voltage was varied between 2.5 V (**A**), 3.0 V (**B**) and 4.0 V (**C;D**) using a constant pulse duration (200 ms) and frequency (40 kHz). NRK cells shown in **A – C** were electroporated using a single pulse protocol and cells in **D** were exposed to a 2nd electroporation pulse with 4.0 V and the time between two sequential pulses was 15 min. The time-courses represent cellular responses, which were determined in a single experiment (T = 37 °C).

Fig. 6.38 shows a survey of fluorescence micrographs for the electroporation-mediated dye-uptake into NRK cells. The position of the circular working electrode is indicated by a white, dashed circle. Fluorescence intensity increased by applying higher voltages independent of the presence of silica particles. In good agreement with previously determined optimal electroporation parameters for NRK cells, also in presence of particles the best parameters were found to be 40 kHz, 200 ms and 4 V. As described in **chapter 5.5.3** an enhanced uptake efficiency of FITC dextran into particle-loaded cells was found using the two-pulse protocol (**A4; B4**). Even if NRK cells showed a densely-packed silica particle loading inside the cytoplasm (**B3 60W**), cells could be successfully loaded with the fluorescent dye and membrane resealing and recovery were not inhibited by the presence of particles.

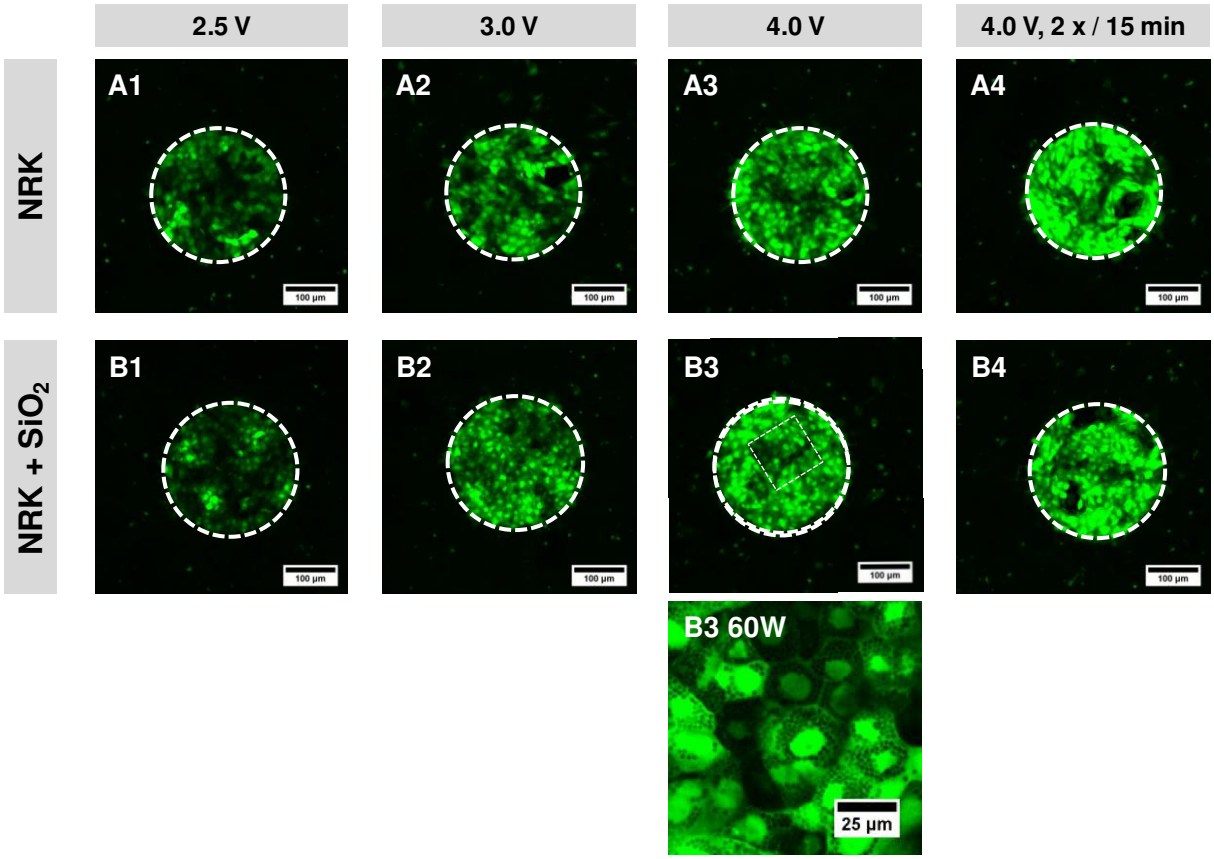

Fig. 6.38: Confocal fluorescence micrographs of NRK cells (**A**) and cells, which were pre-loaded with silica particles (∅ 2 µm; $3.7 \cdot 10^7$ P/cm^2, 24 h; **B**) after electroporation in presence of FITC dextran (4 kDa, 1 mg/mL). Cells were electroporated with a single electroporation pulse of 40 kHz, 200 ms and varying voltages of 2.5 V (**1**), 3.0 V (**2**), 4.0 V (**3**) or using a two pulse protocol (**4**). Images were taken using a 10 x objective and similar gain settings for all images. Additionally, a higher magnification for particle pre-loaded NRK cells from **B3** (white dashed square) is shown which was taken with a 60 x W objective to emphasize the presence of silica particles inside the cytoplasm (**B3 60W**). The position of the 8W1E working electrodes is indicated by the white, dashed circle. The scale bar represents 100 µm (**A; B 1 – 4**) or 25 µm (**B3 60W**).

The results of this preliminary experiment offered the possibility to analyze gap junctional intercellular communication also in presence of silica particles using the developed opto-electrical assay. Therefore, no further modifications of the protocol (**chapter 5.4.2**) were necessary with the exception that cells have to be pre-incubated with the particles 24 h prior to the electroporation experiment.

6.4.7.2.2 Analysis of Cell Attachment and Response to the Addition of Silica Particles to a Confluent Cell Layer Prior to the Opto-Electrical Assay

The experiment was performed with the newly designed 8W4E-GJ electrode layout (**chapter 5.5.4.4.3**) to impedimetrically analyze cell attachment and spreading of NRK cells (600 000 cells/mL) directly after cell seeding (**Fig. 6.39 A**). The formation of a confluent cell layer was recorded over 24 h in a label-free and non-invasive manner. No differences in the time-course of capacitance for all eight wells were found providing similar cellular conditions in all different wells for the following assay.

24 h after cell seeding, NRK populations in two wells were incubated with silica particles (2 µm; $3.7 \cdot 10^7$ P/cm^2), whereas in the remaining wells only culture medium was exchanged (**B**). Using non-invasive ECIS recordings, the response of NRK cells during 24 h of incubation either in fresh culture medium (**black**; Mean ± SD; N = 6) or in presence of silica particles (**blue**; Mean ± SD; N = 2) was monitored (**B**). No significant changes in the time-course of $|Z|_{norm}$ at a monitoring frequency of 16 kHz were found. Cells in presence of silica particles even provided a slightly enhanced impedance value (~ 0.96) compared to control cells (~ 0.92) at the end of experiment (t = 25 h).

Micromotion of NRK cells in presence of silica particles was investigated during (2.75 h; 3.75 h) and at the end of incubation (t = 24 h). Quantification of RTC data was performed as described before. The motility index, as a parameter of the metabolic activity of a cell population, for control cells and after different incubation times with silica particles did not reveal any significant differences (**C**).

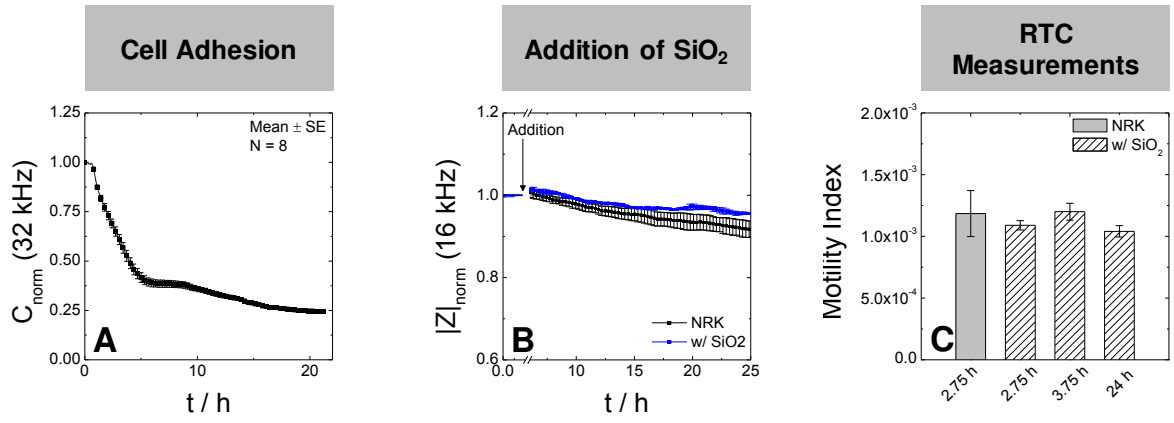

Fig. 6.39: Impedimetric analysis prior to the dye transfer analysis using an ECIS-based sequence of different non-invasive assays in a single experiment: **A:** Analysis of cell adhesion and spreading immediately after cell seeding (600 000 cells/mL) on 8W4E-GJ gold-film electrodes. **B:** Monitoring of cellular response after the addition of silica particles (**blue**) over 24 h (∅ 2 µm; $3.7 \cdot 10^7$ P/cm^2) (N =2; Mean ± SD). **C:** Analysis of cell motility using RTC measurements[k] and quantification of micromotion using the motility index (N =2; Mean ± SD). Here, RTC measurements were performed during (t = 2.75 h and 3.75 h) and at the end (t = 24 h) of silica particle incubation time. No significant differences were obtained independent of the incubation time with silica particles.

[k] In contrast to the RTC experiments presented in **chapter 6.4.4.2** a time resolution of 128 points/s was chosen.

6.4.7.2.3 Dye transfer Analysis to Investigate the Influence of Silica Particles on Gap Junctional Intercellular Communication

The electroporation experiment requires the addition of the fluorescent dyes Lucifer Yellow and TRITC dextran and also the application of an invasive voltage pulse for introduction of the dyes into selected cell populations. The protocol and more information about data analysis were already presented in **chapter 5**.

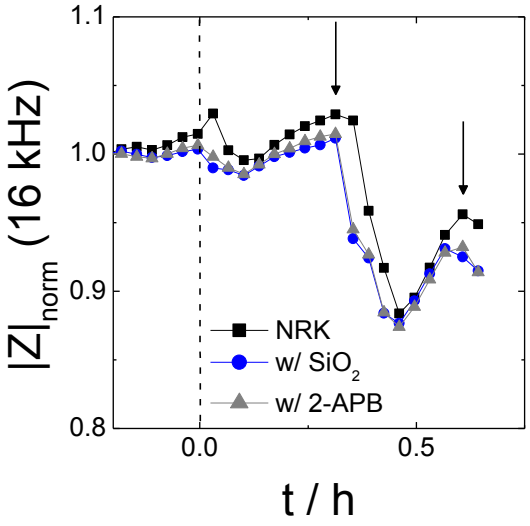

Fig. 6.40: Typical time-courses of normalized impedance |*Z*| at 16 kHz for NRK cells grown on 8W4E-GJ gold-film electrodes before and after two-pulse electroporation (40 kHz, 4 V, 200 ms) in presence of Lucifer Yellow and TRITC dextran. Dye transfer between NRK cells after incorporation of the dyes by electroporation was investigated using different conditions: NRK control cells (■), cells which were pre-loaded with silica particles (●) or cells in presence of 50 µM 2-APB (▲). The experiment was finished 5 min after the 2nd pulse. One exemplary time-course of impedance for each condition is shown. The time-points of electroporation are indicated by the arrow (↓).

ECIS recordings before and after the two-pulse electroporation are shown in **Fig. 6.40**. After electroporation cells were gently washed to remove the extracellular dye and prepared for confocal laser scanning microscopic analysis. **Fig. 6.41** provides a survey of fluorescence micrographs of NRK control cells (**1**), cells pre-loaded with silica particles (**2**) and cells in presence of the gap junction inhibitor 2-APB (**3**). One typical data set for each condition is presented.

Gap junction-mediated dye transfer for Lucifer Yellow, initially incorporated into the cytoplasm of NRK cells on top of the electrode, into the photopolymer-free gap between the two electrodes was found for untreated NRK cells and also when cells were loaded with silica microparticles before (**1; 2**). In both cases, the reference dye TRITC dextran was only detected in cells which were located on the semi-elliptical electrodes (**B1; B2**). Again, the presence of 50 µM 2-APB significantly blocked the dye transfer for Lucifer Yellow into

neighboring cells and a complete overlay between the fluorescence signals in the green and red channel was found (**3**).

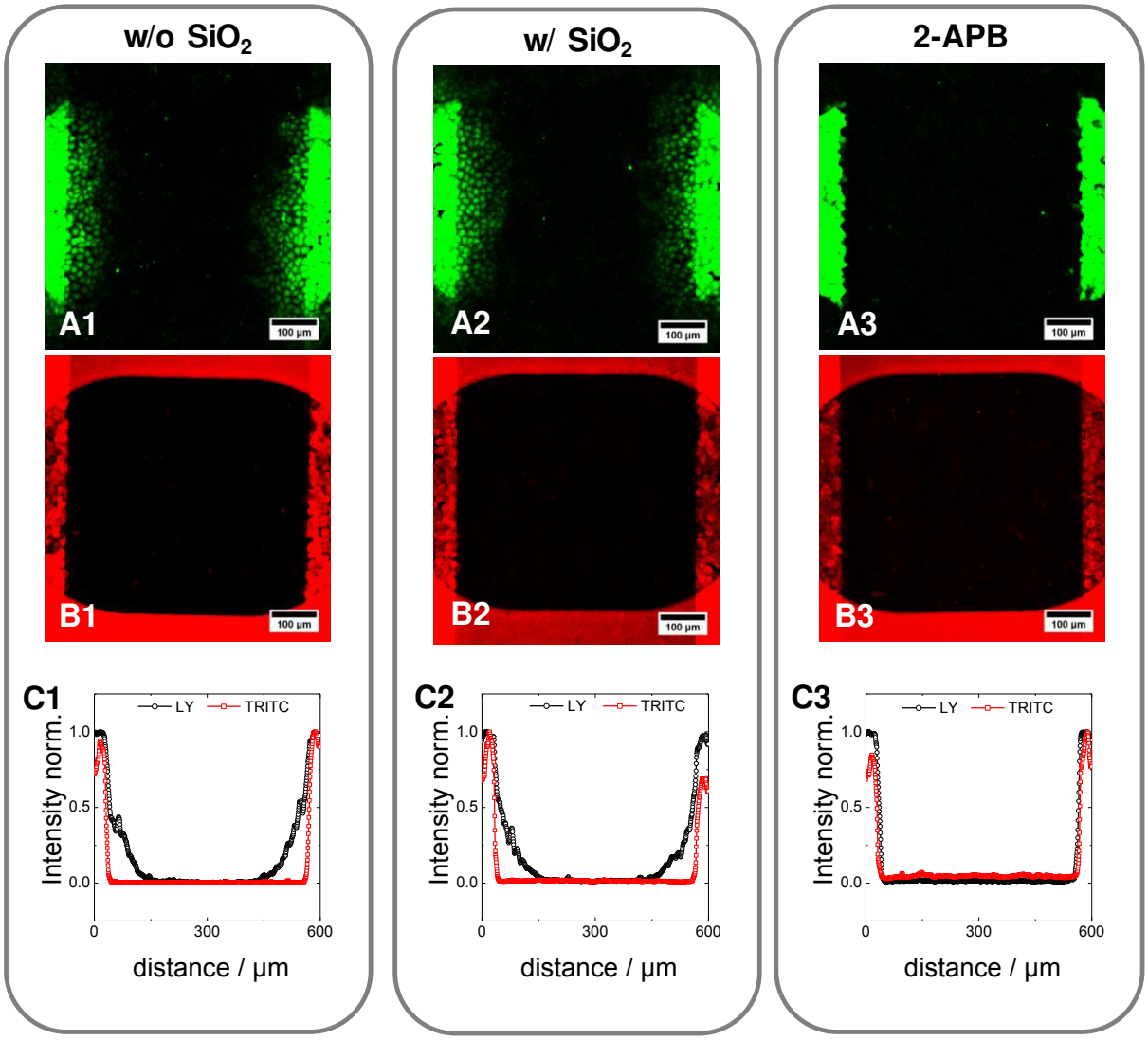

Fig. 6.41: A; B: Typical confocal fluorescence micrographs of NRK cells after two-pulse electroporation in presence of Lucifer Yellow (**A**) and TRITC dextran (**B**). NRK cells were electroporated in $EBSS^{-+}$ (w/o Ca^{2+}) (**1; 2**) or in $EBSS^{-+}$ supplemented with 50 µM 2-APB (**3**). Pre-treatment of NRK cells 24 h in advance was either in culture medium (**1; 3**) or in presence of $3.7 \cdot 10^7$ P/cm^2 silica particles (**2**). **C:** Analysis of a defined ROI and the normalized intensities of the red and green channel were plotted as a function of distance. The scale bar represents 100 µm (**A; B**).

A higher magnification of fluorescence micrographs after performing the electroporation-based analysis of dye transfer between NRK cells and cells in presence of silica particles is shown in **Fig. 6.42**. The different sizes of the fluorophores resulted either in a homogeneous dye distribution into the entire cytoplasm including the cell nuclei (Lucifer Yellow; green) or showed a fluorescence signal where the nuclei remained dark (TRITC dextran; red) due to the size exclusion of the nuclear-pore complex. The silica particles without any label appear as black spots in the green and red channel.

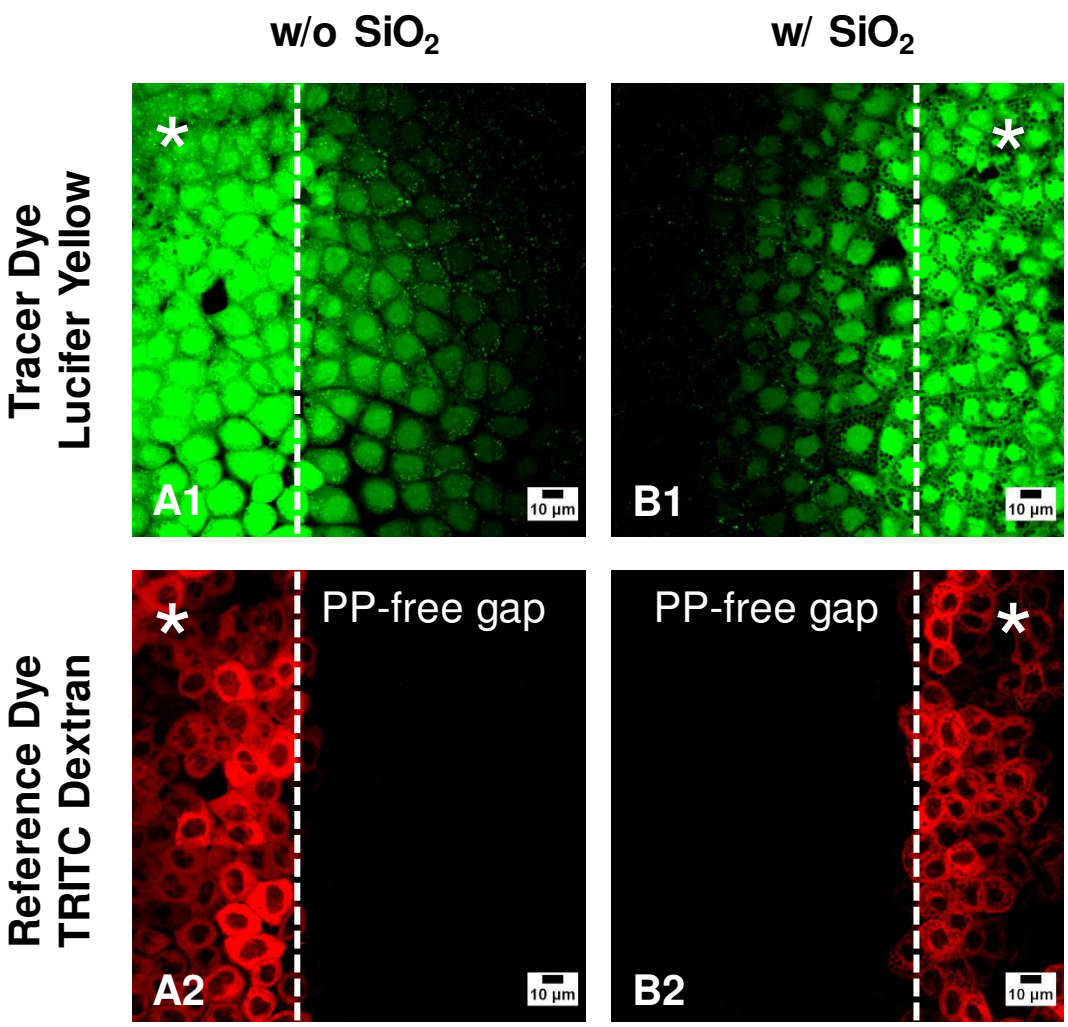

Fig. 6.42: Typical confocal fluorescence micrographs after performing the opto-electrical assay to investigate gap junctional intercellular communication between NRK cells (**A**) and cells after 24 h of pre-loading with silica particles ($3.7 \cdot 10^7$ P/cm^2) (**B**). Cells were electroporated in presence of Lucifer Yellow (green; **1**) and the reference dye TRITC dextran (red; **2**) using the two-pulse protocol. Dye transfer from the initially stained cells on top of the electrode (*) via gap junctions into the photopolymer-free (PP) gap between the two electrodes was investigated. Only the small tracer dye can diffuse via gap junctions whereas the reference dye indicated the efficiency of primary loading. The scale bar represents 10 µm.

Further analysis was performed using the AUC (area under the curve)-approach in a defined ROI (**chapter 5.5.4.5**) for which the intensities of Lucifer Yellow and TRITC dextran were position-dependently plotted (**Fig. 6.41 C**).

Fig. 6.43 summarizes the results of at least three independent experiments where 10 – 16 different sets of images were analyzed regarding their intensity profiles and AUCs.

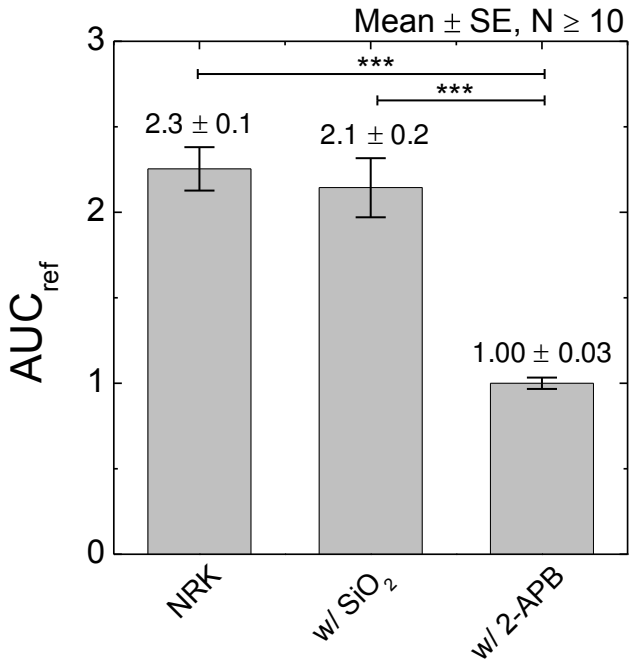

Fig. 6.43: Normalized AUC values for NRK cells, cells pre-loaded with silica particles ($3.7 \cdot 10^7$ P/cm^2) and cells in presence of the gap junction inhibitor 50 µM 2-APB. Individual AUC values from at least three independent experiments were referenced to the AUC of cells in presence of 2-APB. (Mean ± SE; N ≥ 10). Significance was determined by a two-sample t-test using a significance level of 0.01 (***).

Data were normalized using the AUC of cells in presence of the gap junctional intercellular communication inhibitor 2-APB in each experiment. For NRK cells under control conditions the mean AUC_{ref} was (2.3 ± 0.1) and could be clearly distinguished from the populations with inhibited gap junctional intercellular communication in presence of 50 µM 2-APB (1.00 ± 0.03). NRK cells which were pre-loaded with silica particles for 24 h and therefore provided a densely-packed particle distribution inside the cytoplasm did not show a different gap junctions-mediated dye transfer. A mean AUC_{ref} of (2.1 ± 0.2) was found which is not significantly different compared to control cells.

In summary, the common techniques like scrape loading assay, parachute assay and FRAP analysis did not show an inhibition of gap junctional intercellular communication when cells have taken up silica particles during 24 h of incubation. A more intense study using the opto-electrical assay developed in this thesis to quantify dye transfer by calculating the AUC between the intensity profiles of the gap junction-permeable dye Lucifer Yellow and the reference dye TRITC dextran did not show any significant differences. The combination with non-invasive ECIS recordings, which already started after cell seeding, allowed monitoring the cell layer formation, the cellular response to the addition of silica particles and cell motilities. The final assay based on electroporation and subsequent optical analysis of dye transfer via confocal laser scanning microscopy completed the detailed study on the impact of silica particles on NRK cell physiology finding no significant impact of silica microparticles on gap junctional intercellular communication.

6.5 Studying the Beating of Cardiomyocytes Using ECIS

Research on the influence of silica particles on the physiology of adherent cells was extended using cardiomyocytes which are efficiently connected via gap junctions. Cardiomyocytes are a prime example of cells where an intact cell-cell communication via gap junctions is crucial for the functionality of an organ. Gap junctional intercellular communication allows an impulse propagation into neighboring cardiomyocytes which is necessary for a synchronous beating of the heart. The aim of this project was to analyze the contractile performance of beating cardiomyocytes using ECIS and to investigate the influence of silica microparticles on cardiomyocytes during a pre-loading incubation time of 24 h. The setup was validated using Cor.At® cells whose beating efficiency was modulated by adding 100 nM Isoproterenol hydrochloride, by removing Ca^{2+} from the supernatant or by adding 1-heptanol, which is known to inhibit gap junctional intercellular communication.

6.5.1 Beating Analysis Based on RTC Measurements

Cell attachment and spreading of 100 000 cells/cm^2 Cor.At® cells on fibronectin pre-coated ECIS gold-film electrodes was investigated using MFT experiments (**Fig. 6.44 A**).The time-course of normalized capacitance provided a decrease in C_{norm} over 22 h indicating cell layer formation on top of the electrode. The frequency spectra of $|Z|$ for a cell-free and Cor.At® cell-covered 8W4E-GJ electrode layout (**B**) showed an increase in $|Z|$ between 10^3 – 10^5 Hz. The most sensitive frequency for Cor.At® cell-covered 8W4E-GJ and 8W4E-micro gold-film electrodes was determined to ~ 20 kHz with similar maximum values independent of the electrode layout (**C**). **Fig. 6.45 A** shows phase-contrast micrographs of Cor.At® cell-covered 8W4E-micro (**1**) and 8W4E-GJ (**2**) electrodes.

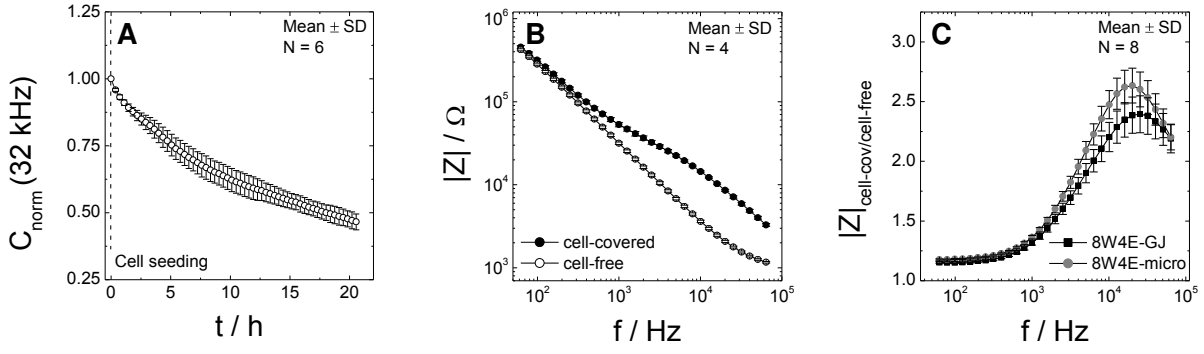

Fig. 6.44: A: Time-course of the normalized capacitance C_{norm} at 32 kHz for cell adhesion and spreading of 100 000 cells/cm^2 Cor.At® cells. Data were normalized to the value of a cell-free fibronectin coated electrode (Mean ± SD, N = 6). **B:** Frequency spectra of $|Z|$ for a cell-covered and cell-free 8W4E-GJ gold-film electrode layout (Mean ± SD, N = 4). **C:** For extraction of the most sensitive frequency the normalized $|Z|$ spectra for 8W4E-GJ and 8W4E-micro gold-film electrodes were obtained by dividing values of cell-covered electrodes by the corresponding cell-free values. This way, the sensitive frequency for $|Z|$ was determined independently of the electrode layout to ~ 20 kHz (Mean ± SD, N = 8).

For the analysis of the synchronous contraction of the Cor.At® cell layer a high time-resolution was required. The software was adjusted by Applied BioPhysics so that a resolution of 64 points per second or 128 points per second was possible. **Fig. 6.45 B1** shows a 10 s snapshot of a RTC experiment of Cor.At® cells where characteristic periodic peaks of similar pulse amplitudes and durations were found. A frequency of 4 kHz was used as it was found to provide a good analysis of cell micromotion before (**chapter 6.4.4.2**). A higher magnification of one peak (**B2**) emphasizes the high time-resolution of 64 points per second which was very beneficial for the impedimetric investigations of beating cardiomyocytes.

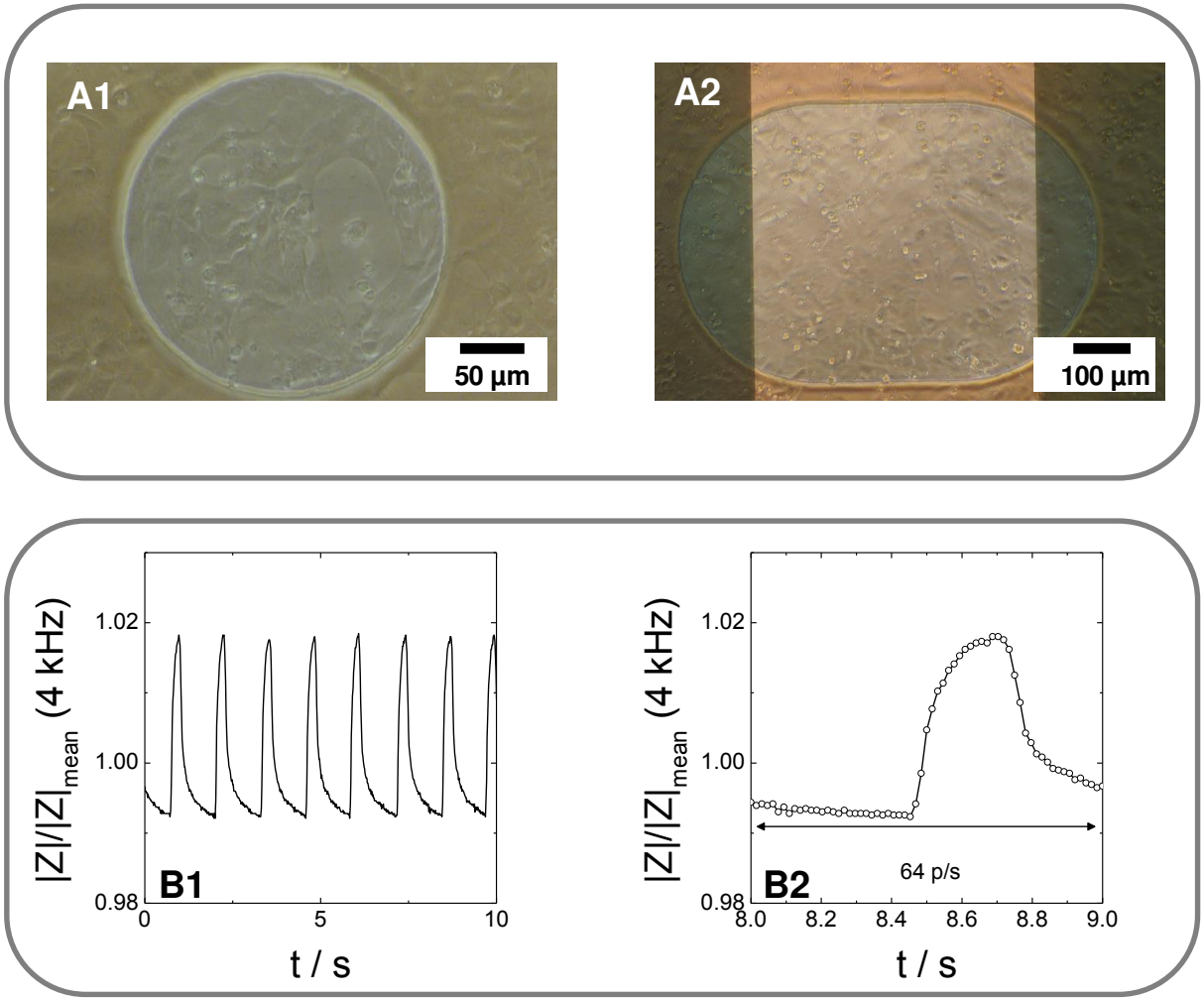

Fig. 6.45: A: Phase-contrast images of Cor.At® cells cultured on 8W4E-micro (**1**) or 8W4E-GJ (**2**) gold-film electrodes. **B:** Time-course of normalized impedance $|Z|/|Z|_{mean}$ for Cor.At® cells cultured on ECIS gold-film electrodes (**1**). Contractile beating efficiency of Cor.At® cells cultivated on 8W4E-micro electrodes was monitored using RTC measurements with a resolution of 64 points/s. A snapshot of 1 s clearly indicates the high temporal resolution to detect contraction of Cor.At® cells (**2**) ∗[I].

[I] An instrumental correction factor was required for some data sets, which were recorded with an earlier software version. The software for data conversion was provided by Applied BioPhysics immediately before the thesis was submitted. The influence of data conversion is exemplarily shown for one data set with respect to beating profiles, beat amplitude and time-course of $|Z|/|Z|_{mean}$ in **Fig. S 12**. Signal shapes and the time-course for beating Cor.At® cells remained unaffected. Only a marginal increase in signal amplitude was observed. Therefore, raw data were used for data presentation without any further conversion. Data sets which should be converted with the software in future are in the following denoted with ∗.

In order to evaluate whether or not the obtained impedance signals (**Fig. 6.45 B**) were indeed related to physical contraction and relaxation of the cardiomyocytes, RTC experiments were performed for a cell-free electrode (**Fig. 6.46**), for 8W4E-micro electrodes after establishment of a confluent NRK cell layer (**Fig. 6.47**) and for a confluent cell layer of beating Cor.At® cells (**Fig. 6.48**). The aim of these preliminary experiments was to find the best frequency to detect synchronous beating of cardiomyocytes and moreover to evaluate the best parameter for data analysis. When cells started to beat on day one after cell seeding RTC experiments were performed at different frequencies and a selection of different measurements using low, middle or high frequencies are presented in **Fig. 6.48**. Furthermore, the RTC measurements allow analysis of the beating efficiency using the parameter $|Z|$, R, C and χ which is the imaginary part of the impedance. The frequency-dependent study of the beating profiles of Cor.At® cells were performed over a broad frequency range and only the results for the popular frequencies of 500 Hz, 4 kHz and 32 kHz are presented below.

Similar experimental settings were chosen for the cell-free and cell-covered measurements. The significant difference of the RTC traces for cardiomyocytes and cell-free or NRK cell-covered electrodes clearly demonstrated that ECIS experiments can be used to detect beating of Cor.At® cells. Although, 20 kHz were determined to the most sensitive frequency in $|Z|_{\text{cell-cov/cell-free}}$, 4 kHz was found to be the optimal frequency to selectively detect the physical contraction of cardiomyocytes. The four different parameters $|Z|$, R, C and χ all provided a characteristic pattern which can be used for further analysis of the RTC data. However, to facilitate the comparison with data from literature, we focused on the analysis of $|Z|$ for the data presentation in this thesis. It should be pointed out that ECIS provides the ability to analyze changes of beating profiles using four different parameters and even the characteristic pattern in the complex analysis where the resistance was plotted against the imaginary part can be used as a description for the beating efficiency of cardiomyocytes.

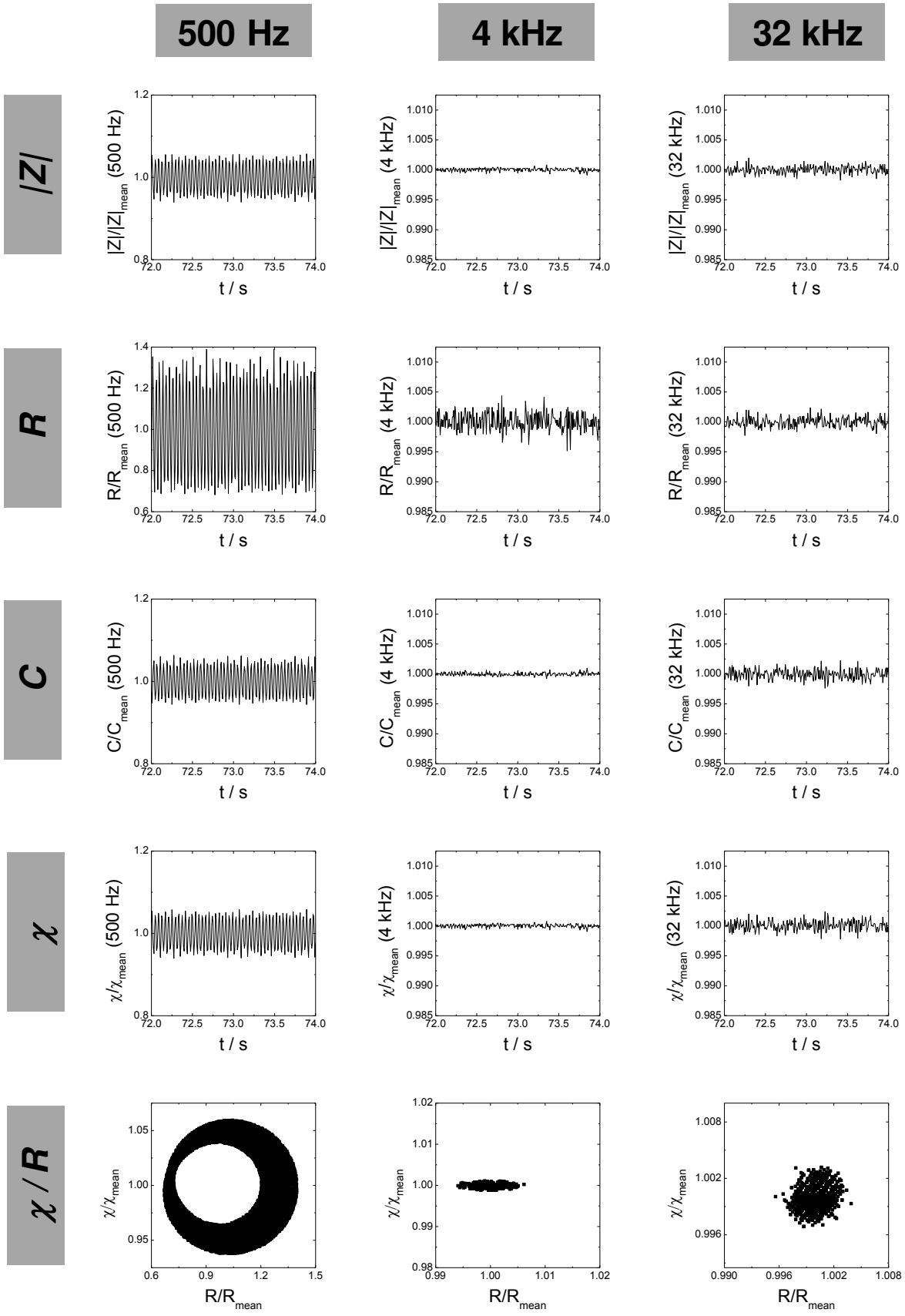

Fig. 6.46: Frequency-dependent RTC measurements for a **cell-free** 8W4E-micro electrode layout*. Data were analyzed using $|Z|$, R, C and χ at 500 Hz, 4 kHz and 32 kHz. Data were recorded with a time-resolution of 128 points/s and were normalized to the respective mean value of the entire measurement.

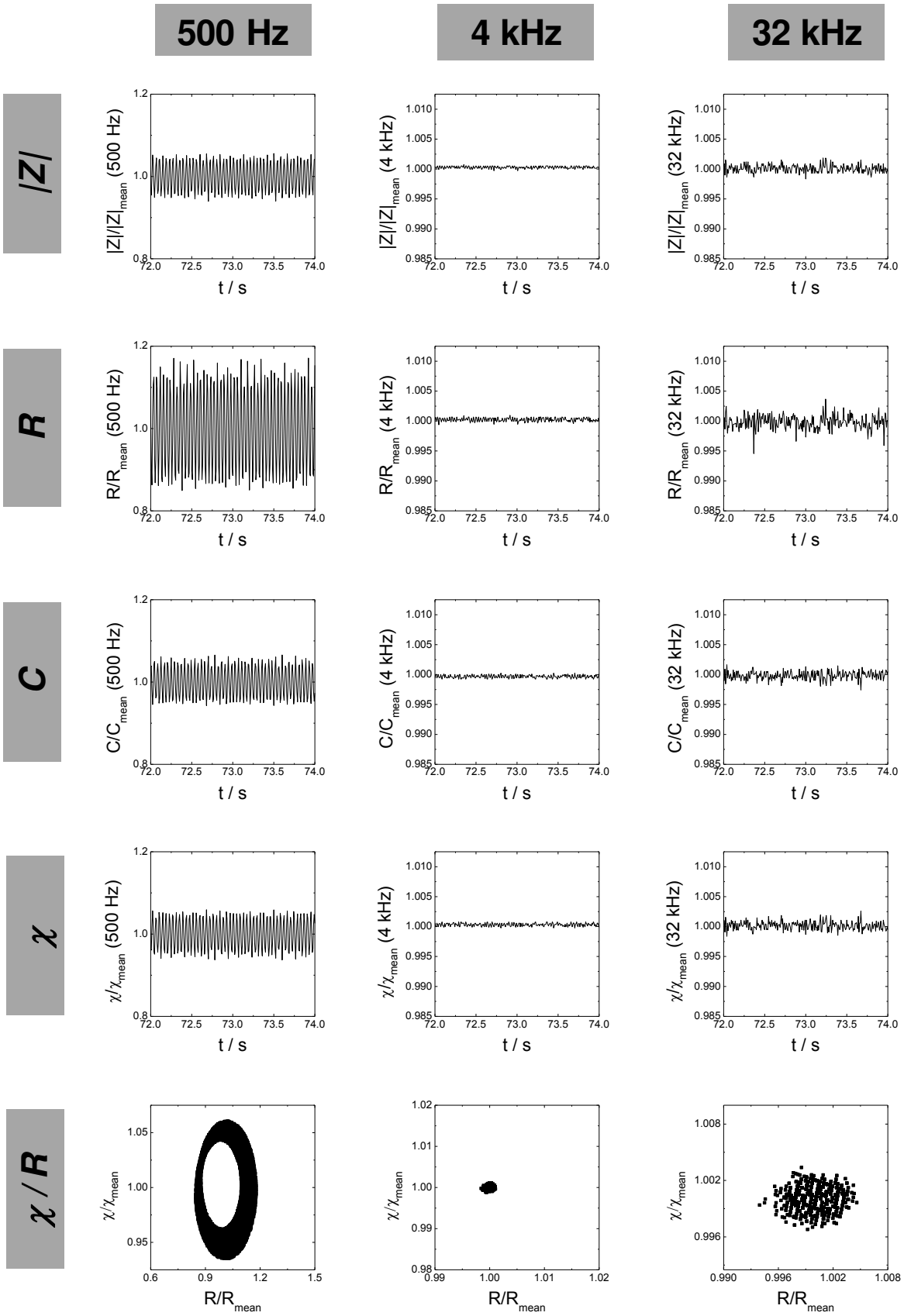

Fig. 6.47: Frequency-dependent RTC profiles for **NRK cells** cultivated on 8W4E-micro gold-film electrodes*. Cell responses were investigated using the parameters |*Z*|, *R*, *C* and χ at 500 Hz, 4 kHz and 32 kHz with a time-resolution of 128 points/s. Data were normalized to the respective mean value of the entire measurement.

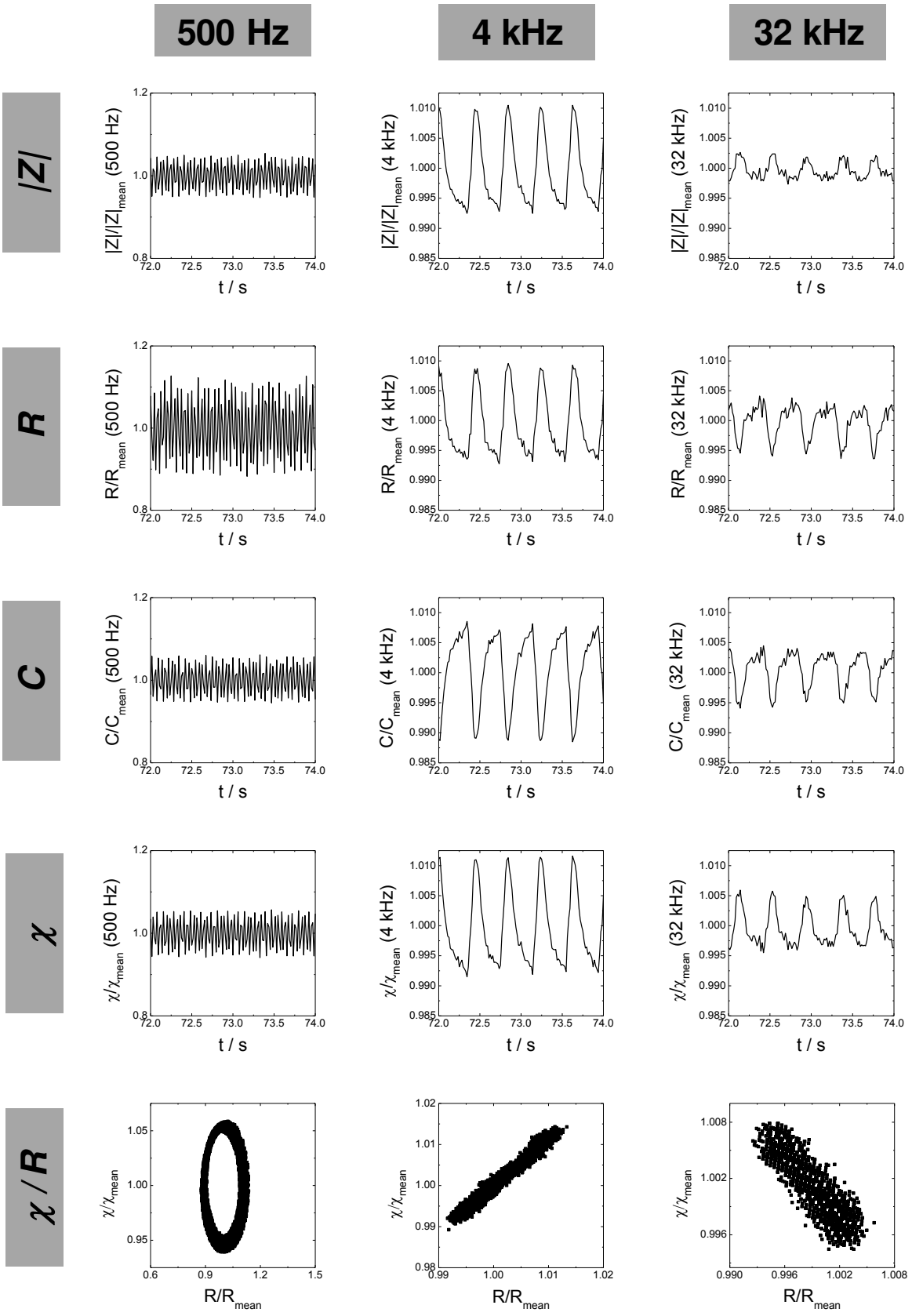

Fig. 6.48: Frequency-dependent beating profiles for **Cor.At® cells** cultivated on 8W4E-micro gold-film electrodes*. Synchronous beating was investigated using the parameters |*Z*|, *R*, *C* and χ at 500 Hz, 4 kHz and 32 kHz. Data were recorded with a time-resolution of 64 points/s and were normalized to the respective mean value of the entire measurement. Data were recorded on day one after cell seeding.

6.5.2 Modulation of the Periodic Beating of Cardiomyocytes

Using 4 kHz for RTC analysis, ECIS is a versatile tool to investigate the synchronous beating of Cor.At® cells. Cardiomyocytes were impedimetrically analyzed upon modulating the beating efficiency by removing extracellular Ca^{2+} ions, which are necessary for the contraction, or by adding selected compounds with well-known effects on cardiomyocytes, like Isoproterenol hydrochloride.

The experimental setup was first evaluated by analyzing beating of cardiomyocytes in medium or in EBSS buffer in absence or presence of Ca^{2+}. The reason for the different beating behavior of Cor.At® cells dependent on extracellular Ca^{2+} is that Ca^{2+} entry through the L-type Ca^{2+}-channel is essential for beating.

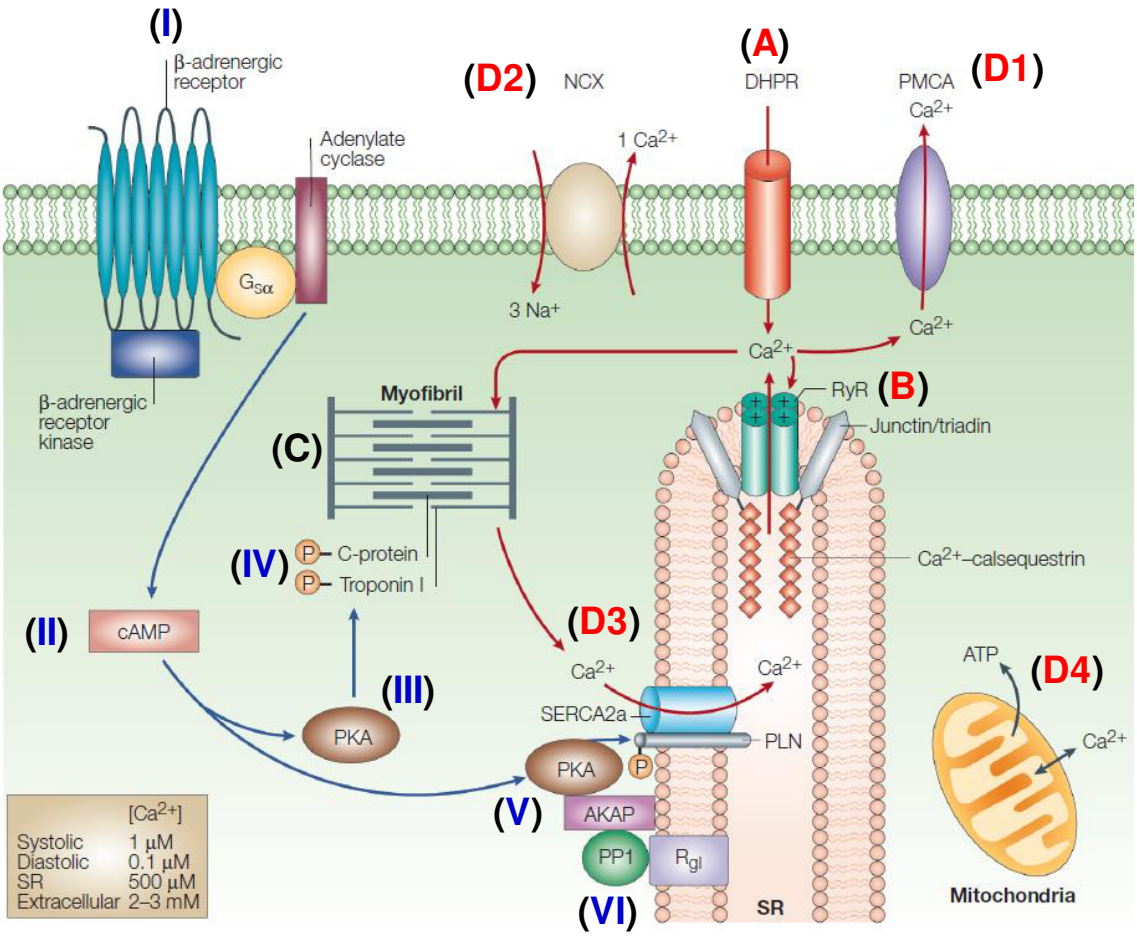

Fig. 6.49: Schematic overview of the Ca^{2+}-signaling pathway (**red arrows**). **A:** Extracellular Ca^{2+} can enter the cytoplasm after depolarization via the Ca^{2+}-channels (*dihydropyridine receptors*; DHPRs). **B:** Ca^{2+} binds to the RyR Ca^{2+}-release channel located in the membrane of the SR (*sarcoplasmic reticulum*) initiating Ca^{2+} release from the SR. **C:** Activation of the muscle contraction by binding to Troponin C. **D**: Ca^{2+}-removal from the myoplasm by Ca^{2+}-ATPases (PMCAs; **1**), Na^{+}/Ca^{2+}-exchangers (NCXs; **2**), SERCA2a (**3**) or storage in the mitochondria (**4**). Schematic overview of the β-adrenergic-receptor pathway (**blue arrows**): Binding of a ß-agonist on the β-adrenergic-receptor (I) initiates the production of cAMP by adenylate cyclase (II). This leads to the activation of the cAMP-dependent protein kinase PKA (**III**) which can phosphorylate a few cardiac proteins. Phosphorylation of Troponin-1 accelerates the dissociation of Ca^{2+} from the myofilaments (**IV**) and phosphorylation of phospholamban (PLN) induces a faster Ca^{2+} re-transport into the SR via SERCA2a (**V**). De-phosphorylation of PLN by protein phosphatase PP1 inhibits the SERCA2a pump at resting Ca^{2+}-concentrations and terminates the stimulation phase (**VI**). The image was taken with permission from MacLennan and Kranias (2003) [497] and was modified.

Already 1883 S. Ringer showed that the heart requires Ca^{2+} for beating [498]. The role of Ca^{2+} is schematically shown in **Fig. 6.49** and briefly summarized in the following (**red arrows)**: Normally, Ca^{2+} influx through the L-type voltage-dependent Ca^{2+}-channel (DHPR) is required. The increase in intracellular Ca^{2+} concentration then triggers a release of Ca^{2+} from the *sarcoplasmic reticulum* (SR) stores via the *ryanodine receptor* (RyR). The high importance of Ca^{2+} was further highlighted by Fabiato and Fabiato (1975) [499] and by Fabiato (1983) who presented the hypothesis of Ca^{2+}-induced Ca^{2+} release (CICR) which is necessary for each beat [500]. This CICR enables an increase of the intracellular Ca^{2+}-concentration from ~ 100 nM to 1 µM [501]. Ca^{2+}, which was released from SR stores can subsequently bind to troponin C which finally enables a muscle contraction. The Ca^{2+}-removal from the cytoplasm allows for relaxation [502]. This can either happen by uptake of Ca^{2+} into SR stores via SR Ca^{2+}-ATPase, transport into mitochondria via the *mitochondrial calcium uniporter* (MCU) or via export into the extracellular compartment using the Na^{+}/Ca^{2+} exchanger (NCX) or Ca^{2+}-ATPase (*plasma membrane Ca^{2+}-ATPase*, PMCA) [497, 502].

Fig. 6.50 summarizes the time-course of normalized impedance $|Z|/|Z|_{mean}$ for a sequence of impedimetric RTC experiments. In the beginning, the contractile performance of two cell populations was monitored in presence of culture medium (**A**). Afterwards, medium was aspirated and replaced by $EBSS^{-+}$ (only containing Mg^{2+}) or $EBSS^{++}$ (w/ Ca^{2+}, w/ Mg^{2+}). RTC measurements were started immediately after the exchange, finding a significant difference between the two Cor.At® populations (**B**). Only when Ca^{2+} was present, the characteristic pattern for beating cardiomyocytes was found, whereas cells in absence of Ca^{2+} showed an almost stable $|Z|/|Z|_{mean}$ value without the characteristic beating profiles. Also microscopic observations confirmed only contractions of the cell monolayer in presence of $EBSS^{++}$. Afterwards, $EBSS^{-+}$ buffer was replaced by culture medium and the time-course of $|Z|/|Z|_{mean}$ recorded immediately after the exchange (**C1**) clearly showed that cells re-started beating and the beating frequency increased with increasing incubation time. The final analysis of both wells showed the characteristic pattern for beating cardiomyocytes indicating that the removal of Ca^{2+} from the extracellular buffer only transiently caused a beating arrest without further consequences on cell viability (**C2**). The time-courses of impedance, which were recorded during the ECIS experiment, were further analyzed with respect to a complex data presentation where $\Delta\chi$ was plotted against ΔR (**Fig. 6.51**). Here, a linear dependency was found in culture medium (**1 + 3**) and in buffer containing Ca^{2+} (**A2**), whereas the signal significantly changed in absence of Ca^{2+} (**B2**).

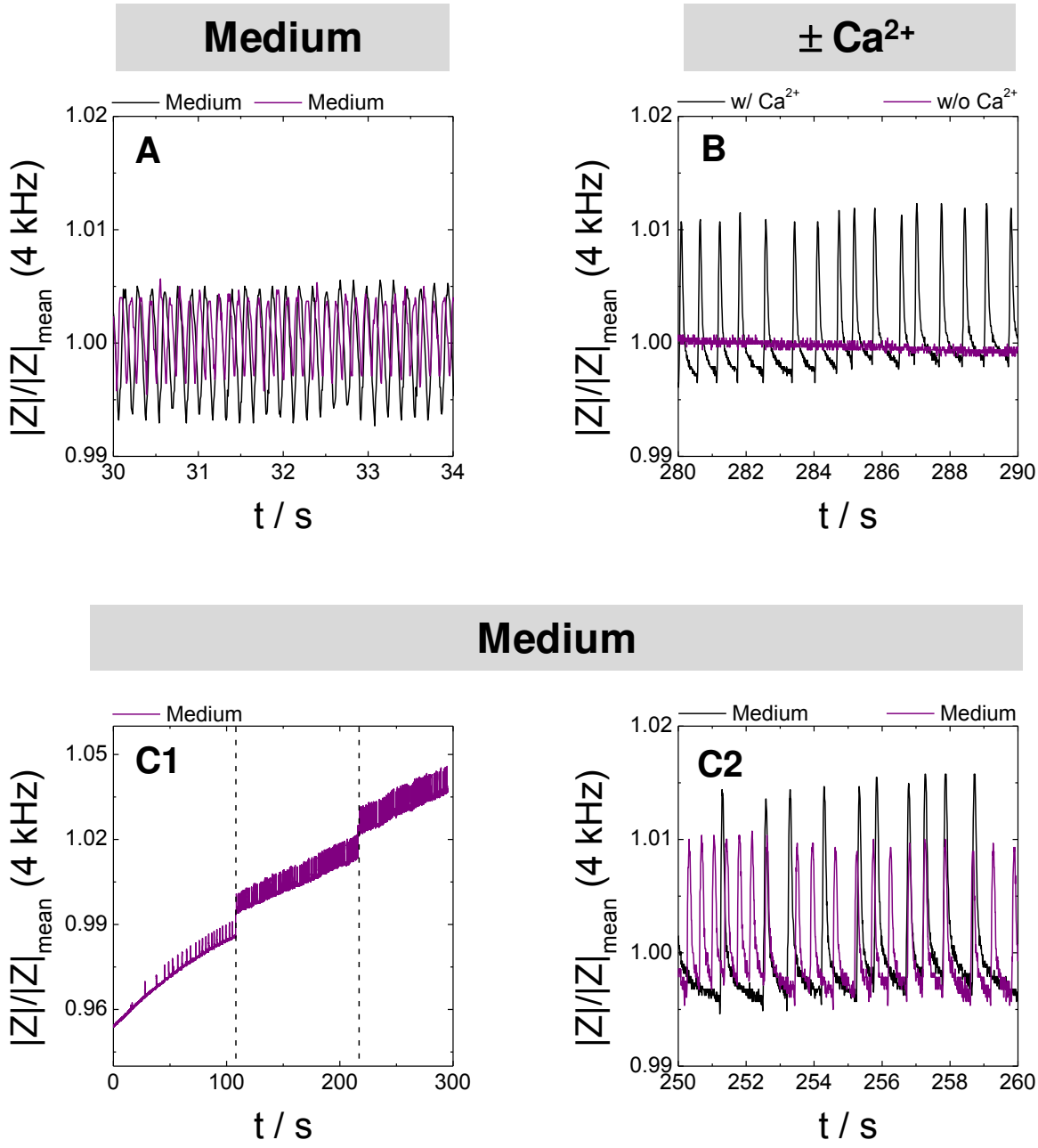

Fig. 6.50: Sequence of ECIS RTC recordings to investigate the synchronous beating of Cor.At® cells cultivated on 8W4E-micro gold-film electrodes in culture medium (**A**), in absence or presence of Ca^{2+} in EBSS buffer (**B**) and after addition of culture medium (**C**)*. When Ca^{2+}-free buffer was exchanged against medium, the cellular response of one cell population was recorded over three cycles indicated by the dotted lines (**C1**). Time-course of normalized impedance for two cardiomyocyte populations in presence of culture medium replacing Ca^{2+}-free (**purple**) or Ca^{2+}-containing buffer (**black**) (**C2**). Data were recorded at 4 kHz using a time-resolution of 128 points/s and were normalized to the respective mean value of the entire experiment.

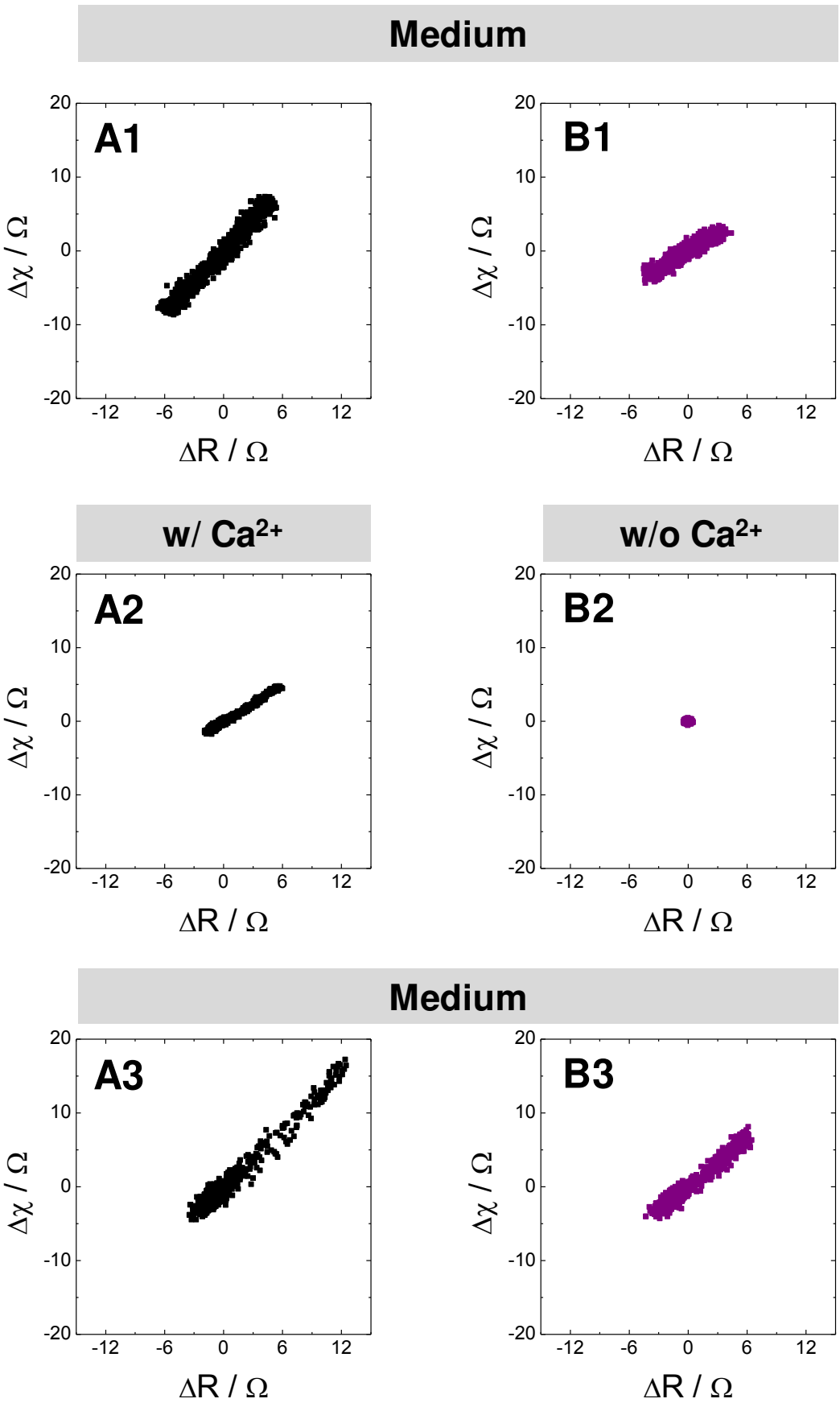

Fig. 6.51: Complex data presentation of $\Delta\chi$ against ΔR of the experiments presented in **Fig. 6.50**. Cor.At® beating was analyzed in presence of culture medium (**A1; B1**), in buffer supplemented with (**A2**) or without (**B2**) Ca^{2+} and after the addition of culture medium (**A3; B3**). In absence of Ca^{2+} no linear dependency between $\Delta\chi$ and ΔR was found.

Moreover, the periodic beating of Cor.At® cells was modulated using Isoproterenol hydrochloride which is an agonist of the β-adrenergic receptor. It is known that the activation of the β-adrenergic receptor on the one hand increases the contractility of cardiomyocytes and on the other hand accelerates the relaxation and the Ca^{2+} decline [497]. The basic signal-transduction pathway is schematically shown in **Fig. 6.49** with the **blue arrows**. Stimulation of the β-adrenergic receptor activates a GTP-binding protein ($G_{s\alpha}$) which initiates the production of cAMP by the *adenylyl cyclase* (AC). This leads to the activation of PKA, a kinase which can phosphorylate several important cardiac proteins and strongly influences their activity [503]. Phosphorylation of troponin-1 facilitates the Ca^{2+}-dissociation from the myofilaments whereas the phosphorylation of *phospholamban* (PLN) accelerates the re-uptake of Ca^{2+} into the SR [504]. The stimulation of the SERCA2a pump located in the membrane of the SR is terminated by the enzyme *protein phosphatase* (PP1) which dephosphorylates PLN. In this form PLN acts as inhibitor for the SERCA2a and inactivates the Ca^{2+}-pump [497].

The beating efficiency of Cor.At® cells, cultivated on 8W4E-GJ gold-film electrodes, was investigated in absence or presence of 100 nM Isoproterenol hydrochloride. Therefore, two cell populations were monitored with time and the sequence of RTC measurements for one experiment is exemplarily summarized in **Fig. 6.52**. In presence of culture medium, Cor.At® cells expressed their prominent beating profiles (**A**). The calculation of the respective beating rate yielded 61.4 BPM for the control population and 46.1 BPM for Cor.At® cells immediately before Isoproterenol hydrochloride was added. Medium was exchanged to fresh culture medium or 100 nM Isoproterenol hydrochloride in culture medium. The influence of the β-adrenergic receptor agonist on the beating efficiency was monitored over time. Snapshots over 10 s of the RTC measurements which were started immediately after the addition (**B**) or after an incubation time of 10 min (**C**) or 60 min (**D**) are provided in **Fig. 6.52**. In presence of Isoproterenol hydrochloride the beat rate increased within the time-frame of 10 s compared to the baseline recording in culture medium. Control cells, where fresh medium was added, showed a decrease in the beat amplitude immediately after the exchange but recovered to baseline values within 60 min.

Unfortunately, the effects due to temperature changes and the addition of fresh medium with or without Isoproterenol hydrochloride resulted in a significant decrease of the pulse amplitude in **B** – **C** and should not be neglected.

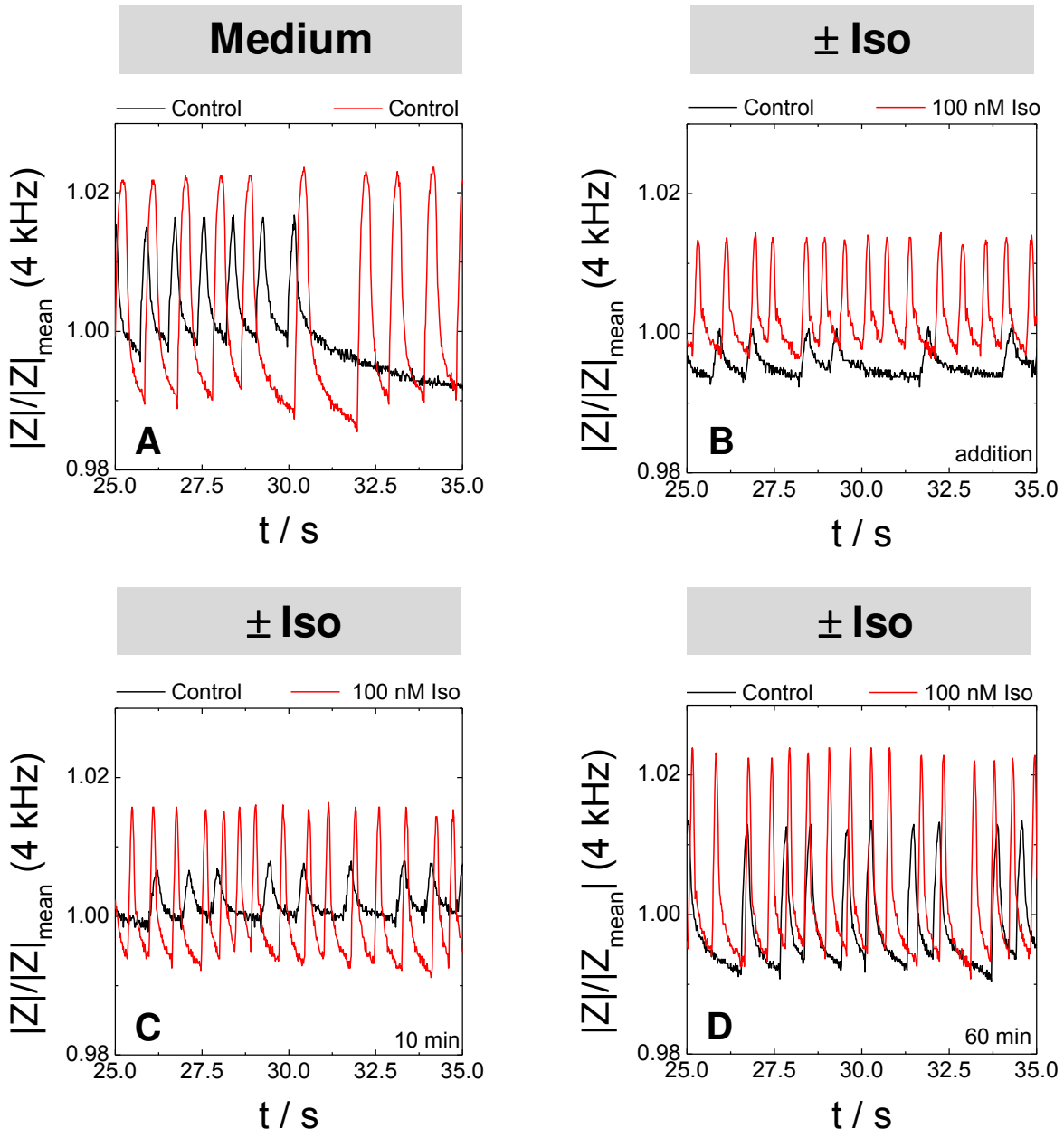

Fig. 6.52: Time-courses of the normalized impedance $|Z|/|Z|_{mean}$ for Cor.At® cells cultivated on 8W4E-GJ gold-film electrodes in presence of culture medium (**A**) and after addition of 100 nM Iso (*Isoproterenol hydrochloride*) (**B-D**). Synchronous beating of cardiomyocytes was monitored immediately (**B**), 10 min (**C**) and 60 min (**D**) after addition of culture medium (**black**) or Iso (**red**) at 4 kHz using a time-resolution of 64 points/s. Data were normalized to the respective mean value of the entire experiment.

Quantification of the impedance data using a LabVIEW-based software also confirmed an increase in beating rate for Cor.At® cells in presence of Isoproterenol hydrochloride. The BPM analysis 60 min after the addition provided 65.3 BPM for cells in presence of medium and 88.3 BPM for cells after Isoproterenol hydrochloride treatment. A summary of the time-dependent changes of the BPM of a single experiment is shown in **Fig. 6.53**.

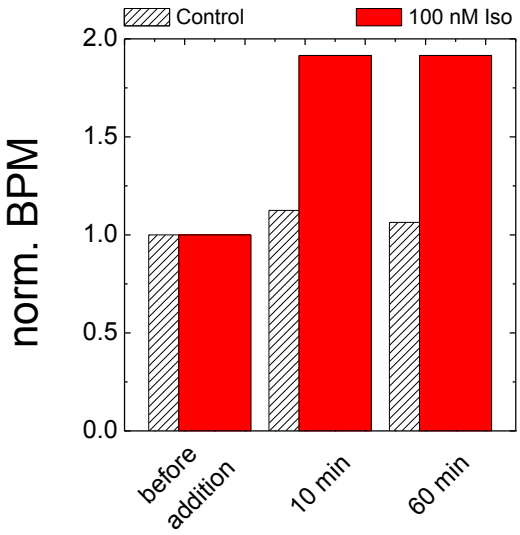

Fig. 6.53: Analysis of beating rate for Cor.At® cells (BPM) in absence or presence of 100 nM Isoproterenol hydrochloride. BPM were calculated before addition, and 10 min or 60 min after addition. BPM were normalized to the respective values immediately before fresh medium (61.4 BPM) or Isoproterenol hydrochloride (46.1 BPM) was added.

In summary, these two preliminary experiments clearly showed that high time-resolution ECIS experiments enable an analysis of the beating rate of Cor.At® cells. In absence of Ca^{2+} a significant difference was found in the beating profiles compared to the control population in presence of Ca^{2+}, which emphasizes the important role of Ca^{2+} during the cardiac excitation-contraction coupling. The model compound Isoproterenol hydrochloride enables an analysis of the stimulation of the β-adrenergic receptor pathway which confirmed the expected increase in beating rate. These two experiments were used to validate the setup and enabled an analysis of gap junctional intercellular communication between cardiomyocytes in absence or presence of silica particles below.

6.5.3 Impact of the Gap Junctions Inhibitor 1-Heptanol on Beating Cardiomyocytes

It is known that gap junctional intercellular communication between cardiomyocytes plays a crucial role in impulse propagation in cardiac tissue. Additionally, cell-cell communication via gap junctions is required to synchronize pacemaker cells and to enable a coordinated contraction of the heart [505, 506].

Fig. 6.54 summarizes the sequence of impedimetric recordings where one population of Cor.At® cells was analyzed in absence or presence of the gap junctional intercellular communication inhibitor 1-heptanol.

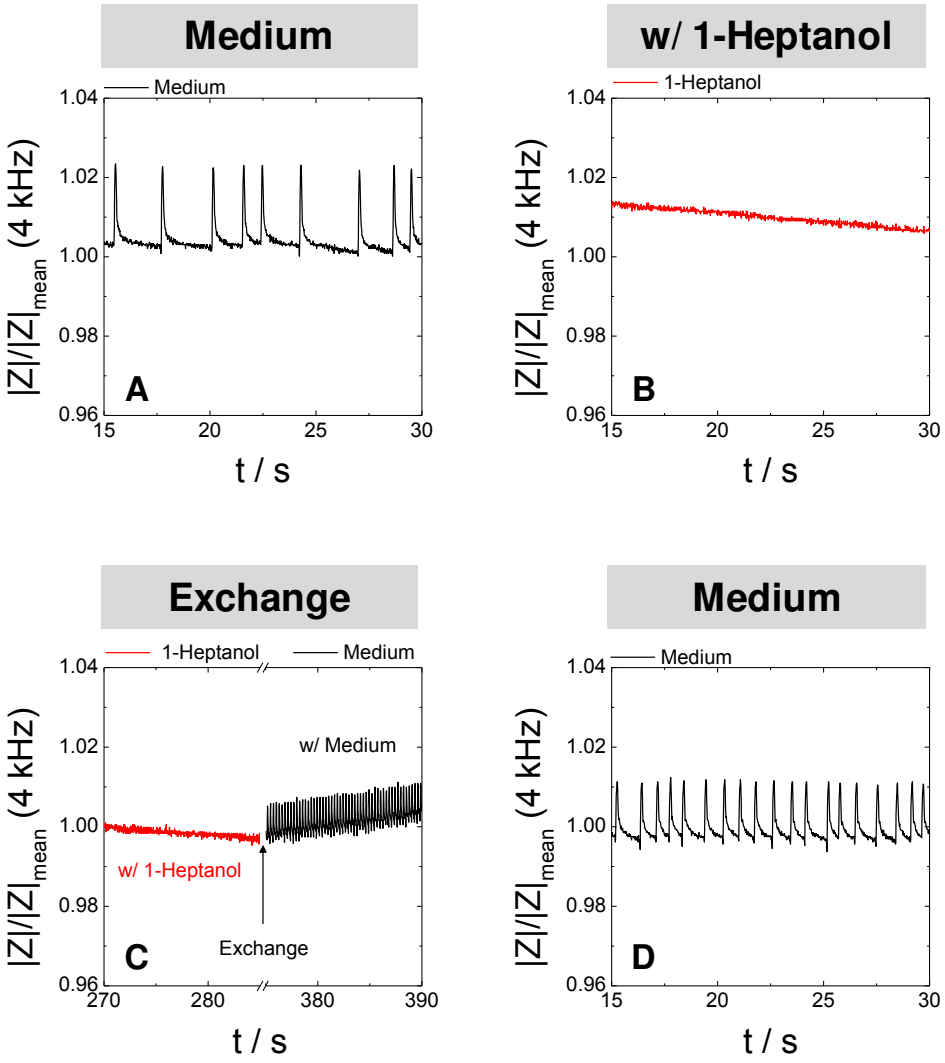

Fig. 6.54: Time-courses of the normalized impedance $|Z|/|Z|_{mean}$ for a single experiment with Cor.At® cells cultivated on 8W4E-GJ gold-film electrodes in presence of culture medium (**A**), after the addition of 1 mM 1-heptanol (**B**) or after removing the gap junction inhibitor from the supernatant (**D**). The detection of Cor.At® beating in presence of 1-heptanol and immediately after the re-exchange (**C**) was realized by recording several cycles where the exchange was performed during the measurement pause directly in the incubator. Cor.At® beating was monitored in a sequence of different experiments at 4 kHz using a time resolution of 64 points/s. Data were normalized to the mean value of the time record analyzed over 1.8 min.

During baseline recordings of Cor.At® cells in medium the characteristic beating profile in $|Z|/|Z|_{mean}$ at 4 kHz was found (**A**). The respective BPM were calculated to 38.4. Afterwards, the culture medium was replaced by 1 mM 1-heptanol in EBSS^{++} and the RTC measurement immediately after the addition showed an almost stable value of $|Z|/|Z|_{mean}$ without any evidence for a regular beating pattern (**B**). Between two cycles of impedance recordings 1-heptanol was replaced by culture medium. The time-course of $|Z|/|Z|_{mean}$ showed a significant difference for cells in presence of 1-heptanol and cells in presence of culture medium (**C**). Cor.At® cells re-started their contractile behavior after removing 1-heptanol indicating a reversible inhibitory effect on gap junctional intercellular communication. When the same cell population was recorded some minutes later, a regular beating profile was confirmed by the ECIS recordings (**D**) with 80.6 BPM.

The complex data presentation of $\Delta\chi$ against ΔR (**Fig. 6.55**) provided the characteristic pattern of beating cardiomyocytes in presence of culture medium (**A**). When 1-heptanol was present in the extracellular buffer, the pattern of $\Delta\chi$ against ΔR changed (**B**) significantly. Cor.At® cells re-started to perform their regular beating when the inhibitor was replaced by culture medium (**C**). Again, a linear dependency between $\Delta\chi$ and ΔR was found indicating a reversible inhibitory effect of 1-heptanol.

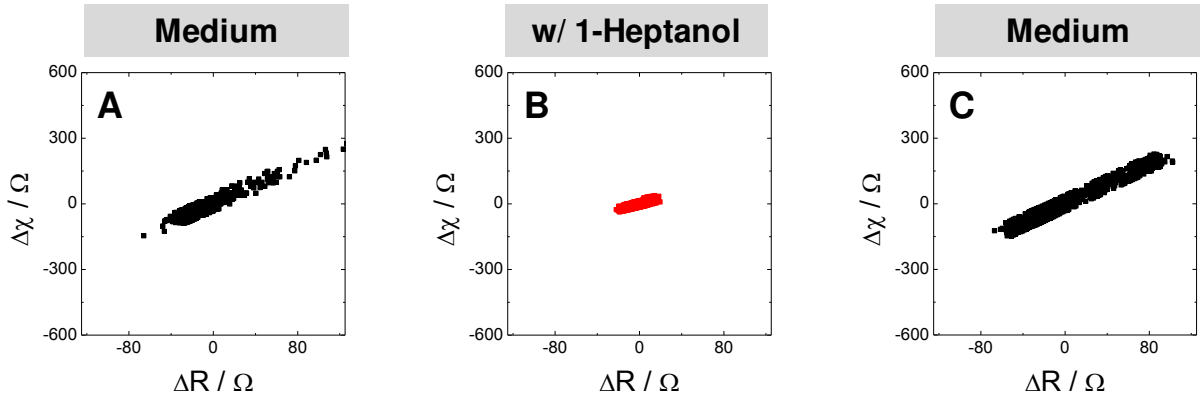

Fig. 6.55: Complex data presentation of $\Delta\chi$ against ΔR of the experiments presented in **Fig. 6.54**. Cor.At® cells were analyzed in presence of culture medium (**A**), after the addition of 1 mM 1-heptanol (**B**) and after replacement of the 1-heptanol solution by culture medium (**C**) at the end of the experiment. In presence of the gap junctional intercellular communication inhibitor 1-heptanol, the signal pattern of $\Delta\chi$ against ΔR changed significantly.

6.5.4 Impact of Silica Particles on the Periodic Beating of Cardiomyocytes

The study on the impact of silica particles on cell physiology was completed by investigating the contraction of Cor.At® cells in absence or presence of silica particles.

First, the response of cardiomyocytes to the addition of silica particles was investigated microscopically. Therefore, Cor.At® cells, which are stably expressing GFP, were incubated with silica particles ($7.5 \cdot 10^6$ P/cm^2). **Fig. 6.56** shows phase-contrast (**A**) and confocal fluorescence micrographs (**B; C**) of Cor.At® cells 23 h after particle exposure. The confocal fluorescence micrographs revealed the presence of silica particles which appeared as black spots inside the cytoplasm. Microscopic observations during particle exposure showed a continuous contraction of Cor.At® cells even in presence of the particles.

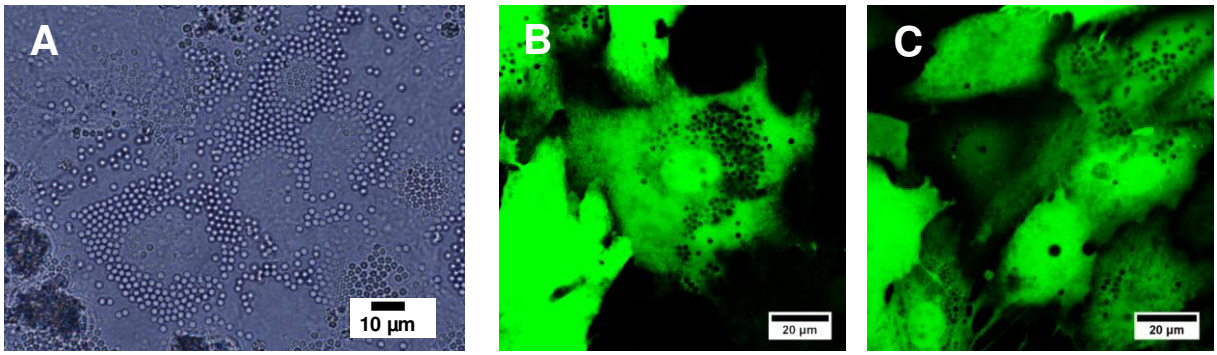

Fig. 6.56: Cor.At® cardiomyocytes expressing GFP after ~23 h of incubation with 2 µm silica particles ($7.5 \cdot 10^6$ P/cm^2) in phase-contrast (**A**) and confocal fluorescence micrographs (**B; C**).

These microscopic findings were further analyzed using time-dependent impedance recordings of control cells (**Fig. 6.57**) and cells in presence of silica particles (∅ 2 µm; $3.7 \cdot 10^7$ P/cm^2) (**Fig. 6.58**). Cells were recorded immediately before medium was exchanged or replaced by the particle solution to obtain baseline values (**A**). The beating pattern of control cells and cells in presence of silica particles was then monitored after 1 h (**B**), 2 h (**C**), 16 h (**D**), 20 h (**E**) and 24 h (**F**) of incubation.

The snapshots of the time-courses of $|Z|/|Z|_{mean}$ at different time-points after medium exchange provided noticeable differences. With increasing incubation time, the amplitude increased and the beat rate was significantly different before (**A**) and 24 h after medium exchange (**F**). A decrease of the beat rate from 112.6 BPM (**A**) to 35.8 BPM at the end of the experiment (**F**) was found. The differences in the BPM over time are likely to result from the nutritional state of the cells and from the age of the cardiomyocytes.

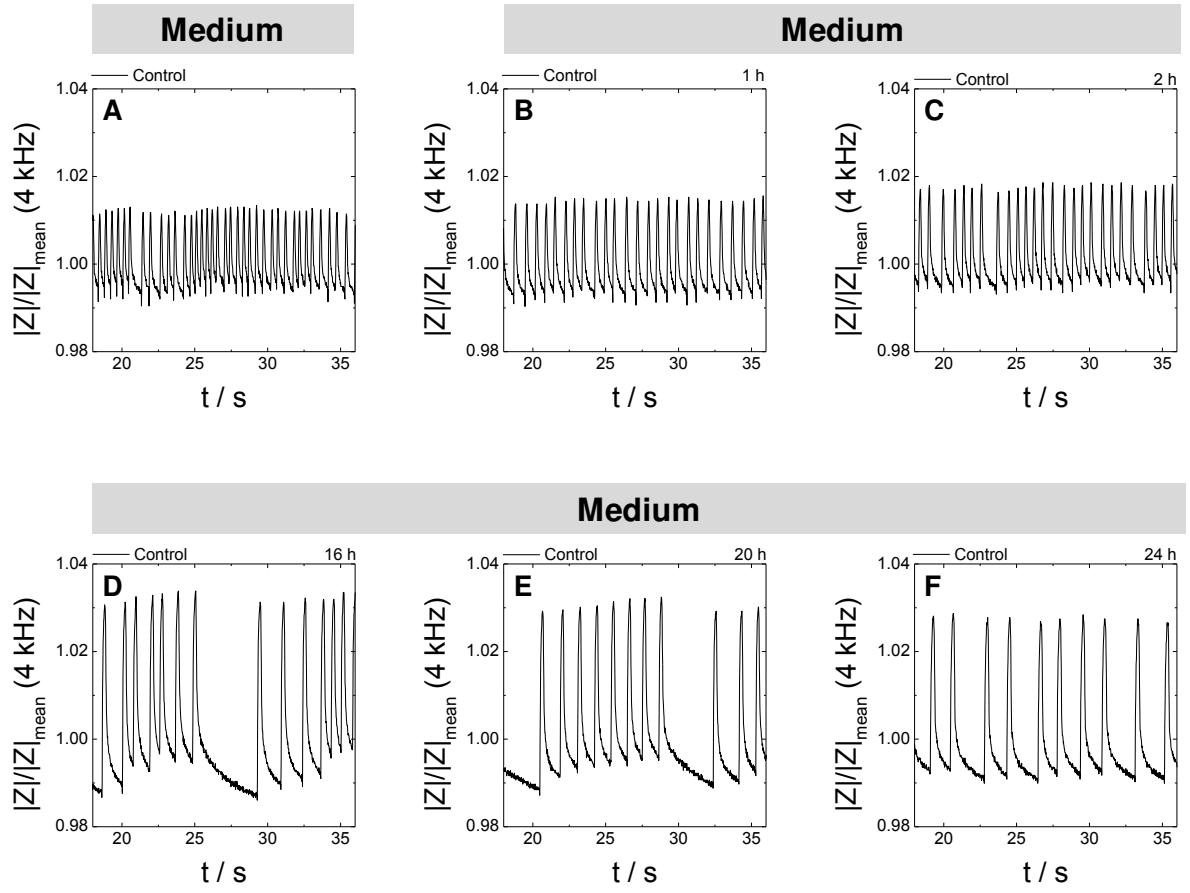

Fig. 6.57: Time-courses of the normalized impedance $|Z|/|Z|_{mean}$ for Cor.At® cells cultivated on 8W4E-GJ gold-film electrodes in presence of culture medium over 24 h. Data were recorded before (**A**) or 1 h – 24 h after medium exchange (**B** – **F**). Cor.At® beating of one cell population was monitored at 4 kHz using a time-resolution of 64 points/s and data were normalized to the respective mean value of the entire experiment.

The influence of silica particles on the physiology of cardiomyocytes was investigated for two different cell populations and the time-dependent snapshots of RTC experiments are provided in **Fig. 6.58**. The time-courses of $|Z|/|Z|_{mean}$ immediately before particle addition showed the characteristic pattern for beating cardiomyocytes with regular signals. The beat rate of two Cor.At® cell populations were determined to 56.3 BPM and 49.9 BPM, respectively. One hour after the addition of $3.7 \cdot 10^7$ P/cm^2 silica particles in culture medium one population showed regular beating profiles, whereas the other population revealed arrhythmia (**B**). These differences were further confirmed in the time courses of $|Z|/|Z|_{mean}$ 2 h after particle exposure (**C**). This temporary anomaly in the contractile performance of Cor.At® cells was not detected for incubation times between 16 – 24 h. Both populations provided a synchronous pattern of contraction and relaxation. The amplitude of the beats in **D** – **F** was higher compared to the signal in the beginning of the experiment and beat rate after 24 h of particle exposure were calculated to 30.7 and 61.4, respectively.

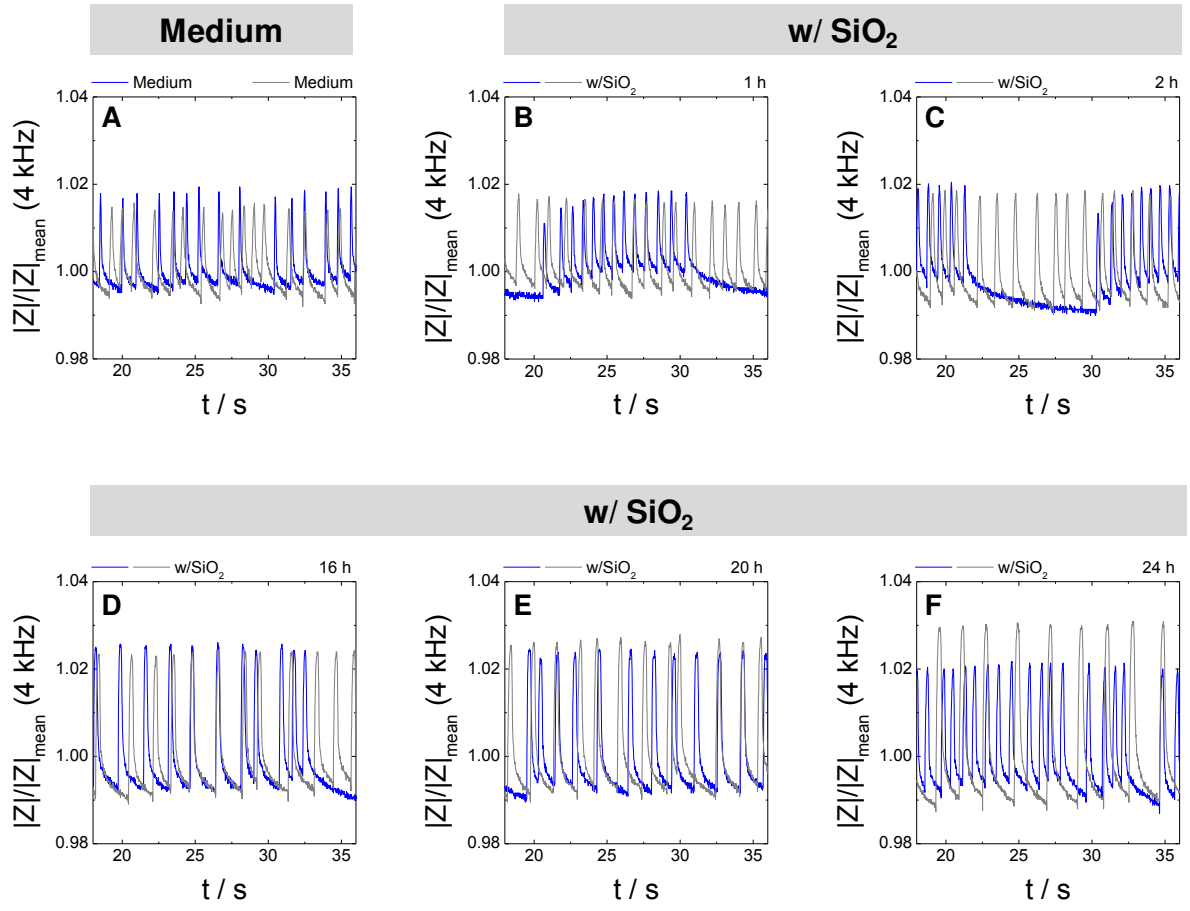

Fig. 6.58: Time-courses of the normalized impedance $|Z|/|Z|_{mean}$ for Cor.At® cells cultivated on 8W4E-GJ gold-film electrodes in presence of silica particles over 24 h. Data were recorded in the beginning of the experiment in culture medium (**A**) or 1 h – 24 h (**B** – **F**) after the addition of 2 µm silica particles ($3.7 \cdot 10^7$ P/cm^2). Cor.At® beating of two different populations was monitored at 4 kHz using a time-resolution of 64 points/s and data were normalized to the respective mean value of the entire experiment.

A summary of the calculated beat rate and the respective raw data before and at the end of particle exposure is provided in **Fig. 6.59**. Even under control conditions, the beat rate significantly changed during 24 h but at the end of the experiment (**B**) Cor.At® cells independent of the culture conditions provided the characteristic pattern of beating cardiomyocytes.

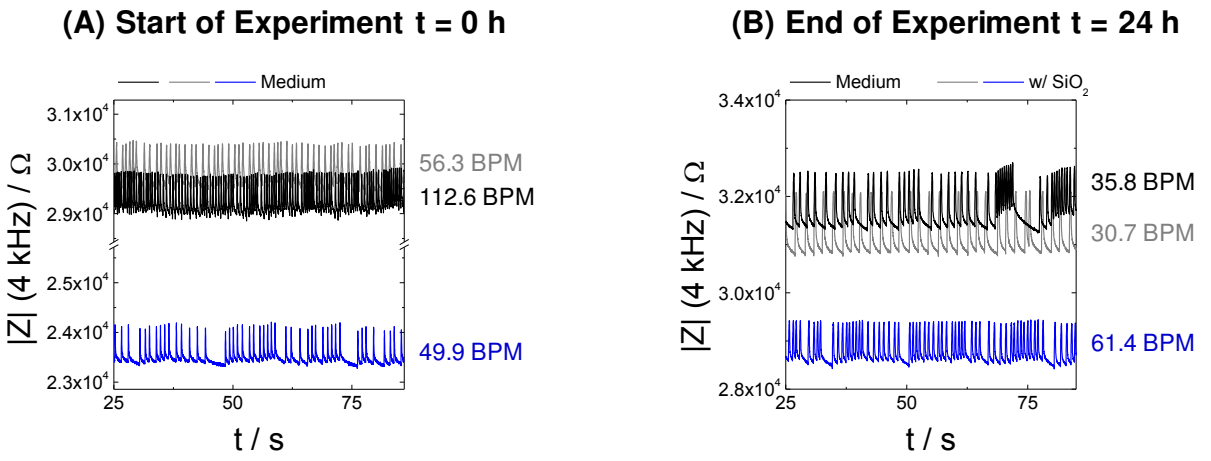

Fig. 6.59: Quantification of RTC data using a LabVIEW-based software to calculate the beat rate for the respective time-courses of |*Z*| presented in **Fig. 6.57** and **Fig. 6.58**. BPM and a snap shot of 1 min of the raw impedance data for control (black) and Cor.At® cells in presence of silica particles (blue; grey) are shown at $t = 0$ h (**A**) and after 24 h of incubation in medium or silica particles (**B**).

The experiments addressing the influence of silica particles on contraction of cardiomyocytes showed no influence of the microparticles on gap junctional intercellular communication, as Cor.At® cells were able to perform synchronous beating after 24 h of particle exposure. In contrast, the addition of the gap junction inhibitor 1 mM 1-heptanol resulted in a reversible beating arrest of the Cor.At® cells, indicating a complete inhibition of gap junctional intercellular communication.

6.6 Discussion

6.6.1 Uptake into Mammalian Cells

The uptake and localization of silica microparticles into NRK cells was investigated using different microscopic approaches like confocal laser scanning microscopy, SEM, TEM and ToF-SIMS analysis. The application of an inhibitor for micropinocytosis and particle exposure at 4 °C significantly reduced or completely inhibited uptake into the cytoplasm of NRK cells.

An important step to evaluate the cytotoxicity of a (nano)-material is to understand the interaction of the test material with the respective cell type [507] and therefore understand and analyze the particle uptake into living cells.

In this thesis the uptake of silica particles into NRK cells was investigated using different microscopic techniques to achieve an in-depth understanding about particle localization and uptake mechanism. Classical cytochemical stainings and phase-contrast microscopy showed a particle localization around the nucleus (**Fig. 6.9**). Cells still provided an intact cytoskeleton and high cell viability. The live-stain with Calcein AM and 3D analysis via confocal laser scanning microscopy confirmed the presence of the silica particles inside green fluorescent cytoplasm (**Fig. 6.11**). Staining of the extracellular compartment and ToF-SIMS analysis further excluded adhesion of the particles to the upper membrane (**Fig. 6.15**). DiI staining revealed a membrane-coating around the individual particles (**Fig. 6.12**). SEM (**Fig. 6.13**) and TEM images (**Fig. 6.14**) of NRK cells after pre- incubation with silica microparticles clearly indicated particle uptake into the cytoplasm. More evidence for the uptake was given by ToF-SIMS analysis. After sputter ablation of the apical membrane, the non-labeled particles could be successfully detected inside the cell (**Fig. 6.15**).

The intracellular localization of spherical mesoporous silica nano- and microparticles with a diameter of 190 nm, 420 nm and 1220 nm in human breast cancer cells was studied by He et al. (2009) [508]. The group found a size-dependent decrease of particle uptake into lysosomes. Only some particles with a diameter of 1220 nm were detected via confocal laser scanning microscopy in lysosomes whereas most particles with a diameter of 190 nm were found inside the cells. Sun et al. (2008) documented time-dependently the endocytosis of mesoporous silica nanoparticles with a diameter of ~ 100 nm into living A549 cells via differential interference contrast (DIC) microscopy without any additional label. By monitoring the motion of a single particle and calculating the corresponding diffusion coefficients the group could clearly differentiate between extracellular and intracellular particle localization [509]. Yu et al. (2009) investigated the size-dependent uptake of silica particles into mouse keratinocytes using TEM images. After 24 h of incubation, particles independent of

their diameter (30 nm – 535 nm) were found to be taken up by the cells and were located in the cytoplasm [510].

However, the particle size is reported to be a critical parameter which clearly influences the uptake mechanism and its efficiency. In literature, many studies focus on the uptake of nanoparticles into mammalian cells, however, only little information is provided about the incorporation of microparticles. Foster et al. (2001) studied the uptake of polystyrene microspheres into A549 and Calu-3 cells, both human cell lines derived from the respiratory epithelium. During their study they applied particles with a diameter of 0.5 µm to 3 µm and successfully showed an uptake into the cytoplasm which was confirmed by TEM images and fluorescence microscopy. Moreover, they used differently-charged particle surfaces and monitored a 10-fold enhanced uptake for positively charged microspheres compared to negative surface functionalities [511]. Using different diameters of polystyrene particles Foster et al. further confirmed findings which were already published in 1996 by Carr et al. [512], that the uptake of microparticles is inversely related to particle size. Vallhov et al. (2007) compared the uptake of mesoporous silica nanoparticles (∅ 270 nm) and microparticles (∅ 2.5 µm) into human monocyte-derived dendritic cells using confocal microscopy and TEM. Whereas at 4 °C no uptake occurred for both particle sizes, at 37 °C an uptake into the cytoplasm but not in the nucleus was found for the microparticles indicating an active mechanism of particle uptake and confirming the size exclusion of the nuclear pore complex. Moreover, TEM images revealed the existence of the 270 nm particles in vesicular structures, whereas microparticles were found inside the cytoplasm without membrane-like structures [513].

The internalization of molecules into cells can happen via different endocytotic pathways like clathrin-mediated endocytosis, caveolin-mediated endocytosis, phagocytosis, macro-pinocytosis as well as via pathways which are independent of clathrin and caveolin [514]. Macropinocytosis is an endocytotic process during which large (> 1 µm) areas of plasma membrane including fluid are internalized into the cells [515]. Therefore, large vesicles with a size > 1 µm are formed, which are termed macropinosomes. The formation of the large macropinosomes requires an intact cytoskeleton and its reorganization [516]. It is crucial to understand the entry mechanism of particles into mammalian cells as well as the intracellular localization after endocytosis. Therefore, different inhibitors are known which can inhibit or influence one specific endocytotic pathway [517].

During this study the uptake of silica microparticles was analyzed in more detail. Due to the large size of the particles, an uptake of 2 µm silica particles via macropinocytosis was considered as the most likely uptake mechanism. To further proof the hypothesis, the uptake

was investigated in presence of *dimethylamiloride* (DMA), which is described in literature to have an influence on macropinocytosis [518]. Normally, amilorides are known to inhibit the Na^+/H^+-exchange [519-521]. Koivusalo et al. (2010) reported about an inhibition of macropinocytosis as a consequence of acidification due to inhibition the Na^+/H^+-exchange. The group found an impairment of small GTPases Rac1 and Cdc42, which are responsible for actin remodeling as a consequence of lowering the submembranous pH-value by an unknown mechanism [518]. Furthermore, inhibition of the actin polymerization by cytochalasin D can be useful for the analysis of this specific endocytotic uptake mechanism but was not applied in the presented study. Using 100 µM DMA, which is reported to lead to mild acidification of the cytosol [518, 522], significantly reduced the uptake of the 2 µm silica particles during 24 h of incubation, analyzed by confocal laser scanning microscopy after cytoplasm stain with Calcein (**Fig. 6.16**).

DMA is often applied to inhibit particle uptake via macropinocytosis [523, 524] but also different amiloride analogues are available which differ in their potency to inhibit the Na^+/H^+-exchange [525]. DMA is known to have a higher potency and is consequently applied in significantly lower concentrations during inhibition experiments compared to amiloride [526]. Whereas macropinocytosis can be blocked using amiloride in millimolar concentrations, DMA is applied in a concentration range between 50 - 100 µM [517]. Zhang et al. (2010) found a significantly impaired uptake of 500 nm-sized silica particles into primary human dermal fibroblasts in presence of 2.5 mM amiloride [527]. The uptake of four different hydrogel particles into HepG2 cells was investigated by Liu et al. (2012) in presence of different inhibitors. The application of 2 mM amiloride significantly decreased the particle uptake to 30 – 40% compared to particle exposure under control conditions [528].

Zhu et al. (2013) found a size-dependent endocytotic uptake mechanism for silica nanoparticles into HeLa cells [529]. For a diameter of ~ 56 nm an energy-independent mechanism was proposed which was not inhibited by incubation at 4 °C. When the diameter increased to ~ 168 nm the uptake was proposed to occur via clathrin-coated vesicles or caveolin-dependent mechanism. In contrast, the internalization of ~ 308 nm-sized silica nanoparticles was found to be clathrin-mediated. By further increasing the particle diameter of silica microparticles to ~ 1.6 µm or ~ 3.2 µm also Serda et al. (2009) suggested a preferred uptake mechanism by endothelial HUVEC cells via phagocytosis and macropinocytosis [530]. In this study, the uptake of the microparticles was significantly reduced by 85 – 88 % when the incubation took place in presence of 2.5 µg/mL cytochalasin B. A label-free study of the time-dependent uptake of 2 µm and 0.5 µm carboxyl-modified polystyrene particles into 3T3 fibroblasts was presented by Byrne et al. (2008). Using *total internal reflection microscopy* (TIRM) the group could visualize the internalization of non-labeled particles [531]. Recently,

Byrne et al. (2015) published a combination of TIRM/TIRF (*total internal reflection microscopy*/ *total internal reflectance fluorescence*) analysis to investigate the uptake of 0.5 µm and 1 µm polystyrene beads into EGFP-clathrin expressing 3T3 cells in more detail. A co-localization of the 0.5 µm particles with EGFP-clathrin pointed to an uptake via clathrin-mediated endocytosis. In contrast, no co-localization was found for 1 µm particles demonstrating a size-dependent uptake mechanism which occurred via a non-clathrin dependent pathway for the larger particles [532].

ECIS recordings during uptake of silica particles clearly showed spikes in the time-course of |Z| at 16 kHz which were significantly reduced when the inhibitor DMA was present. A relationship between these spikes and the uptake into NRK cells was hypothesized. To further support our hypothesis, different concentrations of silica particles were investigated and the particle surface charge was modified.

When the cellular response was monitored over at least 24 h after the addition of silica particles spikes were found in the time-course of impedance which were most prominent at 16 kHz (**Fig. 6.16**). A correlation and mechanistical connection between the spikes and the endocytosis of the particles into NRK cells was considered. The presence of the macropinocytosis inhibitor DMA clearly impaired the uptake, analyzed via confocal laser scanning microscopy and also the appearance of these spikes in the impedance signal decreased. To investigate the concentration-dependency of particle uptake, different particle concentrations were offered extracellularly with the intention that uptake is increased in presence of higher concentrations with a corresponding increase in impedance spikes (**Fig. 6.18**). Lower particle concentrations resulted in a more stable time-course of impedance compared to higher concentrations, where the spikes in $|Z|_{norm}$ were clearly visible. As the silica particles were also taken up after exposure of the cells with particles in a concentration of $1.9 \cdot 10^7$ P/cm^2 without detectable spikes in the time-course of impedance, it was hypothesized that these spikes correlate with the simultaneous uptake of more than one particle. This internalization includes the re-arrangement of the actin cytoskeleton [533, 534] which might lead to a temporary alteration of the current flow.

Furthermore, different surface modifications were tested as these are known to enhance or reduce the uptake efficiency [490, 535]. Commercially available polystyrene beads were investigated, which had negatively or positively-charged surfaces. Microscopic analysis clearly revealed the preferred uptake of amine-modified compared to the carboxylate-modified polystyrene beads (**Fig. 6.19 B**). A stronger interaction of positively-charged particles with the negatively-charged cell membrane has been outlined by Gao et al. (2005)

[492]. Foged et al. (2005) further investigated the uptake of 1 µm polystyrene particles dependent on the surface charge. The group found a significantly enhanced uptake of positively-charged particles into dendritic cells[536]. Also E. Fröhlich (2012) summarized in a review that for most nanoparticles a cationic surface charge increases the uptake efficiency [489].

ECIS experiments during 40 h of exposure of NRK cells to polystyrene beads or silica particles with similar concentrations only showed the spikes in $|Z|_{norm}$ at 16 kHz for NRK cells when incubated in presence of silica particles (**Fig. 6.19 A**).

These results pointed to a material-dependent cell response as particles made of polystyrene did not induce spikes in the time-course of impedance. Additionally, these spikes were not obligatory as in some experiments NRK cells did not provide these characteristic pattern in presence of silica particles. However, still a connection between the occurrence of these spikes and the incorporation of the particles is still likely but requires further investigations.

6.6.2 Determination of Toxicity of Nanoparticles Using Label-Free and Label-Based Techniques

In this study the response of NRK cells to the exposure of silica particles was investigated using the label-free ECIS technique. Time-resolved ECIS measurements revealed no acute cytotoxicity of silica particles with a diameter of 2 µm.

Nanoparticles are applied in many different fields of our daily lifes and, therefore, a careful characterization of the particles and their influence on mammalian cells should be performed. This includes evaluating the potential toxicity resulting from nanomaterial or particles in the micrometer range. The integrative parameter “cytotoxicity” includes the interference with cellular attachment, impact on cell morphology, cell proliferation or the effect of inducing cell death [537]. A variety of endpoint assays are available to analyze cell viability, which is the most commonly analyzed cell-related parameter after exposure to a given test compound. These include classical dye conversion assays (e.g. MTT assay), dye inclusion (e.g. Crystal Violet) or exclusion assays (e.g. Ethidium Homodimer) as well as detection of membrane damages by the release of an enzyme into the media (e.g. LDH assay). These assays require a pre-defined endpoint and offer only information about cell viability after a certain incubation time.

During the MTT assay the reduction of yellow tetrazolium by metabolically active cells to purple formazan is used to quantify cytotoxicity of particles. Napierska et al. (2009) studied the size-dependent cytotoxicity of silica nanoparticles with diameters between 16 nm and 335 nm using an MTT assay. Human endothelial cells (EAHY926) were incubated with silica nanoparticles for 24 h and afterwards the cytotoxic response of the cells was evaluated using MTT assay. Particles with a diameter of 104 nm and 335 nm provided a very low cytotoxicity whereas an enhanced cytotoxicity was found by decreasing the particle diameter [538]. Furthermore, Lin et al. (2006) investigated the cytotoxicity of 15 nm and 46 nm silica nanoparticles using A549 lung cancer cells. Independent of the particle size the group found a dose-dependent decrease in cell viability when applying concentrations between 10 – 100 µg/mL [539]. Yu et al. (2009) analyzed the cytotoxicity of amorphous silica nanoparticles in mouse keratinocytes (HEL-30). In this study HEL-30 cells were exposed to 30 nm – 535 nm silica particles for 24 h and cell viability was investigated using MTT assay. The mitochondrial activity of HEL-30 cells was significantly lower for the smaller particles compared to the 118 nm and 535 nm particles when they were applied in concentrations above 100 µg/mL. Moreover, these particles were investigated with respect to membrane permeabilization and leakage of the intracellular enzyme lactate dehydrogenase (LDH). A size- and dose-dependency of LDH content in the medium was found. A concentration above 50 µg/mL provided a significantly higher cytotoxicity for smaller particles (30 nm; 48 nm)

compared to the larger ones (118 nm; 535 nm) [510]. Lison et al. (2008) analyzed the effect of silica nanoparticles using different label-based cytotoxicity assays. As also determined by other assays, a dose-dependent increase in cytotoxicity was observed for mouse monocyte-macrophages (J774 cells) after 24 h of incubation in presence of 29 nm silica particles using the crystal violet assay, which provided an EC_{50}-value of 37 µg/mL [540]. The necrotic effect of silica nanoparticles with a diameter of 304 nm after 24 h of incubation was investigated by Bauer et al. (2011) using Propidiumiodide staining and FACS analysis. In this assay, the cell death of HUVEC cells was quantified and Bauer et al. found a (4.4 ± 1)-fold increase of cell death after nanoparticle exposure compared to the untreated cell population [541]. This type of assay is based on the fact that vital cells with an intact cell membrane exclude Propidiumiodide from the cell interior. When the cell membrane in necrotic cells is damaged a characteristic red nuclei stain allows an identification of dead cells.

It should be mentioned that often an interference of the test material with *in vitro* label-based toxicity assays is reported [542-544] which can be explained by the high adsorption capacity and optical properteies of nanoparticles [545]. Therefore, it is necessary to ensure that the test materials themselves do not interact with the ingredients of the assay observed causing misinterpretations of the assay results. In contrast, ECIS provides a label-free approach to detect cytotoxicity. Cell shrinkage during apoptosis or loss of membrane integrity during necrosis causes a significant decrease in impedance. Moreover, this technique enables analysis of cytotoxicity without the addition of a colorimetric, fluorogenic or radio-labeled substance, and is advantageous compared to optical assays as the (micro-) particles do not interfere with the electrochemical readout.

In this study, ECIS recordings were performed to analyze the cytotoxicity of silica microparticles with a diameter of 2 µm. NRK cells were grown to confluence on the surface of planar 8W1E gold-film electrodes and incubated with silica particles with increasing concentrations for at least 24 h. The experiments revealed no indication for acute cytotoxicity of the particles (**Fig. 6.21**). Also the long-term study in absence or presence of FCS over 72 h did not show any evidence for an alteration of cell morphology or cytotoxicity due to the presence of 2 µm silica particles (**Fig. 6.26**).

A second parameter which clearly correlates with cell viability is the ability of cells to perform small cell fluctuations which can be recorded as fluctuations in the impedance signal using ECIS. No influence on cell micromotion was found after incubation with different concentrations of silica particles as determined by the calculated motility indices based on RTC measurements.

In 1991, Giaever and Keese reported about the ability to detect micromotion of cells in the nanometer range using the ECIS technique [121]. This is realized by the high time-resolution of at least 1 point per second when one electrode is recorded over a defined period of time using the most sensitive frequency. Further investigations were performed by Lo et al. (1993) who analyzed the ability of the fibroblast cell line WI-38 VA13 to perform micromotion at low temperature or reduced glucose content in the medium. For both conditions, a significantly decreased fluctuation amplitude was found in the impedance recordings compared to control populations, which correlated with the reduced metabolic activity of the cells [546]. Micromotion of cells should be clearly differentiated from wound healing during a migration assay. There, cell migration into a cell-free area is monitored whereas micromotion detects form fluctuations within a confluent cell layer and requires a high time-resolution. These metabolically driven fluctuations are also reported to be mediated by the cytoskeleton. Opp et al. (2009) analyzed the resistance signal of HUVEC cells 20 h after the addition of cytochalasin B (1 µM; 5 µM; 10 µM) with high time-resolution. The group found a dose-dependent decrease in resistance fluctuation indicating a significantly lower micromotion of cells after treatment with the actin-binding drug [493]. Also Lovelady et al. (2009) performed ECIS micromotion experiments using a confluent cell layer of 3T3 fibroblasts incubated with different concentrations of cytochalasin B (0.1 – 10 µM). By analyzing the electric noise within the recorded RTC data, the group was able to characterize the impact of cytochalasin B down to a concentration of 0.1 µM [494].

RTC assays provide a correlation between the observed fluctuation in the resistance signal and cell viability and they have been used to evaluate the impact of nanomaterials on mammalian cells in the past. Tarantola et al. (2011) analyzed the effect of gold nanoparticles on the micromotion of epithelial cells. The group recorded the micromotion of MDCK II cells in absence or presence of gold spheres and gold rods, finding a higher impairment of cell motility by gold spheres [96]. Shukoor et al. (2009) recorded an increase in the micromotion of human kidney cancer cells (Caki-1) after 24 h or 48 h of incubation with pathogen mimicking MnO nanoparticles which are able to enter cancer cells and activate the TLR9 pathway inside [547]. Tarantola et al. (2009) also used the micromotion of MDCK II cells as indicator for the cytotoxicity of quantum dots [548].

In this thesis the acute toxicity of these particles was studied within 24 h of exposure finding no impact on cell viability (**chapter 6.4.4.1**). Therefore, the sequence of impedimetric assay was continued with the analysis of micromotion 24 h after particle addition. This assay provides a more sensitive analysis of changes in the metabolic activity of NRK cells. The interest was driven by the microscopic images which clearly showed a densely-packed arrangement of silica particles in the cytoplasm of NRK cells (**Fig. 6.10**). However, independent of the applied concentration of silica particles (∅ 2 µm) the micromotion analysis always yielded similar motility indexes (**Fig. 6.23**). These results indicated that the particles did not have any influence on the metabolic activity of NRK cells.

The performance of cell micromotion within a confluent cell layer requires an intact cytoskeleton. The metabolically driven cell shape fluctuations are mediated by the cytoskeleton network of adherent cells. The application of actin-binding drugs like cytochalasin B [493, 494,77] or cytochalasin D [546] strongly interferes with cell motility and significantly reduced the fluctuation recorded in micromotion experiments. No effect of silica microparticles on the cytoskeleton was indicated by the results of the RTC measurements, which were further backed up by microscopic analysis of NRK cells after actin cytoskeleton stain (**Fig. 6.29**). It is possible that the impact of silica microparticles on the metabolic activity of a cell layer strongly depends on the cell type. Chang et al. (2007) investigated the impact of nanoparticles on normal fibroblasts and tumor cells by MTT assays. They claim that the cytotoxicity of silica nanoparticles depends on the metabolic activity of the cell type itself. The group detected a higher cytotoxicity in normal human fibroblast cells compared to the cancer cells, which are characterized by a higher metabolic activity [549].

In summary, silica microparticles did neither provide any evidence for cytotoxicity nor affect NRK cells in their cellular dynamics and metabolic activity. Using cells with a higher metabolic activity, as characterized by a more fluctuating resistance signal, RTC measurements are supposedly more sensitive to small changes in cell micromotion and might reveal differences after particle addition. The impact of silica microparticles on different cell types might be an interesting topic for future applications.

6.6.3 Impact of Microparticles on Cell Migration

Migration of NRK cells after incorporation of silica particles was investigated using an ECIS-based analysis during which a circular wound was created by applying an invasive voltage pulse (40 kHz, 5 V, 30 s). After pulsing the re-population of the cell-free electrode was monitored in real time in a non-invasive way. No influence on cell migration was found even when NRK cells have taken up high amounts of particles.

Collective cell migration plays an important role in many physiological processes, like tissue repair, wound healing, angiogenesis and embryogenesis [495, 496] as well as during invasion and metastasis of malignant tumors [550]. Different *in vitro* techniques and assay formats are available [551] to address the collective cell migration within a cell population. One prominent type of assay is the so-called wound healing assay where a wound is created by a mechanical, physical or electrical method [101].

One simple way to introduce a wound in a confluent cell monolayer is to create mechanical injury by physical scraping so that the migration of cells into the cell-free area can be analyzed microscopically. To further improve the reproducibility, a circular wound can be formed using a rotating drill press. Kam et al. (2008) used this assay to study different levels of invasion and wound healing efficiencies for three different cancer cell lines [552]. The stamping assay published by Lee et al. (2010) represents another mechanical wound healing assay. Here, a confluent cell layer is punched by a PDMS stamp to create a defined wound and afterwards migration of an epithelial cell monolayer was monitored in presence of the remaining cell debris in a two-step process. First, a clearing process was observed, followed by cell migration into the cleared, cell-free area [553].

Instead of removing cells from a confluent cell layer physical barrier-based assays include cell seeding in presence of a solid or liquid barrier to prevent the formation of a confluent cell layer. The assay starts immediately after removing the physical barrier, which subsequently allows the cells to migrate into the cell-free area and to create a confluent cell layer. One example of a physical barrier is a Teflon fence which was applied by Pratt et al. (1984) for the investigation of BAEC cell migration [554]. Another method to study migration after removing a physical barrier is the oil droplet migration assay presented by Cai et al. (2000). Here, a small volume of HUVEC cell suspension is pipetted into light mineral oil and the cells subsequently adhere to the matrix surface. After 60 min the oil is removed and replaced by culture medium to initiate cell migration which can be monitored microscopically [555].

In 2004, Keese et al. presented the electrical wound healing assay based on ECIS where the migration of the cells can be analyzed in real-time after the application on an elevated electric field which creates a well-defined wound. In this study the authors clearly showed the

influence of different amounts of FCS on the ability of BS-C-1 cells to migrate and to completely close the circular wound [103]. In this thesis, the ECIS-based wound healing assay was used to analyze the migration of NRK cells in presence of different concentrations of silica particles with a diameter of 2 µm (**Fig. 6.24**). Even though those particles did not cause an immediate toxicity (**Fig. 6.21**) an effect on cell migration seemed possible, due to the fact that microscopic data revealed a dense intracellular localization of particles. However, NRK cells were not inhibited in their ability to migrate even after the uptake of different concentration of silica particles (**Fig. 6.24**).

These findings are in good agreement with studies in literature, where the impact of nanomaterials on cellular processes like cell migration is often correlated with cytotoxic effects. Zhang et al. (2010) analyzed the influence of incorporated 80 nm and 500 nm silica particles on the migration of dermal fibroblasts. After 4 h of incubation with 100 µg/mL a classical wound healing assay was performed where a confluent cell layer was scratched to initiate the migration process. The wound healing efficiency was investigated microscopically 16 h and 24 h later finding a reduced cell migration in presence of nanoparticles. The wound closure was faster for cells in presence of 500 nm silica particles compared to fibroblasts which were pre-incubated with 80 nm particles. This was in good correlation with the detected cytotoxicity, which was significantly higher for cells in presence of the smaller particles [527]. Huang et al. (2010) used a physical barrier-based migration assay. A375 cells were seeded in presence of a PDMS frame. After removing the physical barrier a cell-free gap of (800 ± 50) µm was formed. The wound healing efficiency of A375 cells after 24 h of incubation with 0.1 mg/mL mesoporous silica nanoparticles was enhanced compared to the control population. A375 cells migrated faster in presence of spherical nanoparticles (~ 100 nm) compared to cells incubated with long rod particles with a length of 450 nm. Moreover, both particle types were found to be non-toxic as revealed by MTT assay. Rod-shaped particles were taken up in larger amount and with faster kinetics compared to spherical particles and consequently revealed a greater impact on cell migration [556]. The effect of silver nanoparticles (~ 50 nm) on the migration of bovine retinal endothelial cells (BREC) was studied by Kalishwaralal et al. (2009). In presence of the vascular endothelial growth factor (VEGF) and 500 nM silver nanoparticles the migration of BREC cells was significantly blocked which was evaluated by microscopic scratch assays. In this study silver nanoparticles showed acute cytotoxicity leading to apoptosis [557].

In summary, cell migration of NRK cells was unaffected by silica particles, independent of the applied concentration. Similar wound healing efficiencies were determined relative to migration of NRK cells under control conditions.

6.6.4 Impact of Microparticles on Cell Proliferation

Proliferation of NRK cells in absence or presence of silica particles was investigated using ECIS recordings finding similar proliferation kinetics under both conditions. These results were further confirmed using label-based assays.

Cell proliferation describes the increase in cell number within a population and is strictly controlled and regulated by the cell cycle. The cell cycle can be divided into the interphase consisting of G1-, S- and G2-phase and the M-phase. Mammalian cells run through the cell cycle around 60 times in their lifetime, which is called the Hayflick-limit [558] until they become senescent. Studies on cell proliferation are often used to address the impact of drugs on tumor progression. Moreover, the effect of nanomaterials or microparticles on cell proliferation can be analyzed using label-free or label-based methods. ECIS enables to study cell proliferation without any additional labeling over a long period of time. Cells are seeded in low densities, resulting in sparsely populated gold-film electrodes characterized by a high capacitance value. Due to proliferation of the initially seeded cells the electrode coverage increases, which is indicated by a decrease of capacitance at high frequencies. As already presented in **chapter 4.5.1** the capacitance linearly depends on the electrode coverage providing the kinetics of cell proliferation. Wang et al. (2010) analyzed the cell cycle of HeLa cells in a label-free manner and in real-time using an impedance sensing chip which consisted of interdigitated gold-film electrodes. The group reported that their setup and the time-course of impedance are a sensitive indicator for the different stages during the cell cycle and allowed to calculate the doubling time to ~ 22 h, which can be used to investigate the influence of drugs or toxins on cell proliferation [559].

Huang et al. (2008) published one of the earliest studies about impedimetric analysis of particle influence on cell proliferation. They analyzed the impact of two different quartz particle mixtures with diameters between 0.35 µm – 3.5 µm or 1.2 µm – 20.0 µm on proliferation of two different human carcinoma cell lines (A549 and SK-MES-1) using the real-time cell-electronic sensing (RT-CES) system. RT-CES system allows the analysis of 16 wells simultaneously and quantifies the changes in impedance using the so-called cell index (CI). The CI is the difference between cell-covered and cell-free electrode as ratio to the cell-free electrode for one of the three measuring frequencies that yielded maximum signal. The authors yielded a cell-type specific and dose-dependent impact on cell proliferation. A549 cells were less sensitive to the presence of the particles compared to SK-MES-1 cells which clearly showed an inhibition of the proliferation and evidences for cytotoxic effects when the particles were applied in high concentrations [560]. A cell-type specific response to the presence of nanoparticles was further reported by Chuang et al.

(2013) who analyzed the effect of gold nanoparticles on six different cell lines using an impedance-based proliferation assay [561].

In this thesis, the effect of 2 µm silica particles on NRK cell proliferation was analyzed using ECIS recordings. The interdigitated 8W10E$^+$ electrode layout was chosen with an active electrode area of 1.96 mm^2 per well. Therefore, the detected signal represented the average electrode coverage in the entire growth area of ~ 0.8 cm^2. Around 22 h – 24 h after subconfluent seeding, silica particles or fresh medium were added and the establishment of a confluent cell layer in absence or presence of silica particles was monitored over time. The increase in electrode coverage was analyzed either by the decrease in capacitance or by the increase in impedance at high frequencies (**Fig. 6.27**). In the simulation project a linear dependency between the capacitance decrease and the increase in electrode coverage was found (**Fig. 4.25 C3**). Therefore, the continuous decrease in C_{norm} in absence or presence of silica particles clearly indicated a successively increasing NRK population in the well as the result of cell proliferation. In contrast, the analysis of $|Z|_{norm}$ at 32 kHz showed only a small change in the impedance level within the first 48 hours. Afterwards, the signal increased time-dependently until a confluent cell layer was formed. This was in good agreement with the simulated impedance data for a 8W10E electrode layout presented in **Fig. 4.25 A3** where $|Z|_{norm}$ at 32 kHz started to increase after 60 % of the electrode was covered with cells. From the time-course of impedance and capacitance no influence on the cell proliferation kinetics was found in presence of silica particles compared to the control population. Further analysis evaluated the slope of C_{norm} between 0.7 – 0.5 as well as the time-point when half of the electrode surface was covered with cells (**Tab. 6.5**). Both parameters did not show any significant difference between the control population and cells which proliferated in presence of the microparticles.Although it is known that nanomaterials and microparticles can interfere with the readout of label-based analysis, the majority of studies addressing the impact of nanomaterials on cell proliferation is performed using label-based assays. These assay formats are more time-consuming compared to the ECIS technique as they require to analyze the progress in cell proliferation at defined time-points microscopically or using colorimetric readings. Furthermore, these kinds of end-point assays require a determination of the time-point of analysis in advance. Prominent label-based assays to analyze the impact of nanoparticles on proliferation are BrdU assay [562] which detects the proliferation activity with respect to DNA synthesis or MTT assay [535] which has been found to be sensitive to the cell number under study.

In this assay two label-based strategies were performed to support the proliferation data obtained with ECIS. The readout of these assays was found not to be impaired by the particles. Cell proliferation was stopped after defined periods of proliferation and cell nuclei

were visualized with DAPI. Fluorescence images were analyzed using ImageJ with respect to the number of fluorescence pixels above an arbitrary threshold or the number of cell nuclei within the pictures (**Fig. 6.30 B**). The continuous proliferation of NRK cells with time was confirmed by both approaches. At the end of the experiment (t = 96 h) a slightly decreased value for the number of fluorescence pixels above the threshold and the number of nuclei was found for NRK cells in presence of silica particles compared to the control population. After formation of a confluent cell layer during an ECIS experiment the electrode coverage was analyzed microscopically using cell nuclei stain with DAPI as well as Alexa Fluor 488 Phalloidin to visualize the actin cytoskeleton. In **Fig. 6.29** less cell nuclei were counted on top of the circular electrodes in presence of silica particles compared to the control cells. Nevertheless, the actin cytoskeleton stain and also the capacitance data revealed the presence of a confluent cell layer on top of the electrodes. This led to the hypothesis that due to the incorporation of the silica particles the cell sizes increased compared to the control population. This has an influence on both optical approaches, where the numbers of cell nuclei or the pixels were counted. The influence of silica particles on NRK cell proliferation was further investigated over 94 h using the PrestoBlue® assay (**Fig. 6.31**). Similar $I_{590\,nm}$-values were found until 70 h of cell proliferation for control and particle-loaded cells. After 94 h of proliferation control cells provided a slightly higher signal compared to particle-loaded cells which was found not to be significant.

In summary, no significant influence of silica particles on cell proliferation was found using label-free ECIS recordings which enable a real-time analysis over the entire proliferation time. The label-based experimental approaches based on staining cell nuclei with DAPI showed difference between the control cells and cells in presence of the microparticles at the end of experiment. Microscopic images showed that the cell size increased when NRK cells have taken up silica microparticles that interfere with their cell volume. Consequently, fewer cells occupy the same growth area compared to the control NRK population under particle-free conditions which had an influence on the label-based approaches where cell nuclei were stained with DAPI.

6.6.5 Analysis of Gap Junctional Intercellular Communication in Presence of Microparticles

The impact of silica microparticles on cells' ability to communicate via gap junctions was investigated using common dye transfer assays. Additionally, a new opto-electrical assay developed in this thesis was used to evaluate the impact of silica particles on gap junctional intercellular communication. No significant influence on dye transfer was found for NRK cells in presence of silica microparticles.

When the impact of nanomaterials on cell physiology is analyzed the influence on gap junctional intercellular communication should not be disregarded. But in literature only few studies focus on the impact of (nano-)particles on gap junctional intercellular communication at all. Chang et al. (2009) first analyzed the impact of quantum dot (QD) internalization into human adult mesenchymal stem cells on gap junctional intercellular communication. The QDs were coated with Pep-1, an amphipathic peptide which facilitated the delivery into the cells. As no cytotoxicity was observed for Pep-1-delivered CdSe/ZnS QDs the impact of this nanomaterial on gap junctional intercellular communication was investigated using the scrape loading technique. A significantly reduced transfer of Lucifer Yellow was monitored using a cell monolayer in the scrape loading assay after internalization of Pep-1-QDs compared to the particle-free control population. The dye transfer of Lucifer Yellow was determined to (57 ± 11) µm after QD internalization and to (168 ± 10) µm under particle-free control conditions. When gap junctional intercellular communication was monitored in 3D alginate hollow spheres by FRAP analysis similar dye transfer characteristics were observed indicating a significant difference of QDs' impact on cell-cell communication between 2D and 3D cell models. These results can be explained by the increased density of cell-cell contacts in 3D compared to cell monolayers [563]. The impact of silica particles ($\varnothing < 5$ µm) on Cx43-mediated gap junctional intercellular communication between rat lung epithelial (RLE-6TN) cells was investigated by Ale-Agha et al. (2009). Microinjection experiments revealed the properties of these cells to mediate dye transfer via gap junctions as well as a significant decrease in gap junctional intercellular communication after 2 h – 24 h of incubation with the sub-toxic concentration of 10 µg/cm^2 DQ12 silica particles. The group explained the decrease of gap junctional intercellular communication by the formation of reactive oxygen species, which are known to modulate cell-cell communication [564]. Moreover, Ale-Agha et al. (2010) analyzed the impact of differently sized carbon black or silica-based nanoparticles on gap junctional intercellular communication between RLE-6TN cells based on dye transfer analysis after microinjection. In this study a size-dependent difference was found for carbon black. Whereas fine carbon black ($\varnothing$ 260 nm) did not affect the degree of gap junction-mediated dye transfer the exposure of RLE-6TN cells to ultra-fine carbon black ($\varnothing$ 14 nm)

resulted in a decrease (63 %) of gap junctional intercellular communication. Silica-based fine (∅ < 5 µm) and ultra-fine (∅ 14 nm) particles significantly reduced the ability to mediate dye transfer via gap junctions about 59 % and 77 %, respectively [565]. Alpatova et al. (2010) studied the influence of single-walled carbon nanotubes (SWCNT) on gap junctional intercellular communication between rat liver epithelial (WB-F344) cells. The quantification of the distance of dye transfer into adjacent cells after scrape-loading revealed no influence of SWCNTs on gap junctional intercellular communication between WB-F344 cells independent of the incubation time (30 min; 24 h) [566]. An increase in gap junctional intercellular communication between A549 cells was found by Deng et al. (2010) in presence of silver nanoparticles (∅ 69 ± 3 nm). Using dye transfer analysis based on scrape-loading technique after 24 h of exposure to silver nanoparticles an enhanced ability to transfer Lucifer Yellow via gap junctions was found using 2.0 µg/mL and 4.0 µg/mL silver nanoparticles. Immunofluorescence staining of Cx43 also showed an increase in Cx43 expression in presence of silver nanoparticles [567].

The results obtained in this thesis with the newly developed opto-electrical assay were compared to the results of common dye transfer based methods including scrape loading assay, parachute assay and FRAP assay. Scrape loading provides a simple and fast method, where cells are scratched in presence of a gap junction permeable, but membrane impermeable dye. The dye can diffuse into the cells, which were damaged by the pipette tip. If cells communicate with each other via gap junctions the dye can further diffuse into the cell monolayer perpendicular to the scrape. **Fig. 6.32** summarizes the fluorescence micrographs after performing the scrape loading assay with NRK cells or cells which were pre-loaded with silica particles. When the gap junction inhibitor 2-APB was present the fluorescence signal was strictly limited to the initially stained cells. In contrast, NRK cells and cells in presence of silica particles clearly showed a gap junction-mediated dye transfer into neighboring cells. In this work no further quantification of the dye transfer ability based on the scrape-loading assay was performed as it should only serve as proof that NRK cells are able to communicate via gap junctional intercellular communication and that it was not significantly affected by the presence of microparticles.

Furthermore, the ability of *de novo* formation of gap junctions was investigated in absence or presence of silica particles using the parachute assay. Here, the pre-stained donor population is seeded on a confluent cell layer and the formation of new gap junction channels between the pre-stained donor cells and the confluent acceptor cell layer is analyzed. **Fig. 6.33** clearly showed that NRK cells and cells in presence of silica particles in the acceptor cells are able to form intact gap junctions as dye transfer into the cell monolayer was observed under both conditions. Using this assay a quantification of the obtained data

based on confocal fluorescence micrographs is hard to perform as the results significantly differed dependent on the field of view. In summary, cells with internalized silica microparticles were able to communicate via *de novo* formed gap junctions.

In this study FRAP assays were performed using NRK control cells and cells which have taken up high amounts of silica particles via endocytotic pathways. During the FRAP assay target cells within a Calcein pre-stained cell population were photo-bleached using a high laser intensity. Then, time-resolved images allowed the analysis of fluorescence recovery resulting from Calcein transfer via gap junctions from neighboring cells into the photo-bleached cell. Interestingly, first a bright green fluorescent signal recovered in the nucleus followed by the recovery of fluorescence within the cytoplasm. Up to now, no explanation for the preferential recovery in the cell nuclei was found in literature.

The time-courses of fluorescence recovery and therefore the degree of gap junctional intercellular communication were analyzed using a time-dependent CV value. Therefore, the decrease in fluorescence intensity with time within a reference cell was monitored to correct for inherent decrease in intensity due to permanent microscopic analysis within a field of view. When cells in presence of silica particles were analyzed the reference was selected to be equal to the target cell with respect to cell size and number of internalized particles. Moreover, phototoxicity due to live cell imaging should be kept in mind where reactive oxygen species and radicals can be produced [568] during the time-resolved analysis of recovery. For image analysis, a significant influence of the microparticles became obvious as they appeared as black dots inside the cytoplasm when located intracellularly. We tried to account for this effect by choosing a reference cell with similar properties, however, a complete conformity is impossible to ensure. Nevertheless, **Fig. 6.35** clearly showed that NRK cells and cells in presence of silica particles showed recovery of fluorescence intensity within the photo-bleached cell as long as no inhibitor was present. The summary of seven different cells in absence or presence of silica particles (**Fig. 6.36**) provided a recovery of 54 ± 6 % for control cells and a slightly reduced recovery of 45 ± 16 % within 6.2 min for cells in presence of silica particles. The higher standard deviation for cells pre-incubated with the particles may result from the different amounts of intracellular particles, which were taken up during 24 h of particle exposure. The application of a two-sample t-test did not show a significant difference between the two conditions.

Finally, the opto-electrical assay was applied to investigate the ability of silica particles to manipulate gap junctional intercellular communication. It was found that *in situ* electroporation can be performed with silica pre-loaded NRK cells without any adjustment of the electroporation parameters (**Fig. 6.38**). Within this thesis a new opto-electrical assay was developed which facilitates the multi-parametric readout (**Fig. 6.39**). It is based on the ECIS

technique, which enables a pre-analysis of the cell layer integrity before the test compound, in this study the silica microparticles, is added. Thus, the cytotoxicity of the particles and their impact on cell motility were investigated prior to *in situ* electroporation. Finally the analysis of gap junctional intercellular communication was realized using a two-pulse electroporation in presence of Lucifer Yellow and the reference dye TRITC dextran. The fluorescence micrographs for NRK cells with and without 24 h of pre-loading with silica particles revealed a gap junction-mediated dye transfer in multiple neighboring cells under both conditions (**Fig. 6.41**). The quantification of the ability to transport Lucifer Yellow into neighboring cells was performed by calculating the AUC as described in more detail in **chapter 5.5.4.5**. The quantification of the dye transfer showed similar AUC values for control cells (2.3 ± 0.1) and cells in presence of silica particles (2.1 ± 0.2). However, a significant difference was found for cells in presence of 50 µM 2-APB (1.00 ± 0.03) where the dye transfer was strictly blocked (**Fig. 6.43**).

This electroporation based analysis of gap junctional intercellular communication of NRK cells, grown on gold-film electrodes, completed the in-depth analysis of microparticles' impact on NRK cell physiology. The sequence of impedimetric assays can serve as model for the analysis of nanoparticles or other modulators of gap junctional intercellular communication.

In summary, this chapter provided an analysis of the cell response after the addition of silica microparticles including changes in viability, migration and proliferation finding no influence on NRK cell physiology. The study was further extended analyzing the alteration of intercellular structures which can affect cell-cell communication. The analysis of the dye transfer between NRK cells was not affected by the presence of silica particles.

6.6.6 Impact of Microparticles on Beating Cardiomyocytes

This proof-of-concept study showed that the ECIS setup can be used to analyze the periodic beating of Cor.At® cells. The positive inotropic effect of Isoproterenol hydrochloride and the cessation of beating in absence of Ca^{2+} or after the addition of the gap junctional intercellular communication inhibitor 1-heptanol were detected. Moreover, the effect of silica microparticles on gap junctional intercellular communication between cardiomyocytes was investigated, finding no significant influence on Cor.At® beating over 24 h of exposure.

Gap junctions, presented in detail in **chapter 5,** are responsible for the coordination of several cellular processes in tissue and organs. The main function of the heart is to pump blood through the body what requires repeated, synchronous contraction and relaxation cycles of individual cardiomyocytes. A synchronization of cardiomyocytes is essential for the contraction of the myocardium and is realized via gap junctional intercellular communication [272]. The propagation of the action potential in cardiomyocytes is mediated via ion transport through gap junctions, which are mainly located in the intercalated disc [569]. Cx43 is the predominant connexin isoform but also Cx40 and Cx45 are present in different regions of the mammalian hearts [570].

Cor.At® cells derived from mouse embryonic stem cells were used as a second cell model system to investigate the effect of silica particles. An intact gap junctional intercellular communication is crucial for the synchronous contraction. Thus, an alteration of the gap junction channel properties by addition of silica particles might drastically change their functionality resulting in beating irregularities or even in beating arrest.

Impedance analysis provides a non-invasive method to detect the beating activity of cardiomyocytes and enables a short- or long-term analysis e.g. of the impact of different drugs. One popular real-time system to analyze the contractility of cardiomyocytes based on impedance measurements is the xCELLigence RCTA Cardio System (ACEA Biosciences. Inc.). The xCELLigence RCTA Cardio System allows monitoring of cardiomyocytes in a 96-well microtiter plate with a fast data acquisition rate where the impedance of the entire plate is detected within 12.9 ms. In this setup, the recorded impedance data are converted into so-called Cell Index (CI) values. The detected beating pattern for Cor.At® cells [571] provides a high similarity to the observed pattern in our study.

A proof-of-concept experiment was performed to validate our impedance-based setup to detect the contraction of cardiomyocytes. The removal of Ca^{2+} in the extracellular buffer caused a transient cessation of beating whereas cells re-started their periodic beating when $EBSS^{-+}$ buffer was exchanged to culture medium (**Fig. 6.50**). This experiment confirmed the requirement of the presence of extracellular Ca^{2+} to initiate the contraction of Cor.At® cells by

CICR [500, 501, 503]. The mechanism of Ca^{2+}-influx through the L-type voltage-dependent Ca^{2+}-channel was already presented in **Fig. 6.49**. Abassi et al. (2012) analyzed the effect of isradipine, a well-known voltage-activated L-type calcium channel blocker on Cor.At® cells using impedance analysis. Inhibition of the L-type calcium channels by 40 µM isradipine caused a beating arrest of Cor.At® cells within 30 min, indicating that Ca^{2+}-entry through L-type channel is an unconditional requirement for beating of cardiomyocytes [572].

The synchronous contraction of cardiomyocytes can be modulated by positive inotropes, substances which increase the force of contraction. In this thesis, 100 nM Isoproterenol hydrochloride was applied as one prominent example of a positive inotropic substance. **Fig. 6.52** summarizes the time-courses of $|Z|/|Z|_{mean}$ before and after addition of Isoproterenol hydrochloride. The analysis of the corresponding BPM clearly showed that an enhanced beat rate of Cor.At® cells was found in presence of the β-adrenergic receptor agonist in comparison to control cells (**Fig. 6.53**). Using the xCELLigence System Abassi et al. (2012) investigated the effect of pharmacological modulators on the contractile performance of Cor.At® cells. The β-adrenergic receptor agonist Isoproterenol, which was applied in varying concentrations between 0.41 nM – 300 nM provided a concentration-dependent increase in the beating rate [572]. Jonsson et al. (2011) also investigated the effect of 330 nM Isoproterenol on human induced pluripotent stem cell-derived cardiomyocytes and mouse embryonic stem cell-derived cardiomyocytes using the xCELLigence system and found an increase in the calculated BPM by 77 % and 71 %, respectively [573]. Moreover, Scott et al. (2013) analyzed human induced-pluripotent stem cell-derived cardiomyocytes and rat neonatal cardiomyocytes in presence of 49 compounds with respect to their modulation of the beating properties. Among others, Isoproterenol was found to be a positive inotrope for both cell types since it increased the beating rate detected by impedance measurements [574]. Nguemo et al. (2012) also reported an increase in the beating frequency in induced pluripotent stem cell-derived cardiomyocytes after the addition of 10 µM Isoproterenol hydrochloride using impedance-based real-time monitoring [575].

1-Heptanol is a popular, reversible inhibitor of gap junctional intercellular communication and often applied for cardiomyocytes [272]. The mechanism of uncoupling of gap junctional intercellular communication between cardiomyocytes caused by the addition of 1-heptanol was analyzed systematically by Takens-Kwak et al. (1992). Using patch-clamp analysis, the group pointed to a reversible effect of inhibition and found a concentration-dependent decrease in the junctional current. The group hypothesized that 1-heptanol alters the lipid membrane structure and, thus, the functional state of gap junction channels [240]. Nguemo et al. (2012) applied 0.5 mM 1-heptanol to induced pluripotent stem cell-derived cardiomyocytes and monitored a significant change in the synchronous beating profile during

impedance recordings and completely inhibited the beating activity [575]. Hayakawa et al. (2012) used 2 mM 1-heptanol and reported about a delayed propagation of contraction in neonatal rat cardiomyocytes analyzed by motion vector analysis [576]. This method combines the analysis of cardiomyocyte beating with a high-speed camera via light microscopy and the calculation of motion vectors using block-matching algorithms. Natarajan et al. (2011) confirmed the inhibition of gap junctional intercellular communication between cardiomyocytes in presence of 50 µM 1-heptanol. The group detected the field potential of cardiomyocytes in presence of 1-heptanol and found a drastical increase in the propagation time of action potentials compared to control conditions [577]. In our study, 1 mM 1-heptanol was applied resulting in a significant change of the impedance signal (**Fig. 6.54**). A reversible inhibition of gap junctional intercellular communication was confirmed, as after washing out the drug cells regained the characteristic beating profiles.

In literature, different studies addressed the interaction of nanomaterials with the cardiovascular system. When nanoparticles are inhaled the heart is the first organ where nanoparticles may accumulate after they have entered the pulmonary circulation. The interaction between differently-charged polystyrene nanoparticles of 50 nm diameter and cultured neonatal rat myocytes was investigated by Miragoli et al. (2012). The group found a different impact of the nanomaterial on cardiomyocytes depending on the surface charge. Positively charged, amine-modified nanoparticles could penetrate into the cardiomyocytes and provided a high impact on cell viability. When negatively-charged particles were applied in high concentrations (50 µg/mL) the impulse propagation was significantly reduced. Moreover, cardiomyocytes showed changes in the action potential amplitude with a delayed afterdepolarization [578]. Savi et al. (2014) analyzed the short-term response of rat cardiac tissue after one hour of exposure to TiO_2 nanoparticles (5 – 50 µg/mL). The group found a reduced action potential duration after studying of cardiomyocytes isolated from adult rats via patch-clamp recordings. Moreover, TiO_2 nanoparticles were detected inside cardiomyocytes *in vitro* and in the left and right ventricular cardiomyocytes *in vivo* [579].

In this work the impact of silica particles on gap junctional intercellular communication of Cor.At® cells was investigated based on impedance recordings (**Fig. 6.58**). To the best of our knowledge, it is the first time that the impact of particles on beating periodicity of cardiomyocytes was investigated using label-free and non-invasive impedance recordings. After 24 h of particle exposure the characteristic, regular beating profiles were found in the time-course of impedance indicating no significant influence of microparticles on gap junctional intercellular communication. This short-term influence of silica particles requires further investigations as in some populations beating arrhythmia was found whereas other populations remained unaffected for 2 h of exposure (**Fig. 6.58 B – C**). However, these

transient irregularities were also recorded under control conditions (**Fig. 6.57 D**). For a final statement, further experiments and variations within the experimental procedure are required to guarantee stable beating profiles under control conditions. So far, an acute toxicity of these particles for Cor.At® cells as well as a complete inhibition of gap junctional intercellular communication can be excluded as cells were still able to perform contractions 24 h after particle exposure.

Impedance-based analysis of cardiomyocytes can be combined with other techniques to achieve further information. A well-established label-free and non-invasive method to investigate the electrical activity of cardiomyocytes is the analysis of extracellular field potentials, often performed with microelectrode arrays (MEA) [580-584]. The ion flow across the membrane of cardiomyocytes via voltage-gated ion channels leads to an extracellular field potential which can be detected via an extracellular microelectrode [585]. A comparison between field potential measurements and impedance recordings was presented by Abassi et al. (2012) who monitored the response of Cor.At® cells after the addition of 10 µM blebbistatin, an inhibitor of myosin II. A significant inhibition of Cor.At® beating was found in the impedance signal, but the inhibitor did not alter the duration of the action potential during field potential recordings [572]. This indicates, that impedance analysis is most sensitive to changes in cellular movement due to myosin contraction [586] whereas MEA analyzes the electrical activity of cardiomyocytes by detecting the extracellular field potential [587]. Doerr et al. (2014) presented a new screening platform called CardioExcyte 96, which combines the two non-invasive and label-free techniques of impedance recordings and extracellular field potential (EFP) analysis within one setup. Their setup provided a temporal resolution of 1 ms for the impedance analysis and 0.1 ms for EFP [588]. In order to achieve a multi-parametric analysis of human cardiomyocyte clusters (hCMC) Jahnke et al. (2013) presented a new 3D label-free system to measure tissue-like cardiac material. In their setup, field potential recordings were performed in combination with impedance spectroscopy to analyze 3D samples using a microcavity array [589]. More recently, Rother et al. (2015) presented a combination of ECIS experiments with optical microscopy and investigated the crosstalk between cardiomyocytes and fibroblasts. The group found higher impedance amplitudes and beating frequencies for co-cultures with higher portions of cardiomyocytes [590]. Using a modified ECIS model where cells were regarded as rectangular-shaped with circular caps [125], Rother et al. quantified the cardiac cell-cell contacts (R_b) for different ratios of co-cultures. The group found an increase in R_b with increasing portions of fibroblasts in the respective co-culture [590].

In this thesis some challenges within the analysis of cardiomyocyte beating pattern were unveiled. The presented data are basic studies regarding the ability to monitor synchronous

contraction with ECIS and to analyze the effect of silica particles on beating Cor.At® cells. Prior to the ECIS experiment, optimization of the setting and validation of the measurement setup was necessary. In proof of principle studies, different sensitivities were found using 500 Hz, 4 kHz and 32 kHz as monitoring frequencies (**Fig. 6.48**). However, even with optimized measurement setting, using 4 kHz with a high time-resolution of at least 64 points/s, some challenges became apparent which are highlighted in **Fig. 6.60**.

One parameter which strongly influenced the beating efficiency of Cor.At® cells was the post-incubation time after cell seeding (**A**). When periodic beating of cells for one well was monitored one, two or three days after cell seeding the time-courses of $|Z|/|Z|_{mean}$ and the corresponding calculated BPM differed from each other. The influence of this natural aging on the cellular beating pattern of one cell population should not be disregarded when the influence of one substance is quantified over 24 h. Therefore, it was necessary to additionally monitor one control population after medium exchange over the entire experimental period when the influence of a certain stimulus should be analyzed. A second difficulty was the high well-to-well variation within one experiment (**B**). Even for similar seeding densities and culture conditions different beating frequencies were found in the individual wells within one experiment, indicating a high well-to-well variance. This effect can be addressed by recording the periodic beating immediately before the stimulus was added (baseline). As the Cor.At® cells are non-proliferating cells, only a limited cell number was available for one experiment. After thawing different cryovials of Cor.At® cells, a high batch-to-batch variation was found as well (**C**). Therefore, only single experiments were presented in this thesis as the BPM were significantly different in multiple experiments. The presented results are preliminary experiments and require further optimization. It was found that different parameters affect the beating efficiency like cultivation time, medium exchange, and temperature. As only a limited number of different wells were available for the experimental series to analyze the influence of different compounds, different pre-treatments in prior experiments should not be disregarded.

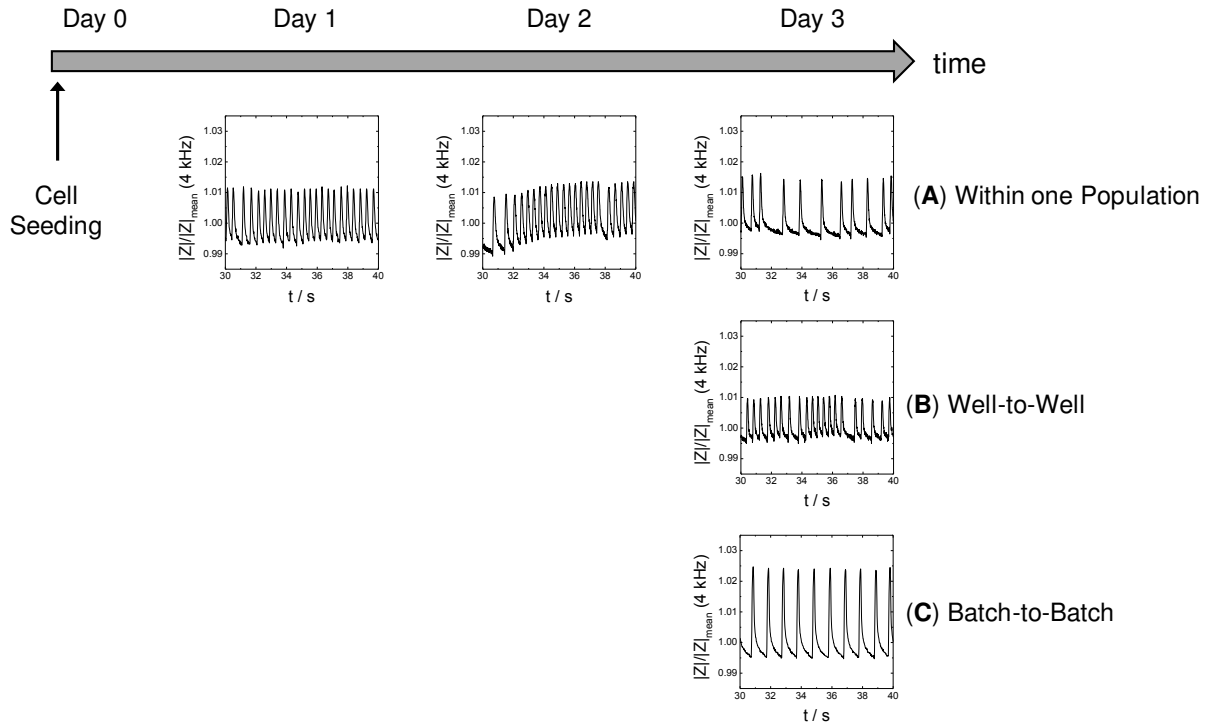

Fig. 6.60: Cor.At® cells cultivated on 8W4E-micro gold-film electrodes in presence of culture medium. Typical time-courses of normalized impedance $|Z|/|Z|_{mean}$ for Cor.At® cells one, two or three days after seeding* (**A**), for two different Cor.At® cell populations three days after seeding indicating a high well-to-well variation* (**B**) and for two different Cor.At® cell populations originating from different cryovials at day 3 after seeding indicating a high batch-to-batch variation* (**C**). (Note: All data was recorded in presence of culture medium, however, different experiments were performed prior to recording these time-courses).

The problems described above were not reported to that extend in other impedimetric studies using Cor.At® cells as they could detect dose-dependent effects for drugs with low standard deviations of the respective beating rate [572, 574]. However, other groups pointed to parameters which can influence the beating frequency. Xi et al. (2011) observed that it can take 1-5 days in culture until reproducible and regular beating profiles for Cor.At® cells were found. When a low coefficient of variation for the beating rate within the entire plate was found, the group added drugs and investigated the Cor.At® cell response to guarantee similar baseline values [571]. Johnson et al. (2011) also reported an impact of the addition of fresh medium and suggested only a partial exchange of medium. Moreover, they also mentioned that seeding density, surface coating, cultivation time and temperature can affect beating. They claim that the optimal time-point of compound screening is after day 12 – 14 in culture [573]. In contrast, Abassi et al. (2012) suggested using a pre-incubation time of 60 – 80 h in medium before contractility modulating drugs were added [572]. In conclusion, it seems that there is no general protocoll for the best time-point of analysis and the different parameters have to be adjusted individually. For our setup the best time-point of compound screening as well as the maximum period of incubation for Cor.At® cells need to be further optimized and studied systematically to achieve a higher reproducibility in particular with respect to beating rate in future experiments.

6.6.7 Multi-Dimensional Analysis to Characterize Biocompatibility of Microparticles

Research about the impact of nanoparticles on biosystems is a challenging project. A comparison with literature data is complex as the studies are performed with variable cell types, culture conditions, nanomaterials and buffer or medium compositions. The characteristics of nanomaterials like surface decoration, size, long-term stability and adhesiveness for proteins or biomolecules should not be neglected. Additionally, often only a single parameter is investigated which makes it difficult to issue a final, general statement.

The complexity of understanding the impact of nanomaterials on cell physiology can be reduced using a data presentation where results from different experiments are combined to one multi-parametric analysis plot. The idea was to create *interaction profiles* to conclude on the impact of a certain nanomaterial on one cell type [591].

Here, the interaction profile summarizes the impact of silica microparticles on different cell-related parameters, which were obtained by different individual experiments or by a sequence of impedimetric assays (**chapter 6.4.4)**.

The interaction profile consists of four different parameters including the

(i) **Toxicity** (Tox_{norm})
(ii) **Cell Migration** (WHE_{norm})
(iii) **Cell Proliferation** ($Prolif_{norm}$)
(iv) **Gap Junctional Intercellular Communication** ($GJIC_{norm}$)

These four cell-related parameters were addressed in this chapter to study the impact of silica particles on the physiology of NRK cells. It is not the aim to create new approaches for data analysis for the different assays but rather combine the obtained results within one profile. The toxicity was evaluated based on the $|Z|_{norm}$-value at the end of experiment after 24 h of particle exposure and was compared to the value of the control population (**chapter 6.4.4.1**). The migration of cells was already quantified in **chapter 6.4.4.3** by the wound healing efficiency 4 h after applying the wounding pulse (WHE_{4h}). This parameter was determined based on the time-course of $|Z|_{norm}$ at 32 kHz. Cell proliferation in absence or presence of silica particles was evaluated by the time-point of half maximum capacitance decrease ($t_{1/2}$) at 32 kHz which corresponds to 50 % electrode coverage with cells (**chapter 6.4.6**). The final application of the opto-electrical assay to investigate the impact of silica

microparticles on the dye transfer ability of NRK cells, data were quantified by calculating the AUC value (**chapter 6.4.7.2**). These parameters were normalized by the following equations:

$$\mathrm{Tox_{norm}} = \left(\frac{|\mathrm{Z}|_{24\,\mathrm{h}}(\mathrm{SiO_2})}{|\mathrm{Z}|_{24\,\mathrm{h}}(\mathrm{Control})} \right)^{-1} \quad \textbf{Eq. 6.5}$$

$$\mathrm{WHE_{norm}} = \left(\frac{\mathrm{WHE}_{4h}(\mathrm{SiO_2})}{\mathrm{WHE}_{4h}(\mathrm{Control})} \right)^{-1} \quad \textbf{Eq. 6.6}$$

$$\mathrm{Prolif_{norm}} = \frac{\mathrm{t}_{1/2}(\mathrm{SiO_2})}{\mathrm{t}_{1/2}(\mathrm{Control})} \quad \textbf{Eq. 6.7}$$

$$\mathrm{GJIC_{norm}} = \left(\frac{\mathrm{AUC}\ (\mathrm{SiO_2})}{\mathrm{AUC}\ (\mathrm{Control})} \right)^{-1} \quad \textbf{Eq. 6.8}$$

It is the idea of this interaction profile to create a graphic in the style of a shooting target. When a (nano-) material does not provide any impact on cell physiology the different parameters are located in the bull's eye. In contrast, harmful particles which show a significant impact on a single or on multiple parameters are located in the outer part. Therefore, values > 1 indicate a negative influence on cell physiology whereas values ≤ 1 characterize a positive or no impact of the particles. The studies presented in this thesis are summarized in the interaction profile in **Fig. 6.61**.

Based on **Fig. 6.21 A** no significant influence on $|Z|_{norm}$ at 4 kHz after 24 h of exposure to different concentrations of silica particles was found. In **Fig. 6.61**, only the impact of silica particles with a concentration of $3.7 \cdot 10^7$ P/cm^2 was analyzed in more detail. NRK cells in presence of the particles even provided a slightly enhanced impedance signal. This resulted in $Tox_{norm} < 1$ located in the green-highlighted part of the graph. In the following experiment the impact of silica particles on cell migration was investigated. During this study the WHE_{4h} was calculated to compare different experiments. Based on the column bars in **Fig. 6.24 B** the wound healing efficiency was not impaired by the presence of silica particles and no influence on cell migration was detected. This resulted in a WHE_{norm}-value of 0.99 for silica particles applied in a concentration of $3.7 \cdot 10^7$ P/cm^2. Furthermore, the impact of microparticles on the proliferation of NRK cells was analyzed. The results of two different experiments are shown in **Tab. 6.5**. The mean value of these two experiments for NRK cells and cells in presence of silica particles did not provide any impact on cell proliferation represented by a $Prolif_{norm}$-value of 1.04. Finally, the impact of silica particles on gap junctional intercellular communication between NRK cells was analyzed using the opto-

electrical assay. Image analysis of the obtained microscopic data only provided a slightly decreased AUC_{ref} value for cells in presence of silica particles compared to control cells. Therefore, the parameter $GJIC_{norm}$ for silica particles is located in the adjacent orange-red part of the interaction profile with a value of 1.11. For the interpretation of this parameter the $GJIC_{norm}$-value for cells in presence of 50 µM of the gap junctional intercellular communication inhibitor 2-APB is included in **Fig. 6.61**. It is located in the outer, dark red-highlighted part of the circle.

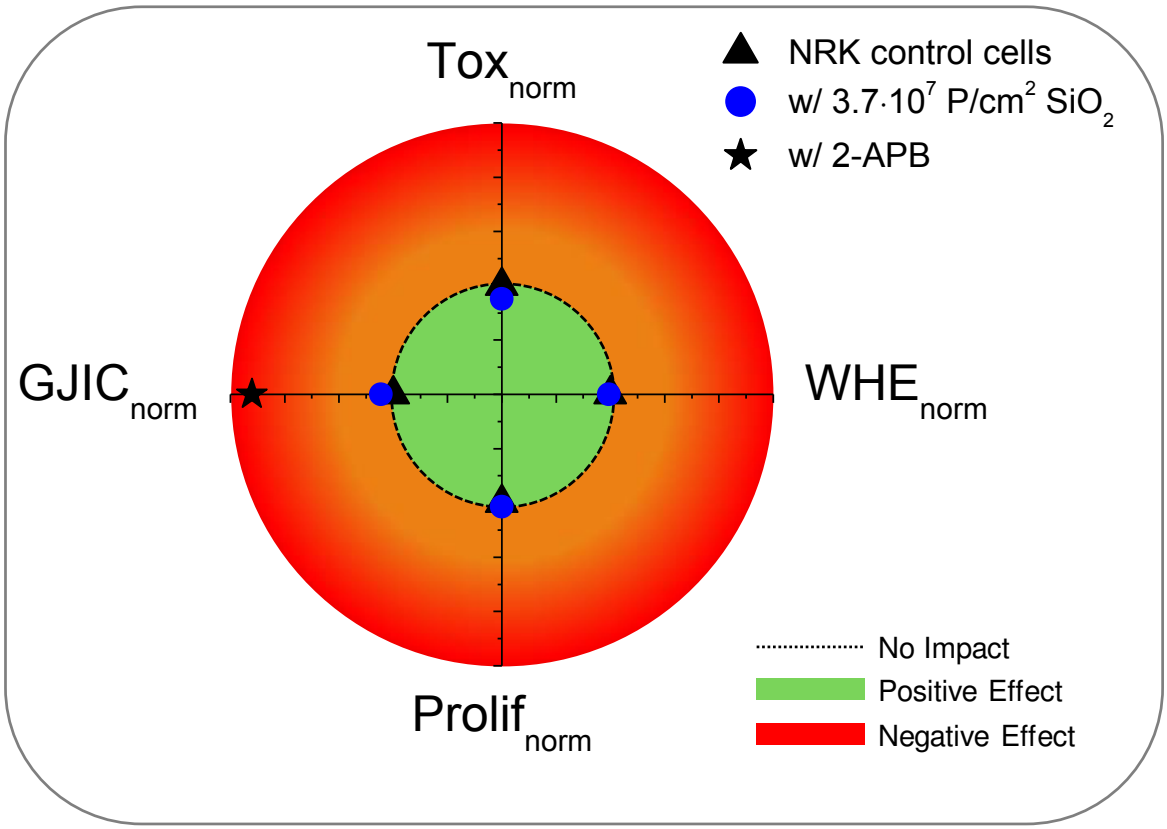

Fig. 6.61: Scheme of an interaction profile that summarizes the interaction between 2 µm silica microparticles and NRK cells as derived from different impedimetric and opto-electrical assays that were performed in individual or sequential experiments. The interaction card can be expanded using the same material in different concentrations, or by investigating other particle material.

The interaction profile provides an excellent visual summary of the presented data, indicating no influence of silica particles on the physiology of NRK cells. Of course the parameters which are included in the interaction profile can be adjusted to the respective experimental conditions and expanded by further cell-related parameters. For this study, it would be interesting to integrate also other concentrations of silica particles or results which were obtained by label-based assays. Moreover, cell motility which was determined by RTC measurements could be included and also the impact of silica particles on other cell types like cardiomyocytes.

Interaction profiles allow an estimation of risks and opportunities for different particles by combining the bio responses obtained by different assays. It facilitates the identification of correlations and dependencies between different cell-related parameters which are not uncovered by single experiments. This may help for a better understanding of the cellular interaction with biomaterials and is crucial for further development of new nanomaterials as well as for their application especially in the field of biomedicine and diagnostic.

6.7 Summary

The goal of this study was to provide a multimodal, label-free analysis of the NRK cell response to the exposure to silica particles. The research was not only limited to changes in cell viability, which is the most intensely studied parameter in literature, but provides a summary of the impact of silica particles on different cell-related parameters. The presented studies are based on different modes of the well-established ECIS technique using NRK cells as biological recognition element.

The uptake of silica particles into the cytoplasm was investigated microscopically indicating an intracellular localization of membrane-coated particles around the nucleus. The exposure of cells to silica particles in varying concentrations and incubation times did not provide any indication of cytotoxic effects. Moreover, the analysis of NRK cell micromotion, a sensitive parameter for the metabolic activity of cells, did not show any significant differences in absence or presence of particles. The final assay of the three-step ECIS experiment sequence focused on the ability of NRK cells pre-loaded with silica microparticles to migrate into an electrically-created wound. The assay returned no influence on the wound healing efficiency independent of the presence of microparticles. Time-resolved ECIS measurements showed no difference in the time-course of proliferation in absence or presence of silica particles and confluent cell layers were formed within a similar time-scale. The in-depth analysis was completed by an analysis of the influence of internalized particles on gap junctional intercellular communication using an impedance-based opto-electrical assay. For this purpose NRK cells, grown on gold-film electrodes were loaded with the gap junction permeable dye Lucifer Yellow by *in situ* electroporation. Dye transfer to NRK cells in the periphery of the electrode was insignificantly different in presence and absence of silica particles.

Within this work RTC measurements based on the ECIS principle were performed after establishment of a confluent Cor.At® cell layer on gold-film electrodes. For both electrode layouts (8W4E-micro, 8W4E-GJ) 4 kHz turned out to be the most sensitive frequency to record the periodic beating of the cardiomyocytes based on the parameter $|Z|$. Further manipulations of the beating efficiency by removing Ca^{2+}, by adding Isoproterenol hydrochloride or the gap junction inhibitor 1-heptanol showed the applicability of high resolution ECIS experiments to detect beating of cardiomyocytes. Within 24 h of exposure to silica microparticles no significant changes of Cor.At® beating was found, indicating no influence of the particles on gap junctional intercellular communication between Cx43-connected cardiomyocytes.

This thesis may serve as a model study on the information content of multimodal impedance-based assays to assess the biological response to particles and can be used as a basis for future investigations addressing different nanomaterials.

6.8 Outlook

The sequential performance of impedimetric assays guarantees a comprehensive analysis of the cell response to the addition of any test compound. Here, we used commercially available silica microparticles, however, the same sequential analysis can be performed for any material or formulation in the future. The impact of particles on mammalian cells strongly depends on the cell type used as recognition element in the cell-based analysis. In this study, normal rat kidney cells were used, but future studies can include investigations with other cell types originating from tissues which are supposed to be in contact with high particle concentrations. When thinking about nanoparticles resulting from the environment like air pollution, the respiratory tract and the lung will receive higher concentrations followed by other organs like brain, liver or heart. In the presented study, ECIS measurements were performed using a 2D NRK cell layer as sensing device, providing an indication about the response of the kidney within the living organism. But a 2D response is not necessarily correlated with similar cell responses in 3D.

Future studies addressing the impact of silica microparticles can include the analysis of cell proliferation by flow cytometry. DNA analysis can be performed using static or dynamic approaches, where the first is the simplest way to determine the DNA content and the latter provides more information about the G1- and G2/M-phase. The results of the flow cytometry experiment can be used to calculate the time period of each phase within the cell cycle and further characterize differences between cell proliferation in absence or presence of silica particles with respect to the doubling time. Moreover, gap junctional intercellular communication can be investigated as a function of particle concentration or particle size using the commercially available silica particles. In future applications also nanomaterials can be investigated which might require an adjustment of the gap junction permeable dye when fluorescently-labeled particles are used and interfere with the readout. However, there is a huge variety of dyes which can be applied to investigate the dye transfer between gap junction-connected cells which differ in their excitation and emission properties. Of course, other cell lines can be used to achieve information about the impact on other tissues, but cells should be evaluated due to their ability to communicate via gap junctions and which might require optimization of the *in situ* electroporation protocol. The analysis of gap junctional intercellular communication between cardiomyocytes using the opto-electrical assay can be an interesting approach. However, optimization of the protocol is impeded by the limited number of non-proliferating Cor.At® cells as well as for reasons of economy and could not be successfully established within this thesis. In future experiments, the beating periodicity of Cor.At® cells in presence of silica particles could be investigated as a function of particle concentration and diameter.

7 Summary

This thesis provides a model study on the information content of multimodal impedance-based assays to assess the impact of microscale particles on cell physiology of mammalian cells. In three main chapters, different approaches to this topic are presented and discussed:

The first chapter focused on the simulation of several scenarios within cell-based assays. These simulations are all based on the so-called ECIS model, originally introduced by Giaever and Keese (1991), describing the impedance contribution of cell-covered gold-film electrodes. This theoretical part of the thesis should help to support the interpretation of impedance data. First, opening and closing of cell junctions (R_b) for different types of barrier-forming cell layers were simulated and the accompanying changes in the complex impedance were extracted at various frequencies. The simulation data for some model epithelial and endothelial cell types showed that the relationship between resistance and barrier tightness may undergo inversion for frequencies above the cell-type specific threshold. Moreover, the influence of incomplete electrode coverage or inhomogeneity within the cell layer was studied systematically. For all experiments a good correlation between the simulated data and the experimental support was found.

The aim of the second project was to establish a new opto-electrical assay to investigate the dye transfer via gap junctions into neighboring cells. The principle of this new assay was based on loading a selected cell population with Lucifer Yellow by *in situ* electroporation. The cell-type specific adjustment of the ac pulse parameters for a temporary permeabilization of the plasma membrane improved the incorporation of Lucifer Yellow into the cytoplasm without affecting NRK cell viability. The assay also required the optimization of the gold-film electrode layout which enabled the application of the ac pulses, the non-invasive impedance recordings before and after pulse application and the microscopic analysis of dye transfer from cells on the electrode into adjacent cells. The final electrode layout (8W4E-GJ) contained four “semi-elliptical” electrodes which were separated by a photopolymer-free gap to facilitate microscopic analysis without any interference from the red autofluorescence of the photopolymer. The development of an appropriate experimental protocol yielded on electroporation in Ca^{2+}-free buffer and the application of two sequential ac pulses, as it was found to enhance the uptake efficiency into primary-loaded NRK cells. The opto-electrical assay was successfully applied to analyze the effect of the well-known gap junctional intercellular communication inhibitor 2-APB. The analysis of dye transfer via gap junctions was based on confocal fluorescence micrographs documenting dye transfer from the electrode into the photopolymer-free gap. The analysis was further improved by the application of the red-fluorescent TRITC dextran as co-electroporated reference dye, which

was trapped in the cytoplasm of primary-loaded cells due to its molecular size. The image analysis of the position-dependent intensities of both dyes (TRITC dextran and Lucifer Yellow) allowed a quantification of gap junctional intercellular communication.

The third chapter contains all sub-projects dealing with a multimodal and label-free analysis of the impact of micrometer-sized silica particles (Ø = 2 µm) on vitality, migration, proliferation and gap junctional intercellular communication of adherent NRK cells *in vitro*. A sequence of different impedimetric assays, all based on the well-established ECIS-technique, was applied for the analysis of particle impact on cell physiology. Microscopic studies addressing the particle uptake revealed the presence of membrane-coated particles in the cytoplasm of NRK cells. Further evidence for particle uptake was gathered from ToF-SIMS analysis that showed a densely-packed particle distribution around the cell nucleus in cells with intact plasma membranes. Time-resolved ECIS measurements revealed no acute cytotoxicity of silica particles as well as no influence on cell migration. Furthermore, the influence of silica particles on NRK proliferation was studied impedimetrically. No differences in the time-course of proliferation were found for particle-loaded or control cells. To study the influence of internalized particles on gap junctional intercellular communication the new opto-electrical assay was applied. Dye transfer to NRK cells in the periphery of the electrode was insignificantly different in absence and presence of silica particles. The results were supported by classical techniques, like FRAP analysis, scrape loading or parachute assay. Superior to other assays, the developed opto-electrical assay allowed for analysis of cell adhesion and cellular response to the presence of particle during an exposure time of 24 h prior to the dye transfer study. This enables the investigation of the impact of internalized particles on different cell-related parameters like viability, motility and gap junctional intercellular communication within one cell population.

8 Zusammenfassung

Die vorliegende Arbeit ist eine Modellstudie, die unter Einsatz multimodaler, labelfreier impedanz-basierter Sensorik eine sequentielle Analyse des Einflusses von Mikropartikeln auf die Zellphysiologie von adhärenten Zellen ermöglicht. Die Studie gliedert sich in drei verschiedene Projekte.

Im ersten Kapitel wurden Impedanzspektren unter Zuhilfenahme des bekannten ECIS Modells von Giaever und Keese (1991) für verschiedenste experimentelle Szenarien berechnet. Dies beinhaltete zum einen die Simulation einer konfluenten Zellschicht hinsichtlich der Fähigkeit, eine starke Zellbarriere auszubilden. Die Analyse der Impedanz- und Widerstandsspektren für eine Zellpopulation mit unterschiedlich starken Zell-Zell Kontakten (R_b) zeigte ein frequenzabhängiges Verhalten des Widerstandes. Dadurch wird bei einer Analyse des Widerstandes bei Frequenzen oberhalb einer zelltyp-spezifischen kritischen Frequenz eine Zerstörung der Zell-Zell Kontakte gegen die Intuition durch einen Anstieg des Widerstandes angezeigt. Die präsentierten Simulationsergebnisse sollten helfen, Fehlinterpretationen vorzubeugen und die Analyse von ECIS Daten zu erleichtern. Im Folgenden wurde die Zellschicht, die im ECIS Model als homogene, konfluente Zellpopulation angenommen wird, gezielt verändert indem schrittweise die Inhomogenität innerhalb einer Population erhöht wurde. Dabei wurde systematisch analysiert, welchen Einfluss kleine zellfreie Bereiche oder Veränderungen innerhalb einer Population auf die komplexe Impedanz ausüben. Dies erfolgte durch Variation des Bedeckungsgrades der Elektrode mit Zellen, durch Etablierung einer Co-Population auf der Elektrode und der Veränderung von deren Membraneigenschaften oder von Zell-Zell-Kontakten.

Der zweite Teil der Arbeit beschäftigte sich mit der Entwicklung eines neuen opto-elektrischen Assays zur Untersuchung der *Gap Junction*-vermittelten Zell-Zell-Kommunikation (GJIC). Die Primärbeladung einer definierten Zellpopulation mit Lucifer Yellow basierte dabei auf dem Prinzip der *in situ* Elektroporation. Dazu wurden konfluente NRK Zellschichten auf Goldfilm-Elektroden etabliert und mittels optimierter Spannungspulse eine kurzzeitige Permeabilität der Zellmembran erzeugt. Dies ermöglichte den Eintrag von Lucifer Yellow in das Zytoplasma von NRK Zellen auf der Elektrode. Die Analyse der GJIC erfolgte mittels fluoreszenz-mikroskopischer Bilder anhand der Farbstoffweitergabe von Lucifer Yellow in benachbarte Zellen. Die Entwicklung des opto-elektrischen Assays erforderte eine Anpassung der Elektrodenstruktur. Das optimierte Layout bestand aus vier „halbelliptischen“ Goldelektroden, die durch einen Photopolymer-freien Spalt voneinander getrennt waren, der für die mikroskopische Analyse der GJIC herangezogen wurde. Das Elektrodenlayout dient dabei als Wachstumssubstrat für die Zellen, ermöglicht die

Applikation von invasiven AC Pulsen, sowie eine nicht-invasive Impedanzanalyse vor und nach Pulsapplikation basierend auf dem ECIS Prinzip. Während der Entwicklung eines geeigneten Protokolls zur Durchführung des Assays zeigte sich, dass durch die Applikation von zwei aufeinander folgenden AC Pulsen die Primärbeladung mit Lucifer Yellow deutlich erhöht werden konnte. Die Analyse der mikroskopischen Bilder wurde durch den Einsatz des rot fluoreszierenden TRITC Dextrans als ko-elektroporierten Referenzfarbstoff erleichtert, der aufgrund seiner molekularen Größe ausschließlich im Zytoplasma der primär beladenen Zellen verbleibt. Mit Hilfe des opto-elektrische Assays konnte die Inhibierung der Farbstoffweitergabe von Lucifer Yellow in benachbarte NRK Zellen in Gegenwart des literaturkannten Hemmstoffes 2-APB erfolgreich nachzuweisen werden.

Das Ziel des dritten Projekts dieser Arbeit war, neben einer klassischen Untersuchung der durch Silikapartikel (∅ = 2 µm) ausgelösten Zytotoxizität, auch deren Einfluss auf ausgesuchte, zellbiologische Fundamentalprozesse wie die Zellmigration, die Proliferation und die GJIC zu charakterisieren. Eine Beeinflussung dieser Grundprozesse würde eine Zelle nicht unmittelbar töten, sehr wohl aber ihre biologische Funktionalität erheblich einschränken und dennoch bei einer reinen Zytotoxizitätsbetrachtung der Beobachtung entgehen. Zur Korrelation der durch die Partikel ausgelösten Veränderungen von Migration, Proliferation und Kommunikation mit der intrazellulären Partikelkonzentration wurde zudem die Partikelaufnahme in die Zellen untersucht und charakterisiert. Die Partikelaufnahme in das Zytoplasma von NRK Zellen wurde mittels lichtmikroskopischer Techniken unter Einsatz klassischer zytochemischer Anfärbe Methoden adressiert. Eine intrazelluläre Lokalisation von Silikapartikeln wurde zusätzlich durch abbildende 3D Massenspektrometrie (ToF-SIMS), TEM- und REM-Studien ermöglicht. Nachdem weder nach einer Expositionszeit von 24 h noch bei Langzeitstudien über 72 h ein Hinweis auf zytotoxische Eigenschaften gefunden wurde, wurde der Einfluss von Silikapartikeln auf weitere zellphysiologische Parameter untersucht. Zellmigration und Proliferation von NRK Zellen wurden unter Verwendung label-freier impedimetrischer Untersuchungsmethoden zeitaufgelöst analysiert. Dabei zeigte sich kein Einfluss der internalisierten Partikel auf die Wundheilungseffizienz von NRK Zellen. Die Etablierung einer konfluenten Zellschicht erfolgte mit gleichen Proliferationskinetiken für NRK Kontrollpopulationen und Zellen in Anwesenheit der Partikel. Um den Einfluss internalisierter Partikel auf die GJIC unter den gleichen experimentellen Bedingungen erfassen zu können, wurde der in Teil 2 entwickelte opto-elektrische Assay erfolgreich eingesetzt und mit vorangehenden, nicht invasiven Untersuchungen hinsichtlich der akuten Toxizität oder Motilität kombiniert. Die Quantifizierung des Farbstofftransports in benachbarte Zellen ergab keine signifikante Änderung der GJIC zwischen NRK Zellen unabhängig von der An- und Abwesenheit von Partikeln. Dieser Befund wurde zusätzlich mit klassischen Methoden, die zur Untersuchung von Zell-Zell-Kommunikation gerne eingesetzt werden, bestätigt.

9 Appendix

9.1 Abbreviations and Symbols

A

A	area; parameter included in CPE
α	ECIS model: parameter for cell-electrode junction
ac	alternating current
ATCC	American Type Culture Collection

B

BSA	*bovine serum albumin*
BPM	beats per minutes

C

C	capacitance
°C	degree Celsius
C_m	ECIS model: specific membrane capacitance
CaAM	*calcein acetoxymethylester*
CE	counter electrode
CICR	calcium-induced calcium release
CLSM	confocal laser scanning microscope
CPE	constant phase element

D

d	diameter
d_h	hydrodynamic diameter
DAPI	*4', 6-diamidino-2-phenylindole*
DM	dichroidic mirror
dc	direct current
DMA	*dimethyl amiloride*
DMEM	Dulbecco's Modified Eagle's Medium
DMSO	*dimethylsulfoxide*
DNA	*desoxyribonucleic acid*
DiI	*1,1'-dioctadecyl-3,3,3',3'-tetramethylindocarboxycyanine*
DSMZ	Deutsche Sammlung von Mikroorganismen und Zellkulturen GmbH

E

E	electric field
EBSS^{++}	Earle's balanced salt solution
EBSS^{-+}	Earle's balanced salt solution (w/o Ca^{2+}, w/ Mg^{2+})
EBSS^{--}	Earle's balanced salt solution (w/o Ca^{2+}, w/o Mg^{2+})
ECIS	Electric Cell-Substrate Impedance Sensing
EDTA	*ethylenediaminetetraacetic acid*
e.g.	for example (Lat.: exempli gratia)
EGTA	*ethylene glycol-bis(2-aminoethyl-ether)-N,N,N',N' tetraacetic acid)*
em.	emission
et al.	and others (Lat.: et alii)
EthD-1	*ethidium homodimer*
EYFP	enhanced yellow fluorescent protein
ex.	excitation

F

f	frequency, shape factor
FCS	*fetal calf serum*
FG	frequency generator
FET	field-effect transistor
Fig.	figure
FITC	*fluorescein isothiocyanate*

G

g	factor in electroporation
GFP	green fluorescent protein

H

h	ECIS model: cell-electrode distance

I

I	current
I_D	drain current
I_{ph}	photo current

i	imaginary factor
Im	imaginary fraction of a complex quantity
IS	impedance spectroscopy
ISFET	ion selective field-effect transistor
ITO	*indium tin oxide*

K

k	time constant

L

L	inductance
LAPS	light addressable potentiometric sensor
LED	light-emitting diode

M

M	normal to the membrane surface
M_w	molecular weight
MDCK II	Madin-Darby canine kidney strain II
MFT	Multi-Frequency/Time
mRNA	*messenger ribonucleic acid*

N

N	number of experiments
n	CPE parameter
NADH	*nicotineamid adenine dinucleotid* (reduced form)
NRK	normal rat kidney

P

PBS^{--}	phosphate buffered saline (without Ca^{2+} and Mg^{2+})
PBS^{++}	phosphate buffered saline (with Ca^{2+} and Mg^{2+})
PC	personal computer
PC	*polycarbonate*
PDMS	*polydimethylsiloxane*
PET	*polyethylene terephthalate*
PFA	*paraformaldehyde*

PMT	photomultiplier tube
pp	*peak to peak*-value
P/cm^2	particle per cm^2
points/s	points per second (resolution of the RTC experiments)

Q

QCM	quartz crystal microbalance
QD	quantum dot

R

ρ	ECIS model: specific resistivity of the electrolyte in the gap
r_c	ECIS model: cell radius
R	resistance
R_b	ECIS model: specific barrier resistance
R_{bulk}	bulk resistance
r_h	hydrodynamic radius
Re	real fraction of a complex quantity
RE	reference electrode
RNA	*ribonucleic acid*
rms	*r*oot mean square
ROS	reactive oxygen species
RT	room temperature
RTC	Rapid Time Collect
rpm	rounds per minute
RWG	resonant waveguide grating

S

SAM	self-assembling monolayer
SCM	serum-containing medium
SD	standard deviation
SEM	scanning electron microscopy
SFM	serum-free medium
SFT	Single Frequency/Time

SPR	Surface Plasmon Resonance
	T
T	Temperature
t	time
Tab.	table
TER	transepithelial/ transendothelial electrical resistance
ToF-SIMS	Time of Flight Secondary Ion Mass Spectrometry
TRITC	*tetramethylrhodamin isothiocyanate*
	U
U	Unit
U	voltage
UV	ultraviolet
	V
VIS	visual
V_{bias}	dc bias voltage
V_{SD}	voltage between source and drain
	W
W	Warburg Impedance
WE	working electrode
	Z
ZO-1	zona occludens protein 1
Z	impedance
Z'	resistance: real fraction of the complex impedance
Z'', χ	reactance: imaginary fraction of the complex impedance
$\|Z\|$	impedance magnitude
Z_{CPE}	impedance of the cell-free electrode assuming a constant phase element
Z_n	impedance of the cell-free electrode
Z_m	total impedance of the apical and basolateral plasma membranes
$\|Z\|_{norm}$	normalized impedance magnitude

Other Abbreviations

8W1E	eight wells each containing one electrode
8W10E	eight wells each containing ten electrode
8W10E^{+}	eight wells each containing an interdigitated electrode structure
8W4E-micro	eight wells each containing four circular electrodes (used for electroporation)
8W4E-GJ	eight wells each containing four “semi-elliptical” electrodes (used for gap junctional intercellular communication analysis)

9.2 Supplementary Figures

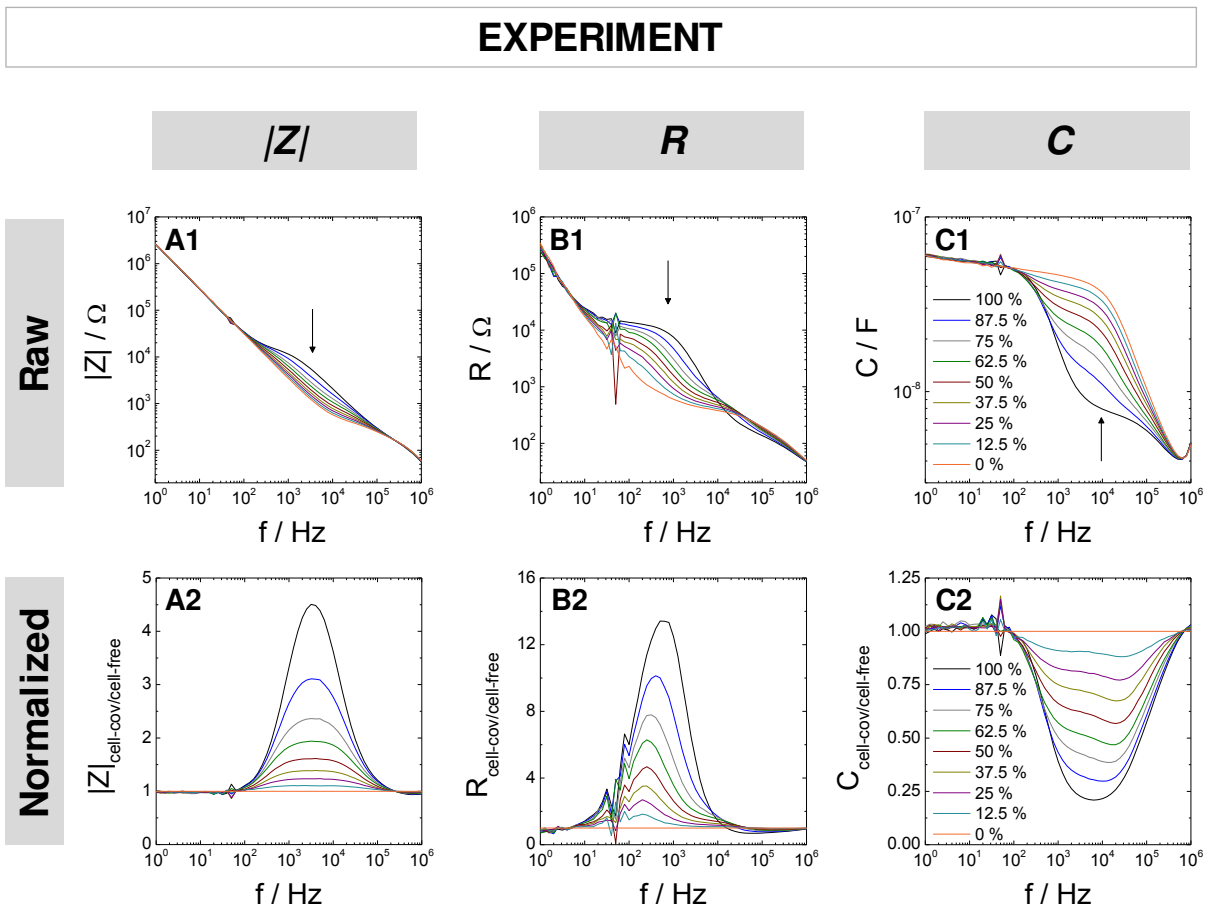

Fig. S 1: Survey of experimental data addressing the influence of varying electrode coverage with MDCK II cells on |*Z*| (**A**), *R* (**B**) and *C* (**C**) using a 8W1E electrode layout surrounded by a PDMS chamber. Electrode were wounded sequentially by an invasive voltage pulse of 40 kHz, 5 V and 1.25 ms. After each wounding step spectra were recorded in the modified "8 against CE" measurement mode. **1:** Frequency-dependent |*Z*| (**A1**), *R* (**B1**) and *C* (**C1**) spectra ($f = 1$ Hz – 10^6 Hz) recorded in the "8 against CE" measurement mode. **2:** Normalized |*Z*|, *R* and *C* spectra: $|Z|_{\text{cell-cov/cell-free}}$ (**A2**), $R_{\text{cell-cov/cell-free}}$ (**B2**), $C_{\text{cell-cov/cell-free}}$ (**C2**) were obtained by dividing values from the respective cell-covered electrodes by the corresponding cell-free values (■).

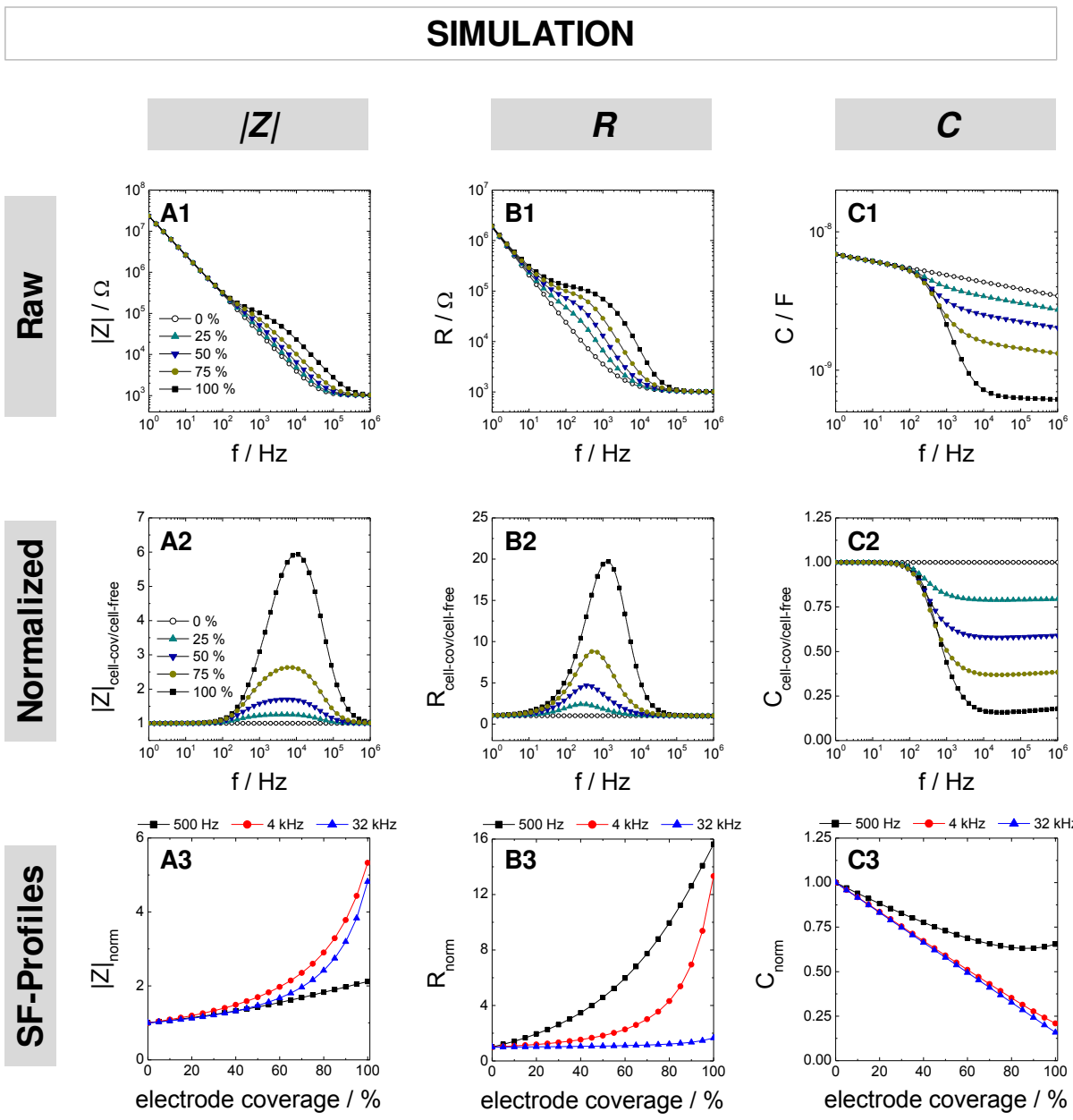

Fig. S 2: 1: Simulated frequency-dependent $|Z|$ (**A**), R (**B**) and C spectra (**C**) (f = 1 Hz – 10^6 Hz) for cell-free (○) and differently cell-covered 8W1E electrode layout. The model cell layer was characterized by R_b = 25 Ωcm^2, α = 15 Ω$^{0.5}$cm, C_m = 3.0 µF/cm^2 and the electrode parameters were used as described in **Tab. 4.1**. **2:** Normalized spectra were obtained by dividing values from cell-covered electrodes by the corresponding cell-free values. **3:** *Single frequency* (SF)-profiles of $|Z|_{norm}$, R_{norm} and C_{norm} at 500 Hz, 4 kHz and 32 kHz depending on the electrode coverage. Data were normalized by the values of a cell-free 8W1E electrode layout.

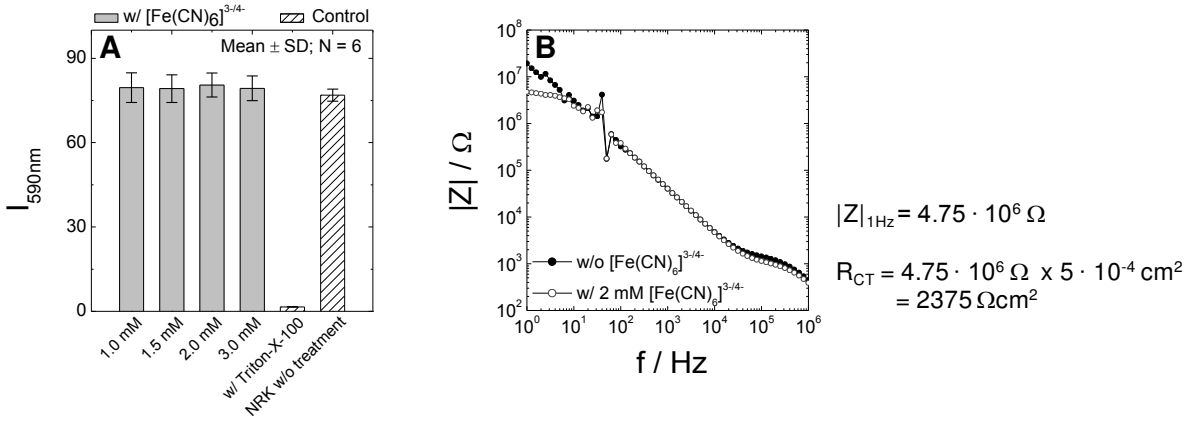

Fig. S 3: A: PrestoBlue® assay to investigate the cellular response of NRK cells to the addition of different concentrations of $[Fe(CN)_6]^{3-/4-}$ (1.0 mM – 3.0 mM). Dilutions were made in culture medium and cells were incubated in presence of the redox mediator for 24 h. Cells incubated in culture medium (negative) or after the addition of 0.5 % Triton-X-100 (positive) served as control. After 2 h of incubation at 37 °C in the dark, fluorescence was recorded at 590 nm using an excitation wavelength of 544 nm. **B:** Impedance spectra of a cell-free 8W1E gold-film electrode layout in medium (●) and in presence of 2 mM $[Fe(CN)_6]^{3-/4-}$(○). The corresponding R_{CT} was calculated based on $|Z|$ at 1 Hz and the corresponding electrode area to 2375 Ωcm^2.

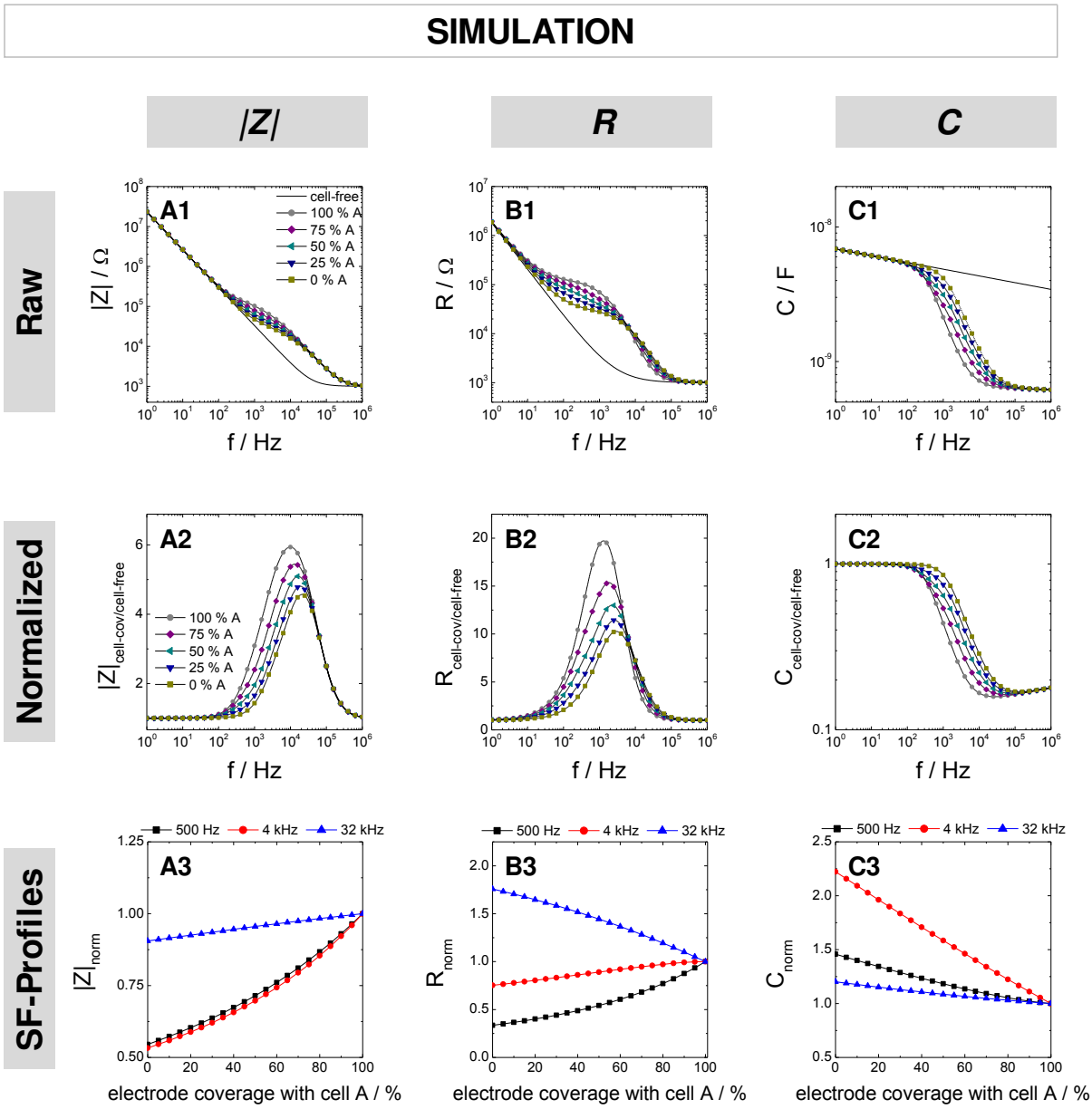

Fig. S 4: 1: Simulated frequency-dependent $|Z|$ (**A**), R (**B**) and C (**C**) spectra ($f = 1$ Hz – 10^6 Hz) for cell-free (line) and cell-covered 8W1E electrode layout. A confluent cell layer was assumed during the simulation where only the content of cell type A ($R_b = 25\ \Omega cm^2$, $\alpha = 15\ \Omega^{0.5}cm$, $C_m = 3\ \mu F/cm^2$) and type B ($R_b = 5\ \Omega cm^2$, $\alpha = 8\ \Omega^{0.5}cm$, $C_m = 3\ \mu F/cm^2$) was varied. The electrode parameters were used as described in **Tab. 4.1**. **2:** Normalized spectra were obtained by dividing values from differently cell-covered electrodes by the corresponding cell-free values. **3:** *Single frequency* (SF)-profiles of $|Z|_{norm}$, R_{norm} and C_{norm} at three 500 Hz, 4 kHz and 32 kHz depending on the electrode coverage. Data were normalized by the values of a confluent cell layer of type A using a 8W1E gold-film electrode layout.

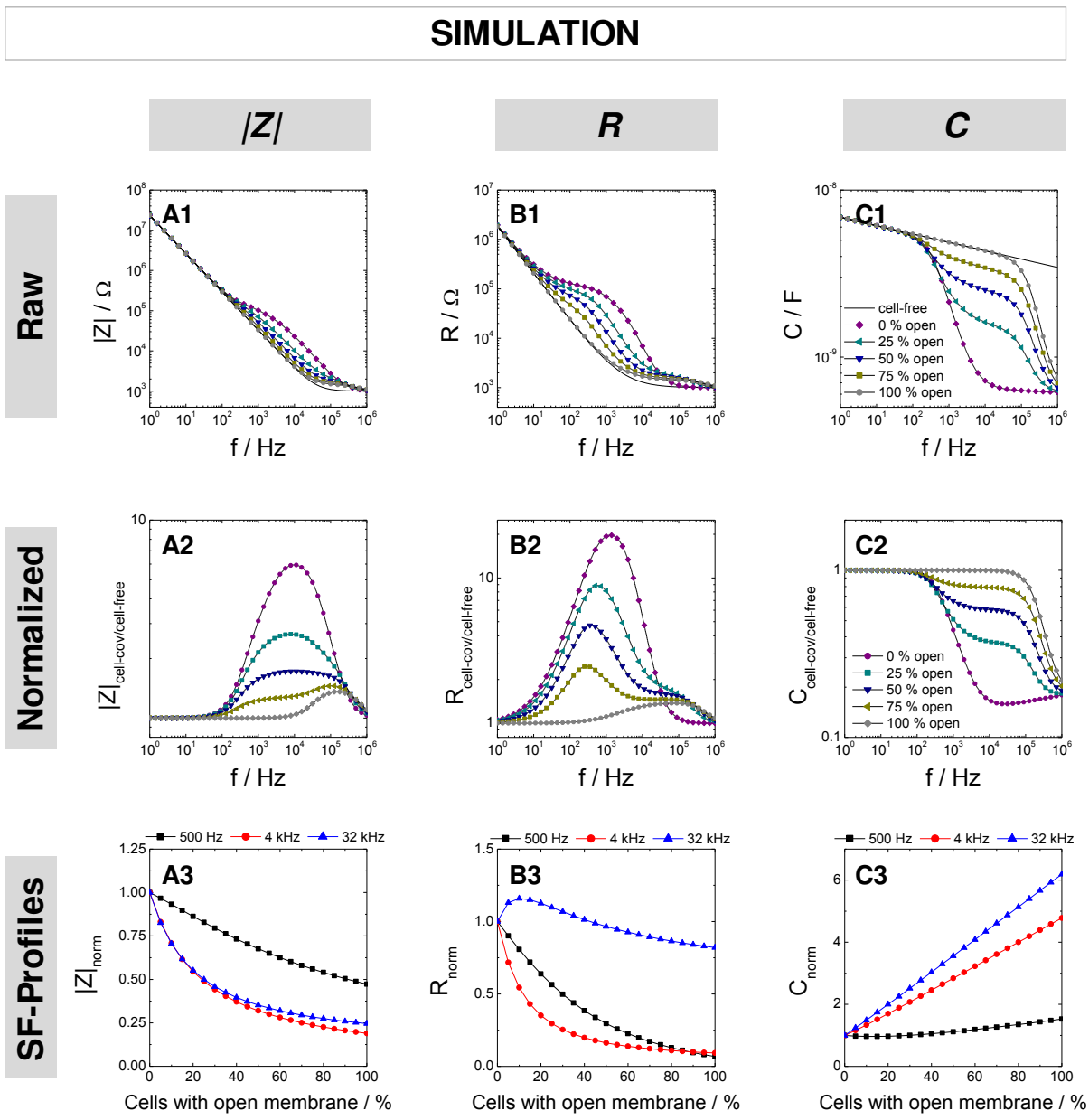

Fig. S 5: 1: Simulated frequency-dependent $|Z|$ (**A**), R (**B**) and C (**C**) spectra ($f = 1$ Hz – 10^6 Hz) for cell-free (line) and cell-covered 8W1E electrode layout. A confluent cell layer was assumed during the simulation and only the content of cells with permeabilized plasma membrane was varied (0 – 100 %). The electrode parameters were used as described in **Tab. 4.1**. **2:** Normalized spectra were obtained by dividing values from differently cell-covered electrodes by the corresponding cell-free values. **3:** *Single frequency* (SF)-profiles of $|Z|_{norm}$, R_{norm} and C_{norm} at 500 Hz, 4 kHz and 32 kHz depending on the electrode coverage. Data were normalized by the values of a confluent cell layer with intact plasma membrane grown on a 8W1E gold-film electrode layout.

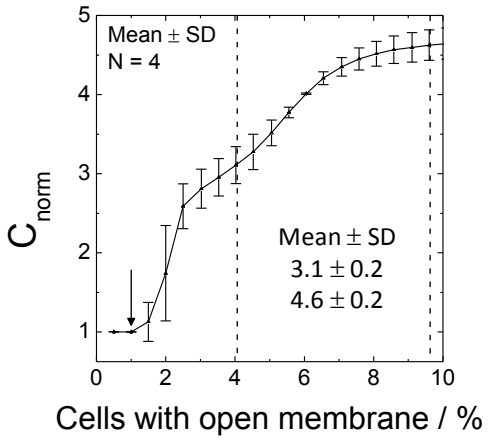

Fig. S 6: Time-course of C_{norm} at 32 kHz for MDCK II cells, grown on a 8W10E electrode layout before, during and after the addition of 0.02 % saponin. Time-point of addition is indicated by the arrow. Mean ± SD of four different wells taken from two different experiments is shown. A first increase to 3.1 ± 0.2 and a second increase to 4.6 ± 0.2 was observed.

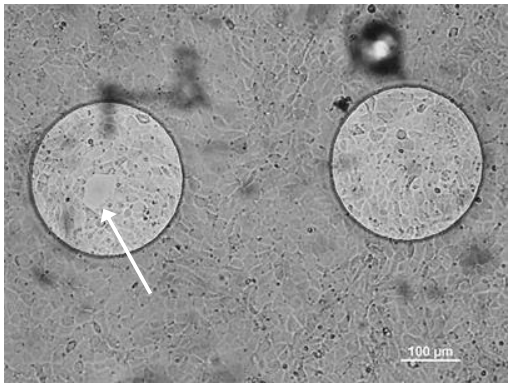

Fig. S 7: Phase contrast images of NRK cells after electroporation in presence of Lucifer Yellow (**H**) (T = 24 °C). The cell-free area, where cell-damages occurred during electroporation is indicated by the arrow. Scale bar represents 100 µm.

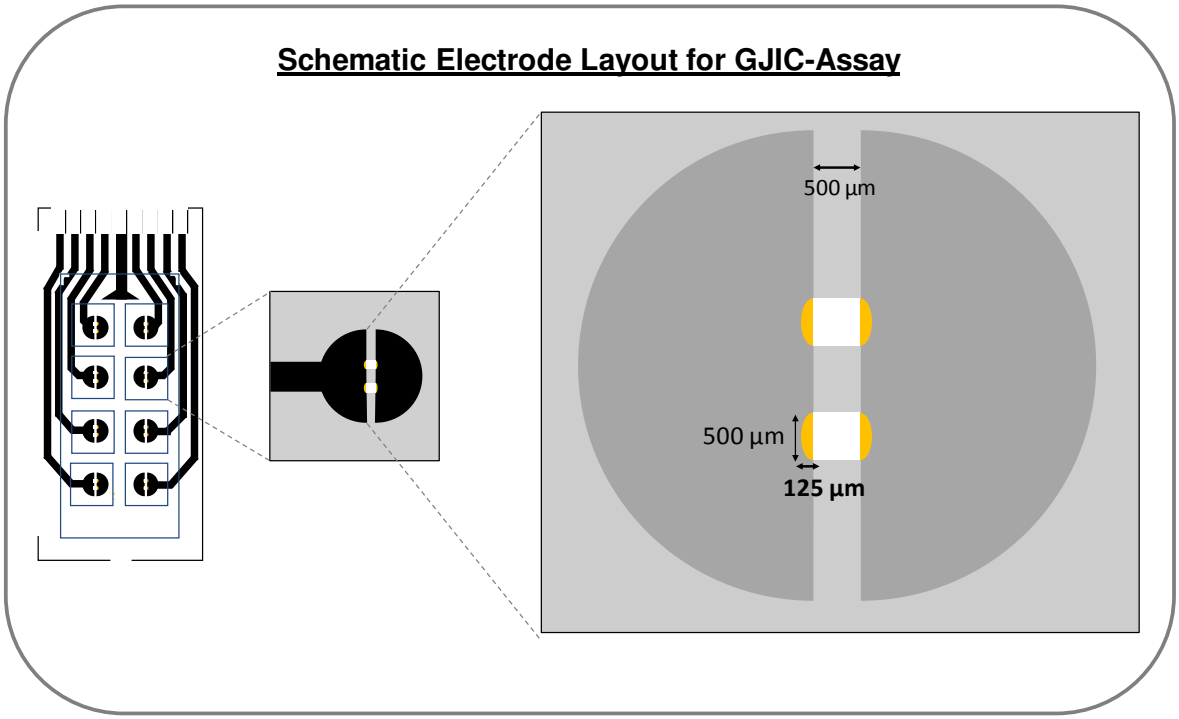

Fig. S 8: Designed electrode layout for the analysis of dye transfer through gap junctions.

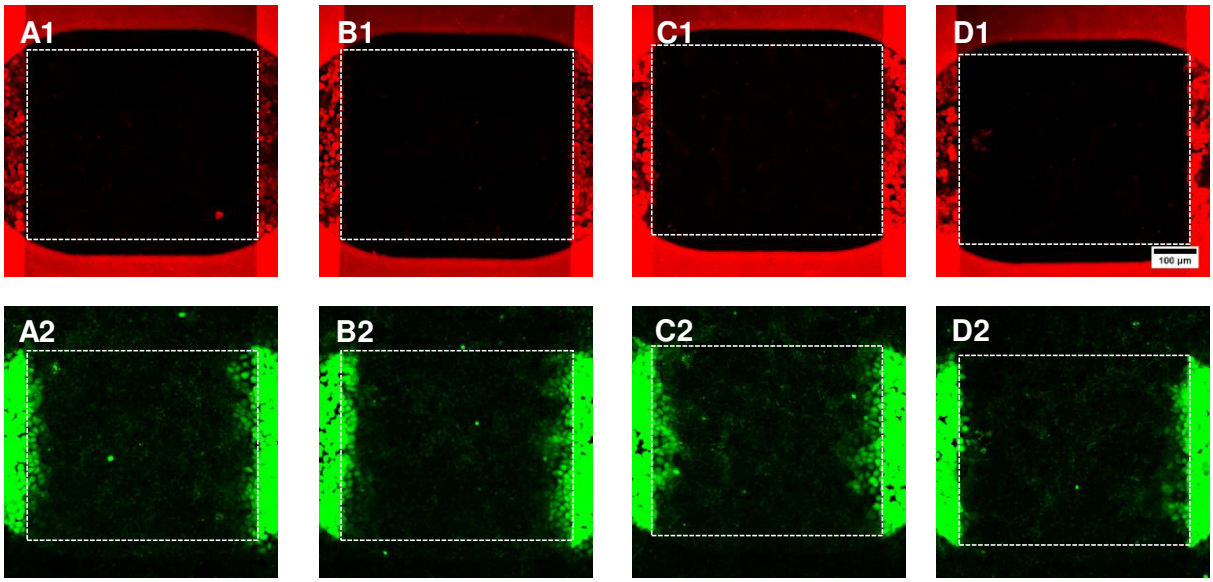

Fig. S 9: Fluorescence micrographs after single pulse (**A**) or two-pulse electroporation (**B-D**) of NRK cells grown on the 8W4E-GJ electrode layout in presence of TRITC dextran (**1**; **red**) and Lucifer Yellow (**2**; **green**) with varying distances of 10 min (**B**), 15 min (**C**) or 30 min (**D**). Dye transfer of Lucifer Yellow was analyzed in the photopolymer-free region between the two electrodes (**2**) whereas fluorescence intensity of TRITC dextran was limited to the position of the "semi-elliptical" electrode (**1**). Scale represents 100 µm.

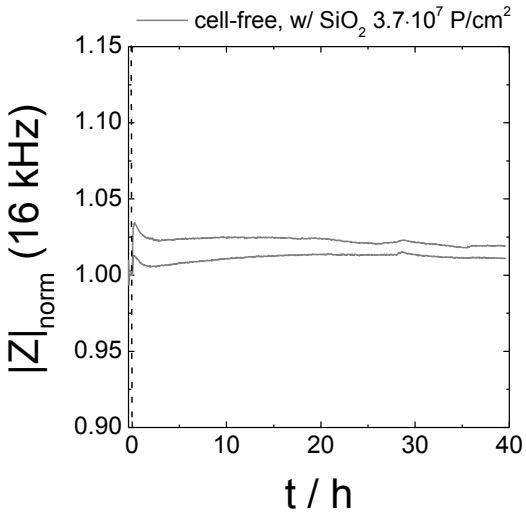

Fig. S 10: Time-course of normalized impedance |*Z*| at 16 kHz of a cell-free 8W1E electrode layout after the addition of silica particles (∅ 2 µm; $3 \cdot 10^7$ P/cm^2) over 40 h. The time-courses of two different wells are provided. Data were normalized to the respective value immediately before addition.

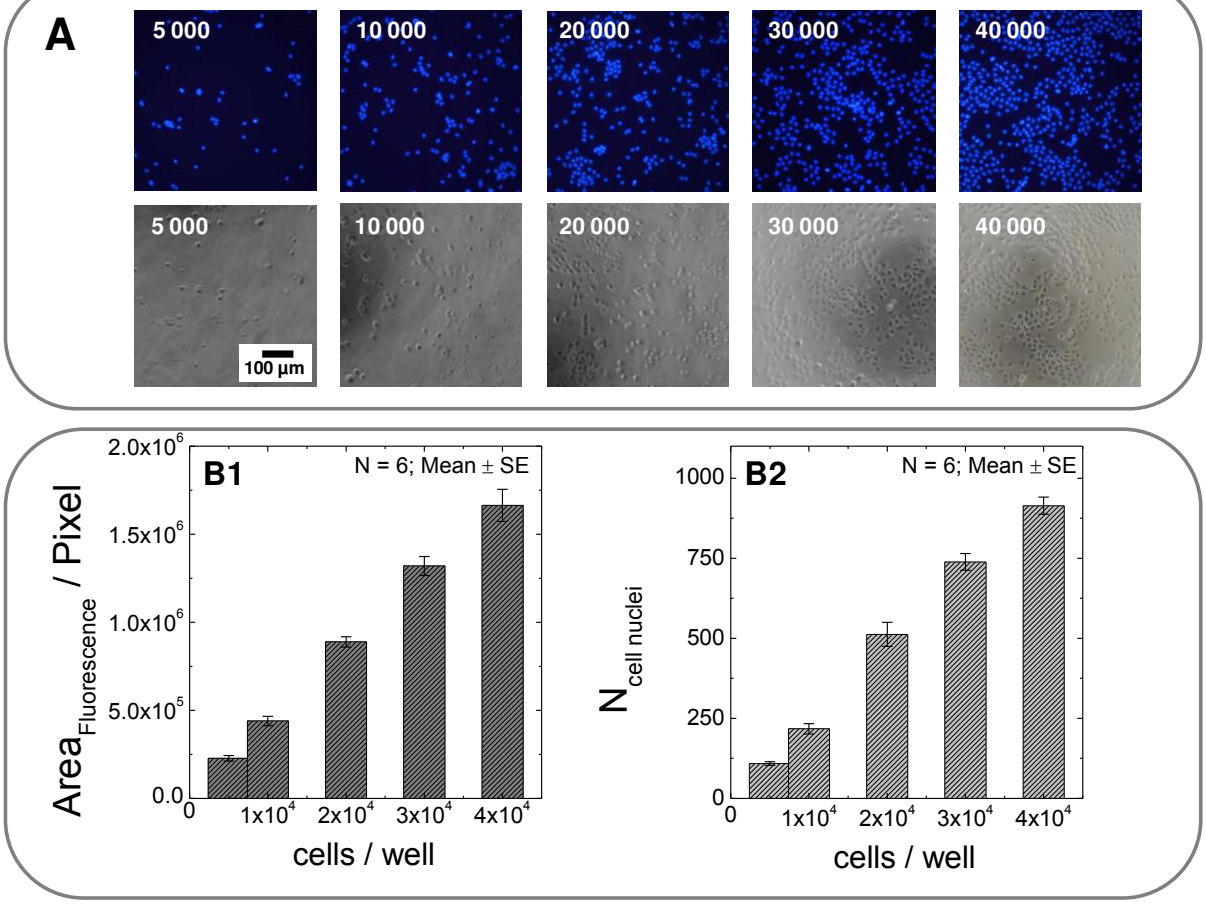

Fig. S 11: Calibration for the analysis of NRK cell proliferation after nuclei stain with DAPI. (**A**) Fluorescence micrographs and phase-contrast images of defined seeding densities of 5000 cells/well, 10 000 cells/well, 20 000 cells/well, 30 000 cells/well and 40 000 cells/well were used. (**B**) Analysis was performed using two different strategies (**1**) quantification of the fluorescence area or (**2**) counting of cell nuclei using ImageJ software.

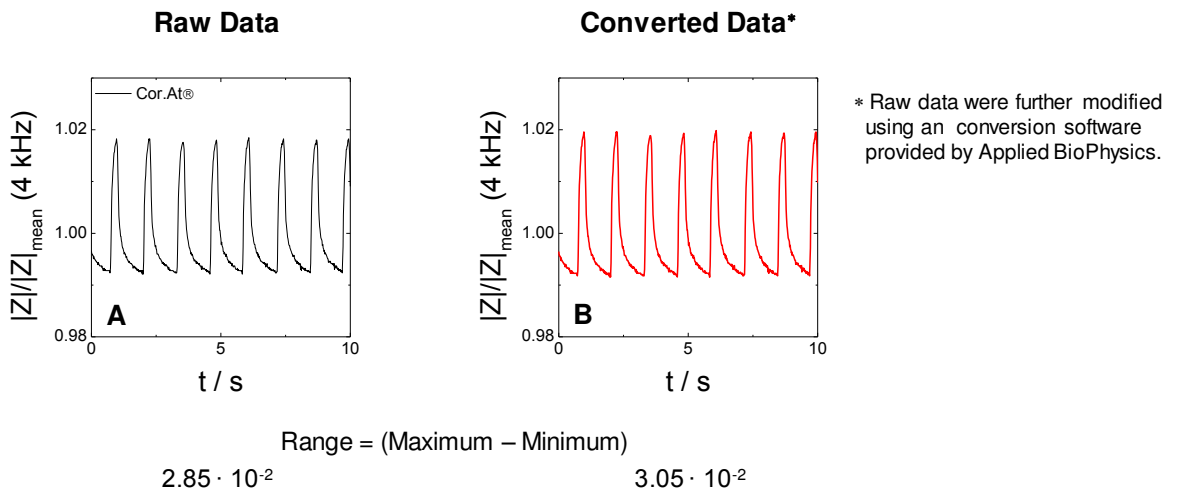

Fig. S 12: Comparison between raw data (**A**) and converted data (**B**). An instrumental, correction factor was required for some data set recorded with an earlier software version to convert the recorded impedance data. The software for data conversion was provided by Applied BioPhysics immediately before the thesis was submitted. The influence of data conversion is shown exemplarily for one data set with respect to beating profiles, beat amplitude and time-course of $|Z|/|Z|_{mean}$. Signal shapes and time-course for beating Cor.At® cells remained unaffected. Only a marginal increase in signal amplitude was observed. The calculated data range, which was determined by the maximum and minimum value of $|Z|/|Z|_{mean}$ provided a small increase from $2.85 \cdot 10^{-2}$ (raw data) to $3.05 \cdot 10^{-2}$ (converted data). Within the experimental part, raw data were used without any further conversion. Later versions of the software version required no further data conversion.

9.3 Materials and Instrumentations

A

Anti-occludin primary, monoclonal Antibody (invitrogen)

Anti-mouse secondary, polyclonal Alexa Fluor® 546 Antibody (invitrogen)

2-APB: *2-Aminoethyl diphenylborinate* (Sigma-Aldrich)

Argon Plasma Cleaner (Harrick Plasma)

Ascent Reader (Labsystems)

Autoclave (DX-45, Systec, Wettenberg)

B

Bleomycinsulfate (Sigma-Aldrich)

BSA: *bovine serum albumin* (Sigma-Aldrich)

Bunsen burner for cell culture (Fireboy Tecnomare, Fernwald)

Bürker hemocytometer (Marienfeld)

C

Calcein AM (Molecular Probes)

Calcium chloride (Sigma-Aldrich)

Cell culture dishes: Greiner bio-one (9.2 cm^2), Sarstedt (60.1 cm^2)

Cell culture flasks (12.5 cm^2) (25 cm^2) (75 cm^2)

Cell culture incubator (Thermo Fisher Scientific Inc.)

Cell culture medium: DMEM, MEM Eagle (Sigma-Aldrich, Biochrom)

Cell culture 6-well plates (Starstedt)

Cell culture 96-well plates (TPP, Greiner)

Centrifuge Heraeus Multifuge 1S-R for cell culture (Thermo Fisher Scientific)

Centrifuge tubes: 15 mL, 50 mL (Sarstedt, Greiner)

Cor.At® Cells (w/ or w/o GFP) (Axiogenesis)

Cor.At® Culture Medium (Axiogenesis)

Cryovials 1.8 mL (Nunc)

Cytochalasin D (Sigma-Aldrich)

D

DAPI: *4',6-diamidino-2-phenylindole* (Sigma-Aldrich)

DiI: *1,1'–dioctadecyl-3,3,3',3'- tetramethylindocarbocyanine* (Fluka Chemie)

Disposable pipettes: 1, 5, 10, 25 ml (Sarstedt)

DMA: *Dimethylamiloride* (Sigma-Aldrich)

DMSO: *dimethyl sulfoxide* (Roth)

E

$EBSS^{++}$ (Sigma-Aldrich)

$EBSS^{--}$ (Life Technologies)

ECIS 1600R or ECIS Zθ (Applied BioPhysics, Troy, NY, USA)

EDTA: *ethylenediaminetetraacetic acid* (Sigma-Aldrich)

Electrode arrays (commercially available): 8W1E, 8W10E, $8W10E^{+}$ (Applied BioPhysics Inc.)

Electrode arrays (custom-made): 8W4E-GJ, 8W4E-micro (Applied BioPhysics Inc.)

EthD-1: Ethidium Homodimer (Molecular Probes)

Eppendorf Centrifuge 5415R

Eppendorf® Combitips advanced pipette tips Biopur®: 2.5 mL, 5 mL, 10 mL

F

FCS: *fetal calf serum* (Biochrom)

$[Fe(CN)_6]^{3-/4}$: *hexacyanoferrate(III) and hexacyanoferrate(II)* (Merck)

Fibronectin from human plasma or bovine plasma (Sigma-Aldrich)

FITC dextran: *Fluorescein isothiocyanate* dextran with average mol wt 4 kDa, 10 kDa, 40 kDa, 70 kDa, 250 kDa, 500 kDa, 2 MDa (Sigma-Aldrich)

Frequency generator 33120 A (HP-Agilent)

G

GDA: Glutaraldehyde (Sigma-Aldrich)

D-Glucose (Merck)

L-Glutamine (Biochrome)

H

1-heptanol (Sigma-Aldrich)

I

Impedance analyzer SI-1260 (Solartron Instruments)

Isoproterenol hydrochloride (Sigma-Aldrich)

ITO-PET foil (Sigma-Aldrich, USA)

L

Laminar flow hood (HERAsafe®, Thermo Scientific, München)

Latex gloves (Roth)

Lucifer Yellow CH dipotassium salt (Sigma-Aldrich)

M

Magnesium chloride hexahydrate (Sigma-Aldrich)

Micro Centrifuge (Roth)

Microscopes: Nikon Diaphot and Nikon Eclipse 90i (Nikon)

Zeiss Axiovert 200M and Zeiss LSM510 (Zeiss)

O

1-octanol (Sigma-Aldrich)

Orbital shaker MaxQ 4450 (Thermo Scientific)

P

PBS^{--}/ PBS^{++} (Sigma-Aldrich)

PDMS: *Polydimethylsiloxan* (Dow Corning)

Penicillin/Streptomycin (Sigma-Aldrich)

PFA: *paraformaldehyde* (Sigma-Aldrich)

Phalloidin: Alexa Fluor® 488-Phalloidin (Invitrogen), TRITC-Phalloidin (Sigma-Aldrich)

Pipette Tips: 10 µL; 100 µL; 1000 µL (Sarstedt)

Polystyrene beads: 2 µm, amine-modified and carboxylate-modified (Sigma-Aldrich)

Porous filter membrane (Corning)

PrestoBlue® cell viability assay (Invitrogen)

Puromycin (Axiogenesis)

R

Reaction Tubes: 500 µL – 2 mL (Sarstedt, Greiner)

S

Saponin (Sigma-Aldrich)

Silica Particles: 2 µm Microparticles based on silicium dioxide (Sigma-Aldrich; Fluka)

Silicon Glue Aquadicht PROBAU (Bauhaus)

Sodium Azide (Merck KGaA, Darmstadt)

Sterile Filter: pore diameter 0.2 µm (TPP)

Sulfinpyrazone (Sigma-Aldrich)

T

ToF-SIMS Instrument: ION-TOF GmbH, Münster

TRITC dextran: *Tetramethylrhodamine isothiocyanate dextran* with with average mol wt 155 kDa (Sigma-Aldrich)

Triton-X-100 (Sigma-Aldrich)

0.05 %; 0.25 % (w/v) Trypsin (Sigma-Aldrich)

U

Ultrasonic Bath: Sonorex Digitech (Bandelin Electronics)

V

Vortex mixer (Heidolph)

W

Waterbath (TW12, Julabo, Seelbach)

Weighing Instrument (Mettler Toledo)

Z

Zetasizer Nano ZS (Malvern Instruments)

9.4 Software

Image J

ECIS Software (Applied BioPhysics, Inc.)

LabVIEW-based Software for the analysis of cardiomyocytes (J. Wegener)

LabVIEW-based Software for the simulation of impedance spectra (J. Wegener)

LabVIEW-based Software for the determination of the motility index (J. Wegener)

EZ-C1 3.90 FreeViewer (Nikon)

LSM Image Browser (Zeiss)

10 References

1. Wang, J. et al. DNA electrochemical biosensors for environmental monitoring. A review. *Analytica Chimica Acta* **347**, 1-8 (1997).
2. Baeumner, A.J. Biosensors for environmental pollutants and food contaminants. *Analytical and Bioanalytical Chemistry* **377**, 434-445 (2003).
3. Velasco-Garcia, M.N. & Mottram, T. Biosensor technology addressing agricultural problems. *Biosystems Engineering* **84**, 1-12 (2003).
4. Tudorache, M. & Bala, C. Biosensors based on screen-printing technology, and their applications in environmental and food analysis. *Analytical and Bioanalytical Chemistry* **388**, 565-578 (2007).
5. Higson, S. Biosensors for medical applications (Elsevier Science, 2012).
6. Vo-Dinh, T. & Cullum, B. Biosensors and biochips: advances in biological and medical diagnostics. *Fresenius' Journal of Analytical Chemistry* **366**, 540-551 (2000).
7. McGrath, T.F., Elliott, C.T. & Fodey, T.L. Biosensors for the analysis of microbiological and chemical contaminants in food. *Analytical and Bioanalytical Chemistry* **403**, 75-92 (2012).
8. Narsaiah, K., Jha, S., Bhardwaj, R., Sharma, R. & Kumar, R. Optical biosensors for food quality and safety assurance - a review. *Journal of Food Science and Technology* **49**, 383-406 (2012).
9. Cooper, M.A. Optical biosensors in drug discovery. *Nature Reviews Drug Discovery* **1**, 515-528 (2002).
10. Fang, Y. Label-free cell-based assays with optical biosensors in drug discovery. *Assay and Drug Development Technologies* **4**, 583-595 (2006).
11. Jianrong, C., Yuqing, M., Nongyue, H., Xiaohua, W. & Sijiao, L. Nanotechnology and biosensors. *Biotechnology Advances* **22**, 505-518 (2004).
12. Hussain, M., Wackerlig, J. & Lieberzeit, P. Biomimetic strategies for sensing biological species. *Biosensors* **3**, 89-107 (2013).
13. Ye, L. & Mosbach, K. Molecular Imprinting: synthetic materials as substitutes for biological antibodies and receptors. *Chemistry of Materials* **20**, 859-868 (2008).
14. Liu, Q. Cell-based biosensors: principles and applications (Artech House, Incorporated, 2014).
15. Pancrazio, J.J., Whelan, J.P., Borkholder, D.A., Ma, W. & Stenger, D.A. Development and application of cell-based biosensors. *Annals of Biomedical Engineering* **27**, 697-711 (1999).
16. Bousse, L. Whole cell biosensors. *Sensors and Actuators B-Chemical* **34**, 270-275 (1996).
17. Widder, M.W. et al. Evaluation and refinement of a field-portable drinking water toxicity sensor utilizing electric cell–substrate impedance sensing and a fluidic biochip. *Journal of Applied Toxicology* **35**, 701-708 (2015).
18. Brennan, L.M., Widder, M.W., Lee, L.E.J. & van der Schalie, W.H. Long-term storage and impedance-based water toxicity testing capabilities of fluidic biochips seeded with RTgill-W1 Cells. *In Vitro Cellular & Developmental Biology-Animal* **48**, 8-9 (2012).
19. Harsanyi, G. Sensors in biomedical applications: fundamentals, technology and applications (CRC Press, 2010).
20. Nath, N., Hyun, J., Ma, H. & Chilkoti, A. Surface engineering strategies for control of protein and cell interactions. *Surface Science* **570**, 98-110 (2004).
21. Liu, Q. et al. Cell-based biosensors and their application in biomedicine. *Chemical Reviews* **114**, 6423-6461 (2014).
22. Michaelis, S., Robelek, R. & Wegener, J. Studying cell-surface interactions *in vitro*: a survey of experimental approaches and techniques. *Tissue Engineering III: Cell-Surface Interactions for Tissue Culture* **126**, 33-66 (2012).

23. Bergveld, P. Development of an ion-sensitive solid-state device for neurophysiological measurements. *IEEE Transactions on Biomedical Engineering* **17**, 70-71 (1970).
24. Fromherz, P., Offenhausser, A., Vetter, T. & Weis, J. A neuron-silicon junction: a Retzius cell of the leech on an insulated-gate field-effect transistor. *Science* **252**, 1290-1293 (1991).
25. Schöning, M.J. & Poghossian, A. Recent advances in biologically sensitive field-effect transistors (BioFETs). *Analyst* **127**, 1137-1151 (2002).
26. Lee, C.S., Kim, S.K. & Kim, M. Ion-sensitive field-effect transistor for biological sensing. *Sensors* **9**, 7111-7131 (2009).
27. Hafner, F. Cytosensor Microphysiometer: technology and recent applications. *Biosensors and Bioelectronics* **15**, 149-158 (2000).
28. Kharitonov, A.B., Zayats, M., Lichtenstein, A., Katz, E. & Willner, I. Enzyme monolayer-functionalized field-effect transistors for biosensor applications. *Sensors and Actuators B-Chemical* **70**, 222-231 (2000).
29. Goncalves, D., Prazeres, D.M.F., Chu, V. & Conde, J.P. Detection of DNA and proteins using amorphous silicon ion-sensitive thin-film field effect transistors. *Biosensors and Bioelectronics* **24**, 545-551 (2008).
30. Schöning, M.J. & Poghossian, A. Bio FEDs (Field-Effect Devices): state-of-the-art and new directions. *Electroanalysis* **18**, 1893-1900 (2006).
31. Martinoia, S. et al. Development of ISFET array-based microsystems for bioelectrochemical measurements of cell populations. *Biosensors and Bioelectronics* **16**, 1043-1050 (2001).
32. Baumann, W.H. et al. Microelectronic sensor system for microphysiological application on living cells. *Sensors and Actuators B-Chemical* **55**, 77-89 (1999).
33. Lehmann, M. et al. Simultaneous measurement of cellular respiration and acidification with a single CMOS ISFET. *Biosensors and Bioelectronics* **16**, 195-203 (2001).
34. Vassanelli, S. & Fromherz, P. Transistor records of excitable neurons from rat brain. *Applied Physics A - Materials Science & Processing* **66**, 459-463 (1998).
35. Sprossler, C., Denyer, M., Britland, S., Knoll, W. & Offenhausser, A. Electrical recordings from rat cardiac muscle cells using field-effect transistors. *Physical Review E* **60**, 2171-2176 (1999).
36. Ingebrandt, S., Yeung, C.K., Krause, M. & Offenhausser, A. Cardiomyocyte-transistor-hybrids for sensor application. *Biosensors and Bioelectronics* **16**, 565-570 (2001).
37. Hafeman, D.G., Parce, J.W. & Mcconnell, H.M. Light-addressable potentiometric sensor for biochemical systems. *Science* **240**, 1182-1185 (1988).
38. Parce, J.W. et al. Detection of cell-affecting agents with a silicon biosensor. *Science* **246**, 243-247 (1989).
39. Piras, L., Adami, M., Fenu, S., Dovis, M. & Nicolini, C. Immunoenzymatic application of a redox potential biosensor. *Analytica Chimica Acta* **335**, 127-135 (1996).
40. Yoshinobu, T. et al. The light-addressable potentiometric sensor for multi-ion sensing and imaging. *Methods* **37**, 94-102 (2005).
41. Owicki, J.C. et al. The light-addressable potentiometric sensor - principles and biological applications. *Annual Review of Biophysics and Biomolecular Structure* **23**, 87-113 (1994).
42. Schöning, M.J. et al. Thin film sensors on the basis of chalcogenide glass materials prepared by pulsed laser deposition technique. *Sensors and Actuators B - Chemical* **68**, 254-259 (2000).
43. Seki, A., Motoya, K., Watanabe, S. & Kubo, I. Novel sensors for potassium, calcium and magnesium ions based on a silicon transducer as a light-addressable potentiometric sensor. *Analytica Chimica Acta* **382**, 131-136 (1999).
44. Smart, D. & Wood, M.D. Cytosensor techniques for examining signal transduction of neurohormones. *Biochemistry and Cell Biology* **78**, 281-288 (2000).

45. Neve, K.A., Kozlowski, M.R. & Rosser, M.P. Dopamine D2 receptor stimulation of Na^+/H^+ exchange assessed by quantification of extracellular acidification. *Journal of Biological Chemistry* **267**, 25748-25753 (1992).
46. Fujii, R. et al. Identification of neuromedin U as the cognate ligand of the orphan G protein-coupled receptor FM-3. *Journal of Biological Chemistry* **275**, 21068-21074 (2000).
47. Yicong, W. et al. A novel microphysiometer based on MLAPS for drugs screening. *Biosensors and Bioelectronics* **16**, 277-286 (2001).
48. Stein, B., George, M., Gaub, H.E. & Parak, W.J. Extracellular measurements of averaged ionic currents with the light-addressable potentiometric sensor (LAPS). *Sensors and Actuators B-Chemical* **98**, 299-304 (2004).
49. Xu, G.X. et al. Cell-based biosensors based on light-addressable potentiometric sensors for single cell monitoring. *Biosensors and Bioelectronics* **20**, 1757-1763 (2005).
50. Liu, Q.J. et al. *In vitro* assessing the risk of drug-induced cardiotoxicity by embryonic stem cell-based biosensor. *Sensors and Actuators B-Chemical* **155**, 214-219 (2011).
51. Liu, Q.J. et al. Embryonic stem cells as a novel cell source of cell-based biosensors. *Biosensors and Bioelectronics* **22**, 810-815 (2007).
52. Wang, P. et al. Cell-based biosensors and its application in biomedicine. *Sensors and Actuators B-Chemical* **108**, 576-584 (2005).
53. Wu, Y.C. et al. Drug evaluations using a novel microphysiometer based on cell-based biosensors. *Sensors and Actuators B-Chemical* **80**, 215-221 (2001).
54. Wu, Y.C. et al. A novel microphysiometer based on MLAPS for drugs screening. *Biosensors and Bioelectronics* **16**, 277-286 (2001).
55. Yanase, Y. et al. Living cell positioning on the surface of gold film for SPR analysis. *Biosensors and Bioelectronics* **23**, 562-567 (2007).
56. Chabot, V. et al. Biosensing based on surface plasmon resonance and living cells. *Biosensors and Bioelectronics* **24**, 1667-1673 (2009).
57. Baumgarten, S. & Robelek, R. Surface plasmon resonance (SPR) sensors for the rapid, sensitive detection of the cellular response to osmotic stress. *Sensors and Actuators B-Chemical* **156**, 798-804 (2011).
58. Robelek, R. & Wegener, J. Label-free and time-resolved measurements of cell volume changes by surface plasmon resonance (SPR) spectroscopy. *Biosensors and Bioelectronics* **25**, 1221-1224 (2010).
59. Hide, M. et al. Real-time analysis of ligand-induced cell surface and intracellular reactions of living mast cells using a surface plasmon resonance-based biosensor. *Analytical Biochemistry* **302**, 28-37 (2002).
60. Cuerrier, C.M. et al. Surface plasmon resonance monitoring of cell monolayer integrity: implication of signaling pathways involved in actin-driven morphological remodeling. *Cellular and Molecular Bioengineering* **1**, 229-239 (2008).
61. Curie, J. & Curie, P. An oscillating quartz crystal mass detector. *Rendu* **91**, 294-297 (1880).
62. Sauerbrey, G. Verwendung von Schwingquarzen zur Wägung dünner Schichten und zur Mikrowägung. *Zeitschrift für Physik* **155**, 206-222 (1959).
63. Nomura, T. & Okuhara, M. Frequency-shifts of piezoelectric quartz crystals immersed in organic liquids. *Analytica Chimica Acta* **142**, 281-284 (1982).
64. Wegener, J. Cell surface interactions (John Wiley & Sons, Inc., 2006).
65. Kanazawa, K.K. & Gordon, J.G. Frequency of a quartz microbalance in contact with liquid. *Analytical Chemistry* **57**, 1770-1771 (1985).
66. Janshoff, A., Wegener, J., Sieber, M. & Galla, H.J. Double-mode impedance analysis of epithelial cell monolayers cultured on shear wave resonators. *European Biophysics Journal with Biophysics Letters* **25**, 93-103 (1996).
67. Martin, S.J., Granstaff, V.E. & Frye, G.C. Characterization of a quartz crystal microbalance with simultaneous mass and liquid loading. *Analytical Chemistry* **63**, 2272-2281 (1991).

68. Redepenning, J., Schlesinger, T.K., Mechalke, E.J., Puleo, D.A. & Bizios, R. Osteoblast attachment monitored with a quartz-crystal microbalance. *Analytical Chemistry* **65**, 3378-3381 (1993).
69. Wegener, J., Janshoff, A. & Galla, H.J. Cell adhesion monitoring using a quartz crystal microbalance: comparative analysis of different mammalian cell lines. *European Biophysics Journal with Biophysics Letters* **28**, 26-37 (1998).
70. Fohlerova, Z., Skladal, P. & Turanek, J. Adhesion of eukaryotic cell lines on the gold surface modified with extracellular matrix proteins monitored by the piezoelectric sensor. *Biosensors and Bioelectronics* **22**, 1896-1901 (2007).
71. Marx, K.A. Quartz crystal microbalance: a useful tool for studying thin polymer films and complex biomolecular systems at the solution-surface interface. *Biomacromolecules* **4**, 1099-1120 (2003).
72. Marx, K.A., Zhou, T., Montrone, A., McIntosh, D. & Braunhut, S.J. A comparative study of the cytoskeleton binding drugs nocodazole and taxol with a mammalian cell quartz crystal microbalance biosensor: different dynamic responses and energy dissipation effects. *Analytical Biochemistry* **361**, 77-92 (2007).
73. Braunhut, S.J., McIntosh, D., Vorotnikova, E., Zhou, T. & Marx, K.A. Detection of apoptosis and drug resistance of human breast cancer cells to taxane treatments using quartz crystal microbalance biosensor technology. *Assay and Drug Development Technologies* **3**, 77-88 (2005).
74. Wegener, J., Seebach, J., Janshoff, A. & Galla, H.J. Analysis of the composite response of shear wave resonators to the attachment of mammalian cells. *Biophysical Journal* **78**, 2821-2833 (2000).
75. Guo, M.L. et al. Enhanced adhesion/spreading and proliferation of mammalian cells on electropolymerized porphyrin film for biosensing applications. *Biosensors and Bioelectronics* **23**, 865-871 (2008).
76. Wei, X.L., Mo, Z.H., Li, B. & Wei, J.M. Disruption of HepG2 cell adhesion by gold nanoparticle and Paclitaxel disclosed by *in situ* QCM measurement. *Colloids and Surfaces B-Biointerfaces* **59**, 100-104 (2007).
77. Giaever, I. & Keese, C.R. Monitoring fibroblast behavior in tissue-culture with an applied electric field. *Proceedings of the National Academy of Sciences of the United States of America-Biological Sciences* **81**, 3761-3764 (1984).
78. Fang, Y. Label-free biosensors for cell biology. *International Journal of Electrochemistry* **vol. 2011** (2011).
79. Wegener, J., Zink, S., Rosen, P. & Galla, H.J. Use of electrochemical impedance measurements to monitor β-adrenergic stimulation of bovine aortic endothelial cells. *Pflugers Archiv-European Journal of Physiology* **437**, 925-934 (1999).
80. Yu, N.C. et al. Real-time monitoring of morphological changes in living cells by electronic cell sensor arrays: an approach to study G protein-coupled receptors. *Analytical Chemistry* **78**, 35-43 (2006).
81. Fang, Y. Non-invasive optical biosensor for probing cell signaling. *Sensors* **7**, 2316-2329 (2007).
82. Goral, V., Wu, Q., Sun, H.Y. & Fang, Y. Label-free optical biosensor with microfluidics for sensing ligand-directed functional selectivity on trafficking of thrombin receptor. *FEBS Letters* **585**, 1054-1060 (2011).
83. Komarova, Y.A., Mehta, D. & Malik, A.B. Dual regulation of endothelial junctional permeability. *Science's signal transduction knowledge environment* **2007**, re8 (2007).
84. Wegener, J., Keese, C.R. & Giaever, I. Electric cell-substrate impedance sensing (ECIS) as a noninvasive means to monitor the kinetics of cell spreading to artificial surfaces. *Experimental Cell Research* **259**, 158-166 (2000).
85. Angstmann, M., Brinkmann, I., Bieback, K., Breitkreutz, D. & Maercker, C. Monitoring human mesenchymal stromal cell differentiation by electrochemical impedance sensing. *Cytotherapy* **13**, 1074-1089 (2011).
86. Holmes, S.D., May, K., Johansson, V., Markey, F. & Critchley, I.A. Studies on the interaction of *staphylococcus aureus* and *staphylococcus epidermidis* with fibronectin

using surface plasmon resonance (BIAcore). *Journal of Microbiological Methods* **28**, 77-84 (1997).
87. Hug, T.S., Prenosil, J.E. & Morbidelli, M. Optical waveguide lightmode spectroscopy as a new method to study adhesion of anchorage-dependent cells as an indicator of metabolic state. *Biosensors and Bioelectronics* **16**, 865-874 (2001).
88. Fang, Y., Ferrie, A.M., Fontaine, N.H., Mauro, J. & Balakrishnan, J. Resonant waveguide grating biosensor for living cell sensing. *Biophysical Journal* **91**, 1925-1940 (2006).
89. Fredriksson, C., Kihlman, S., Rodahl, M. & Kasemo, B. The piezoelectric quartz crystal mass and dissipation sensor: a means of studying cell adhesion. *Langmuir* **14**, 248-251 (1998).
90. Gryte, D.M., Ward, M.D. & Hu, W.S. Real-time measurement of anchorage-dependent cell-adhesion using a quartz crystal microbalance. *Biotechnology Progress* **9**, 105-108 (1993).
91. Hondroulis, E., Liu, C. & Li, C.Z. Whole cell based electrical impedance sensing approach for a rapid nanotoxicity assay. *Nanotechnology* **21**, 315103-315112 (2010).
92. Arndt, S., Seebach, J., Psathaki, K., Galla, H.J. & Wegener, J. Bioelectrical impedance assay to monitor changes in cell shape during apoptosis. *Biosensors and Bioelectronics* **19**, 583-594 (2004).
93. Solly, K., Wang, X.B., Xu, X., Strulovici, B. & Zheng, W. Application of real-time cell electronic sensing (RT-CES) technology to cell-based assays. *Assay and Drug Development Technologies* **2**, 363-372 (2004).
94. Curtis, T.M. et al. A portable cell-based impedance sensor for toxicity testing of drinking water. *Lab on a Chip* **9**, 2176-2183 (2009).
95. Liu, Q.J. et al. Impedance studies of bio-behavior and chemosensitivity of cancer cells by micro-electrode arrays. *Biosensors and Bioelectronics* **24**, 1305-1310 (2009).
96. Tarantola, M. et al. Toxicity of gold-nanoparticles: synergistic effects of shape and surface functionalization on micromotility of epithelial cells. *Nanotoxicology* **5**, 254-68 (2011).
97. Wodnicka, M. et al. Novel fluorescent technology platform for high throughput cytotoxicity and proliferation assays. *Journal of Biomolecular Screening* **5**, 141-152 (2000).
98. Yun, Y.H., Dong, Z.Y., Tan, Z.Q. & Schulz, M.J. Development of an electrode cell impedance method to measure osteoblast cell activity in magnesium-conditioned media. *Analytical and Bioanalytical Chemistry* **396**, 3009-3015 (2010).
99. Gfeller, K.Y., Nugaeva, N. & Hegner, M. Micromechanical oscillators as rapid biosensor for the detection of active growth of *Escherichia coli*. *Biosensors and Bioelectronics* **21**, 528-533 (2005).
100. Gfeller, K.Y., Nugaeva, N. & Hegner, M. Rapid biosensor for detection of antibiotic-selective growth of *Escherichia coli*. *Applied and Environmental Microbiology* **71**, 2626-2631 (2005).
101. Riahi, R., Yang, Y.L., Zhang, D.D. & Wong, P.K. Advances in wound-healing assays for probing collective cell migration. *Journal of Laboratory Automation* **17**, 59-65 (2012).
102. Noiri, E. et al. Permissive role of nitric oxide in endothelin-induced migration of endothelial cells. *The Journal of Biological Chemistry* **272**, 1747-1752 (1997).
103. Keese, C.R., Wegener, J., Walker, S.R. & Giaever, L. Electrical wound-healing assay for cells *in vitro*. *Proceedings of the National Academy of Sciences of the United States of America* **101**, 1554-1559 (2004).
104. Charrier, L. et al. ADAM-15 inhibits wound healing in human intestinal epithelial cell monolayers. *American Journal of Physiology-Gastrointestinal and Liver Physiology* **288**, G346-G353 (2005).
105. Jiang, W.G. et al. Eplin-alpha expression in human breast cancer, the impact on cellular migration and clinical outcome. *Molecular Cancer* **7**, 1-10 (2008).

106. Fang, K.S., Farboud, B., Nuccitelli, R. & Isseroff, R.R. Migration of human keratinocytes in electric fields requires growth factors and extracellular calcium. *Journal of Investigative Dermatology* **111**, 751-756 (1998).
107. Fang, K.S., Ionides, E., Oster, G., Nuccitelli, R. & Isseroff, R.R. Epidermal growth factor receptor relocalization and kinase activity are necessary for directional migration of keratinocytes in DC electric fields. *Journal of Cell Science* **112**, 1967-1978 (1999).
108. Wang, L., Zhu, J., Deng, C., Xing, W.L. & Cheng, J. An automatic and quantitative on-chip cell migration assay using self-assembled monolayers combined with real-time cellular impedance sensing. *Lab on a Chip* **8**, 872-878 (2008).
109. Gumbleton, M. & Audus, K.L. Progress and limitations in the use of *in vitro* cell cultures to serve as a permeability screen for the blood-brain barrier. *Journal of Pharmaceutical Sciences* **90**, 1681-1698 (2001).
110. Hartmann, C., Zozulya, A., Wegener, J. & Galla, H.J. The impact of glia-derived extracellular matrices on the barrier function of cerebral endothelial cells: an *in vitro* study. *Experimental Cell Research* **313**, 1318-1325 (2007).
111. Seebach, J. et al. Endothelial barrier function under laminar fluid shear stress. *Laboratory Investigation* **80**, 1819-1831 (2000).
112. Rempe, R., Cramer, S., Huwel, S. & Galla, H.J. Transport of poly(n-butylcyano-acrylate) nanoparticles across the blood-brain barrier *in vitro* and their influence on barrier integrity. *Biochemical and Biophysical Research Communications* **406**, 64-69 (2011).
113. Weidenfeller, C., Schrot, S., Zozulya, A. & Galla, H.J. Murine brain capillary endothelial cells exhibit improved barrier properties under the influence of hydrocortisone. *Brain Research* **1053**, 162-174 (2005).
114. Sun, T. et al. On-chip epithelial barrier function assays using electrical impedance spectroscopy. *Lab on a Chip* **10**, 1611-1617 (2010).
115. Michaelis, S., Wegener, J. & Robelek, R. Label-free monitoring of cell-based assays: combining impedance analysis with SPR for multiparametric cell profiling. *Biosensors and Bioelectronics* **49**, 63-70 (2013).
116. Flanagan, M.D. & Lin, S. Cytochalasins block actin filament elongation by binding to high affinity sites associated with F-actin. *The Journal of Biological Chemistry* **255**, 835-838 (1980).
117. De Larco, J.E. & Todaro, G.J. Epithelioid and fibroblastic rat kidney cell clones: epidermal growth factor (EGF) receptors and the effect of mouse sarcoma virus transformation. *Journal of Cellular Physiology* **94**, 335-342 (1978).
118. Fuller, S., Vonbonsdorff, C.H. & Simons, K. Vesicular stomatitis-virus infects and matures only through the basolateral surface of the polarized epithelial cell line, MDCK. *Cell* **38**, 65-77 (1984).
119. McAdams, E.T., Lackermeier, A., McLaughlin, J.A., Macken, D. & Jossinet, J. The linear and nonlinear electrical properties of the electrode-electrolyte interface. *Biosensors and Bioelectronics* **10**, 67-74 (1995).
120. Wegener, J. ECIS: Ein variabel einsetzbares elektrochemisches Verfahren - Lebende Zellen als Sensoren. *Forschungsjournal der Westfälischen Wilhelms-Universität Münster*, 11-17 (2003).
121. Giaever, I. & Keese, C.R. Micromotion of mammalian cells measured electrically. *Proceedings of the National Academy of Sciences of the United States of America* **88**, 7896-7900 (1991).
122. Minsky, M. Memoir on inventing the confocal scanning microscope. *Scanning* **10**, 128-138 (1988).
123. Wegener, J., Hakvoort, A. & Galla, H.J. Barrier function of porcine choroid plexus epithelial cells is modulated by cAMP-dependent pathways *in vitro*. *Brain Research* **853**, 115-124 (2000).
124. Wegener, J. Impedance analysis of cell junctions. *Nanotechnology* (2010).
125. Lo, C.M. & Ferrier, J. Impedance analysis of fibroblastic cell layers measured by electric cell-substrate impedance sensing. *Physical Review E* **57**, 6982-6987 (1998).

126. Lo, C.M., Keese, C.R. & Giaever, I. Impedance analysis of MDCK cells measured by electric cell-substrate impedance sensing. *Biophysical Journal* **69**, 2800-2807 (1995).
127. Lo, C.M., Keese, C.R. & Giaever, I. Cell-substrate contact: another factor may influence transepithelial electrical resistance of cell layers cultured on permeable filters. *Experimental Cell Research* **250**, 576-580 (1999).
128. Tiruppathi, C., Malik, A.B., Del Vecchio, P.J., Keese, C.R. & Giaever, I. Electrical method for detection of endothelial cell shape change in real time: assessment of endothelial barrier function. *Proceedings of the National Academy of Sciences of the United States of America* **89**, 7919-7923 (1992).
129. Ellis, C.A., Tiruppathi, C., Sandoval, R., Niles, W.D. & Malik, A.B. Time course of recovery of endothelial cell surface thrombin receptor (PAR-1) expression. *American Journal of Physiology - Cell Physiology* **276**, C38-C45 (1999).
130. Phelps, J.E. & DePaola, N. Spatial variations in endothelial barrier function in disturbed flows *in vitro*. *American Journal of Physiology - Heart and Circulatory Physiology* **278**, H469-H476 (2000).
131. Birukov, K.G. et al. Magnitude-dependent regulation of pulmonary endothelial cell barrier function by cyclic stretch. *American Journal of Physiology - Lung Cellular and Molecular Physiology* **285**, L785-L797 (2003).
132. Shen, L. & Turner, J.R. Actin depolymerization disrupts tight junctions via caveolae-mediated endocytosis. *Molecular Biology of the Cell* **16**, 3919-3936 (2005).
133. Furuse, M., Furuse, K., Sasaki, H. & Tsukita, S. Conversion of Zonulae occludentes from tight to leaky strand type by introducing claudin-2 into Madin-Darby canine kidney I cells. *Journal of Cell Biology* **153**, 263-272 (2001).
134. Balda, M.S. et al. Functional dissociation of paracellular permeability and transepithelial electrical resistance and disruption of the apical-basolateral intramembrane diffusion barrier by expression of a mutant tight junction membrane protein. *Journal of Cell Biology* **134**, 1031-1049 (1996).
135. Cereijido, M., Robbins, E.S., Dolan, W.J., Rotunno, C.A. & Sabatini, D.D. Polarized monolayers formed by epithelial cells on a permeable and translucent support. *The Journal of Cell Biology* **77**, 853-880 (1978).
136. Martinez-Palomo, A., Meza, I., Beaty, G. & Cereijido, M. Experimental modulation of occluding junctions in a cultured transporting epithelium. *The Journal of Cell Biology* **87**, 736-745 (1980).
137. Gonzalez-Mariscal, L., Chavez de Ramirez, B. & Cereijido, M. Tight junction formation in cultured epithelial cells (MDCK). *The Journal of Membrane Biology* **86**, 113-125 (1985).
138. Dehouck, M.P., Meresse, S., Delorme, P., Fruchart, J.C. & Cecchelli, R. An easier, reproducible, and mass-production method to study the blood-brain barrier *in vitro*. *Journal of Neurochemistry* **54**, 1798-1801 (1990).
139. Staddon, J.M., Herrenknecht, K., Smales, C. & Rubin, L.L. Evidence that tyrosine phosphorylation may increase tight junction permeability. *Journal of Cell Science* **108 (Pt 2)**, 609-619 (1995).
140. Yuki, T. et al. Tight junction proteins in keratinocytes: localization and contribution to barrier function. *Experimental Dermatology* **16**, 324-330 (2007).
141. Waschke, J., Curry, F.E., Adamson, R.H. & Drenckhahn, D. Regulation of actin dynamics is critical for endothelial barrier functions. *American Journal of Physiology - Heart and Circulatory Physiology* **288**, H1296-H1305 (2005).
142. Matthews, J.B., Tally, K.J., Smith, J.A. & Awtrey, C.S. F-Actin differentially alters epithelial transport and barrier function. *Journal of Surgical Research* **56**, 505-509 (1994).
143. Stevenson, B.R. & Begg, D.A. Concentration-dependent effects of cytochalasin D on tight junctions and actin-filaments in MDCK epithelial cells. *Journal of Cell Science* **107**, 367-375 (1994).
144. Giaever, I. & Keese, C.R. Micromotion of mammalian cells measured electrically. *Proc Natl Acad Sci U S A* **88**, 7896-900 (1991).

145. Cho, M.J., Thompson, D.P., Cramer, C.T., Vidmar, T.J. & Scieszka, J.F. The madin darby canine kidney (MDCK) epithelial-cell monolayer as a model cellular-transport barrier. *Pharmaceutical Research* **6**, 71-77 (1989).
146. Madara, J.L., Barenberg, D. & Carlson, S. Effects of Cytochalasin D on occluding junctions of intestinal absorptive cells - further evidence that the cytoskeleton may influence paracellular permeability and junctional charge selectivity. *Journal of Cell Biology* **102**, 2125-2136 (1986).
147. Srinivasan, B. et al. TEER measurement techniques for *in vitro* barrier model systems. *Journal of Laboratory Automation* **20**, 107-126 (2015).
148. Kirchhofer, D., Grzesiak, J. & Pierschbacher, M.D. Calcium as a potential physiological regulator of integrin-mediated cell adhesion. *Journal of Biological Chemistry* **266**, 4471-4477 (1991).
149. Gonzalez-Mariscal, L. et al. Role of calcium in tight junction formation between epithelial cells. *American Journal of Physiology* **259**, C978-C986 (1990).
150. Ghosh, P.M., Keese, C.R. & Giaever, I. Morphological response of mammalian cells to pulsed ac fields. *Bioelectrochemistry and Bioenergetics* **33**, 121-133 (1994).
151. Stolwijk, J.A., Matrougui, K., Renken, C.W. & Trebak, M. Impedance analysis of GPCR-mediated changes in endothelial barrier function: overview and fundamental considerations for stable and reproducible measurements. *Pflugers Archiv - European Journal of Physiology* **467**, 2193-2218 (2014).
152. K'Owino, I.O. & Sadik, O.A. Impedance spectroscopy: a powerful tool for rapid biomolecular screening and cell culture monitoring. *Electroanalysis* **17**, 2101-2113 (2005).
153. Zhao, L. et al. Electrochemical impedance spectroscopic measurements of FCCP-induced change in membrane permeability of MDCK cells. *Analyst* **137**, 2199-2204 (2012).
154. Primiceri, E. et al. Automatic transwell assay by an EIS cell chip to monitor cell migration. *Lab on a Chip* **11**, 4081-4086 (2011).
155. Guo, M.L. et al. Monitoring of cell growth and assessment of cytotoxicity using electrochemical impedance spectroscopy. *Biochimica Et Biophysica Acta-General Subjects* **1760**, 432-439 (2006).
156. Feng, L.Y., Chen, Y., Ren, J.S. & Qu, X.G. A graphene functionalized electrochemical aptasensor for selective label-free detection of cancer cells. *Biomaterials* **32**, 2930-2937 (2011).
157. Geng, P. et al. Self-assembled monolayers-based immunosensor for detection of *Escherichia coli* using electrochemical impedance spectroscopy. *Electrochimica Acta* **53**, 4663-4668 (2008).
158. Yang, L.J., Li, Y.B. & Erf, G.F. Interdigitated array microelectrode-based electrochemical impedance immunosensor for detection of *Escherichia coli* O157 : H7. *Analytical Chemistry* **76**, 1107-1113 (2004).
159. Heiskanen, A.R., Spegel, C.F., Kostesha, N., Ruzgas, T. & Emneus, J. Monitoring of *Saccharomyces cerevisiae* cell proliferation on thiol-modified planar gold microelectrodes using impedance spectroscopy. *Langmuir* **24**, 9066-9073 (2008).
160. Yang, W. et al. Label-free detection of telomerase activity in HeLa cells using electrochemical impedance spectroscopy. *Chemical Communications* **47**, 3129-3131 (2011).
161. Seeman, P. Transient holes in the erythrocyte membrane during hypotonic hemolysis and stable holes in the membrane after lysis by saponin and lysolecithin. *Journal of Cell Biology* **32**, 55-70 (1967).
162. Lorent, J.H., Quetin-Leclercq, J. & Mingeot-Leclercq, M.P. The amphiphilic nature of saponins and their effects on artificial and biological membranes and potential consequences for red blood and cancer cells. *Organic and Biomolecular Chemistry* **12**, 8803-8822 (2014).
163. Gogelein, H. & Huby, A. Interaction of saponin and digitonin with black lipid-membranes and lipid monolayers. *Biochimica Et Biophysica Acta* **773**, 32-38 (1984).

164. Wassler, M., Jonasson, I., Persson, R. & Fries, E. Differential permeabilization of membranes by saponin treatment of isolated rat hepatocytes. Release of secretory proteins. *Biochemical Journal* **247**, 407-415 (1987).
165. De Mello, W.C. & Janse, M.J. Heart cell coupling and impulse propagation in health and disease (Springer, 2002).
166. Zimmer, H.G. Theodor Wilhelm Engelmann - Profiles in cardiology. *Clinical Cardiology* **29**, 518-520 (2006).
167. Weidmann, S. The electrical constants of Purkinje fibres. *The Journal of Physiology* **118**, 348-360 (1952).
168. Furshpan, E.J. & Potter, D.D. Mechanism of nerve-impulse transmission at a crayfish synapse. *Nature* **180**, 342-343 (1957).
169. Goodenough, D.A. & Paul, D.L. Gap junctions. *Cold Spring Harbor Perspectives in Biology* **1**, a002576 (2009).
170. Revel, J.P., Olson, W. & Karnovsk.Mj. A 20-Angstrom gap junction with a hexagonal array of subunits in smooth muscle. *Journal of Cell Biology* **35**, A112-& (1967).
171. Beblo, D.A. & Veenstra, R.D. Monovalent cation permeation through the connexin40 gap junction channel - Cs, Rb, K, Na, Li, TEA, TMA, TBA, and effects of anions Br, Cl, F, acetate, aspartate, glutamate, and NO3. *Journal of General Physiology* **109**, 509-522 (1997).
172. Veenstra, R.D. Size and selectivity of gap junction channels formed from different connexins. *Journal of Bioenergetics and Biomembranes* **28**, 327-337 (1996).
173. Veenstra, R.D. Ion permeation through connexin gap junction channels: effects on conductance and selectivity. *Gap Junctions* **49**, 95-129 (2000).
174. Wang, H.Z. & Veenstra, R.D. Monovalent ion selectivity sequences of the rat connexin43 gap junction channel. *Journal of General Physiology* **109**, 491-507 (1997).
175. Gong, X.Q. & Nicholson, B.J. Size selectivity between gap junction channels composed of different Connexins. *Cell Communication and Adhesion* **8**, 187-192 (2001).
176. Weber, P.A., Chang, H.C., Spaeth, K.E., Nitsche, J.M. & Nicholson, B.J. The permeability of gap junction channels to probes of different size is dependent on connexin composition and permeant-pore affinities. *Biophysical Journal* **87**, 958-973 (2004).
177. Goodenough, D.A. & Paul, D.L. Beyond the gap: functions of unpaired connexon channels. *Nature Reviews Molecular Cell Biology* **4**, 285-294 (2003).
178. Sohl, G. & Willecke, K. Gap junctions and the connexin protein family. *Cardiovascular Research* **62**, 228-232 (2004).
179. White, T.W., Bruzzone, R., Wolfram, S., Paul, D.L. & Goodenough, D.A. Selective interactions among the multiple connexin proteins expressed in the vertebrate lens - the 2nd extracellular domain is a determinant of compatibility between connexins. *Journal of Cell Biology* **125**, 879-892 (1994).
180. Friend, D.S. & Gilula, N.B. Variations in tight and gap junctions in mammalian tissues. *Journal of Cell Biology* **53**, 758-776 (1972).
181. Forge, A. et al. Gap junctions in the inner ear: comparison of distribution patterns in different vertebrates and assessement of connexin composition in mammals. *The Journal of Comparative Neurology* **467**, 207-231 (2003).
182. McNutt, N.S. & Weinstei.Rs. Ultrastructure of nexus - a correlated thin-section and freeze-cleave study. *Journal of Cell Biology* **47**, 666-688 (1970).
183. Hoh, J.H., Lal, R., John, S.A., Revel, J.P. & Arnsdorf, M.F. Atomic force microscopy and dissection of gap junctions. *Science* **253**, 1405-1408 (1991).
184. Anderson, E. & Albertini, D.F. Gap junctions between oocyte and companion follicle cells in mammalian ovary. *Journal of Cell Biology* **71**, 680-686 (1976).
185. Bukauskas, F.F. et al. Clustering of connexin 43-enhanced green fluorescent protein gap junction channels and functional coupling in living cells. *Proceedings of the National Academy of Sciences of the United States of America* **97**, 2556-2561 (2000).

186. Lauf, U. et al. Dynamic trafficking and delivery of connexons to the plasma membrane and accretion to gap junctions in living cells. *Proceedings of the National Academy of Sciences of the United States of America* **99**, 10446-10451 (2002).
187. Severs, N.J. et al. Immunocytochemical analysis of connexin expression in the healthy and diseased cardiovascular system. *Microscopy Research and Technique* **52**, 301-322 (2001).
188. Martin, P.E.M., Blundell, G., Ahmad, S., Errington, R.J. & Evans, W.H. Multiple pathways in the trafficking and assembly of connexin 26, 32 and 43 into gap junction intercellular communication channels. *Journal of Cell Science* **114**, 3845-3855 (2001).
189. Jordan, K., Chodock, R., Hand, A.R. & Laird, D.W. The origin of annular junctions: a mechanism of gap junction internalization. *Journal of Cell Science* **114**, 763-773 (2001).
190. Falk, M.M. Connexin-specific distribution within gap junctions revealed in living cells. *Journal of Cell Science* **113**, 4109-4120 (2000).
191. Kumar, N.M. & Gilula, N.B. Cloning and characterization of human and rat liver cDNAs coding for a gap junction protein. *The Journal of Cell Biology* **103**, 767-776 (1986).
192. Paul, D.L. Molecular cloning of cDNA for rat liver gap junction protein. *The Journal of Cell Biology* **103**, 123-134 (1986).
193. Sjostrand, F.S., Andersson-Cedergren, E. & Dewey, M.M. The ultrastructure of the intercalated discs of frog, mouse and guinea pig cardiac muscle. *Journal of Ultrastructure Research* **1**, 271-287 (1958).
194. Robertson, J.D. The occurrence of a subunit pattern in the unit membranes of club endings in mauthner cell synapses in goldfish brains. *The Journal of Cell Biology* **19**, 201-221 (1963).
195. Benedett, E.L. & Emmelot, P. Electron microscopic observations on negatively stained plasma membranes isolated from rat liver. *Journal of Cell Biology* **26**, 299-305 (1965).
196. Revel, J.P. & Karnovsky, M.J. Hexagonal array of subunits in intercellular junctions of the mouse heart and liver. *Journal of Cell Biology* **33**, C7-C12 (1967).
197. Uehara, Y. & Burnstoc.G. Demonstration of gap junctions between smooth muscle cells. *Journal of Cell Biology* **44**, 215-217 (1970).
198. Zimmer, D.B., Green, C.R., Evans, W.H. & Gilula, N.B. Topological analysis of the major protein in isolated intact rat-liver gap junctions and gap junction-derived single membrane structures. *Journal of Biological Chemistry* **262**, 7751-7763 (1987).
199. Kumar, N.M. & Gilula, N.B. The gap junction communication channel. *Cell* **84**, 381-388 (1996).
200. Unger, V.M., Kumar, N.M., Gilula, N.B. & Yeager, M. Three-dimensional structure of a recombinant gap junction membrane channel. *Science* **283**, 1176-1180 (1999).
201. Maeda, S. et al. Structure of the connexin 26 gap junction channel at 3.5 angstrom resolution. *Nature* **458**, 597-604 (2009).
202. Sohl, G., Maxeiner, S. & Willecke, K. Expression and functions of neuronal gap junctions. *Nature Reviews Neuroscience* **6**, 191-200 (2005).
203. Nicholson, B.J. et al. The molecular basis of selective permeability of connexins is complex and includes both size and charge. *Brazilian Journal of Medical and Biological Research* **33**, 369-378 (2000).
204. Elfgang, C. et al. Specific permeability and selective formation of gap junction channels in connexin-transfected HeLa cells. *Journal of Cell Biology* **129**, 805-817 (1995).
205. Goldberg, G.S., Valiunas, V. & Brink, P.R. Selective permeability of gap junction channels. *Biochimica Et Biophysica Acta-Biomembranes* **1662**, 96-101 (2004).
206. Harris, A.L. Connexin channel permeability to cytoplasmic molecules. *Progress in Biophysics and Molecular Biology* **94**, 120-143 (2007).
207. Goldberg, G.S., Moreno, A.P. & Lampe, P.D. Gap junctions between cells expressing connexin 43 or 32 show inverse permselectivity to adenosine and ATP. *Journal of Biological Chemistry* **277**, 36725-36730 (2002).

208. Peracchia, C. Chemical gating of gap junction channels roles of calcium, pH and calmodulin. *Biochimica Et Biophysica Acta-Biomembranes* **1662**, 61-80 (2004).
209. Evans, W.H. & Martin, P.E.M. Gap junctions: structure and function (Review). *Molecular Membrane Biology* **19**, 121-136 (2002).
210. Unwin, P.N.T. & Ennis, P.D. Two configurations of a channel-forming membrane protein. *Nature* **307**, 609-613 (1984).
211. Unwin, P.N.T. & Zampighi, G. Structure of the junction between communicating cells. *Nature* **283**, 545-549 (1980).
212. Delmar, M., Coombs, W., Sorgen, P., Duffy, H.S. & Taffet, S.A. Structural bases for the chemical regulation of connexin43 channels. *Cardiovascular Research* **62**, 268-275 (2004).
213. Morley, G.E., Taffet, S.M. & Delmar, M. Intramolecular interactions mediate pH regulation of connexin43 channels. *Biophysical Journal* **70**, 1294-1302 (1996).
214. Delmar, M. et al. A molecular model for the chemical regulation of connexin43 channels: the "ball-and-chain" hypothesis. *Gap Junctions* **49**, 223-248 (2000).
215. Homma, N. et al. A particle-receptor model for the insulin-induced closure of connexin43 channels. *Circulation Research* **83**, 27-32 (1998).
216. Oshima, A., Tani, K., Hiroaki, Y., Fujiyoshi, Y. & Sosinsky, G.E. Three-dimensional structure of a human connexin26 gap junction channel reveals a plug in the vestibule. *Proceedings of the National Academy of Sciences of the United States of America* **104**, 10034-10039 (2007).
217. Peracchia, C., Wang, X.G. & Peracchia, L.L. Behavior of chemical and slow voltage-sensitive gates of connexin channels: The "cork" gating hypothesis (2000).
218. Sosinsky, G.E. & Nicholson, B.J. Structural organization of gap junction channels. *Biochimica Et Biophysica Acta-Biomembranes* **1711**, 99-125 (2005).
219. Rose, B. & Rick, R. Intracellular pH, intracellular free Ca, and junctional cell-cell coupling. *Journal of Membrane Biology* **44**, 377-415 (1978).
220. Reber, W.R. & Weingart, R. Ungulate cardiac purkinje-fibers - the influence of intracellular pH on the electrical cell-to-cell coupling. *Journal of Physiology-London* **328**, 87-104 (1982).
221. Giaume, C., Spira, M.E. & Korn, H. Uncoupling of invertebrate electrotonic synapses by carbon dioxide. *Neuroscience Letters* **17**, 197-202 (1980).
222. Peracchia, C., Wang, X.G., Li, L.Q. & Peracchia, L.L. Inhibition of calmodulin expression prevents low-pH-induced gap junction uncoupling in *Xenopus oocytes*. *Pflugers Archiv-European Journal of Physiology* **431**, 379-387 (1996).
223. Wang, X.G., Li, L.Q., Peracchia, L.L. & Peracchia, C. Chimeric evidence for a role of the connexin cytoplasmic loop in gap junction channel gating. *Pflugers Archiv-European Journal of Physiology* **431**, 844-852 (1996).
224. Stergiopoulos, K. et al. Hetero-domain interactions as a mechanism for the regulation of connexin channels. *Circulation Research* **84**, 1144-1155 (1999).
225. Loewenstein, W.R., Nakas, M. & Socolar, S.J. Junctional membrane uncoupling - permeability transformations at a cell membrane junction. *Journal of General Physiology* **50**, 1865-1891 (1967).
226. Oliveira, G.M. & Loewenstein, W.R. Junctional membrane permeability - effects of divalent cations. *Journal of Membrane Biology* **5**, 51-77 (1971).
227. De Mello, W.C. Effect of intracellular injection of calcium and strontium on cell communication in heart. *Journal of Physiology-London* **250**, 231-245 (1975).
228. Muller, D.J., Hand, G.M., Engel, A. & Sosinsky, G.E. Conformational changes in surface structures of isolated connexin 26 gap junctions. *The EMBO Journal* **21**, 3598-3607 (2002).
229. Ishihara, Y. et al. Hormonal, pH, and calcium regulation of Connexin 43-mediated dye transfer in osteocytes in chick calvaria. *Journal of Bone and Mineral Research* **23**, 350-360 (2008).
230. Jongen, W.M.F. et al. Regulation of connexin 43-mediated gap junctional intercellular communication by Ca^{2+} in mouse epidermal cells is controlled by E-cadherin. *Journal of Cell Biology* **114**, 545-555 (1991).

231. Juszczak, G.R. & Swiergiel, A.H. Properties of gap junction blockers and their behavioural, cognitive and electrophysiological effects: animal and human studies. *Progress in Neuro-Psychopharmacology & Biological Psychiatry* **33**, 181-198 (2009).
232. Chanson, M., Bruzzone, R., Bosco, D. & Meda, P. Effects of n-alcohols on junctional coupling and amylase secretion of pancreatic acinar-cells. *Journal of Cellular Physiology* **139**, 147-156 (1989).
233. Evans, W.H. & Boitano, S. Connexin mimetic peptides: specific inhibitors of gap-junctional intercellular communication. *Biochemical Society Transactions* **29**, 606-612 (2001).
234. Spray, D.C., Rozental, R. & Srinivas, M. Prospects for rational development of pharmacological gap junction channel blockers. *Current Drug Targets* **3**, 455-464 (2002).
235. Nedergaard, M., Cooper, A.J.L. & Goldman, S.A. Gap-junctions are required for the propagation of spreading depression. *Journal of Neurobiology* **28**, 433-444 (1995).
236. Weingart, R. & Bukauskas, F.F. Long-chain n-alkanols and arachidonic acid interfere with the V-m-sensitive gating mechanism of gap junction channels. *Pflugers Archiv-European Journal of Physiology* **435**, 310-319 (1998).
237. Guan, X.J. et al. The sleep-inducing lipid oleamide deconvolutes gap junction communication and calcium wave transmission in glial cells. *Journal of Cell Biology* **139**, 1785-1792 (1997).
238. Nedergaard, M. Direct signaling from astrocytes to neurons in cultures of mammalian brain cells. *Science* **263**, 1768-1771 (1994).
239. Pappas, C.A., Rioult, M.G. & Ransom, B.R. Octanol, a gap junction uncoupling agent, changes intracellular [H^+] in rat astrocytes. *Glia* **16**, 7-15 (1996).
240. Takens-Kwak, B.R., Jongsma, H.J., Rook, M.B. & Van Ginneken, A.C. Mechanism of heptanol-induced uncoupling of cardiac gap junctions: a perforated patch-clamp study. *The American Journal of Physiology* **262**, C1531-C1538 (1992).
241. Bootman, M.D. et al. 2-Aminoethoxydiphenyl borate (2-APB) is a reliable blocker of store-operated Ca^{2+} entry but an inconsistent inhibitor of InsP(3)-induced Ca^{2+} release. *The FASEB Journal* **16**, 1145-1150 (2002).
242. Iwasaki, H. et al. 2-aminoethoxydiphenyl borate (2-APB) inhibits capacitative calcium entry independently of the function of inositol 1,4,5-trisphosphate receptors. *Receptors and Channels* **7**, 429-439 (2001).
243. Bai, D.L., del Corsso, C., Srinivas, M. & Spray, D.C. Block of specific gap junction channel subtypes by 2-aminoethoxydiphenyl borate (2-APB). *Journal of Pharmacology and Experimental Therapeutics* **319**, 1452-1458 (2006).
244. Yang, Y. et al. The effects of 2-aminoethoxydiphenyl borate and diphenylboronic anhydride on gap junctions composed of connexin43 in TM4 sertoli cells. *Biological and Pharmaceutical Bulletin* **34**, 1390-1397 (2011).
245. Harks, E.G.A. et al. Besides affecting intracellular calcium signaling, 2-APB reversibly blocks gap junctional coupling in confluent monolayers, thereby allowing the measurement of single-cell membrane currents in undissociated cells. *The FASEB Journal* **17**, 941-943 (2003).
246. Ye, N., Bathany, C. & Hua, S.Z. Assay for molecular transport across gap junction channels in one-dimensional cell arrays. *Lab on a Chip* **11**, 1096-1101 (2011).
247. Tao, L. & Harris, A.L. 2-aminoethoxydiphenyl borate directly inhibits channels composed of connexin26 and/or connexin32. *Molecular Pharmacology* **71**, 570-579 (2007).
248. Laird, D.W. The life cycle of a connexin: gap junction formation, removal, and degradation. *Journal of Bioenergetics and Biomembranes* **28**, 311-318 (1996).
249. Qin, H., Shao, Q., Igdoura, S.A., Alaoui-Jamali, M.A. & Laird, D.W. Lysosomal and proteasomal degradation play distinct roles in the life cycle of Cx43 in gap junctional intercellular communication-deficient and -competent breast tumor cells. *Journal of Biological Chemistry* **278**, 30005-30014 (2003).
250. Berthoud, V.A., Minogue, P.J., Laing, J.G. & Beyer, E.C. Pathways for degradation of connexins and gap junctions. *Cardiovascular Research* **62**, 256-267 (2004).

251. Traub, O., Look, J., Paul, D. & Willecke, K. Cyclic Adenosine-Monophosphate Stimulates Biosynthesis and Phosphorylation of the 26 Kda Gap Junction Protein in Cultured Mouse Hepatocytes. *European Journal of Cell Biology* **43**, 48-54 (1987).
252. Vanslyke, J.K., Deschenes, S.M. & Musil, L.S. Intracellular transport, assembly, and degradation of wild-type and disease-linked mutant gap junction proteins. *Molecular Biology of the Cell* **11**, 1933-1946 (2000).
253. Windoffer, R. et al. Visualization of gap junction mobility in living cells. *Cell and Tissue Research* **299**, 347-362 (2000).
254. Laird, D.W., Puranam, K.L. & Revel, J.P. Turnover and phosphorylation dynamics of connexin43 gap junction protein in cultured cardiac myocytes. *Biochemical Journal* **273**, 67-72 (1991).
255. Beardslee, M.A., Laing, J.G., Beyer, E.C. & Saffitz, J.E. Rapid turnover of connexin43 in the adult rat heart. *Circulation Research* **83**, 629-635 (1998).
256. Laird, D.W. Life cycle of connexins in health and disease. *Biochemical Journal* **394**, 527-543 (2006).
257. Thomas, T. et al. Mechanisms of Cx43 and Cx26 transport to the plasma membrane and gap junction regeneration. *Journal of Cell Science* **118**, 4451-4462 (2005).
258. Gaietta, G. et al. Multicolor and electron microscopic imaging of connexin trafficking. *Science* **296**, 503-507 (2002).
259. Marquart, K.H. So-called annular gap junctions in bone cells of normal mice. *Experientia* **33**, 270-272 (1977).
260. Sasaki, T. & Garant, P.R. Fate of annular gap junctions in the papillary cells of the enamel organ in the rat incisor. *Cell and Tissue Research* **246**, 523-530 (1986).
261. Murray, S.A., Nickel, B.M. & Gay, V.L. Endocytosis of connexin protein in adrenal cells. *Endocrine Research* **30**, 647-654 (2004).
262. Leithe, E. & Rivedal, E. Epidermal growth factor regulates ubiquitination, internalization and proteasome-dependent degradation of connexin43. *Journal of Cell Science* **117**, 1211-1220 (2004).
263. Thevenin, A.F. et al. Proteins and mechanisms regulating gap junction assembly, internalization, and degradation. *Physiology* **28**, 93-116 (2013).
264. Trosko, J.E. & Ruch, R.J. Gap junctions as targets for cancer chemoprevention and chemotherapy. *Current Drug Targets* **3**, 465-482 (2002).
265. Vinken, M. et al. Connexins and their channels in cell growth and cell death. *Cellular Signalling* **18**, 592-600 (2006).
266. Trosko, J.E. et al. Gap junctions and the regulation of cellular functions of stem cells during development and differentiation. *Methods* **20**, 245-264 (2000).
267. Krysko, D.V., Leybaert, L., Vandenabeele, P. & D'Herde, K. Gap junctions and the propagation of cell survival and cell death signals. *Apoptosis* **10**, 459-469 (2005).
268. Ruch, R.J. The role of gap junctional intercellular communication in neoplasia. *Annals of Clinical and Laboratory Science* **24**, 216-231 (1994).
269. Ruch, R.J. Role of gap junctions in cellular growth control and neoplasia: evidence and mechanisms. *Gap Junctions* **49**, 535-554 (2000).
270. Lo, C.W. The role of gap junction membrane channels in development. *Journal of Bioenergetics and Biomembranes* **28**, 379-385 (1996).
271. Levin, M. Isolation and community: a review of the role of gap-junctional communication in embryonic patterning. *Journal of Membrane Biology* **185**, 177-192 (2002).
272. Kimura, H., Oyamada, Y., Ohshika, H., Mori, M. & Oyamada, N. Reversible inhibition of gap junctional intercellular communication, synchronous contraction, and synchronism of intracellular Ca^{2+} fluctuation in cultured neonatal rat cardiac myocytes by heptanol. *Experimental Cell Research* **220**, 348-356 (1995).
273. Severs, N.J. Cardiovascular disease. *Gap Junction-Mediated Intercellular Signalling in Health and Disease* **219**, 188-211 (1999).
274. Budd, S.L. & Lipton, S.A. Calcium tsunamis: do astrocytes transmit cell death messages via gap junctions during ischemia? *Nature Neuroscience* **1**, 431-432 (1998).

275. Michon, L. et al. Involvement of gap junctional communication in secretion. *Biochimica Et Biophysica Acta-Biomembranes* **1719**, 82-101 (2005).
276. Benninger, R.K.P., Head, W.S., Zhang, M., Satin, L.S. & Piston, D.W. Gap junctions and other mechanisms of cell-cell communication regulate basal insulin secretion in the pancreatic islet. *Journal of Physiology-London* **589**, 5453-5466 (2011).
277. Laird, D.W. The gap junction proteome and its relationship to disease. *Trends in Cell Biology* **20**, 92-101 (2010).
278. Loewenstein, W.R. & Kanno, Y. Intercellular communication and control of tissue growth - lack of communication between cancer cells. *Nature* **209**, 1248-1249 (1966).
279. Mesnil, M., Crespin, S., Avanzo, J.L. & Zaidan-Dagli, M.L. Defective gap junctional intercellular communication in the carcinogenic process. *Biochimica Et Biophysica Acta-Biomembranes* **1719**, 125-145 (2005).
280. Bergoffen, J. et al. Connexin mutations in x-linked Charcot-Marie-Tooth disease. *Science* **262**, 2039-2042 (1993).
281. Steel, K.P. A new era in the genetics of deafness. *New England Journal of Medicine* **339**, 1545-1547 (1998).
282. Krutovskikh, V. & Yamasaki, H. Connexin gene mutations in human genetic diseases. *Mutation Research* **462**, 197-207 (2000).
283. Giessmann, D., Theiss, C., Breipohl, W. & Meller, K. Microinjection of actin antibodies impaired gap junctional intercellular communication in lens epithelial cells *in vitro*. *Current Eye Research* **27**, 157-164 (2003).
284. Simon, A.M., McWhorter, A.R., Dones, J.A., Jackson, C.L. & Chen, H.D.R. Heart and head defects in mice lacking pairs of connexins. *Developmental Biology* **265**, 369-383 (2004).
285. Valiunas, V., Gemel, J., Brink, P.R. & Beyer, E.C. Gap junction channels formed by coexpressed connexin40 and connexin43. *American Journal of Physiology-Heart and Circulatory Physiology* **281**, H1675-H1689 (2001).
286. Larson, D.M., Carson, M.P. & Haudenschild, C.C. Junctional transfer of small molecules in cultured bovine brain microvascular endothelial cells and pericytes. *Microvascular Research* **34**, 184-199 (1987).
287. Abbaci, M., Barberi-Heyob, M., Blondel, W., Guillemin, F. & Didelon, J. Advantages and limitations of commonly used methods to assay the molecular permeability of gap junctional intercellular communication. *Biotechniques* **45**, 33-62 (2008).
288. Abbaci, M. et al. Gap junctional intercellular communication capacity by gap-FRAP technique: a comparative study. *Biotechnology Journal* **2**, 50-61 (2007).
289. Anagnostopoulou, A., Cao, J., Vultur, A., Firth, K. & Raptis, L. Examination of gap junctional, intercellular communication by *in situ* electroporation on two co-planar indium-tin oxide electrodes. *Molecular Oncology* **1**, 226-231 (2007).
290. Loewenstein, W.R. & Kanno, Y. Studies on an epithelial (gland) cell junction: I. Modifications of surface membrane permeability. *The Journal of Cell Biology* **22**, 565-586 (1964).
291. El-Fouly, M.H., Trosko, J.E. & Chang, C.C. Scrape-loading and dye transfer. A rapid and simple technique to study gap junctional intercellular communication. *Experimental Cell Research* **168**, 422-430 (1987).
292. McKarns, S.C. & Doolittle, D.J. Limitations of the scrape-loading dye transfer technique to quantify inhibition of gap junctional intercellular communication. *Cell Biology and Toxicology* **8**, 89-103 (1992).
293. Djalilian, A.R. et al. Connexin 26 regulates epidermal barrier and wound remodeling and promotes psoriasiform response. *Journal of Clinical Investigation* **116**, 1243-1253 (2006).
294. Meda, P. Probing the function of connexin channels in primary tissues. *Methods* **20**, 232-244 (2000).
295. Bittman, K., Becker, D.L., Cicirata, F. & Parnavelas, J.G. Connexin expression in homotypic and heterotypic cell coupling in the developing cerebral cortex. *Journal of Comparative Neurology* **443**, 201-212 (2002).

296. Goldberg, G.S., Behlberger, J.F. & Naus, C.C.G. A pre-loading method of evaluating gap junctional communication by fluorescent dye transfer. *Biotechniques* **18**, 490-497 (1995).
297. Tomasetto, C., Neveu, M.J., Daley, J., Horan, P.K. & Sager, R. Specificity of gap junction communication among human mammary cells and connexin transfectants in culture. *Journal of Cell Biology* **122**, 157-167 (1993).
298. Wade, M.H., Trosko, J.E. & Schindler, M. A fluorescence photobleaching assay of gap junction-mediated communication between human cells. *Science* **232**, 525-528 (1986).
299. Raptis, L.H., Brownell, H.L., Firth, K.L. & Mackenzie, L.W. A novel technique for the study of intercellular, junctional communication - electroporation of adherent cells on a partly conductive slide. *DNA and Cell Biology* **13**, 963-975 (1994).
300. Hofgaard, J.P., Mollerup, S., Holstein-Rathlou, N.H. & Nielsen, M.S. Quantification of gap junctional intercellular communication based on digital image analysis. *American Journal of Physiology - Regulatory, Integrative and Comparative Physiology* **297**, R243-R247 (2009).
301. Tomai, E. et al. Gap junctional communication in cultured human lung carcinoma cells. *Lung Cancer* **23**, 223-231 (1999).
302. Geletu, M. et al. Stat3 is a positive regulator of gap junctional intercellular communication in cultured, human lung carcinoma cells. *BMC Cancer* **12**, :605 (2012).
303. Brownell, H.L. et al. Ras is involved in gap junction closure in proliferating fibroblasts or preadipocytes but not in differentiated adipocytes. *DNA and Cell Biology* **15**, 443-451 (1996).
304. Vultur, A. et al. Gap junctional intercellular communication in cells isolated from urethane-induced tumors in A/J mice. *DNA and Cell Biology* **22**, 33-40 (2003).
305. De Vuyst, E. et al. *In situ* bipolar electroporation for localized cell loading with reporter dyes and investigating gap junctional coupling. *Biophysical Journal* **94**, 469-479 (2008).
306. Dakin, K., Zhao, Y.R. & Li, W.H. LAMP, a new imaging assay of gap junctional communication unveils that Ca^{2+} influx inhibits cell coupling. *Nature Methods* **2**, 55-62 (2005).
307. Li, W.H. & Zheng, G.H. Photoactivatable fluorophores and techniques for biological imaging applications. *Photochemical and Photobiological Sciences* **11**, 460-471 (2012).
308. Zhao, Y.R. et al. New caged coumarin fluorophores with extraordinary uncaging cross sections suitable for biological imaging applications. *Journal of the American Chemical Society* **126**, 4653-4663 (2004).
309. Yang, S. & Li, W.H. Assaying dynamic cell-cell junctional communication using noninvasive and quantitative fluorescence imaging techniques: LAMP and infrared-LAMP. *Nature Protocols* **4**, 94-101 (2009).
310. Chin, C.D. et al. Microfluidics-based diagnostics of infectious diseases in the developing world. *Nature Medicine* **17**, 1015-1020 (2011).
311. Cheng, X.H. et al. A microfluidic device for practical label-free CD4+T cell counting of HIV-infected subjects. *Lab on a Chip* **7**, 170-178 (2007).
312. Kruger, J. et al. Development of a microfluidic device for fluorescence activated cell sorting. *Journal of Micromechanics and Microengineering* **12**, 486-494 (2002).
313. Pihl, J., Karlsson, M. & Chiu, D.T. Microfluidic technologies in drug discovery. *Drug Discovery Today* **10**, 1377-1383 (2005).
314. Hung, P.J., Lee, P.J., Sabounchi, P., Lin, R. & Lee, L.P. Continuous perfusion microfluidic cell culture array for high-throughput cell-based assays. *Biotechnology and Bioengineering* **89**, 1-8 (2005).
315. Yi, C.Q., Li, C.W., Ji, S.L. & Yang, M.S. Microfluidics technology for manipulation and analysis of biological cells. *Analytica Chimica Acta* **560**, 1-23 (2006).
316. Geng, T. & Lu, C. Microfluidic electroporation for cellular analysis and delivery. *Lab on a Chip* **13**, 3803-3821 (2013).

317. Kang, L.F., Chung, B.G., Langer, R. & Khademhosseini, A. Microfluidics for drug discovery and development: From target selection to product lifecycle management. *Drug Discovery Today* **13**, 1-13 (2008).
318. Chen, S. & Lee, L.P. Non-invasive microfluidic gap junction assay. *Integrative Biology* **2**, 130-138 (2010).
319. Mroue, R.M., El-Sabban, M.E. & Talhouk, R.S. Connexins and the gap in context. *Integrative Biology* **3**, 255-266 (2011).
320. Bathany, C., Beahm, D., Felske, J.D., Sachs, F. & Hua, S.Z. High throughput assay of diffusion through Cx43 gap junction channels with a microfluidic chip. *Analytical Chemistry* **83**, 933-939 (2011).
321. Cooper, G.M. The Cell - A Molecular Approach 2nd Edition (Sunderland (MA): Sinauer Associates, 2000).
322. Neumann, E., Schaeferridder, M., Wang, Y. & Hofschneider, P.H. Gene-transfer into mouse lyoma cells by electroporation in high electric fields. *The EMBO Journal* **1**, 841-845 (1982).
323. Stolwijk, J.A. et al. Impedance analysis of adherent cells after *in situ* electroporation: Non-invasive monitoring during intracellular manipulations. *Biosensors and Bioelectronics* **26**, 4720-4727 (2011).
324. Mir, L.M., Banoun, H. & Paoletti, C. Introduction of definite amounts of nonpermeant molecules into living cells after electropermeabilization - direct access to the cytosol. *Experimental Cell Research* **175**, 15-25 (1988).
325. Dinchuk, J.E., Kelley, K.A. & Callahan, G.N. Flow cytometric analysis of transport activity in lymphocytes electroporated with a fluorescent organic anion dye. *Journal of Immunological Methods* **155**, 257-265 (1992).
326. Belehradek, J. et al. Electropermeabilization of cells in tissues assessed by the qualitative and quantitative electroloading of bleomycin. *Biochimica Et Biophysica Acta-Biomembranes* **1190**, 155-163 (1994).
327. Jaroszeski, M.J. et al. Toxicity of anticancer agents mediated by electroporation *in vitro*. *Anti-Cancer Drugs* **11**, 201-208 (2000).
328. Cemazar, M. et al. *In vivo* imaging of tumor growth after electrochemotherapy with cisplatin. *Biochemical and Biophysical Research Communications* **348**, 997-1002 (2006).
329. Matthews Ii, K.L., Aarsvold, J.N., Mintzer, R.A., Chen, C.-T. & Lee, R.C. Tc-99m pyrophosphate imaging of poloxamer-treated electroporated skeletal muscle in an *in vivo* rat model. *Burns* **32**, 755-764 (2006).
330. Engstrom, P.E., Persson, B.R.R. & Salford, L.G. Studies of *in vivo* electropermeabilization by gamma camera measurements of Tc-99m-DTPA. *Biochimica Et Biophysica Acta-General Subjects* **1473**, 321-328 (1999).
331. Spiller, D.G., Giles, R.V., Grzybowski, J., Tidd, D.M. & Clark, R.E. Improving the intracellular delivery and molecular efficacy of antisense oligonucleotides in chronic myeloid leukemia cells: a comparison of streptolysin-O permeabilization, electroporation, and lipophilic conjugation. *Blood* **91**, 4738-4746 (1998).
332. Chakrabarti, R., Wylie, D.E. & Schuster, S.M. Transfer of monoclonal antibodies into mammalian cells by electroporation. *Journal of Biological Chemistry* **264**, 15494-15500 (1989).
333. Dower, W.J., Miller, J.F. & Ragsdale, C.W. High efficiency transformation of *Escherichia coli* by high voltage electroporation. *Nucleic Acids Research* **16**, 6127-6145 (1988).
334. Saeboe-Larssen, S., Fossberg, E. & Gaudernack, G. mRNA-based electrotransfection of human dendritic cells and induction of cytotoxic T lymphocyte responses against the telomerase catalytic subunit (hTERT). *Journal of Immunological Methods* **259**, 191-203 (2002).
335. Teruel, M.N., Blanpied, T.A., Shen, K., Augustine, G.J. & Meyer, T. A versatile microporation technique for the transfection of cultured CNS neurons. *J Neurosci Methods* **93**, 37-48 (1999).

336. Gothelf, A., Mir, L.M. & Gehl, J. Electrochemotherapy: results of cancer treatment using enhanced delivery of bleomycin by electroporation. *Cancer Treatment Reviews* **29**, 371-387 (2003).
337. Mir, L.M. et al. Electrochemotherapy, a novel antitumor treatment - 1st clinical trial. *Comptes Rendus De L'Academie Des Sciences Serie III Sciences de la Vie* **313**, 613-618 (1991).
338. Domenge, C. et al. Antitumor electrochemotherapy - New advances in the clinical protocol. *Cancer* **77**, 956-963 (1996).
339. Mir, L.M. et al. Effective treatment of cutaneous and subcutaneous malignant tumours by electrochemotherapy. *British Journal of Cancer* **77**, 2336-2342 (1998).
340. Davalos, R.V., Mir, L.M. & Rubinsky, B. Tissue ablation with irreversible electroporation. *Annals of Biomedical Engineering* **33**, 223-231 (2005).
341. Miller, L., Leor, J. & Rubinsky, B. Cancer cells ablation with irreversible electroporation. *Technology in Cancer Research and Treatment* **4**, 699-705 (2005).
342. Al-Sakere, B. et al. Tumor ablation with irreversible electroporation. *PLOS One* **2**, e1135 (2007).
343. Rubinsky, B., Onik, G. & Mikus, P. Irreversible electroporation: A new ablation modality - Clinical implications. *Technology in Cancer Research & Treatment* **6**, 37-48 (2007).
344. Aihara, H. & Miyazaki, J. Gene transfer into muscle by electroporation *in vivo*. *Nature Biotechnology* **16**, 867-870 (1998).
345. Mir, L.M. Therapeutic perspectives of *in vivo* cell electropermeabilization. *Bioelectrochemistry* **53**, 1-10 (2001).
346. Gehl, J. Electroporation: theory and methods, perspectives for drug delivery, gene therapy and research. *Acta Physiologica Scandinavica* **177**, 437-447 (2003).
347. Neumann, E., Sowers, A.E. & Jordan, C.A. Electroporation and electrofusion in cell biology (Springer, 1989).
348. Weaver, J.C. Electroporation theory. Concepts and mechanisms. *Methods Mol Biol* **55**, 3-28 (1995).
349. Rols, M.P. Electropermeabilization, a physical method for the delivery of therapeutic molecules into cells. *Biochimica Et Biophysica Acta-Biomembranes* **1758**, 423-428 (2006).
350. Hibino, M., Itoh, H. & Kinosita, K. Time courses of cell electroporation as revealed by submicrosecond imaging of transmembrane potential. *Biophysical Journal* **64**, 1789-1800 (1993).
351. Rols, M.P., Golzio, M., Delteil, C. & Teissie, J. *In vitro* delivery of drugs and other molecules to cells. *Methods in Molecular Medicine* **37**, 83-97 (2000).
352. Valic, B. et al. Effect of electric field induced transmembrane potential on spheroidal cells: theory and experiment. *European Biophysics Journal with Biophysics Letters* **32**, 519-528 (2003).
353. Kinosita, K. & Tsong, T.Y. Voltage-induced pore formation and hemolysis of human erythrocytes. *Biochimica Et Biophysica Acta* **471**, 227-242 (1977).
354. Bernhardt, J. & Pauly, H. On the generation of potential differences across the membranes of ellipsoidal cells in an alternating electrical field. *Biophysik* **10**, 89-98 (1973).
355. Chen, C., Smye, S.W., Robinson, M.P. & Evans, J.A. Membrane electroporation theories: a review. *Medical and Biological Engineering and Computing* **44**, 5-14 (2006).
356. Gabriel, B. & Teissie, J. Direct observation in the millisecond time range of fluorescent molecule asymmetrical interaction with the electropermeabilized cell membrane. *Biophysical Journal* **73**, 2630-2637 (1997).
357. Teissie, J. & Rols, M.P. An experimental evaluation of the critical potential difference inducing cell membrane electropermeabilization. *Biophysical Journal* **65**, 409-413 (1993).

358. Gabriel, B. & Teissie, J. Time courses of mammalian cell electropermeabilization observed by millisecond imaging of membrane property changes during the pulse. *Biophysical Journal* **76**, 2158-2165 (1999).
359. Kotnik, T., Miklavcic, D. & Slivnik, T. Time course of transmembrane voltage induced by time-varying electric fields - a method for theoretical analysis and its application. *Bioelectrochemistry and Bioenergetics* **45**, 3-16 (1998).
360. Marszalek, P., Liu, D.S. & Tsong, T.Y. Schwan equation and transmembrane potential induced by alternating electric field. *Biophysical Journal* **58**, 1053-1058 (1990).
361. Tsong, T.Y. Electroporation of cell membranes. *Biophysical Journal* **60**, 297-306 (1991).
362. Zimmerma.U, Pilwat, G. & Riemann, F. Dielectric-breakdown of cell membranes. *Biophysical Journal* **14**, 881-899 (1974).
363. Teissie, J., Golzio, M. & Rols, M.P. Mechanisms of cell membrane electropermeabilization: a minireview of our present (lack of ?) knowledge. *Biochimica Et Biophysica Acta-General Subjects* **1724**, 270-280 (2005).
364. Prausnitz, M.R. et al. Millisecond measurement of transport during and after an electroporation pulse. *Biophysical Journal* **68**, 1864-1870 (1995).
365. Powell, K.T., Morgenthaler, A.W. & Weaver, J.C. Tissue electroporation - observation of reversible electrical breakdown in viable frog skin. *Biophysical Journal* **56**, 1163-1171 (1989).
366. Golzio, M., Rols, M.P. & Teissie, J. In vitro and *in vivo* electric field-mediated permeabilization, gene transfer, and expression. *Methods* **33**, 126-135 (2004).
367. Teruel, M.N. & Meyer, T. Electroporation-induced formation of individual calcium entry sites in the cell body and processes of adherent cells. *Biophysical Journal* **73**, 1785-1796 (1997).
368. Sowers, A.E. & Lieber, M.R. Electropore diameters, lifetimes, numbers, and locations in individual erythrocyte ghosts. *FEBS Letters* **205**, 179-184 (1986).
369. Rols, M.P. & Teissie, J. Electropermeabilization of mammalian cells - quantitative analysis of the phenomenon. *Biophysical Journal* **58**, 1089-1098 (1990).
370. Benz, R. & Zimmermann, U. The resealing process of lipid bilayers after reversible electrical breakdown. *Biochimica Et Biophysica Acta* **640**, 169-178 (1981).
371. Rols, M.P., Delteil, C., Golzio, M. & Teissie, J. Control by ATP and ADP of voltage-induced mammalian-cell-membrane permeabilization, gene transfer and resulting expression. *European Journal of Biochemistry* **254**, 382-388 (1998).
372. Dressler, V., Schwister, K., Haest, C.W.M. & Deuticke, B. Dielectric breakdown of the erythrocyte membrane enhances transbilayer mobility of phospholipids. *Biochimica Et Biophysica Acta* **732**, 304-307 (1983).
373. Haest, C.W.M., Kamp, D. & Deuticke, B. Transbilayer reorientation of phospholipid probes in the human erythrocyte membrane. Lessons from studies on electroporated and resealed cells. *Biochimica Et Biophysica Acta-Biomembranes* **1325**, 17-33 (1997).
374. Abidor, I.G. et al. Electric breakdown of bilayer lipid-membranes .1. Main experimental facts and their qualitative discussion. *Bioelectrochemistry and Bioenergetics* **6**, 37-52 (1979).
375. Litster, J.D. Stability of lipid bilayers and red blood cell membranes. *Physics Letters A* **A 53**, 193-194 (1975).
376. Taupin, C., Dvolaitzky, M. & Sauterey, C. Osmotic-pressure induced pores in phospholipid vesicles. *Biochemistry* **14**, 4771-4775 (1975).
377. Neumann, E., Kakorin, S. & Toensing, K. Fundamentals of electroporative delivery of drugs and genes. *Bioelectrochemistry and Bioenergetics* **48**, 3-16 (1999).
378. Lewis, T.J. A model for bilayer membrane electroporation based on resultant electromechanical stress. *Ieee Transactions on Dielectrics and Electrical Insulation* **10**, 769-777 (2003).
379. Tarek, M. Membrane electroporation: a molecular dynamics simulation. *Biophysical Journal* **88**, 4045-4053 (2005).

380. Escoffre, J.M. et al. What is (still not) known of the mechanism by which electroporation mediates gene transfer and expression in cells and tissues. *Molecular Biotechnology* **41**, 286-295 (2009).
381. Tieleman, D.P., Leontiadou, H., Mark, A.E. & Marrink, S.J. Simulation of pore formation in lipid bilayers by mechanical stress and electric fields. *Journal of the American Chemical Society* **125**, 6382-6383 (2003).
382. Raptis, L. & Firth, K.L. Laboratory Methods - Electroporation of adherent cells *in situ*. *DNA and Cell Biology* **9**, 615-621 (1990).
383. Wegener, J., Keese, C.R. & Giaever, I. Recovery of adherent cells after *in situ* electroporation monitored electrically. *Biotechniques* **33**, 348-357 (2002).
384. Olofsson, J. et al. Scanning electroporation of selected areas of adherent cell cultures. *Analytical Chemistry* **79**, 4410-4418 (2007).
385. Ishibashi, T., Takoh, K., Kaji, H., Abe, T. & Nishizawa, M. A porous membrane-based culture substrate for localized *in situ* electroporation of adherent mammalian cells. *Sensors and Actuators B-Chemical* **128**, 5-11 (2007).
386. Lin, Y.C., Li, M., Fan, C.S. & Wu, L.W. A microchip for electroporation of primary endothelial cells. *Sensors and Actuators a-Physical* **108**, 12-19 (2003).
387. Kang, W. et al. Microfluidic device for stem cell differentiation and localized electroporation of postmitotic neurons. *Lab on a Chip* **14**, 4486-4495 (2014).
388. Ghosh, P.M., Keese, C.R. & Giaever, I. Monitoring electropermeabilization in the plasma-membrane of adherent mammalian cells. *Biophysical Journal* **64**, 1602-1609 (1993).
389. Yang, T.A., Heiser, W.C. & Sedivy, J.M. Efficient *in situ* electroporation of mammalian cells grown on microporous membranes. *Nucleic Acids Research* **23**, 2803-2810 (1995).
390. Kanthou, C. et al. The endothelial cytoskeleton as a target of electroporation-based therapies. *Molecular Cancer Therapeutics* **5**, 3145-3152 (2006).
391. Olbrich, M., Rebollar, E., Heitz, J., Frischauf, I. & Romanin, C. Electroporation chip for adherent cells on photochemically modified polymer surfaces. *Applied Physics Letters* **92**, 013901-013903 (2008).
392. Vassanelli, S. et al. Space and time-resolved gene expression experiments on cultured mammalian cells by a single-cell electroporation microarray. *New Biotechnology* **25**, 55-67 (2008).
393. Movahed, S. & Li, D.Q. Microfluidics cell electroporation. *Microfluidics and Nanofluidics* **10**, 703-734 (2011).
394. Fox, M.B. et al. Electroporation of cells in microfluidic devices: a review. *Analytical and Bioanalytical Chemistry* **385**, 474-485 (2006).
395. Raptis, L.H., Liu, S.K.W., Firth, K.L., Stiles, C.D. & Alberta, J.A. Electroporation of peptides into adherent cells *in situ*. *Biotechniques* **18**, 104-106 (1995).
396. Rui, M., Chen, Y.Y., Zhang, Y.M. & Ma, D.L. Transfer of anti-TFAR19 monoclonal antibody into HeLa cells by *in situ* electroporation can inhibit the apoptosis. *Life Sciences* **71**, 1771-1778 (2002).
397. Zheng, Q. & Chang, D.C. High-efficiency gene transfection by *in situ* electroporation of cultured cells. *Biochimica et Biophysica Acta - Gene Structure and Expression* **1088**, 104-110 (1991).
398. Teruel, M.N., Blanpied, T.A., Shen, K., Augustine, G.J. & Meyer, T. A versatile microporation technique for the transfection of cultured CNS neurons. *Journal of Neuroscience Methods* **93**, 37-48 (1999).
399. Jain, T. & Muthuswamy, J. Bio-chip for spatially controlled transfection of nucleic acid payloads into cells in a culture. *Lab Chip* **7**, 1004-1011 (2007).
400. Jain, T., Papas, A., Jadhav, A., McBride, R. & Saez, E. In situ electroporation of surface-bound siRNAs in microwell arrays. *Lab on a Chip* **12**, 939-947 (2012).
401. Brownell, H.L., Lydon, N.B., Schaefer, E., Roberts, T.M. & Raptis, L. Inhibition of epidermal growth factor-mediated ERK1/2 activation by *in situ* electroporation of nonpermeant [(alkylamino)methyl]acrylophenone derivatives. *DNA and Cell Biology* **17**, 265-274 (1998).

402. Kim, T.K. & Eberwine, J.H. Mammalian cell transfection: the present and the future. *Analytical and Bioanalytical Chemistry* **397**, 3173-3178 (2010).
403. Schieffer, B., Paxton, W.G., Chai, Q., Marrero, M.B. & Bernstein, K.E. Angiotensin II controls p21(ras) activity via pp60(c-src). *Journal of Biological Chemistry* **271**, 10329-10333 (1996).
404. Zhou, W., Xiong, Z.G., Liu, Y., Yao, C.G. & Li, C.X. Low voltage irreversible electroporation induced apoptosis in HeLa cells. *Journal of Cancer Research and Therapeutics* **8**, 80-85 (2012).
405. Kinosita, K. & Tsong, T.Y. Voltage-induced conductance in human-erythrocyte membranes. *Biochimica Et Biophysica Acta* **554**, 479-497 (1979).
406. Pavlin, M. et al. Effect of cell electroporation on the conductivity of a cell suspension. *Biophysical Journal* **88**, 4378-4390 (2005).
407. Huang, Y. & Rubinsky, B. Micro-electroporation: improving the efficiency and understanding of electrical permeabilization of cells. *Biomedical Microdevices* **2**, 145-150 (1999).
408. He, H.Q., Chang, D.C. & Lee, Y.K. Nonlinear current response of micro electroporation and resealing dynamics for human cancer cells. *Bioelectrochemistry* **72**, 161-168 (2008).
409. Suntharalingam, M. & Wente, S.R. Peering through the pore: nuclear pore complex structure, assembly, and function. *Developmental Cell* **4**, 775-789 (2003).
410. Chen, S.J., Bradley, M.E. & Lee, T.C. Chemical hypoxia triggers apoptosis of cultured neonatal rat cardiac myocytes: modulation by calcium-regulated proteases and protein kinases. *Molecular and Cellular Biochemistry* **178**, 141-149 (1998).
411. Lizard, G. et al. Kinetics of plasma membrane and mitochondrial alterations in cells undergoing apoptosis. *Cytometry* **21**, 275-283 (1995).
412. Frankfurt, O.S. & Krishan, A. Identification of apoptotic cells by formamide-induced DNA denaturation in condensed chromatin. *Journal of Histochemistry & Cytochemistry* **49**, 369-378 (2001).
413. Wilson, D.F. & Chance, B. Azide inhibition of mitochondrial electron transport I. The aerobic steady state of succinate oxidation. *Biochimica et Biophysica Acta (BBA) - Bioenergetics* **131**, 421-430 (1967).
414. Keilin, D. The action of sodium azide on cellular respiration and on some catalytic oxidation reactions. *Proceedings of the Royal Society of London. Series B, Biological Sciences* **121**, 165-173 (1936).
415. Bennett, M.C., Mlady, G.W., Kwon, Y.H. & Rose, G.M. Chronic in vivo sodium azide infusion induces selective and stable inhibition of cytochrome c oxidase. *Journal of Neurochemistry* **66**, 2606-2611 (1996).
416. Ziabreva, I. et al. Injury and differentiation following inhibition of mitochondrial respiratory chain complex IV in rat oligodendrocytes. *Glia* **58**, 1827-1837 (2010).
417. Berndt, J.D., Callaway, N.L. & Gonzalez-Lima, F. Effects of chronic sodium azide on brain and muscle cytochrome oxidase activity: A potential model to investigate environmental contributions to neurodegenerative diseases. *Journal of Toxicology and Environmental Health-Part A* **63**, 67-77 (2001).
418. Raicu, P. & Mixich, F. Cytogenetic effects of sodium azide encapsulated in liposomes on heteroploid cell cultures. *Mutation Research* **283**, 215-219 (1992).
419. Stolwijk, J.A., Electric manipulation and impedance analysis of adherent cells on gold-film electrodes. (University of Regensburg, 2012).
420. Tounekti, O., Belehradek, J. & Mir, L.M. Bleomycin, an apoptosis mimetic drug. *Bulletin Du Cancer* **81**, 1043-1049 (1994).
421. Gehl, J., Skovsgaard, T. & Mir, L.M. Enhancement of cytotoxicity by electropermeabilization: an improved method for screening drugs. *Anti-Cancer Drugs* **9**, 319-325 (1998).
422. Povirk, L.F. DNA damage and mutagenesis by radiomimetic DNA-cleaving agents: Bleomycin, neocarzinostatin and other enediynes. *Mutation Research-Fundamental and Molecular Mechanisms of Mutagenesis* **355**, 71-89 (1996).

423. Bradley, M.O. & Kohn, K.W. X-ray-induced DNA double strand break production and repair in mammalian cells as measured by neutral filter elution. *Nucleic Acids Research* **7**, 793-804 (1979).
424. Muller, M. et al. p53 activates the CD95 (APO-1/Fas) gene in response to DNA damage by anticancer drugs. *The Journal of Experimental Medicine* **188**, 2033-2045 (1998).
425. Nelson, W.G. & Kastan, M.B. DNA strand breaks - the DNA-template alterations that trigger P53-dependent DNA-damage response pathways. *Molecular and Cellular Biology* **14**, 1815-1823 (1994).
426. Stewart, W.W. Functional connections between cells as revealed by dye-coupling with a highly fluorescent naphthalimide tracer. *Cell* **14**, 741-759 (1978).
427. Bahnson, A.B. & Boggs, S.S. Addition of serum to electroporated cells enhances survival and transfection efficiency. *Biochemical and Biophysical Research Communications* **171**, 752-757 (1990).
428. Divirgilio, F., Fasolato, C. & Steinberg, T.H. Inhibitors of membrane-transport system for organic anions block Fura-2 excretion from Pc12 and N2a cells. *Biochemical Journal* **256**, 959-963 (1988).
429. Neumann, E., Toensing, K., Kakorin, S., Budde, P. & Frey, J. Mechanism of electroporative dye uptake by mouse B cells. *Biophysical Journal* **74**, 98-108 (1998).
430. Ghartey-Tagoe, E.B., Morgan, J.S., Ahmed, K., Neish, A.S. & Prausnitz, M.R. Electroporation-mediated delivery of molecules to model intestinal epithelia. *International Journal of Pharmaceutics* **270**, 127-138 (2004).
431. Canatella, P.J., Karr, J.F., Petros, J.A. & Prausnitz, M.R. Quantitative study of electroporation-mediated molecular uptake and cell viability. *Biophysical Journal* **80**, 755-764 (2001).
432. Kim, J.A. et al. A multi-channel electroporation microchip for gene transfection in mammalian cells. *Biosensors and Bioelectronics* **22**, 3273-3277 (2007).
433. Wang, S., Kara, M. & Krishman, T.R. Transdermal delivery of cyclosporin-A using electroporation. *Journal of Controlled Release* **50**, 61-70 (1998).
434. Rols, M.P. et al. *In vivo* electrically mediated protein and gene transfer in murine melanoma. *Nature Biotechnology* **16**, 168-171 (1998).
435. Suzuki, T., Shin, B.C., Fujikura, K., Matsuzaki, T. & Takata, K. Direct gene transfer into rat liver cells by *in vivo* electroporation. *FEBS Letters* **425**, 436-440 (1998).
436. Mir, L.M. et al. High-efficiency gene transfer into skeletal muscle mediated by electric pulses. *Proceedings of the National Academy of Sciences of the United States of America* **96**, 4262-4267 (1999).
437. Miyahara, M., Aoi, M., Inoue-Kashino, N., Kashino, Y. & Ifuku, K. Highly efficient transformation of the diatom *Phaeodactylum tricornutum* by multi-pulse electroporation. *Bioscience Biotechnology and Biochemistry* **77**, 874-876 (2013).
438. Brown, R.E. et al. Multiple-pulse electroporation - uptake of a macromolecule by individual cells of *Saccharomyces cerevisiae*. *Bioelectrochemistry and Bioenergetics* **28**, 235-245 (1992).
439. Sato, E., Suzuki, T., Hoshi, N., Sugino, T. & Hasegawa, H. Sodium azide induces necrotic cell death in rat squamous cell carcinoma SCC131. *Medical Molecular Morphology* **41**, 211-220 (2008).
440. Selvatici, R. et al. Sodium azide induced neuronal damage *in vitro*: evidence for non-apoptotic cell death. *Neurochemical Research* **34**, 909-916 (2009).
441. Mir, L.M., Tounekti, O. & Orlowski, S. Bleomycin: revival of an old drug. *General Pharmacology* **27**, 745-748 (1996).
442. Todorovic, V., Sersa, G., Flisar, K. & Cemazar, M. Enhanced cytotoxicity of bleomycin and cisplatin after electroporation in murine colorectal carcinoma cells. *Radiology and Oncology* **43**, 264-273 (2009).
443. Tounekti, O., Kenani, A., Foray, N., Orlowski, S. & Mir, L.M. The ratio of single- to double-strand DNA breaks and their absolute values determine cell death pathway. *British Journal of Cancer* **84**, 1272-1279 (2001).

444. Campana, L. et al. Bleomycin-based electrochemotherapy: clinical outcome from a single institution's experience with 52 patients. *Annals of Surgical Oncology* **16**, 191-199 (2009).
445. Glass, L.F. et al. Bleomycin-mediated electrochemotherapy of basal cell carcinoma. *Journal of the American Academy of Dermatology* **34**, 82-86 (1996).
446. Kitamura, A. Bleomycin-mediated electrochemotherapy in mouse NR-S1 carcinoma. *Cancer Chemotherapy and Pharmacology* **51**, 359-362 (2003).
447. Glass, L.F., Jaroszeski, M., Gilbert, R., Reintgen, D.S. & Heller, R. Intralesional bleomycin-mediated electrochemotherapy in 20 patients with basal cell carcinoma. *Journal of the American Academy of Dermatology* **37**, 596-599 (1997).
448. Larkin, J.O. et al. Electrochemotherapy - aspects of preclinical development and early clinical experience. *Annals of Surgery* **245**, 469-479 (2007).
449. Ueki, T.-i. et al. Antitumour effect of electrochemotherapy with bleomycin on human prostate cancer xenograft. *BJU International* **102**, 1467-1471 (2008).
450. Yao, J.A. et al. Disruption of gap junctions attenuates aminoglycoside-elicited renal tubular cell injury. *British Journal of Pharmacology* **160**, 2055-2068 (2010).
451. Shao, Q., Wang, H.L., McLachlan, E., Veitch, G.I.L. & Laird, D.W. Down-regulation of Cx43 by retroviral delivery of small interfering RNA promotes an aggressive breast cancer cell phenotype. *Cancer Research* **65**, 2705-2711 (2005).
452. Feldman, P.A., Kim, J. & Laird, D.W. Loss of gap junction plaques and inhibition of intercellular communication in ilimaquinone-treated BICR-M1R(k) and NRK cells. *Journal of Membrane Biology* **155**, 275-287 (1997).
453. Shin, J.L., Solan, J.L. & Lampe, P.D. The regulatory role of the C-terminal domain of connexin43. *Cell Communication and Adhesion* **8**, 271-275 (2001).
454. Savarin, P. et al. A central role for polyamines in microtubule assembly in cells. *Biochemical Journal* **430**, 151-159 (2010).
455. Berthoud, V.M. et al. Heteromeric connexons formed by the lens connexins, connexin43 and connexin56. *European Journal of Cell Biology* **80**, 11-19 (2001).
456. Chao, D.S. et al. SNARE membrane trafficking dynamics *in vivo*. *Journal of Cell Biology* **144**, 869-881 (1999).
457. Bases, R. & Mendez, F. Repair of ionizing-radiation damage in primate α-DNA transfected into rat cells. *International Journal of Radiation Biology* **62**, 21-32 (1992).
458. Kisurina-Evgenieva, O. et al. Multiple mechanisms regulate NuMA dynamics at spindle poles. *Journal of Cell Science* **117**, 6391-6400 (2004).
459. Weiss, M., Elsner, M., Kartberg, F. & Nilsson, T. Anomalous subdiffusion is a measure for cytoplasmic crowding in living cells. *Biophysical Journal* **87**, 3518-3524 (2004).
460. Erikson, A., Andersen, H.N., Naess, S.N., Sikorski, P. & Davies, C.d.L. Physical and chemical modifications of collagen gels: impact on diffusion. *Biopolymers* **89**, 135-143 (2008).
461. Bouille, C., Mesnil, M., Barriere, H. & Gabrion, J. Gap junctional intercellular communication between cultured ependymal cells, revealed by Lucifer Yellow CH transfer and freeze fracture. *Glia* **4**, 25-36 (1991).
462. Brownell, H.L., Whitfield, J.F. & Raptis, L. Cellular Ras partly mediates gap junction closure by the polyoma virus middle tumor antigen. *Cancer Lett* **103**, 99-106 (1996).
463. Wei, C.-J., Francis, R., Xu, X. & Lo, C.W. Connexin43 associated with an N-cadherin-containing multiprotein complex is required for gap junction formation in NIH3T3 cells. *Journal of Biological Chemistry* **280**, 19925-19936 (2005).
464. Bukauskas, F.F. & Peracchia, C. Two distinct gating mechanisms in gap junction channels: CO2-sensitive and voltage-sensitive. *Biophysical Journal* **72**, 2137-2142 (1997).
465. Spray, D.C., Stern, J.H., Harris, A.L. & Bennett, M.V. Gap junctional conductance: comparison of sensitivities to H and Ca ions. *Proceedings of the National Academy of Sciences of the United States of America* **79**, 441-445 (1982).

466. Peracchia, C., Bernardini, G. & Peracchia, L.L. Is calmodulin involved in the regulation of gap junction permeability. *Pflugers Archiv-European Journal of Physiology* **399**, 152-154 (1983).
467. Peracchia, C., Sotkis, A., Wang, X.G., Peracchia, L.L. & Persechini, A. Calmodulin directly gates gap junction channels. *Journal of Biological Chemistry* **275**, 26220-26224 (2000).
468. Burr, G.S., Mitchell, C.K., Keflemariam, Y.J., Heidelberger, R. & O'Brien, J. Calcium-dependent binding of calmodulin to neuronal gap junction proteins. *Biochemical and Biophysical Research Communications* **335**, 1191-1198 (2005).
469. Török, K., Stauffer, K. & Evans, W.H. Connexin 32 of gap junctions contains two cytoplasmic calmodulin-binding domains. *The Biochemical Journal* **326**, 479-483 (1997).
470. Lurtz, M.M. & Louis, C.F. Intracellular calcium regulation of connexin43. *American Journal of Physiology - Cell Physiology* **293**, C1806-C1813 (2007).
471. Harris, A.L. Emerging issues of connexin channels: biophysics fills the gap. *Quarterly Reviews of Biophysics* **34**, 325-472 (2001).
472. Tsuji, A., Terasaki, T., Tamai, I. & Takeda, K. *In vivo* evidence for carrier-mediated uptake of β-lactam antibiotics through organic anion transport-systems in rat kidney and liver. *Journal of Pharmacology and Experimental Therapeutics* **253**, 315-320 (1990).
473. Sauvant, C., Holzinger, H. & Gekle, M. Prostaglandin E-2 inhibits its own renal transport by downregulation of organic anion transporters rOAT1 and rOAT3. *Journal of the American Society of Nephrology* **17**, 46-53 (2006).
474. Gerard, C., Boudier, J.A., Mauchamp, J. & Verrier, B. Evidence for probenecid-sensitive organic anion transporters on polarized thyroid cells in culture. *Journal of Cellular Physiology* **144**, 354-364 (1990).
475. Steinberg, T.H., Newman, A.S., Swanson, J.A. & Silverstein, S.C. Macrophages possess probenecid-inhibitable organic anion transporters that remove fluorescent dyes from the cytoplasmic matrix. *Journal of Cell Biology* **105**, 2695-2702 (1987).
476. Juszczak, G.R. & Swiergiel, A.H. Properties of gap junction blockers and their behavioural, cognitive and electrophysiological effects: Animal and human studies. *Progress in Neuro-Psychopharmacology and Biological Psychiatry* **33**, 181-198 (2009).
477. Loewenstein, W.R. Junctional intercellular communication: the cell-to-cell membrane channel. *Physiological Reviews* **61**, 829-913 (1981).
478. Rols, M.-P. & Teissié, J. Electropermeabilization of mammalian cells to macromolecules: control by pulse duration. *Biophysical Journal* **75**, 1415-1423 (1998).
479. Hartmann, C., Elektroporation von *in vitro*-transkribierter RNA in adhärente Zellen. (Westfälische Wilhelms-Universität, Münster, 2003).
480. Goldenberg, R.C.S. et al. Modulation of gap junction mediated intercellular communication in TM3 Leydig cells. *Journal of Endocrinology* **177**, 327-335 (2003).
481. Buzea, C., Pacheco, I.I. & Robbie, K. Nanomaterials and nanoparticles: sources and toxicity. *Biointerphases* **2**, MR17-MR71 (2007).
482. Nam, J.-M., Thaxton, C.S. & Mirkin, C.A. Nanoparticle-based bio-bar codes for the ultrasensitive detection of proteins. *Science* **301**, 1884-1886 (2003).
483. You, C.C. et al. Detection and identification of proteins using nanoparticle-fluorescent polymer 'chemical nose' sensors. *Nature Nanotechnology* **2**, 318-323 (2007).
484. Liu, J. & Lu, Y. Preparation of aptamer-linked gold nanoparticle purple aggregates for colorimetric sensing of analytes. *Nature Protocols* **1**, 246-252 (2006).
485. Hagenhoff, B.B., D.; Tallarek, E.; Moellers, R.; Niehuis, E.; Sperber, M.; Goricnik, B.; Wegener, J. . Detection of micro- and nano-particles in animal cells by ToF-SIMS 3D analysis. *Surface and Interface Analysis* **45**, 315 - 319 (2013).
486. Chang, E., Thekkek, N., Yu, W.W., Colvin, V.L. & Drezek, R. Evaluation of quantum dot cytotoxicity based on intracellular uptake. *Small* **2**, 1412-1417 (2006).

487. West, M.A., Bretscher, M.S. & Watts, C. Distinct endocytotic pathways in epidermal growth factor-stimulated human carcinoma A431 cells. *The Journal of Cell Biology* **109**, 2731-2739 (1989).
488. Liu, N.Q. et al. Human immunodeficiency virus type 1 enters brain microvascular endothelia by macropinocytosis dependent on lipid rafts and the mitogen-activated protein kinase signaling pathway. *Journal of Virology* **76**, 6689-6700 (2002).
489. Frohlich, E. The role of surface charge in cellular uptake and cytotoxicity of medical nanoparticles. *International Journal of Nanomedicine* **7**, 5577-5591 (2012).
490. He, C.B., Hu, Y.P., Yin, L.C., Tang, C. & Yin, C.H. Effects of particle size and surface charge on cellular uptake and biodistribution of polymeric nanoparticles. *Biomaterials* **31**, 3657-3666 (2010).
491. Win, K.Y. & Feng, S.S. Effects of particle size and surface coating on cellular uptake of polymeric nanoparticles for oral delivery of anticancer drugs. *Biomaterials* **26**, 2713-2722 (2005).
492. Gao, H.J., Shi, W.D. & Freund, L.B. Mechanics of receptor-mediated endocytosis. *Proceedings of the National Academy of Sciences of the United States of America* **102**, 9469-9474 (2005).
493. Opp, D. et al. Use of electric cell-substrate impedance sensing to assess *in vitro* cytotoxicity. *Biosensors and Bioelectronics* **24**, 2625-2629 (2009).
494. Lovelady, D.C., Friedman, J., Patel, S., Rabson, D.A. & Lo, C.M. Detecting effects of low levels of cytochalasin B in 3T3 fibroblast cultures by analysis of electrical noise obtained from cellular micromotion. *Biosensors and Bioelectronics* **24**, 2250-2254 (2009).
495. Friedl, P. & Gilmour, D. Collective cell migration in morphogenesis, regeneration and cancer. *Nature Reviews Molecular Cell Biology* **10**, 445-457 (2009).
496. Rorth, P. Collective cell migration. *Annual Review of Cell and Developmental Biology* **25**, 407-429 (2009).
497. MacLennan, D.H. & Kranias, E.G. Phospholamban: a crucial regulator of cardiac contractility. *Nature Reviews Molecular Cell Biology* **4**, 566-577 (2003).
498. Ringer, S. A further contribution regarding the influence of the different constituents of the blood on the contraction of the heart. *The Journal of Physiology* **4**, 29-42 (1883).
499. Fabiato, A. & Fabiato, F. Contractions induced by a calcium-triggered release of calcium from the sarcoplasmic reticulum of single skinned cardiac cells. *The Journal of Physiology* **249**, 469-495 (1975).
500. Fabiato, A. Calcium-induced release of calcium from the cardiac sarcoplasmic reticulum. *American Journal of Physiology - Cell Physiology* **245**, C1-C14 (1983).
501. Bodi, I., Mikala, G., Koch, S.E., Akhter, S.A. & Schwartz, A. The L-type calcium channel in the heart: the beat goes on. *Journal of Clinical Investigation* **115**, 3306-3317 (2005).
502. Viola, H.M. & Hool, L.C. Cross-talk between L-type Ca^{2+} channels and mitochondria. *Clinical and Experimental Pharmacology & Physiology* **37**, 229-35 (2010).
503. Bers, D.M. Cardiac excitation-contraction coupling. *Nature* **415**, 198-205 (2002).
504. Li, L., Desantiago, J., Chu, G.X., Kranias, E.G. & Bers, D.M. Phosphorylation of phospholamban and troponin I in beta-adrenergic-induced acceleration of cardiac relaxation. *American Journal of Physiology-Heart and Circulatory Physiology* **278**, H769-H779 (2000).
505. Barr, L., Dewey, M.M. & Berger, W. Propagation of action potentials and structure of nexus in cardiac muscle. *Journal of General Physiology* **48**, 797-823 (1965).
506. Spray, D.C. & Burt, J.M. Structure-activity relations of the cardiac gap junction channel. *American Journal of Physiology - Cell Physiology* **258**, C195-C205 (1990).
507. Nel, A.E. et al. Understanding biophysicochemical interactions at the nano-bio interface. *Nature Materials* **8**, 543-557 (2009).
508. He, Q.J., Zhang, Z.W., Gao, Y., Shi, J.L. & Li, Y.P. Intracellular localization and cytotoxicity of spherical mesoporous silica nano- and microparticles. *Small* **5**, 2722-2729 (2009).

509. Sun, W. et al. Endocytosis of a single mesoporous silica nanoparticle into a human lung cancer cell observed by differential interference contrast microscopy. *Analalytical and Bioanalytical Chemistry* **391**, 2119-2125 (2008).
510. Yu, K. et al. Toxicity of amorphous silica nanoparticles in mouse keratinocytes. *Journal of Nanoparticle Research* **11**, 15-24 (2009).
511. Foster, K.A., Yazdanian, M. & Audus, K.L. Microparticulate uptake mechanisms of *in vitro* cell culture models of the respiratory epithelium. *Journal of Pharmacy and Pharmacology* **53**, 57-66 (2001).
512. Carr, K.E., Hazzard, R.A., Reid, S. & Hodges, G.M. The effect of size on uptake of orally administered latex microparticles in the small intestine and transport to mesenteric lymph nodes. *Pharmaceutical Research* **13**, 1205-1209 (1996).
513. Vallhov, H., Gabrielsson, S., Stromme, M., Scheynius, A. & Garcia-Bennett, A.E. Mesoporous silica particles induce size dependent effects on human dendritic cells. *Nano Letters* **7**, 3576-3582 (2007).
514. Mayor, S. & Pagano, R.E. Pathways of clathrin-independent endocytosis. *Nature Reviews Molecular Cell Biology* **8**, 603-612 (2007).
515. Kirkham, M. & Parton, R.G. Clathrin-independent endocytosis: New insights into caveolae and non-caveolar lipid raft carriers. *Biochimica Et Biophysica Acta-Molecular Cell Research* **1745**, 273-286 (2005).
516. Swanson, J.A. Shaping cups into phagosomes and macropinosomes. *Nature Reviews Molecular Cell Biology* **9**, 639-649 (2008).
517. Ivanov, A.I. Pharmacological inhibition of endocytic pathways: is it specific enough to be useful? *Methods in Molecular Biology* **440**, 15-33 (2008).
518. Koivusalo, M. et al. Amiloride inhibits macropinocytosis by lowering submembranous pH and preventing Rac1 and Cdc42 signaling *Journal of Cell Biology* **188**, 547-563 (2010).
519. Masereel, B., Pochet, L. & Laeckmann, D. An overview of inhibitors of Na+/H+ exchanger. *European Journal of Medicinal Chemistry* **38**, 547-554 (2003).
520. Kleyman, T.R. & Cragoe, E.J. Amiloride and its analogs as tools in the study of ion transport. *Journal of Membrane Biology* **105**, 1-21 (1988).
521. Palandoken, H. et al. Amiloride peptide conjugates: Prodrugs for sodium-proton exchange inhibition. *Journal of Pharmacology and Experimental Therapeutics* **312**, 961-967 (2005).
522. West, M.A., Bretscher, M.S. & Watts, C. Distinct endocytotic pathways in epidermal growth factor-stimulated human carcinoma A431 cells. *Journal of Cell Biology* **109**, 2731-2739 (1989).
523. Breus, V.V., Pietuch, A., Tarantola, M., Basché, T. & Janshoff, A. The effect of surface charge on nonspecific uptake and cytotoxicity of CdSe/ZnS core/shell quantum dots. *Beilstein Journal of Nanotechnology* **6**, 281-292 (2015).
524. Zhang, L.W. & Monteiro-Riviere, N.A. Mechanisms of quantum dot nanoparticle cellular uptake. *Toxicological Sciences* **110**, 138-155 (2009).
525. Lindgren, A.M., Granstein, R.D., Hosoi, J. & Gallo, R.L. Structure-Function relations in the inhibition of murine contact hypersensitivity by amiloride. *Journal of Investigative Dermatology* **104**, 38-41 (1995).
526. Renner, E.L., Lake, J.R., Cragoe Jr, E.J. & Scharschmidt, B.F. Amiloride and amiloride analogs inhibit Na^+/K^+-transporting ATPase and Na^+-coupled alanine transport in rat hepatocytes. *Biochimica et Biophysica Acta - Biomembranes* **938**, 386-394 (1988).
527. Zhang, Y.Y., Hu, L., Yu, D.H. & Gao, C.Y. Influence of silica particle internalization on adhesion and migration of human dermal fibroblasts. *Biomaterials* **31**, 8465-8474 (2010).
528. Liu, W.J. et al. Uptake of hydrogel particles with different stiffness and its influence on HepG2 cell functions. *Soft Matter* **8**, 9235-9245 (2012).
529. Zhu, J. et al. Size-dependent cellular uptake efficiency, mechanism, and cytotoxicity of silica nanoparticles toward HeLa cells. *Talanta* **107**, 408-415 (2013).

530. Serda, R.E. et al. The association of silicon microparticles with endothelial cells in drug delivery to the vasculature. *Biomaterials* **30**, 2440-2448 (2009).
531. Byrne, G.D. et al. Total internal reflection microscopy for live imaging of cellular uptake of sub-micron non-fluorescent particles. *Journal of Microscopy* **231**, 168-179 (2008).
532. Byrne, G.D., Vllasaliu, D., Falcone, F.H., Somekh, M.G. & Stolnik, S. Live imaging of cellular internalization of single colloidal particle by combined label-free and fluorescence total internal reflection microscopy. *Molecular Pharmaceutics* (2015).
533. Swanson, J.A. & Watts, C. Macropinocytosis. *Trends in Cell Biology* **5**, 424-428 (1995).
534. Meier, O. et al. Adenovirus triggers macropinocytosis and endosomal leakage together with its clathrin-mediated uptake. *Journal of Cell Biology* **158**, 1119-1131 (2002).
535. Chung, T.H. et al. The effect of surface charge on the uptake and biological function of mesoporous silica nanoparticles 3T3-L1 cells and human mesenchymal stem cells. *Biomaterials* **28**, 2959-2966 (2007).
536. Foged, C., Brodin, B., Frokjaer, S. & Sundblad, A. Particle size and surface charge affect particle uptake by human dendritic cells in an *in vitro* model. *International Journal of Pharmaceutics* **298**, 315-322 (2005).
537. Horvath, S. Cytotoxicity of drugs and diverse chemical agents to cell cultures. *Toxicology* **16**, 59-66 (1980).
538. Napierska, D. et al. Size-dependent cytotoxicity of monodisperse silica nanoparticles in human endothelial cells. *Small* **5**, 846-853 (2009).
539. Lin, W., Huang, Y.-w., Zhou, X.-D. & Ma, Y. *In vitro* toxicity of silica nanoparticles in human lung cancer cells. *Toxicology and Applied Pharmacology* **217**, 252-259 (2006).
540. Lison, D. et al. Nominal and effective dosimetry of silica nanoparticles in cytotoxicity assays. *Toxicological Sciences* **104**, 155-162 (2008).
541. Bauer, A.T. et al. Cytotoxicity of silica nanoparticles through exocytosis of von Willebrand factor and necrotic cell death in primary human endothelial cells. *Biomaterials* **32**, 8385-8393 (2011).
542. Worle-Knirsch, J.M., Pulskamp, K. & Krug, H.F. Oops they did it again! Carbon nanotubes hoax scientists in viability assays. *Nano Letters* **6**, 1261-1268 (2006).
543. Oh, S.J. et al. Incompatibility of silver nanoparticles with lactate dehydrogenase leakage assay for cellular viability test is attributed to protein binding and reactive oxygen species generation. *Toxicology Letters* **225**, 422-432 (2014).
544. Holder, A.L., Goth-Goldstein, R., Lucas, D. & Koshland, C.P. Particle-induced artifacts in the MTT and LDH viability assays. *Chemical Research in Toxicology* **25**, 1885-1892 (2012).
545. Kroll, A., Pillukat, M.H., Hahn, D. & Schnekenburger, J. Interference of engineered nanoparticles with in vitro toxicity assays. *Archives of Toxicology* **86**, 1123-1136 (2012).
546. Lo, C.M., Keese, C.R. & Giaever, I. Monitoring motion of confluent cells in tissue culture. *Experimental Cell Research* **204**, 102-109 (1993).
547. Shukoor, M.I. et al. Pathogen-mimicking MnO nanoparticles for selective activation of the TLR9 pathway and imaging of cancer cells. *Advanced Functional Materials* **19**, 3717-3725 (2009).
548. Tarantola, M. et al. Cytotoxicity of metal and semiconductor nanoparticles indicated by cellular micromotility. *ACS Nano* **3**, 213-222 (2009).
549. Chang, J.-S., Chang, K.L.B., Hwang, D.-F. & Kong, Z.-L. *In vitro* cytotoxicitiy of silica nanoparticles at high concentrations strongly depends on the metabolic activity type of the cell line. *Environmental Science and Technology* **41**, 2064-2068 (2007).
550. Deisboeck, T.S. & Couzin, I.D. Collective behavior in cancer cell populations. *BioEssays* **31**, 190-197 (2009).
551. Hulkower, K.I. & Herber, R.L. Cell migration and invasion assays as tools for drug discovery. *Pharmaceutics* **3**, 107-124 (2011).

552. Kam, Y., Guess, C., Estrada, L., Weidow, B. & Quaranta, V. A novel circular invasion assay mimics *in vivo* invasive behavior of cancer cell lines and distinguishes single-cell motility *in vitro*. *BMC Cancer* **8**, 1-12 (2008).
553. Lee, J., Wang, Y.-L., Ren, F. & Lele, T.P. Stamp wound assay for studying coupled cell migration and cell debris clearance. *Langmuir* **26**, 16672-16676 (2010).
554. Pratt, B.M., Harris, A.S., Morrow, J.S. & Madri, J.A. Mechanisms of cytoskeletal regulation - modulation of aortic endothelial cell spectrin by the extracellular matrix. *American Journal of Pathology* **117**, 349-354 (1984).
555. Cai, G., Lian, J., Shapiro, S.S. & Beacham, D.A. Evaluation of endothelial cell migration with a novel in vitro assay system. *Methods in Cell Science* **22**, 107-114 (2000).
556. Huang, X.L., Teng, X., Chen, D., Tang, F.Q. & He, J.Q. The effect of the shape of mesoporous silica nanoparticles on cellular uptake and cell function. *Biomaterials* **31**, 438-448 (2010).
557. Kalishwaralal, K. et al. Silver nanoparticles inhibit VEGF induced cell proliferation and migration in bovine retinal endothelial cells. *Colloids and Surfaces B: Biointerfaces* **73**, 51-57 (2009).
558. Hayflick, L. Limited *in vitro* lifetime of human diploid cell strains. *Experimental Cell Research* **37**, 614-636 (1965).
559. Wang, L. et al. Real-time, label-free monitoring of the cell cycle with a cellular impedance sensing chip. *Biosensors and Bioelectronics* **25**, 990-995 (2010).
560. Huang, L., Xie, L., Boyd, J.M. & Li, X.F. Cell-electronic sensing of particle-induced cellular responses. *Analyst* **133**, 643-648 (2008).
561. Chuang, S.M. et al. Extensive evaluations of the cytotoxic effects of gold nanoparticles. *Biochimica Et Biophysica Acta-General Subjects* **1830**, 4960-4973 (2013).
562. Ruizendaal, L. et al. Synthesis and cytotoxicity of silicon nanoparticles with covalently attached organic monolayers. *Nanotoxicology* **3**, 339-347 (2009).
563. Chang, J.C., Hsu, S.H. & Su, H.L. The regulation of the gap junction of human mesenchymal stem cells through the internalization of quantum dots. *Biomaterials* **30**, 1937-1946 (2009).
564. Ale-Agha, N., Albrecht, C. & Klotz, L.O. Loss of gap junctional intercellular communication in rat lung epithelial cells exposed to quartz particles. *Biochemical and Biophysical Research Communications* **390**, 44-47 (2009).
565. Ale-Agha, N., Albrecht, C. & Klotza, L.O. Loss of gap junctional intercellular communication in rat lung epithelial cells exposed to carbon or silica-based nanoparticles. *Biological Chemistry* **391**, 1333-1339 (2010).
566. Alpatova, A.L. et al. Single-walled carbon nanotubes dispersed in aqueous media via non-covalent functionalization: Effect of dispersant on the stability, cytotoxicity, and epigenetic toxicity of nanotube suspensions. *Water Research* **44**, 505-520 (2010).
567. Deng, F. et al. Silver nanoparticles up-regulate Connexin43 expression and increase gap junctional intercellular communication in human lung adenocarcinoma cell line A549. *Nanotoxicology* **4**, 186-195 (2010).
568. Knight, M.M., Roberts, S.R., Lee, D.A. & Bader, D.L. Live cell imaging using confocal microscopy induces intracellular calcium transients and cell death. *American Journal of Physiology-Cell Physiology* **284**, C1083-C1089 (2003).
569. van Veen, T.A.B., van Rijen, H.V.M. & Opthof, T. Cardiac gap junction channels: modulation of expression and channel properties. *Cardiovascular Research* **51**, 217-229 (2001).
570. Martin, P.E.M. & Evans, W.H. Incorporation of connexins into plasma membranes and gap junctions. *Cardiovascular Research* **62**, 378-387 (2004).
571. Xi, B.A. et al. Functional Cardiotoxicity Profiling and Screening Using the xCELLigence RTCA Cardio System. *Journal of Laboratory Automation* **16**, 415-421 (2011).

572. Abassi, Y.A. et al. Dynamic monitoring of beating periodicity of stem cell-derived cardiomyocytes as a predictive tool for preclinical safety assessment. *British Journal of Pharmacology* **165**, 1424-1441 (2012).
573. Jonsson, M.K., Wang, Q.D. & Becker, B. Impedance-based detection of beating rhythm and proarrhythmic effects of compounds on stem cell-derived cardiomyocytes. *Assay and Drug Development Technologies* **9**, 589-599 (2011).
574. Scott, C.W. et al. An impedance-based cellular assay using human iPSC-derived cardiomyocytes to quantify modulators of cardiac contractility. *Toxicological Sciences* **142**, 331-338 (2014).
575. Nguemo, F. et al. *In vitro* model for assessing arrhythmogenic properties of drugs based on high-resolution impedance measurements. *Cellular Physiology and Biochemistry* **29**, 819-832 (2012).
576. Hayakawa, T. et al. Noninvasive evaluation of contractile behavior of cardiomyocyte monolayers based on motion vector analysis. *Tissue Engineering Part C-Methods* **18**, 21-32 (2012).
577. Natarajan, A. et al. Patterned cardiomyocytes on microelectrode arrays as a functional, high information content drug screening platform. *Biomaterials* **32**, 4267-4274 (2011).
578. Miragoli, M. et al. Functional interaction between charged nanoparticles and cardiac tissue: a new paradigm for cardiac arrhythmia? *Nanomedicine* **8**, 725-737 (2012).
579. Savi, M. et al. Titanium dioxide nanoparticles promote arrhythmias via a direct interaction with rat cardiac tissue. *Particle and Fibre Toxicology* **11**, 1-16 (2014).
580. Clements, M. & Thomas, N. High-throughput multi-parameter profiling of electrophysiological drug effects in human embryonic stem cell-derived cardiomyocytes using multi-electrode arrays. *Toxicological Sciences* **140**, 445-461 (2014).
581. Harris, K. et al. Comparison of electrophysiological data from human-induced pluripotent stem cell–derived cardiomyocytes to functional preclinical safety assays. *Toxicological Sciences* **134**, 412-426 (2013).
582. Hescheler, J. et al. Determination of electrical properties of ES cell-derived cardiomyocytes using MEAs. *Journal of Electrocardiology* **37, Supplement**, 110-116 (2004).
583. Reppel, M. et al. Microelectrode arrays: a new tool to measure embryonic heart activity. *Journal of Electrocardiology* **37, Supplement**, 104-109 (2004).
584. Wang, J. et al. Microfabricated electrochemical cell-based biosensors for analysis of living cells *in vitro*. *Biosensors (Basel)* **2**, 127-70 (2012).
585. Myers, F.B., Zarins, C.K., Abilez, O.J. & Lee, L.P. Label-free electrophysiological cytometry for stem cell-derived cardiomyocyte clusters. *Lab on a Chip* **13**, 220-228 (2013).
586. Peters, M., Lamore, S., Guo, L., Scott, C. & Kolaja, K. Human stem cell-derived cardiomyocytes in cellular impedance assays: bringing cardiotoxicity screening to the front line. *Cardiovascular Toxicology* **15**, 127-139 (2015).
587. Spira, M.E. & Hai, A. Multi-electrode array technologies for neuroscience and cardiology. *Nat Nano* **8**, 83-94 (2013).
588. Doerr, L. et al. New easy-to-use hybrid system for extracellular potential and impedance recordings. *Journal of Laboratory Automation* **20**, 175-188 (2015).
589. Jahnke, H.G. et al. A novel 3D label-free monitoring system of hES-derived cardiomyocyte clusters: a step forward to *in vitro* cardiotoxicity testing. *Plos One* **8** (2013).
590. Rother, J. et al. Crosstalk of cardiomyocytes and fibroblasts in co-cultures. *Open Biology* **5**, 150038 (2015).
591. Sperber, M.; Hupf, C.; Lemberger, M.; Goricnik, B.; Hinterreiter, N.; Lukic, S.; Oberleitner, M.; Stolwijk, J. A.; Wegener, J. Monitoring the impact of nanomaterials on animal cells by impedance analysis: A non-invasive, label-free and multi-modal approach. *Bioanalytical Reviews*, (in press) (2015).

Eidesstaatliche Erklärung

Ich erkläre hiermit an Eides statt, dass ich die vorliegende Arbeit ohne unzulässige Hilfe Dritter und ohne Benutzung anderer als der angegebenen Hilfsmittel angefertigt habe; die aus anderen Quellen direkt oder indirekt übernommenen Daten und Konzepte sind unter Angabe des Literaturzitats gekennzeichnet.

Weitere Personen waren an der inhaltlich-materiellen Herstellung der vorliegenden Arbeit nicht beteiligt. Insbesondere habe ich hierfür nicht die entgeltliche Hilfe eines Promotionsberaters oder anderer Personen in Anspruch genommen. Niemand hat von mir weder unmittelbar noch mittelbar geldwerte Leistungen für Arbeiten erhalten, die im Zusammenhang mit dem Inhalt der vorgelegten Dissertation stehen.

Die Arbeit wurde bisher weder im In- noch im Ausland in gleicher oder ähnlicher Form einer anderen Prüfungsbehörde vorgelegt.

Regensburg, 22.12.2015

Ort, Datum

Unterschrift